UNSTEADY CONVECTIVE HEAT TRANSFER IN LIQUID SATURATED AND UNSATURATED POROUS MEDIA WITH REFERENCE TO AN ENERGY STORAGE SYSTEM

A thesis submitted by

CHANPREET SINGH

(Registration No: Ph.D(P) 12/99(1)

in fulfillment of the requirement for the degree of

DOCTOR OF PHILOSOPHY

MECHANICAL ENGINEERING DEPARTMENT
THAPAR UNIVERSITY
PATIALA-147004, INDIA
Oct 2007

THESIS CERTIFICATE

This is to certify that the thesis entitled **UNSTEADY CONVECTIVE HEAT TRANSFER IN LIQUID SATURATED AND UNSATURATED POROUS MEDIA WITH REFERENCE TO AN ENERGY STORAGE SYSTEM** submitted by **CHANPREET SINGH** to Thapar University, Patiala for the award of degree of Philosophy is a bonafide record of research work carried out by him under our supervision. In our opinion, the thesis fulfills all the requirements according to the regulations of this university and has reached the standard necessary for submission. The contents of this thesis have not been submitted and will not be submitted to any other institute or university for the award of any degree or diploma.

The research work is carried out at Thapar University, Patiala and Indian Institute of Technology, Kanpur.

Patiala 147004
Dated: 16.10.07

(Dr. R.G. Tathgir)
Professor (Retd.)
Mechanical Engineering Department
Thapar University
Patiala 147004 (Pb)

(Dr. K. Muralidhar)
Professor
Department of Mechanical Engineering
Indian Institute of Technology, Kanpur
Kanpur 208016 (UP)

DEDICATION

I dedicate this thesis to my family members father, mother, sisters, wife and the beloved son Tamanjit Singh.

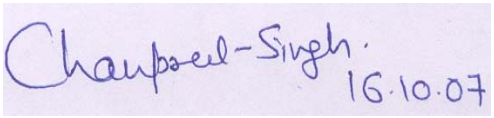

CHANPREET SINGH

ACKNOWLEDGEMENTS

I am grateful to my internal thesis advisor **Dr. R. G. Tathgir,** for his constant encouragement and moral guidance all over the course of this work without which it would have never completed.

I am thankful to my external thesis advisor **Dr. K. Muralidhar**, for suggesting the problem, excellent guidance and encouragement throughout this work. It was only through his benign understanding and patience that I learnt the art of channelising my thinking. I will always cherish pleasant memories of my rewarding association with him.

I am thankful to my doctoral committee member **Dr. D. Gangacharyulu**, Associate Professor, Department of Chemical Engineering, Thapar University, Patiala for his valuable tips regarding Fortran Programming and suggestions to improve the quality of this work.

I render my thanks to **Dr. S.K. Mohapatra**, Prof & Head Mechanical Engineering Department, Thapar University, Patiala for taking keen interest in my work and providing all possible help.

I am glad to acknowledge the kind help and co-operation of all the staff members of Mechanical Engineering Department. I fondly acknowledge the co-operation of **Sh. Sohan Lal**, Lab Supdt, MED for rendering all help for the experimental set up and installing National Instruments Temperature Card & Linux in my PC.

I acknowledge my thanks to **Sh. Charanjit Singh**, Lab Technician, MED for his excellent technical back up and modifications, maintenance and repairs in the experimental set up. I also thank **Sh. Trilok Singh** and **Sh. Sukhdev Chand**, Lab Supdts, MED for their valuable contributions and suggestions in the experimental work.

I humbly place my sincere thanks to **Dr. Abhijit Mukherjee,** Director, Thapar University, Patiala for showing keen interest and providing encouragement in my research work despite his busy schedule.

Finally, I wish to thank my parents and wife for their affectionate support, encouragement and tolerance to all my tantrums and sacrifice in their personal life that they have rendered during the course of my thesis work.

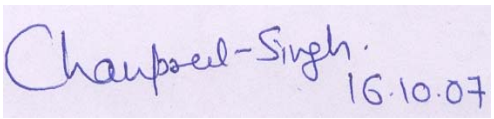

CHANPREET SINGH

ABSTRACT

Flow and heat transfer in porous media has received much attention due to its importance in various fields of engineering: mechanical, chemical, ground water hydrology, petroleum engineering, soil mechanics and environmental science. The examination of transport in porous media relies on the knowledge gained in studying these phenomena in plain media.

The mathematical modeling of convective heat transfer in a porous medium is carried out by volume averaging of governing energy equations for the fluid and the solid phases. The interphase convective heat transfer coefficient h_{sf} couples these two energy equations at the interface. In addition, this model also contains effective thermal conductivity and dispersion tensors and is expected to give reasonably good predictions. This model is called the thermal non-equilibrium model or the 2-equation model. It is advantageous to use this model, as against the thermal equilibrium or 1-equation model, when there is significant heat generation in one of the phases, during sudden heating/cooling of the medium and when the thermal properties of the two phases are distinct.

The volume-averaged energy equations based on thermal equilibrium and thermal non-equilibrium between the two phases are developed. The finite difference discretization of the model is carried out by using implicit format for the time derivatives, central difference scheme for second order partial-spatial derivatives and the upwind scheme and QUICK approaches for modeling of convective terms. The resulting algebraic equations are solved by Gauss-Seidel iterations using sufficiently fine grid in space and large number of time-steps. The numerical simulation is first compared with analytical results obtained by neglecting various terms of the mathematical model such as interphase heat transfer and convection. These include 2-D unsteady state conduction, 1-D & 2-D unsteady advection-diffusion in plain flow i.e. no solid phase present in the medium. Further 1-D form of thermal equilibrium model is compared with the analytical solution. It ensures the accuracy of the numerical simulation and proper selection of grid and time steps.

A laboratory scale experimental set up is developed to validate the results of numerical simulation and provide vital information about the transport phenomenon in porous medium. It ensures that the numerical simulation can model real life problems such as an energy storage system. The validation is performed for two distinct boundary conditions related to

step and frequency response of the porous bed. The step response is the response of an initially cold domain to the hot incoming fluid whereas the frequency response relates to alternate flow of hot and cold fluids through the porous bed. The main components of experimental set up are porous bed, constant head tanks, storage tanks, pumping system, electric immersion heater, temperature controller, thermocouples, data acquisition card, rotameter, electronically controlled solenoid values and electronic timer. The glass beads and steel spheres are closely packed in a PVC tube to make two different porous beds. It ensures that the validation is under widely varying thermal conditions of the bed. An immersion heater of 1 kW capacity is inserted inside the hot water constant head tank. It is controlled by the PID temperature controller and maintains water to a designated constant value within 0.3 K. Electronically controlled solenoid valves are used to supply the cold and the hot water to the bed. The electronic timer actuates the valves for a specific period so that step and frequency response experiments of the porous bed can be conducted. The temperature is measured by *K*-type single sleeve thermocouples inserted in the bed at the required positions. A 16 channel NI-4351 type data acquisition card collects the temperature history of the bed through the thermocouples and stores it in a PC. The flow rate of water is measured by a calibrated rotameter of capacity 170 lph.

The step response refers to the thermal response of an initially cold domain to hot fluid, which flows through one of its ends. For an energy storage system, it relates to charging of the bed. The results of experiments are compared with numerical simulation using the 1 and 2-equation models of heat transfer. The comparison is obtained qualitatively by examining the unsteady temperature profiles at various locations and quantitatively by comparing the front speed and the spread of the thermal front traveling through the bed. The validation is carried out for both the glass-water and the steel-water beds. A sensitivity analysis is performed to find the effect of various parameters on the comparison obtained. The response for glass-water bed is distinct from that of the steel-water bed. The thermal non-equilibrium between the fluid and the solid phases during the step response is discussed.

The response of the bed subjected to a time varying inlet temperature is of waveform having peaks and valleys. During the hot phase, the temperature level of porous medium rises and reaches a maximum value at the end of the phase. During the cold phase; the level falls and reaches a minimum value at the end of the phase. Hence, the frequency response signifies the

unsteady behavior of the porous medium subjected to pulsating boundary conditions. The experimental results of frequency response are compared with numerical simulation using the 1 and 2-equation models of heat transfer. In addition, the global properties such as attenuation of temperature, phase lag, pulse speed and spread are discussed to provide a qualitative validation. The analysis is again carried out for both the glass-water and the steel-water beds. The response is obtained from both the porous beds using distinct Peclet numbers and frequencies of pulsation. A reference frequency is defined as the reciprocal of the time period required for the fluid to travel to the other end of the bed during each phase. The amplitude of pulsations in glass-water bed is higher than that in the steel-water bed but the phase lag is lower. The extent of thermal non-equilibrium between the two phases also varies cyclically in a fashion similar to the temperature fluctuations. The amplitude of this pulse decreases with distance from the inflow plane but increases with Peclet number. Its value for steel-water bed is higher as compared to the glass-water bed.

Energy storage using a porous medium is an attractive method of storing momentarily available excess energy and reusing it at a later point of time. It is obtained by using fixed porous solid mass such as closely packed mesh screens or spherical beads through which hot and cold fluid alternately flow. The storage and the retrieval of energy from the fixed porous solid mass are obtained by back and forth flow of hot and cold fluids through the mass. This type of flow is referred to as oscillatory flow. During the hot phase, heat flows from the fluid to the solid phase and temperature of the fluid phase is higher as compared to that of the solid. During the cold phase, the solid phase temperature is higher. Hence, the estimation of temperature differential between the two phases is important in the working of the storage system. The thermal performance of a porous medium for energy storage is discussed in the present study. It depends on the thermal properties of the solid and the fluid phases. The other parameters of interest are the frequency of oscillation, storage space, Reynolds number, particle size, porosity, number of cycles elapsed, thermal non-equilibrium and the effect of heat loss from the bed. Various thermal properties of the solid phase are considered. Instantaneous temperature distributions inside the porous bed are plotted for judging the thermal performance of the bed. Amplitude of temperature fluctuations in the bed is considered. The extent of thermal non-equilibrium between the two phases is discussed and

the resulting difference between 1 and 2-equation models is also considered. Optimum parameters that yield the maximum effectiveness are obtained.

When the pore space is not fully filled with water and air is present in the pores, the medium is called unsaturated. The flow channels in the unsaturated medium become narrower, the flow path becomes more tortuous as compared to that in the saturated medium, surface tension adds resistance to flow, and the overall flow rate reduces. The main property of the unsaturated medium is the water content present in the pores, c. The relative hydraulic conductivity K_r measures how easily can water flow through this medium as compared to that of the saturated medium. Its value depends on the water content present in the pores and the negative pressure head in the pores. The velocity profiles are obtained in the medium using the continuity equation and flux rate using the modified Darcy's law. The temperature profiles are subsequently obtained using the 2-equation model. The governing equations are solved by finite difference discretization.

Thus, the present study concentrates on energy storage in porous medium. The finite difference based solution is compared with lab scale experiments. The knowledge gained is useful in the design of an energy storage system capable of handling summer air conditioning loads. The problem studied bring out interesting features of convective heat transfer in saturated porous medium and unsaturated soils, which are important from application point of view.

KEYWORDS: 1-equation model, 2-equation model, glass-water bed, steel-water bed, porous medium, forced convection, thermal non-equilibrium, dispersion, Biot number, step response, oscillatory response.

TABLE OF CONTENTS

Table of Contents (continued) **Page**

Table of Contents (continued) **Page**

Table of Contents (continued) **Page**

Table of Contents (continued) **Page**

Table of Contents (continued) **Page**

Table of Contents (continued) **Page**

Table of Contents (continued) **Page**

LIST OF TABLES

List of Tables (continued) **Page**

List of Tables (continued) **Page**

List of Tables (continued) **Page**

LIST OF FIGURES

List of Figures (continued) **Page**

List of Figures (continued) **Page**

List of Figures (continued) **Page**

List of Figures (continued) **Page**

List of Figures (continued) **Page**

List of Figures (continued) **Page**

NOMENCLATURE

English Symbol

A_{IF}	Specific area of the porous insert, m^{-1}
A_f	Non-dimensional value of A_{IF}: $A_{IF} \times R$
Bi	Biot number, $h\ R(k_s)^{-1}$
C_p	Specific heat, $J(kg\ K)^{-1}$
c	Soil water content, cm^3cm^{-3}
d_p	Particle diameter, m
E	Energy, J
h	In Chapter 11, Matrix potential, cm
h_{sf}	Heat transfer coefficient at the particle surface, $Wm^{-2}\ K^{-1}$
k	Thermal conductivity, $W\ (m\ K)^{-1}$
K	In Chapter 9, weighted ratio of thermal storage capacities of the fluid and solid phase, $\frac{(1-\varepsilon)(\rho c_p)_s}{(\varepsilon)(\rho c_p)_f} = \frac{1-\varepsilon}{\varepsilon\,\beta}$
K	In Chapter 11, Hydraulic Conductivity, $cm\ hr^{-1}$
$(k_{eff,f})_z$	Effective thermal conductivity of the fluid in z-direction, $W\ (m\ K)^{-1}$
$(k_{eff,f})_r$	Effective thermal conductivity of the fluid in r-direction, $W\ (m\ K)^{-1}$
$(k_{eff,f})_z / k_f$	Dispersion coefficient of fluid in z-direction
l	Size of the representative elementary volume, REV (V)
L	Length of porous domain scaled by R or y
n_{fs}	A unit normal pointing from the fluid into the solid phase at each point of the interface.
N	Cycle number
Nu	Nusselt number, hR/k
P	Pressure, N/m^2
Pe	Peclet number, Re × Pr
q	Volumetric flux, $cm\ sec^{-1}$
Q	Interphase Heat Transfer

Pr	Prandtl number, $\mu C_p/k$
r	Non-dimensional radial coordinate scaled with R
R	Characteristic length scale, m also the pipe radius
Re	Reynolds number, $\rho UR/\mu$
REV	Representative elementary volume
s	Degree of saturation
t	Time, non-dimensionalized by α_f /R^2
t_p	Time period of oscillations, sec
T	Non-dimensional temperature: $(T - T_C)/\Delta T$
u	Non-dimensional axial velocity scaled with U
U	Characteristic fluid velocity equal to the average velocity in the tube, ms^{-1} and also the temperature at the previous time-step
V	Representative elementary volume
X	Non-dimensional axial distance scaled with y
y	Transverse dimension
z	Non-dimensional axial distance scaled with R

Greek Symbols

α	Thermal diffusivity, m^2sec^{-1}
ϕ	A scalar function in Chapter 4, Phase lag (rad) in Chapter 8 & 9, Energy storage parameter in Chapter 10; see Equation 10.20
ψ	A property in Chapter 3, Energy storage parameter in Chapter 10; see Equation 10.13
Θ	Effective saturation
β	Thermal capacity ratio between the fluid and the solid phases, A phase of the porous medium in Chapter 3
ε	Porosity of the medium
λ	Thermal conductivity ratio between the fluid and the solid phases, $\lambda = n\pi$, a constant in Chapter 4
μ	Dynamic viscosity of the fluid, kg $(m\ s)^{-1}$
ν	Kinematic viscosity of the fluid, m^2s^{-1}

ρ	Material density, kgm^{-3}
ω	Frequency of oscillations, $2\pi/t_p$, rad/s
ωt	Phase angle, radians
ω^*	Non-dimensional frequency of oscillations

Subscripts

c	Cold water temperature, (K)
C	Current grid point (i)
d	Particle diameter
f	Fluid phase
i	Node value in x-direction
j	Node value in y-direction
L	Grid Point at Left Node (i -1)
R	Right Node (i +1)
r	Mean of R and C nodes
l	Mean of L and C nodes
h	Hot water temperature, (K)
m	Porous medium
ND	Non-dimensional quantity
r	Relative
s	Solid phase
sat	Saturation
ref	Reference
res	Residual
in	Incoming energy
out	Outgoing energy

Superscripts

$'$	Spatial deviation component of temperature or velocity within REV
β	Intrinsic volume averaged quantity

CHAPTER 1
INTRODUCTION

1.1 GENERAL

The theory of dynamics of flow and heat transfer in a porous medium is applicable to several disciplines of science and engineering. It is an important subject in many fields of practical interest. Examples can be found in mechanical engineering, petroleum engineering, ground water hydrology, agricultural engineering, chemical engineering, environmental science and soil mechanics. Porous medium is a solid with pores. The fluid flows through interconnected pores. Its path through pores is quite complex, micro level treatment is not possible and a fluid continuum approach is used for analysis. The equations of fluid are solved over an ensemble of many molecules contained in a small volume. The known solutions are useful in understanding the flow and heat transfer phenomena. Lab scale experiments are efficient means for measuring global parameters like thermal dispersion, heat transfer coefficient, pressure drop etc. Experimental developments are costly and time consuming but provide a suitable framework for modeling real life situations. A numerical simulation once tested against experimental data provides an estimate for parameters of field scale problems. Hence, an experimentally validated numerical simulation provides in-depth details of such problems and the results become more meaningful.

There are numerous examples in which fluid flow and heat transfer in porous medium are encountered.

1.2 APPLICATIONS OF POROUS MEDIUM

- Enhanced Oil Recovery

Oil wells are initially allowed to produce crude oil naturally until a certain stage has reached when production rates become uneconomical. This is called the primary stage. Following this, secondary production methods are used by installing high-pressure drives. Pressurized water or gas is injected in the well, which partially or completely displaces the residual oil and gas by intruding into the oil-producing region. At a second well drilled at a distance low pressure conditions are maintained for the oil to come out. This is called Enhanced Oil

Recovery (EOR). The study of interfaces of immiscible fluids moving in a porous medium is of importance here, Lake [1989].

- Stirling Cryocoolers

The regenerator of Stirling Cryocooler stores the energy when available in excess and supplies the stored energy later in the cycle. The regenerator consists primarily of metallic meshes through which fluid flows and gives energy to the mesh. The analysis of regenerator is similar to flow and heat transfer in a porous medium.

- Sea Water Intrusion

In coastal areas, the intrusion of seawater into fresh water reserves is quite common. By pumping from coastal aquifer in excess of replenishment, the water table in the vicinity of the coast is lowered to the extent that piezometric head in the fresh water body becomes less than in the adjacent seawater wedge, and the salt water-fresh water interface starts to advance inland. This is a miscible displacement. So an artificial drive, which can force out the seawater, is needed. Here the analysis of moving interface of the miscible liquids in porous medium is necessitated.

- Chemical Clean up of Soil

Soil is often contaminated by leakage of sewage, contaminated disposals from industries and disposal of solid chemical waste. Various artificial drives are used to clean soil. The study of motion of interface of the two fluids and mass transfer in porous medium is quite useful in this context.

- Hazardous Waste Disposals

Hazardous waste from industries and nuclear plants are disposed off under the surface of earth. During the monsoon period, this waste may be exposed to water. This can lead to the spreading of waste far away from their initial location. The analysis of this problem requires knowledge of flow, heat and mass transfer in a porous medium.

- Cooling of Air using Naturally Occurring Stratified Layers

In stratified layers of earth, air can be cooled using earth-to-air heat exchanger. This arrangement makes use of the lower temperature existing in the layers below the surface of earth. The analysis of heat dissipated to ground through such a system is similar to heat transfer through a porous medium.

- Chilled Water Storage in Porous Formation

This is an attractive method of energy storage. The stored energy is in the form of cold or hot water in the porous formation. This storage system can be used in hot and cold seasons respectively. Energy storage in such a system involves displacing the existing ground water by the water to be stored in the porous formations. During the displacement process, the interface of two fluids moves in the porous media.

- Packed Bed Heat Storage

Packed bed (pebble bed or rock pile) heat storage units have been used extensively in a wide variety of applications. Packed beds as energy storage media are attractive as they have a compact structure due to their relatively greater heat storage capacity offered by large surface area. Both sensible and latent heat storage beds are used. In applications where there is a limitation on size and weight, the packed beds offer a good solution. These are widely used in pulsed space power supplies for heat rejection and spacecraft thermal management system in general.

- Metal Hydride Packed beds

Metal Hydrides ($LaNi_5H_x$, $LaNi_{5-y}$, Al_yH_x, $FeTiH_x$ etc) are used widely for hydrogen storage as an alternative to storage of liquid hydrogen, thermo chemical compressor, and ecologically clean refrigerants, (Kuznetsov and Vafai [1995]). The analysis of the flow and heat transfer through metal hydrides bed is similar to that in porous media.

- Utilization of Porous Layers for Transpiration Cooling by Water for Fire Fighting

The use of porous layers and water to maintain low temperature in fire conditions has been investigated. This is very important for number of applications such as security systems and safety equipments, which demand thermal protection.

- Nuclear Safety

Of late, there is a strong interest to understand and predict the conditions for which it is possible to cool a severely damaged nuclear reactor core, (Duval et al. [2004]).

- Solar receiver devices

It stores the thermal energy derived from solar energy conversion systems. A heated fluid flows from the solar collectors into a bed composed of washed rocks, where the thermal energy is transferred to rocks. The recovery of this stored energy is usually obtained by reversing the flow in the bed, (Spiga and Spiga [1981]).

- Rapid Heat Dissipation

Porous media is used for enhancement of cooling of electrical and electronic equipments. In high speed, electronic equipments the heat dissipated can be up to 25 W/cm^2, which is very difficult to remove by tradional methods of natural or forced convection to air. A channel filled with a high thermal conductivity porous media is subjected to a constant heat flux. An oscillatory flow of air is passed through the channel and the parameters such as, cycle averaged surface temperature of the bed and the cycle averaged local Nusselt number are calculated and compared with those flow when there in no porous material. It is found that surface temperature is lower and Nusselt number is higher in the presence of a porous medium. Hence, porous media is considered as an effective method of rapid heat dissipation, (Fu *et al.* [2001]).

- Heterogeneous Porous Media

The use of heterogeneous porous media of spatially uneven material properties is on the increase. The state of art thermal regenerators consists of composite porous media of spatially uneven meshed screen. It enhances the thermal performance.

- Others

The application of porous medium is also found in building thermal insulation, heat exchangers, ceramic processing, catalytic reactors, and heat pipes.

1.3 PRESENT WORK

In the present study, numerical simulation, experimentation and subsequent analysis of unsteady convective heat transfer in a porous medium is performed. The study focuses on energy storage aspect in a porous medium. The work involves numerical simulation of convective heat transfer in a porous bed. A mathematical model is developed for heat transfer in porous medium. The model is first compared with analytical solutions obtained by omitting various terms in the model such as energy storage and dispersion terms.

Since heat is stored in solid phase of porous medium, which is supplied by/to the fluid phase, the resulting temperature difference between two phases, called thermal non-equilibrium, is important for energy storage system. The simulation considers both step change when temperature at inflow plane increases from a minimum to a maximum value and pulsating change when fluid temperature at inflow plane varies periodically between the same minimum and the maximum values. This is similar to the analysis of Stirling cycle

regenerator where hot and cold air flows alternately through metallic meshes. The numerically generated results are checked against laboratory scale experiments. Experiments are conducted for the step and the pulsating change in temperature at the inflow plane. The repeatability of the beds is studied. The experiments are designed for two distinct materials of solid phase namely glass and steel. The fluid phase is water in each case. The thermo-physical properties of glass and steel are quite different from each other hence the analysis helps in checking the validity of numerical simulation under widely varying conditions. The aim is also to predict the energy storage aspect of these materials. The effect of thermal non-equilibrium is studied by using equilibrium and non-equilibrium models of heat transfer. The effect of, minor heat loss to surroundings, on the unsteady temperature field is also performed. The numerical simulation of oscillatory flow in saturated porous medium is performed. Various solid phase materials are considered and energy storage aspects are studied. The difference between the equilibrium and the non-equilibrium modeling is again addressed. The effect of change in particle diameter, flow rate, length of domain, and minor heat loss to surroundings is studied. The study is extended to flow and heat transfer in unsaturated soils. The presence of air in pore space makes the analysis extremely complex. The velocity field in unsaturated soils is first obtained and later heat transfer model is used to calculate the temperature field. Here the analysis is performed in 1-D format.

Hence, the present study is a detailed analysis of heat transfer aspects in porous medium. The mathematical model is validated against lab scale experiments. One can use simply larger lengths and time scales to simulate the practical storage system.

1.4 ORGANIZATION OF THESIS

The thesis is organized into 12 chapters including the present chapter, which introduces the theme of the work. In Chapter 2, a critical review of literature is presented on flow and heat transfer aspects of porous medium. The studies on interphase heat transfer, hydrodynamic dispersion, non-equilibrium modeling, variable porosity, inertia effects, and effects of presence of solid boundary are presented. The details of mathematical modeling are addressed in Chapter 3. Chapter 4 deals with discretization, code validation and non-dimensional form of mathematical model. The boundary conditions used in mathematical model are discussed. Details of experimentation and instrumentation are presented in Chapter

5. The repeatability of the bed is discussed. Chapters 6 and 7 deals with step response in glass and steel water respectively. The mathematical models are validated with experimentally obtained results. All the aspects of step change in temperature are discussed. Chapter 8 and 9 deal with frequency response of glass and steel water beds. The mathematical models are again validated with experimental results. The aspects of energy storage in oscillatory heat transfer in saturated porous medium are addressed in Chapter 10. The flow and heat transfer in unsaturated soils is discussed in Chapter 11. Finally, in Chapter 12, conclusions from the above studies are drawn and possible future directions of research in this area are indicated.

CHAPTER 2
LITERATURE SURVEY

2.1 INTRODUCTION

Given the wide range of applications of porous medium, as described in Chapter 1, the study of transport in porous medium has become quite important. The very basis of the analysis of transport in porous medium relies on the knowledge of the flow through plain media (absence of the solid phase). The porous medium as such is a heterogeneous system with fluid flowing through solid pores. The path of fluid keeps changing from one pore to another. Hence, the flow through pores provides intense mixing of the fluid and spreading in longitudinal and transverse directions. The flow past solid particles provides additional resistance to flow in addition to fluid- fluid resistance as in a plain flow. It provides drag and vortex shedding in the pores. The porosity of a porous medium, is in general higher near the walls as compared to inside the medium, makes velocity profiles more complex. The phenomenon of increase in porosity near the walls called "Channeling" has been studied. When the porous medium contains a wall at one of its ends, the velocity profile is affected by no-slip boundary condition at the wall. In addition, inertia effects at higher Reynolds number make the flow field quite complex.

Since a porous medium contains a large number of fluid particles contained in the pores, it is very difficult to determine their initial and final positions. So the problem is solved by considering macroscopic level treatment over a representative volume. The governing equations of flow are solved over this volume by various numerical methods. The finite element and finite difference methods are generally used. The analysis of various effects such as inertia, channeling, variable porosity, fluid-fluid & fluid-solid friction, effect of solid wall etc. is reported. The displacement of one fluid by another fluid in porous medium is a very useful study. When pores contain one fluid, only the porous medium is said to be saturated with that fluid. When more than one fluid is present in the pores, the interface between various phases is formed. The analysis then is quite complex.

Heat transfer in a porous medium is also complex due to presence of solid particles. At steady state, the temperatures of fluid and solid phases are equal, but during unsteady

state, heat flows from fluid to solid or vice versa and hence, temperature difference exists between the two phases. A mathematical model for heat transfer is developed at macroscopic level over a representative elementary volume (V). The models are respectively called equilibrium and non-equilibrium. The presence of pores affects the velocity profiles significantly; the spreading of fluid particles is predominantly in longitudinal direction, thus causing mechanical dispersion and it increases the conductivity in this direction. In transverse direction, the spread is mainly due to molecular diffusion. Hence, the effective thermal conductivity increases due to presence of pores and fluid flow. The effects of longitudinal and transverse effective thermal conductivity on transport are studied widely. The effects of inertia, fluid-fluid & fluid-solid friction, variable porosity on heat transfer are studied. Both equilibrium and non-equilibrium modeling are reported. Experiments and numerical simulation both are reported. The effects of storage in solid phase are also reported.

In the following section, the flow and convective heat transfer aspects in porous medium will be reviewed.

2.2 TRANSPORT IN POROUS MEDIUM

In this section, a state of art on various aspects of flow and heat transfer such as Darcy law, thermal non-equilibrium, thermal dispersion, interfacial heat transfer, non-Darcy effects and variable porosity are discussed.

2.2.1 Flow in Porous Medium

When a single fluid fills the pores of the porous medium, it is said to be saturated. For flow of a single fluid through a fixed solid matrix, a commonly used mathematical model is:

$$U = -\frac{K}{\mu}\nabla p \tag{2.1}$$

Darcy [1856] originally discovered it. This equation has found utility in a wide range of applications and is a popular starting point in the analysis of various problems. Here U is the Darcy velocity, different from the true fluid velocity prevailing in the pores. It is an average velocity at a point surrounded by porous region. Further, p is the fluid pressure, μ is the dynamic viscosity and K is the permeability of the porous medium. Darcy Law is valid as

long as Reynolds number based on particle diameter is between *0* and *10*, (Bear [1988]) such that the viscous effects are dominant. Extensions of Darcy law to account for the presence of a wall, inertia and viscous effects in the fluid phase and vortex formation in the pores together called non-Darcy effects have been widely reported. Introducing the effects of inertia, drag and vortex shedding at higher Reynolds number the momentum equation is written as:

$$\rho\left[\frac{1}{\varepsilon}\frac{\partial U}{\partial t}+\frac{1}{\varepsilon}U.\nabla\left(\frac{U}{\varepsilon}\right)\right]=-\nabla p-\frac{\mu}{K}U-\frac{\rho}{K^{0.5}}fU|U| \tag{2.2}$$

The last term in RHS represents the Forchheimer drag term. Finally, the effect of fluid-fluid viscous effects is added as Brinkman corrected Darcy law. The final form of momentum equation is given as (Hsu and Cheng [1990]).

$$\rho\left[\frac{1}{\varepsilon}\frac{\partial U}{\partial t}+\frac{1}{\varepsilon}U.\nabla\left(\frac{U}{\varepsilon}\right)\right]=-\nabla p-\frac{\mu}{K}U+\frac{\mu}{\varepsilon\rho}\nabla^2U-\frac{\rho}{K^{0.5}}fU|U| \tag{2.3}$$

Various forms of this equation are used for analysis of flow in porous medium. The relative importance of each term upon transport, heat transfer etc in porous medium is of great practical interest.

2.2.2 Local Thermal Non-Equilibrium

In this section, the thermal non-equilibrium modeling and related aspects are reviewed.

Riaz [1977] developed analytical solutions of step response of two-phase Schumann model and single-phase conductivity model for rock bed thermal storage system. The analytical solutions for the fluid and the solid phase energy equations are obtained using Laplace transform methods. The single-phase conductivity model is obtained from the Schumann model by setting the interfacial heat transfer coefficient to infinity so that the fluid and the solid phase temperatures coalesce to the same value. A comparison of the step response of these results indicates that for larger times, the two results coincide whereas for shorter times the temperatures difference between the two models is within ten percent. A close agreement between these models suggests that these can be combined together such that the effect of thermal conductivity of the bed can be included in the Schumann model and the effect of solid-fluid heat transfer can be accounted in the single-phase model.

Vafai and Sozen [1990] numerically investigated forced convective heat transfer for gas flow in a packed bed allowing for thermal non-equilibrium between the fluid and the solid phases. At higher flow rate, Darcy formulation is not valid and Ergun formulation is used in order to consider inertial and viscous effects. Finite difference method is used for solving the governing equations. Their studies indicate that the local thermal equilibrium condition is sensitive to particle Reynolds number (*Re*) and Darcy number (*Da*) but insensitive to thermo physical properties. As the Darcy number decreases, the fluid and solid phase temperatures approach each other, hence the thermal equilibrium. Decrease in Darcy number means a decrease in particle diameter and the interphase heat transfer area increases so heat exchange between the two phases become more efficient. At higher flow rates, less time is available for solid to fluid heat interactions thereby less heat exchange and so thermal non-equilibrium. The two dimensional behavior of temperature is very sensitive to thermo physical parameters. If the ratio of thermal diffusivity of solid to fluid phase is high, two-dimensional behavior is obtained but a lesser value of this parameter results to one-dimensional behavior. It is so because the higher value of thermal conductivity of solid phase makes the wall heat loss comparable to convective energy transport in axial direction.

Amiri and Vafai [1994, 98] performed a comprehensive numerical analysis of various effects in a flow field on forced convection heat transfer through porous medium. These include inertia, dispersion, variable porosity and boundary effects, validity of local thermal equilibrium and two dimensionality. The mathematical model for energy transfer is based upon thermal non-equilibrium between the fluid and the solid phases. The boundary conditions in this study the walls are considered at a constant temperature and the entrance temperature of the fluid is lower than wall temperature. The transport in porous medium is largely affected by the mixing and recirculation of the local fluid stream as the fluid flows through tortuous paths offered by the solid particles. This is called thermal dispersion. It is found that axial dispersion has small contribution to overall energy transfer at higher flow rates and important for low Peclet numbers only. This is because the convective heat transfer dominates the axial diffusion at high flow rates. Various particle sizes, Reynolds number, fluids are considered in the study. The governing equations are solved by finite difference scheme. The results of numerical model are compared against analytical solutions available in literature. The analysis shows that considering all the effects in momentum equation, the

velocity is almost uniform in the cross section except some variations near the cold wall. The fluid and solid phase Nusselt number, based upon respective temperature gradients, shows dependence on transverse dispersion. At higher Reynolds number and Darcy number, it is advisable to consider all the non-Darcy effects, to calculate fluid and solid phase Nusselt numbers. The effect of thermal dispersion is only on the energy transport. The effects of transverse dispersion play a significant role in the dispersion phenomenon in porous beds. This is because the thermal boundary layer growth is more dependent on the transverse thermal conductivity as compared to axial thermal conductivity. The local thermal equilibrium [LTE] is sensitive to Reynolds number, Darcy number and shows some sensitivity to the solid to fluid phase thermal diffusivity ratio. The temperature difference is higher at early time since each phase responds differently to abrupt temperature change at entrance. It increases with an increase in Reynolds number and Darcy number. The ratio of thermal conductivity is an important factor for deciding the thermal equilibrium. Two-dimensionality of temperature distribution is a complex function of thermal diffusivity ratio, Darcy and Reynolds numbers. It increases with Reynolds number and Darcy number but decreases as solid to fluid thermal diffusivity ratio approaches unity.

Quintard and Whitaker [1993] analyzed the local thermal equilibrium for transient heat conduction in porous medium. The results are compared with experimental results conducted elsewhere. The temperature difference terms has terms related to conduction, accumulation and heat exchange. The comparison is good except when transport equation for temperature in two phases is of same order but opposite sign.

Nakayama *et al.* [2001] proposed a thermal non-equilibrium model for analyzing conduction and convection in porous media. Thermal non-equilibrium modeling is important when time scales for diffusion in solid and fluid phases are different, significant heat generation in any one of the two phases and in the entrance region of packed beds. Hsu's [1999] closure modeling to account for tortuosity effects in conduction is extended to account for convection terms also. An additional term to account for volumetric heat generation is considered in the respective energy equations for the solid and the fluid phases. The thermal dispersion term $-\left(\rho c_p\right)_f \nabla.\langle u'T'\rangle$ is modeled as:

$$-\left(\rho c_p\right)_f \nabla.\langle u'T'\rangle = k_{dis}.\nabla\left\langle T\right\rangle^f \tag{2.4}$$

Interfacial heat transfer term $\frac{1}{V}\int_{A_{fs}} n_{fs}.k_f \nabla T_f \, dA$ is modeled by Newton's law as:

$$\frac{1}{V}\int_{A_{fs}} n_{fs}.k_f \nabla T_f \, dA = a_{sf} h_{sf} \left(\langle T \rangle^s - \langle T \rangle^f \right) \tag{2.5}$$

The term $\frac{k_f}{V}\int_{A_{fs}} n_{fs} T_f' \, dA$ and the related term in the solid phase represent the tortuosity. It represents the surface integral of interfacial temperature. Quintard and Whitaker [1993] and Hsu [1999] have modeled it as:

$$\frac{1}{V}\int_{A_{fs}} n_{fs} T' \, dA = G\left(\nabla \langle T \rangle^f - \frac{1}{\lambda} \nabla \langle T \rangle^s \right) \tag{2.6}$$

Where G is a scalar quantity and $\lambda = k_f / k_s$ is the thermal conductivity ratio of fluid to solid phases. Combining the terms in Equations 2.4, 2.5 and 2.6, thermal non-equilibrium model is obtained. This equation is solved for steady heat conduction in porous slab saturated with fluid and heat generation in the solid phase. It is shown that this case is an example of thermal non-equilibrium, whose magnitude increases with decrease in λ (increase in solid phase thermal conductivity). This equation is further applied to a thermally developing unidirectional flow through a semi-infinite porous medium. At lower Peclet number, the equilibrium temperature of fluid is less than of inlet temperature. At higher Peclet number, convection dominates the conduction and the equilibrium temperature stays close to the level of inlet fluid temperature.

2.2.3 Temperature Difference between Fluid and Solid Phases

Whereas in the earlier analytical solutions the various terms in the energy equations are neglected, like in Riaz's [1977] work the conduction terms in the solid and fluid phase are neglected. Kuznetsov [1994] obtained the analytical solution of one-dimensional two-phase energy equation using perturbation technique for a step change of inlet fluid temperature considering all the terms in the two-phase energy equation. The long and short-term solutions of fluid phase temperatures are obtained using Laplace transforms. The solid and fluid phase temperatures are like a shock wave propagating from the inlet boundary. The difference of the solid and fluid phase temperatures form a wave localized in space whose amplitude falls

as the wave propagates. Kuznetsov [1996] extended this work for three-dimensional geometry. The temperature difference between the solid and fluid phase forms a thermocline, it has a local maxima and its amplitude decreases as the thermocline propagates downstream.

Lee and Vafai [1999] have obtained the analytical solution of forced convective flow through a porous channel subjected to wall heating using the two-phase model. As the heating is from walls the longitudinal thermal dispersion effects are neglected. The main characteristics of porous medium are extensive interfacial area due to porous structures and the diffusion enhancement due to tortuous flow passages. The analytical solution has two important parameters of equivalent Biot number, which represents the ratio of conduction resistance in the solid phase and thermal resistance of convective heat exchange between the solid and fluid phases, and ratio of conduction resistances between the solid and fluid phases. As the Biot number and ratio of conduction resistances is small, the temperature differential between the solid and fluid phase is large. The Nusselt number variation is plotted as functions of above two parameters. It divides the region into three distinct regions. When the Biot number and resistance ratios are infinitely large: the region 1 is obtained where Nusselt number is small. When the Biot number tends to infinity and resistance ratio is zero, region 2 is obtained where Nusselt number is very large. In addition, when both the above parameters tend to zero the third region is obtained, Nusselt number being small. The individual values of the Nusselt number in each region are different. The heat from the wall in porous medium flows through the conduction in fluid and solid phases. The heat conducted to solid phases eventually transferred to fluid phase through internal heat exchange. Hence, the overall heat exchange is between the heated wall and fluid phase. An electrical-thermal analogy is developed with corresponding resistances. The resistances of solid conduction and internal heat exchange are in series and these two further are in parallel with fluid conduction resistance. In region 1 the resistance of fluid phases is minimum and hence decides the path of dominant heat transfer. In region 2, the solid phase conduction resistance is small and heat flow through solid phase in preference to fluid phase, and the internal heat exchange resistance falls to a minimum hence lower solid-fluid differentials. The solid phase conductivity dominates wall heat transfer coefficient. In region 3, solid phase conduction resistance is minimum, the internal heat exchange resistance approaches the fluid phase resistance and the solid phase temperature is almost same as wall temperature.

The error in using the 1-equation model is essentially large when Biot number and the ratio of thermal conductivities of fluid and solid phases are small. The error in using the 1-equation model is small when Biot number and the conductivity ratio are large. Hence, 2-equation model should be used when Biot number and conductivity ratio tend to zero.

2.2.4 Thermal Dispersion in Porous Medium

Cheng and Zhu [1987] numerically investigated the effects of radial dispersion on fully developed forced convection in packed beds. The results are compared with experiments conducted elsewhere. The presence of heated or cooled wall produced steep radial temperature gradients. Hence, an effective thermal conductivity, which takes into account radial variations in thermal conductivity, axial velocity and porosity, near the wall should be considered. The effects of transverse thermal dispersion and variable stagnant thermal conductivity are taken into consideration in the energy equation for thermally fully developed flow for constant wall temperature and constant heat flux. The presence of wall modifies the velocity distribution because of no slip boundary conditions and non-uniform porosity. It reduces the lateral mixing of the fluid. By considering a wall function in radial thermal dispersion conductivity the agreement with experiments improves.

Hunt and Tien [1988] analyzed non-Darcian effects related to dispersion and resulting heat transfer in high porosity fibrous media which is a form of porous media with constant porosity throughout a given section. Using higher porosity mediums offers advantage as the heat transfer is independent of the solid phase conductivity. The non-Darcian effects such as thermal dispersion and inertial drag are important for modeling the forced convection in compact heat exchangers. The dispersion phenomenon is treated as an additional diffusive term added to the stagnant component. It is modeled as the product of average velocity, fiber thickness and a constant dependent on the porosity. The flow in a porous medium is along tortuous paths, which increases with Reynolds number. The heat transfer rate in fluid increases with dispersion in the fluid, which increases with permeability as compared to slug flow and laminar flow in a tube. The volume averaged momentum and energy equations are obtained using the empirical relations for drag and recirculation or dispersion. The steady state single-phase energy equation models stagnant thermal conductivity and thermal dispersion, which arises from fluid separation and recirculation around the solid particles.

The diffusive flux in stream wise direction is neglected, as the Reynolds number is high. The fiber media is heated from the lower wall and the length averaged Nusselt number is calculated using slug flow approximation. The experiments are designed to supply water into a porous bed with one wall heated. The experiments are first performed without any porous medium to evaluate heat losses and the results are compared with the solutions available in literature with one constant temperature wall and other adiabatic wall. The velocity profile without the porous medium is parabolic and with porous medium, it is almost uniform with steep gradient near the wall. A higher permeability material, the momentum boundary layer slightly thicker with mainstream velocity higher. The effect of presence of porous medium reflects in transverse profile between the heated and adiabatic wall. This profile is sharper and penetrates more in transverse direction as compared to slug and parabolic flow. Hence net transport increases with dispersion in porous medium. This gain increases with increase in permeability. The local bulk temperature Nusselt number is higher for a porous medium as compared to parabolic flow and similarly increases with permeability. The bulk temperature Nusselt number based upon the fluid phase conductivity increases with the presence of porous medium and increases with flow rate and permeability.

Hus and Cheng [1990] derived relationship for thermal dispersion conductivity tensor for convection in porous medium. Microscopic continuity, momentum and energy equations are solved by the local volume averaging technique. In this work, the thermal dispersion conductivity tensor is derived from volume averaging of the velocity and temperature deviations in the pores. Transverse thermal dispersion conductivity at high Reynolds number is correlated as:

$$\left(k_T'\right)_{av} / k_f = C_T Pe_m \tag{2.7}$$

where $\left(k_T'\right)_{av}$ is the cross-sectional average of the radial thermal dispersion conductivity and C_T is a constant. It has been observed that steep radial temperature gradients exist near the heated or cooled wall in the packed column. These gradients are influenced by thermal dispersion, variable porosity and non-uniform velocity distribution. The closure scheme for the thermal dispersion conductivity tensor is based upon the model of flow over a dilute random array of spheres. The Navier-Stokes equation is solved by closure modeling of drag force due to the presence of solid particles. The energy equation is solved considering the deviations in velocity and temperature in the pores. At higher Reynolds number ($Re_d >> 10$),

the thermal dispersion tensor is proportional to Peclet number and local porosity variations whereas at lower Reynolds number it is proportional to square of Peclet number. For a hydro dynamically and thermally fully developed flow in a packed tube or channel, the thermal conductivity tensor reduces to a scalar, which is the radial thermal dispersion conductivity in the form:

$$k_r = D\frac{[1-\varepsilon]}{\varepsilon}\mathrm{Pe}_m k_f (u/u_m) \tag{2.8}$$

where local variation in porosity ε is considered and Peclet number is based upon mean velocity of flow. The value of the constant D can be found by comparing the predicted heat transfer characteristics with experimental results.

It is found that axial dispersion has small contribution to overall energy transfer at higher flow rates and is important for low Peclet number flows only, (Amiri and Vafai [1994, 98]).

Kuwahara *et al*. [1996] studied numerically the thermal dispersion in convective flow in porous media using a two-dimensional periodic model. A macroscopic uniform flow is assumed to pass through a lattice of square rods placed regularly in an infinite space, where a macroscopically linear temperature gradient is imposed perpendicular to the flow direction. The lattice of square rods allows changing the porosity virtually from zero to unity. The continuity, momentum and energy equation is solved for flow over solid body. The direction of flow is changed to investigate the geometric effect on the dispersion coefficient. The calculations are performed over one structural unit (pore level). The governing equations are discretized by finite volume approximation. The single-phase microscopic energy equation is integrated over an elementary control volume and tortuosity and dispersion coefficient in transverse direction are calculated. The velocity profile over the solid squares remains laminar at low Reynolds number such that viscous forces dominate the inertial forces. The pressure gradient becomes high as Reynolds number increases beyond ten. The temperature field at low Reynolds number is similar to the conduction heat transfer. At higher Reynolds number, it becomes complex where dispersion effects dominate. Tortuosity conductivity in transverse direction decreases as Peclet number increases. At lower Peclet number it depends upon $\mathrm{Pe}^{1.7}$ whereas at higher Peclet number on Pe only. The results combine well with experimental data available in literature.

Kuwahara and Nakayama [1996] have extended their work to find the thermal dispersion in axial direction. The thermal dispersion in axial direction is much larger than in transverse direction. In this study, the macroscopically linear temperature gradient is imposed parallel to macroscopic flow direction. It is found that the temperature gradients parallel to flow are considerably distorted even at low Reynolds number as compared to those perpendicular to flow as discussed in previous case. It is stated that the unique feature of axial dispersion renders boundary layer theory failure to be applied to porous medium. The axial thermal dispersion coefficient again depends upon Peclet number. For lower Peclet number it depends on Pe^2 and for higher Peclet number on Pe only. These results again compare well with experimental results for packed beds.

Metzger *et al*. [2004] investigated the thermal dispersion coefficients using one temperature model for flow of water through glass spheres. The uncertainties in velocities and thermocouple position are dealt with Gauss-Markov method. The longitudinal thermal dispersion coefficient is estimated to a high degree of accuracy. The lateral thermal dispersion is roughly estimated. Monte Carlo simulations assess the estimation error. The one-temperature model for thermal dispersion is also valid in case of local thermal non-equilibrium if the average temperature is defined as the calorimetric mean of the solid and fluid average temperatures. Such a one-temperature model is solved by using exponential transforms and Green's function. The heating zone remains relatively confined in lateral direction. The temperature response shows sensitivity to axial and lateral dispersion. But the sensitivity to lateral dispersion is more.

2.2.5 Interphase Heat Transfer

Lage [1993] derived Nusselt numbers for transient heat transfer in a rectangular porous enclosure using scale analysis. The flow model is based on generalized Darcy model. Kuwahara *et al.* [2001] had done a numerical study to determine the interfacial convective heat transfer in the two-energy equation model for convection in porous media for solid phase conductivity to be infinitely large. The thermal equilibrium assumption fails when there is significant heat generation in any one of the two phases, in the entrance region of the packed column when hot fluid flows in, when temperature at bounding surface changes significantly with respect to time and when the solid and fluid heat capacities and thermal

conductivities differ significantly. The interfacial heat transfer is very important under these conditions. The heat transfer coefficient is defined from the pore level treatment by using two-energy equation model in two-dimensional form. A macroscopically uniform flow through infinite square rods placed in staggered fashion. The temperature of the rods is assumed constant and is either higher or lower than the temperature of fluid. In other words, the thermal conductivity of the solid phase is much higher than the fluid phase. The governing equations are discretized by integrating them over a grid volume. The numerical code with its boundary conditions is checked by comparing it with results of flow in a channel with walls maintained at constant temperature with results available in literature. At lower Reynolds number, the flow over the square rod is laminar. At higher Reynolds number, recirculation bubbles expand further behind the rods. The interfacial heat transfer coefficient is calculated and functional relationship similar to Wakao and Kaguei [1982] are developed. The results are compared with available experimental data and good agreement is obtained.

2.2.6 **Non-Darcian Effects and heat Transfer**

Vafai *et al*. [1985] investigated experimentally the effects of variable porosity on heat transfer. The experiments are designed for heat flux 1at boundary and a numerical model is developed. A variable porosity means that velocity is high near the solid wall. It affects the convective heat transfer in region close to wall. With inclusion of non-Darcian effects, such as variable porosity and wall effect, in the model, the increase of average fluid phase Nusselt number with particle Reynolds number is large. The corresponding temperature rise in transverse direction is also larger. The Nusselt number in longitudinal direction is also higher. Poulikakos and Renken [1987] analyzed numerically forced convection in a channel filled with porous medium. In the modeling the flow inertia, variable porosity and Brinkman friction terms are taken into account. In the high porosity regions near the wall, the fluid flows at higher rates and significantly affect the heat transfer characteristics. This effect increases with an increase of the ratio of particle diameter to half the channel width. Brinkman friction term affects channeling significantly. Channeling enhances the fluid phase Nusselt number by 22 % in a circular pipe. The temperature propagation in circular pipes is faster as compared to parallel plates. The thermal entry length is estimated and seen that it increases with an increase in pressure gradients and bead diameter. For fully developed flow,

the thermal communication between the fluid and the solid boundary falls using the Darcy model.

Alazmi and Vafai [2000] analyzed variants within the porous media transport. These variants are constant porosity, variable porosity, thermal dispersion and local thermal non-equilibrium. The effects of Darcy number, inertia parameter, Reynolds number, porosity, particle diameter and the fluid-to-solid conductivity ratio on these variants are analyzed. A parallel plate configuration of porous media with constant heat flux and constant wall temperature is analyzed numerically. The models accounting for Brinkman and Forchheimer terms in momentum equations of constant porosity have negligible effect on temperature and Nusselt number variations. For a constant porosity medium, the inertia factor, Darcy number, Brinkman and Forchheimer terms in momentum equations do not affect temperature profiles and Nusselt number variations significantly. Variable porosity affects the velocity profile such that the velocity increases towards the solid boundary, thereby increasing the convective energy transfer and the Nusselt number. When the particle diameter increases the channeling effect increases due to reduction in fluid flow resistance. An increase in pressure gradient increases the centerline velocity as compared to actual velocity and thinner boundary layer, which increases the Nusselt number. The factors such as inertia number, Darcy number affect the velocity profiles and consequently the dispersion effects. Increasing the particle diameter increase the thermal dispersion. A lower solid-to-fluid thermal conductivity ratio enhances thermal equilibrium.

2.2.7 Thermally Developing Forced Convection in Porous Medium

Renken and Poulikakos [1988] investigated numerically and experimentally the forced convective heat transport in porous medium occupying heated channel. The thermal dispersion is not considered. Observation regarding the thermal entry length is made, it is the entrance length such that mixed mean temperature and Nusselt number become independent of the axial position (fully developed). It is much larger as compared to hydrodynamic length. The Nusselt number in the development region increases with flow rates. The presence of porous medium results into higher Nusselt number as compared to plain flow or slug flow (flow without porous medium). The slug flow coincides with Darcy flow model. Nield *et al.* [2002] investigated the effects of thermal non-equilibrium on thermally

developing forced convection in porous medium using Graetz methodology. Fluid flows through a constant wall channel and the effects such as local thermal non-equilibrium and Nusselt number are investigated. It is found that the Nusselt number is affected by solid fluid conductivity ratio. It decreases markedly as the solid fluid conductivity ratio increases. Nusselt number increases with increase in Peclet number and this effect is particularly large if the solid fluid conductivity ratio is small. The local thermal non-equilibrium is insignificant if Nusselt number is large. It is always small for constant temperature boundary condition.

2.2.8 Step response in porous bed

Levec and Carbonell [1985] were amongst the first to carry out extensive numerical modeling and experiments for step response through a porous medium. At higher Peclet numbers, the input response is similar to unit step. Longitudinal and lateral effective thermal conductivities are calculated from numerical modeling. The values under steady and transient conditions are quite different. Experiments are conducted for step change in temperature fluid and solid phase temperature responses are obtained. Longitudinal and lateral effective thermal conductivities are calculated from experimental data and compared with theoretical predictions. Fluid and solid temperature pulses move at equal speed but a spatial separation exits between the two pulses. A spatial difference also exists between the solid and the fluid temperature fronts. Longitudinal and lateral effective thermal conductivities are calculated from the experimental data.

2.2.9 Porous Medium for cooling purposes

In the earlier works of Koh and Colony [1974], the use of porous medium for cooling of high temperature surfaces is identified. The governing energy equations: one each for the fluid and the solid phases, without the thermal dispersion, are discretized by finite difference method. A solid phase of high thermal conductivity when inserted in the path of coolant flowing over a heated surface, the resulting wall temperature is much less as compared to channel (plain) flow. A high thermal conductivity solid material conducts local heat away from the wall with a minimum temperature gradient and hence the cooling effectiveness increases. A high value of interphase heat transfer is desirable. Koh and Stevens [1975]

further verified this effect experimentally. With the insertion of porous material, much lower hot wall temperature is resulted though the coolant temperature increases. Thus, the use of porous material in the coolant passage of regenerative cooled surfaces such as the space shuttle engines increases the heat flux capability, reduces the maximum wall temperature and therefore reduces the possibility of engine failure due to thermal stresses.

Fu *et al.* [1996] studied numerically the effect of a porous block mounted on a heated wall in a laminar flow channel on convective heat transfer rate. A high thermal conductivity porous block, whose width is half the channel width, is inserted in a laminar heated channel at a sufficient distance from inflow and outflow planes such that flow is fully developed. The heat transfer from heated wall increases with inserting the porous block as compared to without porous block. Higher porosity of porous block and higher particle size enhances the heat transfer rate, which may be attributed to lower drag force and larger velocity. However if the porous block width is equal to channel width, the effects become opposite to above-mentioned effects.

Kim and Kim [1999] had used the porous medium model for thermal optimization and prediction of the thermal resistance of the micro channel heat sink they have obtained the analytical solutions for velocity and temperature profiles in micro channel heat sinks by modeling them as fluid saturated porous medium. Electronic equipment require efficient cooling for their working. A laminar fully developed flow in a micro channel heat sink subjected to a constant heat flux at its bottom is studied. The Darcy model for fluid flow and two-equation model for heat transfer is used. The analytical solutions are compared with solutions available in literature under similar conditions.

In a similar work by Kim *et al.* [2000], the validity of thermal equilibrium is checked so that the analysis can be done by 1-equation model only. The temperature difference between the two phases is a function of Darcy number and effective thermal conductivity ratio, $C \{ \varepsilon k_f / (1- \varepsilon) k_s \}$. As Darcy number decreases, the aspect ratio increases and channel width falls. It means that fin base wetted area increases and more heat transfer takes place. It increases the interstitial heat transfer coefficient and hence the difference between solid and fluid temperatures falls.

The effective thermal conductivity ratio increases with porosity and ratio of fluid and solid thermal conductivities. As porosity increases, the fin base area decreases and decrease

in heat transfer rate between fin and fluid and the temperature difference falls. As the ratio of thermal conductivities increase the temperature difference decreases hence, 1-eqiuaion model can be used. As the ratio of thermal conductivities between fluid and solid phases, increase the heat conductance through the fluid phase increases as compared to solid phase. So less heat passes to solid phase and consequently from the solid to fluid phase. It results into decrease in the temperature differences. The optimization of thermal performance of micro channel heat fins relates to its lower thermal resistance. The thermal resistance can be lowered by minimizing the heat sink base temperature at exit. Various geometries that lower the thermal resistance are obtained under the constraints of previous work. Based upon this theory error maps are drawn. Hence, local thermal equilibrium is assumed when Darcy number is low and effective thermal conductivity ratio is large. For high porosity heat sinks, 1-equation model can be used.

2.2.10 Composite Porous and Fluid regions

Vafai and Kim [1990] studied convective flow and heat transfer through a composite porous and fluid system. The fluid layer is placed over the porous substrate. The numerical algorithm is checked against similar results available in literature. Two distinct boundary layers exist: one in porous medium and other in fluid region. The presence of porous medium results into very slow velocity gradients as compared to fluid region. The porous medium offers greater frictional drag. The slower velocity profile lowers the convective heat transfer. However, when the conductivity ratio between the porous medium and fluid is higher, this trend can be changed. Huang and Vafai [1993] analyzed numerically the use of porous block array over a plate to control flow and heat transfer from the plate. It acts as a good thermal insulator by changing the convection characteristics.

2.2.11 Transport in Metal Hydrides

Kuznetsov and Vafai [1995] have developed a mathematical model for transport in a metal hydride packed bed. Metal hydrides such as ($LaNi_5H_x$, $LaNi_{5-y}$, Al_yH_x, $FeTiH_x$ etc) have high technological potentials such as creating safe hydrogen storage systems (as an alternate to storage of liquid hydrogen), devising highly effective thermo chemical compressors and heat pumps and ecologically clean refrigeration system. The flow of hydrogen through hydride

pores is similar to flow through porous medium. Using local averaging technique, they have developed an equation of motion similar to Darcy law, a two-phase energy equation besides equation of state and continuity equation. The process of hydration occurs due to temperature distribution. Of interest in this paper is the criterion for thermal non-equilibrium in the metal hydride bed. For analyzing the thermal non-equilibrium between gas and the solid matrix, the heat generated due to hydration is removed at location $z = 0$. An inlet layer is considered which is next to inlet boundary where the thermal non-equilibrium effects are considerable. A very short inlet length signifies thermal equilibrium in the bed. This length depends upon the inlet temperature of gas. In the following section, the energy storage aspects in porous medium are reviewed.

2.3 PULSATING AND OSCILLATORY FLOW IN POROUS MEDIUM

Pulsating flow refers to periodic change of boundary condition at inflow plane from cold to hot and vice-versa. Hence, it is unidirectional flow. In an oscillatory flow on the other hand, the cold and hot fluids flow periodically through opposite ends of a domain. These flows have a wide range of applications in the field of energy storage, Stirling cycle regenerators, waste heat recovery units in gas turbines, enhancement of cooling of electrical and electronic equipments and automobile catalytic reactors. For an energy storage system, the pulsating and oscillatory flows have two phases: hot and cold. In the hot phase, the hot fluid enters a medium, the energy is thus stored, and in the cold phase, the cold fluid enters the medium and stored energy is retrieved. When used for cooling purposes, only cold fluid is flowing through the medium. The use of oscillatory flow for plain medium (no solid phase) are also reported. The energy storage in a porous medium involves successive pulses of hot and cold fluids flowing through the solid porous mass at a suitable frequency.

The individual effects of such pulsating boundary conditions reduces to an ideal boundary condition of constant temperature if the frequency of oscillations is large and amplitude of temperature fluctuations is small, (Sozen [1991]). Kim *et al.* [1993, 94] analyzed numerically the pulsating flow (pulsations added to a mean flow) subjected to a porous medium. As compared to non-pulsating flow, it brings enhancement in heat transfer at moderate downstream regions, which increases with amplitude of pulsations. Zhao and

Cheng [1996] have analyzed numerically and experimentally the oscillatory flow heat transfer in a pipe subjected to a laminar reciprocating flow. The oscillatory flow of air takes place across a heated test section, the resulting temperature profiles and cycle averaged Nusselt number is analyzed. A correlation of space-cycle averaged Nusselt number of an oscillatory flow is obtained. Averaged heat transfer rate increases with Reynolds number and amplitude of oscillations. Bradean *et al*. [1996] used 1-equation model for studying flow and heat transfer from periodically heated and cooled, vertical and horizontal surfaces adjacent to a porous medium.

Muralidhar and Suzuki [1997] reviewed the models for flow and heat transfer in regenerators of Stirling cycle. Two models for regenerator are proposed. First considers flow and heat transfer at the scale of the wire that constitutes the mesh and second is a complete non-Darcy, thermal non-equilibrium model for the mesh to be treated as a porous medium. Peak, Kang and Hyun [1999] have done the experimental study of cool-down characteristics of a porous medium in a uniform pulsating flow, where an oscillating component is added to a mean flow. The application of this type of flow is quite common in engineering. An initially hot porous medium is subjected to pulsating air through-flow at low temperature to cool the porous media. Various sets of amplitude and frequency are used for analysis. When the amplitude of the pulsations is quite large such that backward flow is induced, temperature oscillations are produced which decrease the average heat transfer rate. As the diameter of spheres increases, less heat is recovered from the bed.

Muralidhar and Suzuki [2001] analyzed oscillatory flow and heat transfer in a regenerator using the thermal non-equilibrium model treating mesh screen as porous inserts. An oscillatory flow of gas was used with metallic mesh screens over a wide range of Reynolds number, domain lengths and frequencies Quantities such as the friction factor and regenerator effectiveness have been calculated.

Fu *et al.* [2001] analyzed experimentally the heat transfer in a porous channel subjected to oscillating flow. A heated porous section is subjected to oscillatory airflow at inlet bulk temperature. The experimental results show that the surface temperature distribution for oscillating flow is more uniform than that for steady flow. The length averaged Nusselt number in oscillatory flow is higher than that for steady flow. A porous media subjected to oscillatory flow can act as a good heat sink. It is seen that using a porous

material of lower thermal conductivity a higher surface temperature is obtained. Therefore, a channel filled with high conductivity porous material subjected to oscillating flow is a new and effective method of cooling electronic devices. The oscillatory flow is compared with steady state. The cooling increases with an increase in Reynolds number and effective thermal conductivity of porous medium. Similarly, Leong and Jin [2005] have analyzed experimentally the heat transfer in oscillating flow through a channel filled with aluminum foam. The channel is subjected to a constant heat flux and the parameters such as cycle averaged surface temperature of the bed and the cycle averaged local Nusselt number are calculated and compared with those flow when there in no porous material. It is found that surface temperature is lower and Nusselt number is higher in the presence of aluminum foam. The increase in effective Reynolds number brings a reduction in the surface temperature. The temperature also falls with increase in the amplitude of flow and the corresponding Nusselt numbers increase. Hence, porous media in presence of oscillatory flow is considered as an effective method of rapid heat dissipation. A porous media has a large effective solid surface area that can store and retrieve energy during oscillatory flow.

Bouvier *et al.* [2005] have analyzed experimentally and theoretical the heat transfer parameters in an oscillating fluid in a pipe with a time mean velocity of zero. A specially designed instrumentation test rig measures temperatures in the fluid at various locations from heated wall, solid fluid interface temperature, and instantaneous heat flux near the wall measured in an oscillating flow, subjected to wall heating. A comparison with analytical results is good. An assumption of constant wall temperature is not valid in their studies.

Byun *et. al* [2006] studied analytically the thermal behavior of porous medium under oscillating flow conditions; flow changes its direction in a porous medium whose two ends are maintained at hot and cold temperatures. The oscillations in solid and fluid phase vary with thermal properties, interphase heat transfer of the porous medium. It varies with ratio of thermal storage capacities of solid and fluid phases and that of interphase heat transfer and energy convected downstream.

2.4 ENERGY STORAGE IN POROUS MEDIUM

Bejan [1978] states that a second law technique should be used for analyses of the storage system and the purpose of the storage system is not just to store energy but also to store

thermodynamic availability. The design of an energy storage system should be based upon maximum available energy rather than maximum stored energy. There exists an optimum well-defined quantity of hot fluid to be used in order to maximize the useful work stored and an optimum number of heat transfer units in order to minimize the stored energy losses. Hence, a packed bed based energy storage system is widely used for energy storage. Beasley and Clark [1984] have investigated the transient response of a packed bed for energy storage using experimental and numerical techniques. The temperature profiles show sensitivity to Nusselt number variations when the thermal storage capacity of the solid phase is much higher than the fluid phase. The thermal dispersion in axial direction is determined by the heat transfer coefficient. Gong and Majumdar [1997] discuss whether the pulsating flow of hot and cold fluids should occur from the same or the opposite ends. A finite element based analysis of cyclic heat transfer in a shell and tube latent heat energy storage system is carried out. The effects of fluid flow rate, inlet temperature and duration of charging upon the energy stored is calculated using the two approaches. Better results are obtained when hot and cold fluids flow through the same end. Al-Juwayhel and Refaee [1998] have done a numerical study of combined packed bed and solar pond system. A packed bed is inserted at the bottom of a solar pond system that improves the overall thermal performance of the system. The use of low thermal diffusivity rocks such as Bakelite improves the performance of the combined system. In addition, a low porosity rocks give higher temperatures in the storage zone and hence improves the performance of the system. Ismail and Stuginsky [1999] have done numerical analysis of the phase change and sensible heat storage systems in fixed beds using four different models. They have considered a two-dimensional continuous solid phase model in which solid is assumed to behave as a continuous medium with distinct energy equations for solid and fluid phases. The second model used by them is the Schumann's one-dimensional model. In this model, there is no heat conduction in radial direction in the fluid and the solid phases. Thirdly, they have discussed single-phase model with no heat transfer between fluid and solid phase and the instantaneous temperatures of fluid and solid phases are equal. The fourth model considers a thermal gradient in solid phase and no inter phase heat transfer. A comparison of all the models is done in terms of particle size, mass flow rate, working fluid, storage material, varying void fraction, cyclic variations of fluid inlet temperature and thermal wall losses. The effect of particle size variations is more in the

models that considers thermal gradients in the solid phase. Similarly, the two dimensional continuous solid phase model gives better results for variation of heat stored, exit temperature changes with change in mass flow rate particularly for solid-fluid systems whose thermal conductivity ratio ($\lambda = k_f/k_s$) is much less than unity such as air steel system. The two dimensional continuous solid phase model also requires a larger CPU time for simulation as compared to other models.

Using a suitable storage system based upon cold water or ice storage, the running cost of the plant is reduced by as much as 50%, it lowers the peak hour's demand of electricity. Based upon the size of the storage system, the plant can run partially or even fully shut during peak hours. The cooling system thus requires less capacity chillers with fewer amounts of refrigerants. Hence, an energy storage system can be used to reduce the peak load demands and lesser amount of energy is needed for its running (Dincer [2001]). Yumrutas and Unsal [2005] have analyzed numerically the thermal performance of a chiller system coupled with an underground storage tank, which acts as a heat sink. It is found that COP of the system with an underground storage tank is higher than a traditional system. A ground-coupled chiller can operate at higher COP as the heat is rejected at lower temperature. In addition, this temperature remains nearly constant throughout the year. The storage temperature of underground water tank is calculated numerically for different months of a year, various soils types, volume of water in the tank and various ambient air temperatures. An underground storage tank as a heat sink increases the COP of the cooling unit.

2.5 FLOW IN UNSATURATED SOILS

The flow in unsaturated soils is briefly reviewed in this section.

When the pore space is not fully filled with water and air is present in the pores, the medium is called unsaturated. The mathematical formulation for flow through unsaturated medium is considerably involved. The additional factor is the surface tension between air and water interface. The transport in unsaturated mediums is discussed in the text by Tindall and Kunkel [1999]. The main property of the unsaturated medium is the water content present in the pores, c, the relative hydraulic conductivity (K_r) and pressure head h. The relationship between the K_r and h as a function of the dimensionless water content (Θ) as derived by Mualem [1976] is given as

$$K_r = \Theta^{1/2}\left[\int_0^{\Theta} \frac{1}{h(x)}dx \Big/ \int_0^{1} \frac{1}{h(x)}dx\right]^2 \tag{2.9}$$

An expression relating the dimensionless water content to the pressure head is needed. A commonly used expression is of the form given by Van Genuchten [1980]:

$$\Theta = \left[\frac{1}{1+(\alpha h)^n}\right]^m \tag{2.10}$$

Muralidhar [1988] developed an equation for flow into a naturally formed fault in earth using continuity equation and Darcy law for flow in unsaturated soils. Here the formulation of relative permeability as suggested by Van Genuchten [1980] is used.

2.6 CLOSURE

A state of art in flow and heat transfer in porous medium is presented. Wide range of numerical modeling and experiments are considered. The topics like thermal non-equilibrium, dispersion, fluid and solid phase Nusselt number, Interphase Nusselt number and non-Darcy effects are addressed. The issues of flow development are also addressed. The oscillatory and pulsating flow through the porous medium is reviewed. Unsaturated flow and heat transfer is a developing area and needs to be addressed separately. The whole research seems to point that porous medium offers large interfacial area between the fluid and the solid phases with dispersion in the pore spaces enhancing the thermal conductivity of solid and fluid phases. The thermal properties of fluid and solid phases affect the transport in pore spaces. The dispersion in lateral direction plays an important role in energy transfer even when the flow is longitudinal. The presence of heated walls/ heat loss through walls makes the lateral transport even more important. As such, the transport in porous medium has attracted a large attention. However, some problems need to be addressed in detail especially the difference between 1 and 2 equation models for various solid phase materials, effect of heat loss on transport, oscillatory flow and energy storage in porous medium. The application of energy storage is for summer air-conditioning in the form of storage of cold water in winter and reuse in summer. This aspect seems to be an extension of regenerator of Stirling cycles.

The present study addresses the difference between 1 and 2 equation models of heat transfer, the effect of properties of solid phase on energy transfer, pulsating, oscillatory flow and associated energy storage. The analysis is performed both numerically and experimentally. The flow and heat transfer in unsaturated porous medium is numerically studied.

CHAPTER 3
MATHEMATICAL MODEL

3.1 INTRODUCTION

The examination of transport in porous media relies on the knowledge we have gained in studying these phenomena in plain media. The presence of rigid and stationary solid influences these phenomena significantly. A porous medium is a heterogeneous system made of a solid matrix with its voids filled with fluid. It can be treated as a continuum by properly accounting for the role of the fluid and the solid phases. Hence, the mathematical modeling for transport in porous medium is complex. Mathematical models for flow and heat transfer are widely used by Amiri and Vafai [1994], Nakayama *et al*. [2001] and others to analyze various associated problems. Kuznetsov [1994] and Nakayama *et al*. [2001] also developed analytical solutions for certain simplified problems. The thrust in the present work is on mathematical modeling of heat transfer in porous medium, each associated model being validated against the analytical solutions available in literature. The validation against benchmark solutions and experimental results is also performed. The knowledge gained from mathematical modeling is used to analyze an energy storage system capable of storing cold water in winter months to be used for summer air-conditioning. The mathematical model in this chapter is developed from conduction and advection diffusion equations. The derivation of thermal equilibrium and non-equilibrium models for heat transfer is discussed in this chapter. The PDEs and thermal equilibrium and non-equilibrium models are subsequently converted to non-dimensional form for analysis in next chapters.

3.2 LOCAL VOLUME AVERAGING METHOD

The fluid contained in porous medium has a large number of molecules that move about colliding with each other. The geometry of the pore space is complex. Given the large number of molecules in fluid contained in the pores, it is very difficult to determine their initial and final positions, velocities and momenta. Instead, of treating the problem at the molecular level, an approach based on statistical averaging is used. Thus, the molecular level of treatment is abandoned and a fluid continuum approach at macroscopic level is used. For

the treatment of porous medium as a continuum, the concept of representative volume (REV) is used. REV is an ensemble of many molecules contained in a small volume. Its size should be much larger than mean free path of a single molecule and it should be sufficiently small as compared to fluid domain such that by averaging fluid and flow properties over the molecules included in it, bulk fluid properties will be obtained. Such an approach is called Local Volume Averaging. It is based on averages taken over a representative elementary volume, i.e. the smallest volume that represents the local average properties. The addition of extra pores and surrounding solid to this volume does not change the average value.

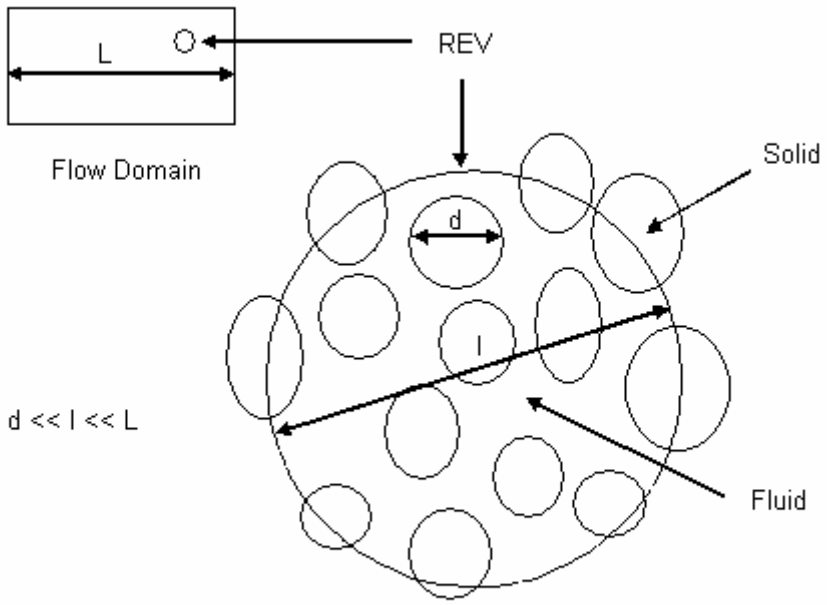

Figure 3.1: The representative elementary volume (REV): The figure illustrates the intermediate size relative to the sizes of the flow domain and the pores.

Figure 1 shows representative elementary volume contained in a flow domain. The size of the pores or the solid particles is represented by d and the size of the representative elementary volume, REV (V) is represented by l. This size is much larger than the size of pores or the solid particles. The size of flow domain L is much larger than the size of the REV l. Thus, macroscopic transport equations are obtained by averaging the pore scale transport equations over this volume REV. Consider a property ψ associated with β- phase in REV. We define two different averages as:

Phase Average $$\langle \psi_\beta \rangle = \frac{1}{V} \int_{V_\beta} \psi_\beta \, dV \tag{3.1}$$

Intrinsic Phase Average $$\langle \psi_\beta \rangle^\beta = \frac{1}{V_\beta} \int_{V_\beta} \psi_\beta \, dV \tag{3.2}$$

and $$\langle \psi_\beta \rangle = \varepsilon_\beta \langle \psi_\beta \rangle^\beta \tag{3.3}$$

in which V_β represents the volume of β- phase contained within REV V and ε_β is the volume fraction of β- phase.

3.3 LOCAL THERMAL EQUILIBRIUM

The energy equation can be applied to a point and integrated over the representative elementary volume. At the pore level, there will be a difference ΔT_d between the temperature at a point in the solid and in the fluid. Similarly, across the representative elementary volume, we have a maximum temperature difference ΔT_l. However, we assume that these temperature differences are much smaller than those occurring over the system dimension, ΔT_L. Thus, local thermal equilibrium is imposed by requiring that

$$\Delta T_d < \Delta T_l << \Delta T_L \tag{3.4}$$

This condition is valid at steady state and for slow transients. With this assumed negligible local temperature difference between the phases, we assume that within the representative elementary volume, the fluid and the solid phases are in local thermal equilibrium, i.e.

$$\frac{1}{V_f} \int_{V_f} T_f \, dV = \frac{1}{V_s} \int_{V_s} T_s \, dV = \frac{1}{V} \int_{V} T \, dV \tag{3.5}$$

For saturated porous medium, when a single fluid is occupying the pore space, the above assumption leads to a homogeneous energy equation, which is called 1 - equation model.

3.4 THERMAL NON-EQUILIBRIUM

When there is a significant heat generation occurring in any one of the phases, then the local volumes of the fluid and the solid phases will be far from being in local thermal equilibrium. Hence, separate temperatures are assigned to the individual phases and energy equations are written for each phase. In a fluid saturated porous medium the thermal diffusivity of the fluid phase may be much lower or higher than that of the solid phase. Therefore, the time scale for

thermal diffusion in the fluid phase can be quite different from the solid phase. In such transient heat transfer processes, the assumption of local thermal equilibrium must be discarded.

It is assumed that each phase is continuous and represented with an appropriate effective thermal conductivity that depends upon the thermal conductivity of the individual phases and the pore microstructure. A model based on the individual energy equations is developed and called 2-equation model. It contains a modeling parameter h_{sf} that represents the interfacial convective heat transfer coefficient. In addition, this model also contains effective thermal conductivity and dispersion tensors and is expected to give reasonably accurate predictions.

The volume averaged energy equation is solved in the next section. The principal modes of heat transfer considered in this thesis are conduction and convection. We first consider the volume averaging of pure conduction equation in a porous medium and subsequently the convection term is added to the equation. The analysis can be reduced to 1 and 2-equation models by assuming either thermal equilibrium or thermal non-equilibrium between the fluid and the solid phases.

3.5 CONDUCTION EQUATION

3.5.1 Local Volume Averaging

The heat conduction through fully saturated porous media is similar to heat conduction through any heterogeneous media, which depends on the structure of the matrix and the thermal conductivity of each phase. For the analysis of the macroscopic heat flow through heterogeneous media, the local volume averaged properties such as the effective thermal conductivity $\langle k \rangle$ are used. Consider the energy equation for transient conduction for each phase as discussed in Welty *et al*. [1976].

$$\left(\rho c_p\right)_f \frac{\partial T_f}{\partial t} = \nabla.\left(k_f \nabla T_f\right) \tag{3.6}$$

$$\left(\rho c_p\right)_s \frac{\partial T_s}{\partial t} = \nabla.\left(k_s \nabla T_s\right) \tag{3.7}$$

where $\frac{\partial T}{\partial t}$ represents the local change in temperature in a given phase and $\nabla.k\nabla T$ is the diffusion energy transfer of the phase. Here all the symbols have usual dimensions.

The boundary conditions on the interfacial area between the fluid and solid phase, A_{fs} are the continuity of temperature and heat flux, i.e.

$$T_f = T_s \quad \text{on } A_{fs}, \tag{3.8}$$

$$n_{fs}.k_f \nabla T_f = n_{fs}.k_s \nabla T_s \quad \text{on } A_{fs}. \tag{3.9}$$

here n_{fs} is a unit normal pointing from the fluid into the solid phase at each point of the interface.

The volume of REV is $V = V_f + V_s$. The fluid or solid temperature within V is decomposed using

$$T_f = \langle T \rangle^f + T_f' \tag{3.10}$$

where T_f' is the spatial deviation component. Assuming that over V, the thermal conductivities and heat capacities remain constant and by taking volume averages of LHS of Equation 3.6, we get

$$\begin{aligned} \frac{1}{V}\int_{V_s} (\rho c_p)_f \frac{\partial T_f}{\partial t} dV &= \frac{V_f}{V}(\rho c_p)_f \frac{\partial}{\partial t}\left(\frac{1}{V_f}\int_{V_f} T_f \, dV\right) \\ &= (\varepsilon)(\rho c_p)_f \frac{\partial \langle T \rangle^f}{\partial t} \end{aligned} \tag{3.11}$$

The Slattery theorem [1981] for volume average can be used for a scalar, vector or a second order tensor as.

$$\langle \nabla.b \rangle = \nabla.\langle b \rangle + \frac{1}{V}\int_{A_{sf}} b.n \, dA \tag{3.12}$$

where n is a unit normal to the surface. The volume averaging of RHS of Equation 3.6 can be obtained by using Slattery theorem as

$$\begin{aligned} \left\langle \nabla.k_f \nabla T_f \right\rangle &= \nabla.\left\langle k_f \nabla T_f \right\rangle + \frac{1}{V}\int_{A_{fs}} n_{fs} \,.\, k_f \nabla T_f \, dA \\ &= \nabla.\left[k_f \nabla \left\langle T_f \right\rangle + \frac{k_f}{V}\int_{A_{fs}} n_{fs} T_f \, dA \right] + \frac{1}{V}\int_{A_{fs}} n_{fs}.k_f \nabla T_f \, dA \end{aligned} \tag{3.13}$$

Since $\langle T_f \rangle = \varepsilon \langle T \rangle^f$ the term $k_f \nabla \langle T_f \rangle$ can be written as

$$k_f \nabla \langle T_f \rangle = k_f \nabla \varepsilon \langle T \rangle^f = k_f \varepsilon \nabla \langle T \rangle^f + k_f \langle T \rangle^f \nabla \varepsilon \tag{3.14}$$

Using Equation 3.14, Equation 3.13 becomes

$$\langle \nabla . k_f \nabla T_f \rangle = \nabla . \left[k_f \varepsilon \nabla \langle T \rangle^f + k_f \langle T \rangle^f \nabla \varepsilon + \frac{k_f}{V} \int_{A_{fs}} n_{fs} T_f \, dA \right] + \frac{1}{V} \int_{A_{fs}} n_{fs} . k_f \nabla T_f \, dA \tag{3.15}$$

Carbonell and Whitaker [1984] have shown that

$$\frac{1}{V} \int_{A_{fs}} n_{fs} T_f \, dA \approx \frac{1}{V} \int_{A_{fs}} n_{fs} T'_f \, dA - \langle T \rangle^f \nabla \varepsilon \tag{3.16}$$

Using the above assumption, the Equation 3.15 can be written as

$$\langle \nabla . k_f \nabla T_f \rangle = \nabla . \left[k_f \varepsilon \nabla \langle T \rangle^f + \frac{k_f}{V} \int_{A_{fs}} n_{fs} T_f' \, dA \right] + \frac{1}{V} \int_{A_{fs}} n_{fs} . k_f \nabla T_f \, dA \tag{3.17}$$

Using Equations 3.11 and 3.17, the volume averaged energy equation for fluid phase becomes

$$(\varepsilon)(\rho c_p)_f \frac{\partial \langle T \rangle^f}{\partial t} = \nabla . \left[k_f \varepsilon \nabla \langle T \rangle^f + \frac{k_f}{V} \int_{A_{fs}} n_{fs} T_f' \, dA \right] + \frac{1}{V} \int_{A_{fs}} n_{fs} . k_f \nabla T_f \, dA \tag{3.18}$$

The first term in RHS represents the energy transfer due to molecular diffusion, the second term the tortuosity term in the fluid phase and the last term represents the interphase heat transfer in the fluid.

Similarly, the solid phase energy equation is

$$(1-\varepsilon)(\rho c_p)_s \frac{\partial \langle T \rangle^s}{\partial t} = \nabla . \left[k_s (1-\varepsilon) \nabla \langle T \rangle^s + \frac{k_s}{V} \int_{A_{fs}} n_{sf} T_s' \, dA \right] + \frac{1}{V} \int_{A_{fs}} n_{sf} . k_s \nabla T_s \, dA \tag{3.19}$$

The first term in RHS of the above equation represents the energy transfer due to molecular diffusion, the second term the tortuosity and the third term represents the interphase heat transfer. From the above two equations 1 and 2 equation model can be derived.

3.5.2 1-Equation Model

Since REV comprises the fluid and the solid phases, the one-equation model can be obtained by adding Equations 3.18 and 3.19 and considering on $A_{fs}, n_{fs} = -n_{sf}$, we get

$$(\varepsilon)(\rho c_p)_f \frac{\partial \langle T \rangle^f}{\partial t} + (1-\varepsilon)(\rho c_p)_s \frac{\partial \langle T \rangle^s}{\partial t} = \nabla.\left[\varepsilon k_f \nabla \langle T \rangle^f + k_s (1-\varepsilon) \nabla \langle T \rangle^s\right] + \nabla.\left[\frac{1}{V}\int_{A_{fs}} n_{fs}\left(k_f T_f{}' - k_s T_s{}'\right) dA\right] + \frac{1}{V}\int_{A_{fs}} n_{fs}.\left(k_f \nabla T_f - k_s \nabla T_s\right) dA \quad (3.20)$$

Since within REV, the fluid and solid phases have equal average temperatures

$$\langle T \rangle^f = \langle T \rangle^s = \langle T \rangle \quad (3.20)$$

On A_{fs}, the phase deviations are equal

$$T_f{}' = T_s{}' \quad (3.21)$$

In addition, the continuity of heat flux on interface as given by Equation 3.9, Equation 3.20 reduces to

$$\left[\varepsilon(\rho c_p)_f + (1-\varepsilon)(\rho c_p)_s\right]\frac{\partial \langle T \rangle}{\partial t} = \nabla.\left\{\left[\varepsilon k_f + (1-\varepsilon)k_s\right]\nabla \langle T \rangle + \frac{k_f - k_s}{V}\int_{A_{fs}} n_{fs} T_f{}' \, dA\right\} \quad (3.22)$$

Here the terms $\left[\varepsilon(\rho c_p)_f + (1-\varepsilon)(\rho c_p)_s\right]$ and $\left[\varepsilon k_f + (1-\varepsilon)k_s\right]$ represent respectively the thermal storage and the thermal conductivity of porous medium represented by $(\rho c_p)_m$ and k_m and the other term represents the trotuosity. Hence, the 1-equation model for pure conduction is written as

$$(\rho c_p)_m \frac{\partial \langle T \rangle}{\partial t} = \nabla.\left(k_{eff,m}.\nabla \langle T \rangle\right) \quad (3.23)$$

where $k_{eff,m}$ is the effective thermal conductivity of the porous medium given by

$$k_{eff,m} = \left[\varepsilon k_f + (1-\varepsilon)k_s\right] I + \frac{k_f - k_s}{V}\int_{A_{fs}} n_{fs} b_f \, dA \quad (3.24)$$

3.5.3 2-Equation Model

Equations 3.18 and 3.19 represent the fluid and the solid phase energy equation within REV for pure conduction in porous medium. There are two conduction terms and one interphase heat transfer term in RHS of both the equations. Using an effective thermal conductivity of

each phase and an interphase heat transfer term, the fluid and the solid phase equations can be written as

$$Fluid: \quad (\varepsilon)(\rho c_p)_f \frac{\partial \langle T \rangle^f}{\partial t} = \nabla.\left[k_{eff,f}.\nabla \langle T \rangle^f\right] + Q_{s \to f} \tag{3.25}$$

$$Solid: \quad (1-\varepsilon)(\rho c_p)_s \frac{\partial \langle T \rangle^s}{\partial t} = \nabla.\left[k_{eff,s}.\nabla \langle T \rangle^s\right] - Q_{s \to f} \tag{3.26}$$

where $k_{eff,f}$ and $k_{eff,s}$ is the effective thermal conductivity of the fluid and solid phases corrected for tortuosity and $Q_{s \to f}$ is the interphase heat transfer. The values are respectively given as

$$k_{eff,f} = \left(\varepsilon k_f + \frac{k_f}{V}\int_{A_{fs}} n_{fs} T_f' \, dA\right) \tag{3.27}$$

$$k_{eff,s} = \left((1-\varepsilon)k_s - \frac{k_s}{V}\int_{A_{fs}} n_{fs} T_s' \, dA\right) \tag{3.28}$$

$$\frac{1}{V}\int_{A_{fs}} n_{fs}.k_f \nabla T_f \, dA = Q_{s \to f} \tag{3.29}$$

3.6 ADVECTION DIFFUSION EQUATION

3.6.1 Local Volume Averaging

The advection diffusion is an equation, which considers conduction as well as convection in porous media. Only the fluid phase energy equation changes with convection and the solid phase energy equation remains same. Consider energy equation for fluid and solid phases as

$$(\rho c_p)_f \left[\frac{\partial T_f}{\partial t} + \nabla.uT\right] = \nabla.k_f \nabla T_f \tag{3.30}$$

$$(\rho c_p)_s \frac{\partial T_s}{\partial t} = \nabla.k_s \nabla T_s \tag{3.31}$$

here $\nabla.uT$ the convective energy transfer. Here u is the fluid velocity in ms^{-1}.

The boundary conditions on the interfacial area A_{fs} are the continuity of temperature and heat flux are

$$T_f = T_s \quad \text{on } A_{fs}, \tag{3.32}$$

$$n_{fs}.k_f \nabla T_f = n_{fs}.k_s \nabla T_s \quad \text{and } u = 0 \qquad \text{on } A_{fs}. \tag{3.33}$$

The fluid or solid temperature and velocity within V is decomposed using respective deviations as

$$T_f = \langle T \rangle^f + T' \tag{3.34}$$

$$T_s = \langle T \rangle^s + T' \tag{3.35}$$

$$u = \langle u \rangle^f + u' \tag{3.36}$$

where the volume averages of the above variables is zero i.e.

$$\frac{1}{V_f} \int_{V_f} T' \, dV = \langle T' \rangle^f = 0 \tag{3.37}$$

Consider volume averaging of Equation 3.30 over V. Assume that the thermal properties are constant over REV

$$\left(\rho c_p\right)_f \left[\frac{\partial \langle T \rangle}{\partial t} + \langle \nabla . uT \rangle \right] = \left\langle \nabla . k_f \nabla T_f \right\rangle \tag{3.38}$$

Equation 3.11 gives the volume averaging of local change in temperature, consider now the convection term in LHS of above equation, its volume averaging can be written as

$$\langle \nabla . uT \rangle = \nabla . \langle uT \rangle + \frac{1}{V} \int_{A_{fs}} (uT) . n \, dA \tag{3.39}$$

Since on the interface velocity is zero, hence volume averaging of second term of RHS of above equation vanishes. The first term is written as

$$\langle uT \rangle = \frac{1}{V} \int_V uT \, dV = \frac{\varepsilon}{V_f} \int_{V_f} \left(\langle u \rangle^f + u' \right) \left(\langle T \rangle^f + T_f' \right) dV \tag{3.40}$$

Using Equation 3.37, the volume averages of deviation terms vanishes, hence we get

$$\nabla . \langle uT \rangle = \nabla . \left[\varepsilon \left(\langle u \rangle^f \langle T \rangle^f + \langle u' T' \rangle^f \right) \right] \tag{3.41}$$

Using Equation 3.39, we get

$$\langle \nabla . uT \rangle = \nabla . \left[\varepsilon \langle u \rangle^f \langle T \rangle^f + \langle u' T' \rangle \right] \tag{3.42}$$

Since the porosity is locally constant, the fluid is incompressible, the above equation reduces to

$$\langle \nabla . uT \rangle = \varepsilon \langle u \rangle^f . \nabla \langle T \rangle^f + \nabla . \langle u' T' \rangle \tag{3.43}$$

The volume averaging of RHS of Equation 3.30 is discussed in section 3.5 and is given by Equation 3.17. Using Equations 3.17 and 3.41, Equation 3.38 reduces to

$$\left(\rho c_p\right)_f\left[\frac{\partial\langle T\rangle}{\partial t}+\varepsilon\langle u\rangle^f.\nabla\langle T\rangle^f+\nabla.\langle u'T'\rangle\right]=\nabla.\left[k_f\varepsilon\nabla\langle T\rangle^f+\frac{k_f}{V}\int_{A_{fs}}n_{fs}T_f'\,dA\right]+\frac{1}{V}\int_{A_{fs}}n_{fs}.k_f\nabla T_f\,dA \tag{3.44}$$

Substituting the volume average of temperature over V in terms of intrinsic value over V_f as $\langle T\rangle=\varepsilon\langle T\rangle^f$ further substituting $V=\frac{V_f}{\varepsilon}$ we get

$$\left(\rho c_p\right)_f\left[\varepsilon\frac{\partial\langle T\rangle^f}{\partial t}+\varepsilon\langle u\rangle^f.\nabla\langle T\rangle^f+\nabla.\langle u'T'\rangle\right]=\nabla.\left[k_f\varepsilon\nabla\langle T\rangle^f+\frac{k_f}{V}\int_{A_{fs}}n_{fs}T_f'\,dA\right]+\frac{1}{V}\int_{A_{fs}}n_{fs}.k_f\nabla T_f\,dA \tag{3.45}$$

Rearranging, we get

$$\varepsilon\left(\rho c_p\right)_f\left[\frac{\partial\langle T\rangle^f}{\partial t}+\langle u\rangle^f.\nabla\langle T\rangle^f\right]=\nabla.\left[k_f\varepsilon\nabla\langle T\rangle^f+\frac{k_f}{V}\int_{A_{fs}}n_{fs}T_f'\,dA\right]-\left(\rho c_p\right)_f\nabla.\langle u'T'\rangle+\frac{1}{V}\int_{A_{fs}}n_{fs}.k_f\nabla T_f\,dA \tag{3.46}$$

The above equation represents the fluid phase energy equation. There are two diffusion terms in RHS of the above equation; the first term $\varepsilon k_f\nabla\langle T\rangle^f$ represents the molecular diffusion. The second term $\frac{k_f}{V}\int_{A_{fs}}n_{fs}T_f'\,dA$ is the thermal tortuosity, which is the area integral of the spatial deviations in temperature along the interface. The term $\left(\rho c_p\right)_f\nabla.\langle u'T'\rangle$ represents thermal dispersion, which is the volume average of the product of spatial deviations in velocity and temperature. The last term $\frac{1}{V}\int_{A_{fs}}n_{fs}.k_f\nabla T_f\,dA$ represents the heat exchange term between the phases, which is the area integral of the heat flux at the phase interface. See Levec and Carbonell [1985] and Kuwahara *et al.* [1996].

The tortuosity is modeled by Hsu [1999], Nakayama [2001] by adding the term $(1-\sigma)G$ to molecular diffusion term where $\sigma = \frac{1}{\lambda}$ is the thermal conductivity ratio of solid to fluid and $G = \left((k_{stg}/k) - \varepsilon - \sigma(1-\varepsilon)\right)/(1-\sigma)^2$ is a scalar quantity.

The parameter k_{stg} is the effective stagnant thermal conductivity of the saturated porous medium and given by

$$\frac{k_{stg}}{k_f} = 1-(1-\varepsilon)^{2/3} + \frac{(1-\varepsilon)^{2/3}\sigma}{\sigma+(1-\sigma)(1-\sigma)^{2/3}} \tag{3.47}$$

The dispersion term is related to velocity and temperature deviations but add additional diffusive term as

$$\left(\rho c_p\right)_f \nabla.\langle u'T'\rangle = k_{dis}.\nabla\langle T\rangle^f \tag{3.48}$$

Wakao and Kaguei [1982] recommended the following formula for dispersion in longitudinal and lateral directions.

Longitudinal Direction:
$$\frac{(k_{dis})_z}{k_f} = 0.5\,\mathrm{Pe} \tag{3.49}$$

Lateral Direction:
$$\frac{(k_{dis})_r}{k_f} = 0.1\,\mathrm{Pe} \tag{3.50}$$

Where Pe is the Peclet number.

Finally the interface heat exchange is modeled as, Kuwahara *et al*. [1996].

$$\frac{1}{V}\int_{A_{fs}} n_{fs}.k_f \nabla T_f \, dA = a_{sf} h_{sf}\left(\langle T\rangle^s - \langle T\rangle^f\right) \tag{3.51}$$

$$h_{sf} = \frac{\frac{1}{V}\int_{A_{fs}} n_{fs}.k_f \nabla T_f \, dA}{a_{sf}\left(\langle T\rangle^s = \langle T\rangle^f\right)} \tag{3.52}$$

Wakao and Kaguei [1982] recommended the following relation

$$Nu_p = 2+1.1\mathrm{Pr}^{0.33}\mathrm{Re}_p^{0.6} \tag{3.53}$$

where Nu_p is the particle based Nusselt number based upon inter-particle convective heat exchange, hence interphase heat transfer coefficient is given as

$$h_{fs} = \frac{1}{d}\left(2 + 1.1 \mathrm{Pr}^{0.33} \mathrm{Re}_p^{0.6}\right) k_f \tag{3.54}$$

The effective thermal conductivity of fluid phase corrected for tortuosity and thermal dispersion effect can be written as

$$k_{eff,f} = \varepsilon k_f + k_{torr} + k_{dis} \tag{3.55}$$

Considering the individual effects of the above parameters, the fluid phase energy equation modifies to

$$\begin{aligned} \varepsilon\left(\rho c_p\right)_f \left[\frac{\partial \langle T \rangle^f}{\partial t} + \langle u \rangle^f . \nabla \langle T \rangle^f\right] = \nabla . \left[(\varepsilon + (1-\sigma)G) k_f \nabla \langle T \rangle^f + k_{dis} . \nabla \langle T \rangle^f\right] \\ + a_{sf} h_{sf} \left(\langle T \rangle^s - \langle T \rangle^f\right) \end{aligned} \tag{3.56}$$

Similarly, the solid phase energy equation can be written as

$$(1-\varepsilon)\left(\rho c_p\right)_s \left[\frac{\partial \langle T \rangle^s}{\partial t}\right] = \nabla . \left[(1-\varepsilon) k_s \nabla \langle T \rangle^s + \frac{k_s}{V} \int_{A_{fs}} n_{sf} T_s' \, dA\right] + \frac{1}{V} \int_{A_{fs}} n_{sf} . k_s \nabla T_s \, dA \tag{3.57}$$

Using $n_{fs} = - n_{sf}$, we get

$$(1-\varepsilon)\left(\rho c_p\right)_s \left[\frac{\partial \langle T \rangle^s}{\partial t}\right] = \nabla . \left[(1-\varepsilon) k_s \nabla \langle T \rangle^s - \frac{k_s}{V} \int_{A_{fs}} n_{fs} T_s' \, dA\right] - \frac{1}{V} \int_{A_{fs}} n_{fs} . k_s \nabla T_s \, dA \tag{3.58}$$

The above equation represents the solid phase energy equation. The term $(1-\varepsilon) k_s \nabla \langle T \rangle^s$ represents the molecular diffusion in the solid phase, the term $\frac{k_s}{V} \int_{A_{fs}} n_{fs} T_s' dA$ represents thermal tortuosity and the term $\frac{1}{V} \int_{A_{fs}} n_{fs} . k_f \nabla T_f \, dA$ is the heat exchange, being opposite and equal to that in the fluid phase. Considering the individual effects, the solid phase energy equation modifies to

$$(1-\varepsilon)\left(\rho c_p\right)_s \left[\frac{\partial \langle T \rangle^s}{\partial t}\right] = \nabla . \left[((1-\varepsilon) + (\sigma - 1)G) k_s \nabla \langle T \rangle^s\right] - a_{sf} h_{sf} \left(\langle T \rangle^s - \langle T \rangle^f\right) \tag{3.59}$$

where the tortuosity and the heat transfer terms are opposite to that in fluid phase; Hsu [1999], Nakayama [2001]. The 1 and 2-equation models can now be written.

3.6.2 1-Equation Model

This model is based upon the local thermal equilibrium between the solid and fluid phases in REV and contains only one governing energy equation. The individual effects of the solid and fluid phases modify the governing equation.

From the assumption of local thermal equilibrium, we have

$$\langle T \rangle^{f} = \langle T \rangle^{s} = \langle T \rangle \tag{3.60}$$

And on A_{fs}

$$T_f' = T_s' \tag{3.61}$$

$$n_{fs}.k_f \nabla T_f = n_{fs}.k_s \nabla T_s \tag{3.62}$$

Adding Equations 3.46 and 3.58, we get

$$\left[\varepsilon(\rho c_p)_f + (1-\varepsilon)(\rho c_p)_s\right]\frac{\partial \langle T \rangle}{\partial t} + \varepsilon(\rho c_p)_f \langle u \rangle^f .\nabla \langle T \rangle = \nabla .\left\{\left[\varepsilon k_f + (1-\varepsilon)k_s\right]\nabla \langle T \rangle + \frac{k_f - k_s}{V}\int_{A_{fs}} n_{fs} T_f'\, dA\right\} - (\rho c_p)_f \left(\varepsilon \langle u'T' \rangle^f\right) \tag{3.63}$$

Using the analysis as suggested by Hsu [1999], Nakayama [2001], the above equation reduces to

$$\left[\varepsilon(\rho c_p)_f + (1-\varepsilon)(\rho c_p)_s\right]\frac{\partial \langle T \rangle}{\partial t} + \varepsilon(\rho c_p)_f \langle u \rangle^f .\nabla \langle T \rangle = \nabla .\begin{bmatrix}\left(\varepsilon k_f + (1-\varepsilon)k_s + k_f (1-\sigma)^2 G\right)\nabla \langle T \rangle \\ + k_{dis}.\nabla \langle T \rangle\end{bmatrix} \tag{3.64}$$

Using the effective terms for thermal storage and conductivity, the 1-equation model for heat transfer becomes

$$\left[(\rho c_p)_m\right]\frac{\partial \langle T \rangle}{\partial t} + \varepsilon(\rho c_p)_f \langle u \rangle^f .\nabla \langle T \rangle = \nabla .\left[\left(k_{eff,m}\right).\nabla \langle T \rangle\right] \tag{3.65}$$

where $k_{eff,m} = \left[\left(\varepsilon k_f + (1-\varepsilon)k_s + k_f (1-\sigma)^2 G\right)I + k_{dis}\right]$ is the effective thermal conductivity of the porous medium.

3.6.3 2-Equation Model

Equations 3.46 and 3.58 represent the 2-equation model. It is written for fluid and solid phases as

$$Fluid: \quad \varepsilon(\rho c_p)_f \left[\frac{\partial \langle T \rangle^f}{\partial t} + \langle u \rangle^f . \nabla \langle T \rangle^f \right] = \nabla . \left[(\varepsilon + (1-\sigma)G) k_f \nabla \langle T \rangle^f + k_{dis} . \nabla \langle T \rangle^f \right] + a_{sf} h_{sf} \left(\langle T \rangle^s - \langle T \rangle^f \right) \tag{3.66}$$

$$Solid: \quad (1-\varepsilon)(\rho c_p)_s \left[\frac{\partial \langle T \rangle^s}{\partial t} \right] = \nabla . \left[((1-\varepsilon) + (\sigma - 1)G) k_s \nabla \langle T \rangle^s \right] - a_{sf} h_{sf} \left(\langle T \rangle^s - \langle T \rangle^f \right) \tag{3.67}$$

3.6.4 Parameters of Mathematical Model

Wakao *et al.* [1979] and Wakao and Kaguei [1982] recommended the following relationship for effective thermal conductivity of fluid and solid phases.

$$\text{Longitudinal Direction:} \quad k_{eff,f_z} = \varepsilon k_f + 0.5 \, \text{Pe} \, k_f \tag{3.68}$$

$$\text{Transverse Direction:} \quad k_{eff,f_r} = \varepsilon k_f + 0.1 \, \text{Pe} \, k_f \tag{3.69}$$

In these relationships the effect of tortuosity of the fluid and solid phases are neglected but theses are widely used for analysis. Kuwahara and Nakayama [1999] derived numerically the following relationship for longitudinal thermal dispersion.

$$\frac{(k_{dis})_z}{k_f} = 0.022 \frac{\text{Pe}_D^2}{(1-\varepsilon)} \qquad \text{for } (\text{Pe}_D < 10) \tag{3.70}$$

$$\frac{(k_{dis})_z}{k_f} = 2.7 \frac{\text{Pe}_D}{\varepsilon^{1/2}} \qquad \text{for } (\text{Pe}_D > 10) \tag{3.71}$$

Nakayama *et al.* [1996] numerically investigated thermal dispersion using two-dimensional periodic model of porous structure and recommended the following relationship for thermal dispersion in lateral direction.

$$\frac{(k_{dis})_r}{k_f} = 0.022 \frac{\text{Pe}_D^{1.7}}{(1-\varepsilon)^{1/4}} \qquad \text{for } (\text{Pe}_D < 10) \tag{3.72}$$

$$\frac{(k_{dis})_r}{k_f} = 0.052 (1-\varepsilon)^{1/2} \text{Pe}_D \qquad \text{for } (\text{Pe}_D > 10) \tag{3.73}$$

where the relationship $\text{Pe}_D = \text{Pe}(1-\varepsilon)^{1/2}$ and Pe is the based upon the size of structural unit that generally varies from 1mm to 1cm.

The interphase heat transfer is modeled as recommended by Wakao and Kaguei [1982], which is given by Equation 3.53. Kuwahara *et al*. [2001] derived the following relationship for interphase heat transfer.

$$Nu_p = \left(1 + \frac{4(1-\varepsilon)}{\varepsilon}\right) + \frac{1}{2}(1-\varepsilon)^{1/2} Re_p^{0.6} Pr^{1/3} \qquad \text{for } (0.2 < \varepsilon < 0.9) \qquad (3.74)$$

where Re_p is the particle based Reynolds number.

The interface area A_{fs} can be obtained from the specific surface area of the porous bed A_{IF} i.e. the surface area per unit bulk volume of the porous bed. It is expressed in terms of the particle diameter and porosity as Dullien [1979].

$$A_{If} = \frac{6(1-\varepsilon)}{d_p} \qquad (3.75)$$

The corresponding non-dimensional value is given by

$$A_f = \frac{6(1-\varepsilon)R}{d_p} \qquad (3.76)$$

3.7 NON-DIMENSIONALISATION OF GOVERNING EQUATIONS

The non-dimensional form of governing equations and mathematical models is discussed in this section. The use of non-dimensional groups makes the analysis easier and the results become independent of the individual parameters used. As an example the individual temperatures of hot and cold water are grouped together to make a non-dimensional temperature which varies from zero to unity. Here zero and unity refers respectively to the cold and cold hot water temperatures. Similarly, the length of a domain is made non-dimensional by dividing it by transverse dimension and time is made non-dimensional by multiplying it with the factor α/R^2 for pure conduction and α Pe $/R^2$ for advection-diffusion.

3.7.1 Unsteady State Conduction

Consider the unsteady state conduction equation in 2-D from as

$$(\rho c_p)\frac{\partial T}{\partial t} = k\left(\frac{\partial^2 T}{\partial x^2} + \frac{\partial^2 T}{\partial y^2}\right) \qquad (3.77)$$

Here the terms appearing the above equation have usual units. This equation is similar to diffusion through a solid phase, which does not have any pores in it. Since there is no velocity terms in this equation, Reynolds and Peclet numbers are not used. Using the

following non-dimensional groups for temperature, distance and time. Non-dimensional values are indicated by subscript *ND*.

T_{ND}: Dimensionless temperature, $(T\text{-}T_{\text{cold}})/(T_{\text{hot}}\text{-}T_{\text{cold}})$, where T_{hot}, T_{cold} are temperature assigned to stationary hot and cold fluids.

x_{ND}: Dimensionless distance, (x/Y), where Y is the transverse dimension.

t_{ND}: Dimensionless time, $\alpha t/Y^2$

The dimensional values are written in terms of non-dimensional values as

$$T = T_{ND}\left(T_{hot} - T_{cold}\right) + T_{cold} \tag{3.78}$$

$$x = x_{ND} Y \tag{3.79}$$

$$t = Y^2 t_{ND} / \alpha \tag{3.80}$$

Substituting the dimensional values in terms of non-dimensional values, we get

$$\rho c_p \left[\frac{\alpha}{Y^2}\frac{\partial T_{ND}}{\partial t_{ND}}\right]\left(T_{hot} - T_{cold}\right) = \frac{k}{Y^2}\left[\frac{\partial^2 T_{ND}}{\partial x^2{}_{ND}} + \frac{\partial^2 T_{ND}}{\partial y^2{}_{ND}}\right]\left(T_{hot} - T_{cold}\right) \tag{3.81}$$

Here the non-dimensional values are indicated by subscript *ND*. The non-dimensional energy equation thus becomes

$$\left[\frac{\partial T}{\partial t}\right] = \left[\frac{\partial^2 T}{\partial x^2} + \frac{\partial^2 T}{\partial y^2}\right] \tag{3.82}$$

3.7.2 Unsteady Advection Diffusion Equation

Consider 1-D advection diffusion equation as

$$\left(\rho c_p\right)\left(\frac{\partial T}{\partial t} + u\frac{\partial T}{\partial x}\right) = k\left(\frac{\partial^2 T}{\partial x^2}\right) \tag{3.83}$$

Here u is the velocity is m/s. All the variables have usual units.

The above equation can be non-dimensionlised by assuming a suitable scale for temperature, distance and time. The non-dimensional temperature and distance obtained as in pure conduction. The time and velocity can be non-dimensioned as below.

t_{ND}: Dimensionless time, $(t\ u/Y)$. From the definition of Peclet number, $\text{Pe} = uY/\alpha$, where α is the thermal diffusivity. Hence t: Dimensionless time is $\alpha t\text{Pe}/Y^2$

u_{ND}: Dimensionless velocity, (u /|u|). In two-dimensional field |u | is obtained as square root of sum of squares of velocities in x and y directions. For one-dimensional field it is equal to u itself.

The dimensional temperature and distance in terms of non-dimensional values is given by Equations 3.78, 3.79 and the corresponding time and velocity are substituted in terms of non-dimensional values as

$$t = Y^2 t_{ND} / \alpha \mathrm{Pe} \tag{3.84}$$

$$u = u_{ND} |u| \tag{3.85}$$

substituting the above values in Equation 3.83, we get

$$\rho c_p \left[\frac{\alpha \mathrm{Pe}}{Y^2} \frac{\partial T_{ND}}{\partial t_{ND}} + \frac{|u|}{Y} (\vec{u}) \frac{\partial T_{ND}}{\partial x_{ND}} \right] (T_{hot} - T_{cold}) = \frac{k}{Y^2} \frac{\partial^2 T_{ND}}{\partial x^2{}_{ND}} (T_{hot} - T_{cold}) \tag{3.86}$$

Canceling common factors and substituting |u | as $Pe\alpha/Y$, we get

$$\frac{\alpha \mathrm{Pe}}{Y^2} \rho c_p \left[\frac{\partial T_{ND}}{\partial t_{ND}} + (\vec{u}) \frac{\partial T_{ND}}{\partial x_{ND}} \right] = \frac{k}{Y^2} \frac{\partial^2 T_{ND}}{\partial x^2{}_{ND}} \tag{3.87}$$

from the definition of $\alpha = k/\rho c_p$ we get and canceling common terms.

$$\left[\frac{\partial T_{ND}}{\partial t_{ND}} + (\vec{u}) \frac{\partial T_{ND}}{\partial x_{ND}} \right] = \frac{1}{\mathrm{Pe}} \frac{\partial^2 T_{ND}}{\partial x^2{}_{ND}} \tag{3.88}$$

$$\left[\frac{\partial T}{\partial t} + (\vec{u}) \frac{\partial T}{\partial x} \right] = \frac{1}{\mathrm{Pe}} \frac{\partial^2 T}{\partial x^2} \tag{3.89}$$

In 2-D it can be written as:

$$\left[\frac{\partial T}{\partial t} + \vec{u} \frac{\partial T}{\partial x} + \vec{v} \frac{\partial T}{\partial y} \right] = \frac{1}{\mathrm{Pe}} \left(\frac{\partial^2 T}{\partial x^2} + \frac{\partial^2 T}{\partial y^2} \right) \tag{3.90}$$

and in vector form, it can be written as:

$$\frac{\partial T}{\partial t} + u.\nabla T = \frac{1}{\mathrm{Pe}} \left(\nabla^2 T \right) \tag{3.91}$$

3.7.3 1-Equation Model

Consider 1-D form of 1-equation model in Cartesian co-ordinates as

$$(\rho Cp)_m \frac{\partial T}{\partial t} + (\rho Cp)_f u \frac{\partial T}{\partial x} = k_{eff,m} \frac{\partial^2 T}{\partial x^2} \tag{3.92}$$

Here T and u are volume-averaged quantities. The parameters $\left(\left(\rho c_p\right)_m\right)$ and $\left(k_{eff,m}\right)$ are respectively the thermal storage capacity and effective thermal conductivity of the porous medium. The later being considered constant with respect to the spatial position. The non-dimensionalisation of the model is obtained as

$$\left[\left(\rho c_p\right)_m \frac{\alpha \mathrm{Pe}}{R^2}\frac{\partial T_{ND}}{\partial t_{ND}} + \left(\rho c_p\right)_f \frac{|u|}{R}(\vec{u})\frac{\partial T_{ND}}{\partial x_{ND}}\right]\left(T_{hot}-T_{cold}\right) = \frac{k_{eff,m}}{R^2}\frac{\partial^2 T_{ND}}{\partial x^2{}_{ND}}\left(T_{hot}-T_{cold}\right) \tag{3.93}$$

Here the non-dimensional model is obtained with respect to tube radius R.

As $|u| = Pe\ \alpha/R$, which results to

$$\left[\left(\rho c_p\right)_m \frac{\alpha \mathrm{Pe}}{R^2}\frac{\partial T_{ND}}{\partial t_{ND}} + \left(\rho c_p\right)_f \frac{\alpha \mathrm{Pe}}{R^2}(\vec{u})\frac{\partial T_{ND}}{\partial x_{ND}}\right]\left(T_{hot}-T_{cold}\right) = \frac{k_{eff,m}}{R^2}\frac{\partial^2 T_{ND}}{\partial x^2{}_{ND}}\left(T_{hot}-T_{cold}\right) \tag{3.94}$$

Canceling the common terms, we get

$$\alpha Pe\left(\rho c_p\right)_f\left[\frac{\left(\rho c_p\right)_m}{\left(\rho c_p\right)_f}\frac{\partial T}{\partial t} + (\vec{u})\frac{\partial T}{\partial x}\right] = k_{eff,m}\frac{\partial^2 T}{\partial x^2} \tag{3.95}$$

$$\text{substituting}\ \frac{1}{\beta_m} = \frac{\left(\rho c_p\right)_m}{\left(\rho c_p\right)_f} = \frac{\varepsilon\left(\rho c_p\right)_f + (1-\varepsilon)\left(\rho c_p\right)_s}{\left(\rho c_p\right)_f} = \varepsilon + \frac{(1-\varepsilon)}{\beta} \tag{3.96}$$

Hence, the above equation becomes

$$\left[\frac{1}{\beta_m}\frac{\partial T}{\partial t} + (\vec{u})\frac{\partial T}{\partial x}\right] = \frac{1}{\mathrm{Pe}}\left(\frac{k_{eff,m}}{k_f}\right)\frac{\partial^2 T}{\partial x^2} \tag{3.97}$$

$$\text{where}\ \lambda_m = \frac{\left(k_f\right)}{\left(k_m\right)} = \frac{\left(k_f\right)}{\left(\varepsilon\left(k_f\right) + (1-\varepsilon)\left(k_s\right)\right)} = \frac{1}{\varepsilon + \dfrac{(1-\varepsilon)}{\lambda}} \tag{3.98}$$

In 2-D form the 1-equation model becomes

$$\left[\frac{1}{\beta_m}\frac{\partial T}{\partial t} + (\vec{u})\frac{\partial T}{\partial x} + (\vec{v})\frac{\partial T}{\partial y}\right] = \frac{1}{\mathrm{Pe}}\left(\left(\frac{\left(k_{eff,m}\right)_x}{k_f}\right)\frac{\partial^2 T}{\partial x^2} + \left(\frac{\left(k_{eff,m}\right)_y}{k_f}\right)\frac{\partial^2 T}{\partial y^2}\right) \tag{3.99}$$

In vector form the equation becomes

$$\left[\frac{1}{\beta_m}\frac{\partial T}{\partial t} + \vec{u}.\nabla T\right] = \frac{1}{\mathrm{Pe}}\left(\nabla.\left(\frac{k_{eff,m}}{k_f}\right)\nabla T\right) \tag{3.100}$$

3.7.4 2-Equation Model

Consider the fluid or solid phase of a porous medium with interfacial heat transfer Q. The energy equation for the fluid phase and the solid phases in 1-D form is given as

$$Fluid: \varepsilon(\rho Cp)_f\left(\frac{\partial T}{\partial t}+u\frac{\partial T}{\partial x}\right)=k_{eff,f}\frac{\partial^2 T}{\partial x^2}+Q_{f\leftarrow s} \tag{3.101}$$

$$Solid \;\; : (1-\varepsilon)(\rho Cp)_s\frac{\partial T}{\partial t}=k_{eff,s}\frac{\partial^2 T}{\partial x^2}+Q_{f\rightarrow s} \tag{3.102}$$

In the above equation, $Q_{f\leftarrow s}$ represents heat transfer from solid to fluid phase. The heat flow from fluid to solid phase per unit volume of the porous medium is written as:

$$Q_{f\rightarrow s}=h\,A_{IF}\,(T_f - T_s) \tag{3.103}$$

Here it is assumed that fluid temperature is higher than solid phase. The Nusselt number can be defined as $Nu=\frac{hR}{k_f}$

A_{IF} is the specific surface area of the porous insert given by Equation 3.75

Substituting the non-dimensional parameters in this equation, we get,

$$Q=\mathrm{Nu}\frac{k}{R}A_{IF}(T_f-T_s)(T_{hot}-T_{cold}) \tag{3.104}$$

Using non-dimensionlisation of other parameters as discussed in last sections, the fluid phase energy equation thus becomes

$$\begin{aligned}\varepsilon(\rho c_p)_f\left[\frac{\alpha\mathrm{Pe}}{R^2}\frac{\partial T_{ND}}{\partial t_{ND}}+\frac{|u|}{R}(\vec{u})\frac{\partial T_{ND}}{\partial x_{ND}}\right](T_{hot}-T_{cold})&=\frac{k_{eff,f}}{R^2}\frac{\partial^2 T_{ND}}{\partial x^2{}_{ND}}(T_{hot}-T_{cold})\\&+\mathrm{Nu}\frac{k}{R}A_{IF}(T_s-T_f)(T_{hot}-T_{cold})\end{aligned} \tag{3.105}$$

Non-dimensional specific surface area is obtained as $A_f=A_{IF}R$, the above equation becomes

$$\begin{aligned}\varepsilon(\rho c_p)_f\left[\frac{\alpha\mathrm{Pe}}{R^2}\frac{\partial T_{ND}}{\partial t_{ND}}+\frac{|u|}{R}(\vec{u})\frac{\partial T_{ND}}{\partial x_{ND}}\right](T_{hot}-T_{cold})&=\frac{k_{eff,f}}{R^2}\frac{\partial^2 T_{ND}}{\partial x^2{}_{ND}}(T_{hot}-T_{cold})\\&+\mathrm{Nu}\frac{k}{R^2}A_F(T_s-T_f)(T_{hot}-T_{cold})\end{aligned} \tag{3.106}$$

Canceling the common terms, the non-dimensional fluid phase equation becomes

$$\varepsilon\left(\frac{\partial T}{\partial t}+u.\nabla T\right)=\frac{1}{\mathrm{Pe}}\left(\left(\frac{k_{eff,f}}{k_f}\right)\frac{\partial^2 T}{\partial x^2}\right)-\frac{1}{\mathrm{Pe}}\mathrm{Nu}\ A_f(\mathrm{T}_f-T_s) \tag{3.107}$$

In 2-D format it written as

$$\varepsilon\left(\frac{\partial T}{\partial t}+u\frac{\partial T}{\partial x}+v\frac{\partial T}{\partial y}\right)=\frac{1}{\mathrm{Pe}}\left(\left(\frac{\left(k_{eff,f}\right)_x}{k_f}\right)\frac{\partial^2 T}{\partial x^2}+\left(\frac{\left(k_{eff,f}\right)_y}{k_f}\right)\frac{\partial^2 T}{\partial y^2}\right)-\frac{1}{\mathrm{Pe}}\mathrm{Nu}\ A_f(\mathrm{T}_f-T_s) \tag{3.108}$$

in vector notation

$$\varepsilon\left(\frac{\partial T}{\partial t}+u.\nabla T\right)=\frac{1}{\mathrm{Pe}}\left(\nabla.\left(\frac{k_{eff,f}}{k_f}\right)\nabla T\right)-\frac{1}{\mathrm{Pe}}\mathrm{Nu}\ A_f(\mathrm{T}_f-T_s) \tag{3.109}$$

Here T stands for fluid phase temperature. The second term in RHS represents the energy leaving the fluid phase.

The solid phase energy equation can be non-dimensionlized by similar procedure, the solid phase Equation 3.102 becomes,

$$\begin{aligned}(1-\varepsilon)(\rho c_p)_s\left[\frac{\alpha\mathrm{Pe}}{R^2}\frac{\partial T_{ND}}{\partial t_{ND}}\right](T_{hot}-T_{cold})&=\frac{k_{eff,s}}{R^2}\frac{\partial^2 T_{ND}}{\partial x^2{}_{ND}}(T_{hot}-T_{cold})\\&+\mathrm{Nu}\frac{k_f}{R^2}A_F(T_f-T_s)(T_{hot}-T_{cold})\end{aligned} \tag{3.110}$$

Using the fluid phase thermal diffusivity, the above equation becomes,

$$\begin{aligned}(1-\varepsilon)(\rho c_p)_s\frac{k_f}{(\rho c_p)_f}\left[\frac{\mathrm{Pe}}{R^2}\frac{\partial T_{ND}}{\partial t_{ND}}\right](T_{hot}-T_{cold})&=\frac{k_s}{R^2}\frac{\partial^2 T_{ND}}{\partial x^2{}_{ND}}(T_{hot}-T_{cold})\\&+N\mathrm{u}\frac{k_f}{R^2}A_F(T_f-T_s)(T_{hot}-T_{cold})\end{aligned} \tag{3.111}$$

and using $\beta=\dfrac{(\rho c_p)_f}{(\rho c_p)_s}$, we get the non-dimensional solid phase energy equation as

$$(1-\varepsilon)\left[\frac{\partial T}{\partial t}\right]=\frac{\beta}{\lambda}\frac{1}{\mathrm{Pe}}\frac{\partial^2 T}{\partial x^2}+\frac{\mathrm{Nu}A_f\beta}{\mathrm{Pe}}(T_f-T_s) \tag{3.112}$$

The corresponding 2-D for of equation is

$$(1-\varepsilon)\left(\frac{\partial T}{\partial t}\right)=\frac{\beta}{\lambda}\frac{1}{\mathrm{Pe}}\left(\left(\frac{\left(k_{eff,s}\right)}{k_s}\right)\frac{\partial^2 T}{\partial x^2}+\left(\frac{\left(k_{eff,s}\right)}{k_f}\right)\frac{\partial^2 T}{\partial y^2}\right)+\frac{1}{\mathrm{Pe}}\mathrm{Nu}\ A_f\beta(\mathrm{T}_f-T_s) \tag{3.113}$$

and in vector notation, the equation is

$$(1-\varepsilon)\left(\frac{\partial T}{\partial t}\right)=\frac{\beta}{\lambda}\frac{1}{\mathrm{Pe}}\left(\nabla.\left(\frac{k_{eff,s}}{k_s}\right)\nabla T\right)+\frac{1}{\mathrm{Pe}}\mathrm{Nu}\,A_f\beta(\mathbf{T}_f-T_s) \tag{3.114}$$

3.8 CLOSURE

The thermal equilibrium and non-equilibrium models for heat transfer in porous medium are derived. The analysis is based upon local volume averaging over REV, of the conduction and the advection diffusion equations. The parameters such as thermal dispersion, tortuosity, interphase heat transfer and specific surface area so obtained are discussed and various relationships for these parameters are obtained from literature. The model is unsteady in nature in the sense that time scale is very important for the analysis. At steady state, the analysis becomes comparatively easy. The models can be used to evaluate step and frequency responses of the porous bed by considering widely varying properties of the porous medium. These results will then be compared with experimental data. Further all the discussed partial differential equations and mathematical model are converted to non-dimensional form.

The numerical discretization of the above models is discussed in the next chapter.

CHAPTER 4
NUMERICAL SIMULATION

4.1 INTRODUCTION

There has been a phenomenal increase in the use of computational methods for engineering applications in recent years. This is particularly true for problems in heat transfer and fluid flow. The complexity of the governing equations generally allows analytical solutions to be obtained only for very simple cases, making it necessary to use numerical techniques for most problems of practical interest.

Many important physical processes in nature are governed by partial differential equations (PDEs). PDEs of various types are encountered in fluid mechanics and heat transfer. PDEs for problems in heat transfer are classified into two domains (i) Equilibrium Problems in which a solution of a given PDE is desired in a closed domain subject to a prescribed set of boundary conditions. Equilibrium problems are boundary value problems. Examples of such problems include steady state temperature distributions and equilibrium stress distributions in solids. (ii) Marching or Propagation problems are transient or transient-like problems where the solution of a PDE is required on an open domain subject to a set of initial domain and marching direction for the case. Problems in this category are initial value or boundary value problems. Mathematically, these problems are governed by either hyperbolic or parabolic PDEs. Typical examples of marching problems include transient heat conduction, unsteady invisid flow and boundary-layer flow.

In this chapter, the problems marching in time as applicable to an energy storage system are solved by finite differences and compared with corresponding analytical solutions, which are either developed or available in literature. The problems include 2-D unsteady state conduction, 1-D and 2-D unsteady advection-diffusion in plain flow, and unsteady advection-diffusion in porous medium etc. The discretization of 1 and 2-equation models is also discussed. The method of discretization used in this analysis is finite differences. An introduction to this method for the present analysis is presented.

4.2 FINITE DIFFERENCE METHOD

The analytical solution of partial differential equations provides us with a closed-form expression, which depicts the variations of dependent variables at all points in the domain. However, these solutions are only available for a few simple cases. The finite difference solutions, on the other hand, provide us with values of the dependent variables at discrete points in the domain, which are known as grid points. This is done by replacing the derivatives of the governing equations by algebraic difference quotients. The system of algebraic equations is then solved for the dependent variables at the discrete grid points in the flow field.

Figure 4.1 shows a finite difference grid in x-y plane. The spacing of the grid points in x and y directions are uniform. These are given by Δx and Δy respectively. The grid points are identified by an index i which increases in the positive x-direction, and an index j which increases in the positive y-direction. If (i, j) is the index of point P in the Figure 4.1, then the point immediately to the right of P is designated as $(i+1, j)$ and the point immediately to the left is $(i-1, j)$. Similarly the point directly above is $(i, j+1)$ and the point below is $(i, j-1)$. The algebraic equations are obtained at all the grid points and subsequently solved by various numerical methods. In the next section, the use of finite difference methods for obtaining common algebraic difference quotients related to discretization of PDE is discussed.

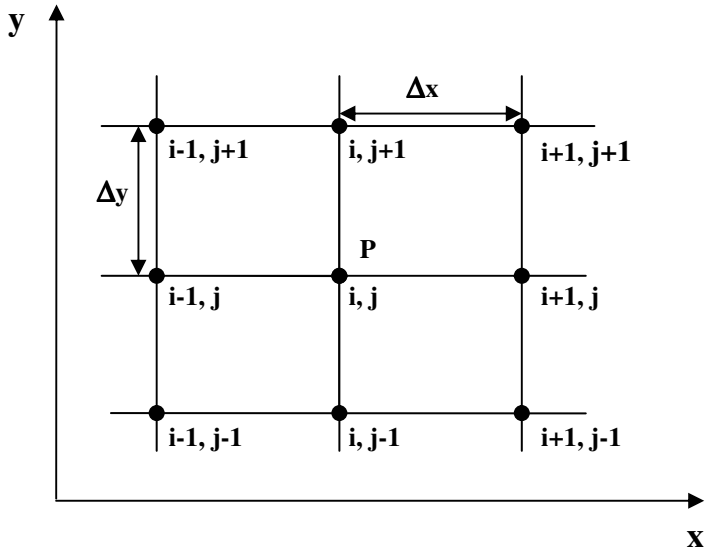

Figure 4.1: A finite difference grid.

4.2.1 Elementary Finite Difference Quotients

Finite difference representations of the derivatives are derived from Taylor series expansions. For example, if $u_{i,j}$ is the x-component of velocity at point (i, j) then the velocity $u_{i+1,j}$ at point $(i+1, j)$ can be expressed in the terms of Taylor series expansion about point (i, j) as

$$u_{i+1,j} = u_{i,j} + \left(\frac{\partial u}{\partial x}\right)_{i,j} \Delta x + \left(\frac{\partial^2 u}{\partial x^2}\right)_{i,j} \frac{(\Delta x)^2}{2} + \left(\frac{\partial^3 u}{\partial x^3}\right)_{i,j} \frac{(\Delta x)^3}{6} + \ldots\ldots\ldots\ldots \quad (4.1)$$

Mathematically, Equation 4.1 is an exact expression for $u_{i+1,j}$ if the series converges. In practice, Δx is small and any higher order term of Δx is smaller than Δx. Hence, for any function $u(x)$, Equation 4.1 can be truncated after a finite number of terms. For example, if the terms of magnitude $(\Delta x)^3$ and higher order are neglected, Equation 4.1 becomes

$$u_{i+1,j} \approx u_{i,j} + \left(\frac{\partial u}{\partial x}\right)_{i,j} \Delta x + \left(\frac{\partial^2 u}{\partial x^2}\right)_{i,j} \frac{(\Delta x)^2}{2} \quad (4.2)$$

Equation 4.2 is second order accurate, because the terms of order $(\Delta x)^3$ and higher have been neglected. If the terms of magnitude $(\Delta x)^2$ and higher order are neglected, Equation 4.2 becomes

$$u_{i+1,j} \approx u_{i,j} + \left(\frac{\partial u}{\partial x}\right)_{i,j} \Delta x \quad (4.3)$$

Equation 4.3 is first order accurate. In Equations 4.1 and 4.2, the neglected terms represent truncation error. Therefore the truncation errors for Equations 4.2 and 4.3 are

$$\sum_{n=3}^{\infty} \left(\frac{\partial^n u}{\partial x^n}\right)_{i,j} \frac{(\Delta x)^n}{n!} \quad (4.4)$$

and

$$\sum_{n=2}^{\infty} \left(\frac{\partial^n u}{\partial x^n}\right)_{i,j} \frac{(\Delta x)^n}{n!} \quad (4.5)$$

It is now clear that the truncation error can be reduced by retaining more terms in the Taylor series expansion of the corresponding derivative and reducing the magnitude of Δx.

Solving Equation 4.1 for $(\partial u / \partial x)_{i,j}$, we get

$$\left(\frac{\partial u}{\partial x}\right)_{i,j} = \frac{u_{i+1,j} - u_{i,j}}{\Delta x} - \left(\frac{\partial^2 u}{\partial x^2}\right)_{i,j} \frac{(\Delta x)}{2} - \left(\frac{\partial^3 u}{\partial x^3}\right)_{i,j} \frac{(\Delta x)^2}{6} + \ldots\ldots\ldots\ldots \quad (4.6)$$

or

$$\left(\frac{\partial u}{\partial x}\right)_{i,j} = \frac{u_{i+1,j} - u_{i,j}}{\Delta x} + O(\Delta x) \quad (4.7)$$

In Equation 4.7, the symbol O(Δx) stands for "terms of the order of Δx". The first order accurate difference representation for the derivative $(\partial u / \partial x)_{i,j}$ can be identified as first-order- forward difference.

Consider a Taylor series expression for $u_{i-1,j}$ about $u_{i,j}$

$$u_{i-1,j} = u_{i,j} + \left(\frac{\partial u}{\partial x}\right)_{i,j} (-\Delta x) + \left(\frac{\partial^2 u}{\partial x^2}\right)_{i,j} \frac{(-\Delta x)^2}{2} + \left(\frac{\partial^3 u}{\partial x^3}\right)_{i,j} \frac{(-\Delta x)^3}{6} + \ldots\ldots\ldots\ldots$$

or

$$u_{i-1,j} = u_{i,j} - \left(\frac{\partial u}{\partial x}\right)_{i,j} (\Delta x) + \left(\frac{\partial^2 u}{\partial x^2}\right)_{i,j} \frac{(\Delta x)^2}{2} - \left(\frac{\partial^3 u}{\partial x^3}\right)_{i,j} \frac{(\Delta x)^3}{6} + \ldots\ldots\ldots\ldots \quad (4.8)$$

Solving for $u_{i,j} - u_{i-1,j}$, we obtain

$$\left(\frac{\partial u}{\partial x}\right)_{i,j} = \frac{u_{i,j} - u_{i-1,j}}{\Delta x} + O(\Delta x) \quad (4.9)$$

Equation 4.9 is the first–order-backward difference expression for the derivative $(\partial u / \partial x)_{i,j}$ at grid point (i, j).

Subtracting Equation 4.8 from Equation 4.1

$$u_{i+1,j} - u_{i-1,j} = 2\left(\frac{\partial u}{\partial x}\right)_{i,j} (\Delta x) + \left(\frac{\partial^3 u}{\partial x^3}\right)_{i,j} \frac{(\Delta x)^3}{3} + \ldots\ldots\ldots \quad (4.10)$$

and solving for $(\partial u / \partial x)_{i,j}$, we obtain

$$\left(\frac{\partial u}{\partial x}\right)_{i,j} = \frac{u_{i+1,j} - u_{i-1,j}}{2(\Delta x)} + O(\Delta x)^2 \quad (4.11)$$

Equation 4.11 is the second-order-central difference for the derivative $(\partial u / \partial x)_{i,j}$ at grid point (i, j).

In order to obtain a finite difference expression for the second order partial derivative of $\left(\partial^2 u / \partial x^2\right)_{i,j}$, add Equations 4.1 and 4.8.

$$u_{i+1,j} + u_{i-1,j} = 2u_{i,j} + \left(\frac{\partial^2 u}{\partial x^2}\right)_{i,j} (\Delta x)^2 + \left(\frac{\partial^4 u}{\partial x 4}\right)_{i,j} \frac{(\Delta x)^4}{12} + \ldots\ldots\ldots\ldots \tag{4.12}$$

Solving for $\left(\partial^2 u / \partial x^2\right)_{i,j}$, we obtain

$$\left(\frac{\partial^2 u}{\partial x^2}\right)_{i,j} = \frac{u_{i+1,j} - 2u_{i,j} + u_{i-1,j}}{(\Delta x)^2} + O(\Delta x)^2 \tag{4.13}$$

Equation 4.13 is second-order-central difference for the derivative of $\left(\partial^2 u / \partial x^2\right)_{i,j}$ at grid point (i, j).

Hence, many other forms of finite difference approximations can be obtained for the derivatives, which constitute the governing equations for fluid flow and heat transfer. More details in this topic are available in Tannehill *et al*. [1997].

4.2.2 Finite Difference Quotients for Time Derivatives

Marching problems result in algebraic equations that usually can be solved one at a time. Consider Equation 4.14, the unsteady state conduction, the spatial derivative can be substituted by second order central difference scheme and time derivative with a forward difference scheme as

$$\frac{\partial T}{\partial t} = \alpha \frac{\partial^2 T}{\partial x^2} \tag{4.14}$$

$$\frac{T_{i,j}^{n+1} - T_{i,j}^{n}}{\Delta t} = \alpha \left(\frac{T_{i+1,j}^{n} + T_{i-1,j}^{n} - 2T_{i,j}^{n}}{\Delta x^2} \right) \tag{4.15}$$

The index for time appears in as a superscript, where n denotes condition at time t, $(n+1)$ denotes condition at time $(t+\Delta t)$. Thus, the dependent variable at time $(t+\Delta t)$ can be obtained explicitly from the results at time t. This is an example of explicit finite-difference method. This approach is very simple but requires for convergence the value of parameter $\alpha \Delta t / \Delta x^2 \leq 0.25$. This problem is overcome in Implicit Method. Consider the finite difference solution of Equation 4.14 in the following form

$$\frac{T_{i,j}^{n+1} - T_{i,j}^{n}}{\Delta t} = \alpha \left(\frac{T_{i+1,j}^{n+1} + T_{i-1,j}^{n+1} - 2T_{i,j}^{n+1}}{\Delta x^2} \right) \tag{4.16}$$

Here all the temperature values in RHS of above equation are evaluated at time ($t+\Delta t$). This approach converges for all the values of the parameter $\alpha \Delta t / \Delta x^2$. It requires more CPU time as temperatures at each node for ($n+1$) time level are to be assumed first and then to be converged using suitable convergence criterion.

4.2.3 Fluid Flow Modeling

The problems of fluid mechanics are more complex in character. The governing partial differential equations form a nonlinear system, which must be solved for the unknown pressures, densities, temperature and velocities. These equations have convective, diffusive and time dependent terms. A good finite difference scheme for fluid flow should have conservative property. It should preserve the integral conservation relations of the continuum. The quality of preserving the conservative property is of special importance in finite difference equations. Most methods of convective modeling are used for conservative form of partial differential equations. The finite difference scheme should also possess the transportive property to convect any perturbation only in the direction of the velocity. The use of central differencing, second order upwind and QUICK approaches for convective modeling are discussed in this section.

4.2.3.1 Upwind Differencing

The upwind method of discretization is very much necessary for convection-dominated flows in order to obtain numerically stable results. The upwind bias retains the transportive property of flow equation. One may use space centered differences which seems more accurate than upwind differencing, as indicated by the Taylor series expansion, but it is not more accurate if criteria for accuracy includes the transportive property as well. The central differencing is not suitable for convection terms as it fails to provide diagonal dominance in the coefficient matrix.

Consider the transport of a scalar function ϕ. For preserving the conservative property of ϕ, the convective term ($u.\nabla\phi$) can be written as $\nabla.(u\phi)$, since in most applications the flow

is incompressible and $\nabla.u = 0$. Figure 4.2 denotes the values of the variable ϕ along the x-direction. Consider three grid points having the values ϕ_L, ϕ_C and ϕ_R and the convecting velocities u_l and u_r, which are obtained by linear interpolation. The Second Order Upwind approximation for the convective term is stated as

$$\frac{\partial(u\phi)}{\partial x} = \frac{u_r\phi_r - u_l\phi_l}{\Delta x} \tag{4.17}$$

where
$$u_r = \frac{1}{2}(u_R + u_C) = \frac{1}{2}(u_{i+1} + u_i), u_l = \frac{1}{2}(u_L + u_C) = \frac{1}{2}(u_{i-1} + u_i) \tag{4.18}$$

The values of the transported scalar ϕ are taken to be adjacent upstream node values, where the upstream direction is based on sign of the linearly interpolated u-value. Thus

$$\phi_r = \phi_C = \phi_i \quad \text{for} \quad u_r > 0, \qquad \phi_r = \phi_R = \phi_{i+1} \quad \text{for} \quad u_r < 0 \tag{4.19}$$

$$\text{and } \phi_l = \phi_L = \phi_{i-1} \quad \text{for} \quad u_l > 0, \qquad \phi_l = \phi_C = \phi_i \quad \text{for} \quad u_l < 0 \tag{4.20}$$

Hence, the velocity is taken as the arithmetic mean of adjacent grid points and temperature is the next upstream point as shown in Figure 4.2. The corresponding first order upwind differencing is obtained if the velocity is taken as constant. It is written as

$$u\frac{\partial(\phi)}{\partial x} = u\frac{\phi_r - \phi_l}{\Delta x} \quad \text{for} \quad u > 0 \tag{4.21}$$

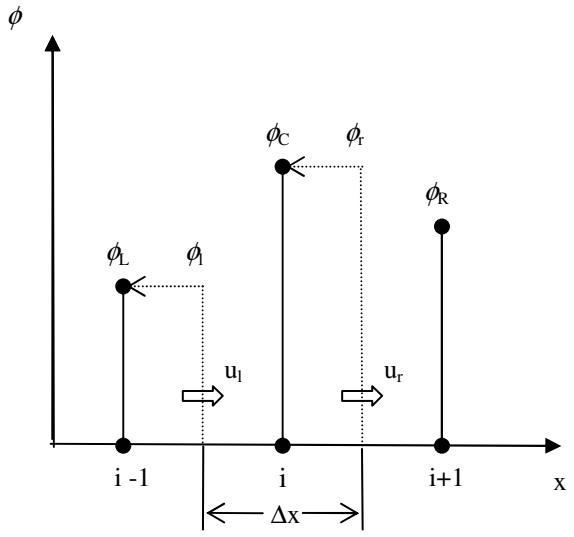

Figure 4.2: The cell values for upwind differencing when velocities are positive to right.

Hence, the upwind scheme uses the first order interpolation for u and convective parameters are of zeroth order based on upstream values of u_r and u_l. It reduces the artificial diffusion errors and improves its performance with respect to the classical first order upwind method. The upwind method maintains transportive property but suffer from false diffusion errors. The method has directional dependence, which gives stable convective sensitivity.

4.2.3.2 Quadratic Upstream Interpolation for Convective Kinematics (QUICK) Approach

Though the upwind approach has directional dependence, it suffers from a first order truncation error. In the context of control volume approach, the QUICK scheme of Leonard [1979] is simple. This approach is used for the governing equations in the conservative form. The QUICK approach possesses good accuracy and directional properties associated with stable convective sensitivity. It is a quadratic fit to the three node values ϕ_L, ϕ_C and ϕ_R . It is asymmetrically placed interpolation having upstream shifting. Hence, it is a three-point upstream-weighted quadratic interpolation. The QUICK approximation for the convection terms is based upon the first order interpolation of u linear interpolation of convective term corrected by a term proportional to upstream weighted curvature, Thus preserving the conservative property of ϕ. Figure 4.3 denotes the values of the transported variable ϕ along the x-direction. Consider three grid points having the convective parameters ϕ_L, ϕ_C and ϕ_R and the velocities u_l and u_r, which are obtained by linear interpolation between velocity node values. The QUICK approximation for the convective term is stated as

$$\frac{\partial(u\phi)}{\partial x} = \frac{u_r\phi_r - u_l\phi_l}{\Delta x} \tag{4.22}$$

$$\text{where } u_r = \frac{1}{2}(u_R + u_C) = \frac{1}{2}(u_{i+1} + u_i), u_l = \frac{1}{2}(u_L + u_C) = \frac{1}{2}(u_{i-1} + u_i) \tag{4.23}$$

$$\begin{aligned} \phi_r &= \frac{1}{2}(\phi_C + \phi_R) - \beta(\phi_L + \phi_R - 2\phi_C) \\ &= \frac{1}{2}(\phi_i + \phi_{i+1}) - \beta(\phi_{i-1} + \phi_{i+1} - 2\phi_i) \end{aligned} \tag{4.24}$$

$$\begin{aligned}\phi_l &= \frac{1}{2}(\phi_L + \phi_C) - \beta(\phi_{FL} + \phi_C - 2\phi_L) \\ &= \frac{1}{2}(\phi_{i-1} + \phi_i) - \beta(\phi_{i-2} + \phi_i - 2\phi_{i-1})\end{aligned} \tag{4.25}$$

where β is a constant which is selected suitably. The QUICK scheme has β = 1/8, while the value $\beta = 0$ corresponds to pure central differencing.

Figure 4.3 shows the basic interpolation scheme for ϕ_r, where u_r is positive to the right. Figure 4.4 shows the corresponding interpolation scheme for ϕ_l, when u_l is positive to the right. In the nodal form, the nodes *C*, *L*, *R* and *FL* refers to ith, (i-1) th, (i+1) th and (i-2) th node.

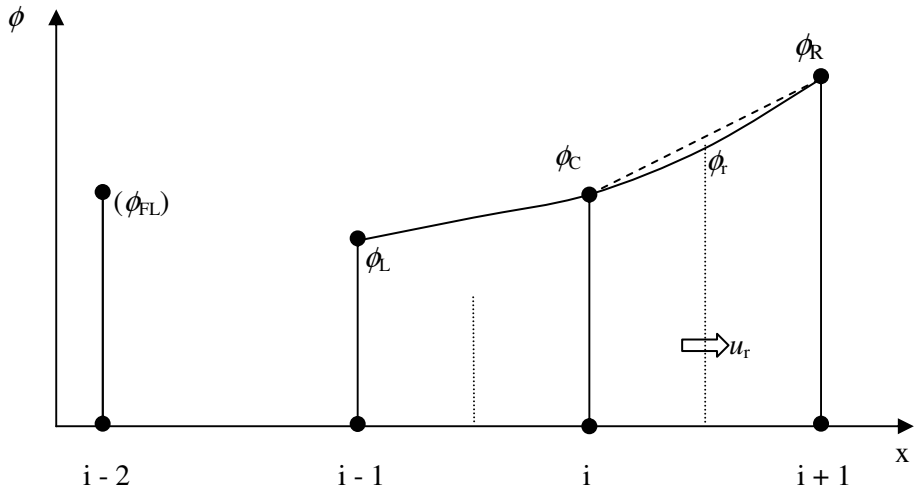

Figure 4.3: Quadratic upstream interpolation for ϕ_r

Substituting the value of β in Equations 4.24 and 4.25, the values of temperature at right and left walls become

$$T_r = \left(\frac{3}{4}\right)T_i + \left(\frac{3}{8}\right)T_{i+1} - \left(\frac{1}{8}\right)T_{i-1} \qquad \text{and} \qquad T_l = \left(\frac{3}{8}\right)T_i + \left(\frac{3}{4}\right)T_{i-1} - \left(\frac{1}{8}\right)T_{i-2} \tag{4.26}$$

In the next sections the solutions of various equations is obtained by finite difference and analytical methods and subsequently they are compared.

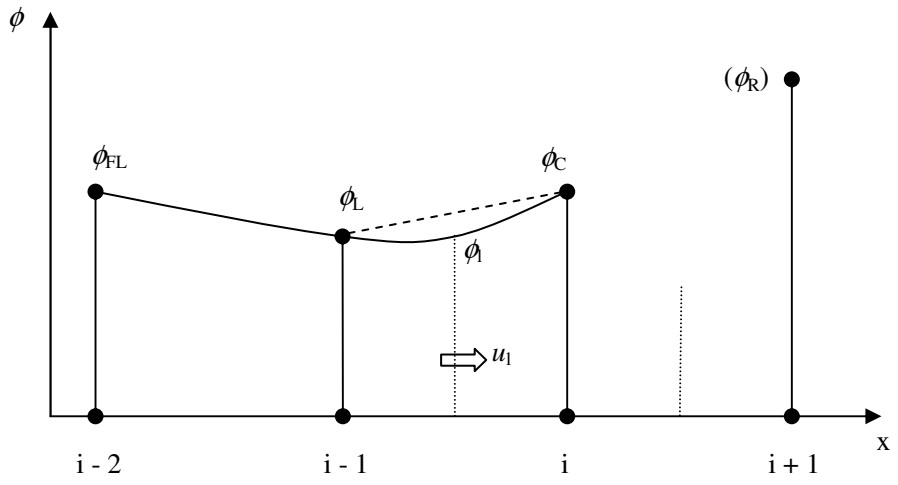

Figure 4.4: Quadratic upstream interpolation for ϕ_l

4.3 2-D UNSTEADY STATE CONDUCTION

An energy storage system constitutes a domain in which hot fluid enters an initially cold domain. The corresponding problem in pure conduction refers to a square domain whose one surface is exposed to hot surface and the thermal disturbances travel purely by conduction i.e. a temperature gradient exists in a material and energy transfers by the thermal motion of the microscopic particles of the solid material, see Figure 4.5. The corresponding analysis is done by a 2-D unsteady state conduction in a square domain given by the following PDE

$$\frac{\partial^2 T}{\partial x^2} + \frac{\partial^2 T}{\partial y^2} = \frac{1}{\alpha}\frac{\partial T}{\partial t} \tag{4.27}$$

where T is the temperature at any point in the domain, α the thermal diffusivity and t the time. The terms have usual units. The terms in LHS of the above equations indicates the diffusive transport of energy and RHS the unsteady local change in temperature. The solution of the problem can be obtained by numerical and analytical methods. The analytical solution is the exact solution whereas the numerical solution can approach the exact solution under ideal conditions. It is convenient to convert the above equation into non-dimensional form so that result is independent of individual values of the parameters. Temperature can be non-dimensionlized as $(T\text{-}T_{cold})/(T_{hot}\text{-}T_{cold})$ where T_{hot} and T_{cold} are temperature assigned to stationary hot and cold fluids. Time as $\alpha t/ L^2$, L being the dimension of square domain and distance as (x/L). The non-dimensional differential equation thus becomes

$$\frac{\partial^2 T}{\partial x^2}+\frac{\partial^2 T}{\partial y^2}=\frac{\partial T}{\partial t} \tag{4.28}$$

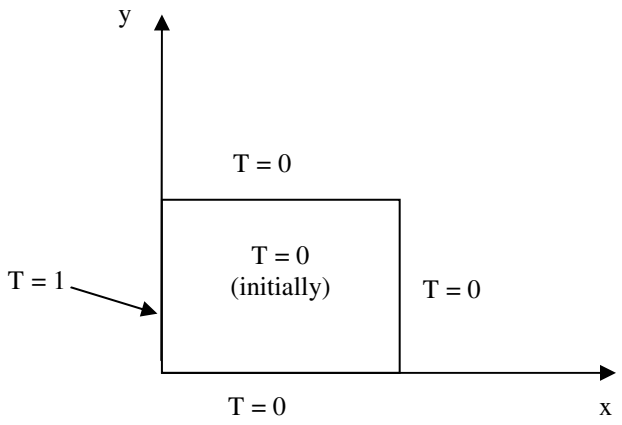

Figure 4.5: Unsteady heat conduction in a square domain.

This equation is subjected to following initial and boundary conditions.

Initial conditions

$$T = 0 \text{ in } 0 \le x \le 1 \text{ and } 0 \le y \le 1, \text{ for } t = 0 \tag{4.29}$$

Boundary conditions

$$T = 1 \text{ at } x = 0, \text{ for } t > 0 \tag{4.30}$$

$$T = 0 \text{ at } x = 1;\ T = 0 \text{ at } y = 0,\ 1 \text{ for } t > 0 \tag{4.31}$$

4.3.1 Analytical Solution

The principal of superposition is used to find the analytical solution, as a sum of a steady state solution(θ_s), that results as the time becomes very large, and a transient solution (θ) that dies out at large times.

Thus, we can write

$$T(x, y, t) = \theta_s(x, y) + \theta(x, y, t) \tag{4.32}$$

Substituting this decomposition into the governing PDE, we find that because θ_s is independent of time

$$\frac{\partial^2 \theta_s}{\partial x^2} + \frac{\partial^2 \theta_s}{\partial y^2} = 0 \tag{4.33}$$

Boundary conditions are

$$\theta_s = 1 \text{ at } x = 0,\ \theta_s = 0 \text{ at } x = 1;\ \theta_s = 0 \text{ at } y = 0,\ 1 \tag{4.34}$$

and unsteady state partial differential equation

$$\frac{\partial^2 \phi}{\partial x^2} + \frac{\partial^2 \phi}{\partial y^2} = \frac{\partial \phi}{\partial t} \tag{4.35}$$

with initial condition in the domain

$$\phi = -\theta_s(x, y) \text{ for } t = 0, \text{ in the region} \tag{4.36}$$

and boundary conditions

$$\phi = 0 \text{ at } x = 0,1;\ \phi = 0 \text{ at } y = 0,1, \quad \text{for } t > 0 \tag{4.37}$$

The solution of steady state problem is discussed first.

Applying separation of variables technique to Equation 4.33 by assuming that the desired solution can be expressed as product of two functions, one of which depends only on *x*, while other depends only on *y* as

$$\theta_{\text{steady}}(x,y) = X(x)^*\ Y(y) \tag{4.38}$$

If a solution of this form can be found that satisfies both the Equation 4.33 and the boundary conditions given by Equation 4.34, then it can be shown that this is the one and only solution to the problem. After this form of the temperature is substituted into Equation 4.33, two differential equations are obtained.

$$\frac{\partial^2 X}{\partial x^2} - \lambda^2 X = 0 \tag{4.38}$$

$$\frac{\partial^2 Y}{\partial y^2} + \lambda^2 Y = 0 \tag{4.39}$$

λ^2 arises from the separation process and must be determined as part of solution to the problem. The solution of two differential equation may be written as

$$Y(\gamma) = A\cos(\lambda y) + B\sin(\lambda y) \quad \text{and} \quad X(x) = CExp(-\lambda x) + DExp(\lambda x) \tag{4.40}$$

Any linear combination of the above equation corresponding to different values of (λ) will satisfy Equation (4.33)

$$\theta_s(x, y) = [A\cos(\lambda y) + B\sin(\lambda y)]X[C\,Exp(-\lambda x) + D\,Exp(\lambda x)] \tag{4.41}$$

$\lambda = n\pi$, where n = 1, 2, 3-------

using the boundary conditions as given by Equation 4.34, we get the analytical solution of steady state problem as

$$\theta_{steady}(x,y) = \sum_{n=1}^{\infty} (-2)\,X\,\frac{(\cos(n\pi)-1)}{(1-Exp(2n\pi))X(n\pi)}\,X\,Sin(n\pi y)\,X\,(Exp(n\pi x)-Exp(n\pi)X(2-x))) \quad (4.42)$$

Consider the unsteady part as given by Equation 4.35

$\phi(x, y, t)$ can be written as product of function $\phi(x, t)$ and $\phi(y, t)$ such that

$$\phi(x,t) = Exp(-\lambda^2 t)\,[A\sin(\lambda x) + B\cos(\lambda x)] \quad (4.43)$$

$$\phi(y,t) = Exp(-\beta^2 t)\,[A'\sin(\beta y) + B'\cos(\beta y)] \quad (4.44)$$

$$\phi(x,y,t) = Exp(-(\lambda^2+\beta^2)t)\,[A\sin(\lambda x) + B\cos(\lambda x)]\,[A'\sin(\beta y) + B'\cos(\beta y)] \quad (4.45)$$

Using the boundary conditions as given by Equation 4.37

$$\phi(x,y,t) = \sum\sum Exp\,[-(\lambda^2 + m^2\pi^2)]^2 t \quad X A_{mn} \sin m(x\pi \sin n(y\pi) \quad (4.46)$$

Further using the initial condition as given by Equation 4.36, we get

$$-\theta_s(x,y) = \sum_{m=1}^{\infty}\sum_{n=1}^{\infty} A_{mn}\sin(m\pi x)\sin(n\pi y) \quad (4.47)$$

The value of the constant A_{mn} using the condition $\int_0^1 \sin^2 m\pi x = \frac{1}{2}$, we get

$$A_{mn} = 4X\int_0^1\int_0^1 [(-\theta_{steady}(x,y))]\,X\sin(m\pi x)\,X\sin(n\pi y)dxdy \quad (4.48)$$

Substituting for $\theta_s(x, y)$ from Equation 4.42, A_{mn} is given

$$A_{mn} = 8\sum_{l=1}^{\infty}\frac{(\cos(l\pi)-1)}{l\pi}X\frac{1}{1-Exp(2l\pi)}$$
$$X\int_0^1 \sin(l\pi y)X\sin(m\pi y)dy\;X\int_0^1 \sin(n\pi x)\,X\,(Exp(l\pi x)-Exp((l\pi)\,X\,(2-x))dx \quad (4.49)$$

Therefore, the unsteady part of the equation from Equation 4.46 is given by

$$\phi_{unsteady}(x,y,t) = \sum_{m=1}^{\infty}\sum_{n=1}^{\infty} Exp\left[-(n^2+m^2)\pi^2 t\right]X\,A_{mn}X\sin(m\pi x)\,X\sin(n\pi y) \quad (4.50)$$

Substituting for Equations 4.50 and 4.42 in Equation 4.32, the complete analytical solution of Equation 4.28 is obtained.

4.3.2 Finite Difference Solution

The finite difference solution of Equation 4.28 is obtained by using implicit format for time derivative and central difference for spatial derivatives as

$$\frac{T_{i,j} - U_{i,j}}{\Delta t} = \left(\frac{T_{i+1,j} + T_{i-1,j} - 2T_{i,j}}{\Delta x^2} + \frac{T_{i,j+1} + T_{i,j-1} - 2T_{i,j}}{\Delta y^2} \right) \tag{4.51}$$

and $$T_{i,j}\left(1 + 2\Delta t\left(\frac{1}{\Delta x^2} + \frac{1}{\Delta y^2} \right) \right) = U_{i,j} + \left(\frac{T_{i+1,j} + T_{i-1,j}}{\Delta x^2} + \frac{T_{i,j+1} + T_{i,j-1}}{\Delta y^2} \right) \tag{4.52}$$

Here T refers to temperature at time $(t+\Delta t)$ and U the temperature at (t). The grid size in x and y direction is taken to be same. The governing algebraic equations are written at each grid point and are solved by Gauss Seidel iterations and unsteady solution is obtained. The space grid size used is 101 x 101 and number of time steps used are 1001.

4.3.3 Comparison of analytical and finite difference solutions

The temperatures at various locations are plotted using analytical and finite difference solutions as discussed in sections 4.3.1 and 4.3.2 respectively. The unsteady temperatures are plotted as a function of time at various locations. The temperature at a location increases as a function of time and distance from heat influx plane and subsequently reaches a steady state. Figure 4.6 shows the comparison at various locations of a square domain. Figure 4.6(a) shows the comparison of temperature build-ups at locations (*0.25*, *0.25*) and (*0.5*, *0.5*). The steady state temperatures at these locations are 0.43 and 0.25 respectively. Similarly, in Figure 4.6(b), the comparison at locations (*0.1*, *0.1*) and (*0.75*, *0.75*) is shown and the corresponding steady state temperatures are 0.49 and 0.07 respectively. The temperature profiles predicted by finite differences and analytical approaches show a good comparison indicating thereby the accuracy of the finite difference method.

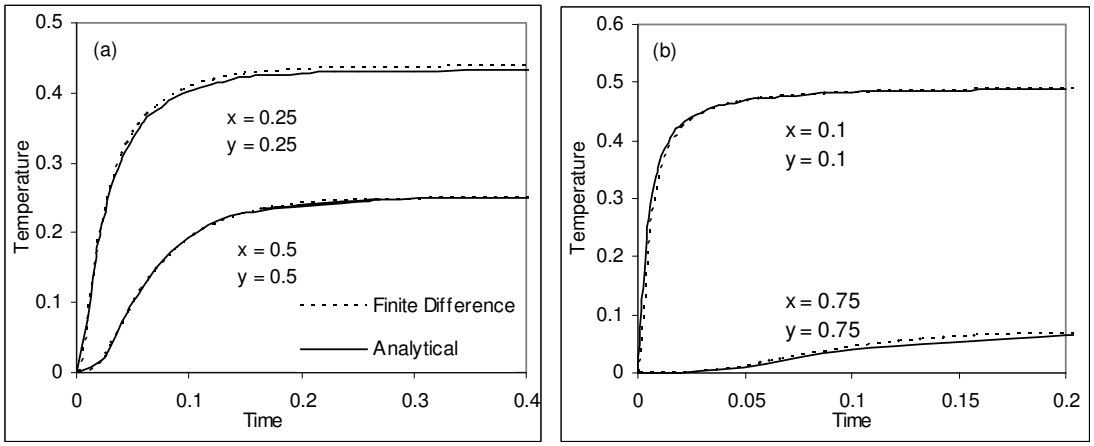

Figure 4.6: Comparison of finite difference and analytical solutions for unsteady state conduction in a square domain.

4.4 1-D ADVECTION-DIFFUSION EQUATION

Consider now the case when the hot fluid flows through an initially cold domain with a velocity u, the corresponding energy equation in 1-D format is

$$\left(\rho c_p\right)\left(\frac{\partial T}{\partial t}+u\frac{\partial T}{\partial x}\right)=k\left(\frac{\partial^2 T}{\partial x^2}\right) \tag{4.53}$$

The first term in LHS represents the partial derivative of temperature with respect to time, the second term represents the convective transport of energy and the right hand side represents the diffusive transport of energy.

The corresponding equation in non-dimensional form is

$$\frac{\partial T}{\partial t}+u.\nabla T=\frac{1}{\mathrm{Pe}}\left(\frac{\partial^2 T}{\partial x^2}\right) \tag{4.54}$$

Here u is dimensionless velocity, T is dimensionless fluid temperature, Pe is the Peclet number and t is dimensionless time.

The initial and boundary conditions are

$$T=0 \text{ in } 0\le x<\infty, \text{ for } t=0 \tag{4.55}$$

$$T=1 \text{ at } x=0;\ T\to 0 \text{ as } x\to\infty \text{ , for } t>0 \tag{4.56}$$

Like 2-D Unsteady state Conduction Equation, this equation is solved by two approaches namely the analytical and the finite differences approach.

4.4.1 Analytical Solution

Using transformation

$$T = exp\left(-\left(-\mathrm{Pe}\,\frac{x}{2}\right)+0.25\mathrm{Pe}\,t\right)U \tag{4.57}$$

Equation 4.54 becomes

$$\frac{1}{\mathrm{Pe}}\frac{\partial^2 U}{\partial x^2}=\frac{\partial U}{\partial t} \tag{4.58}$$

This is an unsteady conduction equation over a semi-infinite region, having the following initial and boundary conditions

$$U = 0 \text{ in } 0 \le x < \infty, \text{ for } t = 0 \tag{4.59}$$

$$U = \mathrm{Exp}\ (\mathrm{Pe}\ t/4) \text{ at } x = 0;\ \boldsymbol{U} \to 0 \text{ as } x \to \infty, \text{ for } t > 0 \tag{4.60}$$

Here the source at $x = 0$ contains a time varying factor.

Consider the equation

$$\frac{\partial^2 \phi}{\partial u^2} = \mathrm{Pe}\frac{\partial \phi}{\partial t} \tag{4.61}$$

with the conditions

$$\phi = 0 \text{ in } 0 \le x < \infty, \text{ for } t = 0 \tag{4.62}$$

$$\phi = 1 \text{ at } x = 0;\ \phi \to 0 \text{ as } x \to \infty,\ \text{for } t > 0 \tag{4.63}$$

The solution of Equation 4.58 is obtained in terms of the solution of Equation 4.61 by using Duhamel's Principle as, (Ozisik [1980]).

$$U(x,t) = \int_{\tau=0}^{t} f(\tau)\frac{\partial \phi(x,t-\tau)}{\partial t}\partial\tau \tag{4.64}$$

where

$$\begin{aligned}\phi(x,t) &= 1 - erf\left(\frac{x}{\sqrt{4\alpha t}}\right)\\ &= erfc\left(\frac{x}{\sqrt{4\alpha t}}\right)\\ &= \frac{2}{\sqrt{\pi}}\int_{\frac{x}{\sqrt{4\alpha t}}}^{\infty} Exp\left(-\xi^2\right)d\xi\end{aligned} \tag{4.65}$$

$\frac{2}{\sqrt{\pi}}\int_{0}^{\frac{x}{\sqrt{4\alpha t}}} Exp\left(-\xi^2\right)d\xi$ is called error function of argument $\frac{x}{\sqrt{4\alpha t}}$ and its solution is expressed in the form $T(x,t) = erf\left(\frac{x}{\sqrt{4\alpha t}}\right)$

which gives $U(x,t)$ as

$$U(x,t) = \frac{2}{\sqrt{\pi}}\int_{\frac{x}{\sqrt{4\alpha t}}}^{\infty} Exp\left(-\xi^2\right) * Exp\left(\frac{\mathrm{Pe}}{4}\left(t - \frac{x^2}{4\alpha\xi^2}\right)\right)d\xi \tag{4.66}$$

Substituting the above equation in Equation 4.57, temperature is obtained at the as function of x and t.

4.4.2 Finite Difference Solution

The partial differential Equation 4.54 can be solved by an implicit form of finite difference method. The second order partial derivative is approximated by the central difference scheme. The convective term ($u.\nabla T$) is represented in the present study by two methods namely the Upwind and the QUICK approach as discussed in Section 4.2.3.

4.4.2.1 Upwind Formulation

Here The Upwind formulation, as given in section 4.2.3.1, is used for discretizing the convective term in Equation 4.54. Using implicit formulation for time derivative, central difference formulation for the second order partial derivative and Upwind formulation for convective term, Equation 4.54 becomes

$$\frac{T_i - U_i}{\Delta t} + \frac{u_r T_i - u_l T_{i-1}}{\Delta x} = \frac{1}{\mathrm{Pe}}\left(\frac{T_{i+1} + T_{i-1} - 2T_i}{\Delta x^2}\right) \tag{4.67}$$

T and U are temperatures calculated at times (n+1) and (n) respectively. Upon rearrangement the above equation results to

$$T_i\left[1 + \frac{\Delta t}{\Delta x}u_r + 2\frac{\Delta t}{\Delta x^2}\frac{1}{\mathrm{Pe}}\right] = U_i + \frac{\Delta t}{\Delta x^2}\frac{1}{\mathrm{Pe}}\left(T_{i+1} + T_{i-1}\right) + \frac{\Delta t}{\Delta x}u_l T_{i-1} \tag{4.68}$$

for a constant known velocity, the terms

$u_r = u_l = u$ = constant everywhere hence the above equation becomes

$$T_i\left[1+\frac{\Delta t}{\Delta x}u\ +2\frac{\Delta t}{\Delta x^2}\frac{1}{\mathrm{Pe}}\right]=U_i+\frac{\Delta t}{\Delta x^2}\frac{1}{\mathrm{Pe}}\left(T_{i+1}+T_{i-1}\right)+\frac{\Delta t}{\Delta x}u\ T_{i-1} \tag{4.69}$$

4.4.2.2 QUICK Formulation

Using the QUICK formulation, as given in section 4.2.3.2 for the convection term, central differencing for the conduction term and implicit time differencing for time derivative Equation 4.54 becomes

$$\frac{T_i-U_i}{\Delta t}+\frac{u_rT_r-u_lT_l}{\Delta x}=\frac{1}{\mathrm{Pe}}\left(\frac{T_{i+1}+T_{i-1}-2T_i}{\Delta x^2}\right) \tag{4.70}$$

using the formulation for T_r and T_l as given by Equation 4.26,we get

$$\frac{T_i-U_i}{\Delta t}+\frac{u_r\left(\left(\frac{3}{4}\right)T_i+\left(\frac{3}{8}\right)T_{i+1}-\left(\frac{1}{8}\right)T_{i-1}\right)-u_l\left(\left(\frac{3}{8}\right)T_i+\left(\frac{3}{4}\right)T_{i-1}-\left(\frac{1}{8}\right)T_{i-2}\right)}{\Delta x}=\frac{1}{\mathrm{Pe}}\left(\frac{T_{i+1}+T_{i-1}-2T_i}{\Delta x^2}\right) \tag{4.71}$$

which upon rearrangement gives

$$\begin{aligned}T_i\left[1+\frac{3}{4}\frac{\Delta t}{\Delta x}u_r-\frac{3}{8}\frac{\Delta t}{\Delta x}u_l+2\frac{\Delta t}{\Delta x^2}\frac{1}{\mathrm{Pe}}\right]&=U_i+\frac{\Delta t}{\Delta x^2}\frac{1}{\mathrm{Pe}}\left(T_{i+1}+T_{i-1}\right)\\&\quad-\frac{3}{8}\frac{\Delta t}{\Delta x}u_lT_{i+1}+\frac{\Delta t}{\Delta x}\left(\frac{1}{8}u_r-\frac{3}{4}u_l\right)T_{i-1}-\frac{1}{8}\frac{\Delta t}{\Delta x}u_lT_{i-2}\end{aligned} \tag{4.72}$$

Using the condition of constant velocity, the above equation becomes

$$T_i\left[1+\frac{3}{8}\frac{\Delta t}{\Delta x}u+2\frac{\Delta t}{\Delta x^2}\frac{1}{Pe}\right]=U_i+\frac{\Delta t}{\Delta x^2}\frac{1}{Pe}\left(T_{i+1}+T_{i-1}\right)-\frac{3}{8}\frac{\Delta t}{\Delta x}uT_{i+1}+\frac{\Delta t}{\Delta x}\left(-\frac{5}{8}u\ \right)T_{i-1}-\frac{1}{8}\frac{\Delta t}{\Delta x}u\ T_{i-2} \tag{4.73}$$

The algebraic equations resulting from Equations 4.69 and 4.73 are solved by Gauss-Seidel iterations. The temperature field is obtained for a domain of unit length on a grid size of 101, the time step for each calculation being 0.01% of the total time. The Peclet number is varied from 1 to 1000.

4.4.3 Comparison of Upwind and QUICK approaches with Analytical solution

A comparison of the Upwind and the QUICK approaches for the approximation of the convection terms has been carried out with the analytical solution for Pe = 7, 100, 200, 500, 700 and 1000. The comparison is shown in Figure 4.7. The temperature profiles with respect to the longitudinal coordinate are drawn at various points of time, in the dimensionless form. It is to be noted that the length is scaled by the channel height Y and the time by Y^2/α;

specifically the length and time scales are independent of the fluid velocity. Figure 4.7(a) shows the temperature profiles at Pe = 7, for a longitudinal dimension of 1.0 using the upwind, QUICK and analytical methods. It shows the temperature profile at $t = 0.021$, at this time it has reached $x = 1$. The three figures are overlapping and so the upwind and Quick approaches are similar to the analytical solution for the low Pe of 7.0. Figure 4.7(b) shows the corresponding profiles for Pe=100 at $t = 0.0057$. This figure shows that by using QUICK the solution nearly matches the analytical solution whereas the upwind approach deviates from the analytical solution. It is initially slower and faster later on. The same trend is seen at Pe = 200 in Figure 4.7(c) and the corresponding time is 0.00325 The QUICK approach matches well with the analytical solution. Almost identical trends are seen in Figures 4.7(d) and (e) at Pe = 500 and 700 respectively. It shows that QUICK is very accurate under these conditions. At Pe = 1000, there is only a small deviation of QUICK from the analytical solution near $x = 1$, see Figure 4.7(f). It is clear that the QUICK approach of convective discretization is accurate and matches well with the analytical solution. It can thus be used to model 2-D convection –diffusion equation for various applications.

A comparison of upwind and QUICK methods can be carried out in the following manner. Both methods introduce false diffusion to eliminate oscillations inherent to central differencing. In this respect, they stabilize the calculation. Being a higher order method, QUICK has lower discretization error and hence a smaller false diffusion. Thus, it matches the analytical solution better than upwind.

At lower Peclet numbers, convective terms are themselves unimportant when compared to the diffusion terms. Hence, the nature of discretization of the convective terms is unimportant. Another issue discussed in Leonard [1979] is the response of the two methods to grid refinement. Both methods strictly converge to exact solution at the limit of the zero grid size. However, there are differences in their sensitivity to grid refinement, QUICK being a better approximation of the convective terms than upwind. Thus on a fairly course meshes as well, QUICK performs better than upwind. It is clear that the QUICK approach of convective discretization is accurate and matches well with the analytical solution. It can thus be used to model 2D convection–diffusion equation for various applications.

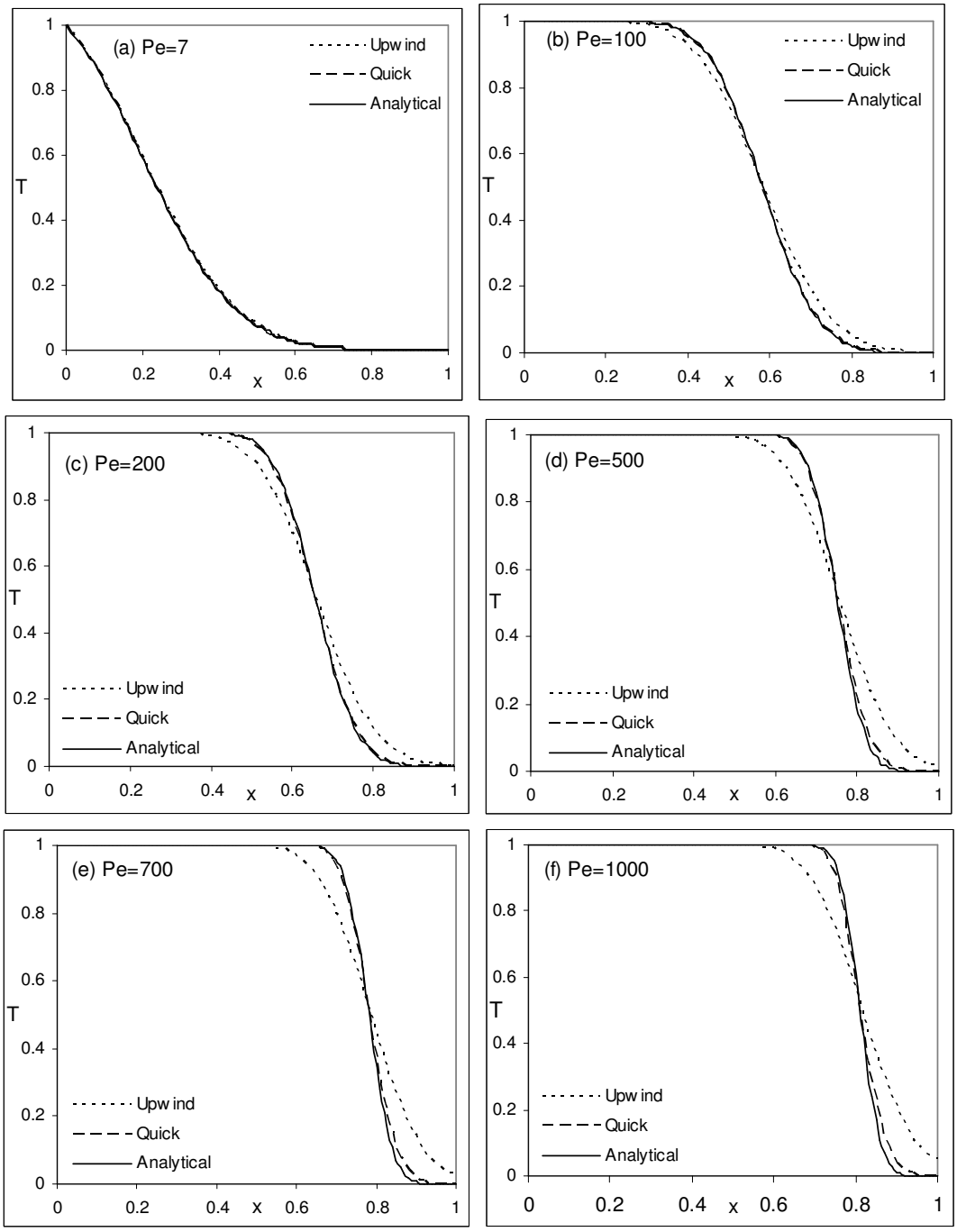

Figure 4.7: Comparison of Upwind, Quick and analytical solutions for 1-D Unsteady Convection (a) $t = 0.021$, (b) $t = 0.0057$, (c) $t = 0.00325$, (d) $t = 0.0015$, (e) $t = 0.001$ and (f) $t = 0.00081$.

4.5 2D ADVECTION-DIFFUSION EQUATION

The comparison of Upwind and QUICK approaches is done for a benchmark problem involving thermal mixing as shown in Figure 4.8. Consider 2-D advection diffusion equation in non-dimensional form as

$$\frac{\partial T}{\partial t} + u\frac{\partial T}{\partial x} + v\frac{\partial T}{\partial y} = \frac{1}{\mathrm{Pe}}\left(\frac{\partial^2 T}{\partial x^2} + \frac{\partial^2 T}{\partial y^2}\right) \tag{4.74}$$

Here u is dimensionless velocity in longitudinal direction and v is the corresponding velocity in transverse direction, T is dimensionless fluid temperature, Pe is the Peclet number and t is dimensionless time. The first term represents the partial derivative of temperature with respect to time, the second and third terms represent the convection transport of energy in longitudinal and lateral directions respectively and the right hand side represents the diffusion energy transfer.

A brief study of two-dimensional flow at an angle of 45 ^{o} to the grid is considered here. This configuration along with the thermal boundary conditions is shown in Figure 4.8. A thermal mixing layer forms along the diagonal parallel to the flow, and its thickness δ decreases with increasing Peclet number. For an unbounded flow problem, the steady state temperature distribution along the diagonal normal to the mean flow is obtained by solving the equation (Muralidhar *et al.* [1993]).

$$u\frac{\partial T}{\partial x} + v\frac{\partial T}{\partial y} = \frac{1}{\mathrm{Pe}}\left(\frac{\partial^2 T}{\partial x^2} + \frac{\partial^2 T}{\partial y^2}\right) \tag{4.75}$$

where x and y are measured parallel and perpendicular to the flow, respectively. The solution using Upwind and QUICK schemes is compared with analytical solution. This problem is solved to show the advantages of the later approach. The analytical solution of the above problem is obtained as

$$T(x,y) = \frac{1}{2}\left\{1 + erf\left[\frac{y}{2}\left(\frac{\mathrm{Pe}}{x}\right)^{0.5}\right]\right\} \tag{4.76}$$

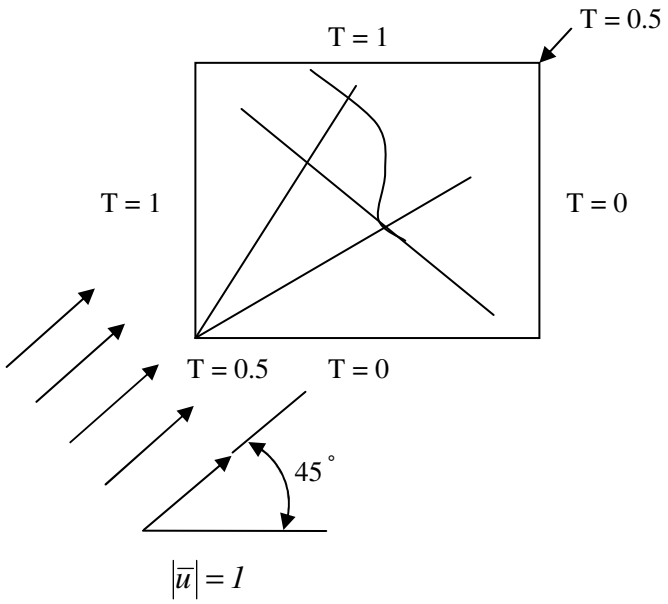

Figure 4.8: Configuration of flow in the study of flow-orientation effect.

Upwind and QUICK discretization is obtained as

Upwind Formulation

$$\frac{u_r T_{i,j} - u_l T_{i-1,j}}{\Delta x} + \frac{v_r T_{i,j} - v_l T_{i,j-1}}{\Delta y} = \frac{1}{\mathrm{Pe}}\left(\frac{T_{i+1,j} + T_{i-1,j} - 2T_{i,j}}{\Delta x^2} + \frac{T_{i,j+1} + T_{i,j-1} - 2T_{i,j}}{\Delta y^2} \right) \tag{4.77}$$

QUICK Formulation

$$\begin{aligned} &\frac{u_r\left(\left(\frac{3}{4}\right)T_{i,j} + \left(\frac{3}{8}\right)T_{i+1,j} - \left(\frac{1}{8}\right)T_{i-1,j}\right) - u_l\left(\left(\frac{3}{8}\right)T_{i,j} + \left(\frac{3}{4}\right)T_{i-1,j} - \left(\frac{1}{8}\right)T_{i-2,j}\right)}{\Delta x} \\ &+ \frac{v_r\left(\left(\frac{3}{4}\right)T_{i,j} + \left(\frac{3}{8}\right)T_{i,j+1} - \left(\frac{1}{8}\right)T_{i,j-1}\right) - v_l\left(\left(\frac{3}{8}\right)T_{i,j} + \left(\frac{3}{4}\right)T_{i,j-1} - \left(\frac{1}{8}\right)T_{i,j-2}\right)}{\Delta y} \\ &= \frac{1}{\mathrm{Pe}}\left(\frac{T_{i+1} + T_{i-1} - 2T_i}{\Delta x^2} + \frac{T_{i,j+1} + T_{i,j-1} - 2T_{i,j}}{\Delta y^2} \right) \end{aligned} \tag{4.78}$$

and
$$u_r = u_l = v_r = v_l = 0.5 \tag{4.79}$$

A comparison of three approaches is obtained at Pe = 1000. A grid 101 x 101 over a square region of 5 x 5 is solved. Figure 4.9 shows the comparison of the three approaches. The sharp temperature profile expected from the analytical solution is realized in QUICK solution. The

Upwind solution shows considerable transverse broadening. Hence, QUICK approach gives accurate solution of the benchmark problem. This method of convective modeling is used in discretization of 1 and 2-equtaion models.

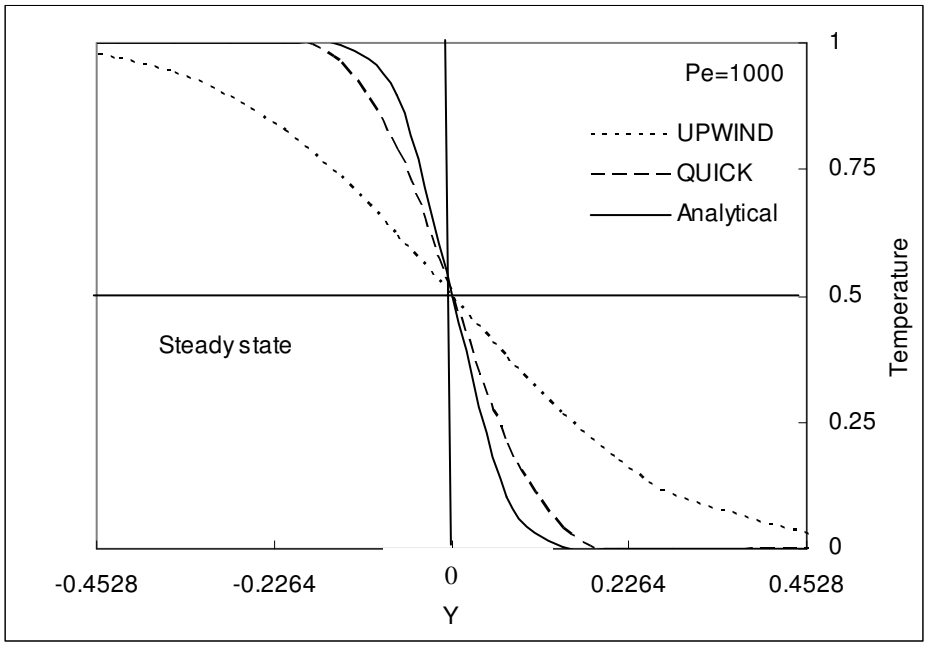

Figure 4.9: Temperature distribution in steady two-dimensional flow at $x = 1.414$

4.6 1-EQUATION MODEL

In the earlier problems, either there were no convective terms in the governing equations or the convection was plain i.e. no solid phase present in the fluid flow. In this section, a comparison for finite difference based solution for advection-diffusion through porous medium is done with corresponding analytical solution. Consider the local volume averaged advection-diffusion equation based upon local thermal equilibrium between the fluid and the solid phases as discussed in Section 3.6.2, in non-dimensional 1-D form as

$$\frac{1}{\mathrm{Pe}\beta_m}\frac{\partial T}{\partial t} + u\frac{\partial T}{\partial x} = \frac{1}{\mathrm{Pe}\ \lambda_m}\left(\frac{\partial}{\partial x}\left(\left[\frac{k_{eff,m}}{k_m}\right]\frac{\partial T}{\partial x}\right)\right) \tag{4.80}$$

This model is called 1-equation model for advection-diffusion in porous medium. Here β_m and λ_m stands respectively for ratio of thermal storage capacity and thermal conductivity of the fluid to porous medium, the derivation of this equation is discussed in section 3.6.2

Consider the boundary conditions in which hot fluid enters an initially cold domain as

$$T = 0 \text{ in } 0 \le x < \infty, \text{ for } t = 0 \tag{4.81}$$

$$T = 1 \text{ at } x = 0;\ T \to 0 \text{ as } x \to \infty \text{ , for } t > 0 \tag{4.82}$$

Its analytical and finite differences based solution is obtained as

4.6.1 Analytical Solution

The analytical solution of 1-equation model is similar to that of advection-diffusion equation as discussed in section 4.5.1.

Using the transformation

$$T(x,t) = exp\left[\left\{\frac{\text{Pe}\,\lambda_m}{2\left(\frac{k_{eff,m}}{k_m}\right)}\right\}\left\{x - \frac{t\beta_m}{2}\right\}\right] W(x,t) \tag{4.83}$$

and solving this equation with modified boundary conditions**,** as discussed in section 4.4.1**,** the expression for the transformed variable W is obtained as follows

$$W(x,t) = \frac{2}{\sqrt{\pi}} \int_{\frac{x}{\sqrt{4\psi t}}}^{\infty} exp\left(-\xi^2\right) \times exp\left(\frac{\text{Pe}}{4}\left(t - \frac{x^2}{4\psi\xi^2}\right)\right) d\xi \tag{4.84}$$

where the term ψ is given as

$$\psi = \frac{\beta_m}{\text{Pe}\ \lambda_m} \frac{k_{eff,m}}{k_m} \tag{4.85}$$

and the term ξ is

$$\xi = \frac{x}{\sqrt{4\psi(t-\tau)}} \tag{4.86}$$

The parameter $K_{eff,m}$ represents the effective thermal conductivity of the porous medium, it is modeled as $k_{eff,m} = \varepsilon\, k_m + 0.5\ \text{Pe}\ k_m$.

Substituting Equation 4.84 in Equation 4.83, the analytical solution is obtained.

4.6.2 Finite Difference Solution

The time derivative is approximated by implicit form of forward difference scheme, convective term by QUICK scheme and the conduction term by central difference scheme at time level (n +1) as

$$\frac{1}{\mathrm{Pe}\,\beta_m}\frac{T_i - U_i}{\Delta t} + \frac{u_r\left(\left(\frac{3}{4}\right)T_i + \left(\frac{3}{8}\right)T_{i+1} - \left(\frac{1}{8}\right)T_{i-1}\right) - u_l\left(\left(\frac{3}{8}\right)T_i + \left(\frac{3}{4}\right)T_{i-1} - \left(\frac{1}{8}\right)T_{i-2}\right)}{\Delta x} = \frac{1}{\mathrm{Pe}}\frac{1}{\lambda_m}\left(\frac{k_{eff,m}}{k_m}\right)\left(\frac{T_{i+1} + T_{i-1} - 2T_i}{\Delta x^2}\right) \tag{4.87}$$

for a constant velocity u, the above equation modifies to

$$\frac{1}{\mathrm{Pe}\,\beta_m}\frac{T_i - U_i}{\Delta t} + \frac{u\left(\left(\frac{5}{8}\right)T + \left(\frac{3}{8}\right)T_{i+1} - \left(\frac{7}{8}\right)T_{i-1}\right) + \left(\frac{1}{8}\right)T_{i-2}}{\Delta x} = \frac{1}{\mathrm{Pe}}\frac{1}{\lambda_m}\left(\frac{k_{eff,m}}{k_m}\right)\left(\frac{T_{i+1} + T_{i-1} - 2T_i}{\Delta x^2}\right) \tag{4.88}$$

The algebraic equations are subjected to boundary conditions as given by Equations 4.81 and 4.82. Sufficiently fine space grid and large time steps are chosen such that results are independent of this selection.

4.6.3 Comparison of Finite Difference and Analytical Solutions

The temperature profiles are obtained as a function of longitudinal distance from inflow plane at various points of time. The values of Peclet number is varied from 100 to 1500. The comparison is done for various values of β_m and λ_m indicating various solid phase materials. Figure 4.10(a, b) shows the comparison at a Peclet number of 100 and 1500 respectively with the values of parameters β_m and λ_m as 1.0 and 0.062. These properties refer to a steel-water system. The temperature front is not very sharp because of large thermal conductivity of the solid phase. The match between the finite difference and analytical solutions is quite close. In Figures 4.10(c, d), the value of the parameter λ_m is raised to 0.68, and that of β_m remains same at 1.0. The values of Peclet numbers in these figures are 100 and 1500 respectively. The effect, of decrease of solid phase thermal conductivity relative to that of the fluid phase,

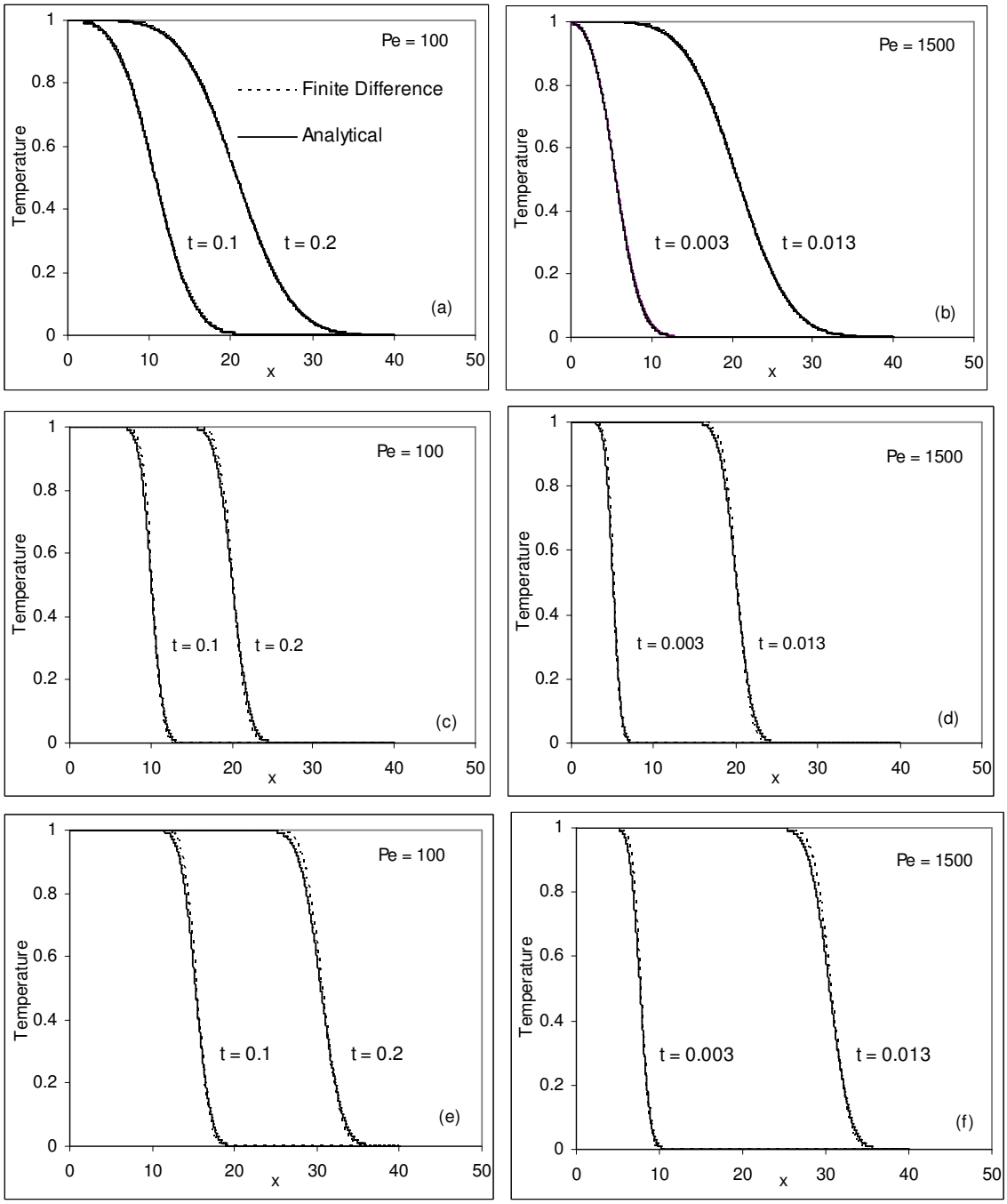

Figure 4.10: Comparison of finite difference solution of 1-equation model with the analytical solution. (a, b) β_m=1.0, λ_m= 0.062 (steel-water system), (c, d) β_m=1.0, λ_m= 0.68, (e, f) β_m=1.52, λ_m= 0.68 (glass-water system). D = 0.0514 m, d_P = 0.00225 m, ε = 0.37.

is clearly visible in the temperature front. It becomes quite sharp as compared to the previous case. The finite difference based solution deviates slightly from the analytical solution near the start and end of the front. Overall, the match between the two results is quite good. In

Figure 4.10(e, f), the values of the parameters β_m is increased to 1.52 and that of λ_m remains same at 0.68. These properties resemble a glass-water system, indicating decrease of the thermal storage capacity of the solid phase relative to the fluid phase as compared to the previous case in Figure 4.10(c, d). This has resulted into an increase in front speed relative to previous cases. Overall, the temperature front remains quite sharp indicating λ_m being a governing factor in the nature of temperature front. Some deviations between the two solutions are again visible near the start and end of the front, the comparison between the finite difference and the analytical solutions being quite good.

The above analysis shows that the importance of using QUICK approach for discretization of the convective terms. In addition, the finite difference based solution is an effective method for simulating flow and heat transfer in a porous medium.

4.7 DISCRETIZATION OF MATHEMATICAL MODELS FOR HEAT TRANSFER IN POROUS MEDIUM

4.7.1 Discretization of 1-Equation Model

The discretization of 1-equation model is discussed in this section. Consider the non-dimensional form of 1-equation model in *r*-*z* co-ordinates as

$$\frac{1}{\mathrm{Pe}\beta_m}\frac{\partial T}{\partial t}+u\frac{\partial T}{\partial z}+v\frac{\partial T}{\partial r}=\frac{1}{\mathrm{Pe}}\left(\frac{\partial}{\partial z}\left(\left[\frac{\left(k_{eff,m}\right)_z}{k_f}\right]\frac{\partial T}{\partial z}\right)+\frac{1}{r}\frac{\partial}{\partial r}\left(\left[\frac{\left(k_{eff,m}\right)_r}{k_f}\right]r\frac{\partial T}{\partial r}\right)\right) \tag{4.89}$$

This model is now discretized by methods as discussed in previous sections i.e. time derivative is approximated by the implicit scheme, convective term by the QUICK scheme and the conduction term by the central difference scheme as

$$\begin{aligned}\frac{1}{\mathrm{Pe}\,\beta_m}\frac{T_{i,j}-U_{i,j}}{\Delta t}+&\frac{u_r\left(\left(\frac{3}{4}\right)T_{i,j}+\left(\frac{3}{8}\right)T_{i+1,j}-\left(\frac{1}{8}\right)T_{i-1,j}\right)-u_l\left(\left(\frac{3}{8}\right)T_{i,j}+\left(\frac{3}{4}\right)T_{i-1,j}-\left(\frac{1}{8}\right)T_{i-2,j}\right)}{\Delta z}\\&+\frac{v_rT_{i,j}-v_lT_{i,j-1}}{\Delta r}\\&=\frac{1}{\mathrm{Pe}}\left(\begin{array}{l}\left(\frac{k_{eff,m}}{k_f}\right)_z\left(\frac{T_{i+1,j}+T_{i-1,j}-2T_{i,j}}{\Delta z^2}\right)\\+\left(\frac{k_{eff,m}}{k_f}\right)_r\left(\frac{T_{i,j+1}+T_{i,j-1}-2T_{i,j}}{\Delta r^2}+\frac{T_{i,J+1}-T_{i,j-1}}{2(j-1)\Delta r^2}\right)\end{array}\right)\end{aligned} \tag{4.90}$$

As the flow is longitudinal, QUICK formulation is used for convection in *z*-direction but Upwind formulation in *r*-direction.

4.7.2 Discretization of 2-Equation Model

Consider 2-equation model as derived in Section 3.6.3, the fluid and solid phase energy equations in *r*-*z* co-ordinates can respectively be written as

$$\varepsilon\left(\frac{1}{\mathrm{Pe}}\frac{\partial T}{\partial t}+\frac{u}{\varepsilon}\frac{\partial T}{\partial z}+\frac{v}{\varepsilon}\frac{\partial T}{\partial r}\right)=\frac{1}{\mathrm{Pe}}\left(\frac{\partial}{\partial z}\left(\left[\frac{\left(k_{eff,f}\right)_z}{k_f}\right]\frac{\partial T}{\partial z}\right)+\frac{1}{r}\frac{\partial}{\partial r}\left(\left[\frac{\left(k_{eff,f}\right)_r}{k_f}\right]r\frac{\partial T}{\partial r}\right)\right) - \frac{\mathrm{Nu}\,A_f}{\mathrm{Pe}}\left(T_f-T_s\right) \tag{4.91}$$

$$\frac{(1-\varepsilon)}{\mathrm{Pe}}\frac{\partial T}{\partial t}=\frac{\beta/\lambda}{\mathrm{Pe}}\left(\frac{\partial}{\partial z}\left(\left[\frac{k_{eff,s}}{k_s}\right]\frac{\partial T}{\partial z}\right)+\frac{1}{r}\frac{\partial}{\partial r}\left(\left[\frac{k_{eff,s}}{k_s}\right]r\frac{\partial}{\partial r}\right)\right)+\frac{\mathrm{Nu}A_f\beta}{\mathrm{Pe}}\left(T_f-T_s\right) \tag{4.92}$$

Here in the fluid phase energy equation, the actual velocity prevailing in the pores is considered instead of the Darcy velocity by dividing the Darcy velocity by the porosity of the medium. The above equations are discretized in a manner similar to 1-equation model using QUICK formulation in *z*-direction and Upwind formulation in *r*-direction.

<u>Fluid Phase</u>

$$\varepsilon\left(\frac{1}{\mathrm{Pe}}\frac{T_{i,j}-U_{i,j}}{\Delta t}+\frac{\frac{u_r}{\varepsilon}\left(\left(\frac{3}{4}\right)T_{i,j}+\left(\frac{3}{8}\right)T_{i+1,j}-\left(\frac{1}{8}\right)T_{i-1,jj}\right)-\frac{u_l}{\varepsilon}\left(\left(\frac{3}{8}\right)T_{i,j}+\left(\frac{3}{4}\right)T_{i-1,j}-\left(\frac{1}{8}\right)T_{i-2,j}\right)}{\Delta z}+\frac{\frac{v_r}{\varepsilon}T_{i,j}-\frac{v_l}{\varepsilon}T_{i,j-1}}{\Delta r}\right)$$
$$=\frac{1}{\mathrm{Pe}}\left(\left(\frac{k_{eff,f}}{k_f}\right)_z\left(\frac{T_{i+1,j}+T_{i-1,j}-2T_{i,j}}{\Delta z^2}\right)+\left(\frac{k_{eff\,f}}{k_f}\right)_r\left(\frac{T_{i,j+1}+T_{i,j-1}-2T_{i,j}}{\Delta r^2}+\frac{T_{i,J+1}-T_{i,j-1}}{2(j-1)\Delta r^2}\right)\right) \tag{4.93}$$
$$-\frac{\mathrm{Nu}A_f}{\mathrm{Pe}}\left(T_{i,j}-T^s_{i,j}\right)$$

<u>Solid Phase</u>

$$\left(\frac{(1-\varepsilon)}{\mathrm{Pe}}\frac{T_{i,j}-U_{i,j}}{\Delta t}\right)=\frac{\beta/\lambda}{\mathrm{Pe}}\left(\left(\frac{k_{eff,s}}{k_s}\right)\left(\frac{T_{i+1,j}+T_{i-1,j}-2T_{i,j}}{\Delta z^2}+\frac{T_{i,j+1}+T_{i,j-1}-2T_{i,j}}{\Delta r^2}+\frac{T_{i,J+1}-T_{i,j-1}}{2(j-1)\Delta r^2}\right)\right) \tag{4.94}$$
$$+\frac{\mathrm{Nu}A_f\beta}{\mathrm{Pe}}\left(T^f_{i,j}-T_{i,j}\right)$$

Here the temperatures T^s and T^f in the fluid phase and the solid phase energy equations are calculated at previous time level.

4.7.3 Boundary Conditions

The 1 and 2-equation models are subjected to the following boundary conditions**.** Consider the grid size in z and r direction to be m and n respectively.

The initial condition for the problem is

$$T(i, j) = 0 \quad 1 \le i \le m \text{ and } 1 \le j \le n, \quad \text{at } t = 0 \tag{4.95}$$

The boundary conditions for the problem are given by

$$T(1, j) = 1 \text{ at } t > 0 \tag{4.96}$$

Since the fully developed profile is invariant in the axial direction, the derivative in the z-direction is assumed to be equal to zero

$$\frac{\partial T}{\partial z} = 0 \text{ at } i = m \tag{4.97}$$

The continuity of heat flow at the axis of the tube in radial direction

$$T(i, j) = T(i, j+1) \text{ at } j = 1 \tag{4.98}$$

The boundary condition at the tube wall is a heat loss condition in terms of Biot number and is given

Fluid phase
$$-\left(\frac{\partial T}{\partial r}\right) = \frac{Bi}{\lambda}(T - T_a) \text{ at } j = 1 \tag{4.99}$$

Solid phase
$$-\left(\frac{\partial T}{\partial r}\right) = Bi(T - T_a) \text{ at } j = 1 \tag{4.100}$$

4.8 SPACE GRID AND TIME STEPS INDEPENDENCE

The space grid used in finite difference should be quite fine such that a small increase or decrease in its value does not affect the results. Similarly, in a marching problem, the value of time step (Δt) should again be fine so that results are independent of its change. These are respectively called as space grid and time steps independence. The idea here is to find the independent space grid and time steps. Since in this study, the various terms of the mathematical model are taken to be non-dimensional, the corresponding space grid and time steps are also non-dimensional. The expected range of the values of the lengths and time scales encountered in the experiments are considered. A space grid and time steps are obtained by dividing the total length and time into number of finite parts. The grid

independence is subsequently checked. The effect of variation of grid size is considered first. Figure 4.11 shows the effect of varying the grid size on a step response through a porous medium at various locations. Here the analysis is done for a tube. The grid size is varied from 100 to 1000, a grid refinement from 1 to 0.1% over a length of 30. Figure 4.11(a) shows the effect over a distance of 15 and Figure 4.11(b) over a length of 30, at a Peclet number of 500. The response becomes slower by grid refinement. It becomes slightly dominant at points away from inflow plane as shown in Figure 4.11(b). Hence, this grid size is selected for numerical simulation.

Figure 4.12 shows the effect of varying the time steps on the step response in porous medium at a Peclet number of 500. The time steps are varied form 1000 to 10000. The corresponding percentages of the total times changes from 0.1 to 0.01%. The figure 4.12(a) shows the time steps variation effect at location z = 15 and the figure 4.12(b) at z = 30. The results at two locations are almost identical. Time steps of 1000 gives highly unreliable results. The results improve as the number of time steps are increased. It seems independent of location Similar trends are observed at higher Peclet number of 5000, though the three curves are closer to each other. Hence, it can be concluded that the time steps for accurate discretization should be less than 0.1 %. Hence, a time steps of 0.01 % are selected for numerical simulation.

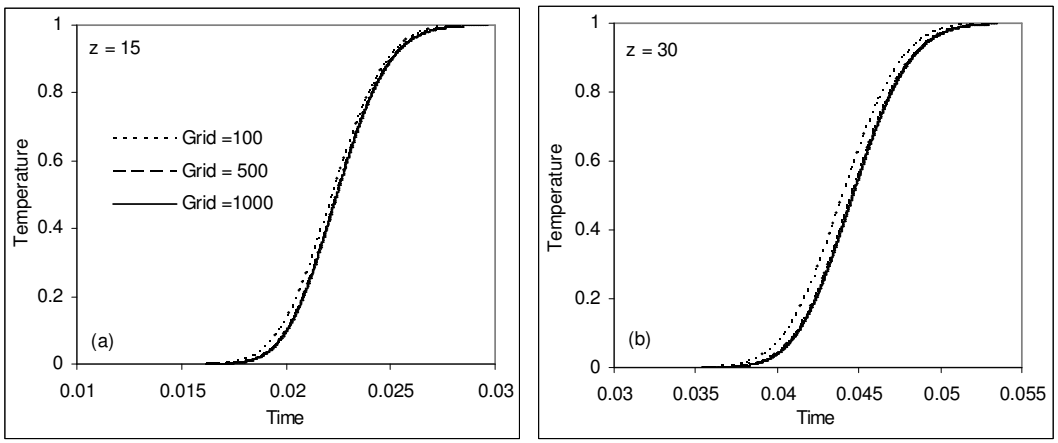

Figure 4.11: The effect of grid size on the results of step change in temperature at inflow plane. Pe = 500. (a) z = 15; (b) z = 30.

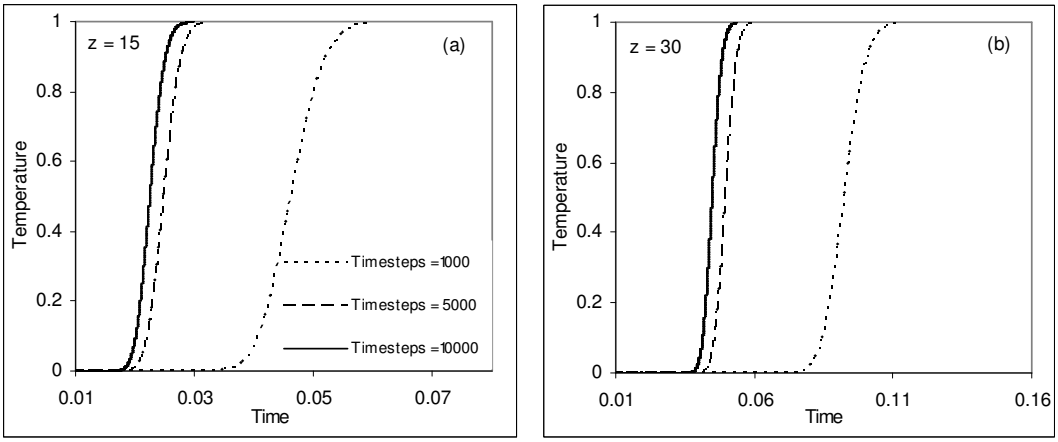

Figure 4.12: The effect of time steps variation on the results of step change in temperature at inflow plane. Pe = 500; (a) z = 15; (b) z = 30.

4.9 CLOSURE

In this chapter, finite difference discretization of the governing partial differential equations is discussed. The discretization of both the 1 and the 2-equation models is discussed. The analytical solutions of 2-D unsteady conduction, 1-D unsteady conduction and 2-D unsteady convection subjected to the given boundary conditions are compared with finite difference based solutions. The convective terms in mathematical model are discretized using Upwind and Quick approaches and further compared with analytical solutions. The QUICK approach of convective modeling is stable and accurate and compares well with analytical solution. This fact is further strengthened by comparing the Upwind and QUICK approaches for a Benchmark problem. The knowledge gained by discretization of plain flow and corresponding heat transfer is used for modeling of heat transfer in porous medium. The analytical solution of 1-D 1-equation model is developed on the lines of corresponding solution of 1-D unsteady conduction equation. It is compared with finite difference based solution where QUICK approach for convective modeling is used. This method is used in the present work. A grid size of 0.1% of the total length and time steps of 0.01 % of the total time are used in the present work. Hence, the discretization of mathematical models is checked so that it can be validated against lab scale models in the next chapter.

CHAPTER 5

APPARATUS AND INSTRUMENTATION

5.1 INTRODUCTION

An apparatus for experimental set up is made for validating the results of numerical simulation. It helps in checking the accuracy of the mathematical model generated; else it helps to improve the experimental set up. In the present study, the apparatus for the experimental set up is generated to check the numerical simulation for two distinct boundary conditions namely the step and the frequency response. The step response refers to the thermal response of an initially cold domain to a hot fluid, which flows through one of its ends. The frequency response, on the other hand, refers to the thermal response of the porous domain to hot and cold fluids, which flow alternately through one of its ends. Further, for each of these boundary conditions, two distinct types of materials comprising the solid phase of the porous bed are considered. These two materials refer here to uniform spherical beads made of either glass or steel. These two materials are selected, as their thermal properties are quite distinct from each other, thereby the validation is under widely varying conditions of the bed. Whereas the glass has low thermal conductivity and the steel has low thermal storage capacity but high thermal conductivity, see Table 5.1 for details of the thermal properties of the two materials. In this way, a comprehensive validation is obtained. The experiments, in general are iterative in nature with the results of one helps to improver those of the next ones. In this chapter, the details of apparatus and instrumentation comprising the experimental set up are discussed. In addition, the experimental procedure and repeatability of the recorded data is also discussed.

Table 5.1: The thermal properties of glass and steel used as a solid phase of the porous bed.

Solid Phase	Specific Heat $\rho\, c_p$ [kJ m^{-3} K^{-1}]	Thermal Conductivity k [W (m K)$^{-1}$]
Glass	1869	1.09
Steel	3768.3	14.9

Before taking up the details of the experimentation, we discuss the boundary conditions related to the step and the frequency responses.

5.2 STEP AND FREQUENCY RESPONSE OF POROUS BED

Figure 5.1 shows a physical model of a porous bed subjected to the flow of hot and cold fluids. In a step response, a single flow of hot fluid is passed through the initially cold bed through one of the ends, the other end acts as the exit end. In the problem analyzed, the porous bed is initially saturated with water at room temperature that also serves as the minimum temperature at any point in the porous medium during the experiment. Figure 5.1(b) shows the step response of porous bed where hot fluid flows through initially cold domain and temperature at a point in the bed rises as a function of time and reaches a constant value as shown. At location $z = 0$, the temperature is maintained at unit value.

This statement can be expressed in dimensionless form as

$$z,(r,t\quad)=0 \text{ in } 0\le z\le \quad \text{and} \quad 0\le r\le \quad \text{for} \quad t \quad \le 0 \tag{5.1}$$

The boundary condition for step response simulation is that hot water is introduced through the inlet plane for all times. Hence

$$,(0,t\quad)=1 \quad \text{for} \quad t \quad >0 \tag{5.2}$$

In a frequency response, the hot and cold fluids flow alternately through the inflow plane and the other end again acts as the exit end. Assuming that the hot and the cold fluids flow for equal times respectively called as hot and cold phases, the total time is the time-period (t_P) of the cycle. Figure 5.1(c) shows the frequency response of a porous bed. The temperature varies as a function of time at all downstream points as a function of forcing frequency. The maximum and minimum level of temperatures being less than the hot but more than the cold fluid temperature as shown.

The initial conditions for the problem are same as given by Equation 5.1, the boundary conditions can be mathematically written as

$$\underline{\text{Hot Phase}} \qquad O,(r,t\quad)=1 \qquad \text{for} \quad 0< \le(\ _p/2) \tag{5.3}$$

$$\underline{\text{Cold Phase}} \qquad O,(r,t\quad)=0 \qquad \text{for } t\ (\ _p/2)t< \le t_p \tag{5.4}$$

The apparatus has to be prepared for these boundary conditions and it requires many individual components for its working.

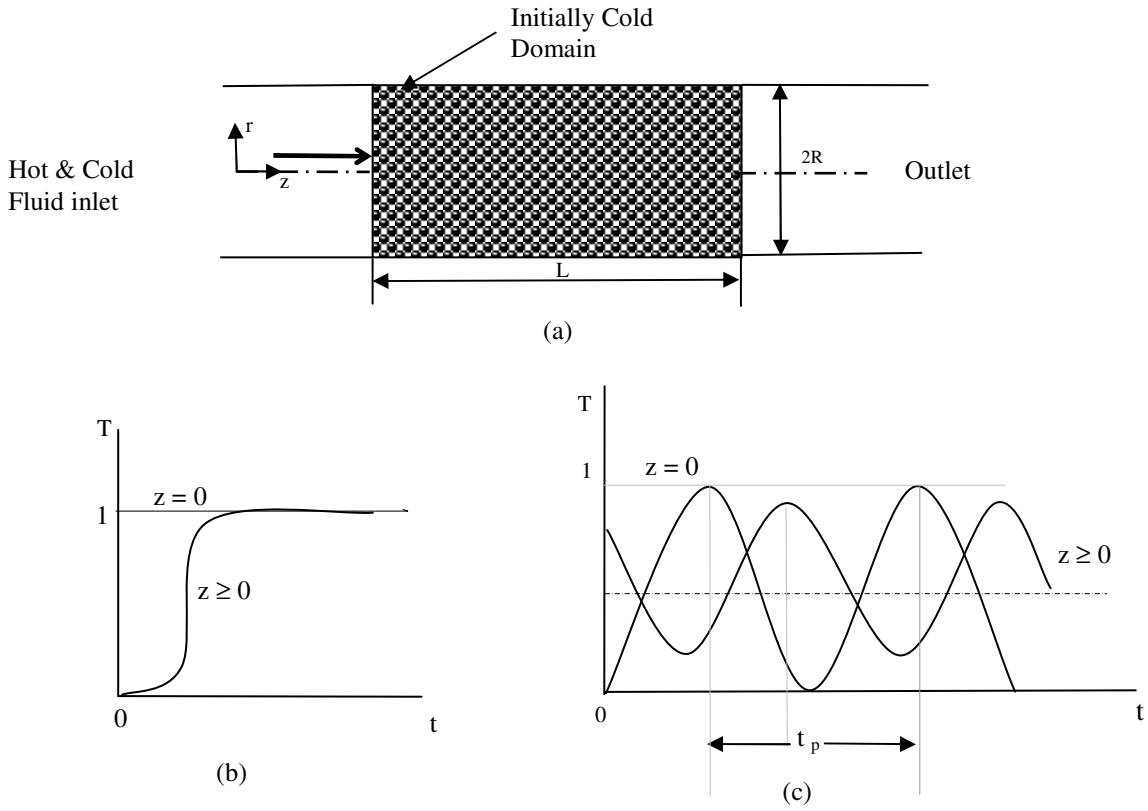

Figure 5.1: (a) Physical Model and coordinate system, and resulting change in temperature of the domain for a (b) Step response (c) Frequency Response.

5.3 REQUIREMENTS FOR EXPERIMENTAL SET UP

In order to obtain the validation, we need an experimental set up capable of achieving the above boundary conditions. The most important component of the set up is a porous bed, which contains an insulated tube closely packed with uniform diameter beads of either the glass or the steel. It should be supplied with cold or hot water under a fixed head. It can be done by using separate cold and hot water constant head tanks. The hot water constant head tank needs an electric immersion heater along with a temperature controller for maintaining constant temperature in tank under flow conditions. Two storage tanks one each for the cold and the hot water constant head tanks are also needed for supplying water to the beds through respective constant head tanks. These would also receive water from the bed, thereby making

it a closed system of flow of the cold and the hot water. This needs a pumping system for supplying water from the storage tanks to the constant head tanks. For temperature measurements in the bed, thermocouples are to be inserted in the porous bed. The thermocouples should be connected with a data acquisition system for converting the signal from analog to digital form and interfaced with a PC for storing the data permanently in it. Flow measurement system for calculating the flow rate through the bed is needed. Solenoid valves along with an electronic timer for actuating the valves are also needed which can change periodically the supply of hot and cold water to the bed as needed in frequency response experiments.

The various components of the experimental set up should work with following considerations.

5.3.1 Constraints for the Components of Experimental Set Up

Before going into details of each of the above-mentioned components, we want to discuss the important constraints of the experimental set up.

- The tube should be filled with closely packed with glass or steel beads and the beads should be perfect spheres.
- The diameter of the tube should be at least ten times the diameter of the beads so that wall effects on the velocity profile are minimum. In addition, resulting velocity profile is nearly flat.
- Some initial length of the bed should be considered as a settling length for the flow and only afterwards, the thermocouples should be inserted for validation. Similarly the temperature near the end of the bed should be avoided for minimizing end effects on the temperature measurement.
- The bed should be fully saturated with water; there should be no trace of air in the bed.
- The cold and hot water tanks should maintain equal levels for the supply of water for supply to the bed; the level should remain constant during the experiment.
- The most important consideration of the experimental set up is to maintain constant hot water temperature to the bed such that the temperature should remain constant within a tolerance of around 3-5 % of difference of hot and cold water temperatures (T_h-T_c) for full duration of the experiment.

- For longevity of the experimental set up, the water, being used should be free from chemicals and suspended impurities. The set up should work as a closed system so that same water can be used repeatedly.
- As the experiments are involving both water and current, avoid leakages of water and current at all costs.
- All the electrical and electronic equipments like thermocouples, heater, preheater etc. should be earthed properly.
- The data acquisition system is delicate and costly equipment; it should be protected from stray current, which can flow in through thermocouples in contact with hot water.
- Apply proper kit-kat switches to electric circuits to avoid over voltage. It will increase the life of the set up.
- The thermocouple wire should be of small diameter so that its time constant is small. Its length should be checked that it does not effect the response time. Else its time constant should be checked and compensated for.

We now take the details of each component of the experimental set-up.

5.4 MAIN COMPONENTS OF EXPERIMENTAL SET UP

5.4.1 Porous Bed

It is the most important part of the set up. It contains the beads in a pipe, which allows the passage of hot and cold water through it. The material used for the pipe were chosen from either glass or PVC. The glass has good surface finish and transparency but it is very fragile so its handling is not easy. The PVC pipe is strong and easy to handle but is opaque. In the first bed, glass tube was used but later on PVC was preferred for both type of beds. The diameter of the tube has a nominal value of 50 mm. To ensure that the diameter of tube is at least ten times the diameter of the glass and the steel beads, the diameter of the spheres should be less than 5 mm. The diameter of glass beads used in the experiments is 2.25 mm and that of steel beads is 4.76 mm. Around five thermocouples are inserted in a bed at its central plane. The thermocouples are first passed through a small metallic pipe and consequently put in the tube. The glass or steel spheres are subsequently filled in the tube by carefully compacting them. A thermocouple is inserted in the pipe supplying water to the bed immediately before it is called as lead thermocouple. The data acquisition card being costly

and sensitive equipment must be protected against excessive current leakages through electrical equipments like heater. This is performed by checking the level of voltage developed at the thermocouples by connecting them with a data logger. A typical voltage level is around 1.00 *m*V, which is due to voltage generated by the thermocouples. A value close to this value shows that no stray currents in the system and the data acquisition system can be connected to the bed. All the thermocouples are properly ground and joined to National instruments data acquisition card. The bed is supplied water with its outlet closed for few hours to remove air from it. We now consider the layout of all the beds used in the experimental set ups.

Glass Water Bed-1

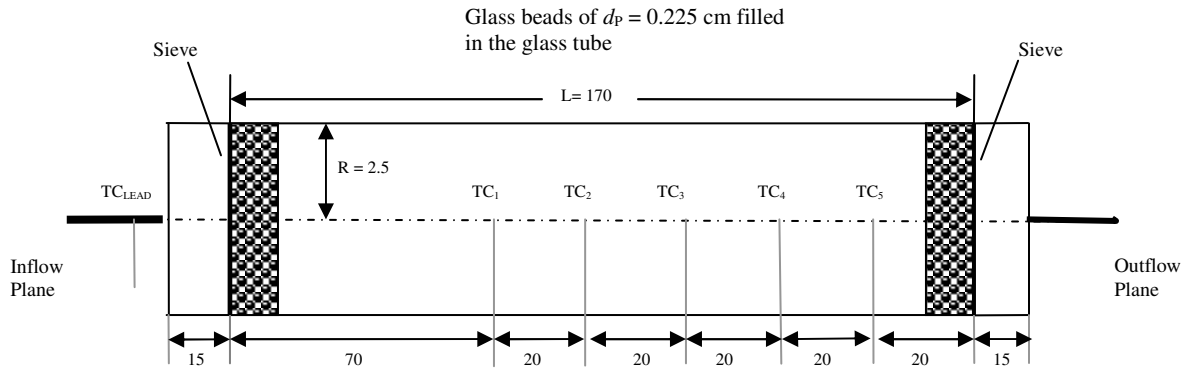

Figure 5.2: Layout of glass-water bed-1.

Figure 5.2 shows the layout of the glass water bed-1. Glass beads of diameter 2.25 mm are filled inside an insulated glass tube of radius 2.5 cm. A fine sieve is placed at the ends in order to avoid the loss of glass beads with flow of water. The length of the bed is 1.7 m, which excludes plain tube at both ends of the pipe as shown in the figure. Five thermocouples are inserted in the bed; first, one is at a distance of 70 cm from the start of the bed to allow for flow development and afterwards thermocouples are inserted at distance of 20 cm each. A pipe of 1.2 cm diameter supplies water to the bed and a similar pipe takes the

water out. Table 5.2 shows the distance of each thermocouple from bed inlet and the corresponding distances in the nondimensional form.

Table 5.2: The distance of the thermocouples from inflow plane and corresponding non-dimensional distances for glass-water bed-1. Non-dimensional length, $L = 66.1$.

Thermocouple No.	Position of thermocouple from inflow to bed, [cm]	Non-dimensional distance from the inflow to bed
1	70	27.2
2	90	35.01
3	110	42.8
4	130	50.58
5	150	58.36

Glass Water Bed-2

As a glass tube was used in glass water bed-1, the handling of this bed became very difficult. It was difficult to close pack the beads in it and minor repairs difficult to carry out. It is also observed if bed is not used for a long period of time, say a few months, the beads in the bed in the presence of moisture form a group and does not allow the flow of water. Some experiments on the step response were carried out with this bed but afterwards a new bed was constructed using a PVC tube. Figure 5.3 shows the layout of glass water bed-2. The plain portion is not there in the bed and the beads are filled in the tube from end to end for compact packing. The use of PVC tube also allow for near perfect insulation on its surface as compared to a glass tube. Six thermocouples are inserted at the centre of the PVC tube of radius 2.9 cm. The length of this bed is 1.76 m. A thermocouple is placed near the start of the bed but thermocouples sufficiently away from start and end of the bed are chosen for analysis. The position of the various thermocouples inserted in the bed is shown in the figure. The frequency response and the remaining step response experiments carried out in this bed. Table 5.3 shows the position of the thermocouples from bed inlet and corresponding non-dimensional distances.

Steel Water Bed-1

Figure 5.4 shows the layout of steel water bed-1. The steel spheres of 4.76 mm (AISI-304) are filled inside a PVC pipe. The question of using a glass pipe for filling steel spheres does

not arise as the density of steel is very high, see Table 1. A PVC tube of 3 cm radius is filled closely with the steel spheres, the length of the bed is 71 cm. Five thermocouples are placed at the centre of the tube as shown in the figure. Space is left vacant for plug flow on each side of the bed. Some step response experiments were carried out with this bed. Table 5.4 shows the position of the thermocouples from bed inlet and corresponding non-dimensional distances.

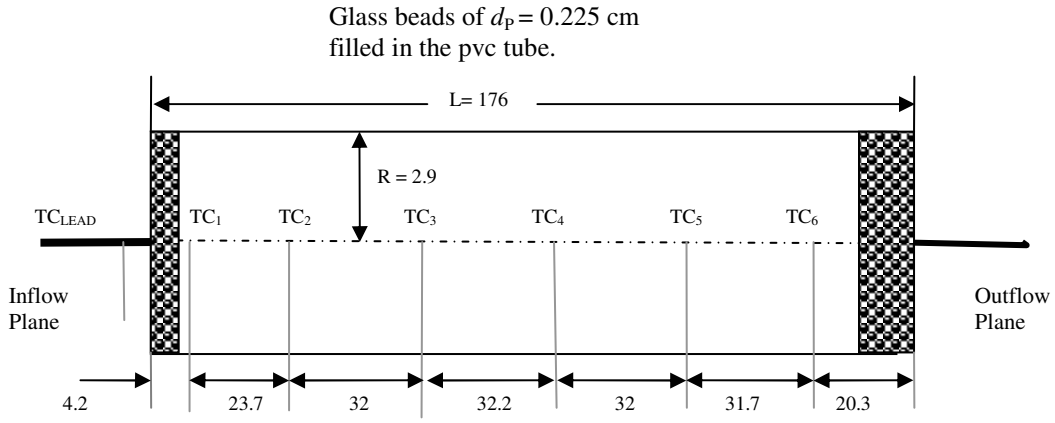

Figure 5.3: The layout of glass water bed-2.

Table 5.3: The distance of the thermocouples from inflow plane and corresponding non-dimensional distances for glass-water bed-2. Non-dimensional length, L = 60.7

Thermocouple No.	Position of thermocouple from inflow to bed, [cm]	Non-dimensional distance from inflow to bed
1	4.2	1.4
2	27.9	9.6
3	59.9	20.6
4	92.1	31.7
5	124.4	42.8
6	155.8	53.7

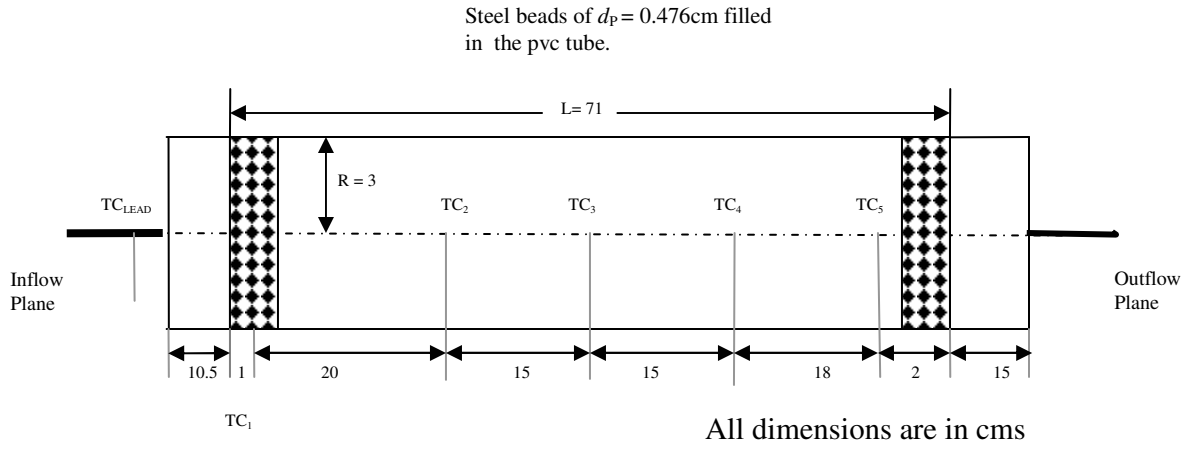

Figure 5.4: The layout of steel water bed-1

Table 5.4: The distance of the thermocouples from inflow plane and corresponding non-dimensional distances for steel-water bed-1. Non-dimensional length, L = 23.7.

Thermocouple No.	Position of thermocouple from inflow to bed, [cm]	Non-dimensional distance from inflow to bed
1	1	0.33
2	21	7.0
3	36	12.0
4	51	17.0
5	69	23.0

Steel Water Bed-2

Figure 5.5 shows the layout of steel water-2 bed. In the bed-1, the steel beads become loose with use. Some air pockets were developed. The first and last thermocouples were too close to start and end of the bed leaving only three thermocouples for analysis. The end effects were visible with the last thermocouple, which were traveling upstream at lower flow rates. In the new bed the beads are filled very closely by mechanical agitation. In addition, the first and last thermocouple are sufficiently away from respective ends. The tube has a radius of 3 cm and the length of the bed is 69 cm. In all five thermocouples are placed in the bed. Table 5.5 shows the position of the thermocouples from bed inlet and corresponding non-dimensional distances.

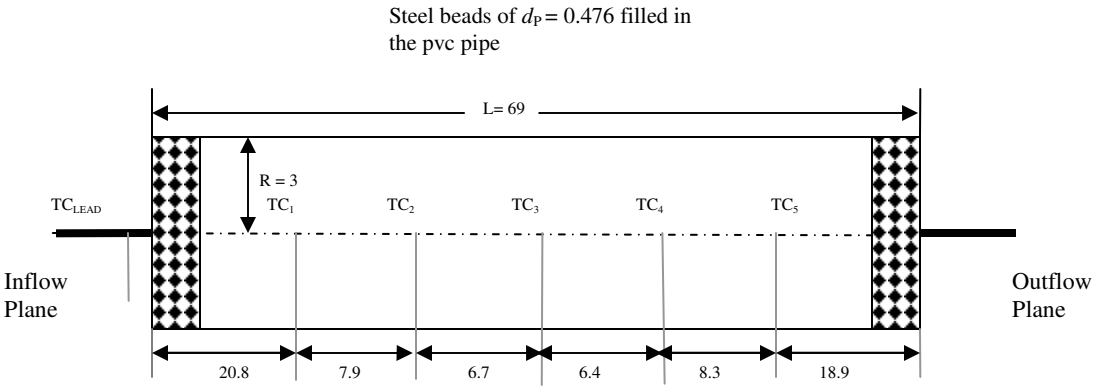

All dimensions are in cms

Figure 5.5: The layout of steel water bed-2.

Table 5.5: The distance of the thermocouples from inflow plane and corresponding non-dimensional distances for steel-water bed-2. . Non-dimensional length, L = 23.0

Thermocouple No.	Position of thermocouple from inflow to bed, [cm]	Non-dimensional distance from inflow to bed
1	20.8	6.9
2	28.7	9.6
3	35.4	11.8
4	41.8	13.9
5	50.1	16.7

5.4.2 Constant Head Tanks

Two constant head tanks one each for the cold and the hot water are used in the experimental set up. These tanks are connected to steel channels fixed on a wall, so that their height can be changed. Figure 5.6 shows the layout of the cold water constant head tanks. The tank has one inlet connection and two outlet connections. Through the inlet connection water flows into the tank and one of the outlet connections is for supplying cold water to the bed through a valve and other one is for overflow of water to the storage tanks. The tank is covered with a lid on the top. The height of water level in the tanks above the bed is 95 cm.

Figure 5.7 shows the layout of the hot water constant head tank. Its layout and dimensions are similar to the cold-water tank but it differs from the cold tank in the

respect that the water comes through a preheater, which raises the temperature of water to a reasonable level. It has an immersion heater inserted, which is automatically controlled by the PID temperature controller, see the figure for details. The controller has a sensor to sense the hot water temperature and hence varying the supply voltage. The hot water tank is well insulated and properly earthed. The use of preheater is to reduce the time required for heating and to make up for thermal losses taking place in the system.

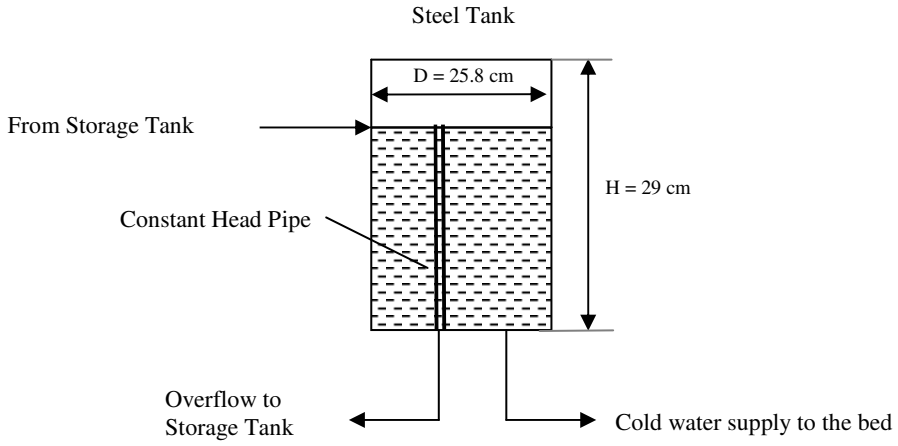

Figure 5.6: Layout of cold-water constant head tank.

5.4.3 Storage Tanks and Pumping System

The purpose of the storage tanks is to make the flow of the cold and the hot water as a closed one avoiding thereby the wastage of water. It also stores a large quantity of water for storage purposes. Two steel tanks are used as storage tanks one each for cold and hot water constant head tanks. Figure 5.8 shows the layout of the storage tank. A centrifugal pump attached to the tank supplies the stored water to the respective constant head tanks. Valves can control the flow rate. The overflow from the constant head tanks flows back to the storage tanks by gravity. The cold and hot water tanks are identical but the hot water tank is well insulated to avoid heat loss. The level of water in the storage tanks is 80 cm below the level of the bed.

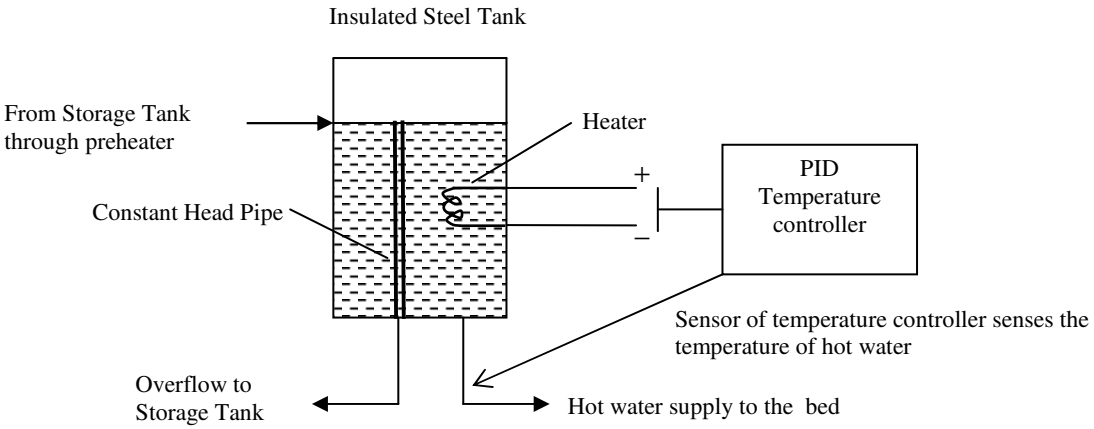

Figure 5.7: Layout of hot water constant head tank.

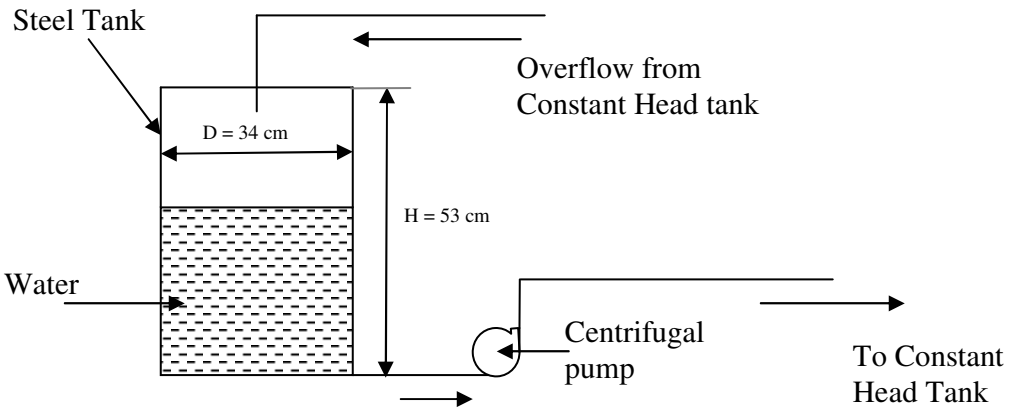

Figure 5.8: Layout of storage tank and pump.

5.4.4 Electric Immersion Heater and Temperature Controller

An immersion heater of 1 kW capacity and 220V is installed in the hot water constant head tank. It heats the water to a desired temperature as set in the PID temperature controller. The temperature controller controls the voltage of the heater such that the outlet temperature is always maintained to the set point, see Figure 5.7 for details. The outlet point where the sensor is inserted is kept close to the bed thereby reducing the time of travel of water to the bed. The sensor is accurate to 0.3 °C of hot water temperature.

As the water is flowing in and out of the tank, it takes a lot of time for heater to heat water to the required temperature, so a preheater is used between hot water storage tank and the constant head tank, which raises the temperature to a permissible limit, see Figure 5.7.

5.4.5 Thermocouples

The temperature is measured by *K*-type single sleeve wire thermocouples inserted in the bed at the required position. The thermocouples are connected to the junction box of the NI data acquisition card. The thermocouples are highly sensitive and have low response time. The wire of the thermocouples is 0.32 mm diameter and a bead diameter of 0.62 mm. The dimensions involved are quite small, with estimated time constant in the range of 10-100 ms. Since the time scales in experiments are of the order of 1 hour (step-response) and 1-2 hrs (frequency response), transient effects associated with the thermocouple itself are expected to be negligible for the present work. Each thermocouple is passed through a 1 mm diameter copper sheath and introduced at the centre plane of the bed.

The temperatures indicated by the thermocouple are checked for errors by various means. The length of lead wire in the thermocouples is changed to see the effect on readings. The *K*-type along with a *P*-type thermocouple is inserted in a bare tube at the same location and hot water is passed. The two thermocouples respond identically to the hot pulse. Further the time constant of the thermocouples being quite small, their suitability for use in the experiments is established.

5.4.6 High Precision Data Acquisition System

A 16 channel-NI-4351 type data acquisition card collects the temperature history from the bed and stores in a PC. It is supplied along with junction box and a cable. It has an interface with PC thereby temperature record is stored in PC.

5.4.7 Flow Measurement

The flow measurement is obtained by a rotameter of capacity 170 lph. The flow rate can be converted to the respective Reynolds number of flow in the pipe. Its calibration is checked by comparing the flow rate with a calibrated jar and a stopwatch. The comparison is found to be satisfactory.

5.4.8 Solenoid Valves and Electronic Timer

Electronically controlled solenoid valves are used to supply the cold and the hot water to the beds. The electronic timer actuates the cold and hot valves for a specific period of time. It is set in such a way that only one of the two valves is open at a time. For the step response experiments, it opens the hot valve and closes the cold valve for the supply of the hot water to the bed. Whereas in a frequency response experiment, it opens and closes the cold and the hot solenoid valves alternately for a fixed period of time.

In addition to the above-discussed components of the experimental set up, a number of valves, pipes, switches and earthing wires for safety and other related purposes are used.

5.5 LAYOUT OF WATER CIRCUITS AND SOLENOID VALVES

In this section, the layout of the cold and hot water circuits are discussed along with that of the solenoid valves.

5.5.1 Cold Water Circuit

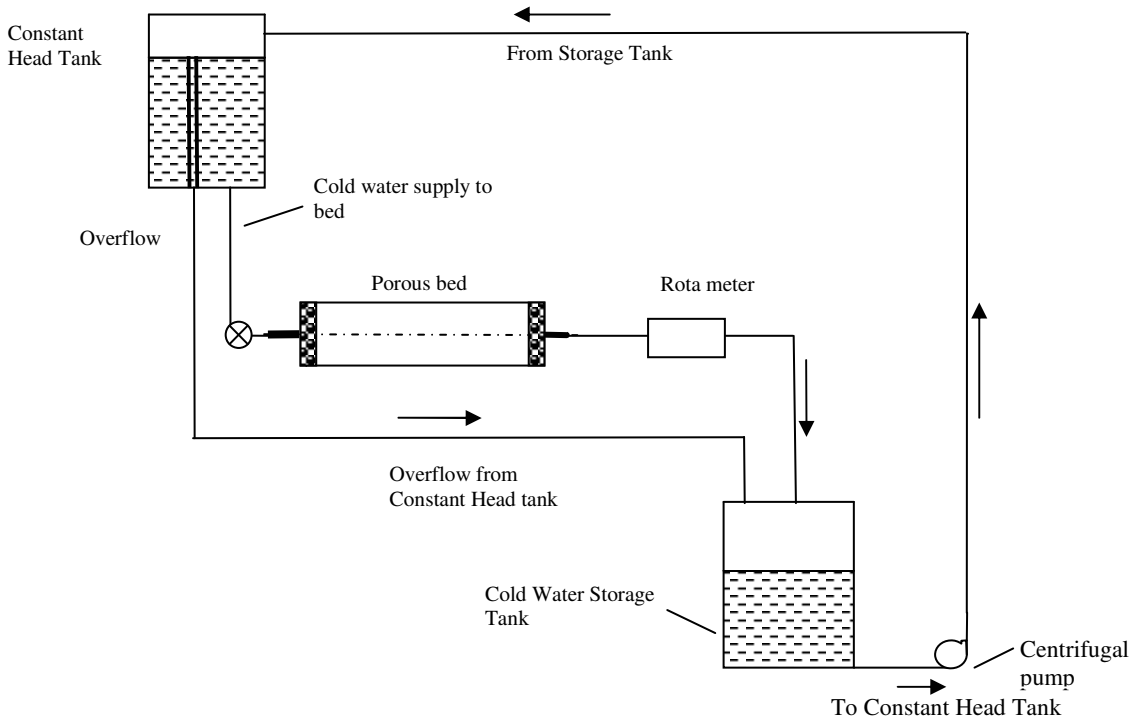

Figure 5.9: Layout of cold-water circuit

Figure 5.9 shows the details of cold-water circuit. The water from constant head tank flows through the solenoid valve to the bed and subsequently through the rotameter to the storage tank. From this tank, it is re-circulated through a centrifugal pump to the constant head tank. The overflow from constant head tank flows directly to the storage tank.

5.5.2 Hot Water Circuit

The layout of hot water circuit is shown in Figure 5.10. The hot water at a preset temperature flows to porous bed from the constant head tank. Two valves, V_1 and V_2, are arranged before the hot water flows to the bed. It insures that hot water at a preset temperature is always available at a point nearest to the bed. When the hot water is not in use, V_1 is open and V_2 is closed, thereby water flows down to the storage tank. At the start of step or frequency response experiments, the valve V_2 is opened and the water flows to the bed.

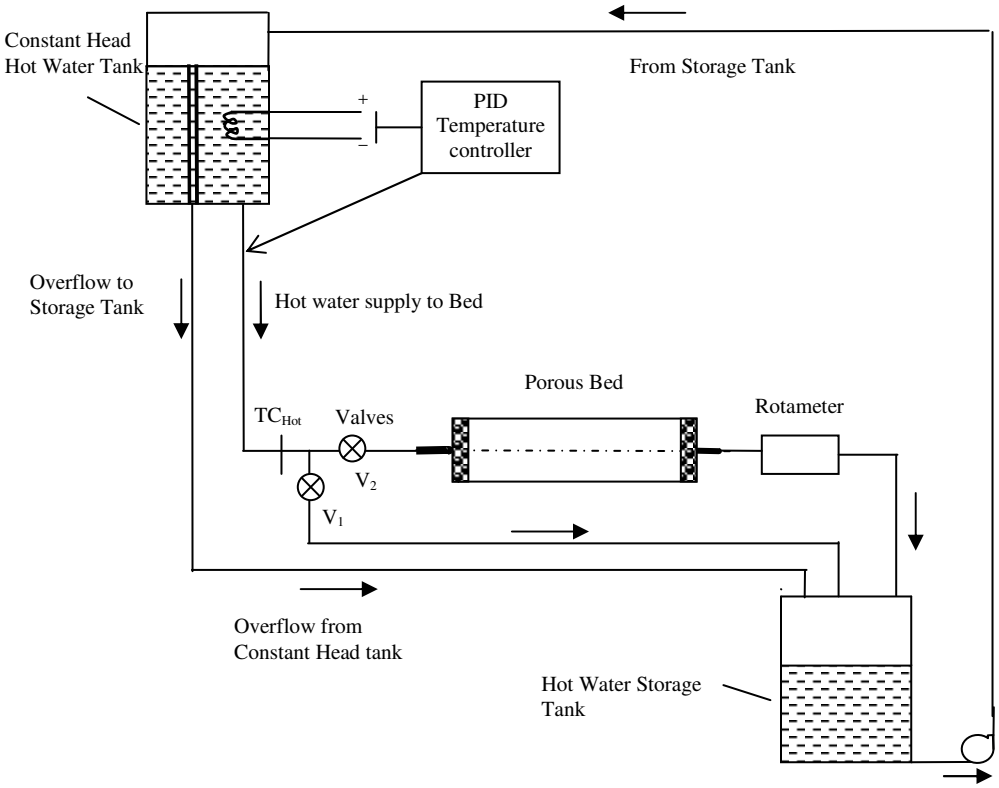

Figure 5.10: Layout of hot water circuit.

5.5.3 Layout of Solenoid Valves

The solenoid valves are used in addition to the above-mentioned valves. It opens and closes to supply the cold and hot water to the bed. The setting can control the timing for a particular valve to remain open. Figure 5.11 shows layout of solenoid valves and the electronic timer. The figure shows that when the hot solenoid valve is closed, the cold valve is open for flow of water to the bed. Electronic timer can control the opening and closing time. Further, at the exit of the bed, an arrangement for air vent is made to remove air present in the bed. The air can be removed by opening air-vent valve from the system. For normal working, the air vent valve is closed and water flows through another valve to the storage tanks.

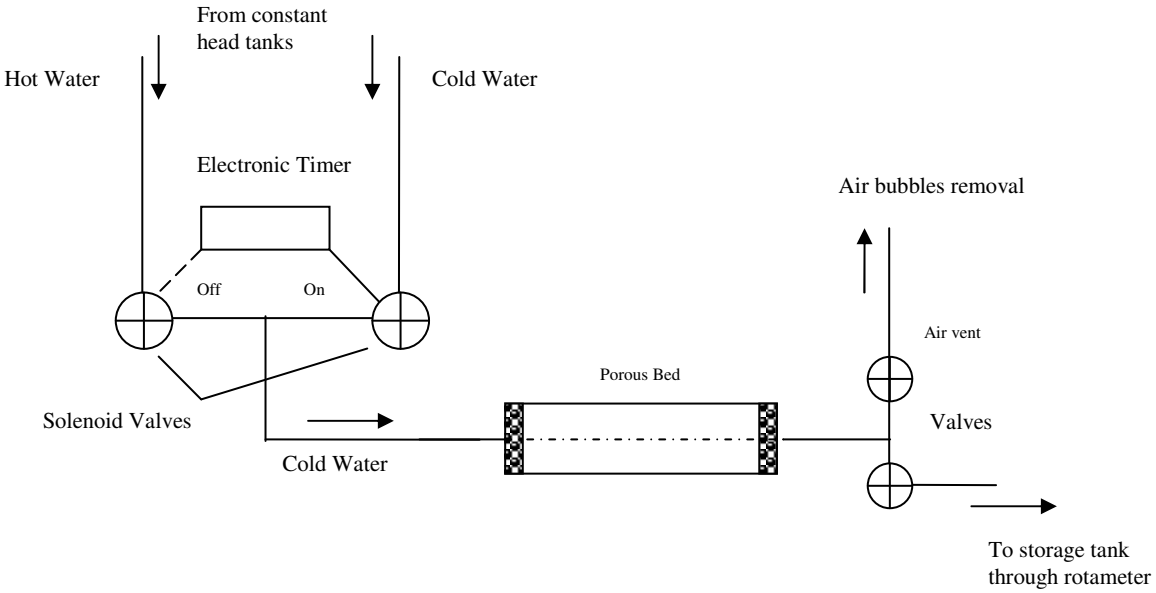

Figure 5.11: The layout of solenoid and the air vent valves.

5.6 LAYOUT OF APPARATUS AND EXPERIMENTAL PROCEDURE

The details of complete experimental set up is shown in Figure 5.12. All the components are numbered and subsequently shown in a table below the figure. The water flows from the constant head tanks to the bed and then passes through a two-way valve for subsequent flow to the respective storage tank. From the storage tanks, it is pumped to constant head tanks and again flows through the bed. The thermocouples inserted in the bed records the temperature of fluid and subsequently stored in PC through the data acquisition card.

5.6.1 Experimental Procedure

The experimental procedure involves the various precautionary checks in the system and the subsequent running of set up for various step and frequency response of the bed.

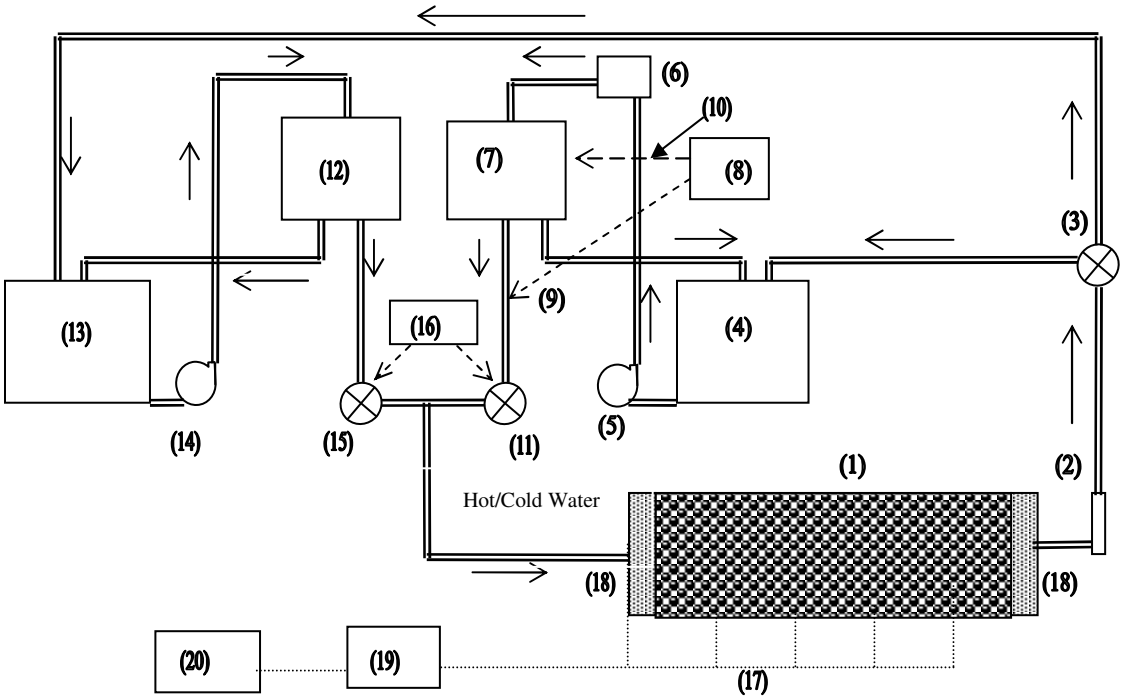

1	Porous bed	8	Temperature controller	15	Cold water solenoid valve
2	Rota-meter	9	Sensor of temperature controller	16	Electronic timer
3	Two-way valve	10	Voltage control of the heater	17	Thermocouples inserted in the centre of the bed
4	Hot water storage tank	11	Hot water solenoid valve	18	Sieve
5	Centrifugal pump for hot water	12	Constant head cold water tank	19	Data acquisition card
6	Preheater	13	Cold water storage tank	20	PC
7	Constant head hot water tank with heater	14	Centrifugal pump for cold water		

Figure 5.12: Schematic layout of apparatus for the experimental set up.

The precautionary checks involve checking the air in the bed, water leakages and level in the tanks, grounding of the electrical equipments. After all the checks have been made, cold water is supplied to the bed with its end valve closed. It is done to fill the bed completely with water and remove air from the system. This is done for a long period of around 1 hour

depending upon the condition of the bed. This time is less in case the experiments are done in a bed continuously for a few days. It is also ensured that the opening of cold and hot valves is identical so that flow rate through them is same.

The experimental procedure is as follows

- Start the power supply.
- Set the temperature controller to the required temperature of the hot water.
- Check the thermocouple wires for stray currents by connecting them with data-logger. This is done mainly for a new bed.
- Start the PC and log on to the data acquisition card. Keep the files ready to record the data.
- Check the water levels in the storage and constant head tanks if required add additional distilled water.
- Start the hot and cold-water centrifugal pumps.
- Open the cold water supply to the bed; keep the outlet valve of the bed closed. It will help to remove air through the bed.
- Open the outlet valve and ensure that air is removed from the bed.
- The timer can be set as to whether a step or a frequency response is to be performed. For a step response experiment, the hot valve would remain open for a time much longer than the duration of the experiment and for a frequency response experiments, timer is set so that hot and cold valves open alternately for a specific period as required for the experiment.
- Switch on the preheater and main heater.
- Monitor the temperature of hot water through PC. It should reach a constant value under flow conditions. Also, monitor the bed temperature at all points. It should be equal to the cold water temperature at each location. Check the flow rate in the rotameter and set it to the required value using the valves.
- Remove air bubbles from the bed as and when they are visible.
- After about one hour, the hot water temperature will become nearly constant. Ensure that remain constant throughout the duration of experiment.
- The experiment can now be started by opening the hot valve to supply the water to the bed.

- Record the temperature data of the experiment in the PC.
- Record the flow rate through the rotameter. Adjust the minor variations in flow rate, if any.
- In a frequency response experiment, the water from the outlet is either hot or cold so it should not be mixed with cold and hot storage tanks respectively. A separate collecting tank is used for the outlet water to ensure that the temperature of water in storage tanks remains unchanged.
- The data is now recorded in the PC. After the experiment is over log off the NI card, close the supply of hot water to the bed and close the outlet valve of the bed.
- Switch off the preheater and heater. Stop the centrifugal pumps.
- Switch off the main supply.
- Plot graphs for the experiments, in case the results are satisfactory record the data permanently in the PC.

5.7 REPEATABILITY OF THE BEDS

Accuracy and *repeatability* are the most important attributes of an experimental set up. Accuracy refers to the closeness or conformity to the true value of the quantity under measurement and repeatability refers to degree of agreement within a group of measurement. Repeatability refers to the ability of a measurement set up to reproduce its readings repeatedly for a constant input signal. It is worthwhile to check the accuracy and repeatability of an experiment set up before its results are to be considered valid.

The accuracy of an experimental set up can be checked by comparing its results with an instrument/model whose level of accuracy is supposed to be of much higher than the given experimental set up. In contrast, repeatability can only be checked by comparing the measured values of variables for nominally identical inputs.

5.7.1 Procedure for Repeatability

In our case, the controlled input is the flow rate, which is measured by the rotameter. The flow rate can be expressed in dimensionless form as a Reynolds number but in a heat transfer study, it is more convenient to use Peclet number. For a given Peclet number, the repeatability of the apparatus is examined by varying the temperature of the hot water. The

non-dimensional temperature will vary between zero and unity irrespective of the absolute temperatures of hot and cold water. Repeatability of the set up is assessed, separately for step and frequency response through a given bed, by plotting the non-dimensional temperature as a function of time for a given Peclet number. In step response experiments, Peclet numbers are kept nominally equal but in frequency response experiments, time-period of pulsations is kept constant and Peclet numbers are varied marginally by varying the hot water temperature. As the temperature is non-dimensional, the corresponding time should also be non-dimensional. The nondimensional time is obtained by multiplying time with a factor α/R^2, where α is the thermal diffusivity of water at mean temperature of hot an cold water and R is the pipe radius. The repeatability of the beds for step response is discussed first.

5.7.2 Repeatability of Step Response Experiments

5.7.2.1 Glass-Water Bed-1

The repeatability of glass-water bed-1 is discussed here. It is checked at distinct flow rates and hot water temperatures. The experiments are carried with various flow rates of nominal values of 30, 50 and 70 lph. These flow rates are respectively called as low, intermediate and high flow rates. At each flow rate, different hot water temperatures are considered such that the difference between the hot and the cold temperatures keep varying. This is done to vary The Peclet number marginally at nominally similar flow rate. The repeatability is checked by the step responses of the bed to a similar set of Peclet numbers corresponding to each flow rate. The change in temperature at a particular location is studied as a function of Peclet number.

Low Flow Rate

Recalling Figure 5.2 showing the layout of the glass-water porous bed, the step response at locations of 27.2, 35, 50.8 and 58.3 from the inflow plane is recorded. Figure 5.13 shows the repeatability of the bed at low flow rate. The flow rate is nominally equal to 30 lph. The repeatability is shown at the above-mentioned four locations in the bed. Three nominally equal Peclet numbers are considered and the step response is plotted at these locations as a function of time. At location z = 27, in Figure 5.13(a), the difference between the individual step responses of the three Peclet number is the minimum.

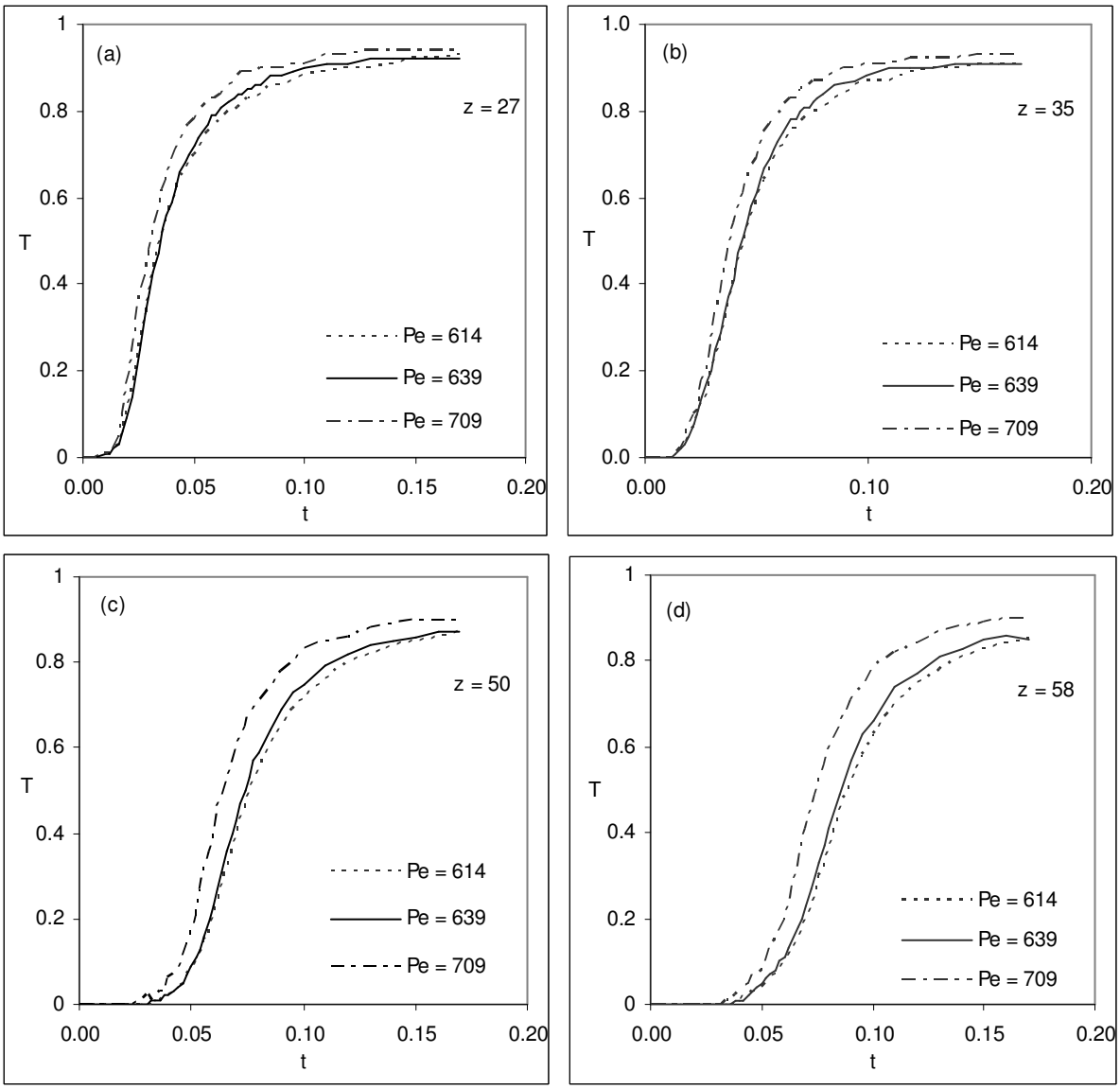

Figure 5.13: The repeatability of glass water bed-1 at low flow rate.

Table 5.6: Details of the parameters related to repeatability of glass-water bed-1 at low Peclet number.

Sr. No	Peclet number, Pe	Flow rate, Q [lph]	Reynolds number, Re	Particle Reynolds number, Re_d	Difference between the hot and cold water temperatures, ΔT [^oC]
1	614	27	132.2	11.6	10.6
2	639	28	134.3	11.8	9
3	709	31	144.9	12.7	7.4

It gradually builds up at location z = 35 and becomes maximum at z = 58. This clearly shows that the repeatability of the bed falls away from inflow plane. In each of the figures, the step response corresponding to a Peclet number of 614 is the slowest and that of 709 is the fastest, which is on the expected lines. The temperature rises from zero at each location and approaches unity but settles to a value less than unity indicating minor heat loss in the bed. The maximum temperature attained at points nearer to inflow plane are higher than those at farther away from the plane. The values of the flow rate, hot and cold water temperature and other related parameters are given in Tables 5.6 and 5.7. It is also interesting to note the degree of control over the hot water temperature during these experiments. A good control over this temperature indicates high reliability of the temperature controller. Figure 5.6 gives the details of parameters related to the difference between the hot and the cold water temperature from 7.4 to 10.6 °C. Similarly, Table 5.7 gives the degree of control over the hot water temperature supplied to the bed. During an the experiments, the cold water temperature remains practically constant but the hot water temperature keeps fluctuating above and below a nominal value. These variations become smaller with time. It is seen that the maximum variation of this temperature is 0.4 ° C during the experiment. The nominal time for the conduct of the experiment is around 1000 sec. The temperature control is obtained for this time. This excludes the time for initial checking of the set up and heating up of water to desired temperature experiments at this flow rate. The flow rate in these experiments varies from 27 to 31 lph. Overall, the repeatability and the control over the hot water temperature are good.

Table 5.7: Maximum variation of the hot water temperature at the inlet plane during experiments on glass-water bed-1 at low Peclet number.

Sr No	Peclet Number, Pe	Hot water Temperature, T_h [^oC]	Cold water Temperature, T_c [^oC]	Variation in hot water temperature during experimentation, T [^oC]	
				Maximum	Minimum
1	614	42.3	31.7	42.5	42.1
2	639	40.7	31.7	40.9	40.5
3	709	38.4	31	38.7	38.3

Intermediate Flow rate

Figure 5.14 shows the repeatability of the bed at intermediate flow rate. The temperature response is faster here as compared to that at low flow rate. The flow rate in this case is nominally equal to 50 lph and the temperature difference between the hot and the cold fluids is again varied. The step response at three nominally equal Peclet numbers as shown in the figure. The difference between the curves increases with distance from inflow plane indicating lower repeatability at these locations. At a Peclet number of 1095, the response is the slowest and the fastest at a Peclet number of 1200. The maximum value of temperature achieved at a location, is less than unity, and falls with distance from the inflow plane. This is attributed to minor heat losses. Table 5.8 shows the parameters related to repeatability at this flow rate. The flow rate varies from 48 to 53 lph and the temperature difference between the hot and cold fluids from 6.1 to 10.8°C. The duration of experiments is around 500 sec. The variation between the maximum and the minimum values of hot water temperature during the experiments is 0.3°C, indicating a good control over this temperature, see Table 5.9 for details.

Table 5.8: Details of the parameters related to repeatability of glass-water bed-1 at intermediate Peclet number.

Sr. No	Peclet number, Pe	Flow rate, Q [lph]	Reynolds number, Re	Particle Reynolds number, Re_d	Difference between the hot and cold water temperatures, ΔT [^oC]
1	1095	48	230.3	20.2	6.1
2	1194	52.5	257	22.5	8.7
3	1200	53	267.9	23.4	10.8

High Flow rate

In the following section, the repeatability of the experiments at high Peclet numbers is discussed. The experiments are carried out at the full opening of the gate valve. Three experiments are performed at this flow rate. Figure 5.15 shows the repeatability at high flow rate. The temperature difference between the hot and cold fluids is varied. The transient response of the porous bed is shown nominally equal Peclet numbers of 1505, 1576 and

1591. The temperature response at these Peclet numbers is almost identical at location z = 27, see Figure 5.15(a) and increases to a maximum value at location z = 58 as shown in Figure 5.15(d). The individual temperatures at each location reach a value quite close to unity. Table 5.10 gives the details of the parameters related to repeatability at this flow rate. The flow rates are nearly same for the three cases but the temperature difference between the hot and cold water varies from 6.4°C to 12.1°C. The duration of individual step response is around 400 sec. Table 5.11 gives the details of control over the hot water temperature at the inlet plane, which is again quite good.

From the above analysis, it is clear that repeatability of the bed is good and the control over hot water temperature is quite good. We now discuss the repeatability of steel-water bed-1.

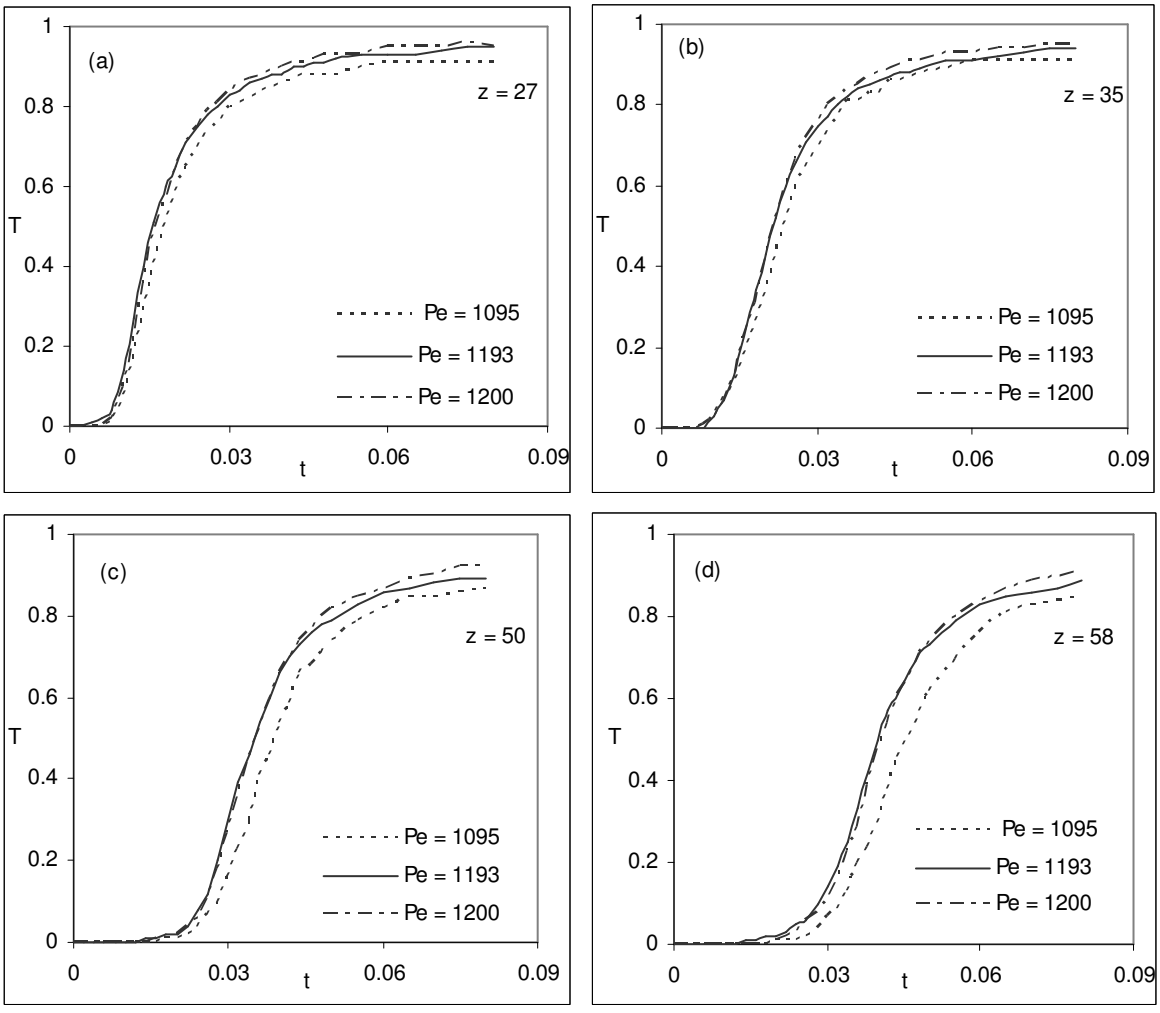

Figure 5.14: The repeatability of glass-water bed 1 at intermediate flow rate.

Table 5.9: Maximum variation of the hot water temperature at the inlet plane during experiments on glass-water bed-1 at intermediate Peclet number

Sr. No	Peclet Number, Pe	Hot water Temperature, T_h [^oC]	Cold water Temperature, T_c [^oC]	Variation in hot water temperature during experimentation, ΔT [^oC]	
				Maximum	Minimum
1	1095	39.1	33	39.3	39
2	1194	41.2	32.5	41.3	41
3	1200	43.8	33	43.9	43.7

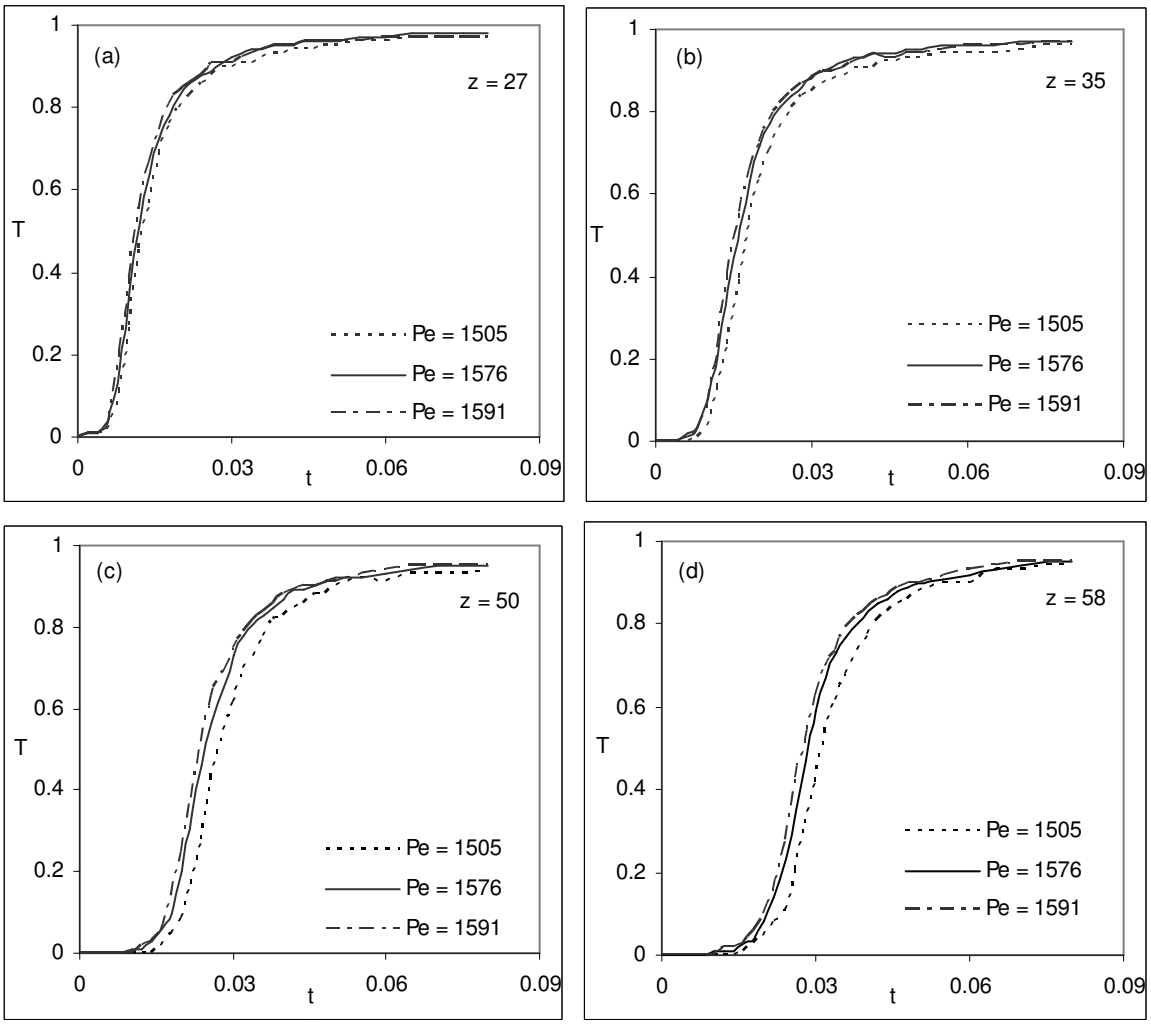

Figure 5.15: The repeatability of glass-water bed-1 at high flow rate.

Table 5.10: Details of the parameters related to repeatability of glass-water bed-1 at high Peclet number

Sr. No	Peclet number, Pe	Flow rate, Q [lph]	Reynolds number, Re	Particle Reynolds number, Re_d	Difference between the hot and cold water temperatures, ΔT [^oC]
1	1505	66	317	27.7	6.4
2	1576	70	366	32	12.1
3	1591	70	343	30	8.5

Table 5.11: Maximum variation of the hot water temperature at the inlet plane during experiments on glass-water bed-1 at high Peclet number.

Sr No	Peclet Number, Pe	Hot water Temperature, T_h [^oC]	Cold water Temperature, T_c [^oC]	Variation in hot water temperature during experimentation, ΔT [^oC]	
				Maximum	Minimum
1	1505	39.3	32.9	39.4	39.2
2	1576	45.8	33.7	46	45.7
3	1591	41.2	32.7	41.4	41

5.7.2.2 Repeatability of Steel-Water Bed-1

The procedure for repeatability is same as discussed for the glass-water bed-1. The repeatability at three distinct flow rates of 40, 80 and 160 lph is considered. These flow rates are respectively called low, intermediate and high flow rates. At each flow rate, three different hot water temperatures are considered such that the difference between the hot and cold temperatures varies. Figure 5.4 shows the layout of the steel-water bed-1. The repeatability at non-dimensional distances of 0.3,7, 12, 17 and 23 from the inflow plane is discussed.

Low Flow Rate

In this section, the repeatability of the steel-water bed-1 at low Peclet number is discussed. Three experiments are performed at a nominal flow rate of 40 lph and temperature difference between the hot and cold fluids is varied. The Peclet number varies from 769 to 816. Figure 5.16 indicates the extent of the repeatability at this flow rate. Referring to Figure 5.16(a), the thermal response corresponding to the three Peclet numbers at the location z = 0.3, is

identical and at location z = 17, the individual differences are the maximum indicating the lowest repeatability. Table 5.12 gives the details of parameters related to the experiments conducted at this flow rate.

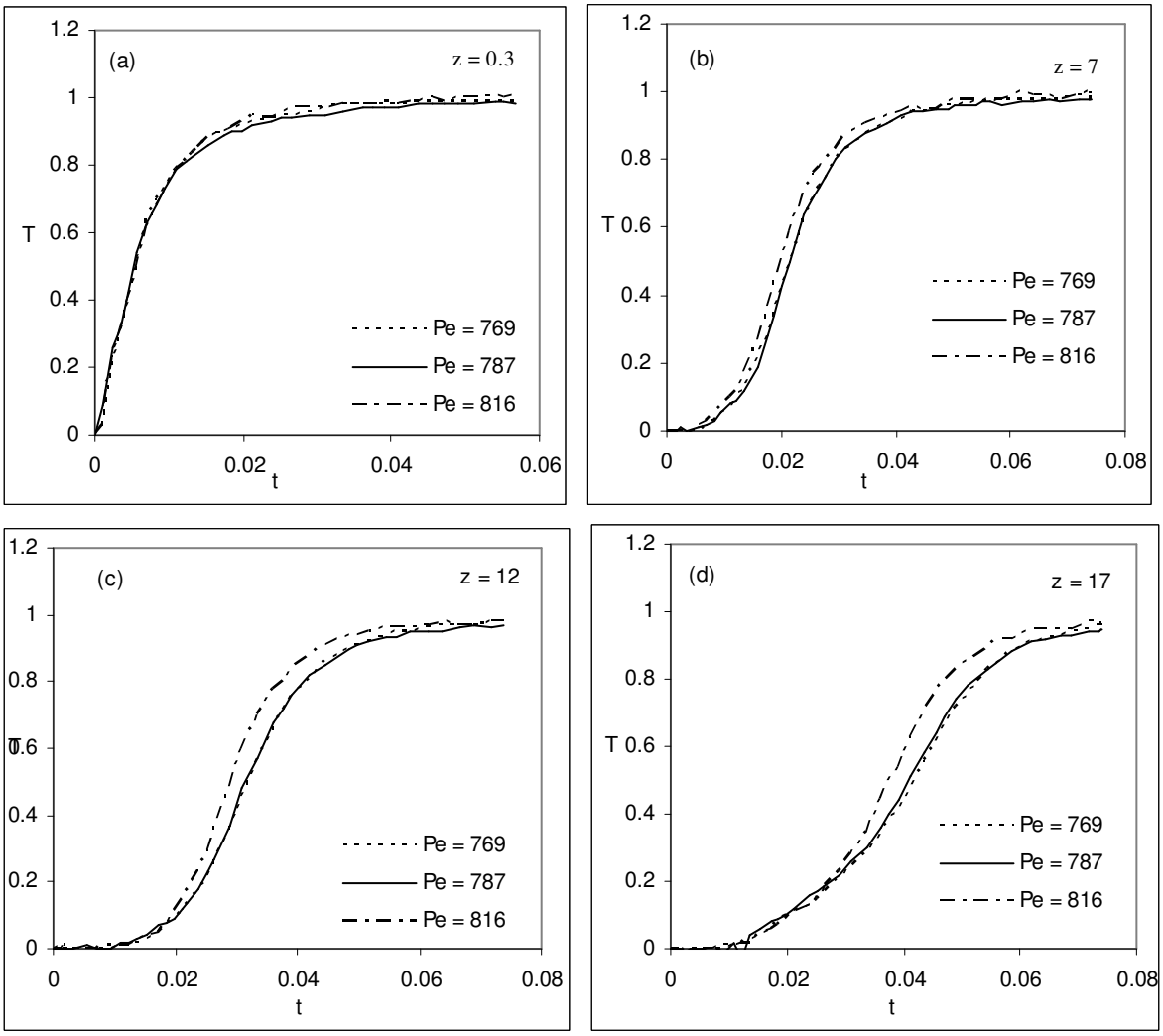

Figure 5.16: The repeatability of steel-water bed-1 at low flow rate.

The flow rate varies between 38 and 40 lph, and the corresponding difference between the hot and the cold water varies from 5.9°C to 15.1°C. Table 5.13 gives the details of control over the hot water temperature indicating that it is again quite good. The duration of the step response is around 500 secs.

Table 5.12: Details of the parameters related to repeatability of steel-water bed-1 at low Peclet number

Sr. No	Peclet number, Pe	Flow rate, Q [lph]	Reynolds number, Re	Particle Reynolds number, Re_d	Difference between the hot and cold water temperatures, ΔT [^oC]
1	769	38.5	139.76	22.24	15.1
2	787	39	132.28	21.05	9.9
3	816	40	127.85	20.35	5.9

Table 5.13: Maximum variation of the hot water temperature at the inlet plane during experiments on steel-water bed-1 at low Peclet number.

Sr No	Peclet Number, Pe	Hot water Temperature, T_h [^oC]	Cold water Temperature, T_c [^oC]	Variation in hot water temperature during experimentation, ΔT [^oC]	
				Maximum	Minimum
1	769	37.2	22.1	37.4	37
2	787	31.7	21.8	31.8	31.5
3	816	26.8	20.9	27	26.7

Intermediate Flow Rate

In this section, the repeatability at intermediate Peclet number is discussed. The flow rate in the experiments varies from 82 to 90 lph. Three experiments are performed at this flow rate having Peclet numbers of 1643, 1648 and 1803. The temperature difference between the hot and cold fluid varies from 6 to 10 ^oC. Figure 5.17 shows the repeatability at intermediate Peclet number. The responses at Peclet numbers of 1643 and 1648 are almost identical but faster corresponding to Peclet number of 1803. The individual temperatures approach unity at every location indicating no heat loss to surrounding conditions. Table 5.14 gives the details of the parameters related to repeatability at this flow rate. Table 5.15 gives the details about the control over the hot water temperature at the inlet plane of the bed. The total time for step response is around 250 sec. Overall, the repeatability is good at this flow rate.

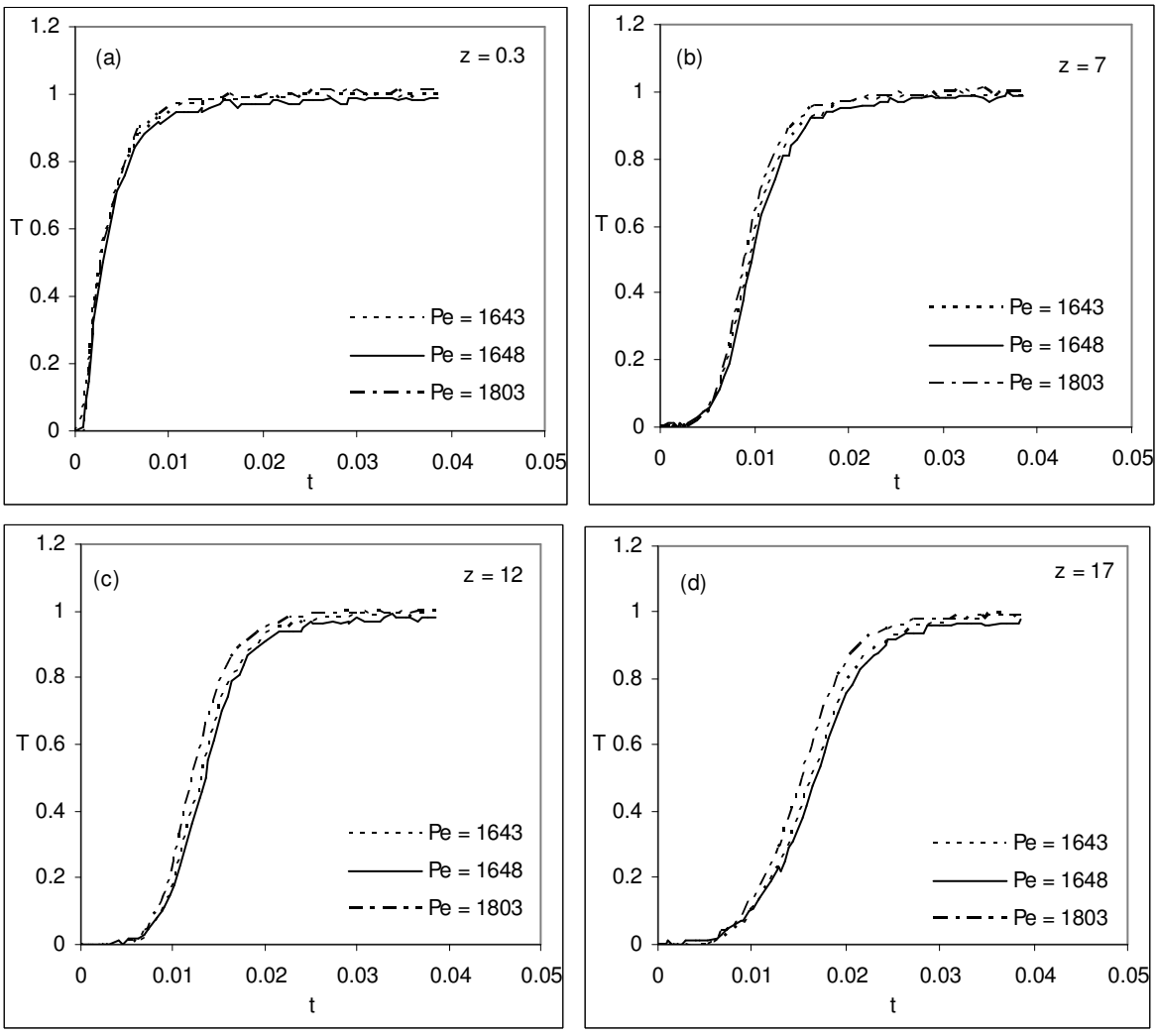

Figure 5.17: The repeatability of steel-water bed-1 at intermediate flow rate.

Table 5.14: Details of the parameters related to repeatability of steel-water bed-1 at intermediate Peclet number.

Sr. No	Peclet number, Pe	Flow rate, Q [lph]	Reynolds number, Re	Particle Reynolds number, Re_d	Difference between the hot and cold water temperatures, ΔT [^oC]
1	1643	82	291.83	46.45	9.9
2	1648	82	284.55	45.29	6.2
3	1803	90	318.63	50.72	6.8

Table 5.15: Maximum variation of the hot water temperature at the inlet plane during experiments on steel-water bed-1 at intermediate Peclet number.

Sr No	Peclet Number, Pe	Hot water Temperature, T_h [^oC]	Cold water Temperature, T_c [^oC]	Variation in hot water temperature during experimentation, ΔT [^oC]	
				Maximum	Minimum
1	1643	33.7	23.8	33.9	33.5
2	1648	30.7	24.5	30.8	30.5
3	1803	31.8	25	32	31.7

High Flow Rate

Experiments are performed at full valve opening. The flow rate varies from 151 to 161 and the temperature difference between the hot and cold fluids from 5.9°C to 15.6°C. The thermal response of the porous bed is discussed at nominally similar Peclet numbers of 3019, 3143 and 3186. In Figure 5.18 gives the degree of repeatability at this flow rate at various locations. In Figure 5.18(a), the degree of repeatability at z = 0.3, the temperature build-ups corresponding to three Peclet numbers are almost similar. The build up here is quite fast and nearly resemble an ideal response in plain flow (no solid phase). At z = 17, the three curves are almost identical. Table 5.16 gives the details of the parameters related to repeatability at this flow rate and Table 5.17 gives the details of control over the hot water temperature at the inlet plane. The duration of the step response is around 150 sec.

Table 5.16: Details of the parameters related to repeatability of steel-water bed-1 at high Peclet number.

Sr. No	Peclet number, Pe	Flow rate, Q [lph]	Reynolds number, Re	Particle Reynolds number, Re_d	Difference between the hot and cold water temperatures, ΔT [^oC]
1	3019	151	540.15	85.99	5.9
2	3143	160	649.36	103.37	15.6
3	3186	161	566.86	90.24	10

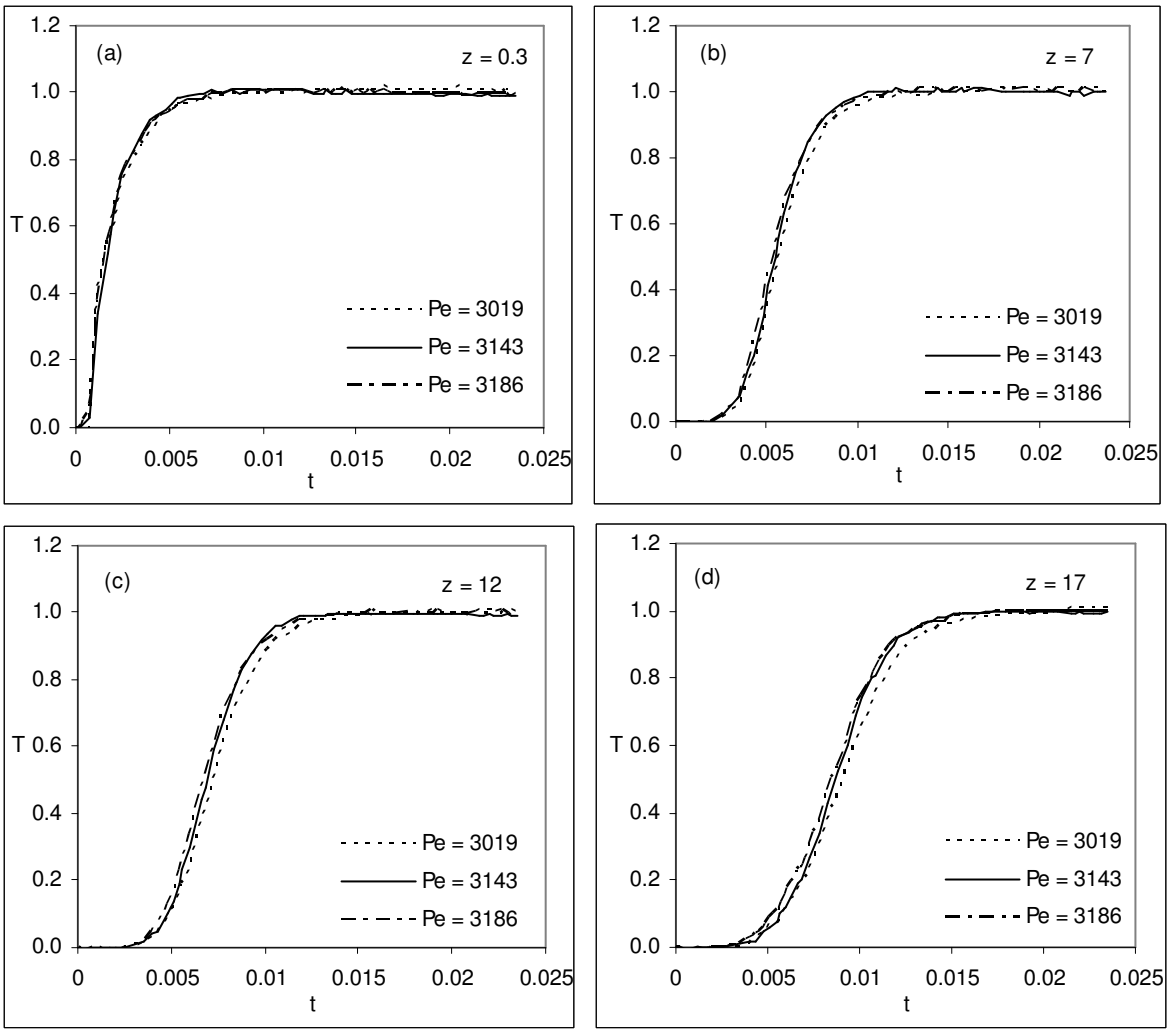

Figure 5.18: The repeatability of steel-water bed-1 at high flow rate.

Table 5.17: Maximum variation of the hot water temperature at the inlet plane during experiments on steel-water bed-1 at high Peclet number.

Sr No	Peclet Number, Pe	Hot water Temperature, T_h [^oC]	Cold water Temperature, T_c [^oC]	Variation in hot water temperature during experimentation, ΔT [^oC]	
				Maximum	Minimum
1	3019	31.8	25.9	32	31.8
2	3143	43	27.4	43.2	42.9
3	3186	33.8	23.6	33.9	33.7

In general, the steel water bed-1 responds well to nominally identical inputs. Hence, the results of this bed can be considered for validation. We now discuss briefly the repeatability of steel-water bed-2.

5.7.2.3 Repeatability of Steel Water Bed-2

The repeatability of steel water bed-2 is discussed in this section. The configuration of the bed is shown in Figure 5.5 and details of the position of the thermocouples in Table 5.5. Three sets of experiments are performed at low, intermediate and high opening of the valve.

Low Flow Rate

Here the flow rate is around 30 lph and the temperature difference between the hot and cold fluid varies from 6.9 to 8.6°C. The Peclet number varies from 514 to 641. Figure 5.19 shows the repeatability at the low flow rate. The various locations indicated in the figure are chosen such that no entrance and end effects are visible on the individual step responses. The individual differences between the curves increase with distance from inflow plane. Minor heat losses are also visible. The variations of the temperature difference between the hot, the cold fluids are shown in Table 5.18, and the Table 5.19 shows the degree of control over the hot temperature at the inflow plane. The control is very good. The duration of these experiments after steady state is around 600 sec.

Table 5.18: Details of the parameters related to repeatability of steel-water bed-2 at low Peclet number.

Sr. No	Peclet number, Pe	Flow rate, Q [lph]	Reynolds number, Re	Particle Reynolds number, Re_d	Difference between the hot and cold water temperatures, ΔT [^oC]
1	541	27.5	116.76	21.62	6.9
2	572	29	121.3	22.46	8.6
3	614	31.2	143.8	26.63	7.2

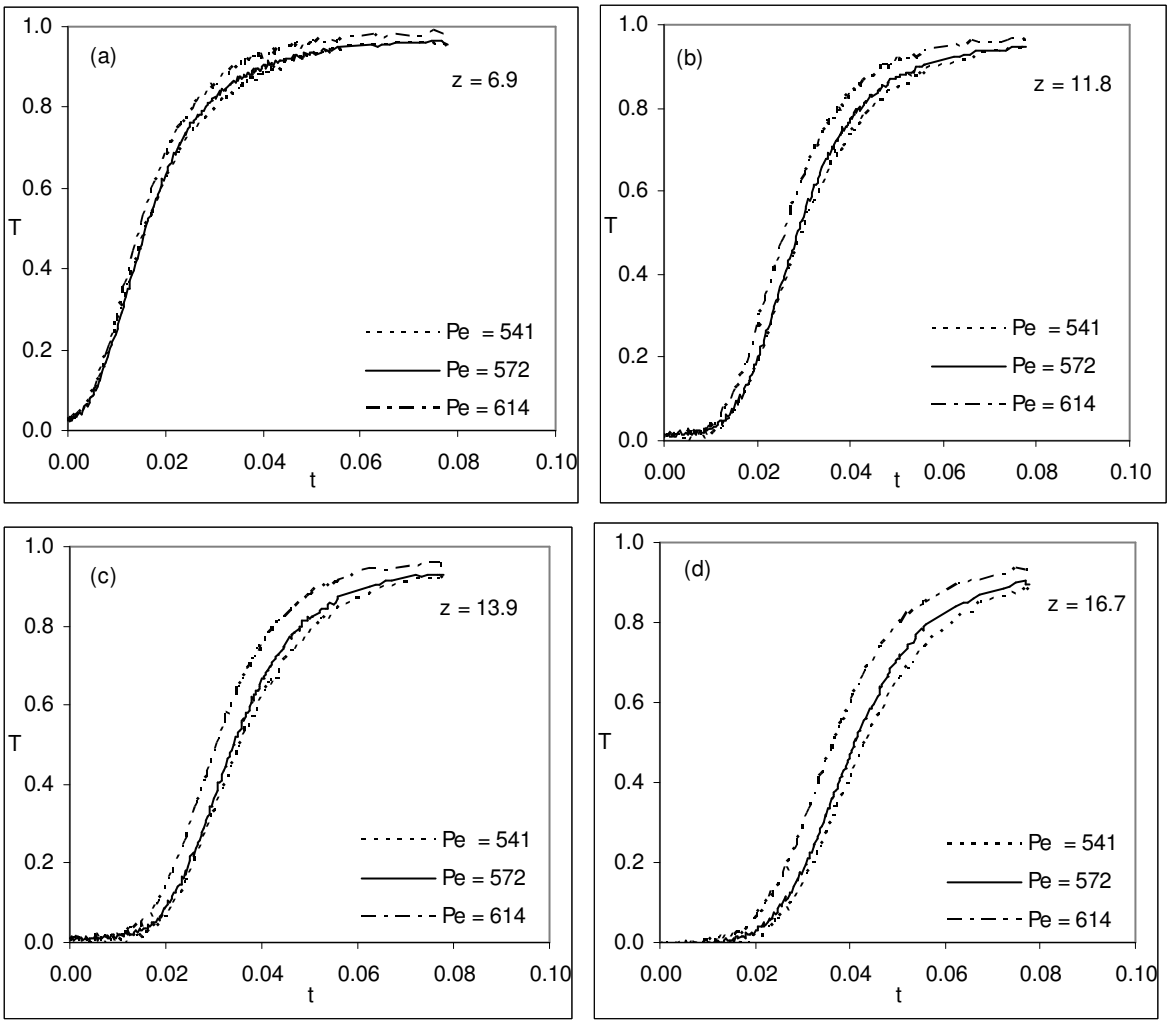

Figure 5.19: The repeatability of steel-water bed-2 at low flow rate.

Table 5.19: Maximum variation of the hot water temperature at the inlet plane during experiments on steel-water bed-2 at low Peclet number.

Sr No	Peclet Number, Pe	Hot water Temperature, T_h [^oC]	Cold water Temperature, T_c [^oC]	Variation in hot water temperature during experimentation, ΔT [^oC]	
				Maximum	Minimum
1	541	40.7	33.8	40.9	40.54
2	572	40.75	32.1	40.97	40.55
3	614	40.86	33.63	40.99	40.71

Intermediate Flow Rate

The flow rate is varied form 48 to 64 lph and the temperature difference from 7.8 to 9.6°C. The Peclet number varies from 961 to 1260. Figure 5.20 shows the repeatability at this flow rate and Table 5.20 shows the parameters related to repeatability at this flow rate. The temperature control over the hot water is again within permissible limits as shown in Table 5.21.

Table 5.20: Details of the parameters related to repeatability of steel-water bed-2 at intermediate Peclet number.

Sr. No	Peclet number, Pe	Flow rate, Q [lph]	Reynolds number, Re	Particle Reynolds number, Re_d	Difference between the hot and cold water temperatures, ΔT [^oC]
1	961	48	191	30.4	9.6
2	1171	60	263.6	41.9	7.8
3	1260	64	279.5	44.5	8.9

Table 5.21: Maximum variation of the hot water temperature at the inlet plane during experiments on steel-water bed-2 at intermediate Peclet number.

Sr No	Peclet Number, Pe	Hot water Temperature, T_h [^oC]	Cold water Temperature, T_c [^oC]	Variation in hot water temperature during experimentation, ΔT [^oC]	
				Maximum	Minimum
1	961	38.51	28.89	38.63	38.40
2	1171	42.94	35.11	43.25	42.39
3	1260	42.85	33.96	43.0	42.42

High Flow Rate

Here the flow rate is around 110 lph. Figure 5.21 shows the extent of repeatability at this flow rate. The temperatures at various locations approach unity, which indicates that minor heat losses do not affect the thermal response at this flow rate. Table 5.22 shows the parameters related to repeatability at the high flow rate and Table 5.23 the extent of control over the hot water temperature during the experiments. The duration of these experiments is around 180 sec.

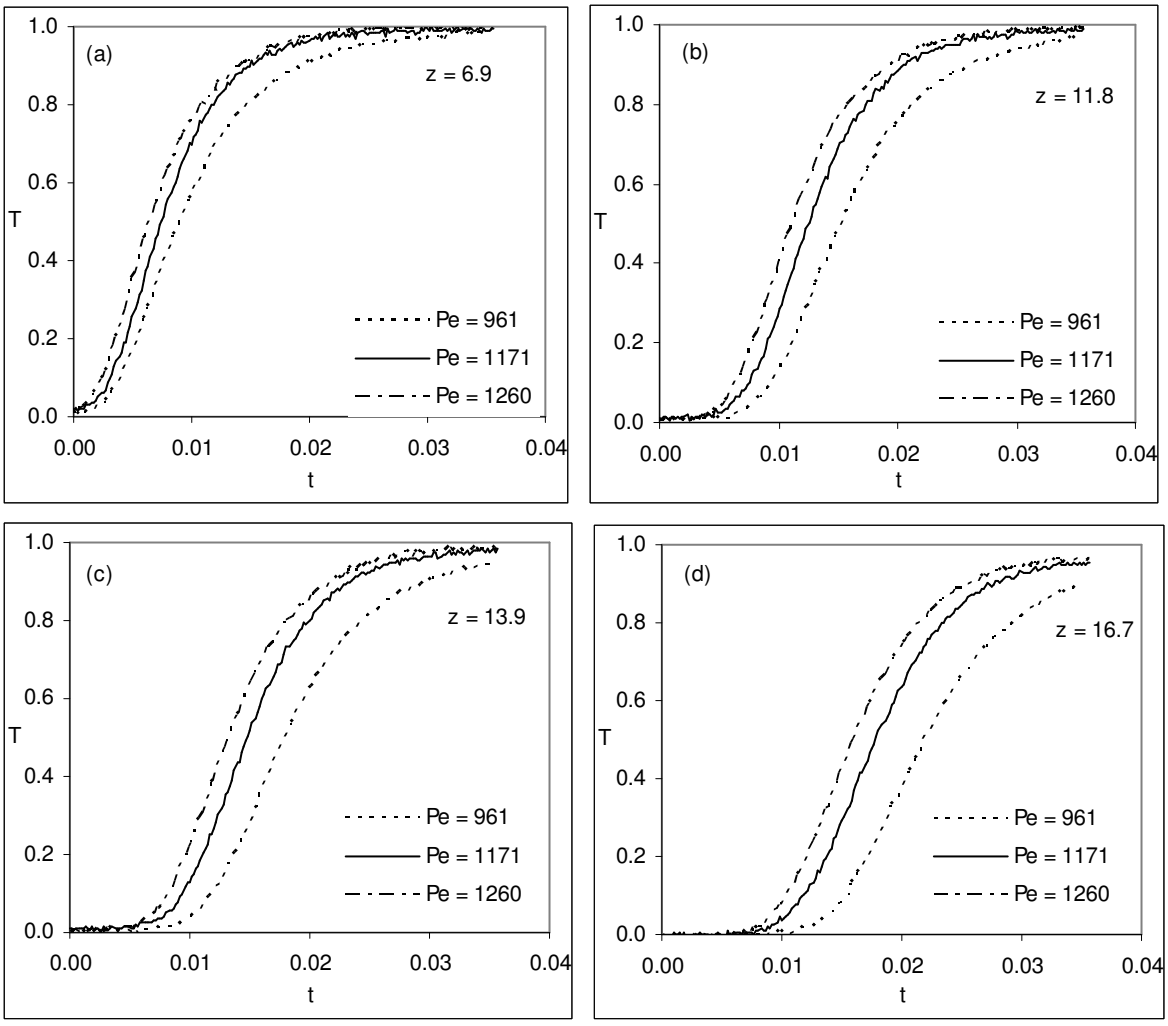

Figure 5.20: The repeatability of steel-water bed-2 at intermediate flow rate.

From the above analysis on repeatability it is clear that the beds response well to almost identical inputs. As the bed is supplied with water through the experimental set up, it may be concluded that the repeatability of the experimental set up as a whole is good. Further, the non-dimensional temperature is independent of the absolute temperature levels chosen. It always varies between zero and unity values. The nondimensional time chosen makes the analysis independent of the velocity of fluid in the bed. Overall, the repeatability of the whole experimental set-up is quite good. Hence the results obtained from the experiments can be used for validation of the mathematical model.

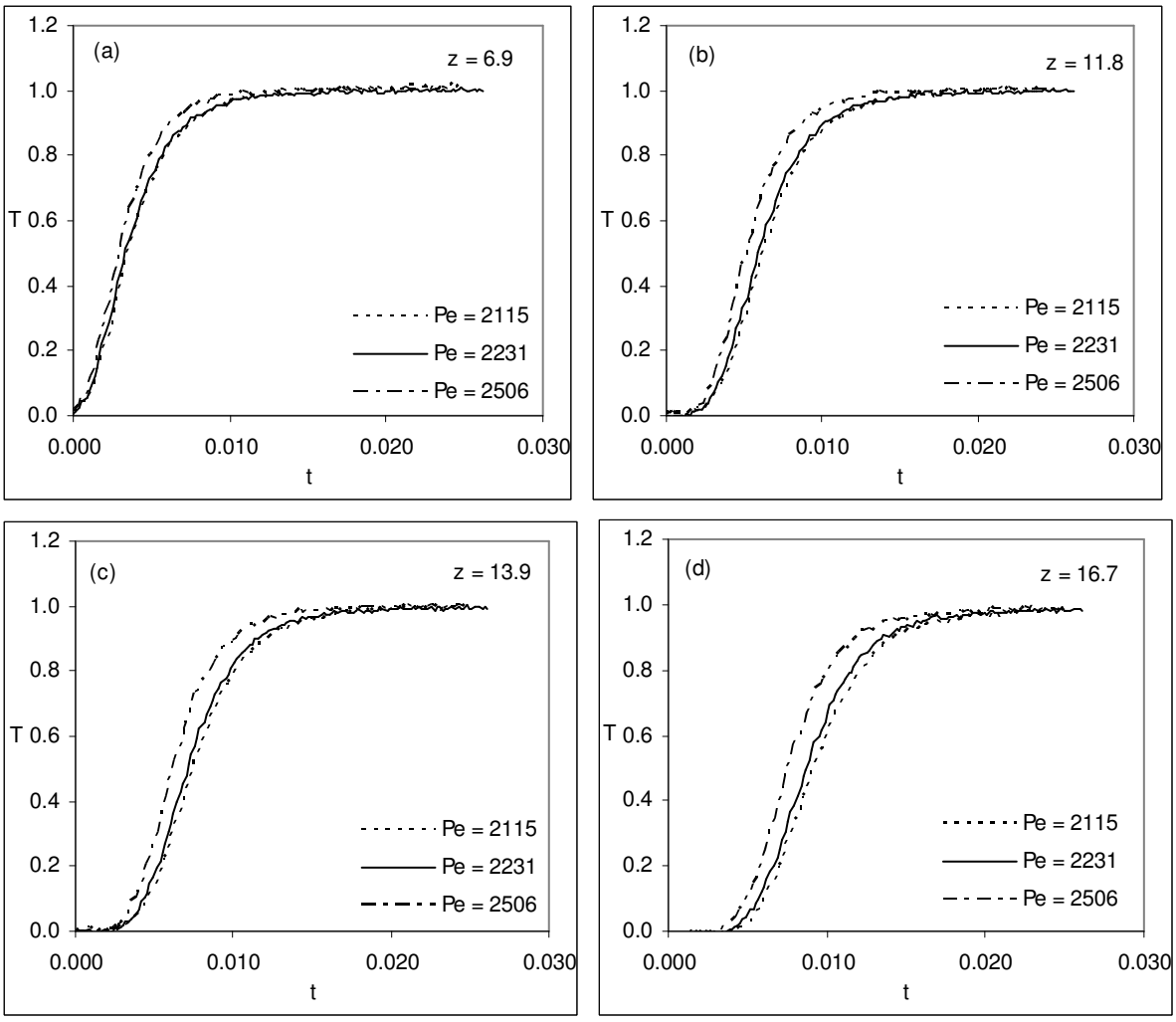

Figure 5.21: The repeatability of steel-water bed-2 at high flow rate.

Table 5.22: Details of the parameters related to repeatability of steel-water bed-2 at high Peclet number.

Sr. No	Peclet number, Pe	Flow rate, Q [lph]	Reynolds number, Re	Particle Reynolds number, Re_d	Difference between the hot and cold water temperatures, ΔT [^{o}C]
1	2115	107.5	455.2	72.46	7.4
2	2231	113	471.45	75	9.2
3	2506	128.8	575.6	91.63	7.77

Table 5.23: Maximum variation of the hot water temperature at the inlet plane during experiments on steel-water bed-2 at high Peclet number.

Sr No	Peclet Number, Pe	Hot water Temperature, T_h [^oC]	Cold water Temperature, T_c [^oC]	Variation in hot water temperature during experimentation, ΔT [^oC]	
				Maximum	Minimum
1	2115	40.84	33.44	40.96	40.76
2	2231	40.84	31.68	40.94	40.75
3	2506	43.76	35.99	43.99	43.7

5.7.3 Repeatability of Frequency Response Experiments

The repeatability of frequency response experiments is discussed briefly in this section. For these experiments, the time-period of pulsations is first selected for a particular flow rate. The repeatability is assessed by varying the hot water temperature, which thereby varies the Peclet number marginally. This procedure is repeated for various time-periods of pulsations. These experiments are performed for respective beds-2 only.

5.7.3.1 Glass-Water Bed

Figure 5.3 shows the layout of glass-water bed-2. In order to minimize the entrance and exit effects, the profiles are plotted for third and fifth thermocouples only. These thermocouples are well away from the start and the end of the bed. Figure 5.22 assesses the repeatability of the bed when the frequency of pulsations is set to 0.073 rad/s. The flow rate through the bed is varied from 57.5 to 80 lph and temperature profiles are plotted for the locations of z = 20.6 and 42.8. Figure 5.22(a & b) shows the plots for Peclet numbers of 1115 and 1228 and Figure 5.22(c & d) for 1505 and 1605. In Figure 5.22(a & b), the profiles corresponding to Peclet number of 1115 are slower as compared to those of 1228. Similarly in Figure 5.22(c & d), the profiles corresponding to Peclet numbers of 1505 are slower. The difference between the individual curves increases with distance from the inflow plane. Table 5.24 gives the corresponding values of Peclet number, Reynolds number and difference between the hot and the cold water temperatures.

Table 5.24: Details of the parameters related to repeatability of glass-water bed at a frequency of 0.073 rad/s.

Sr. No	Peclet number, Pe	Flow rate, Q [lph]	Reynolds number, Re	Particle Reynolds number, Re_d	Difference between the hot and cold water temperatures, ΔT [^oC]
1	1115	57.5	264.92	20.55	8.42
2	1228	62	283.1	21.96	7.77
3	1505	75	346.77	26.90	6.05
4	1605	80	369.81	28.69	6.22

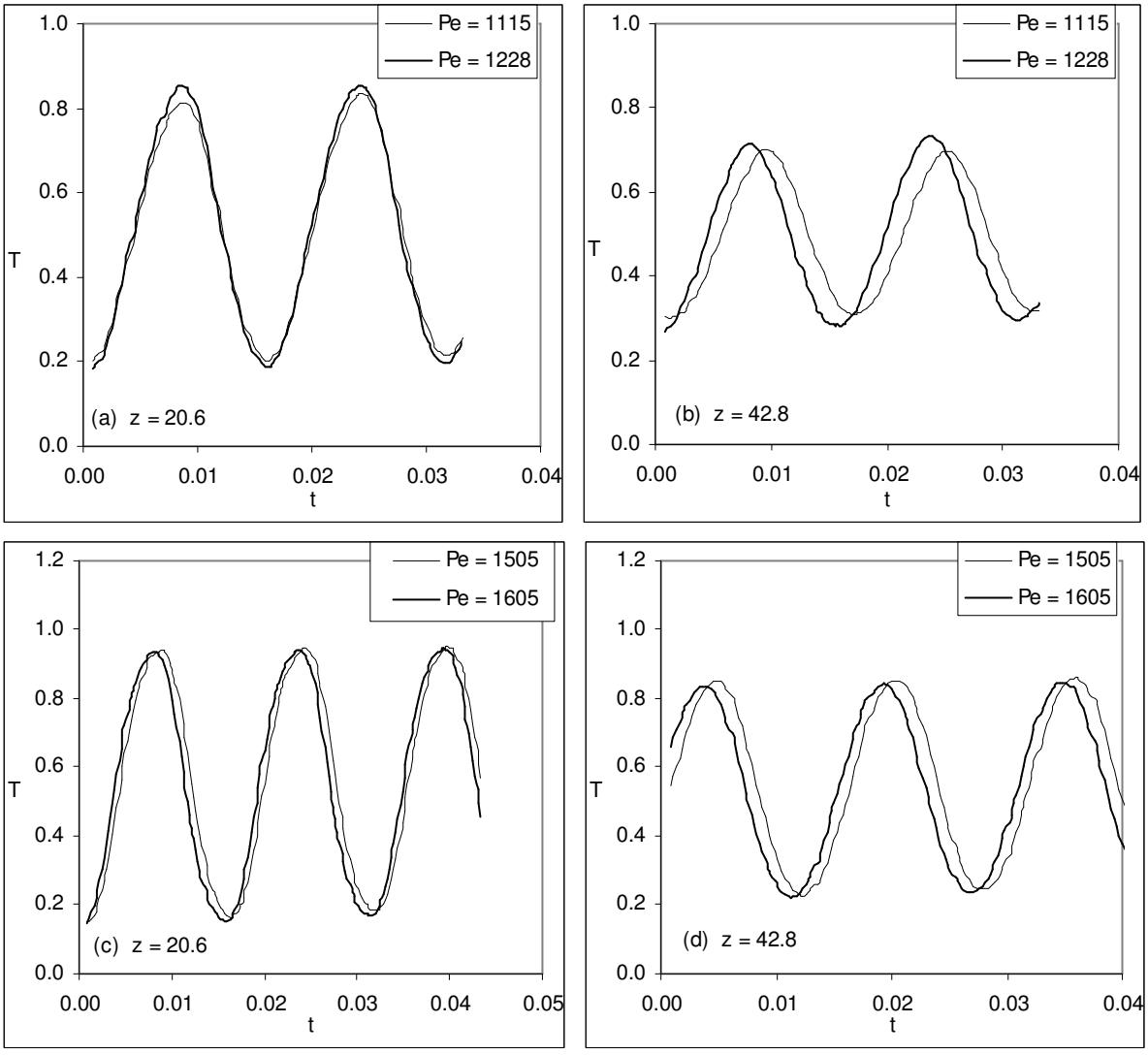

Figure 5.22: Repeatability of glass-water bed for frequency response experiments. $\omega = 0.073$ rad/s.

5.7.3.2 Steel-Water Bed

The layout of steel-water bed-2 is shown in Figure 5.5. The temperature profiles are plotted for first and fifth thermocouples in the bed. The flow rate through the bed is varied from 42.5 to 75 lph. Figure 5.23 shows the repeatability of the bed for a frequency of 0.053 rad/s. The profiles are plotted at locations of 6.9 and 16.7. Figure 5.23(a & b) shows the profiles for Peclet numbers of 837 and 890 and Figure 5.23 (c & d) for 1373 and 1467. In Figure 5.23(a & b), the profiles corresponding to Peclet number of 890 are faster as compared to those of 837. Similarly in Figure 5.23(c & d), the profiles corresponding to Peclet number of 1467 are faster. Table 5.25 gives the details of the related parameters.

Table 5.25: Details of the parameters related to repeatability of steel-water bed at a frequency of 0.053 rad/s.

Sr. No	Peclet number, Pe	Flow rate, Q [lph]	Reynolds number, Re	Particle Reynolds number, Re_d	Difference between the hot and cold water temperatures, ΔT [^oC]
1	837	42.5	178.50	28.41	8.02
2	890	45	186.54	29.69	9.37
3	1373	70.6	317.69	50.57	9.23
4	1467	75	326.38	51.95	8.47

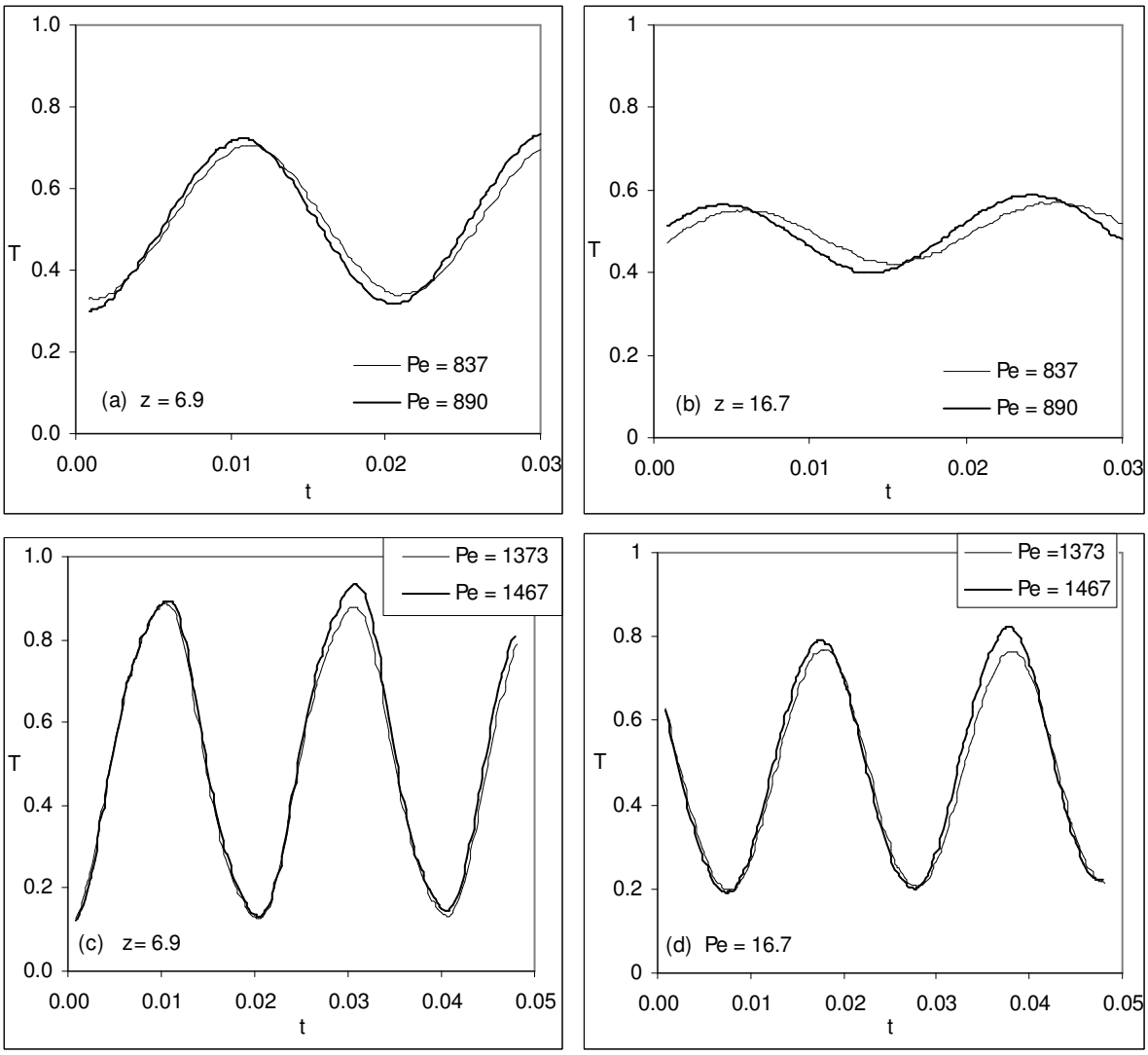

Figure 5.23: Repeatability of steel-water bed for frequency response experiments. $\omega = 0.053$ rad/s.

5.8 CLOSURE

The apparatus and instrumentation discussed in this chapter is developed with an aim of validating the mathematical model. Hence, its components are checked for providing accurate outputs. The individual components of this experimental set-up are fabricated by the author at his parent institute. Some of the components such as thermocouple, data acquisition card and temperature controller are purchased through various sources. During assembly of the set up, various checks are incorporated in the set up so that losses are minimized. Compact packing is used for filling respective beads in the tubes. The experimental set up is

used to generate step and frequency response of the glass-water and steel-water beds. The experimental set up in general and data acquisition card in particular is safeguarded against excessive stray currents. It is ensured that voltage indicated by the thermocouples is due to Seeback effect only and not due to current leakages from the heater which travels through water. The procedure for the experimentation is notified. The control over hot water temperature during experiments is also very good. In the end, the repeatability of the bed is assessed and found to be good. In general, the experimental set-up provides repeatable and reliable results and can be used for validating the mathematical model in the next chapters.

CHAPTER 6

STEP RESPONSE OF GLASS-WATER BED

6.1 INTRODUCTION

In this chapter, the step response of the glass-water bed is discussed. The aim is to compare the results with that of numerical simulation and gather vital information regarding the propagation of thermal front through the bed. For a particular experimental step response of the bed, the corresponding numerical models are generated and the results of the two approaches are compared. The step response as discussed in Section 5.2 where temperature at inflow plane rises to unity instantaneously is an ideal step response, which is obtained only at high flow rates. In actual practice, the temperature at the inflow takes some time to reach this value. Hence, the boundary conditions of the step response in the experiments and the numerical simulation are modified with the actual temperature response obtained at the inflow plane. With this modified boundary condition, the results of both 1 and 2-equation models are obtained and the comparison is carried out at various locations in the bed. To see the effect of the modified boundary condition, a comparison with the ideal step response is also performed.

The solid phase used in these experiments is glass beads. Its thermal conductivity k and thermal storage capacity ρc_p are lower than that of steel; the other solid phase used in this study, see Table 5.1 for details. Since water is the common fluid phase used in all the experiments, it is necessary to compare the thermal properties of the respective solid phases with it. For convenience, the comparison can be obtained by a single thermal property of a phase; namely thermal diffusivity α. Its value for glass and steel are 0.00583 cm^2s^{-1} and 0.0395 cm^2s^{-1} respectively. For water its value is 0.00146 cm^2s^{-1}. Hence, the thermal properties contrast in glass-water bed is lower as compared to that in steel-water bed.

The results obtained from both the glass-water beds, as discussed in Chapter 5, are compared with those of numerical simulation. The comparison is obtained qualitatively by comparing the unsteady temperature profiles at various locations and quantitatively by comparing speed and spread of the thermal front travelling through the bed. A sensitivity analysis is performed to find the effect of various parameters on the comparison obtained. In

addition, the thermal non-equilibrium between the fluid and the solid phase is also discussed. A complete analysis of step response in a glass-water bed is presented in this chapter so that the numerical simulation can be used to predict real life effects related to an energy storage system. We now discuss the thermo-physical properties of glass-water bed.

6.2 THERMO-PHYSICAL PROPERTIES OF GLASS-WATER BED

Table 5.1 gives the thermal properties of glass beads used in the experimental set up. Using the thermo physical properties of water at 300 K as: ρ = 995.7 kg m^{-3}, c_p = 4178 J (kg. K)$^{-1}$, k = 0.61 W (m. K)$^{-1}$, ν = 0.00802 cm^{2}s^{-1}, α = 0.00146 cm^{2}s^{-1} and Pr = 5.46; the values of parameters such as thermal storage capacity ratio β and thermal conductivity ratio λ are obtained. Table 6.1 gives the thermo-physical properties of the bed. In addition, the values of particle diameter, particle to tube diameter, porosity and specific surface area of the bed are also given.

Table 6.1: Thermo-physical properties of glass-water porous bed.

Thermal capacity ratio, β	Thermal conductivity ratio, λ	Particle diameter, d_P [mm]	Tube to particle diameter ratio, D/d_P		Porosity, ε	Non-dimensional specific surface area, A_f
			Bed-1	Bed-2		
2.2	0.55	2.25	22.8	25.7	0.37	43.16

The thermal storage capacity of water is higher than that of glass but its thermal conductivity is lower. The tube to particle diameter ratio is quite large so the velocity profile in the bed is nearly flat. A porous medium provides a large interphase surface area, for the particle size of 2.25 mm the specific surface area is 43.16 relative to the pipe radius. The length of the bed-1 is 66.1 and that of bed-2 is 60.7. A test section of suitable length is considered in the bed so that entrance and end effects are minimized.

We discuss the experimental step response of the glass-water beds. For both the beds, the step responses are obtained at three distinct flow rates starting from the minimum to the maximum value.

6.3 EXPERIMENTAL STEP RESPONSE

6.3.1 Glass-Water Bed-1

Figure 5.2 shows the layout of the glass-water bed-1 and Table 5.2 gives the position of thermocouples from the inflow plane of the bed. The step response of the bed is recorded at these positions. Figure 6.1 shows the experimentally obtained step response in the glass-water bed-1 at three distinct Peclet numbers. The x-axis shows the non-dimensional time and the y-axis the non-dimensional temperature. The temperature at a location rises as a function of time and approaches the maximum value of unity. The zero time in this figure is based on lead thermocouple's response and the corresponding distance from the lead thermocouple and the start of the bed. The other way of setting this time is choosing a thermocouple away from inflow plane and starting its response from zero time onwards. Such as location $z = 27$ can be set as an inflow plane and the corresponding point of time for start of temperature build up is set as zero.

Figure 6.1(a) shows the step response at a Peclet number of 614. The temperature profiles at various locations are shown in the figure. These profiles rise from a zero value and reach a steady state whose value is less than unity. The steady state temperature reached at each location decreases with distance from the inflow plane. It may be attributed to minor heat losses taking place in the bed. At a higher Peclet number of 1194 in Figure 6.1(b), the rate of temperature rise is faster and the corresponding steady state temperatures are higher when compared to those at lower Peclet number of 614. Figure 6.1(c), shows the step response when Peclet number is increased to 1591. The temperature profiles rise sharply and reach higher steady state temperatures when compared to lower Peclet numbers.

Figure 6.2 shows the temperature evolution in the bed for various Peclet numbers. Figure 6.2(a) shows the evolution when Peclet number is 614. Temperature in the bed rises with time and reaches a steady state at $t = 0.224$. At higher Peclet number of 1194 in Figure 6.2(b), the temperature rise in the bed is faster and the steady state is reached at $t = 0.1386$. The steady state at a Peclet number of 1591 is reached at $t = 0.0448$, see Figure 6.2(c). In

Figure 6.2(d), the steady state temperature profiles for each Peclet number are shown. These profiles fall with distance from the inflow plane due to minor heat loses taking place in the bed. Further, the corresponding temperatures increase with Peclet number.

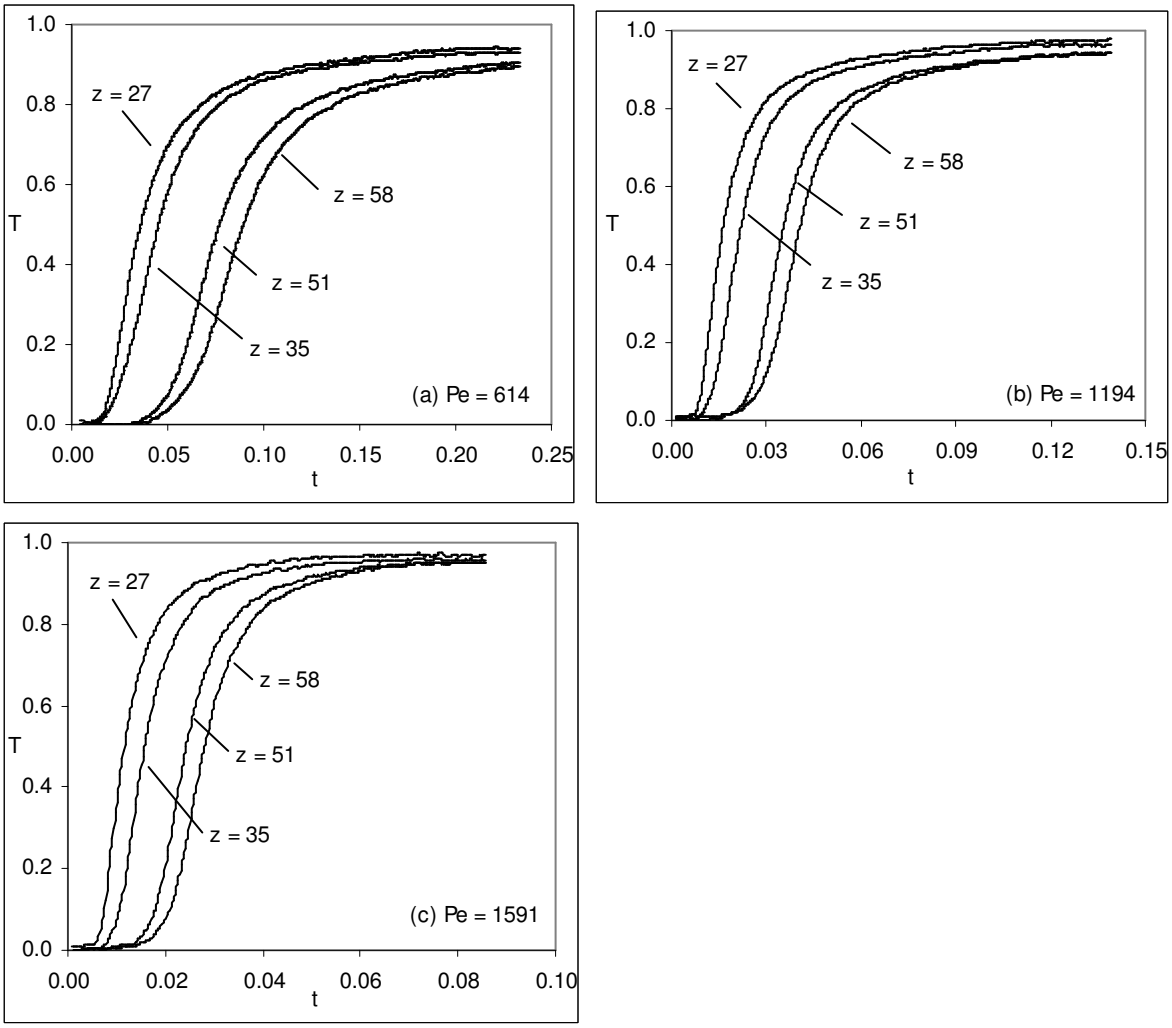

Figure 6.1: Experimental step response of glass-water bed-1.

6.3.2 Glass-Water Bed-2

Figure 5.3 shows the layout of the glass-water bed-2 and Table 5.3 gives the position of the thermocouples from the inflow plane. In this bed, there is no plain portion in the tube and is closely packed with glass beads from start to end. The step response is obtained by considering a test section from third to sixth thermocouple in the bed. The position of third thermocouple is set as an inflow plane and the point of start of the thermal response is set as

zero time. The location of subsequent thermocouples change with respect to the third thermocouple as shown in Table 6.2. With this approach, the flow development effects in the entrance region of the bed are minimized.

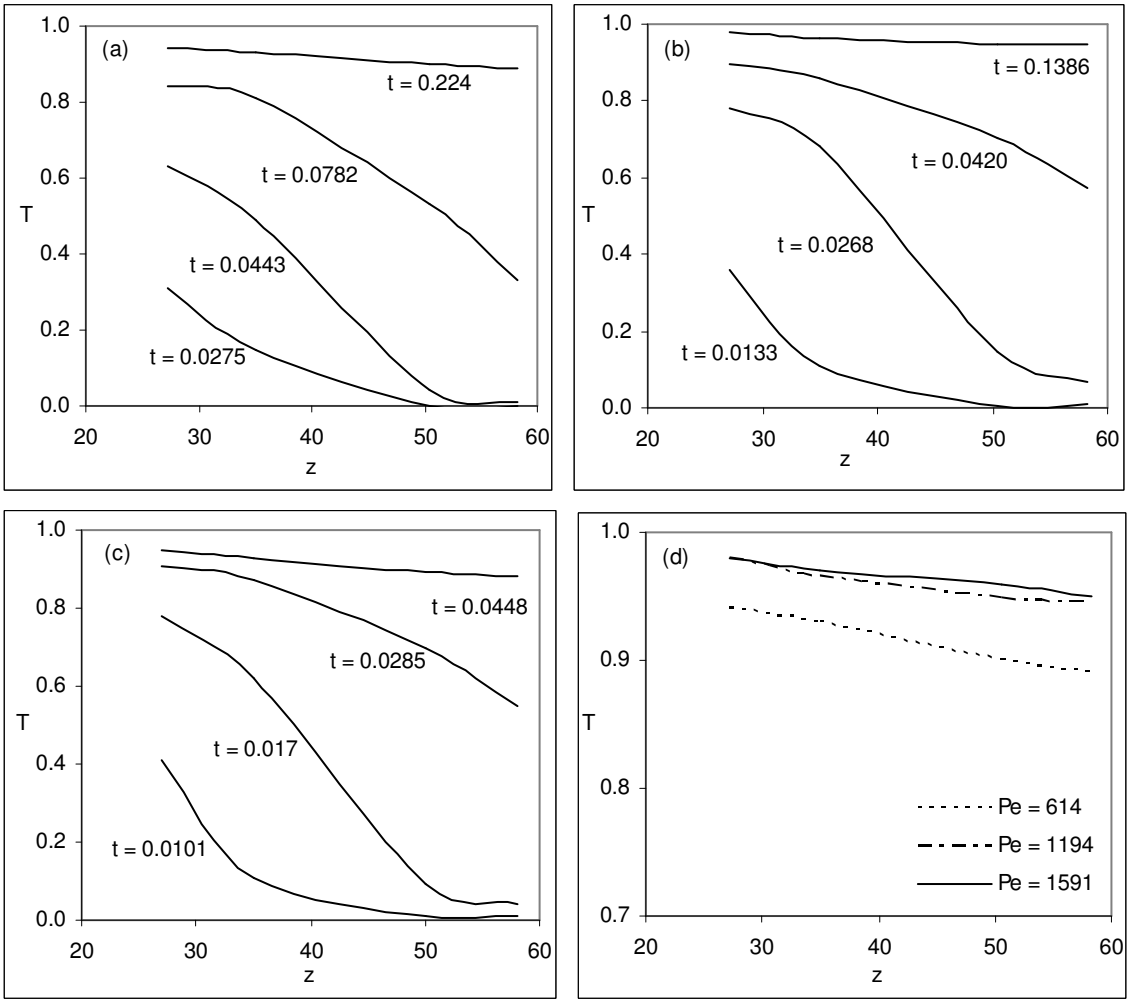

Figure 6.2: Temperature variation as a function of distance from inflow plane for experimental step response in glass-water bed-1. (a) Pe = 614; (b) Pe = 1194; (c) Pe = 1591 and (d) Steady state.

Figure 6.3 shows the experimental step response in this bed for three distinct Peclet numbers. The response at low Peclet number of 513 is shown in Figure 6.3(a). Here the steady state temperatures at all the locations are less than unity. The profiles become slower when approaching the respective steady states indicating that the diffusive energy transfer dominates the advective energy transfer at this Peclet number. At higher Peclet number of 915, in Figure 6.3(b), dominance of convective energy transfer is established. Here the steady

state temperatures almost reach the maximum value of unity and the rate of temperature build up is faster than that at a lower Peclet number of 513. In Figure 6.3(c), the step response at a Peclet number of 1615 in shown. Here the temperature profiles look quite sharp and the steady state temperatures approach unity. Hence, at this Peclet number, the convective energy transfer dominates the diffusive energy transfer.

Figure 6.4 shows the temperature evolution in the bed for various Peclet numbers. At a lower Peclet number of 513 in Figure 6.4(a), the temperature profiles have gentle slope as compared to those at higher Peclet numbers as shown in Figures 6.4(b & c). For example at t = 0.0403 in Figure 6.4(a), the profile extends up to a location of z = 33 whereas the corresponding profiles in Figures 6.4(b & c) show a sharp fall terminating at z = 22.1. It shows the dominance of diffusion energy at lower Peclet number. The steady state temperature profiles are shown in Figure 6.4(d) where the corresponding temperatures increase with Peclet number. Hence, the heat losses are less at higher Peclet numbers.

The above analysis shows the importance of convective heat transfer in porous medium at higher Peclet numbers. We can measure the relative strength of diffusive and convective energy transfers in porous medium by using terms such as front speed and spread.

Table 6.2: Position of thermocouple in the glass-water bed-2 and corresponding distances from third thermocouple.

Thermocouple No.	Non-dimensional distance from inflow to bed	Non-dimensional distance from third thermocouple onwards
1	1.44	-
2	9.62	-
3	20.65	0
4	31.75	11.1
5	42.79	22.1
6	53.72	33.0

6.4 FRONT SPEED AND SPREAD

In order to quantitatively measure the diffusive and the advective transport in porous medium the terms such as front speed and front spread are used. Further, these are also helpful in comparing the numerical simulation with the experimental results. These are defined as

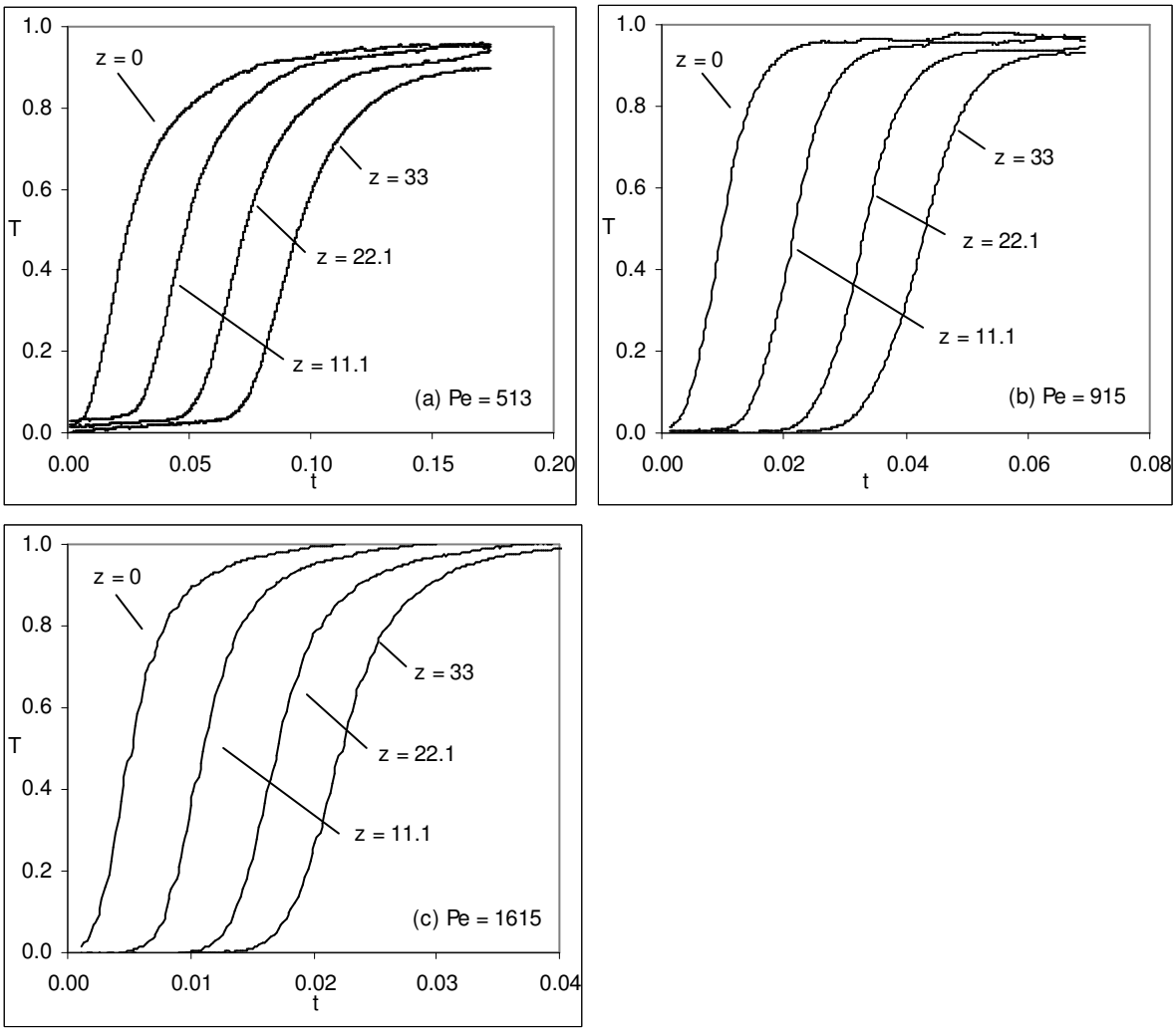

Figure 6.3: Experimental step response of glass-water bed-2.

Front Speed: Spatial distance between the given locations divided by difference in time elapsed for fluid to reach a temperature of 0.5 at each location. Nondimensional value of the front speed is given as

$$\text{Front Speed} = \frac{1}{\text{Pe}}\left(\frac{\Delta z}{\Delta t}\right) \tag{6.1}$$

In experiments, it is calculated by dividing the distance between the two successive thermocouples by the corresponding time elapsed. Similarly, in simulation, the grid numbers for each thermocouple are identified and the front speed is obtained from the thermal response at these grid points.

Front Spread: Time for fluid temperature to rise from 0.25 to 0.75 at a particular location. Its non-dimensional value is given as

$$\text{Front Spread} = (\Delta t)\text{Pe} \tag{6.2}$$

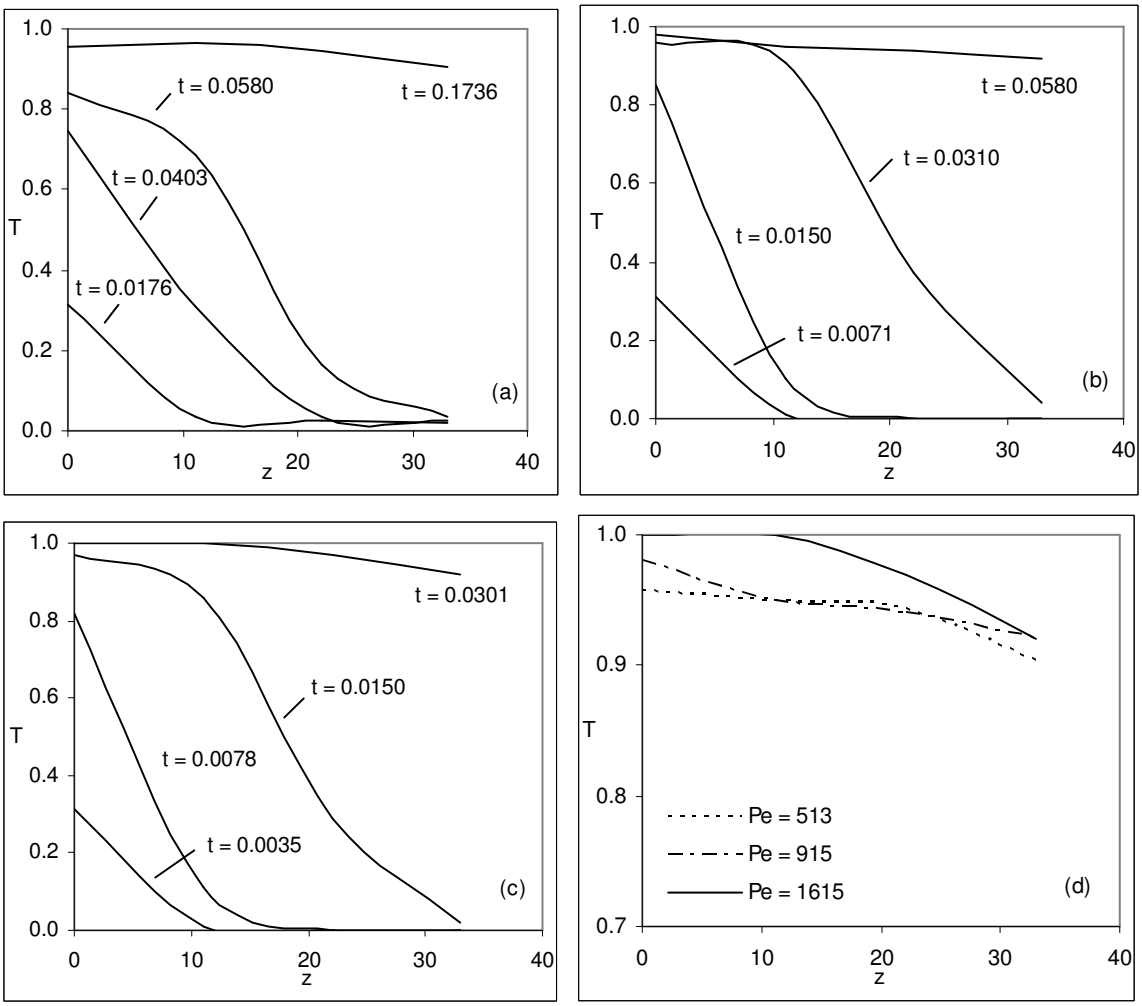

Figure 6.4: Temperature variation as a function of distance from inflow plane for experimental step response in glass-water bed. (a) Pe = 513; (b) Pe = 915; (c) Pe = 1615 and (d) Steady state.

The front speed is the speed at which thermal front travels in the bed and is generally different from the true fluid speed. The diffusive energy transfer slows the front speed. The

spread of the front at a location indicates role of diffusion in the overall energy transfer. A higher spread at a location indicates higher energy transfer due to diffusion. Hence, at lower Peclet numbers, where the energy transfer is predominantly by diffusion, the front spread is an important parameter. An ideal step response will show a zero spread when the corresponding Peclet number is very high.

6.4.1 Glass-Water Bed-1

Figure 6.5 shows the experimentally obtained front speed and spread. In Figure 6.5(a) shows the front speed for different Peclet numbers. Since front speed is calculated between two locations where the temperature profiles are recorded, the *x*-coordinate is the average of the two locations considered. At a Peclet number of 614, it first falls and then increases with distance. At a higher Peclet number of 1194, it again falls but marginally and subsequently increases. The rate of increase is higher as compared to that at lower Peclet number of 614. At a Peclet number of 1591, the corresponding deviations are small. In general, the front speed shows variations along the length and increases with Peclet number. Figure 6.5(b) shows the front spread. It is highest for the lowest Peclet number of 614 and decreases with an increase in Peclet number. For a particular Peclet number, the spread increases with distance from the inflow plane.

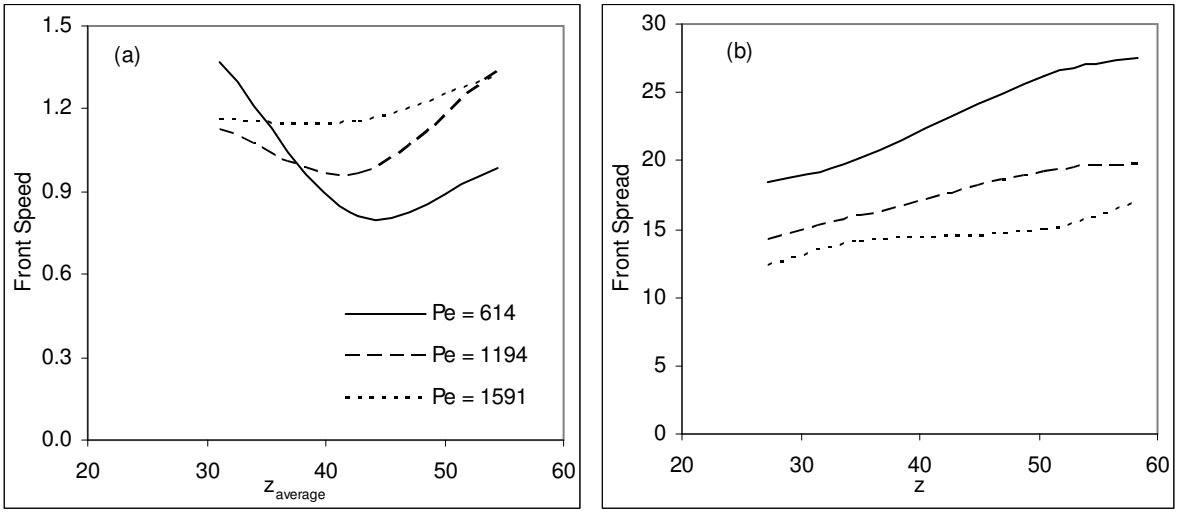

Figure 6.5: Experimental front speed and spread in glass-water bed-1.

The physical origin of the spread is in hydrodynamic dispersion in the pores through which fluid movement takes place, as well as thermal non-equilibrium between the fluid and the solid phases. Heat loss from the tube walls to the ambient also contribute to the spread of the thermal front. These three factors are cumulative in the sense that the spread increases with distance, though at a given location, a steady state is attained. The front speed in a porous bed is a function of Peclet number, dispersion, heat loss to the atmosphere and the thermal properties of fluid and solid phases. In general, higher the heat loss, lower is the front speed. The front spread is indicative of dispersion and decreases with an increase in Peclet number. The dispersion in radial direction causes an increase in spread with distance. In general, the above figure depicts the behavior of spread as increasing with distance but that of front speed is first decreases and then increases with distance. Theoretically, it should only decrease with distance due to dispersion, thermal non-equilibrium and heat loss to ambient. Higher front speed may be caused due to channeling in the bed which causes, the flow of fluid through plain tube in preference to the porous medium, Bear [1988]. This bed is using a glass tube and the glass beads are not close packed in it; hence the channeling is not ruled out. The increase in front speed may also be caused due to end effects on the flow. Flow development near the axis can increase the fluid speed towards the end of the bed. Consequently the portion of the bed beyond location $z = 50$ is not considered for validation and the consequent front speed does not increase with distance. Bed-2 can provide accurate information in this regard.

6.4.2 Glass-Water Bed-2

Here the front speed and spread as observed in bed-2 are discussed. The analysis is based on choosing thermocouples sufficiently away from the inflow and outflow planes as discussed in Section 6.3.2. This will help in selecting a group of thermocouples whose response is suitable for validation such that the front speed is free from the effect of flow development in the entrance region and further it is not increasing with distance due to end effects. Figure 6.6 shows the front speed and spread in this bed. Figure 6.6(a) shows the front speed for various Peclet numbers. It increases with the Peclet number and for a particular Peclet number it decreases marginally with distance except from locations 22.1 to 33, where it increases. It may be attributed to end effects as these locations are near to the exit end of the bed. The exit

effect seems to be increasing with Peclet number. Hence, for validation the portion from 22.1 to 33 is neglected. The front spread is shown in Figure 6.6(b); showing higher spread at lower Peclet numbers. For a particular Peclet number, the front spread increases with distance from the inflow plane. At higher Peclet number, the spread becomes independent of Peclet number and remains constant of it. Overall, the trends in this bed are consistent and can provide vital information about validation.

6.4.3 Comparison of the Two Beds

A comparison of front speed and the spread is carried out for the two beds. An increase in front speed with Peclet number is observed for both the beds. It increases from 0.9 to 1.2 as Peclet number increases from 600 to 1500. In some regions in bed-1, the front speed is relatively large due to channeling particularly at lower Peclet numbers. Overall, the mean values of front speeds in the two beds are almost identical. Similarly, a decrease in front spread with Peclet number is observed for both the beds. It increases with distance from the inflow plane in both the beds. For almost the same flow rates and distance from inflow plane, the spread of bed-1 is higher when compared to that in the bed-2. There is a proportionate decrease in spread with Peclet number in bed-1, but in bed-2 the results converge with Peclet number, such that they almost become independent of Peclet number. It may be attributed to higher heat loss through glass tube as used in bed-1. PVC tube used in bed-2 seems not altering the behavior of the front. In general, both the beds provide meaningful information though the results of bed-2 seem more consistent.

We now compare the experimental results with the numerical simulation. For this purpose, the temperature-time profiles as shown in Figures 6.1 and 6.3 are redrawn by adding the corresponding numerical simulation profiles showing thereby a qualitative validation. A quantitative validation is performed by adding the results of numerical simulation to the profiles of experimental front speed and spread as shown in Figures 6.5 and 6.6. The comparison is carried out for both the beds.

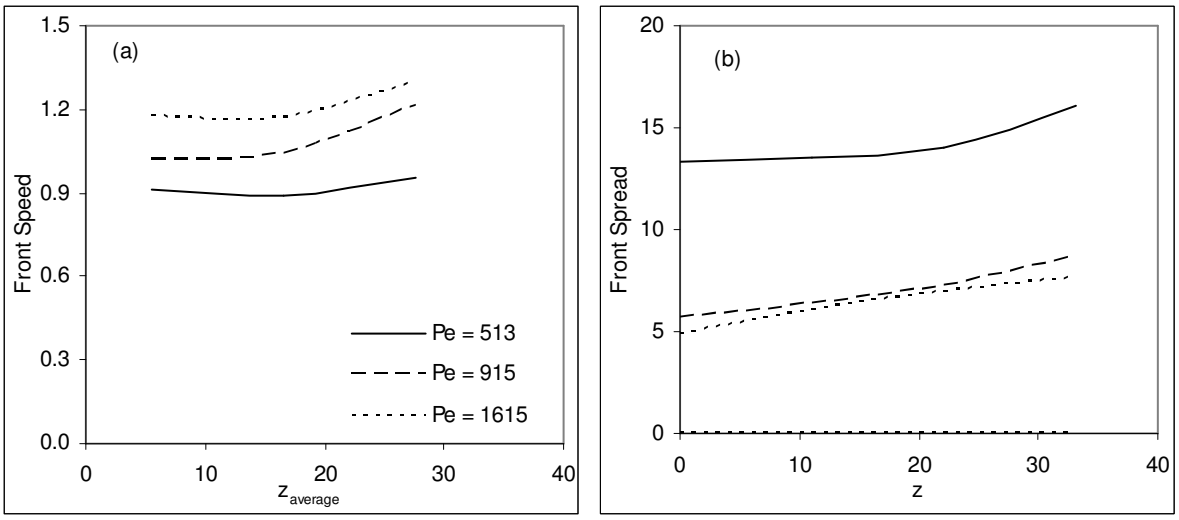

Figure 6.6: Experimental front speed and spread in glass-water bed-2

6.5 VALIDATION OF NUMERICAL MODELS USING GLASS-WATER BED-1

Here the comparison of experimental results of bed-1 is carried out with numerically generated results. The comparison is in the form of temperature-time and the front speed and spread profiles for various Peclet numbers. The validation is based upon both the ideal step response at the inflow plane and actual step response of a thermocouple far away from the inflow plane. In the comparison, the effect of heat loss is included by increasing the Biot number in the numerical models form zero onwards such that meaningful changes in these profiles occur. The comparison based on the ideal step response is carried out first.

6.5.1 Comparison For Ideal Step Response

Here the comparison of experimental results with numerical models is carried out with the boundary conditions pertaining to an ideal step response as given by Equations 5.1 and 5.2. It is assumed that temperature at the inflow plane rises to its maximum value of unity instantaneously. Figure 6.7 shows the comparison of temperature-time profiles at three distinct Peclet numbers. Here the Biot number is set to zero. The profiles corresponding to experiments, 1 and 2-equation models are shown in the figure. For each Peclet number, the comparison is shown at four distinct locations in the bed. The first of the two curves of each category in all the figures correspond to nearer location i.e. in Figure 6.7(a) to z = 27 and in

Figure 6.7(b) to z = 51, the experimental profiles are indicated by corresponding slashes. In these figures, the numerical models predict a faster temperature rise as compared to that of the experiments. The numerical profiles are almost vertical and hence are dominated by the convective effects. Of the two numerical models discussed, 1-equation model predicts a faster temperature response as compared to that of 2-equation model. A close look at the experimental profiles shows that these start gradually from a zero value such that its build up is very gentle until a temperature of around 0.1 is attained and afterwards the build up is at faster rate until a temperature of around 0.7 is attained. In the end as approaching the maximum temperature, the build up is again very slow. Hence, the experimental profiles have three distinct regions, a central region where the build up is faster separated by regions of slower build up on the either side. The profiles corresponding to the experiments are largely diffusive type. The numerical profiles for this boundary condition do not show regions of gradual build up but show very steep temperature profiles.

Figure 6.7(a & b) shows the comparison at a Peclet number of 614. Figure 6.7(a) shows the comparison at z = 27 and 35 and Figure 6.7(b) at z = 51 and 58. The rate of temperature builds up in the numerical simulation is faster as compared to that in the experiments, and the two curves intersect with each other. It is found that at z = 27.2, the point of intersection of 2-equation model and experiments occur at a temperature of 0.5 and it falls with distance. For example, at z = 51 and 58, the points of intersection occur at temperatures of 0.3 and 0.2 respectively. This is because of perhaps the excessive diffusion in the experiments as compared to that in the simulation. The maximum temperature predicted by numerical models is equal to unity at each location whereas in experiments it is less than unity. It is observed that the rate of diffusive transport in the experimental profiles increases with distance such that the build up becomes slower. The difference between 1 and 2-equation models increases marginally with distance. The absence of interphase heat transfer in this model could be one of the reasons.

Figure 6.7(c & d) shows the corresponding comparison at a Peclet number of 1194. In experiments, an increase in Peclet number indicates an increase in advection relative to diffusion, particularly at locations nearer to the inflow plane. It is demonstrated by the profile at z =27 in Figure 6.7(c), which intersects 2-equation model profile at a temperature of 0.6, which is higher than that at a Peclet number of 614. The point of intersection falls with

distance from the inflow plane. For example, at farther locations of z = 51 and 58 in Figure 6.7(d), the intersection occurs at temperatures of 0.35 and 0.3 respectively. Hence, the diffusive effects increase with distance. Overall, the comparison at all locations at this Peclet number improves relative to lower Peclet number of 614. The difference between 1 and 2-equation model is now less as compared to that at the lower Peclet number.

Figure 6.7(e & f) shows the comparison at a Peclet number of 1591. Here the advection rate increases and difference between the 1 and 2-equation models reduces to a minimum value. The difference between the experimental profiles and those of numerical simulation also decreases. The profiles of experiments and 2-equation model at various locations intersect at higher temperatures as compared to lower Peclet numbers of 614 and 1194. Overall, the trends are similar to those at lower Peclet numbers but the comparison improvers.

It is clear from the above analysis that though the numerical models predict the time of start of the step response at a location well but the consequent temperature build up is not well matched, particularly at lower Peclet numbers. The numerical models show steeper temperature build up as compared to that in the experiments. The experimental profiles become even slower approaching the maximum temperature at respective locations. The comparison of temperature profiles of experiments and numerical model reveals that the nature of the two is distinct, the experimental profiles are dominated by diffusion and those of simulation by advection. Recalling the principle of hydrodynamic dispersion, the fluid path in a porous medium is not linear but spreads in transverse and longitudinal direction due to presence of pores. The true path of the fluid as against the linear path implied by the flow model leads to larger spreading rates of energy. As the flow continues, it occupies ever-increasing volume of flow domain. This is further enhanced by heat loss through tube wall and thermal non-equilibrium.

1-equation model predicts a faster temperature front as compared to 2-equation model. The difference between the two models is large at lower Peclet numbers and it increases with distance from the inflow plane. The comparison of the experiments and the numerical simulation is better at higher Peclet numbers. It is also better for locations closer to the inflow plane. This comparison is at zero Biot number in numerical simulation, the

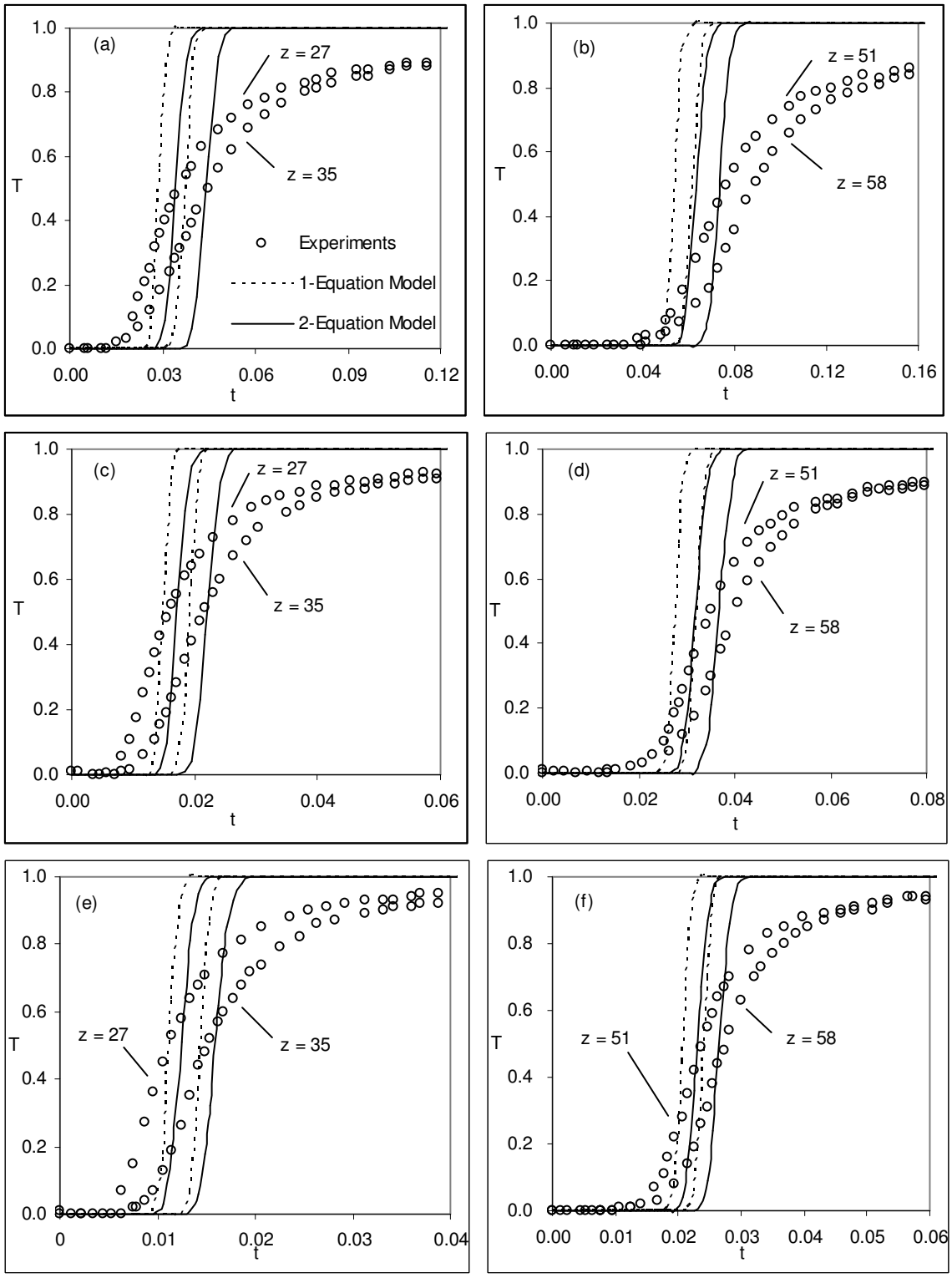

Figure 6.7: Variation of temperature with time in experiments, 1 and 2- equation model for glass-water bed-1 for an ideal step change at inflow plane in simulation. *Bi* = 0. (a,b) Pe = 614; (c,d) Pe =1194 and (e,f) Pe = 1591.

comparison when it is increased to unity is shown in Figure 6.8. It only effects the simulation and the experimental profiles remain unchanged as before. This value of Biot number is chosen such that the effect on the temperature profiles at various locations varies considerably. A zero Biot number signifies that the external convective resistance to heat loss is much higher as compared to internal conductive resistance and no heat loss takes place across the tube. With an increase in Biot number, the external convective resistance decreases proportionally and heat loss starts. The effect of heat loss is to lower the energy flow rate downstream, which is evident from the maximum temperature attained at a location and the corresponding front speed and spread. The maximum temperature attained at a location in simulation falls and it now becomes lower than that in the experiments. This temperature also falls with distance from the inflow plane. The front speed in simulation falls but the front spread increases in comparison to zero Biot number and hence the thermal response at a location becomes slower. The thermal response at a location as predicted by 1-equation model is faster as compared to 2-equation model and the corresponding maximum temperature attained is higher. Overall, the match between the experiments and simulation improves but the maximum temperature predicted by simulation is lower than that of the experiments.

6.5.1.1 Front Speed and Spread

Figure 6.9 compares the experimental front speed and spread with that in numerical simulation when Biot number in simulation varies from zero to unity. The comparison is carried out excluding the last thermocouple at z = 58 from the inflow plane. At zero Biot number, there is no heat loss from the tube and the front speed is the maximum and the corresponding spread is the minimum. The front speed as predicted by 1-equation model is higher as compared to that of 2-equation model and the experiments. The front spread in experiments is much higher as compared to that in numerical simulation.

Figure 6.9(a & b) compares the experimental and numerical front speed and spread at a Peclet number of 614. Figure 6.9(a & b) respectively show the front speed and the spread. The front speed for 1-equation model is the highest, followed by 2-equation model and the experiments. In simulation, it falls with an increase in Biot number. The front spread in experiments is large as compared to that in the simulation. In simulation, it increases with

Biot number, but its value remains lower as compared to that in the experiments. It is higher for 2-equation model as compared to that of 1-equation model.

At a Peclet number of 1194 in Figure 6.9(c & d), the similar trends are observed except that the difference between the experiments and simulation falls. The front speed increases marginally in simulation and the spread falls. For region between the locations z = 27 and 35, the experimental front speed is 1.12 whereas the corresponding value of 2-equation model for unity Biot number is 1.25.

By increasing the Peclet number to 1591 as shown in Figure 6.9(e & f), the front speed as predicted by 2-equation model for Biot number of unity is only marginally faster than that of experiments.

Hence, at higher Peclet numbers the validation improves. It also improves by increasing the Biot number from zero onwards. Though, the front speed in numerical simulation is marginally higher but the spread is much lower than that in the experiments Hence, a validation based on the modified boundary condition is needed.

6.5.2 Validation using Modified Step Response

In this section, the validation is based upon the thermal response of a thermocouple far away from the inflow plane. For this bed the thermocouple at location z = 27.2 is considered as the inflow plane. This thermocouple is at 70 cm away from the actual inflow plane and it is free from flow development in the entrance region. Its response is set as boundary condition for subsequent thermocouples at times greater than zero and the position of this thermocouple is set as z = 0. As this thermocouple is set as an inflow plane, the position of next thermocouples changes with respect to this thermocouple to 7.7, 23.2 and 31.1 respectively. The thermal response at these locations is compared.

6.5.2.1 Inflow Profile at Various Peclet Numbers

The thermal response at location z = 27 in Figure 6.1 is set as modified step boundary condition for subsequent locations. In simulation, curve fitting is used to obtain this profile as a function of time. Figure 6.10 shows the experimental profiles and corresponding values obtained by curve fitting for simulation. Hence temperature at the new location of z = 0 approaches unity temperature as a function of time. This time varies with Peclet numbers as

shown in the figure. At a lower Peclet number of 614, the step response is very slow but for a Peclet number of 1591, it becomes almost an ideal step response. The thermal response at subsequent locations is obtained in simulation and compared with the corresponding experimental results.

6.5.2.2 Unsteady Temperature Profiles

Figure 6.11 compares the experimental results with those of numerical simulation in bed-1 with the modified boundary condition. Here the Biot number is set to zero. The comparison looks better than that for ideal boundary condition. It improves with Peclet number and is better at locations nearer to the inflow plane. The time of start of the experimental and numerical simulation profiles is quite close and the slope of two looks alike particularly at higher Peclet numbers. The time of start of a profile at a location relates to its speed and the slope, in particular relates to the spread of the front traveling through the porous medium. The experimental and numerical profiles during initial phase of temperature build up are almost identical but afterwards the experimental profile becomes diffusive type.

Figure 6.11(a & b) shows the comparison for a Peclet number of 614. The profiles related to the experiments, 1 and 2-equation model are shown in the figure. Figure 6.11(a) shows the comparison at locations z = 0 and 7.8 whereas Figure 6.11(b) at the locations z = 23.3 and 31.1. At location z = 0, in figure 6.11(a), the three profiles are set same. At location z = 7.8, the profiles of 1 and 2-equation models are almost identical and close to the experimental profile. At location z = 23.3, 1 and 2- equation model results are slightly faster as compared to the experimental results. Overall, the simulation matches with the experiments well particularly nearer to the inflow plane. For locations away from the inflow plane, the simulation is faster as compared to the experiments. The maximum temperature in numerical simulation and experimental results is also well matched.

Figures 6.11(c & d) show the comparison at a higher Peclet number of 1194. At locations z = 7.8 and 23.2 in Figures 6.11(c & d), the match is quite good. 1-equation model is marginally faster as compared to 2-equation model and the difference increases with distance. At location z = 31.1, in Figure 6.11(d), the simulation results seems slightly faster as compared to the experimental results. Overall, the comparison is better at this Peclet number as compared to lower Peclet number of 614.

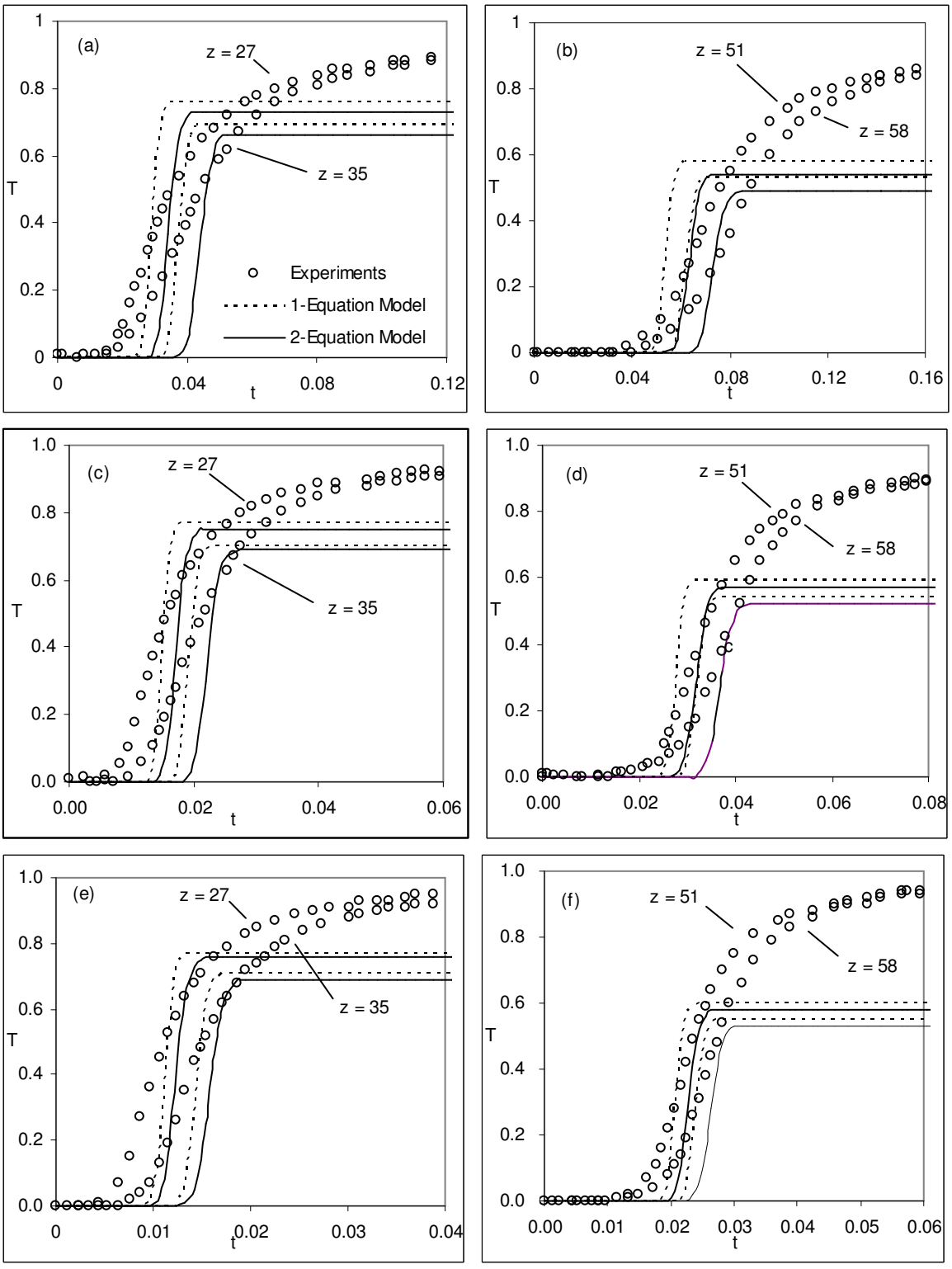

Figure 6.8: Variation of temperature with time in experiments, 1 and 2 equation model for glass-water bed -1 for an ideal step change at inflow plane in simulation. *Bi* = 1. (a,b) Pe = 614; (c, d) Pe = 1194 and (e, f) Pe = 1591.

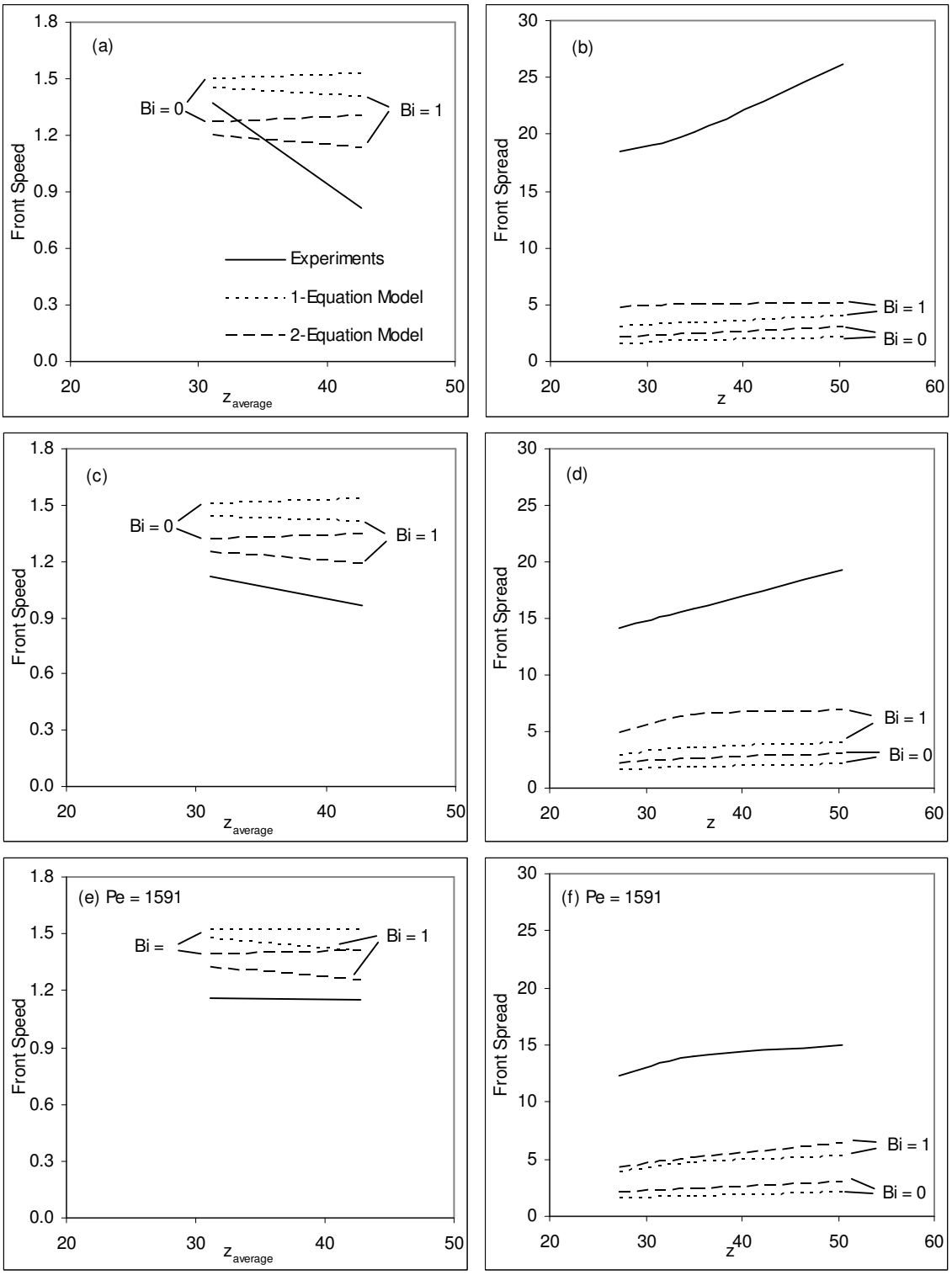

Figure 6.9: Speed and spread of front experiments, 1-equation model and 2-equation model for glass-water bed-1 for an ideal step change at inflow plane in simulation (a,b) Pe = 614; (c, d) Pe = 1194 and (e, f) Pe = 1591.

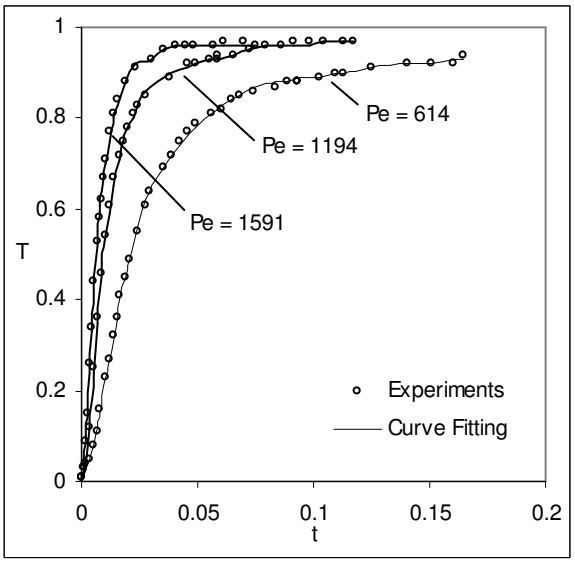

Figure 6.10: Experimental step response at new inflow plane of bed-1 and corresponding points obtained by curve fitting in simulation.

Similarly Figure 6.11(e & f) show the comparison at a Peclet number of 1591. At z = 7.8, in Figure 6.11(e), here is hardly any difference between the numerical simulation and experimental results. In figure 6.11(f), only minor differences at locations z = 23.2 and 31.1 are visible. 1- equation model results are marginally faster than 2-equation model results at this Peclet number. Hence, with an increase in flow rate, the validation has improved.

The difference between 1 and 2-equation model is though looks small in these figures but it is actually substantial. At the intermediate Peclet number of 1194, the maximum difference between the two results at location z = 23.3 is 0.11. Hence the difference between the two models is observable.

It is important to see the effect of heat loss on validation. Figure 6.12 shows the comparison at Biot number of 0.5 in numerical simulation, which means that heat loss is taking place to the surroundings. The experimental profiles are unchanged but the numerical results show fall in the rate of temperature build and subsequent maximum temperature attained. The effect of heat loss is cumulative in nature and hence observable at locations away from the inflow plane and the maximum temperature falls relative to the experiments.

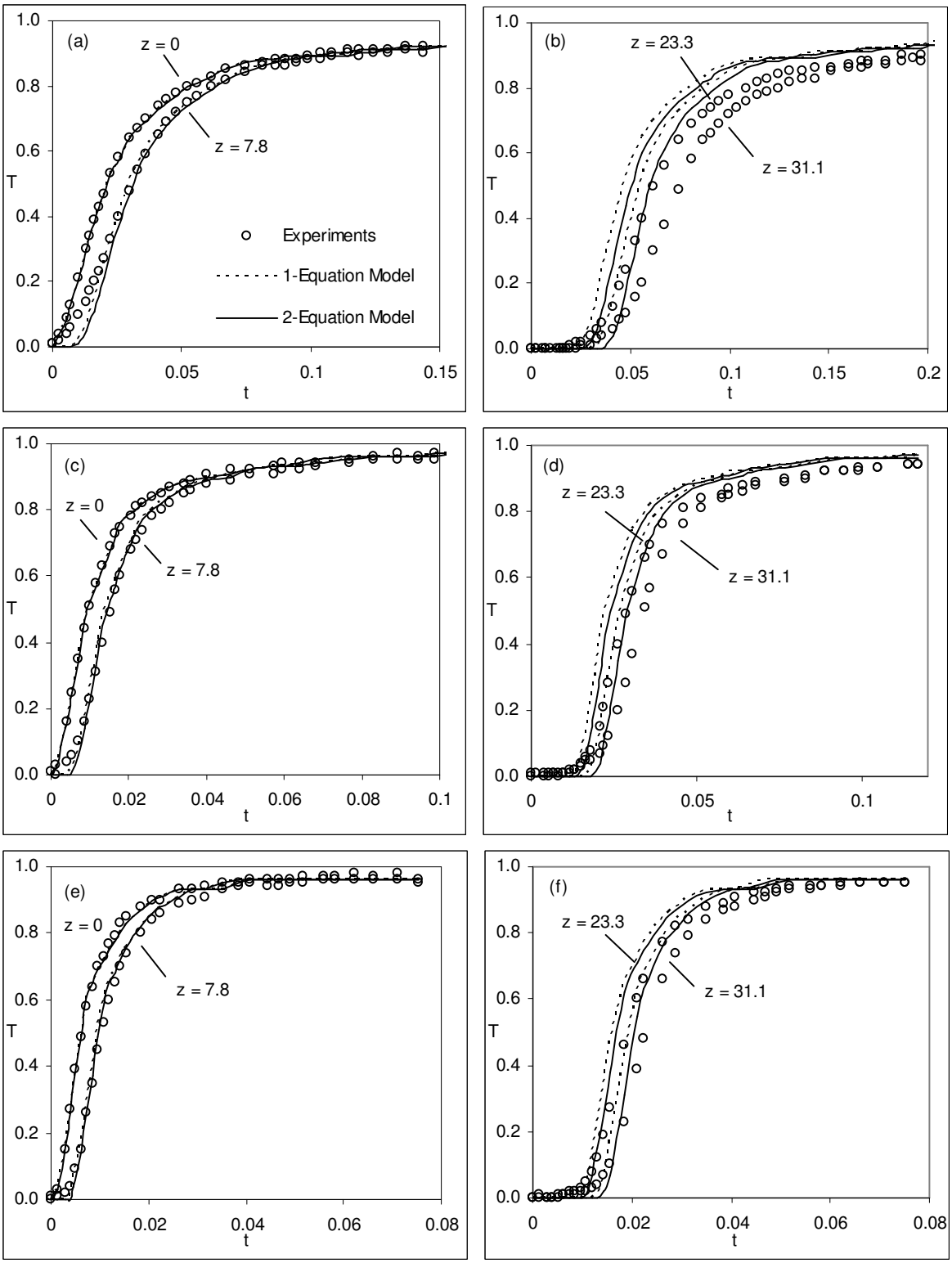

Figure 6.11: Variation of temperature with time in experiments, 1 and 2 equation model for glass-water bed-1 with modified boundary condition. *Bi* = 0. (a, b) Pe = 614; (c, d) Pe = 1194 and (e, f) Pe = 1591.

The maximum temperature of 1-equation model at a location is higher than that of 2-equation model. The heat loss results into a reduction in the front speed and an increase in the front spread.

In figure 6.12(a & b), the comparison for a Peclet number of 614 is shown. At location z = 7.8, the profiles are almost identical to that at zero Biot number. At location z = 23.3, in Figure 6.12(b), the simulation results are now closer to the experimental profiles as compared to that at zero Biot number. But the corresponding maximum temperature falls marginally below that of the experiments. At location z = 31.1, the simulation again comes closer to the experiments and the maximum temperature falls.

Similarly, Figure 6.12(c & d) shows the comparison at a Peclet number of 1194. In Figure 6.12(c), the match at location z = 7.8 is almost perfect both in terms of build up and the maximum temperature attained. At location z = 23.3, in Figure 6.12(d), 2-equation model results is slightly faster compared to that of the experiments but predicts a lower maximum temperature. The maximum temperature of 1-equation model now comes closer to that of 2-equation model. At location z = 31.1, again the results of 2-equation model is quite close to the experiments the only mismatch being the maximum temperature attained which is lower in the model.

Figure 6.12(e & f) show the comparison for a Peclet number of 1591. Here the match between the experiments and 2-equation model is almost perfect but for the maximum temperature attained which is lower in the model. Otherwise the match is quite good. In numerical simulation, the maximum temperature attained at a location falls with distance. Hence, the effect of increase in Biot number is visible for temperature build up as well as maximum temperature attained in simulation and both these fall. The maximum temperature attained decreases with distance from the inflow plane such that this effect seems to be cumulative in nature. A comparison of front speed and spread provides true picture about the quality of validation.

6.5.2.3 Front Speed and Spread

The front speed and spread for the modified inflow plane boundary condition is compared in this section. Figure 6.13 shows the corresponding front speed and spread. The experimentally observed front speed and spread remains same as discussed in Section 6.5.1.1. There seems

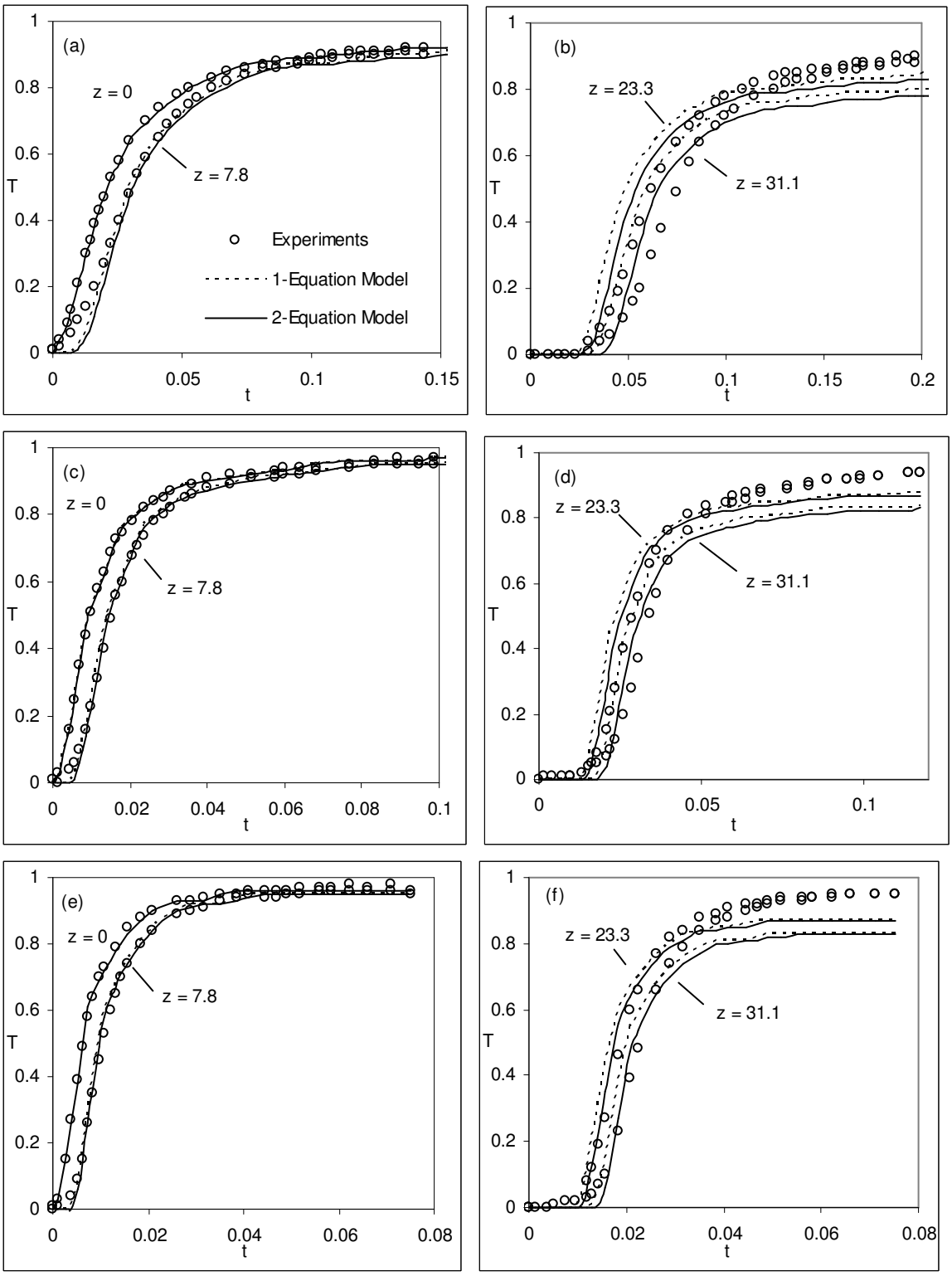

Figure 6.12: Variation of temperature with time in experiments, 1 and 2 equation model for glass-water bed-1 using modified boundary condition. *Bi* = 0.5 (a,b) Pe = 614; (c,d) Pe = 1194 and (e, f) Pe = 1591.

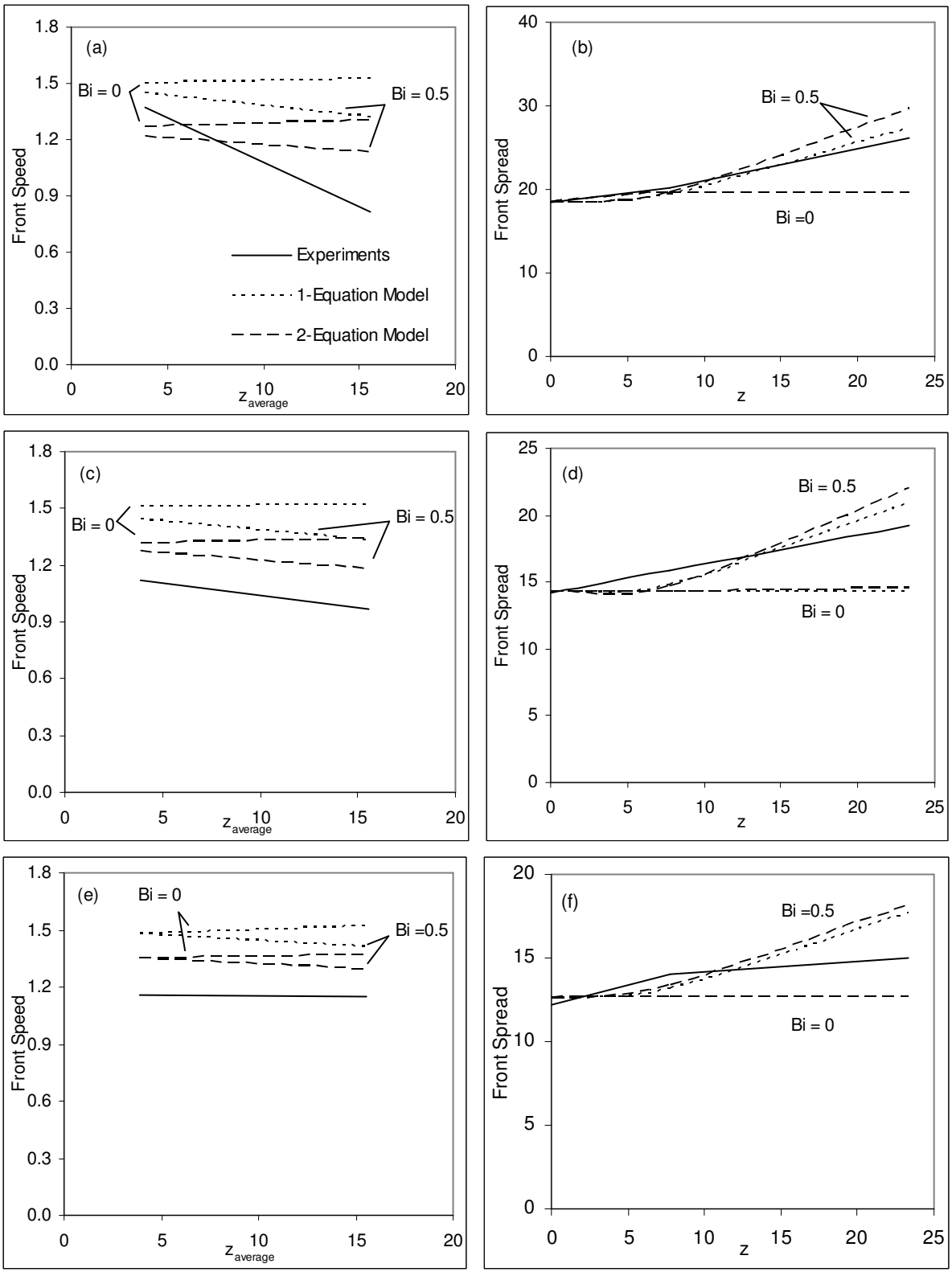

Figure 6.13: Speed and spread of front in glass-water bed-1 for experiments, 1-equation model and 2-equation model.

hardly any change in the front speed predictions in numerical simulation but the corresponding spread changes.

Figure 6.13(a & b) shows front speed and spread at Peclet number of 614. The front speed as shown in Figure 6.13(a) falls with an increase in Biot number. These results are almost identical to the corresponding results with ideal step response as indicated by Figure 6.9(a) except for the value of Biot number is 0.5 here. Hence, the front speed remains unchanged with the change in boundary conditions. However, spread as shown by Figure 6.13(b) shows a good comparison with the experiments. At zero Biot number, 1 and 2-equation model results are almost identical. With an increase in its value to 0.5, the spread exceeds the corresponding experimental value. The same results are seen at higher Peclet number of 1194. Here the front speed for 2-equation model at Biot number of 0.5 is quite close to that in the experiments. The front spread at this Peclet number is also quite close to the experiments and the spread of 2-equation model is higher than that of 1-equation model. The spread at a Peclet number of 1591 becomes larger than experiments as shown in Figure 6.13(f). The front speed however remains unchanged as in Figure 6.9, hence no effect of the change in boundary condition.

From the above discussion, it is concluded that with change in boundary conditions, the spread as shown by 1 and 2-equation models matches well with the experiments but the front speed remains almost unchanged and remains more than that in experiments. At higher Peclet number, it comes closer to that of the experiments. At Biot number of 0.5, the front speed by 2-equation model is around 12-15 % higher as compared to that of the experiments.

Overall, the agreement between experiments and simulation is good, particularly at points closer to inflow plane at higher Peclet numbers. At far off points, the effects of heat loss, dispersion and interphase heat transfer adds up and lowers the agreement with the experiments. Though the agreement is good but this glass-water-bed fabricated using a glass tube does not allow the particles to be close packed. The loose packed particles could be seen near the walls of the tube near the end. The resulting channeling increased the front speed near the end of the bed. It also increases with end effects when the last thermocouple is close to the end of the bed and water falls freely under gravity to storage tanks.

The insulation material added on the glass tube again could not be tightened for the fear of breaking the tube, hence heat losses takes place through the bed. A new bed is constructed using PVC as the tube material and the particles were closely packed in this bed.

After filling the bed with glass beads, the pipe was held vertically and mechanical agitation was performed from the top so that beads settle in the interspaces. It was ensured that glass beads are close packed in the tube and is subsequently well insulated with glass wool.

6.6 VALIDATION OF NUMERICAL MODELS FOR GLASS-WATER BED-2

The comparison of the experimental results of bed-2 is performed here with the numerical simulation. Consider the layout of bed-2 as shown in Figure 5.3 and the corresponding distances in non-dimensional form in Table 5.3. In this bed, the plain flow at the entrance and end of the pipe is not used which ensures close packing of beads in the tube. In all six thermocouples are inserted in the bed. For validation, the third thermocouple is set as location $z = 0$ and its response is set as boundary conditions for the subsequent thermocouples as shown in Section 6.3.2. The modified location of next thermocouples with respect to the third thermocouple becomes 11.1, 22.14 and 33.07 as shown in Table 6.2. The response at last thermocouple is not considered for validating the front speed and the spread as it is close to the outflow plane.

The validation in the form of unsteady temperature profiles is carried out by adding the results of numerical simulation in the corresponding experimental profiles as shown in Figure 6.3. The quantitative comparison is obtained by adding again the results of numerical simulation in the corresponding experimental results as shown in Figure 6.6. The effect of heat loss on validation is studied by increasing the Biot number from zero onwards. As it is clear from the validation using bed-1 that the ideal step response is only possible for very high Peclet numbers, consequently the validation based upon the modified boundary condition is only considered for this bed.

6.6.1 Validation Using Modified Step Response

The third thermocouple in this bed is at a distance of 59.9 cm from the inflow plane as shown in Table 5.3. Its response is free from the flow development in the entrance region of the bed. The thermal response of this thermocouple is set as boundary condition in simulation. Curve fitting is used to obtain the profiles at various Peclet numbers as a function of time.

6.6.1.1 Inflow Profiles at Various Peclet Numbers

Figure 6.14 shows the inflow profiles at new location $z = 0$ at various Peclet numbers. The figure shows the experimental profiles and corresponding profile obtained by curve fitting in numerical simulation. The profile at a Peclet number of 513 is very slow and takes large time to reach a steady state, which is lower than the maximum value of unity. The inflow profiles at higher Peclet numbers of 915 and 1615 are fast and the corresponding maximum temperature attained is higher as compared to that at lower Peclet number of 513.

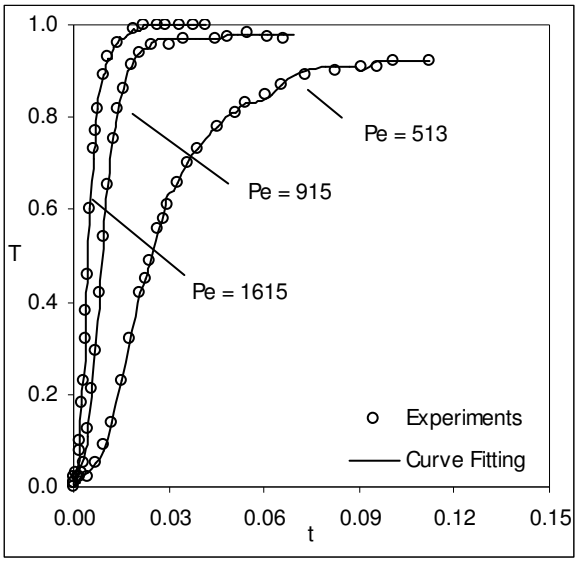

Figure 6.14: Experimental step response at new inflow plane of bed- 2 and corresponding points obtained by curve fitting in simulation.

6.6.1.2 Unsteady Temperature Profiles

Figure 6.15 compares the experimental step responses with numerical models at various Peclet numbers. The Biot number is set to zero. The profiles of the experiments and the numerical simulation are close to each other except at location $z = 33$ where the experimental profile is slow. The difference between the experiments and simulation decreases with an

increase in Peclet number. The comparison is better at locations near the inflow plane. 1-equation model is faster as compared to 2-equation model and the difference increases with distance from the inflow plane but decreases with an increase in Peclet number. Figures 6.15(a & b) show the comparison for a Peclet number of 513. In Figure 6.15(a), the comparison at location z =11.1 is shown, Here the experimental profiles are slower than that of numerical simulation. At locations z = 22.1 and 33 the difference has increased. In Figure 6.15(c & d), the comparison at a Peclet number of 915 is shown. At location z = 11.1, the difference between simulation and experiments is small. The slope of the 2-equation model is quite close to that of experiments at this location. With increase in distance from inflow plane, the corresponding difference between the simulation and experiments increases as shown in Figure 6.15(d). At a Peclet number of 1615, the comparison at location z = 11.1 is quite good. At location z = 22.1, the difference increases slightly. However, it is smaller than that at lower Peclet numbers of 513 and 915. With an increase in Biot number to unity, the corresponding temperature profiles become slower and the maximum temperature attained at a location becomes less than unity.

6.6.1.3 Front Speed and Spread

Figure 6.16 gives the front speed and front spread for glass-water bed-2 using experiments, 1-equation and 2-equation model results. The results are indicated at various Peclet number and at two distinct Biot numbers of zero and unity. The front speed of the experiments is slower as compared to that in simulation and the difference falls with Peclet number. The front speed of 1-equation model is higher as compared to 2-equation model. The front spread in simulation varies almost as in the experiments.

At lower Peclet number of 513 in Figures 6.16, the diffusive transport of energy dominates the advective transport and this coupled with higher dispersion makes the front speed in experiments less as compared to the numerical models. The speed in the models at a Biot number of unity is more than that of the experiments.

At a Peclet number of 915, in Figure 6.16(c & d), the experimental front speed has increased marginally and the comparison is better. The front spread comparison is also good. The spread predicted by simulation is quite close to that in the experiments.

At a Peclet number of 1615 in Figures 6.16(e & f), the front speed and spread is reasonably close to the numerical values. Hence, the comparison improves at higher Peclet number, where convective effects dominate the diffusive effects.

From the above discussion, it is clear that the front speed in simulation is more as compared to that in the experiments. In this bed, there is no channeling hence the front speed in experiments is lower and the corresponding difference is more. The difference decreases with an increase in Peclet number. At the lowest Peclet number of 513, the front speed in the experiments is 21 % slower as compared to that in the simulation. This value falls to 14.8 % at a Peclet number of 1615. The difference between 1 and 2-equation models is the highest at lower Peclet numbers. The results of 1-equation models are 17 % faster as compared to those of 2-equation model at a Peclet number of 513. This value falls to 6.6 % at a Peclet number of 1615.

The dependency of the front speed on the Biot number is also shown in the figures. At lower Peclet number, the front spread increases with increase in Biot number and the front speed decreases, particularly at points far away from inlet plane. At higher Peclet numbers, the effect of increase in Biot number upon front speed and spread is negligible, particularly at points closer to inlet plane.

1-equation model assumes a homogeneous single phase, and has therefore no interphase heat transfer present. As the interphase heat transfer between fluid and solid slows the front movement, it predicts a higher value of front speed as compared to 2-equation model. The difference decreases with an increase in Peclet number, indicating a higher interphase heat transfer at lower Peclet number. The energy flowing from water to glass is predominately stored which results in slowing the thermal front. This aspect is not present in 1-equation model because it a homogeneous single-phase model and consequently the front speed is faster than that of 2-equation model. 1-equation model considers effective thermal properties, whose value is obtained by weighted mean of the fluid and solid phases properties, see Sections 3.5 and 3.6. In general, 1-equation model, being faster, has lower front spread. The 1 and 2-equation models for glass-water bed are quantitatively similar in the sense that both profiles have similar in nature. They only differ by front speed and spread. The response to increase in Biot number in glass-water bed is also similar.

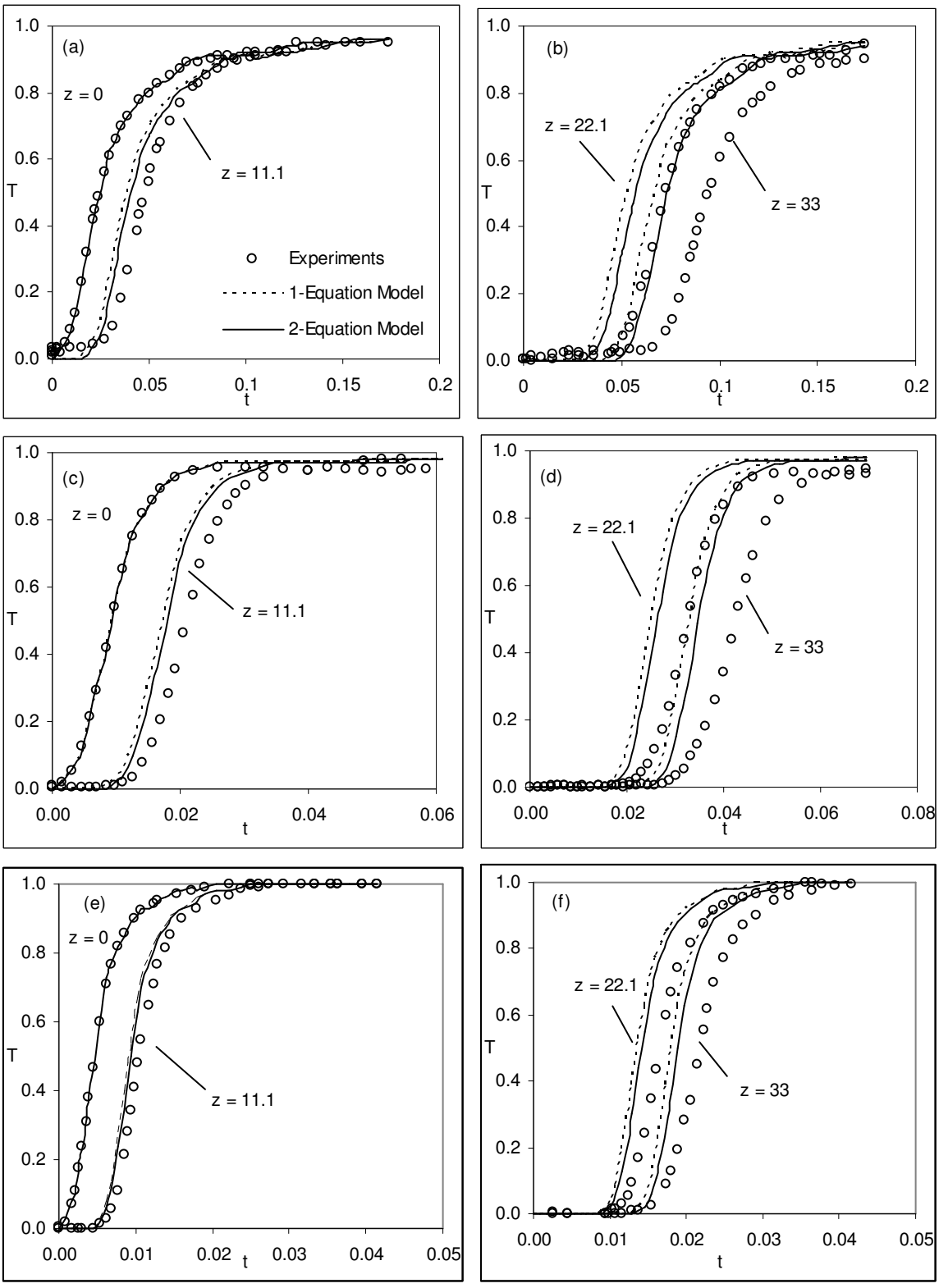

Figure 6.15: Variation of temperature with time in experiments, 1 and 2 equation model for glass-water bed. *Bi* = 0 (a,b) Pe = 513; (c,d) Pe = 915 and (e, f) Pe = 1615.

The front speed as seen in the analysis exceeds unity in both experiments and numerical models. In 1-equation model, see Equation 3.100, the front speed is a function of β_m, a value of 1.53 for glass-water bed and the front speed approaches this value. For 2-equation model, Equation 3.109, it is function of ε^{-1}, so it approaches a value of about 2.7. The actual value of front speed is much less than this value as source terms in fluid phase 2-equation model makes it nonlinear. It also depends upon other thermo-physical properties of the medium.

Front spread arises from the flow of fluid particles in the presence of pore system. It results into spreading of fluid particles in longitudinal and transverse directions collectively called as dispersion. The spread in respective directions arises from flow of fluid in longitudinal direction and velocity and temperature fluctuations in the pore system. Though the dispersion in transverse direction is lower than that in the longitudinal direction but it is significant as it represents heat flow in this direction. The spread increases with distance, which results from ever increasing spreading fluid particles in transverse direction. In general, higher the dispersion and the heat loss the higher is the front spread. The front spread, an indicative of dispersion, decreases with increase in Peclet number. The higher value of front spread lowers the front speed. The front spread in the experiments, in general, matches well with the numerical models. The dispersion increases the effective thermal conductivity of the fluid and solid phases**,** Alazmi and Vafai [2000], which in turn, decreases the front speed.

Since the results of simulation show faster temperature rise than in the experiments, a sensitivity analysis is carried out, where the thermal properties and other parameters are changed slightly to see their effect on degree of validation.

6.7 SENSITIVITY ANALYSIS

A sensitivity analysis is carried out for the numerical simulation in order to see its effect on degree of validation. It is carried out for the data generated from bed-2. The variables for analysis are the thermal storage capacity ratioβ, thermal conductivity ratio λ, Biot number *Bi*, thermal dispersion in longitudinal $(k_{\text{eff,f}})_z$ and transverse directions $(k_{\text{eff,f}})_r$ and the interphase heat transfer coefficient Nu.

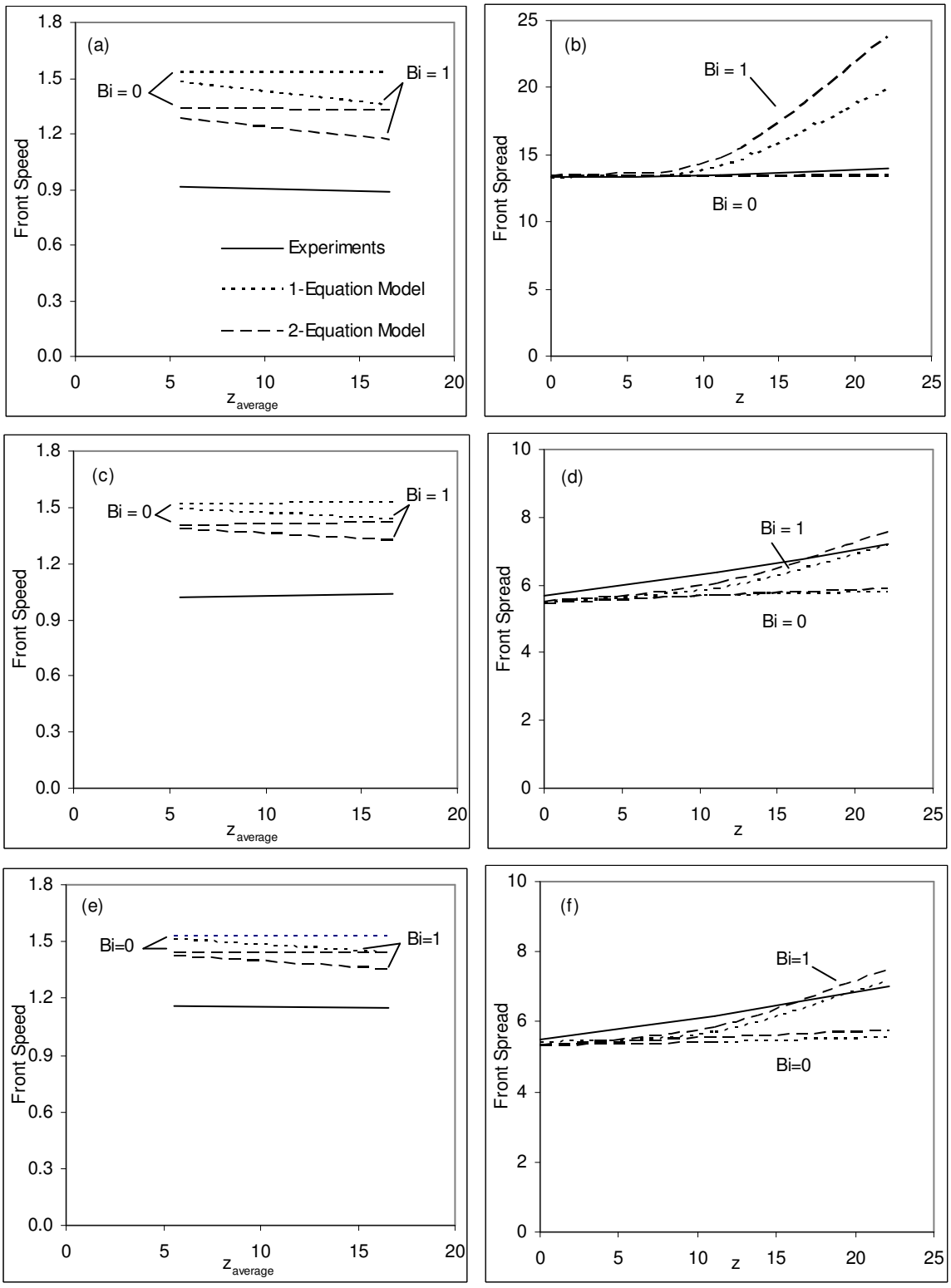

Figure 6.16: Speed and spread of front in glass-water experiments, 1-equation model and 2-equation model of the glass-water bed-2. (a,b) Pe = 513; (c,d) Pe = 915 and (e, f) Pe = 1615.

These values are varied until some visible change occurs in the results and the comparison with experiments is carried out.

The comparison is carried out for an intermediate Peclet number of 914 in bed-2. To account for heat loss in numerical simulation, Biot number is set at 0.5. The front speed and spread is calculated for each case and temperature time profiles are studied. This will further clear the role and relative weightage of each component for transport in porous medium. Recalling the properties of glass-water bed in Table 6.1, the thermal storage capacity ratio, β of the bed is 2.2. The effect of a change in its value on the thermal response of the bed is considered. Assuming a constant value of thermal storage of water, an increase in the corresponding value of glass results to a fall in the value of β. It means that for a particular temperature rise of the solid phase, more energy is extracted from the fluid phase. It results in a decrease in front speed and an increase in front spread. This also means more time needed to attain a particular temperature in the solid phase. Similarly, a lower value of thermal storage of the solid phase means a higher front speed and a lower spread. Figure 6.17 shows the effect of change in β on front speed and spread. As β decreases from its normal value to 1.8, the front speed falls by as much as 8 % from the normal value. The front spread also increases as shown in Figure 6.17(b). On the other hand, the front speed increases as β is increased to 2.6. The corresponding increase is 5.7 %. As the fluid flows through the bed, it encounters the solid phase as well as the walls of the PVC material. PVC has high storage capacity hence its effect is equivalent to an increase in solid phase storage capacity, it results to a decrease in front speed. The change in front speed with β is almost equal at all locations. The front spread also does not show much change with distance. It shows that the effect of change in thermal storage on thermal front is localized in nature. The decrease in front speed seems more as compared to an increase in front spread. Hence, a higher value of thermal storage of the solid phase slows the thermal front. Figure 6.18 shows the sensitivity to change in thermal conductivity ratio λ, on the thermal front flowing through the bed. The normal value of λ for glass-water bed is 0.56. This value is changed in either direction to 0.3 and 0.8 to see the effect on front speed and spread. A decrease in this value to 0.3 means that the thermal conductivity of the solid phase increases relative to the fluid phase.

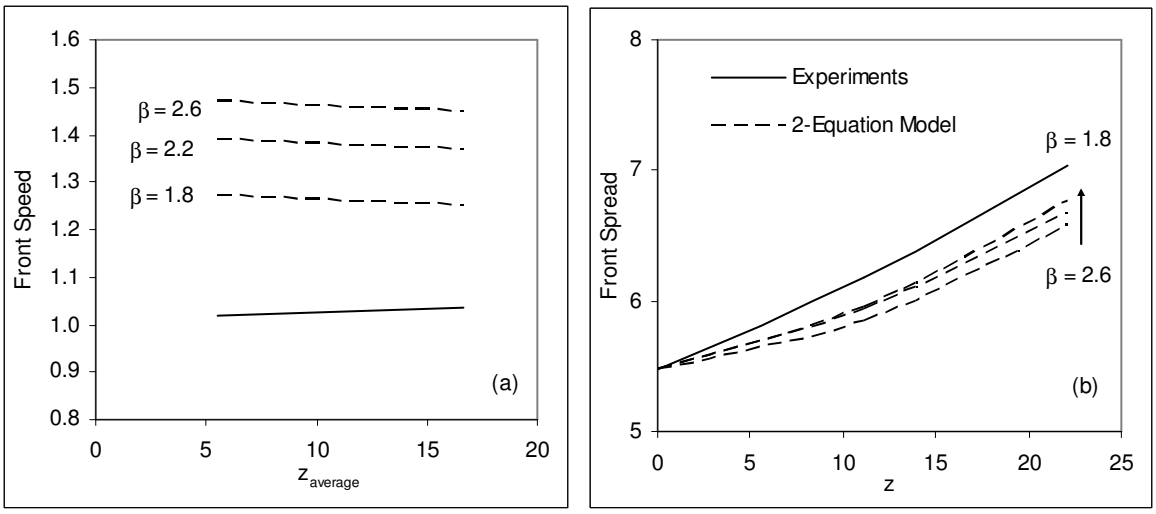

Figure 6.17: Sensitivity of thermal front to thermal storage capacity ratio (β) in glass-water bed. Pe = 914, Bi = 0.5.

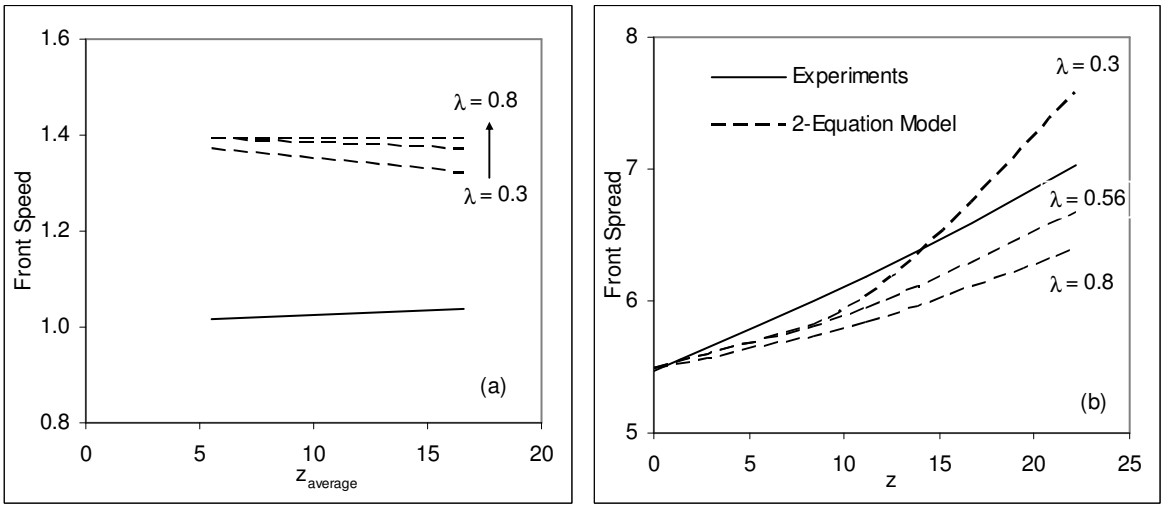

Figure 6.18: Sensitivity of thermal front to thermal conductivity ratio (λ) in glass-water bed. Pe = 914, Bi = 0.5.

It increases the heat flowing to the solid phase for similar temperature profiles in the solid phase. Hence the thermal front flowing through the bed losses more energy. It is reflected by a decrease in front speed and an increase in front spread. The increase in spread seems to be more as compared to a decrease in front speed. Both the changes seem to be increasing with distance and hence cumulative in nature. On the other hand, thermal storage is localized means falls equally with distance.

The above discussion shows the thermal front behaves differently to change in thermal storage and thermal conductivity. Hence, it is not advisable to combine to two factors

into thermal diffusivity. Storage is local and conductivity is cumulative over distance in nature. Hence, the steel phase which has higher thermal storage as compared to glass will have slower thermal front. Further its thermal conductivity is also higher than that of glass, the spread will increase with distance more and minor fall in speed can occur due to higher conductivity of the solid phase.

Whereas the above changes occur in the solid phase, we now look as to what happens when the dispersion in the fluid phase is changed. The thermal dispersion arises from pore level velocity and temperature deviations and its effect is equivalent to adding additional conduction terms in the fluid phase, Alazami & Vafai [2000]. Equations 3.68 and 3.69 respectively give the effective thermal conductivity of the fluid phase in longitudinal and transverse direction. The first factor in RHS of each equation is identical, gives molecular thermal conductivity whereas the second factor is distinct in each direction, and represents the thermal dispersion. Its value is higher in the longitudinal direction as compared to that in the transverse direction. The effect of change in thermal dispersion in either direction on front speed and spread is observed. As the numerical simulation is slower as compared to the experiments the thermal dispersion is only increased from the normal values as given by the above equations. The effect of an increase in thermal dispersion in transverse direction is considered first. Figure 6.19 shows the resulting change by increasing the dispersion. The effect on the front speed is to decrease it marginally and the corresponding effect on front spread is considerable. By increasing the dispersion by 25 % over the normal value, the spread approaches the experimental values at locations away from the inflow plane. By increasing it by 50 %, the spread exceeds the experimental values. By increasing the thermal dispersion in longitudinal direction, the change in speed and spread is very small. When the longitudinal dispersion is increased by 100 % (double the normal value), the front speed does not change at all but the spread increases only marginally. Hence, the thermal dispersion in transverse direction is very important for heat transfer in porous medium. Similarly increasing the interphase heat transfer affects the front speed and its effect on front spread is minor. Hence, transverse dispersion and inter-phase heat transfer can affect speed and spread but longitudinal dispersion can only affect spread.

Levec and Carbonell [1985] calculated the front speed, in one-dimensional form, in the fluid and solid phases, which move at equal speed, but a spatial separation exits between the two. The front speed is given as

$$\text{Front Speed} = \frac{\text{Fluid Speed}}{1+K} \tag{6.4}$$

Here K stands for weighted ratio of thermal storage capacities of the fluid and solid phase and is given as

$$K = \frac{(1-\varepsilon)(\rho c_p)_s}{(\varepsilon)(\rho c_p)_f} \tag{6.5}$$

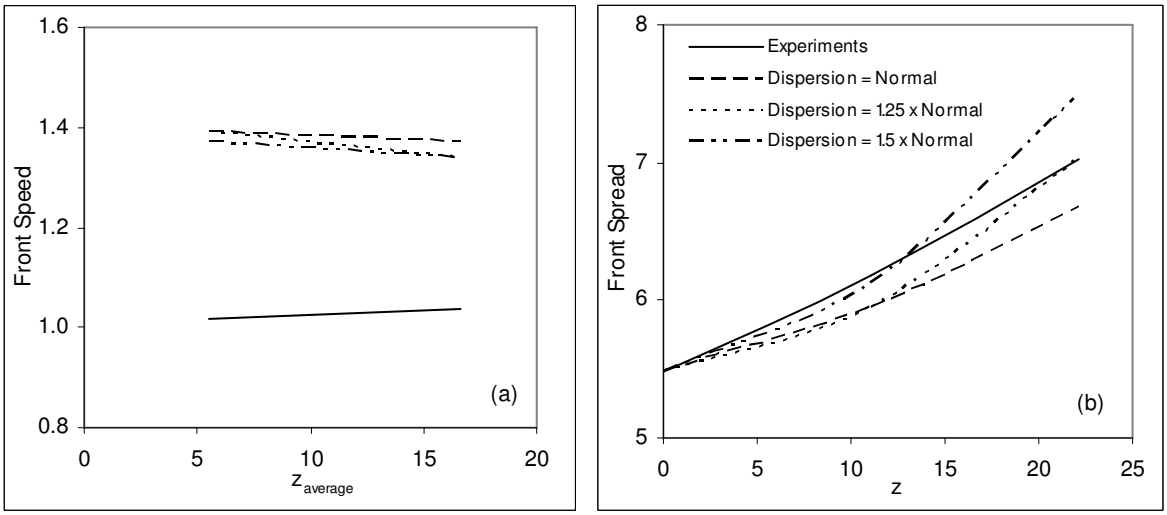

Figure 6.19: Sensitivity of thermal front to thermal dispersion in transverse direction in glass-water bed. Pe = 914, Bi = 0.5.

The value of K for glass-water bed is 0.76. Since the fluid speed in the REV (V) is different from the average fluid speed and obtained by dividing Darcy velocity U by the porosity and the corresponding front speed is 1.53. In the absence of heat loss this value is constant. Figure 6.20 shows the comparison of front speed in the present experiments and 2-equation model with that of Levec and Carbonell. The speed predicted by Levec and Carbonell is slightly higher as compared to the 2-equation model. At a higher Peclet number of 1615, the front speed in experiments increases and approaches the Levec and Carbonell values. The above relation shows clearly that front speed decreases with a decrease in β as discussed above. The front speed in the present experiments is less as compared to the above results owing to heat loss and dispersion.

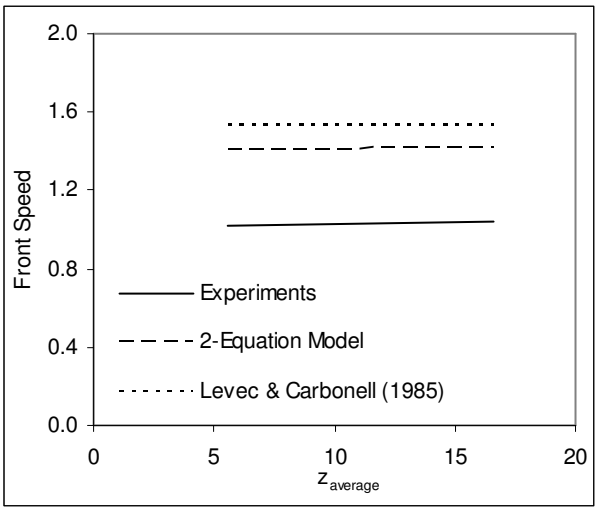

Figure 6.20: Comparison of front speed with the results of Levec and Carbonell (1985). Pe = 951.

6.8 THERMAL NON-EQUILIBRIUM

Thermal non-equilibrium conditions between the fluid and solid phase is dominant during transient heating and cooling of the porous bed. Energy exchange between the two phases takes place during the transient processes. At steady state, the energy exchange is minimal and consequently 1-equation model can be used to predict the corresponding temperature field. The 2-equation model can predict the individual temperatures of fluid and solid phases during the transient process as well.

The thermal properties difference between the two phases also affects thermal non-equilibrium. The 2-equation model uses fluid and solid phases properties for the corresponding phase equations. The 1-equation model treats porous medium as homogeneous single phase having effective thermal properties through which the fluid flows. These properties are obtained by weighted mean of the fluid and the solid phase properties as discussed in Sections 3.5.2 and 3.6.2. In case the fluid and the solid phase properties are widely different, the thermal properties used in the two models becomes distinct. Table 6.3 shows the effective properties of porous medium, the corresponding properties of fluid and solid phases are also shown for easy reference.

Hence, the effective thermal storage capacity of porous medium is 2716 kJ (kg K)$^{-1}$, which is more than the that of the solid phase hence the value of β_m is 1.53 instead of 2.2 as used in 2-equation model. The thermal conductivity of porous medium is 0.912 W (m K)$^{-1}$

instead of 1.09 as of solid phase. The value of λ_m is to 0.66 instead of 0.56 as used in 2-equation model. Hence, the difference between the two models is due to change in these values. A lower value of β lowers the front speed and a higher value of λ increases the front speed and decreases the spread. Both the above factors changes by major amount. β falls by 30 % and λ increase by 17 %. The above changes along with the interphase heat transfer determine the relative difference between the two models.

Table 6.3: Effective Thermal Properties of the glass-water bed as used in 1-equation model.

Thermal Storage Capacity [kJ $(m)^{-3}(K)^{-1}$]			Thermal Conductivity [W $(m\ K)^{-1}$]		
Fluid Phase $(\rho c_p)_f$	Solid Phase $(\rho c_p)_s$	Effective Porous Medium $(\rho c_p)_m$	Fluid Phase (k_f)	Solid Phase (k_s)	Effective porous medium (k_m)
4160	1869	2716	0.61	1.09	0.912

The thermal non-equilibrium is analyzed considering a glass-water bed of length z = 30. The Peclet number is varied from 500 to 4000. These values are chosen as it represents the range in which the experimental data varies. The results of 1 and 2-equation models are obtained using an ideal step response at the inflow plane. 1-equation model gives a single homogeneous temperature field for fluid flowing through the porous medium whereas the 2-equation model gives distinct temperature profiles for the fluid and the solid phases. An analysis of the above three temperature profiles is carried out. In addition, the interphase heat transfer, the temperature difference between the fluid and the solid phases and between 1 and 2-equation models is also obtained.

Figure 6.21 gives the unsteady temperature profiles using 1 and 2-equation models. In each figure temperature profiles of 1-equation model and the fluid and solid phase obtained from 2-equation model are shown. The profiles are drawn at three distinct locations in the bed. These locations are near the start, mid and end of the bed.

Figure 6.21(a-c) gives the temperature profiles for a lower Peclet number of 500. At location z = 3 in Figure 6.21(a), the 1-equation model profile is faster as compared to that of the fluid phase profile. The temperature difference rises from a zero value at the start of step response, reaches a maximum, and falls again to zero value at the end of step response at this location. The solid phase temperature profile is slower than the fluid phase temperature profile. At location z = 15 in Figure 6.21(b), the difference between the temperatures of 1 and 2-equation models has increased but that of fluid and solid phases have fallen. At location near the end of the bed, the difference between 1 and 2-equation models increases further but that of fluid and solid phases almost fall to a negligible value. This may be attributed to cumulative nature of the profiles where the 2-equation model becomes slower with distance due to interphase heat transfer even though the thermal non-equilibrium has fallen.

Figure 6.21(d-f) shows corresponding temperature profiles for a higher Peclet number of 4000. At this Peclet number, the temperature profiles of 1-equation model are starting later as compared to that of the fluid phase. The thermal non-equilibrium has increased as compared to lower Peclet number of 500 and it falls with distance. The difference between 1 and 2-equation models increases with distance but by a lesser margin as compared to that at lower Peclet number of 500. Figure 6.21(d) shows the profiles for location of z =3. The initial response of 1-equation model to inlet boundary condition is slower as compared to 2-equation model. Afterwards it rises fast and overtakes the 2-equation model. Overall, the difference is marginally larger as compared to that at lower Peclet number of 500. The temperature difference between fluid and solid phases increases. At location z = 15, in Figure 6.21(e), the difference between 1 and 2-equation models increases marginally but that of fluid and solid phases falls considerably. At location z = 27 in Figure 6.21(f), the difference between 1 and 2-equation model increases further though marginally but the thermal non-equilibrium falls.

Table 6.5 shows the thermal non-equilibrium at various locations. Clearly, it is function of Peclet number and distance from the inflow plane. Thermal non-equilibrium arises due to heat transfer between the fluid and the solid phase, it is higher at locations near the inflow plane as shown in Table 6.6. The temperature difference between the two phases forms a wave whose amplitude falls with distance and but increases with Peclet number. At higher flow rates, less time is available for solid to fluid heat interactions thereby less heat

exchange and so thermal non-equilibrium, Vafai and Sozen [1990]. This result is similar to that of Kuznetsov [1994, 96] where a wave of temperature difference is said to be propagating from the inlet boundary. Its amplitude falls as the wave propagates downstream.

Table 6.4: Maximum degree of thermal non-equilibrium between the fluid and the solid phases at various locations.

Peclet number	$z = 3$	$z = 15$	$z = 27$
500	0.026	0.011	0.009
4000	0.062	0.028	0.021

Whereas the thermal non-equilibrium is large for high Peclet of 4000 but the corresponding heat transfer is less as compared to that at a lower Peclet number, see Table 6.6. It may be attributed to high dimensionless convective resistance to heat flow at this Peclet number. At higher Peclet number, the step response time falls so the interphase heat transfer also acts over a lower time period. This heat transfer also form a wave like pattern whose amplitude falls with distance and Peclet number.

The difference between the 1 and 2-equation models increases with distance because of cumulative effect of heat transfer to the solid phase. At higher Peclet number of 4000, the difference is almost constant with distance, which may be attributed to lower interphase heat transfer and lower corresponding time for which this occurs, see Table 6.7.

Further, the energy from solid phase due to conduction can also flow to the fluid phase and increase the front speed. The role of this energy can be estimated by considering the time scale for diffusion through the solid phase and for residence time in pores during advection of fluid around the solid particles.

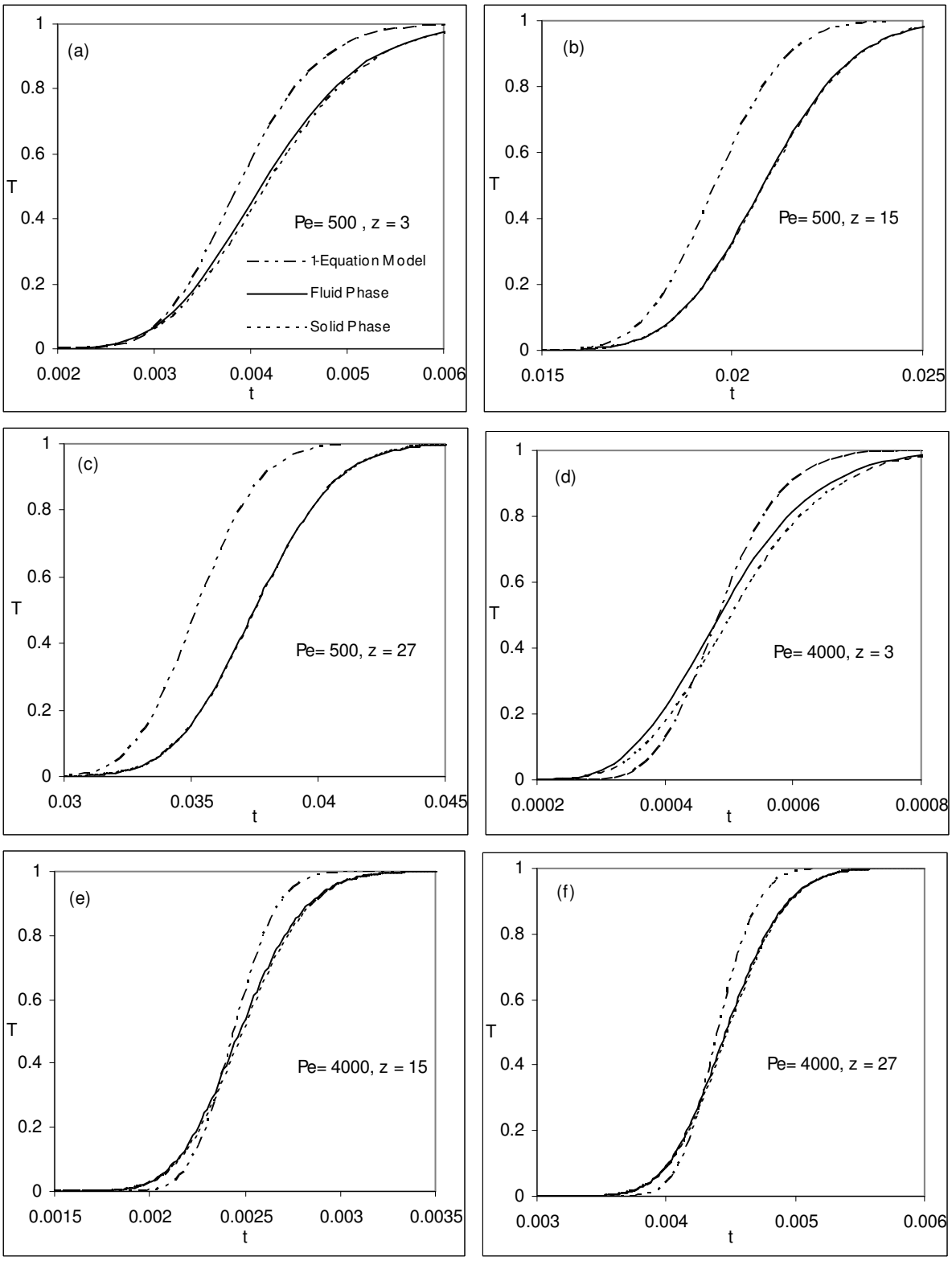

Figure 6.21: The temperature profiles of 1-equation model, the fluid and solid phases for assessment of thermal non-equilibrium in glass-water bed.

The diffusion time scale is given by $\frac{d^2}{\alpha_s}$ and that of residence time in pores by $\frac{d\varepsilon}{U_D}$. The value of diffusion time scale is 8.6 secs whereas the residence time for hot pulse in the pores is 0.29 and 0.035 secs respectively for Peclet number of 500 and 4000. So diffusion in the solid phase takes much longer time as compared to residence time for advection.

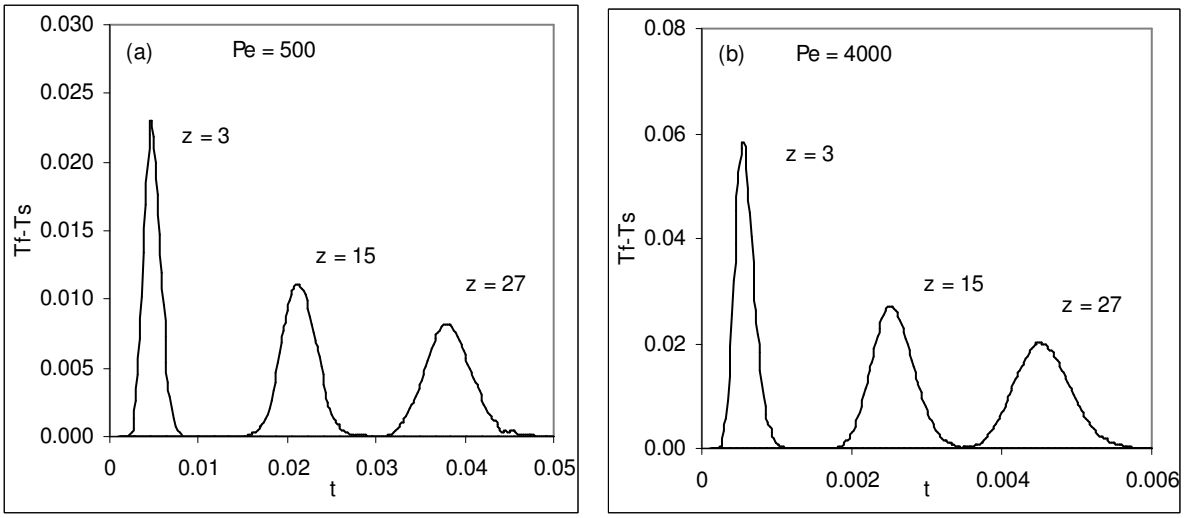

Figure 6.22: The wave of temperature difference in glass-water bed.

Table 6.5: Convective resistance and corresponding maximum interphase heat transfer at various locations.

Peclet Number Pe	Dimensionless Convective Resistance (Pe / Nu A_f)	Dimensionless Interphase Heat Transfer (Nu A_f/Pe*(T_f-T_s))		
		z = 3	z = 15	z = 27
500	0.094	0.275	0.116	0.095
4000	0.261	0.237	0.107	0.080

Table 6.6: Maximum difference between 1 and 2-equation model results at various locations.

Peclet number	z = 3	z = 15	z = 27
500	0.151	0.299	0.391
4000	0.194	0.198	0.202

Hence, the role of energy conducted through the solid phase back to fluid is minimal. It occurs when the fluid has covered a large distance.

6.9 CLOSURE

A detailed validation of numerical simulation models using 1 and 2-equation models are is carried out. The experimental results are obtained for two separate beds constructed using glass and PVC tubes. The comparison is in terms of unsteady temperature profiles and front speed and spread. It is carried out for distinct Peclet numbers in the bed. The boundary conditions used for comparison are the ideal step change and actual change of a thermocouple located away from the inflow plane. The second boundary condition gives better comparison between the simulation and the experiments. From the above analysis, it is clear that 2-equation model is an accurate method of simulation for heat transfer in porous medium. The 1-equation model is also qualitatively similar to 2-equation model such that its response is similar to 2-equation model but it is less accurate. During steady state, 1-equation model can be used but for unsteady state, only 2-equation model should be used. A sensitivity analysis of the comparison is carried out to see on what factors the results depend. In the end, thermal non-equilibrium between the fluid and the solid phases is assessed.

The front speed in experiments is slower as compared to that in 2-equation model for normal properties of the porous medium. It approaches the later as various parameters are changed suitably. The difference may be attributed to the wall effects of PVC tube containing the beads, velocity fluctuations near the walls, presence of air pockets in the bed and effects related to channeling and heat loss.

Overall, the comparison provides good information about the convective heat transfer in porous medium for a solid phase whose properties are similar to those of the fluid phase. A similar comparison when these properties are distinct is carried out in the next chapter.

CHAPTER 7

STEP RESPONSE OF STEEL-WATER BED

7.1 INTRODUCTION

The experimental step response in steel-water bed is discussed in this section. The results obtained from experimental step response are compared with those of numerical simulation. The comparison is based on the modified boundary condition of actual temperature response obtained at the inflow plane. Table 5.1 gives the thermal properties of glass and steel beads used in the experiments. Steel has higher thermal conductivity and thermal storage capacity as compared that of glass. However, its thermal conductivity being very high, dominates the thermal storage capacity and hence the thermal diffusivity of steel is much higher than that of glass. The properties contrast of steel and water is also higher as compared to that between glass and water. In this bed, the highly conductive solid particles actively participate in the overall energy transfer. Whereas in glass-water bed the solid particles have low thermal conductivity and hence do not participate actively in the energy transfer. They only store the energy without conducting it forward. Hence, the step response in this bed is distinct from that in a glass-water bed.

The comparison is carried out for results obtained from both the beds; bed-1 and bed-2, as discussed in Chapter 5. It is based upon both the unsteady temperature profiles and the corresponding front speed and spread of the thermal front traveling through the bed. A sensitivity analysis of the comparison is carried out by varying the various governing variables in numerical simulation. The thermal non-equilibrium between the fluid and the solid phase is discussed. The results of step response in this bed are also compared with those in glass water bed. We now discuss the thermo-physical properties of steel-water bed.

7.2 THERMO-PHYSICAL PROPERTIES OF STEEL-WATER BED

Using the properties of water at 300 K as given in Section 6.2 and that of steel as given in Table 5.1, we get the thermal properties of steel-water bed. Table 7.1 gives all the related thermo-physical properties of the bed.

Table 7.1: Thermo-physical properties of steel-water porous bed.

Thermal capacity ratio, β	Thermal conductivity ratio, λ	Particle diameter, d_P [mm]	Tube to particle diameter ratio, D/d_P	Porosity, ε	Specific surface area, A_f
1.1	0.04	4.76	12.56	0.40	22.47

The thermal storage capacity ratio of water is marginally higher as compared to that of steel but its thermal conductivity is much lower. Overall, the thermal diffusivity of steel, 0.0395 cm^2s^{-1} is much higher as compared to that of water, 0.00583 cm^2s^{-1}. Hence, the movement of thermal front through the steel-water bed is expected to be distorted. The particle diameter is 4.76 mm giving a tube to particle diameter ratio of higher than twelve. The specific surface area of both the beds used is 22.47 in the dimensionless form. The length of bed-1 is 23.7 and that of bed-2 is 23 in the dimensionless form. Tables 5.4 & 5.5 respectively give the position of the thermocouples from the inflow plane in these beds. We now discuss the experimental step response in steel-water bed.

7.3 EXPERIMENTAL STEP RESPONSE

7.3.1 Steel-Water Bed-1

Figure 5.4 shows the layout of the steel-water bed-1 and Table 5.4 gives the corresponding position of thermocouples from the inflow plane of the bed. The step response of the bed is recorded at these locations. Figure 7.1 shows the experimentally obtained step response in the steel-water bed-1 at three distinct Peclet numbers. In each figure, the step response at four locations in the bed is shown. Peclet number for this bed is higher as compared to that for glass water beds. It is attributed to higher porosity and shorter length of this bed. The temperature at a location rises as a function of time and reaches a maximum value of unity in most cases. Figure 7.1(a) shows the step response in the bed for a Peclet number of 816. At location z = 0.3, the response is quite fast and resembles an ideal step response. At farther locations of z = 12 & 17, the corresponding responses are slower and maximum temperatures are marginally less than unity. At a Peclet number of 1803 in Figure 7.1(b), the response at all locations becomes faster and the corresponding maximum temperatures almost reach

unity. Similarly, Figure 7.1(c) shows the step response at a Peclet number of 3143. Here the temperature build up at various locations is fast and the corresponding maximum temperatures reach unity. It is observed during the experiments that occasionally the response at location $z = 17$, becomes faster as compared to that at location $z = 12$, hence end effects are observed in this bed at this location.

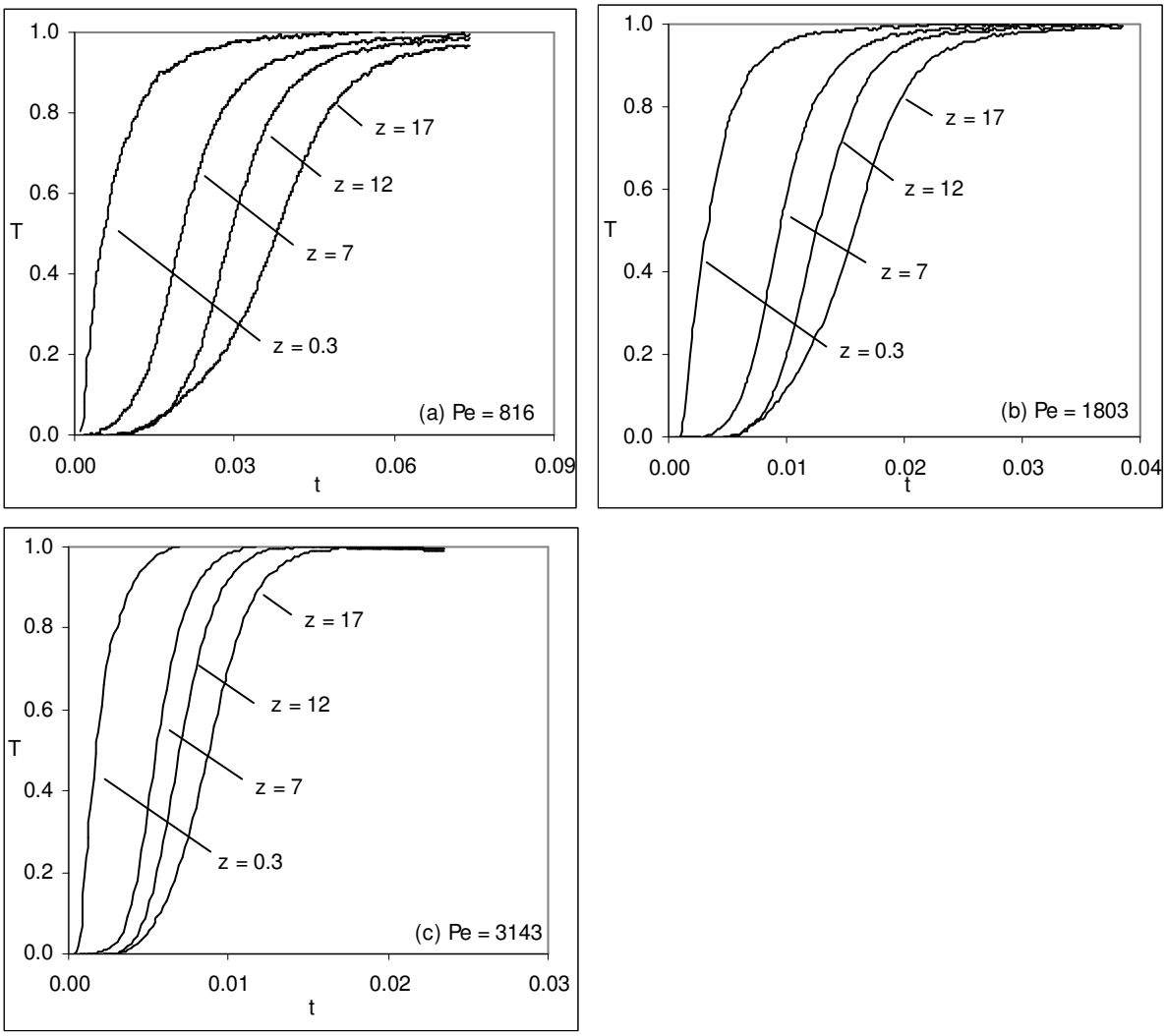

Figure 7.1: Experimental step response of steel-water bed-1.

Figure 7.2 shows the temperature evolution in the bed at various points of time. Figure 7.2(a) shows the evolution when Peclet number is 816. The temperature in the bed rises and reaches a steady state after $t = 0.717$. At a Peclet number of 1803, in Figure 7.2(b), the steady state is reached at $t = 0.371$. Similarly for a Peclet number of 3143 in Figure 7.2(c), the steady state is reached at $t = 0.023$ which is quite fast as compared to that for lower Peclet numbers.

Figure 7.2(d) shows the corresponding steady state temperature profiles at these Peclet numbers. The effect of heat loss through the bed is more at lower Peclet numbers such that for a Peclet number of 816 the steady state temperatures are lower than those at higher Peclet numbers. For a Peclet number of 3143, it is almost unity everywhere.

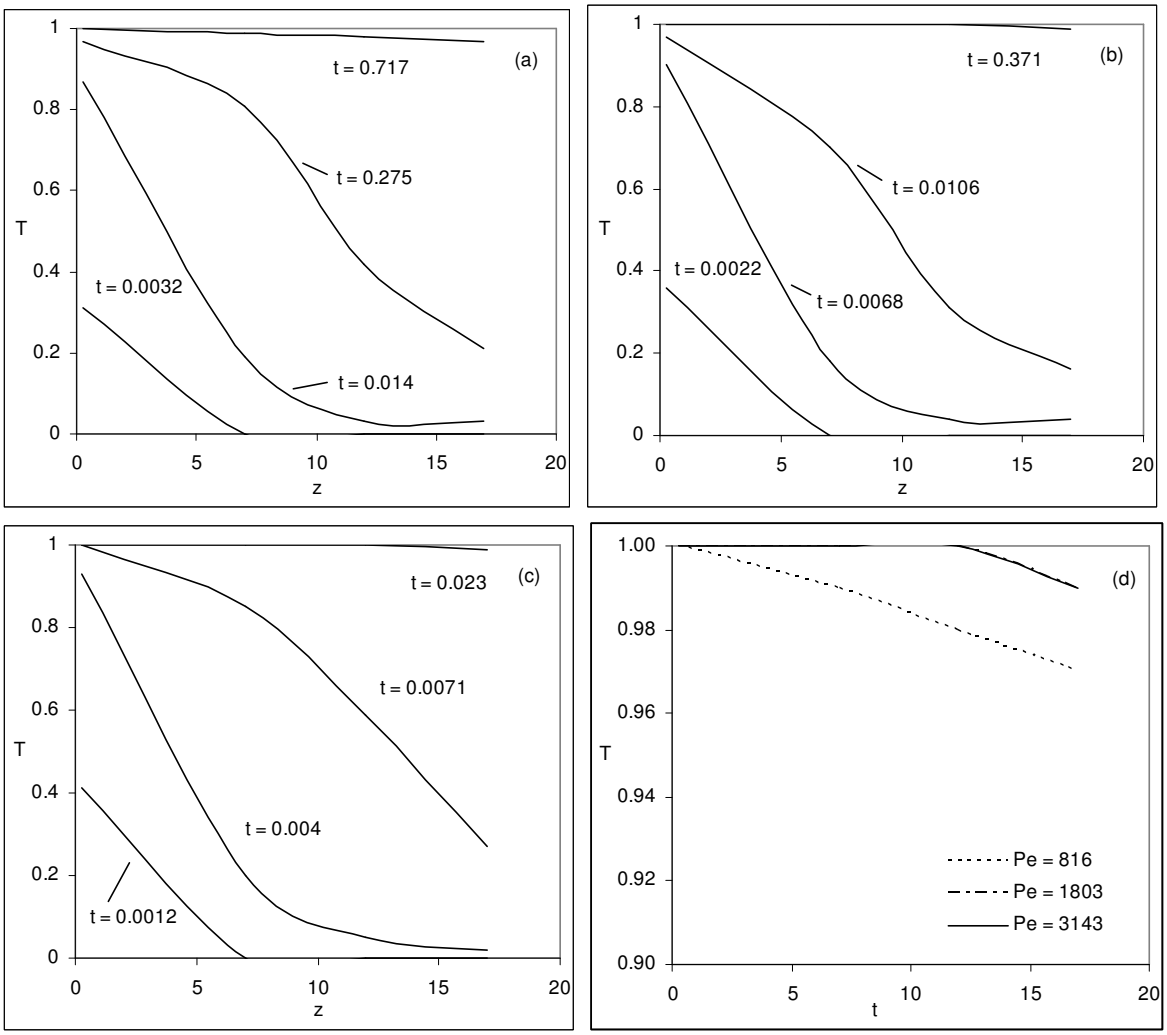

Figure 7.2: Temperature variation as a function of distance from inflow plane for experimental step response in steel-water bed-1. (a) Pe = 816; (b) Pe = 1803; (c) Pe = 3143 and (d) Steady state.

For validation of the results of this bed, the second thermocouple is set as an inflow plane and its response is set as the boundary conditions in simulation. Table 7.2 shows the subsequent position of the thermocouples in this bed.

Table 7.2: Position of thermocouple in the steel-water bed-1 and corresponding distances from second thermocouple.

Thermocouple No.	Non-dimensional distance from inflow to bed	Non-dimensional distance from second thermocouple onwards
1	0.33	-
2	7.0	0
3	12.0	5
4	17.0	10
5	23.0	16

7.3.2 Steel-Water Bed-2

Figure 5.5 shows the layout of steel-water bed-2 and Table 5.5 shows the position of thermocouples in the bed. In this bed, the steel beads are closely packed in the tube without plain portions at the start and the end. A test section is considered by setting the first thermocouple as an inflow plane. Table 7.3 gives the non-dimensional distances when this thermocouple is set as an inflow plane.

Table 7.3: Position of thermocouple in the steel-water bed-2 and corresponding distances from the first thermocouple.

Thermocouple No.	Non-dimensional distance from inflow to bed	Non-dimensional distance from first thermocouple onwards
1	6.9	0
2	9.6	2.7
3	11.8	4.9
4	13.9	7.0
5	16.7	9.8

Figure 7.3 shows the step response in this bed at three distinct Peclet numbers. At each Peclet number, the response at locations z = 0, 4.9, 7.0 & 9.8 are shown. The individual profiles are similar to those in bed-1 except that end effects at location z = 17 are not observed in bed-2. The location z = 9.8 in bed-2 is almost at the same distance from the inflow plane as z = 17 in bed-1 and is free from end effects and hence, its results are consistent. At lower Peclet

numbers, the rate of temperature build up is slower and the maximum temperature reached is lower than unity. As Peclet number increases the build up becomes faster and the maximum temperature approaches unity. Figure 7.4 shows the temperature evolution in the bed with time.

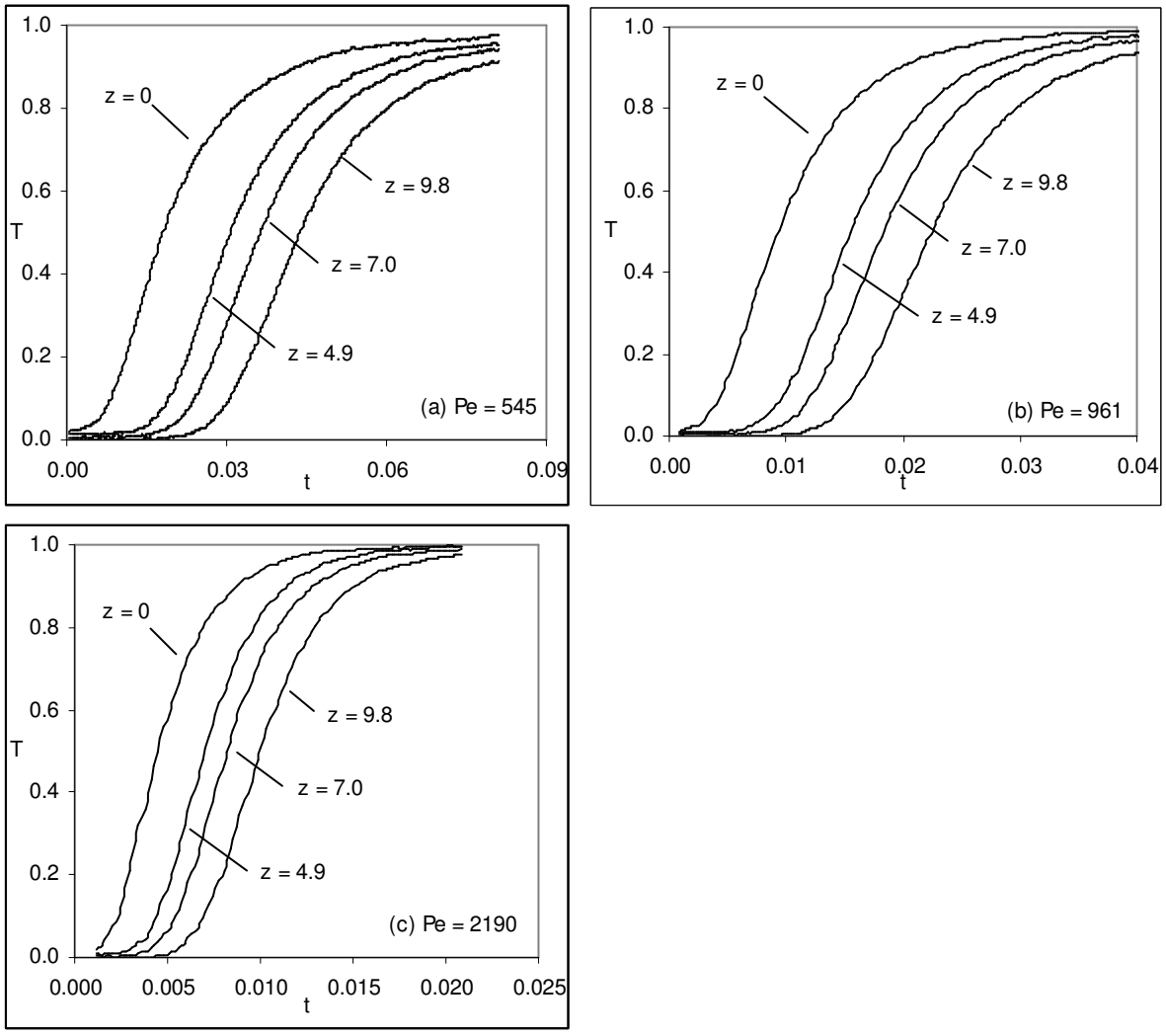

Figure 7.3: Experimental step response of steel-water bed-2.

At a Peclet number of 545, in Figure 7.4(a), the temperature rise in the bed is slower as compared to those at higher Peclet numbers. The effect of diffusion is seen at t = 0.0436 where the slope of the temperature profile is gentle when compared to similar profiles at higher Peclet numbers. At a Peclet number of 2190 in Figure 7.4(c), the temperature profiles are almost similar to those at a Peclet number of 961 in Figure 7.4(b) except that the steady state temperatures are higher and the corresponding times are lower. Figure 7.4(d) shows the

steady state temperature profiles for various Peclet numbers. It is the highest at a Peclet number of 2190 and varies as a function of Peclet number.

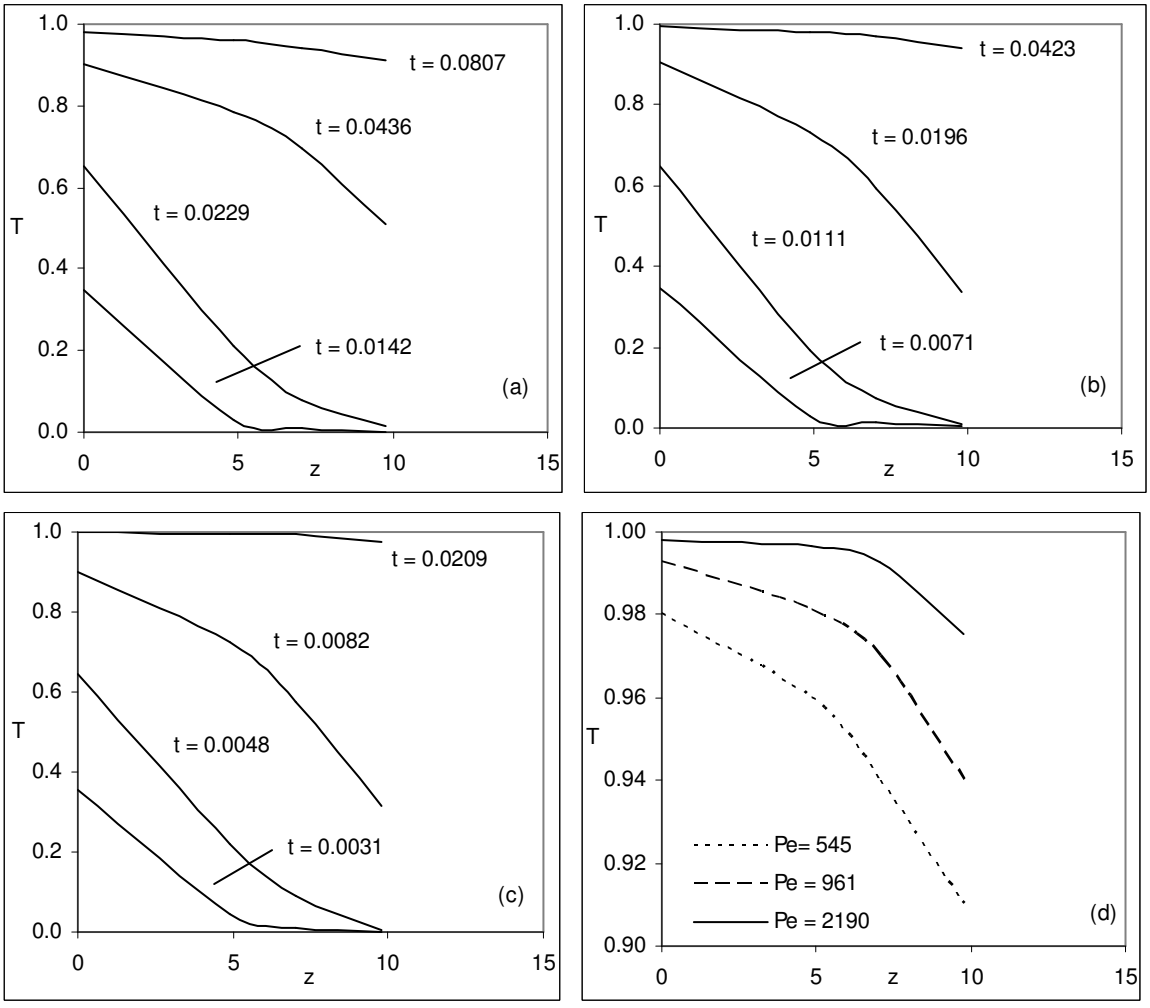

Figure 7.4: Temperature variation as a function of distance from inflow plane for experimental step response in steel-water bed-2. (a) Pe = 545; (b) Pe = 961; (c) Pe = 2190 and (d) Steady state.

7.4 FRONT SPEED AND SPREAD

7.4.1 Steel-water Bed-1

Figure 7.5 shows the front speed and spread as observed in bed-1 for three distinct Peclet numbers. The front speed as shown in Figure 7.5(a) varies as a function of Peclet number. At the lowest observed Peclet number of 816, the front speed is the lowest. It seems to be increasing marginally with distance. At a Peclet number of 1803, the front speed is higher though it decreases marginally with distance. It is highest for a Peclet number of 3143 and falls sharply with distance. The front spread as shown in Figure 7.5(b) varies inversely with Peclet number. It is the highest for a lowest Peclet number of 816. For each Peclet number, it increases with distance.

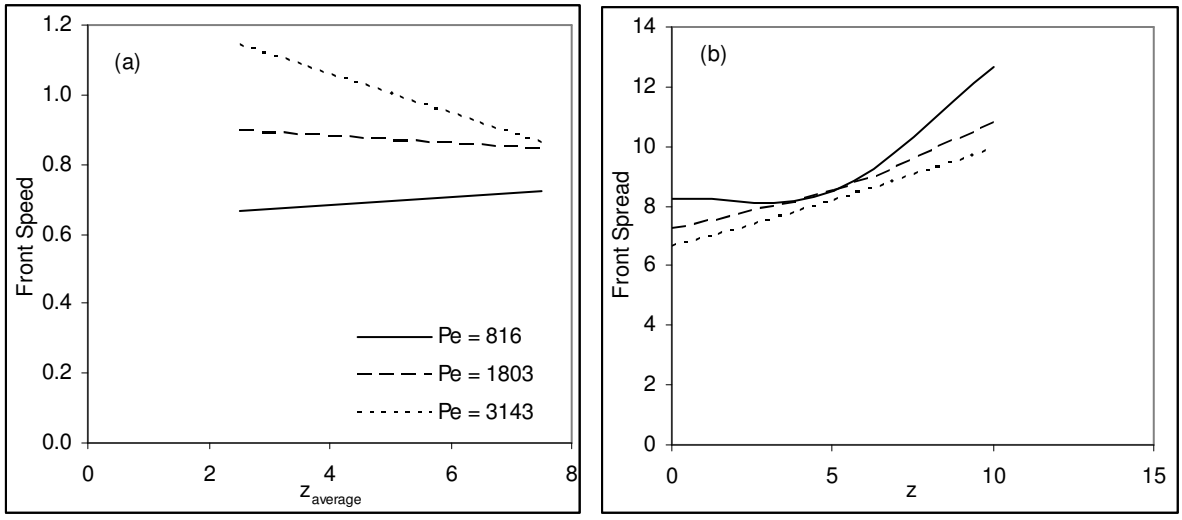

Figure 7.5: Experimental front speed and spread in steel-water bed-1.

7.4.2 Steel-Water Bed-2

Figure 7.6 shows the experimental front speed and spread in bed-2. The front speed as shown in Figure 7.6(a) is again a function of Peclet number but it is lower when compared to that in bed-1. At each Peclet number, it falls with distance, the fall being more at higher Peclet numbers. As an example, for a Peclet number of 2190, it reaches the maximum but falls at locations away from the inflow plane. The front spread is shown in Figure 7.6(b); varies inversely with Peclet number. At higher Peclet numbers, it almost becomes independent of the flow rate. It also increases with distance from the inflow plane.

7.4.3. Comparison of the Two Beds

The variation of the speed as a function of Peclet number is observed in both the beds. In bed-1 the corresponding values of front speed are higher as compared to those in bed-2. For higher Peclet numbers, the front speed falls rapidly with distance being higher in bed-1. The spread in both the beds varies inversely with Peclet number and directly with distance from the inflow plane. Some deviation in bed-1 is observed from normal trend at low Peclet number of 816. The mean value of spread in bed-1 is higher than that in bed-2. In bed-1, the end effects are observed at locations away from the inflow plane but these are absent in bed-2. Hence, the results of bed-2 are consistent as compared to bed-1.

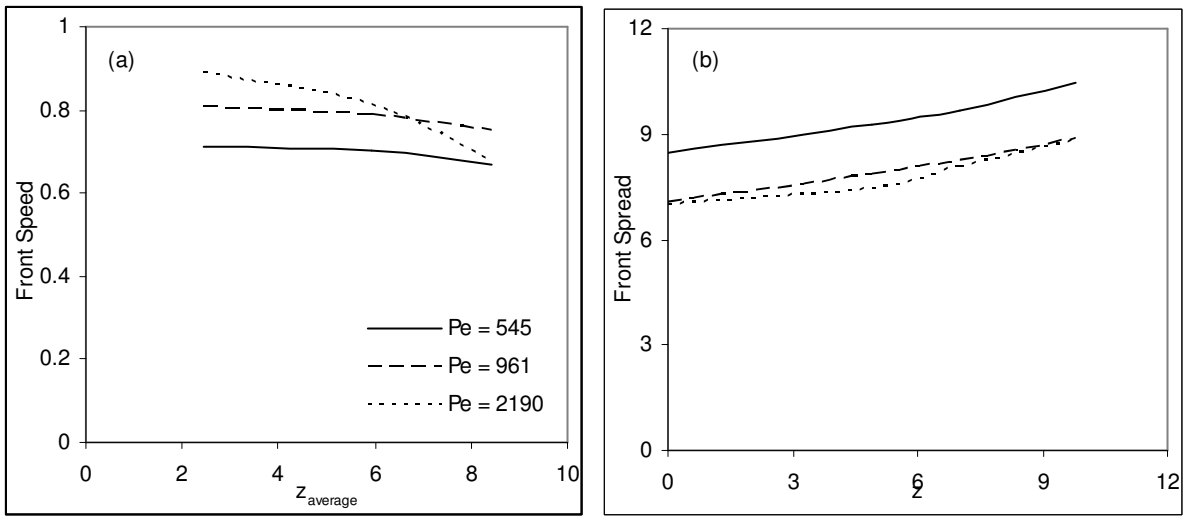

Figure 7.6: Experimental front speed and spread in steel-water bed-2.

7.5 VALIDATION OF NUMERICAL MODELS FOR STEEL-WATER BED-1

Here the comparison of experimental results of bed-1 is performed with numerical simulation. The comparison is performed using temperature time profiles and the corresponding speed & spread of the thermal front trevelling through the bed. The comparison is obtained using the results of both 1 and 2-equation models. Since the actual step response of a thermocouple is far from being ideal, so comparison is based upon the actual response of a thermocouple located away from the inflow plane as boundary condition.

7.5.1 Validation Using Modified Step Response

The validation is obtained using the actual thermal response of the bed as recorded by a thermocouple located away from the inflow plane. This response is set as boundary condition in simulation. The corresponding location in this bed is $z = 7$ and Table 7.2 gives the location of subsequent thermocouples with respect to this thermocouple. The thermal response at these locations is compared with simulation. It is important to consider the nature of inflow profiles at various Peclet numbers at this location.

7.5.1.1 Inflow Profile at Various Peclet numbers

The thermal response at new location $z = 0$ for various Peclet numbers is shown in Figure 7.7; the corresponding profiles generated in simulation by curve fitting are also shown. The step response at a Peclet number 816 is very slow and that at 3143 is almost like ideal step response. The steady state temperatures at each location approach unity as a function of time.

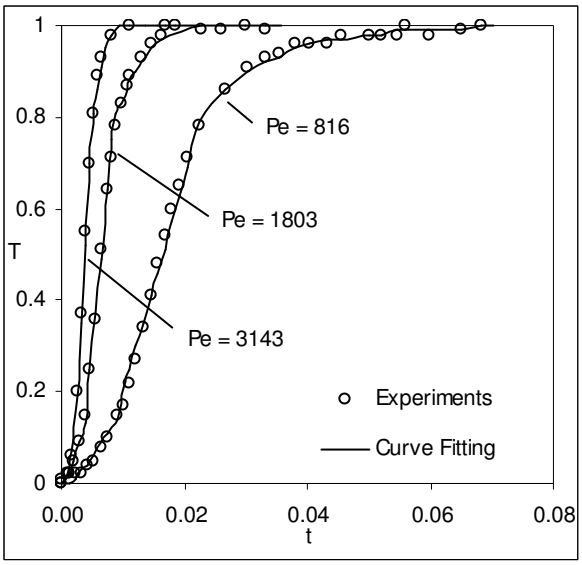

Figure 7.7: Experimental step response at new inflow plane of bed- 1 and corresponding points obtained by curve fitting in simulation.

7.5.1.2 Unsteady Temperature Profiles

Figure 7.8 compares the experimental step response with that of numerical simulation at various Peclet numbers. The Biot number in numerical simulation is set to zero. In each figure, a comparison is shown at two distinct locations in the bed. The profiles corresponding

to 1 and 2-equation models are shown along with the those of experiments. The profiles of 2-equation model are distinct from those of 1-equation model. These profiles are similar to those of experiments though marginally faster at this Biot number. The experimental profiles as shown in Figures 7.8(b & f) show end effects such at location z = 16, these profiles are faster as compared to those at z = 10. In such cases, the comparison is discussed for location z = 10 only.

Figure 7.8(a & b) shows the comparison for a Peclet number of 816. At location z = 0 in Figure 7.8(a), the profiles corresponding to the experiments and the simulation are set identical. At location z = 5, the experiments and 2-equation model profiles are similar to each other though the experimental profile is slower. The profile of 1-equation model is distinct from the other two such that initially it is coinciding with 2-equation model but afterwards with experiments. Figure 7.8(b) shows the comparison at locations of z = 10 & 16. Here the effects appearing at location z = 5 are magnified. At location z = 10, though the profiles of experiments and 2-equation model are similar in nature but the corresponding difference has increased. The profile of 1-equation model is close to that of the experiments. Overall, the temperature profiles for 1 and 2-equation models are quite and latter being faster. Recalling the similar comparison for a glass water bed as discussed in Section 6.5.2, 1-equation model is faster as compared to 2-equation model though qualitatively similar. However, for a steel-water bed, this difference increases much faster with time during unsteady temperature build up.

Figure 7.8(c & d) shows the comparison for a Peclet number of 1803. At location z = 5 in Figure 7.8(c), the experimental profile becomes faster as compared to that at lower Peclet number of 816 and approaches 2-equation model profile. 2-equation model is again faster as compared to 1-equation model and the difference between 1 and 2 equation models looks similar when compared to that at a Peclet number of 816. At location z = 10 in Figure 7.8(d), the effect similar to that for a Peclet number of 816 is observed. The experimental profile is closer to 2-equation model as compared to that at lower Peclet number. 1-equation model seems the slowest of the three profiles.

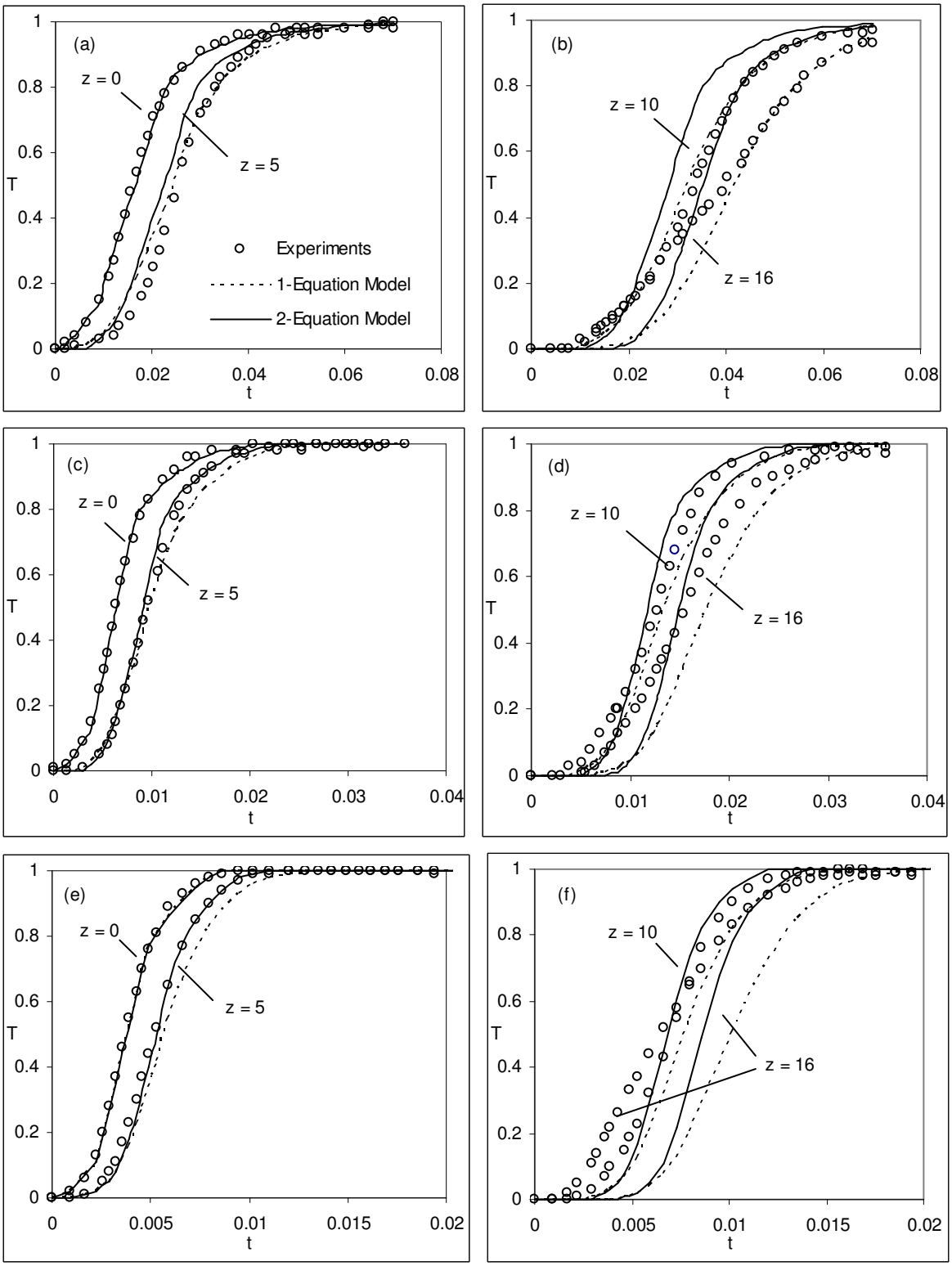

Figure 7.8: Variation of temperature with time in experiments, 1 and 2- equation model for steel-water bed-1 with modified boundary condition. *Bi* = 0. (a,b) Pe = 816; (c,d) Pe = 1803 and (e,f) Pe = 3143.

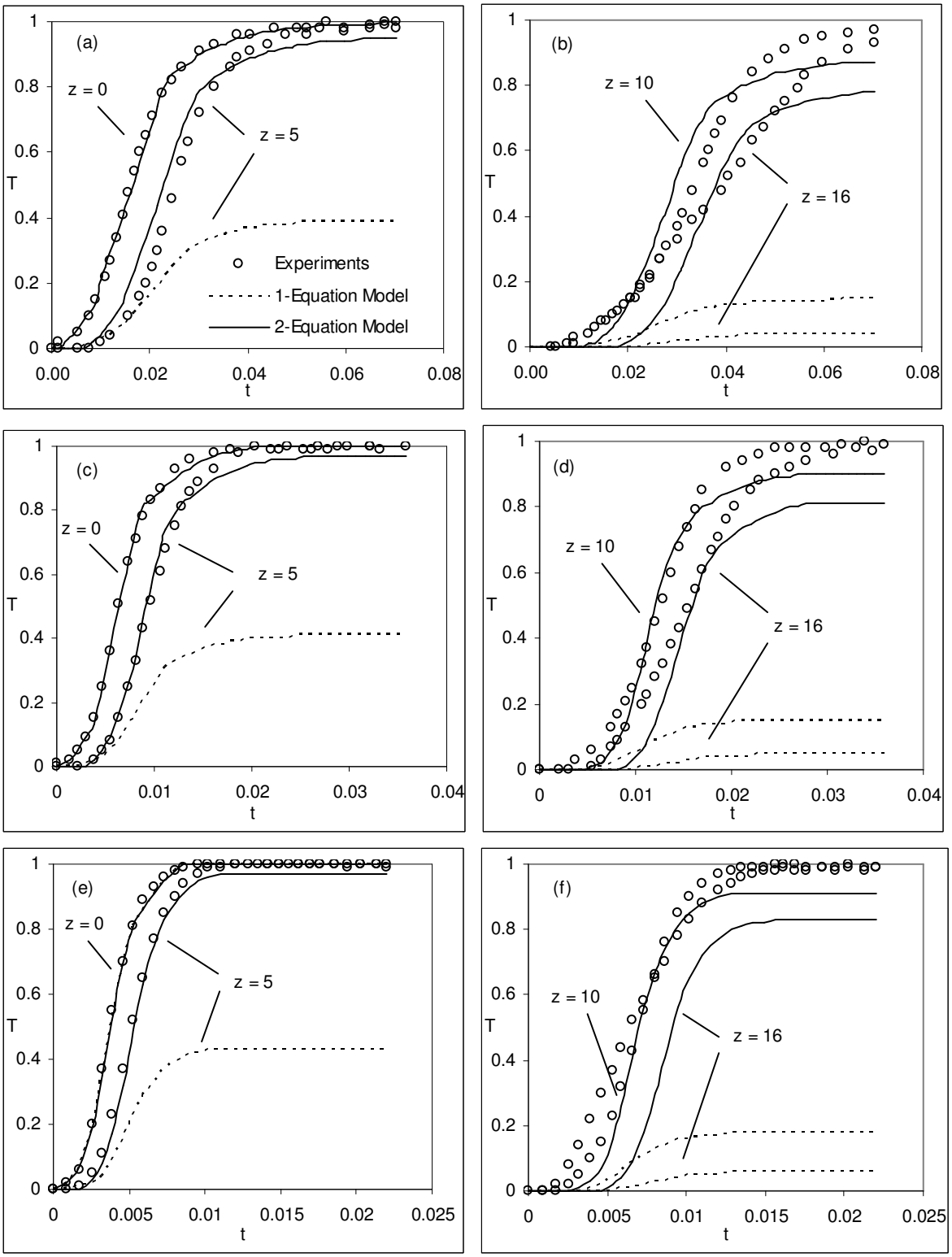

Figure 7.9: Variation of temperature with time in experiments, 1 and 2- equation model for steel-water bed-1 with modified boundary condition. *Bi* = 0.05. (a,b) Pe = 816; (c,d) Pe = 1803 and (e,f) Pe = 3143.

This effect is again seen at a location of z =16 and the difference between the experimental and 2-equation model profiles increases and 1- equation model is again the slowest. The end effects at location z =16 are not observed at this Peclet number.

Similarly, Figure 7.8(e & f) shows the comparison for a Peclet number of 3143. At location z = 5, the profiles of experiments and 2-equation model match each other and that of 1-equation model is slower. At location z = 10 in Figure 7.8(f), experimental and 2-equation model profiles are close to each other.

The effect of minor heat loss on the comparison is shown in Figure 7.9. Here the Biot number is increased to 0.05. At location z = 5, the comparison between the experiments and 2-equation model improves but the 1-equation model shows excessive slowing with time and its maximum temperature falls significantly. At location z =10 in Figures 7.9(b, d &f) there seems to be small improvement in comparison between experiment and 2-equation model. It also improves at location z = 16 as shown in Figure 7.9(d) for a Peclet number of 1803. However, 1-equation model does not show appropriate results and completely fails to predict experiments profiles. It shows excessive sensitivity to minor heat losses.

Table 7.4: Effective Thermal Properties of the steel-water bed.

Thermal Storage capacity of fluid phase, $(\rho c_p)_f$ [kJ $(m)^{-3}(K)^{-1}$]	Thermal Storage capacity of solid phase, $(\rho c_p)_s$ [kJ $(m)^{-3}(K)^{-1}$]	Effective Thermal Storage capacity of porous medium, $(\rho c_p)_m$ [kJ $(kg\ K)^{-1}$]	Thermal Conductivity of fluid phase, k_f [W $(m\ K)^{-1}$]	Thermal Conductivity of solid phase, k_s [W $(m\ K)^{-1}$]	Effective thermal conductivity of porous medium, k_m [W $(m\ K)^{-1}$]
4160	3768	3924	0.61	14.9	9.18

The temperatures build up and consequent front speed in 2-equation model is faster as compared to that of 1-equation model. This may be explained by considering the thermal properties as used in two models. In 2-equation model, the thermal properties used are those of individual phases but in 1-equation model, effective thermal properties are used which are obtained as weighted mean of the individual phase properties as given in Table 7.4. The effective thermal conductivity of the porous medium is much larger as compared to that of the fluid phase. It results in a larger dispersion and hence a large spread of the thermal front. It also reflects a lowered internal conduction resistance with respect to heat losses to the

ambient. Hence, the Biot number experiences rise in conductivity term and consequent rise in convective heat transfer coefficient and so higher heat loss and dispersion. Hence, it is slower than 2-equation model.

7.5.2.3 Front Speed and Spread

Figure 7.10 compares the experimental front speed with that of numerical simulation for the three Peclet numbers considered. The comparison is shown for the above-mentioned Biot numbers of 0 and 0.05 in simulation. The results of 1-equation model at a Biot number of 0.05 do not conform to the definition of front speed and spread as defined in Section 6.4 as the corresponding temperatures of 0.75 and 0.5 are not attained in this model, hence are not shown in these figures. The front speed in 2-equation model falls with an increase in Biot number and the corresponding spread increases. At lower Peclet numbers of 816 and 1803 in Figures 7.10(a & c), the front speed of 2-equation model remains higher than that of the experiments but for a Peclet number of 3143 in Figure 7.10(e) it is nominally equal to that of the experiments. The front speed of 1-equation model is much slower than that of 2-equation model at Biot number of zero such that it falls below the experiments at higher Peclet numbers. The front spread for Biot number of 0.05 for 2-equation model is quite close to that of the experiments. Whereas the 1-equation model shows higher spread as compared to experiments at zero Biot number it is attributed to higher dispersion accounted for in this model. The other difference comes through the interphase heat transfer.

Since in this bed, the steel beads are not closely packed and in bed-2 it is assured that beads are closely packed and the results of the bed-2 are reliable. We now discuss the validation in steel-water bed-2.

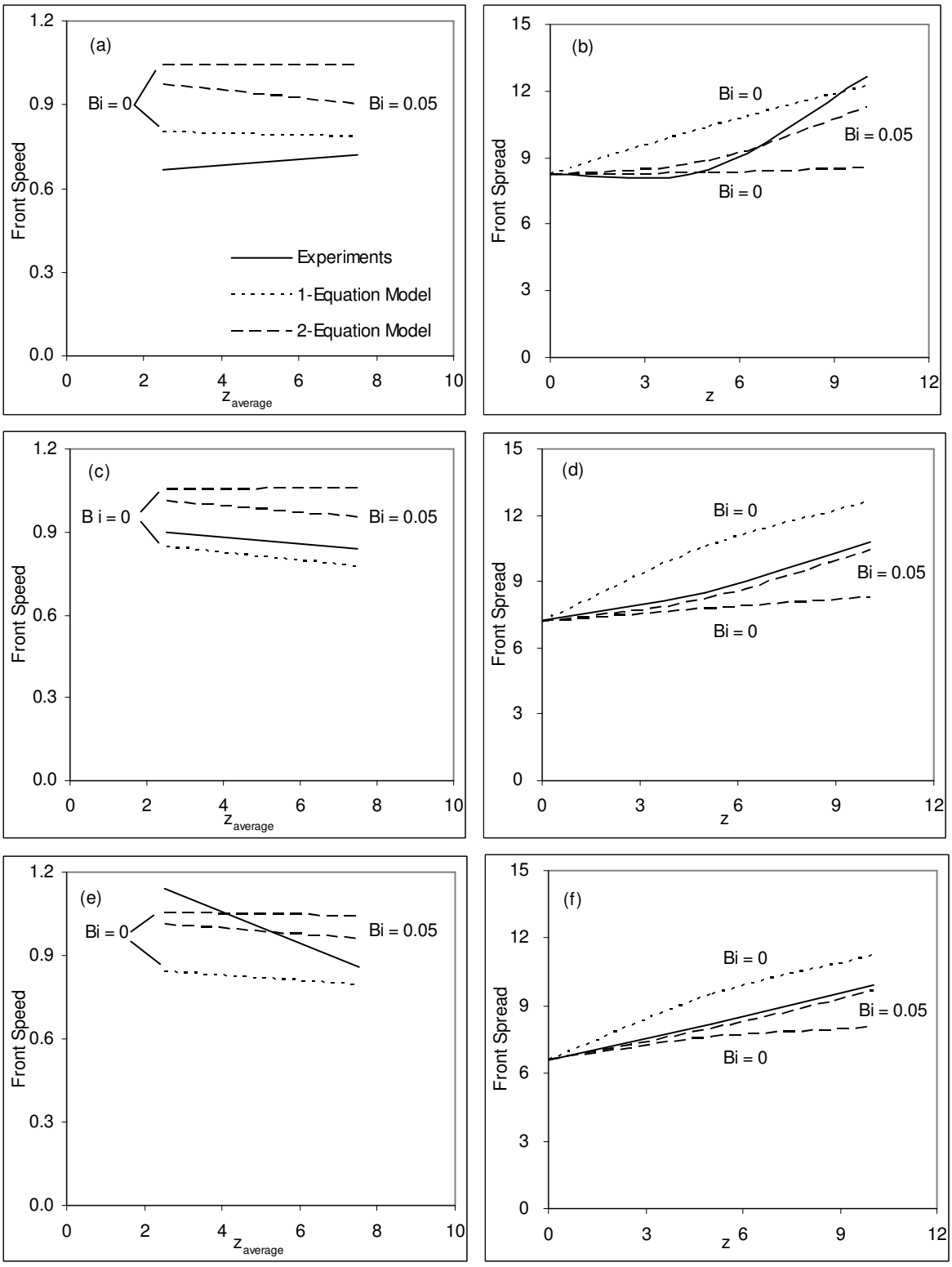

Figure 7.10: Speed and spread of front in steel-water bed-1 for experiments, 1-equation model and 2-equation model. (a,b) Pe = 816; (c,d) Pe = 1803 and (e,f) Pe = 3143.

7.6 VALIDATION OF NUMERICAL MODELS FOR STEEL-WATER BED-2

The validation using the results of steel-water bed-2 is discussed in this section. The comparison is obtained using modified step response technique. The thermal response of first thermocouple in this bed is again set as boundary condition for comparison at subsequent locations in simulation and compared with experiments.

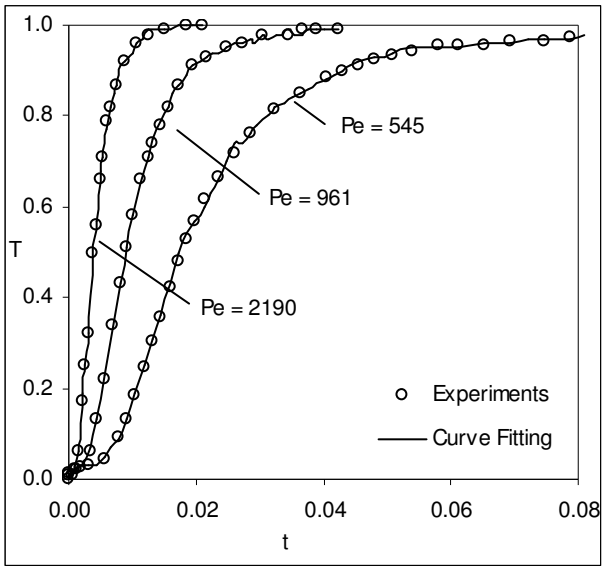

Figure 7.11: Experimental step response at new inflow plane of bed- 2 and corresponding points obtained by curve fitting in simulation.

7.6.1 Inflow Profiles

Figure 7.11 shows the inflow profiles at location z =0 for various Peclet numbers in this bed. Both the experimental profiles and those obtained by curve fitting are shown in the figure. At lower Peclet numbers, the profiles are dominated by diffusion and those at higher Peclet numbers by convection. The change in profiles when reaching the maximum temperature is visible in all the three curves. Here the conduction energy transfer from fluid to fluid becomes quite slow as the driving force; the temperature difference is low. Hence, at higher flow rates the profiles are sharper than those at lower Peclet numbers. The minor heat loss through the bed severely affects the profiles at lower Peclet numbers.

7.6.1.2 Unsteady Temperature Profiles

Figure 7.12 gives the unsteady temperature profiles at various Peclet numbers when the Biot number is set to zero. At a particular location, 1-equation model predicts a slow temperature build up when compared to 2-equation model. This is quite opposite to what happened for a glass water bed. The difference goes increasing with distance from the inflow plane. The profile of 1-equation model at this Biot number is closer to experiments as compared to 2-equation model though its nature of the profile is distinct. The profile of 2-equation model is fast but its slope is similar to that of experiments. The difference between the two decreases with an increase in Peclet number but increases with distance from inflow plane. The comparison between the 2-equation model and experiments in general is better at locations close to inflow plane. At locations away from inflow plane, the effects such as heat loss, dispersion, thermal non-equilibrium and tube wall effects add up to make the experimental profiles slower. With a minor increase in Biot number from 0 to 0.05, the comparison between the 2-equation model and experiments improves but that of 1-equation model deteriorates significantly. The comparison at an intermediate Peclet number of 961 is shown in Figure 7.13. At location z = 4.9, the comparison is quite good and quite permissible at locations z = 7 & 9.8.

7.6.3 Front Speed and Spread

Figure 7.14 shows the comparison of front speed and spread for experiments and numerical simulation in this bed. It is presented for two Biot numbers of 0 and 0.05. For 1-equation model, it is shown for zero Biot number only. This change in Biot number affects the front speed and spread in 2-equation model. The front speed falls but remains marginally more than that of the experiments and the resulting spread increases but exceeds than that of the experiments. In 1-equation model the corresponding change is very large such that front does not show any significant propagation and falls rapidly with distance. Hence, it fails when heat losses are taking place in the bed. At zero Biot number, its predictions are close to that of experiments but the corresponding spread is more. At lower Peclet numbers, the difference between experiments and simulation is more as compared to that at higher Peclet numbers.

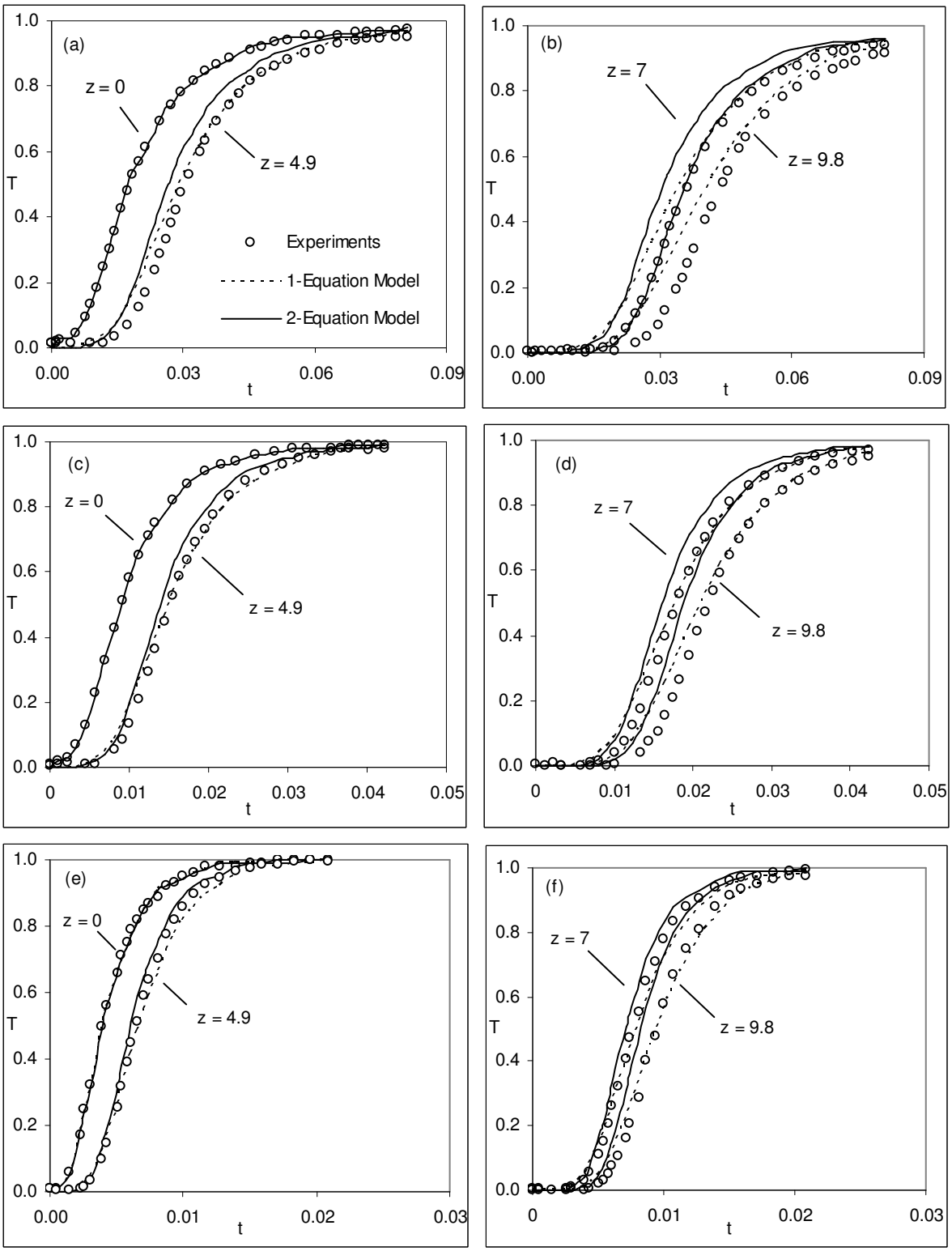

Figure 7.12: Variation of temperature with time in experiments, 1 and 2 equation model for steel-water bed-2 with modified boundary condition. *Bi* = 0. (a, b) Pe = 545; (c, d) Pe = 961 and (e, f) Pe = 2190.

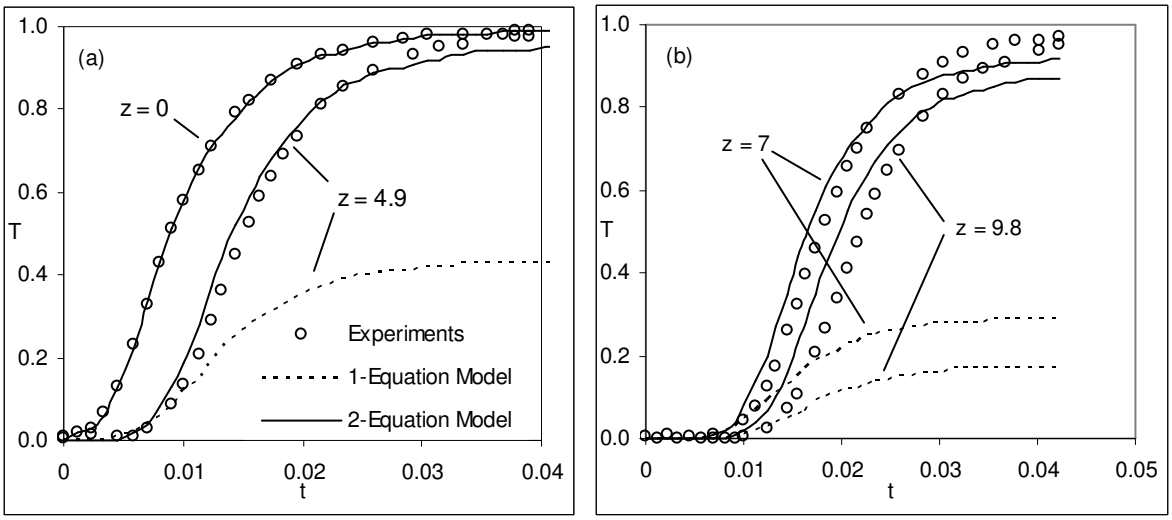

Figure 7.13: Variation of temperature with time in experiments, 1 and 2-equation models for steel-water bed-2 with modified boundary condition. Bi = 0.05, Pe = 961.

The anomalous behavior of the 1-equation model can be explained in terms of the effective medium properties employed. The model accounts for energy storativity in the fluid as well as the solid phases, while advection is present in the liquid phase. It uses an effective thermal conductivity, whose value for this bed is very large such that the value of β_m (1.06) is almost unchanged but there is a major change in the value of λ_m (0.066) hence this factor along with interphase heat transfer determines the relative difference between the two models. It results to a higher dispersion coefficient, large spread and higher heat losses in 1-equation model. In the 2-equation model, the phase energy equations are linked through the interphase Nusselt number that in turn depends on Peclet number. The stored energy in the highly conductive solid phase flows back to fluid phase and hence further increases the front speed in 2-equation model. Thus, the 2-equation model, while predicting the direction of heat transfer between phases correctly is not excessively sensitive to the disparity of their thermo physical properties.

A complete validation using the results of step response in two beds is carried out in this section. As the results of 2-equation model are marginally different from those of the experiments, a sensitivity analysis is carried out by varying various parameters in this model and comparison is again performed.

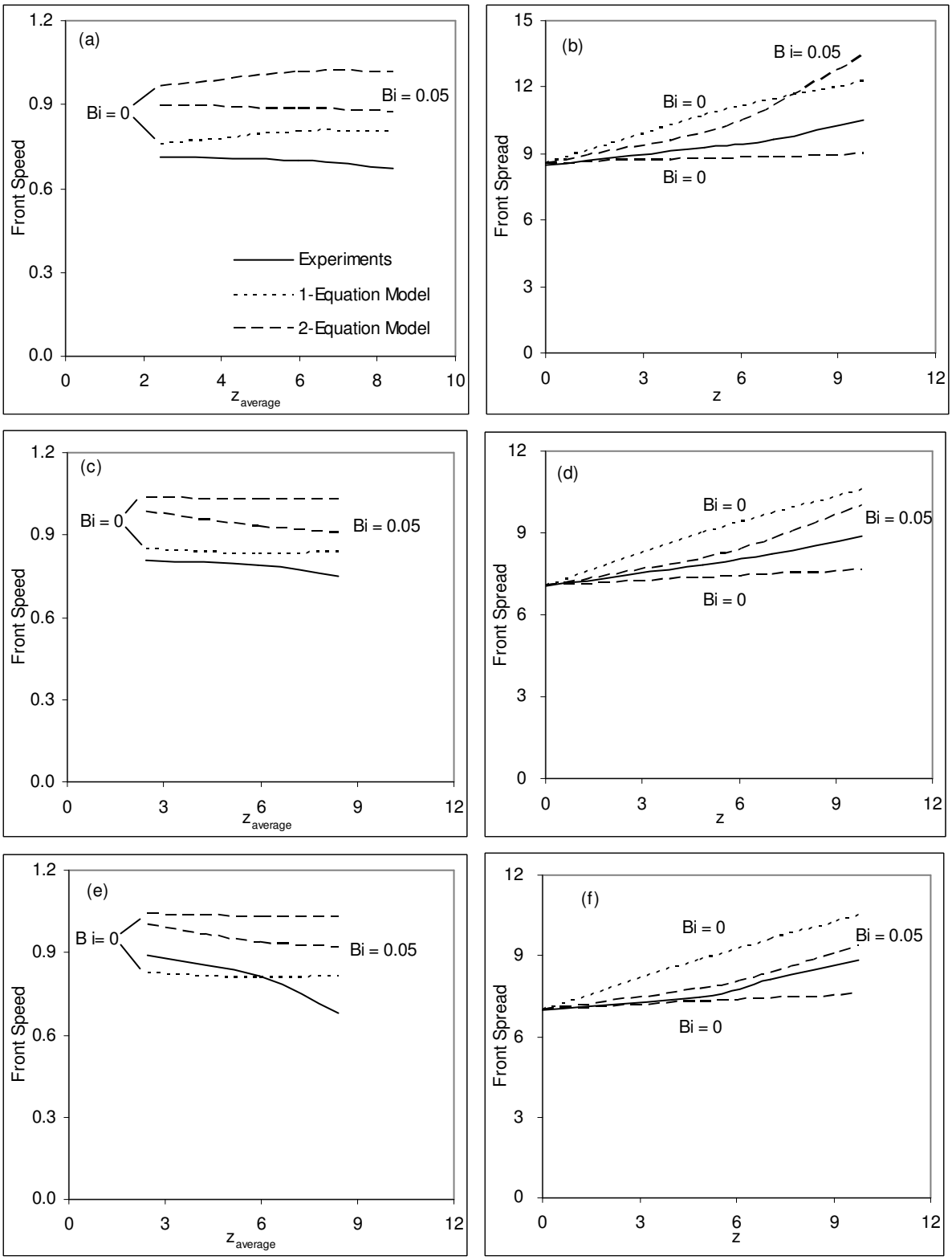

Figure 7.14: Speed and spread of front in steel-water bed-2 for experiments, 1-equation model and 2-equation model. (a, b) Pe = 545; (c, d) Pe = 961 and (e, f) Pe = 2190.

7.7 SENSITIVITY ANALYSIS

A sensitivity analysis is carried out by varying various parameters such as thermal storage capacity ratio β, thermal conductivity ratio λ, Biot number Bi , thermal dispersion in longitudinal $(k_{eff,f})_z$ and transverse $(k_{eff,f})_r$ directions and the interphase heat transfer from the normal values. The aim is to see their effect on degree of validation. The intermediate Peclet number of 961 in bed-2 is selected and the corresponding experimental results are compared with those of 2-equation model. The values of parameters are varied until visible changes occur in the results and a comparison with experiments is performed. The front speed and spread is calculated for each case and temperature time profiles are studied. To account for heat loss in numerical simulation, Biot number is set at 0.05.

Figure 7.15 shows the effect of a change in thermal storage capacity ratio (β) on the front speed and spread. Its value is changed from its normal value of 1.1 in either direction. A fall in its value to 0.9 decreases the front speed and increases the front spread.

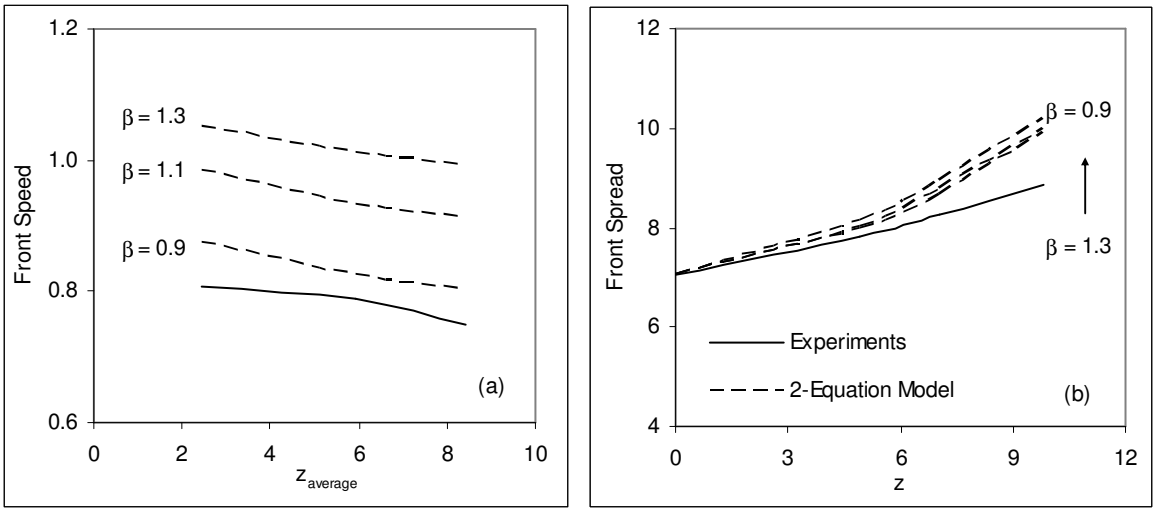

Figure 7.15: Sensitivity of thermal front to thermal storage capacity ratio (β) in steel-water bed. Pe = 961, Bi = 0.05.

A fall in β represents increases in thermal storage capacity of the solid phase relative to the fluid phase and hence the front speed falls. Similarly when the value of β increases, the front speed increases and the corresponding spread falls. These results are similar to the corresponding results in glass water bed as shown in Figure 6.17. The fall in the values of front speed with distance is more as compared to those in glass water bed.

Figure 7.16 shows the sensitivity of the results to thermal conductivity ratio (λ). A decrease in its value to 0.02, below the normal value of 0.04, results to corresponding decrease in the front speed and an increase in the front spread. The front spread for this value of λ becomes very large as shown in Figure 7.16(b). As the value of λ is increased to 0.06 the front speed increases and spread falls. The increase in fluid phase thermal conductivity relative to the solid phase means temperature rise is faster in fluid phase. The changes in this bed are relatively more as compared to the glass water bed owing to higher thermal conductivity of the solid phase.

Figure 7.17 shows the sensitivity to a change in the value of thermal dispersion in the transverse direction $(k_{\text{eff,f}})_{\text{r}}$. An increase in its value over the normal value shows a corresponding decrease in front speed and an increase in front spread. It represents the volume average of the product of spatial deviations in velocity and temperature in REV. A higher value over the normal represents more heat consumed due to the deviations in the respective components. Hence, it decreases the front speed and increases the spread. An increase in the thermal dispersion in longitudinal direction does not affect the thermal front significantly. The heat loss from the bed affects front speed as well as spread. The longitudinal dispersion affects only the spread.

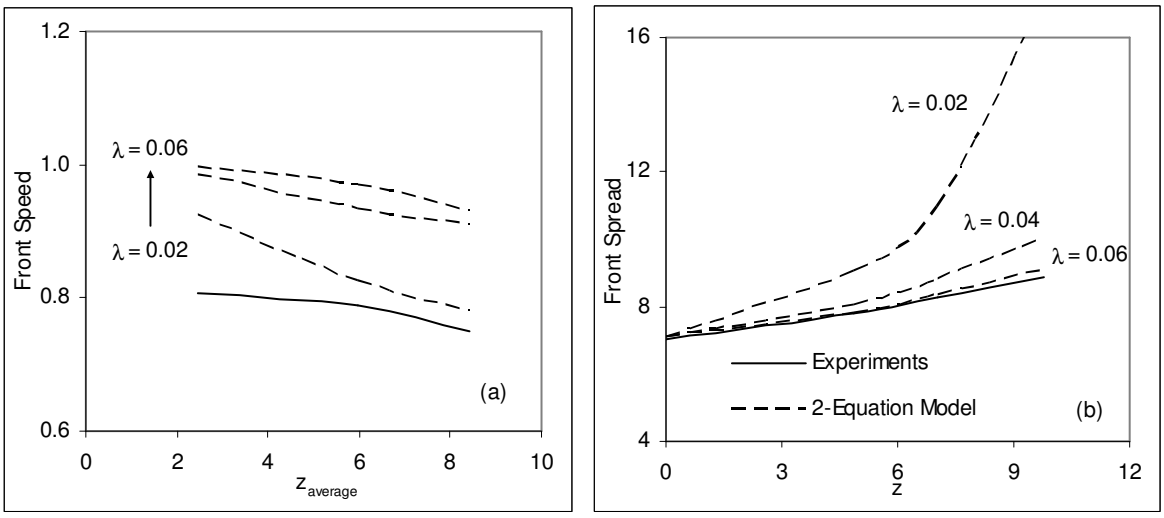

Figure 7.16: Sensitivity of thermal front to thermal conductivity ratio (λ) in steel-water bed. Pe = 961, Bi = 0.05.

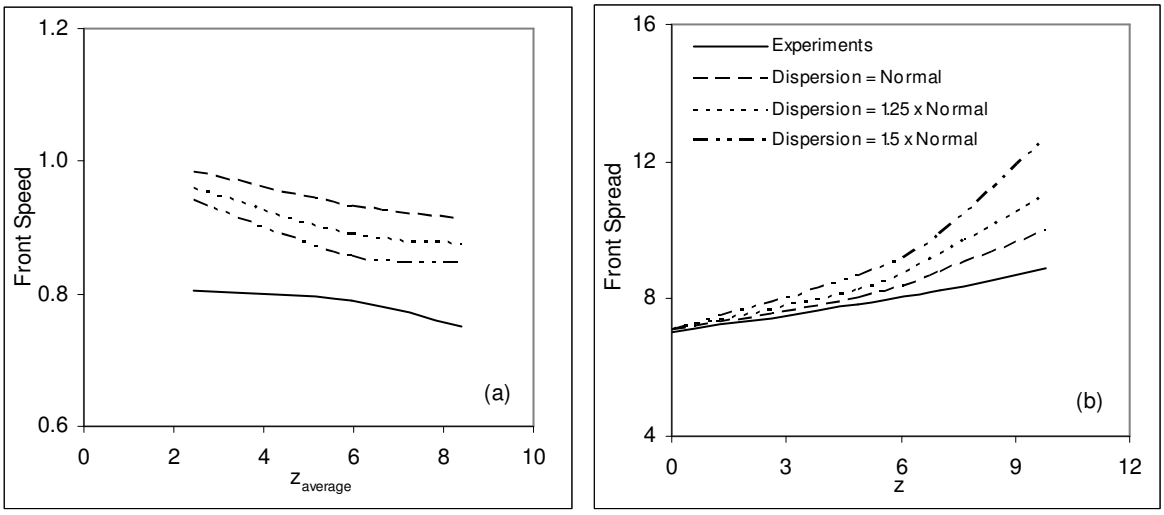

Figure 7.17: Sensitivity of thermal front to thermal dispersion in transverse direction in steel-water bed. Pe = 961, Bi = 0.05.

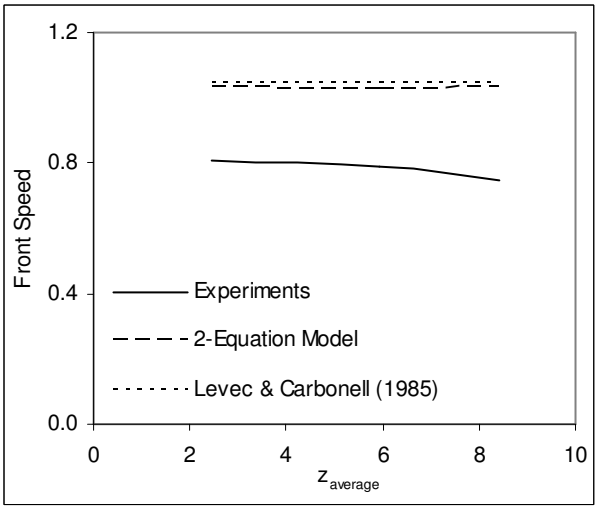

Figure 7.18: Comparison of front speed with the results of Levec and Carbonell [1985]. Pe = 961.

Figure 7.18 compares the present numerical simulation and experiments results with Levec and Carbonell [1985] in the form of front speed. The value of 2-equation model is considered at zero Biot number. Its value is quite close to that predicted by Levec and Carbonell. The front speed in experiments is lower which may be attributed to various factors such as heat loss, tube wall effect, velocity variations near the wall, channeling etc.

7.8 THERMAL NON-EQUILIBRIUM

The temperature difference between the fluid and the solid phases is dominant during unsteady state of the porous medium. It also arises due to the difference between the thermal properties of the two phases. The effect of heat transfer between the two phases is to slow down the thermal propagation in the bed. During this time, the heat flows from one phase to the other. In the present analysis, it flows from fluid to solid phase. When the thermal conductivity of the solid is high, the diffusion time scale approaches the inter-pore convective time scale, which minimizes the effect of heat transfer to solid phase by conducting the stored energy back to the fluid phase.

The thermal non-equilibrium is analyzed considering a steel-water bed of length $L = 30$. The Peclet number is varied from 500 to 4000. The Biot number is set to zero and the particle diameter d_P is 2.25 mm. 1-equation model gives a single homogeneous temperature for porous medium and fluid flowing through it whereas the 2-equation model gives distinct temperature profiles for the fluid and the solid phases. An analysis of these temperatures along with interphase heat transfer is carried out.

Table 7.5: Maximum thermal non-equilibrium between the fluid and the solid phases at various locations.

Peclet number	$z = 3$	$z = 15$	$z = 27$
500	0.031	0.013	0.01
4000	0.070	0.031	0.023

Figure 7.19 shows the temperature profiles of 1-equation model, fluid and solid phase temperature at various locations of the bed for Peclet numbers of 500 and 4000. Figure 7.19(a-c) shows the profiles for a Peclet number of 500 and Figure(d-f) for a Peclet number of 4000. For each Peclet number the profiles near the start, at mid-point and near the end of the bed are shown. The temperature profiles of 1-equation model are distinct from those of 2-equation model. The difference between the fluid and the solid phase temperature is higher near the inflow plane as compared to those away from it, which increases with Peclet number. Table 7.5 gives the corresponding value of the difference between the two phases.

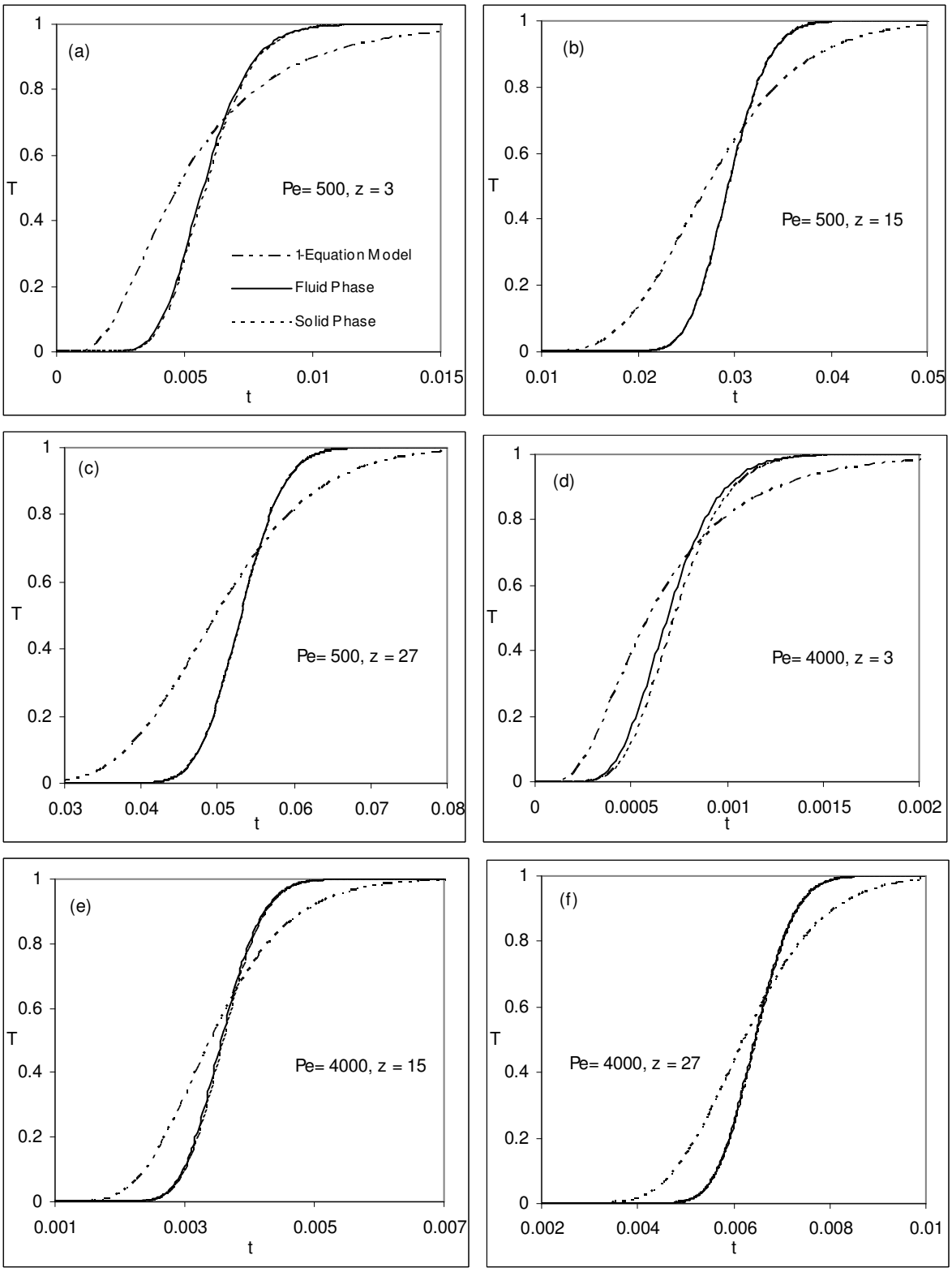

Figure 7.19: The temperature profiles of 1-equation model, the fluid and solid phases for assessment of thermal non-equilibrium in steel-water bed.

At a Peclet number of 500, the difference at a location of z =15 is 0.013 and it rises to 0.070 at a Peclet number of 4000. The difference falls with distance from the inflow plane. The thermal non-equilibrium for this bed is higher as compared to that in glass water bed. The resulting interphase heat transfer is given in Table 7.6 whose values are again higher as compared to that in glass water bed. The Table 7.7 gives the maximum difference between 1 and 2-equation models in the bed. The difference in this case is quite large and increases with distance but falls with Peclet number. It is again higher as compared to that in glass water bed.

Since the thermal conductivity of the solid phase is large in this bed, the heat transferred to the solid phase is conducted back to the fluid phase, and hence affecting the thermal front. The front speed can increase with distance, which is observed at low Peclet numbers in this bed. The corresponding time for conduction through the solid phase and residence time of the thermal front in the pores are comparable in this bed.

Table 7.6: Convective resistance and corresponding maximum interphase heat transfer at various locations.

Peclet Number Pe	Dimensionless Convective Resistance (Pe / Nu A_f)	Dimensionless Interphase Heat Transfer (Nu A_f/Pe*(T_f-T_s))		
		z = 3	z = 15	z = 27
500	0.094	0.328	0.138	0.106
4000	0.261	0.268	0.119	0.088

Table 7.7: Maximum difference between 1 and 2-equation model results at various locations.

Peclet number	z = 3	z = 15	z = 27
500	0.419	0.428	0.432
4000	0.327	0.336	0.338

The diffusion time scale $\frac{d^2}{\alpha_s}$ is 1.28 secs and residence time in pores $\frac{d\varepsilon}{U_D}$ is 0.29 and 0.035 secs respectively for Peclet number of 500 and 4000. Hence, there are chances that heat

conducted can flow back to the fluid though at a slight upstream of the current position of the front.

Figure 6.22 gives the wave of temperature difference at various locations in the bed. This wave flows through the bed and decays with distance from the inflow plane as shown by Kuznetsov [1994, 96]. The amplitude of this wave increases with Peclet number.

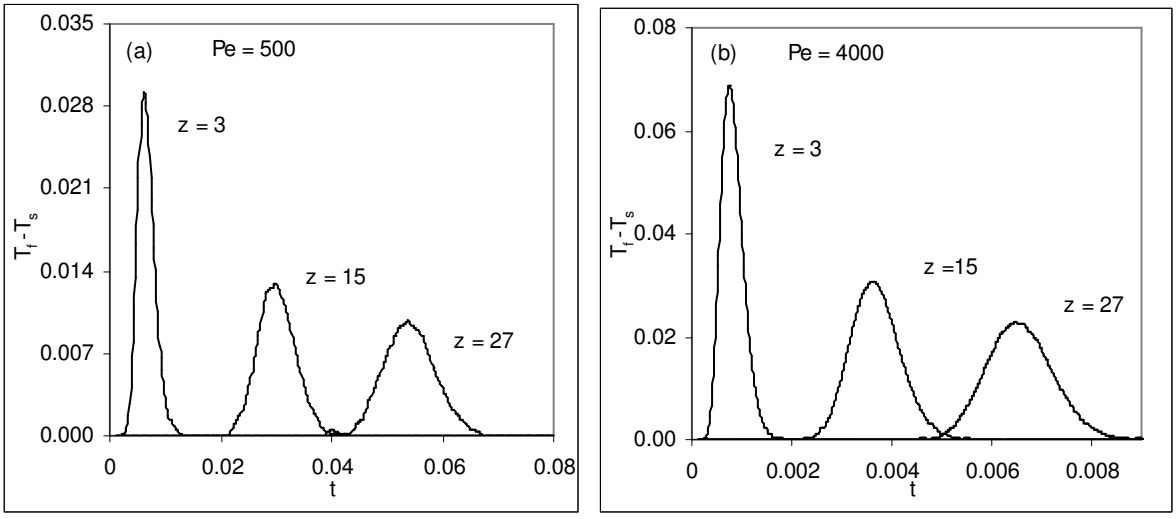

Figure 7.20: The wave of temperature difference in steel-water bed.

7.9 COMPARISON OF STEP RESPONSE IN GLASS AND STEEL-WATER BEDS

A comparison of step responses in glass and steel-water beds is performed in this section. It is obtained by using temperature-time profiles and front speed and spread in the two beds. The comparison for temperature time profiles is performed separately in simulation using an ideal step response through the two beds under similar conditions. For experiments, these profiles are not easy to plot as it requires same flow rate through the two beds and corresponding distance from the inflow plane should also be same. A comparison for nominally similar Peclet numbers through the beds is plotted.

7.9.1 Temperature-Time Profiles

7.9.1.1 Numerical Simulation

For simulation, the comparison is accurate as it is performed under similar conditions. The configuration of the bed considered is similar to one discussed in Section 7.8 on thermal non-equilibrium. Figure 7.21 shows the comparison between the step response as obtained in glass and steel-water beds. The profiles of fluid phase as obtained in 2-equation model are shown along with respective 1-equation model profiles. The results of glass water bed are faster as compared to that of steel-water bed. For a glass water bed, the results of 1-equation model are qualitatively similar to 2-equtaion model but those of steel-water bed are quite distinct from 2-equation model.

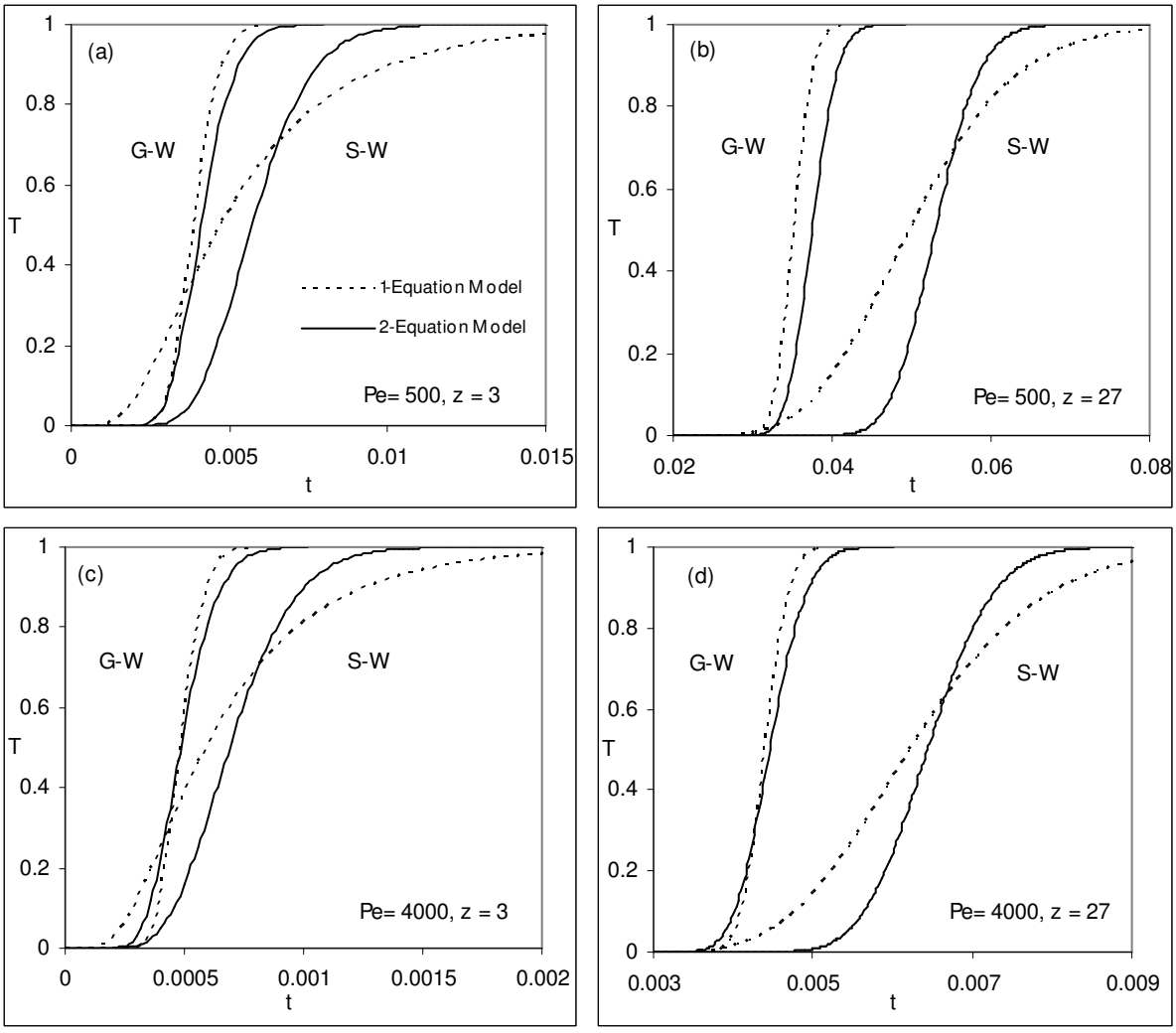

Figure 7.21: The temperature profiles for step response in glass water and steel-water porous beds using 1 and 2-equation models. d_p = 2.25 mm, Bi = 0

This comparison is shown at zero Biot number, with an increase in its value, the comparison for glass water bed maintains the similar trends but for steel-water bed, it deteriorates further.

Figure 7.21(a & b) shows the comparison for a Peclet number of 500 and Figure 7.21(c &d) for 4000. For a particular Peclet number, the difference between the profiles of glass and steel-water beds increases with distance. At higher Peclet number of 4000, the difference has increased marginally.

7.9.1.2 Experiments

Figure 7.22 gives the difference as obtained in experiments in the two beds. It is obtained by selecting nominally similar Peclet number in both the beds and the corresponding distance from the inflow plane is also same. The Peclet number is nominally equal to 500. Its actual value in glass and steel-water beds is 513 and 540 respectively. This comparison is obtained at location z = 9.6 in glass and steel-water bed-2. The time of start of response is set same in the two beds. The response of glass water bed is faster as compared to that of steel-water bed. Though approaching the maximum temperature, the steel-water response becomes faster, which may be attributed to marginally higher Peclet number in this bed.

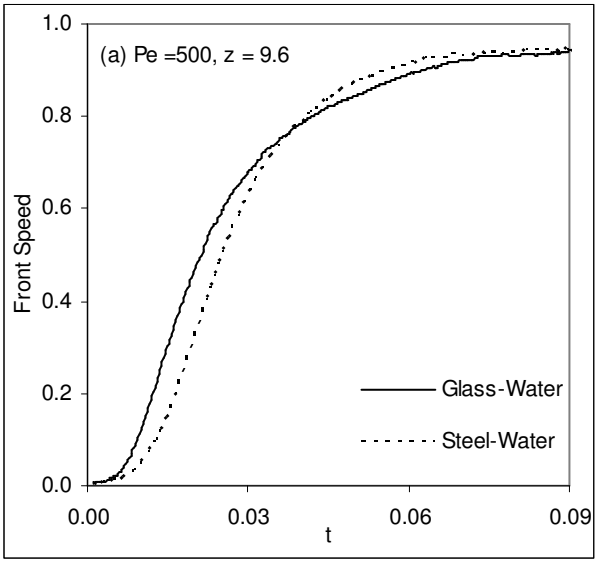

Figure 7.22: The temperature profiles for step response between glass and steel-water beds as obtained in experiments.

7.9.2 Front Speed and Spread

A comparison of front speed and spread in glass and steel-water beds is presented. Figures 7.23 and 7.24 compare the front speed and spread in these beds. The results of experiments and 1 and 2-equation models are presented. The values shown in these figures are obtained at positive Biot numbers except for 1-equation model in steel-water bed where this value is zero. Further, the results are obtained at almost same distance from the inflow plane.

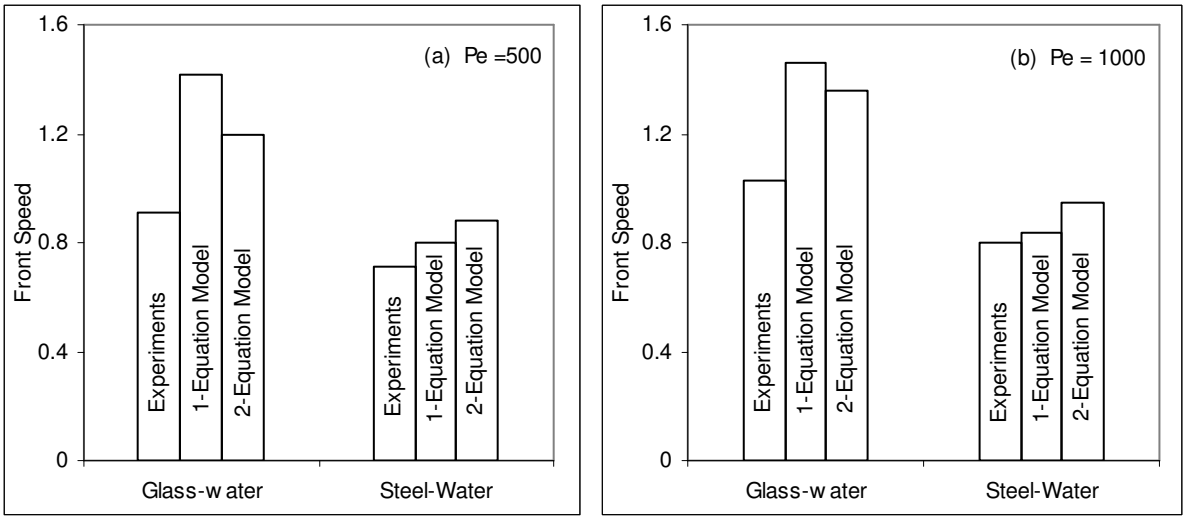

Figure 7.23: The comparison of front speed in glass and steel-water beds; z =10.

Figure 7.23 compares the front speed at two distinct Peclet number in these beds. The Peclet number in Figure 7.23(a) is nominally equal to 500 and that in Figure 7.23(b) to 1000. At a Peclet number of 500, the front speed in glass water bed is higher than that in steel-water bed. The results of 2-equtaion model are faster than those of experiments in both the beds; the difference, however, is less in steel-water bed. 1-equation model predicts the highest value of front speed in glass water bed, but in steel-water bed its value is lower than that of 2-equation model. At a higher Peclet number of 1000 in Figure 7.23(b), the similar trends are observed and but the individual differences become smaller. In general, experiments predict lower front speed as compared to numerical simulation. For steel-water bed, the experimental values are closer to simulation as compared to that in glass water bed. The results of 1-equation model for steel-water bed at a positive value of Biot number gives a very slow thermal response and does not predict correctly the front speed. Hence, only 2-equation model results should be used for steel-water bed.

Figure 7.24 compares the front spread in the two beds. The comparison is carried out by using relative front spread, which at a location of z is defined as

Relative front spread at z = (Front spread at z - Front spread at the inflow plane)/Pe (7.1)

Hence, the relative spread is independent of absolute spread and the Peclet number. The location z is again chosen such that it is almost at same distance from the inflow plane in both the beds. Its value is $z = 10$ for both the beds.

Figure 7.24(a) shows the comparison at a Peclet number of 500 and the relative spread in glass water bed is much lower than in steel-water bed. In glass water bed, the trends are opposite to that of the corresponding front speed in the bed such that 2-equation model predicts lower spread than experiments & 1-equation model the lowest spread. For steel-water bed, the simulation predicts higher spread than that in the experiments and 2-equation model predicts higher value of spread than that in the experiments. 1-equation model, at zero Biot number, predicts the highest spread in this bed. At higher Biot number, its value becomes excessively higher. At a higher Peclet number of 1000, in Figure 7.24(b), the relative spread increases in glass water bed but decreases in steel-water bed. The other trends remain the same.

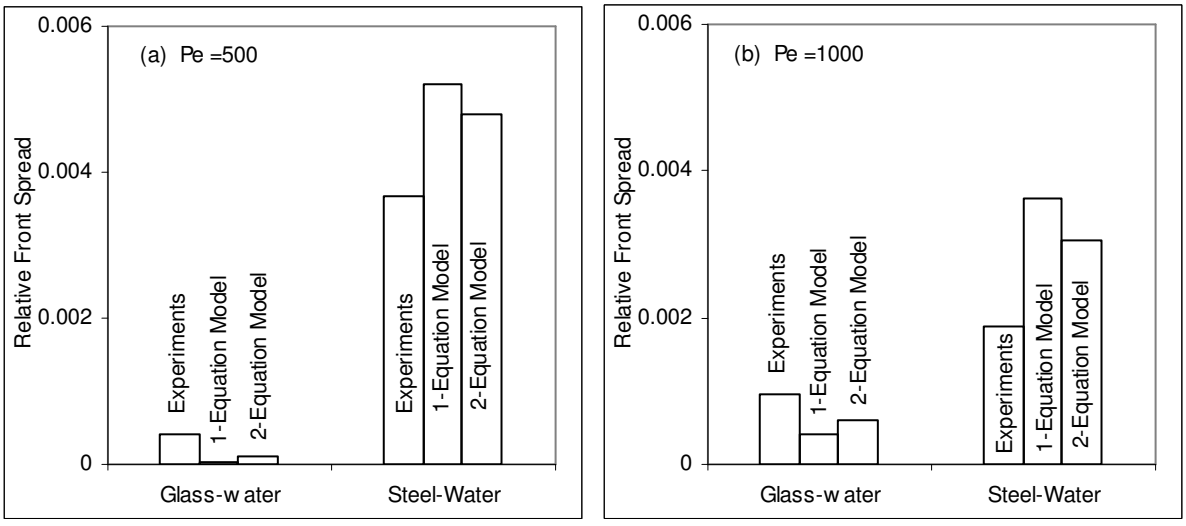

Figure 7.24: The comparison of relative front spread in glass and steel-water beds; $z = 10$.

7.10 CLOSURE

A comparison of numerical simulation with step response experiments in a steel-water bed is presented in this chapter. Experimental results are obtained from two separate steel-water beds. The results of 1and 2-equation model are compared with those of the experiments using unsteady temperature profiles and corresponding speed and spread of the thermal front trevelling through the bed. The modified boundary condition is used for comparison. The results of 2-equation model are uniformly superior to those of 1-equation model. 1-equation model presents results that are distinct to 2-equation model. It predicts poor results when heat loss is taking place in the bed. It is attributed to high weighted thermal conductivity as used in 1-equation model for this bed. Hence, the results of 2-equation model should be used for simulation. Overall, the comparison of numerical simulation with experiments in this bed is better than that in glass water bed. The thermal non-equilibrium in this bed is higher as compared to that in glass-water bed. A comparison of the results of glass-water and steel-water bed is also presented. The front speed in this bed is slower when compared to that in glass water bed and the corresponding spread is higher. The step response in a porous bed provides knowledge when there is single flow of hot water through an initially cold domain. When hot and cold fluids flow alternately through the porous bed, the resulting response, called the frequency response, is distinct from the step response. A detailed analysis of this response in the two beds is presented in the following chapters.

CHAPTER 8

FREQUENCY RESPONSE OF GLASS-WATER BED

8.1 INTRODUCTION

The dynamic behavior of porous medium has applications in many technical fields such as solar thermal energy storage, chemical reactors, Stirling cycle regenerators, underground energy storage reservoirs. In chemical reactors design, it is important to know the thermal transport characteristics of the porous medium in order to predict the reaction rates caused by inlet temperature fluctuations. In the design of packed bed thermal storage systems, it is again desirable to have good estimates of the heat transfer coefficients and effective thermal conductivities so that one can predict the time required to heat up the solid particles. In most of these applications, hot and cold fluids flow alternately through the porous bed. Thermal energy transfers to the solid phase during the flow of the hot fluid through the bed and subsequently it is retrieved during the flow of the cold fluid. The alternative flow of the hot and the cold fluids set up thermal transients in the bed.

Spiga and Spiga [1981] obtained analytically the frequency response of the bed subjected to a time varying inlet temperature. The subsequent temperature evolution in the porous medium is of waveform having peaks and valleys. The maximum temperature falls with distance from the inflow plane and the minimum temperature rises. Ultimately, the two values approach each other and the response of the bed dies out. The time-period of the wave is obtained from the total time for single flow of hot and cold fluids; each being equal to half of the time-period. It depends upon the flow rate of the fluids and the thermo-physical properties of the porous medium. Levec and Carbonell [1985] studied the response of porous medium to a pulse of temperature in the fluid phase. It subsequently heats the solid phase until it reaches the maximum temperature. At this time, the fluid and the solid pulses travel at equal velocities and spread at equal rates, but with a spatial separation; a phase difference exists between the two pulses. Hence, the response of the fluid and the solid phases in the bed is distinct. Byun *et al.* [2006] studied analytically the thermal behavior of porous medium under oscillating flow conditions; flow changes its direction in a porous medium

whose two ends are maintained at hot and cold temperatures. The pulsation in the fluid and the solid phases varies with thermal properties of the porous medium. It is a function of the ratio of thermal storage capacities of the fluid and the solid phases and that of interphase heat transfer and energy convected downstream. In a frequency response, the fluid and the solid pulses are expected to change as a function of the above parameters. The fluid pulse enters the bed through one of its ends and subsequently interacts with the fluid and the solid phases existing in the bed. The fluid pulse is expected to displace and heat up the existing fluid in the bed. The solid phase, the stationary medium, is heated up with this pulse and consequently a phase difference is expected to occur between the pulses traveling through the two phases.

In this chapter, the frequency response of a glass-water bed is discussed. The aim is to compare the experimental results of the frequency response with that of numerical simulation. In addition, global properties such as attenuation of temperature, phase lag, pulse speed and spread are discussed. The thermal non-equilibrium existing between the two phases during the frequency response is also studied. The results of frequency response as obtained from bed-2 are used for analysis. These results are compared with numerical simulation using the results of 1 and 2-equation models. As seen in the step response of glass-water bed, the temperature profiles as predicted by the 1-equation model are faster as compared to those for the 2-equation model. It is interesting to see the nature of the results for time periodic boundary conditions.

Equations 5.3 and 5.4 give the ideal boundary conditions for frequency response of the bed, zero and unity being the minimum and the maximum fluid temperatures. In experiments, the temperature at the inflow plane does not change instantaneously from zero to unity and subsequently to zero, see Figure 5.1(c). Hence, the boundary conditions of the frequency response in the experiments and the numerical simulation are modified with the actual temperature response obtained at the inflow plane.

The study is carried by considering a reference time-period during which both the hot and the cold fluids traverse the bed completely. The time-period of pulsations is varied with respect to this value. We now discuss the frequency of pulsations and reference frequency as used for a frequency response experiment.

8.2 FREQUENCY OF PULSATIONS AND REFERENCE FREQUENCY

Figure 5.1(c) shows frequency response of a porous bed. Here the temperature at $z = 0$ fluctuates between zero and unity; the maximum fluctuation. At a downstream location, the fluctuation is smaller as compared to that at $z = 0$. The time-period of the pulsations, t_P is obtained from the time gap of occurrence of successive peaks or valleys in the temperature response curve. It is divided into two equal halves called the hot and the cold phases. They show the response to the flow of the respective fluids. The frequency of pulsations in the porous bed is a function of forcing frequency, which is thus defined as

$$\omega = \frac{2\pi}{t_P} \quad \text{[rad/s]} \tag{8.1}$$

In addition, one can introduce a reference frequency for each experiment in terms of the time period required for the hot and the cold pulses to travel the entire length of the bed while moving at the average fluid speed. Its value is given as

$$\omega_{ref} = \frac{2\pi}{(t_P)_{ref}} \tag{8.2}$$

$$\text{where } (t_p)_{ref} = \frac{2L}{\text{Average fluid speed}}$$

$$= \frac{2L\,R}{\text{Pe}\alpha} \tag{8.3}$$

Here R is the radius of the tube containing porous medium having length L. The reference frequency is thus given as

$$\omega_{ref} = \frac{2\pi\pi\text{P}\alpha}{2LR} = \frac{\pi\text{Pe}\alpha}{zR^2} \tag{8.4}$$

The corresponding dimensionless reference frequency is given as

$$\omega_{ref} = \frac{\pi R\text{Pe}}{L} = \frac{\pi\text{Pe}}{z} \tag{8.5}$$

where z is the non-dimensional length of the bed.

Hence, the reference frequency depends on length of the bed and the flow rate. Alternately, for each flow rate and frequency a reference length of the bed should be specified. For applications related to energy storage as in Stirling cycle regenerators, solar energy storage and underground energy storage reservoirs an optimum frequency, a value

close to reference, needs to be selected such that the energy levels at the end of the hot and the cold phases reach an optimum value. In case the frequency exceeds the optimum value, the corresponding time-period is smaller such that the storage capacity of the bed is not fully utilized. However, when it is lower than the optimum, the corresponding time-period is higher and supply of energy exceeds the storage capacity. Hence, the frequency should be properly selected so that energy is stored to the optimum level.

8.3 FRONT AMPLITUDE AND PHASE LAG

The response of the bed subjected to a time varying inlet temperature is of waveform having peaks and valleys. During the hot phase, the temperature level of porous medium rises and reaches a maximum value at the end of the phase and during the cold phase, the level falls and reaches a minimum value at the end of the phase. The maximum and the minimum temperatures vary with distance from the inflow plane. The difference between the maximum and the minimum temperatures at a location is called the amplitude. The amplitude at a downstream location is always less than that at $z = 0$.

The propagation of the pulse through the porous medium is similar to that of hot fluid front as in a step response experiment. In a step response, as the hot fluid front flows through initially cold bed, its spread increases with distance from the inflow plane and the corresponding maximum temperature falls. Over a distance, as the front gives its energy to the solid phase, its own energy level falls and subsequently the front will die in the porous medium. In the same way, for a pulse traveling through the bed as in a frequency response, the spread of the hot and the cold phases of the pulse increases and its amplitude fall with distance. Over a distance, the amplitude of the pulse falls to zero and consequently the pulse dies out.

As the pulse moves downstream, it encounters new porous medium to heat or cool to the required temperature. During the hot phase, the hot fluid gives its energy to the bed but the maximum temperature falls with distance from the inflow plane due to increased spread caused by dispersion and heat loss. Similarly, during the cold phase, the cold fluid extracts the stored energy but encounters new porous domain and the minimum temperature increases with distance. A decrease in the maximum temperature and an increase in the minimum temperature results in a fall in temperature amplitudes and pulsation will ultimately die in the

porous medium. The decrease in amplitude of temperature is called the attenuation. The resulting temperature reached when the amplitude of the pulse falls to zero lies in between the hot and cold values. The individual effects of such pulsating boundary conditions reduce to an ideal boundary condition of constant temperature if the frequency of pulsations is large and amplitude of temperature fluctuations is small, Sozen [1991]. On the other hand, for lower frequencies, the attenuation is small.

The pulsations in porous medium are distinct from those in a plain flow. In plain flow the rise and fall of temperature during hot and cold phases is very fast. Whereas in a porous medium, the rise and fall of temperature profile is gentle as both the phases are being heated or cooled. In a plain flow, the corresponding temperature changes are sharp. However in both cases, when the respective maximum and minimum temperatures are approached, the slope of the curves drop markedly. It is because of low driving force; the temperature difference between the hot and the cold fluids with those of the solid phase, Figure 8.1(a). The curves of the hot and the cold phases are mirror images of each other. The maximum and the minimum temperatures in plain flow are closer to the hot and the cold fluid temperatures than those for the porous medium.

Phase lag (ϕ) The maximum and the minimum temperatures at a downstream location occur after some time gap of its occurrence at an upstream location. It represents a time lag of occurrence of respective point on the curve. It is called the phase lag (ϕ), which is obtained, by the corresponding angle of separation between the two locations. Hence, it is defined as the average time elapsed between successive peaks or valleys (expressed in terms of an angle). A phase lag of π indicates that when a peak is occurring at the location, a valley is occurring at the same time for the upstream location. It depends on the time period of pulsations, a larger time period results to a smaller phase lag. In a conduction-dominated transport process, the phase lag increases linearly with distance from the inflow plane. Using this result, phase lag has been non-dimensionalized by the multiplicative factor $\sqrt{\frac{2\alpha_f}{\omega}}\frac{1}{z}$, where z is the separation between the two points.

In addition to amplitude and phase lag, the pulse speed and its spread as discussed in Chapters 6 & 7 can provide vital information about the transport in porous medium.

8.2 EXPERIMENTAL FREQUENCY RESPONSE

The experimental frequency response of glass-water bed is discussed in this section. The results are obtained at various flow rates and frequencies. The response of the bed to a time varying pulse at the inflow plane is plotted and the resulting amplitude, phase lag and front speed and spread are discussed.

The hot and the cold fluids flow alternately through one end of bed initially maintained at zero temperature. When the hot fluid flows in, the temperature at various locations rises as in a step response experiment. Later the temperature at various locations fall due to the flow of cold water through the inflow plane. As the hot water flows again, it raises the temperature at various locations in the bed but from a non-zero initial temperature. Consequently, the maximum temperature reached at various locations increases marginally as compared to that in the first cycle. Gradually, after a few cycles, the level of fluctuations at a location becomes identical from one cycle to another. This is called the cyclic steady state.

Figure 8.1 shows the frequency response of the bed at a Peclet number of 1202, the frequency of pulsations being 0.052 rad/s. The response at various locations in the bed along with that at a lead location in the supply line to the bed is shown in the figure. For the comparison of amplitudes at various locations, the hot fluid temperature of unity is also shown in each figure. The response starts from zero temperature and reaches a maximum value, which depends upon the distance from the inflow plane. The temperature fluctuates between the maximum and the minimum values and the cyclic steady state is reached after 4 to 5 cycles.

Figure 8.1(a) shows the response at a lead location near the bed and $z = 1.4$ from start of the bed. The response at the lead location is very fast and the profile has almost vertical slope. Approaching the maximum and the minimum temperatures, the profiles change due to low driving force at these points. In the first cycle, the maximum temperature for lead location is marginally less than unity; hot fluid temperature. The minimum temperature however is more than zero. In second cycle, the maximum temperature rises further and reaches a unit value. The minimum temperature remains higher than zero. At location $z = 1.4$, the maximum temperature reached is less than that for the lead location and the minimum temperature is higher. The corresponding rates of temperature rise and fall are lower. Figure 8.1(b) shows the frequency response at locations $z = 9.6$ and 20.6 from the start of the bed.

The temperature again rises from zero value and the maximum temperature attained is lower than that at z = 1.4 but the corresponding minimum temperature is higher. Similarly Figure 8.1(c), the response at locations z = 31 and 42 is shown. The respective changes at theses locations occur at a later point of time as compared to the upstream locations and the amplitude of pulsations reduces further.

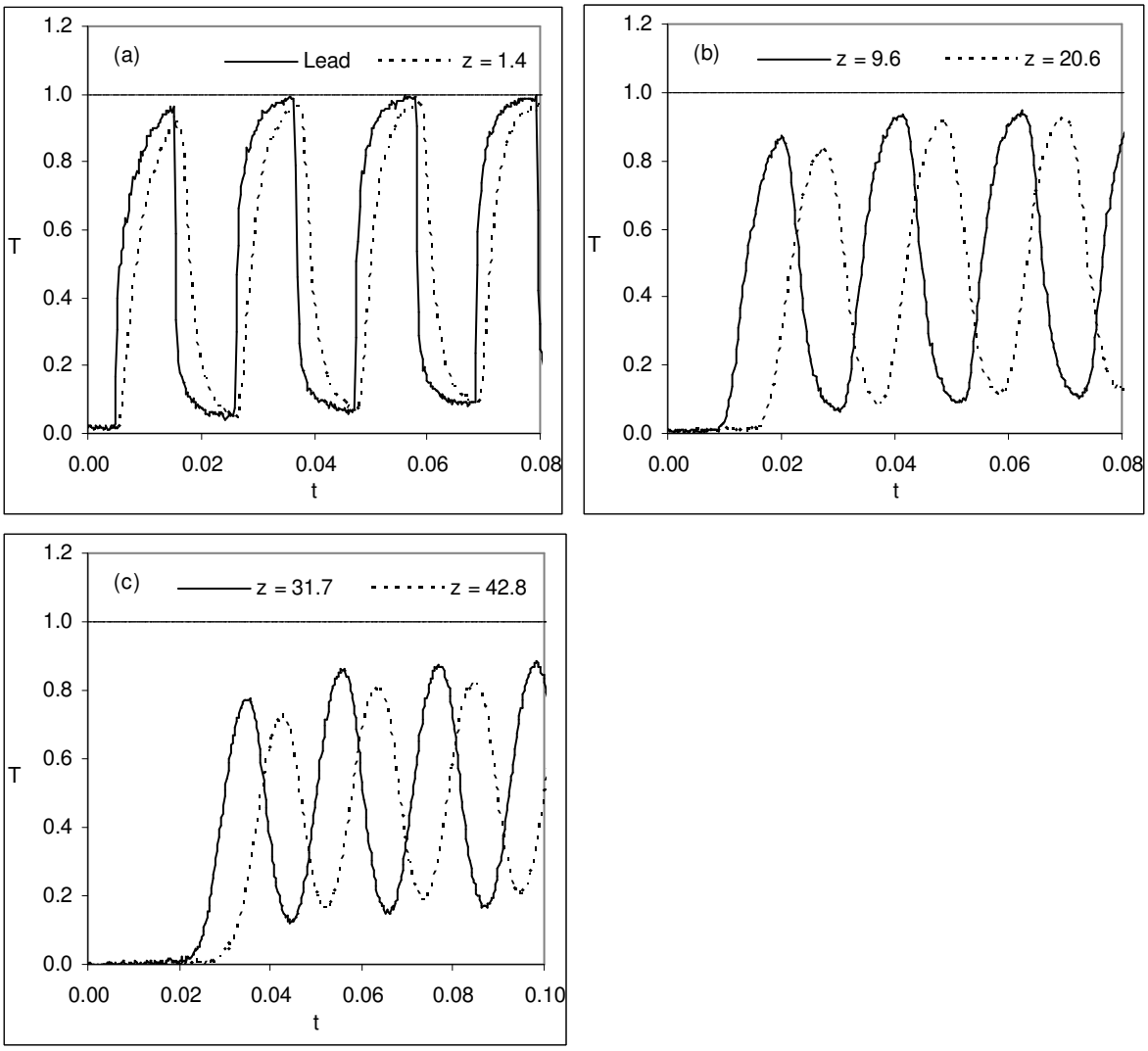

Figure 8.1: The unsteady and cyclic steady states for the frequency response in glass-water bed. Pe = 1202, ω = 0.052 rad/s.

We now plot the experimental frequency response at various frequencies. The plots are drawn after cyclic steady state is reached. The aim is to show the amplitudes, attenuation of temperature, phase lag and pulse speed and spread for various Peclet numbers and frequencies.

8.2.1 Cyclic Temperature Profiles

The cyclic steady state for various Peclet numbers and frequencies are shown. Two distinct Peclet numbers are chosen which are nominally equal to 950 and 1550. For each Peclet number, the response is discussed for three frequencies of pulsations relative to the reference value. These graphs are plotted such that the position of third thermocouple in glass-water bed-2 is set to zero as shown in Table 6.2. The reference frequency as given in these figures is with respect to location z = 33. The response at modified locations of z = 0, 11 and 22 is shown in these figures. Figures 8.2 to 8.4 show the frequency response when Peclet number is 950 and in Figures 8.5 to 8.7, its value is 1550.

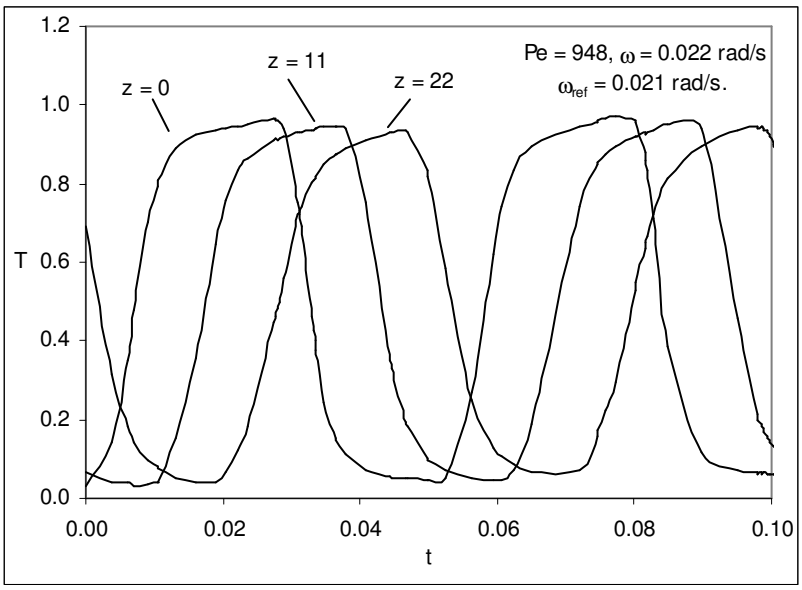

Figure 8.2: The frequency response of glass-water bed. Pe = 948, ω/ω_{ref} = 1.04.

Figure 8.2 shows the frequency response for a Peclet number of 948, the frequency of pulsations being 0.022 rad/s. The reference frequency for this Peclet number is close to the frequency of pulsation at 0.021 rad/s, consequently the two fluids have sufficient time to reach the other end of the bed during the respective phases. The temperature profiles when approaching the maximum and the minimum values experience a drop in slope. The amplitude at z = 0 is marginally less than 0.5; the maximum value possible. The maximum temperature decreases with distance and minimum temperature increases. The decrease in amplitude is however small. The phase lag between the two locations; say z = 11 and 0 is

estimated from the temperature at z = 0 when a peak is occurring at z =11. The corresponding phase lag is 67°.

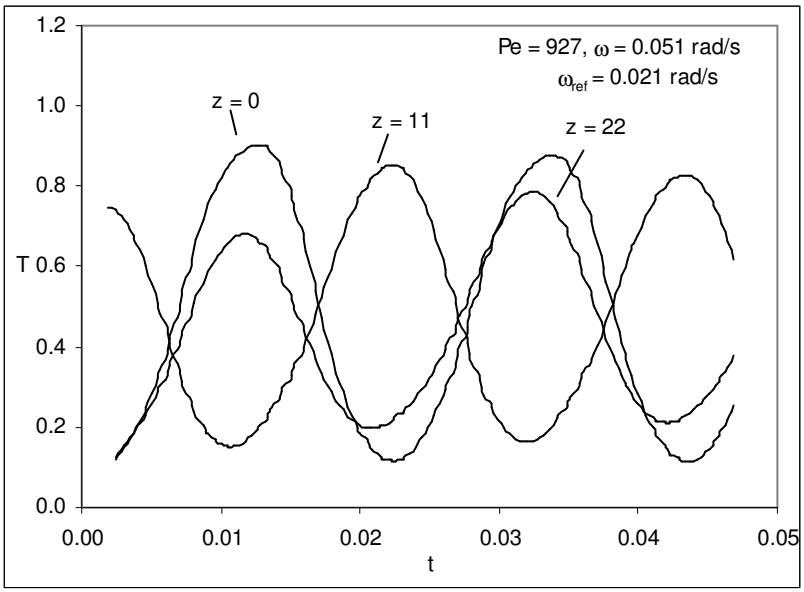

Figure 8.3: The frequency response of glass-water bed. Pe= 927, ω/ω_{ref} = 2.21.

Figure 8.3 shows the frequency response for a Peclet number of 927 and a frequency of 0.051 rad/s. Here the frequency of pulsations is 2.21 times the reference value so the time-period is smaller as compared to the reference value. The amplitudes at various locations are smaller and its fall with distance is more as compared to that for the previous case. The corresponding phase lag is also more such that when a peak occurs at location z = 11, a valley occurs at z = 0; a phase lag of π radians. In Figure 8.4, the frequency of pulsations is increased to 0.072 rad/s at a Peclet number of 981. As the frequency is much larger as compared to reference value, the amplitudes at various locations in the bed are small. The corresponding attenuation is more as compared to the previous cases and the phase lag between locations z = 11& 0 rises to 169°.

Figures 8.5 to 8.7 show the frequency response of the bed at a higher Peclet number having nominal value of 1550. The reference frequency is higher for this flow rate as compared to that for lower Peclet number of 950. In general, as the frequency approaches the reference frequency, the amplitude of the pulsations increases and the corresponding attenuation is lower. For higher frequencies, the amplitudes fall and attenuation of temperature is higher.

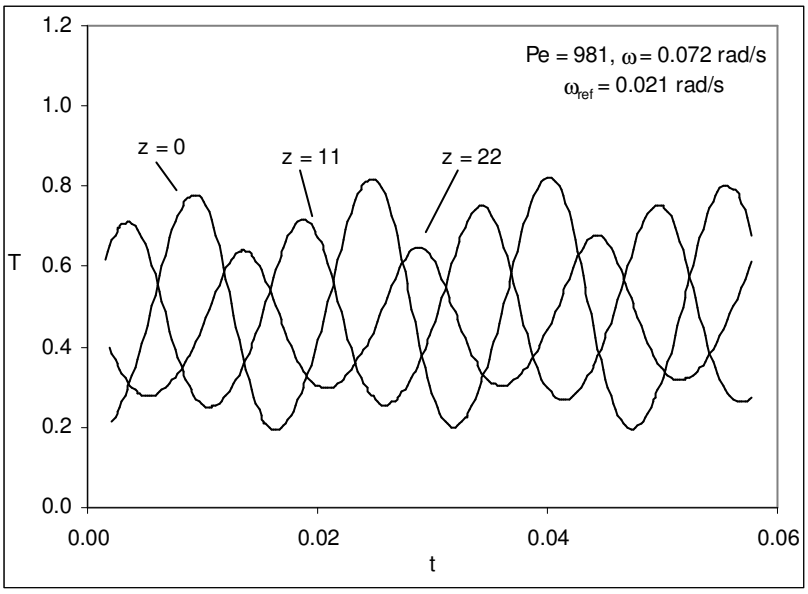

Figure 8.4: The frequency response of glass-water bed. Pe= 981, $\omega/\omega_{ref} = 3.42$.

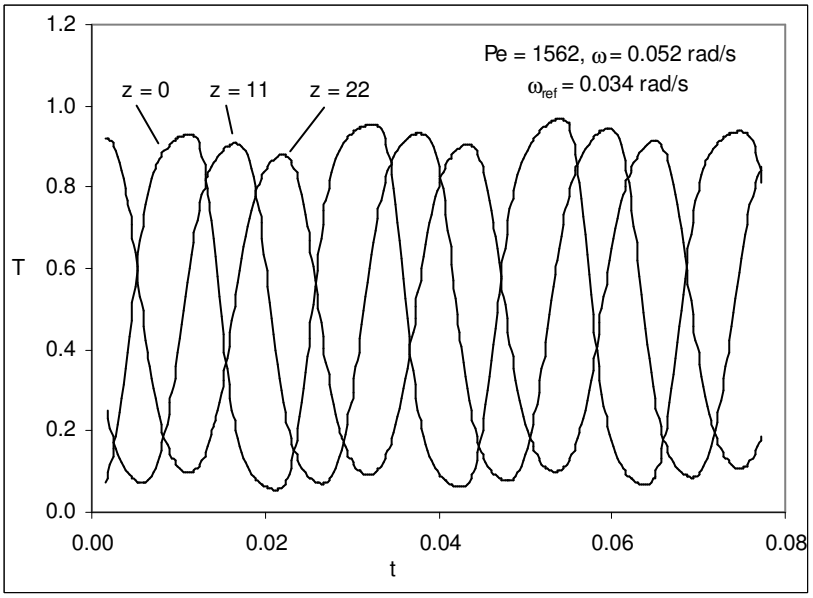

Figure 8.5: The frequency response of glass-water bed. Pe = 1562, $\omega/\omega_{ref} = 1.52$.

In Figure 8.5, the frequency response at a Peclet number of 1562 is shown and the frequency of pulsations is close to reference value though marginally higher. The amplitude at $z = 0$ is marginally lower than 0.5. The maximum temperature at $z = 11$ is marginally lower and the minimum temperature is marginally higher and hence the amplitude falls. The fall in amplitude seems gentle and the corresponding phase lag is small.

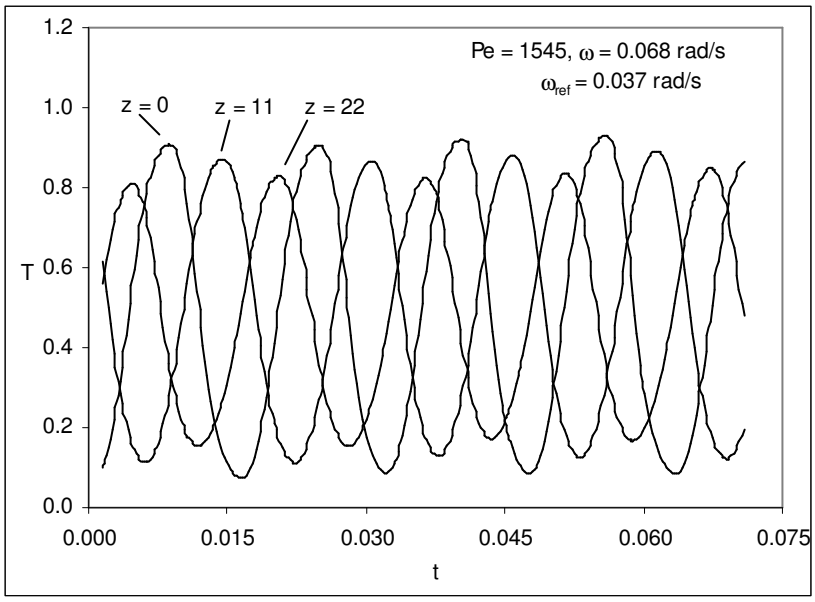

Figure 8.6: The frequency response of glass-water bed. Pe= 1545, ω/ω_{ref} =1.83.

As the frequency is increased to 0.068 rad/s, the amplitudes at respective locations fall and the attenuation of temperature and phase lag increases. Figure 8.7 shows the frequency response at a frequency of 0.096 rad/s and the Peclet number is 1589. Here the frequency is 2.46 times the reference value and the resulting time-period being very small, the amplitude at $z = 0$ is small and falls rapidly with distance. The phase lag is also higher as compared to that for the previous cases.

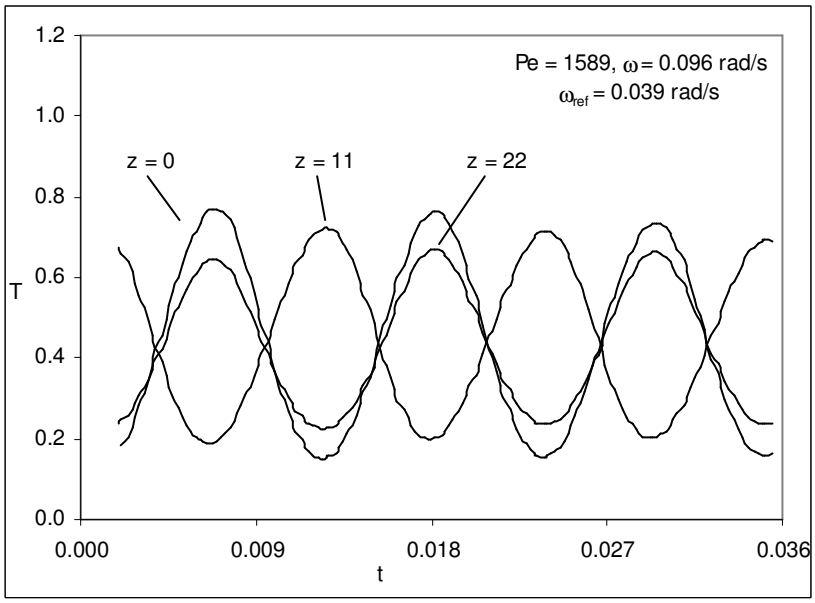

Figure 8.7: The frequency response of glass-water bed. Pe= 1589, ω/ω_{ref} =2.46.

From the above analysis, it is clear that the response of porous medium to temperature pulse is in waveform with amplitude falling with distance. The frequency response in the medium is a function of frequency of pulsations, distance from the inflow plane and the thermal properties of the solid phase of the porous medium. We now compare the amplitudes phase lag and pulse speed and spread for the above mentioned cases.

8.2.2 Amplitude and Phase Lag

The amplitude of pulsations indicates the maximum variation of temperature at a location. In the non-dimensional form, it varies between 0 and 0.5. It increases with the time period of pulsations and flow rate. The phase lag of a location with respect to an upstream location signifies the angle of separation between these locations in the terms of time period of pulsations. A non-dimensional phase lag as discussed in Section 8.3 is presented in this section. Figures 8.8 and 8.9 show the attenuation of temperature amplitudes and the corresponding phase lag for Peclet numbers having nominal values of 950 and 1550 respectively.

Figure 8.8(a) shows the attenuation of temperature for various frequencies as a function of distance from the inflow plane. The respective amplitudes increase with a decrease in frequency and reach a maximum value as the frequency approaches the reference value. For a particular frequency, it falls with distance from the inflow plane. Figure 8.8(b) shows the non-dimensional phase lag with respect to location $z = 0$. It decreases with a decrease in frequency of pulsations and reaches a minimum value for a frequency close to reference value. For a particular frequency, it remains constant with distance from the inflow plane indicating that, the corresponding phase lag in radians increases linearly with distance.

Figure 8.9 shows the results when the Peclet number is increased to 1550. As the frequency approaches the reference value, the amplitude increases and the corresponding phase lag decreases. For a particular frequency, the amplitude falls with distance but the phase lag remains constant. The phase lags are higher when compared to those at lower Peclet number of 950, but the respective amplitudes look similar.

8.4.3 Pulse Speed and Spread

The speed of the pulse traveling through the porous medium and the corresponding spread is presented in this section. The speed of the pulse is calculated corresponding to a temperature of 0.5 at various locations and the spread for the corresponding temperature range of 0.25 to 0.75. These are calculated for both the hot and the cold phases.

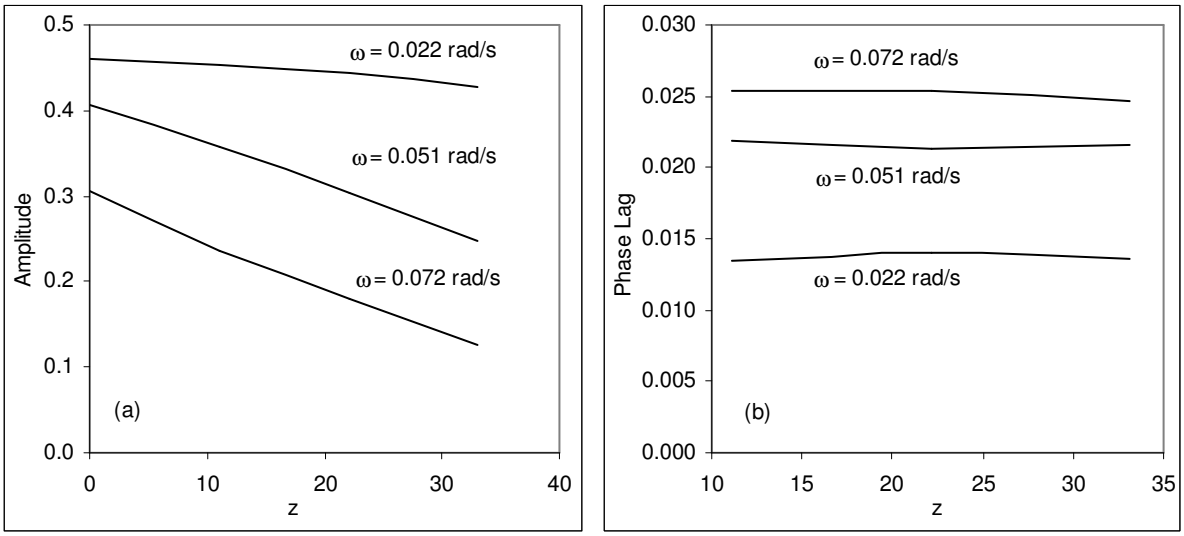

Figure 8.8: Attenuation of temperature and phase lag as a function of distance for glass-water bed. Pe = 950; ω_{ref} = 0.023 rad/s.

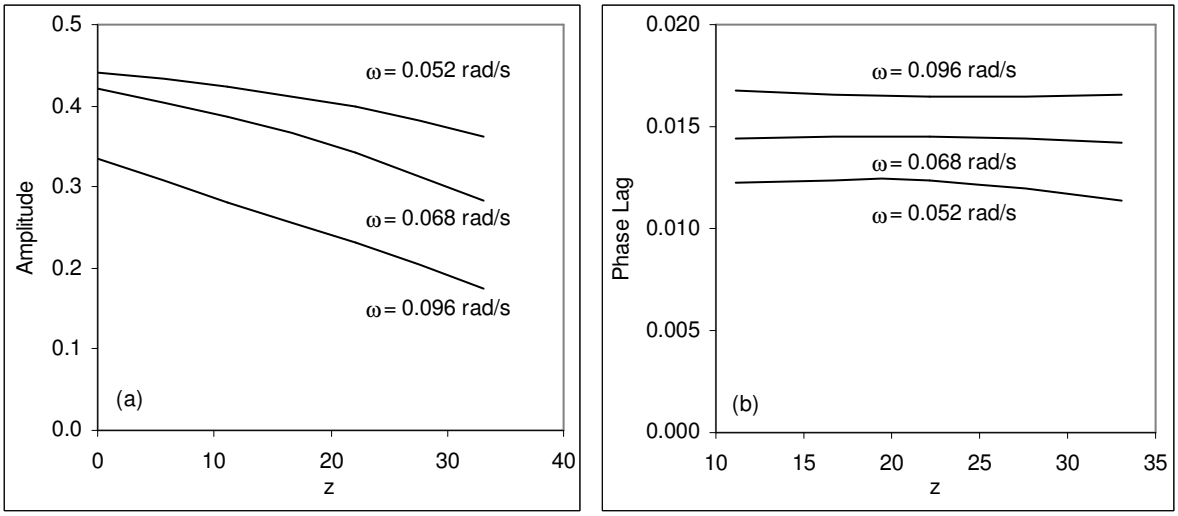

Figure 8.9: Attenuation of temperature and phase lag as a function of distance for glass-water bed. Pe = 1550; ω_{ref} = 0.038 rad/s.

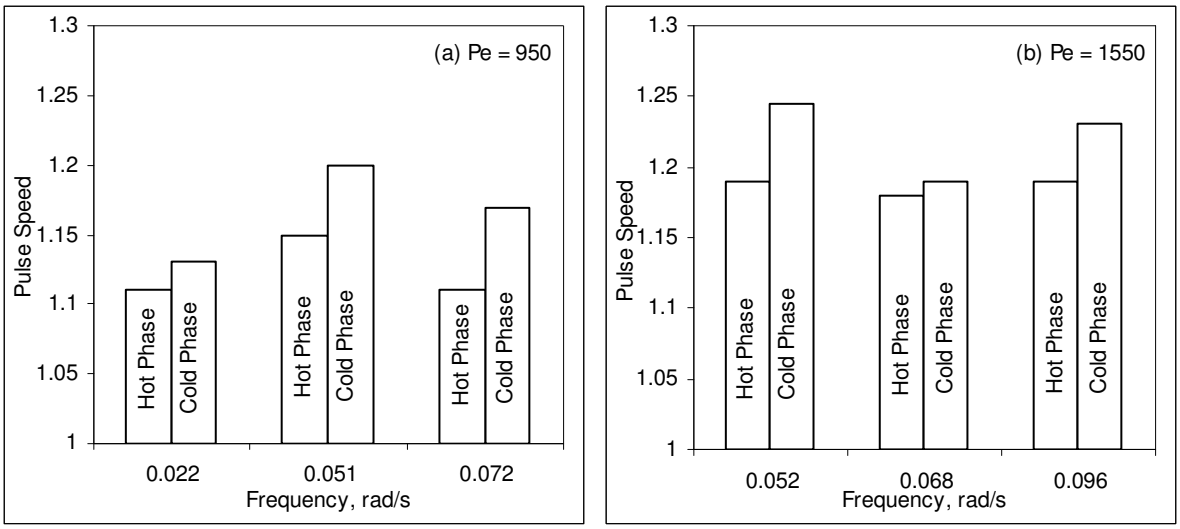

Figure 8.10: Pulse speed as a function of frequency of pulsation in glass-water bed.

Figures 8.10(a & b) show the pulse speed in the bed for Peclet numbers of 950 and 1550 respectively. The pulse speed for the hot and the cold phases are shown for various frequencies. The pulse speed is higher for the cold phase as compared to that for the hot phase. In general, it increases with Peclet number.

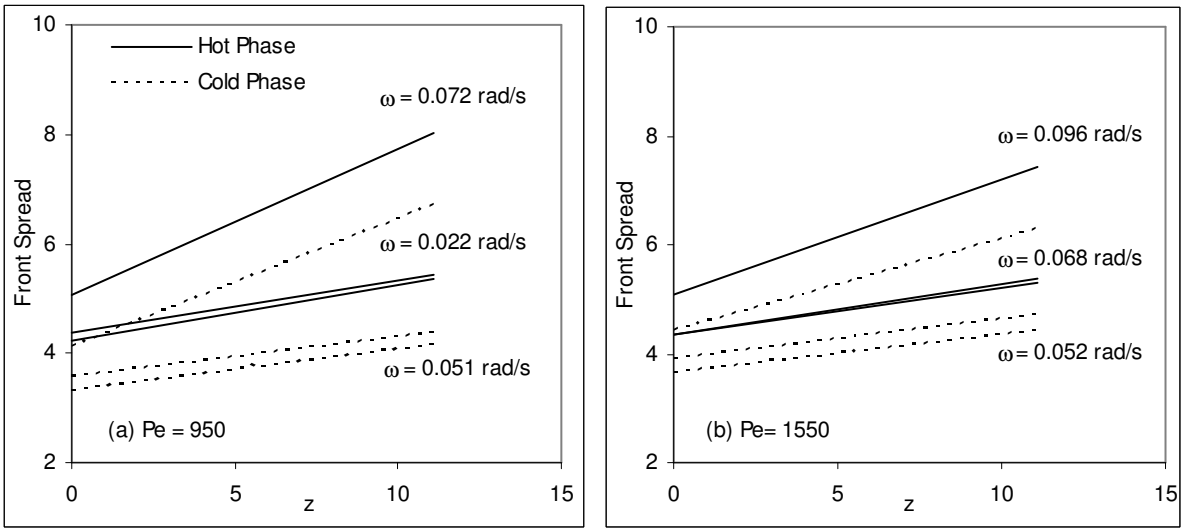

Figure 8.11: Pulse spread as a function of distance in glass-water bed.

Figures 8.11 show the variation of pulse spread with distance for the respective Peclet numbers. The spread for the hot and the cold phases is shown in the figure. The spread for the hot phase is higher as compared to that for the cold phase. Both the spreads, however, increase at equal rate with distance and hence remain parallel to each other. For lower range

of frequencies, the spread seems independent of it. However, it becomes large for higher frequencies. In Figure 8.11(a), the spread is almost similar for frequencies of 0.022 and 0.051 rad/s but it becomes very large when frequency rises to 0.072 rad/s. The similar trends are observed at higher Peclet number of 1550.

We now compare the experimental results with the numerical simulation. For this purpose, the cyclic temperature profiles as shown in Figures 8.2 to 8.7 are drawn by adding the corresponding numerical simulation profiles showing thereby a qualitative validation. A quantitative validation is obtained by comparing measurable parameters such as amplitude, phase lag, pulse speed and spread.

8.3 VALIDATION OF NUMERICAL MODELS

A detailed validation of numerical simulation is performed in this section. The results of both the 1 and 2-equation models are compared with experiments under similar conditions. In numerical simulation, the response at first thermocouple in bed-2 is set as boundary condition for subsequent locations and the results are compared with experiments. The time-temperature profiles are drawn and resulting amplitude and phase lag is calculated at each location. The comparison of pulse speed and its spread is obtained. In addition, the thermal non-equilibrium between the fluid and the solid phase is predicted and the role of interphase heat transfer between the two phases is assessed.

8.5.1 Boundary Conditions

In the numerical simulation, the two distinct boundary conditions are tested. In the first case, the unsteady temperature profiles of the two phases are same at the inflow plane time but in the second case, the fluid phase heats the solid phase hence the two temperature profiles are different. The two boundary conditions do not show any visible differences as far as the time-temperature profiles are concerned. But the thermal non-equilibrium is different. Here the second boundary condition is used for validation. The other parameter such as effective thermal conductivities and interphase heat transfer is used as the normal values.

8.3.1 Cyclic Temperature Profiles

A comparison between the numerical simulation and the experimental results as obtained at cyclic steady state is performed for various frequencies and Peclet numbers. Figure 8.12 shows the temperature profiles as predicted by 1 and 2-equation models for a frequency of 0.021 rad/s, the value of Peclet number being 948. Here the Biot number is set to unity to account for minor heat losses. The idea here is to show the nature of cyclic temperature profiles as predicted by the numerical simulation. At location z =0, the two profiles are set similar. The profiles at locations z =11 & 22 are shown in the figure. 1-equation model predicts faster temperature response as compared to 2-equation model and the difference is increases with distance. The fall of maximum temperatures attained at a given location with respect to z =0 is more as compared to corresponding rise of the minimum temperatures. Figure 8.13 shows the comparison of these results with corresponding experimental profiles. For clarity, the results are shown over single time-period.

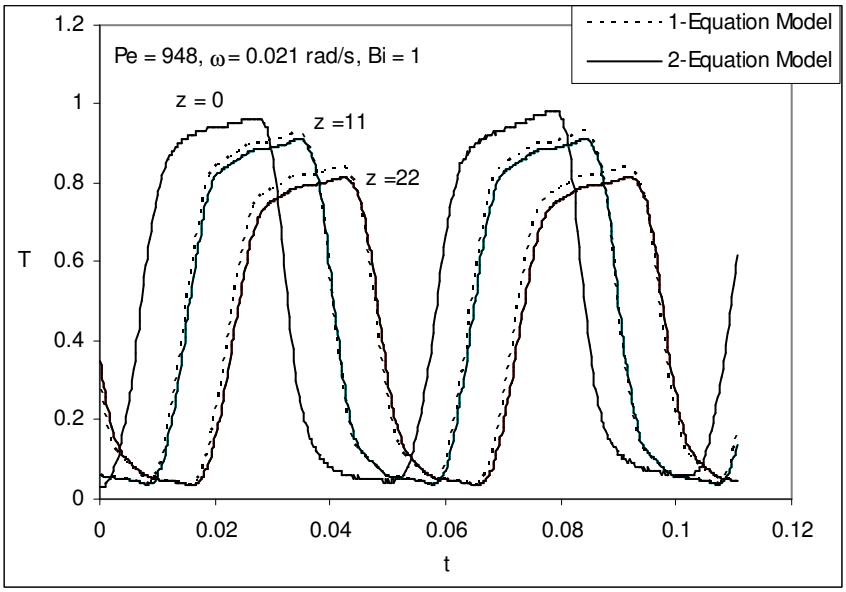

Figure 8.12: Variation of temperature with time as predicted by numerical simulation for frequency response of glass-water bed. Pe = 948; ω = 0.021 rad/s.

At location z =0, the three curves are identical and are set as boundary condition for the response at subsequent locations. The profiles related to experiments are slower as compared to those of numerical simulation such that the difference between the respective curves increases with distance. 1-equation model predicts faster temperature response as compared to that of 2-equation model such that during the hot phase it predicts higher temperature but

lower temperature during the cold phase. However, in both cases the 2-equation model is closer to experiments. The maximum temperature in simulation is lower than that in the experiments.

Figure 8.14 shows the comparison for a frequency of 0.051 rad/s and the corresponding Peclet number is 927. As the frequency increases the difference between the experiments and the numerical simulation also increases. At location z = 11, 2-equation model is closer to the experiments as compared to the 1-equation model though the respective differences are large. This has magnified over a distance of 22. Whereas for a frequency of 0.021 rad/s, the experimental amplitudes are more than those of numerical simulation but here the case the numerical simulation predicts higher amplitudes, see the profiles corresponding to location z =22 in the figure.

Figure 8.15 shows the similar comparison when the frequency of pulsations is increased to 0.072 rad/s. The amplitudes have fallen and the phase lag is increased. The results of numerical simulation are faster as compared to those of the experiments.

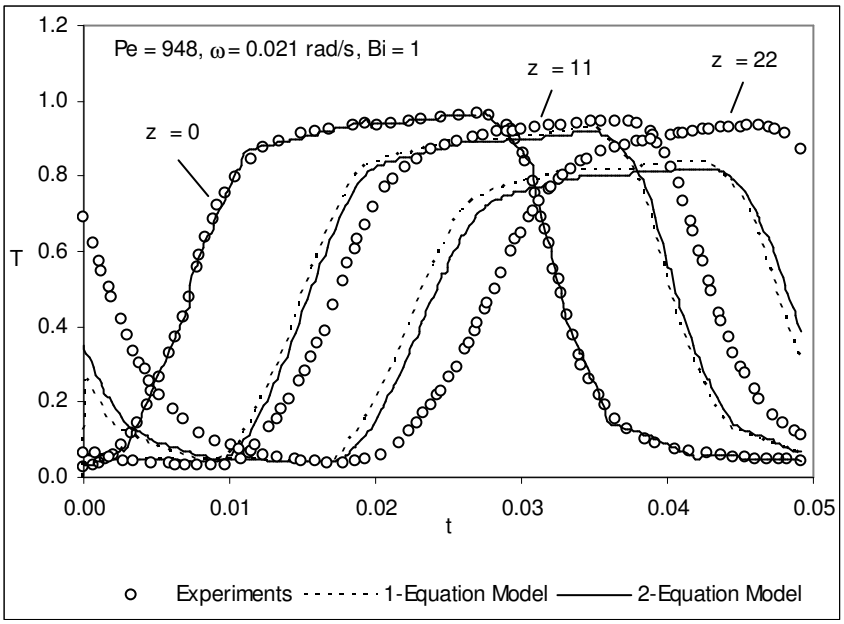

Figure 8.13: Variation of temperature with time in experiments, 1 and 2-equation models for frequency response of glass-water bed. Pe = 948, ω = 0.021 rad/s.

Figures 8.16 to 8.18 show the comparison for a higher Peclet number having nominal value of 1550. In Figure 8.16, the comparison for a frequency of 0.052 rad/s is shown. At location z =11, the simulation is marginally faster as compared to experiments. Of the numerical

simulation, 1-equation model again predicts faster temperature response as compared to 2-equation model. The differences increases over a distance of z =22.

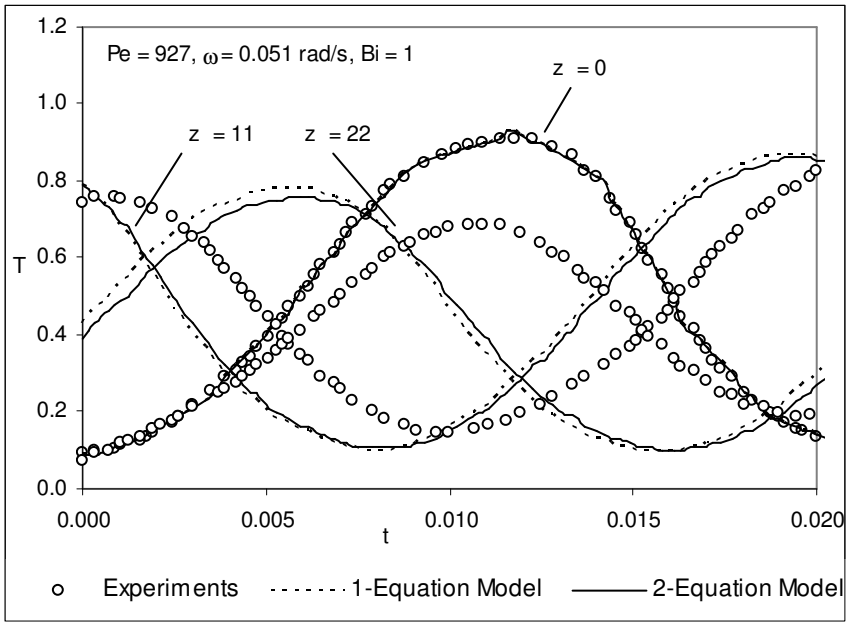

Figure 8.14: Variation of temperature with time in experiments, 1 and 2-equation models for frequency response of glass-water bed. Pe = 927, ω = 0.051 rad/s.

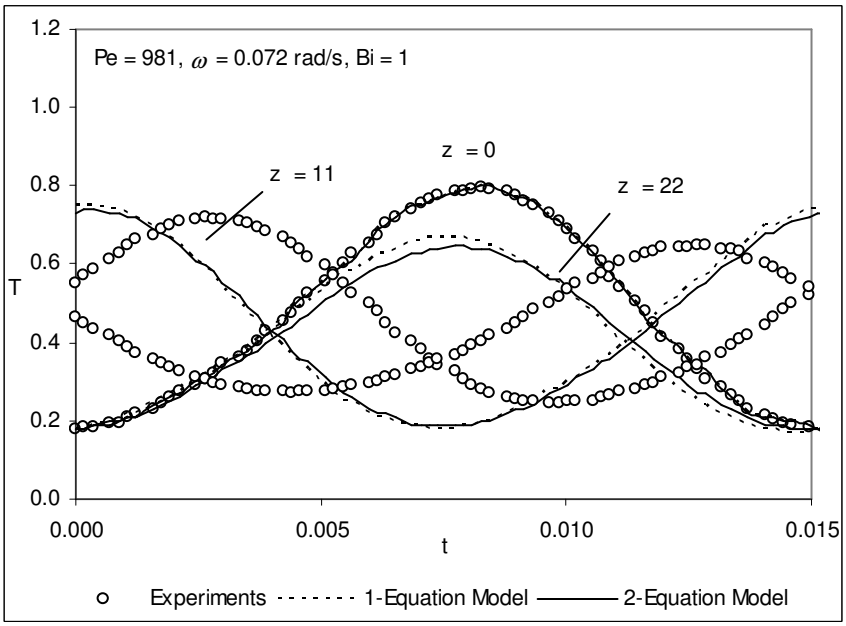

Figure 8.15: Variation of temperature with time in experiments, 1 and 2-equation models for frequency response of glass-water bed. Pe = 981, ω = 0.072 rad/s.

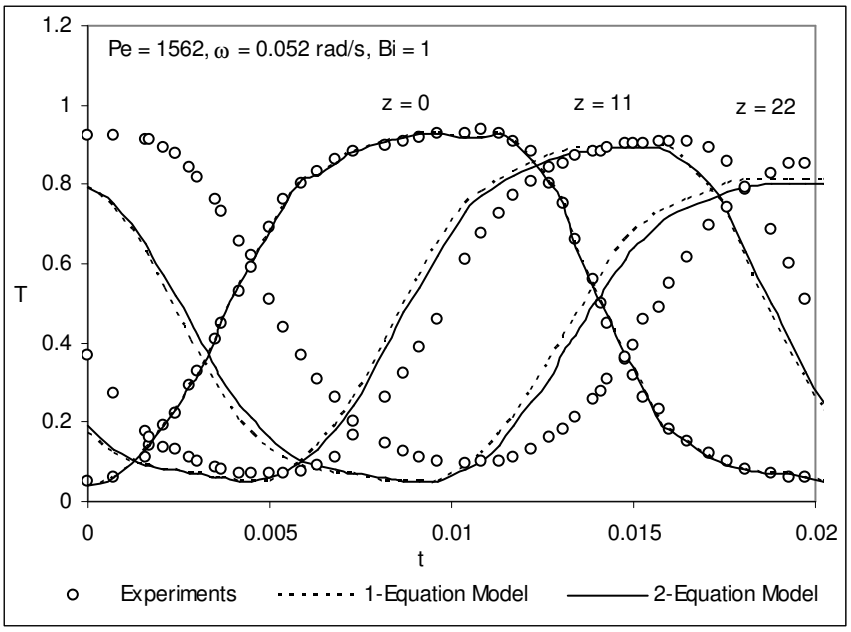

Figure 8.16: Variation of temperature with time in experiments, 1 and 2-equation models for frequency response of glass-water bed. Pe = 1562, ω = 0.052 rad/s.

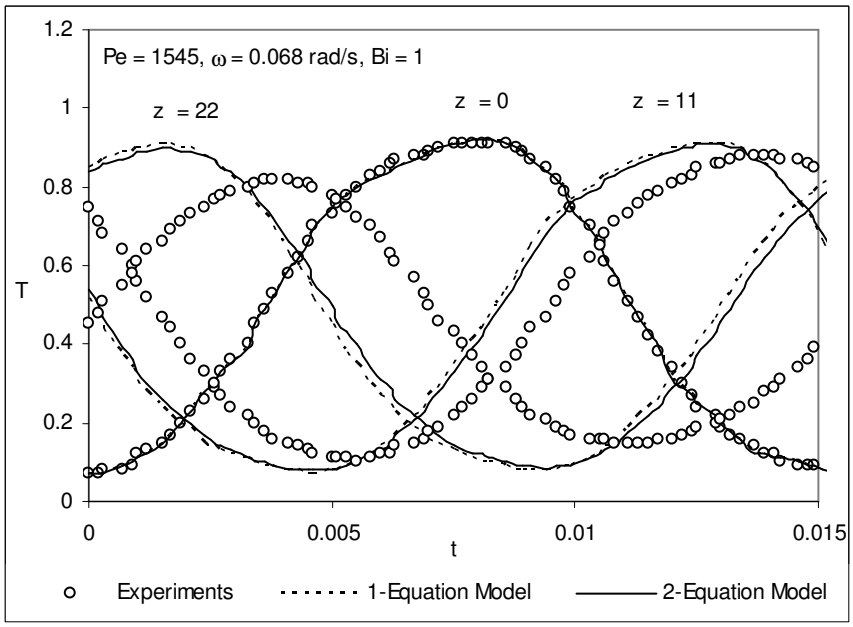

Figure 8.17: Variation of temperature with time in experiments, 1 and 2-equation models for frequency response of glass-water bed. Pe = 1545, ω = 0.068 rad/s.

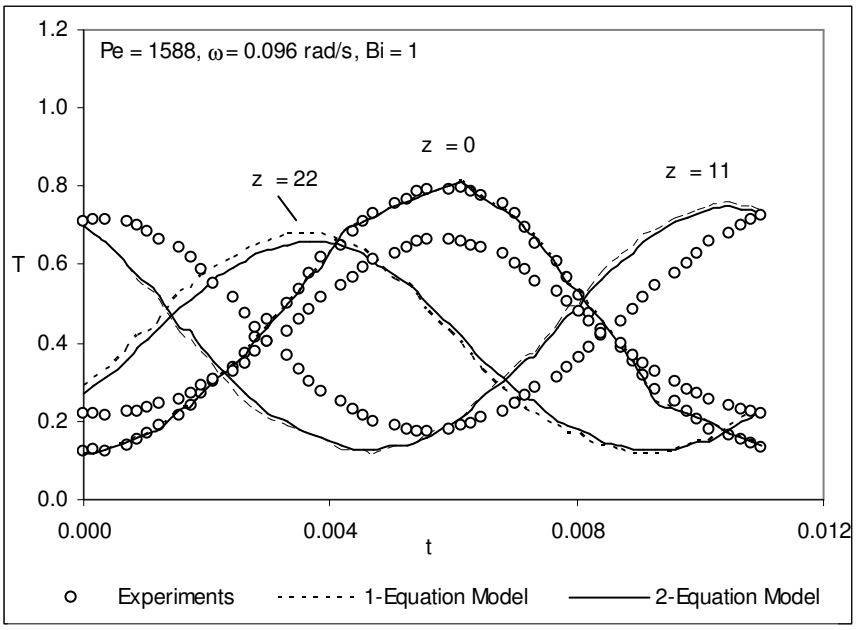

Figure 8.18: Variation of temperature with time in experiments, 1 and 2-equation models for frequency response of glass-water bed. Pe = 1588, ω = 0.096 rad/s.

As the frequency is increased to 0.068 rad/s as shown in Figure 8.17, the differences seem to have increased marginally. It is seen that, simulation show lower temperatures at valleys, which does not increase with distance, see the profile, for location z =22. The comparison for a frequency of 0.096 rad/s is shown in Figure 8.18. The experiments curve is nominally similar to simulation and but slower. The phase lag in experiments is clearly higher as compared to that in simulation such that the peaks in simulation occur earlier than those in the experiments.

Figure 8.19 shows the abstract of validation plotted over 2-3 cycles at location z = 11 for various frequencies. The results of experiments, 1 and 2-equation models are shown in this figure. At lower Peclet number of 950 in Figures 8.19(a-c), the differences between the results of simulation and experiments is higher as compared to those at higher Peclet number of 1550, Figures 8.19(d-f). In general, the experimental results are marginally slower as compared to those of simulation. The valleys in experiments increase at a higher rate as compared to simulation where there is no much change in the lower temperature. Looking in this figure, there is hardly any difference between the 1 and 2-equation models and they practically look similar.

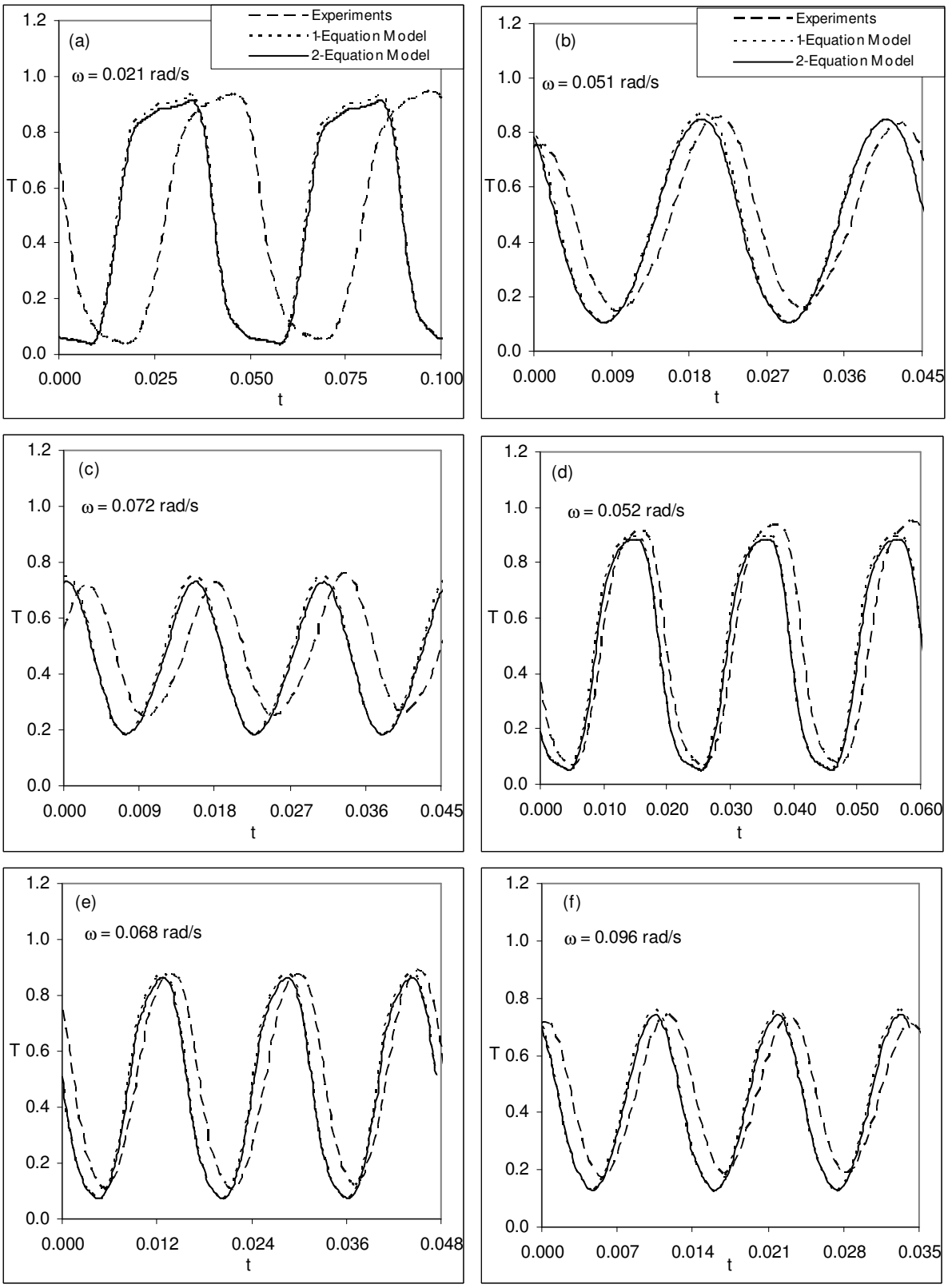

Figure 8.19: Comparison of temperature profiles in experiments, 1 and 2-equation models for frequency response of glass-water bed at z =11. (a-c) Pe = 950; (d-f) Pe = 1550.

8.3.2 Amplitude and Phase Lag

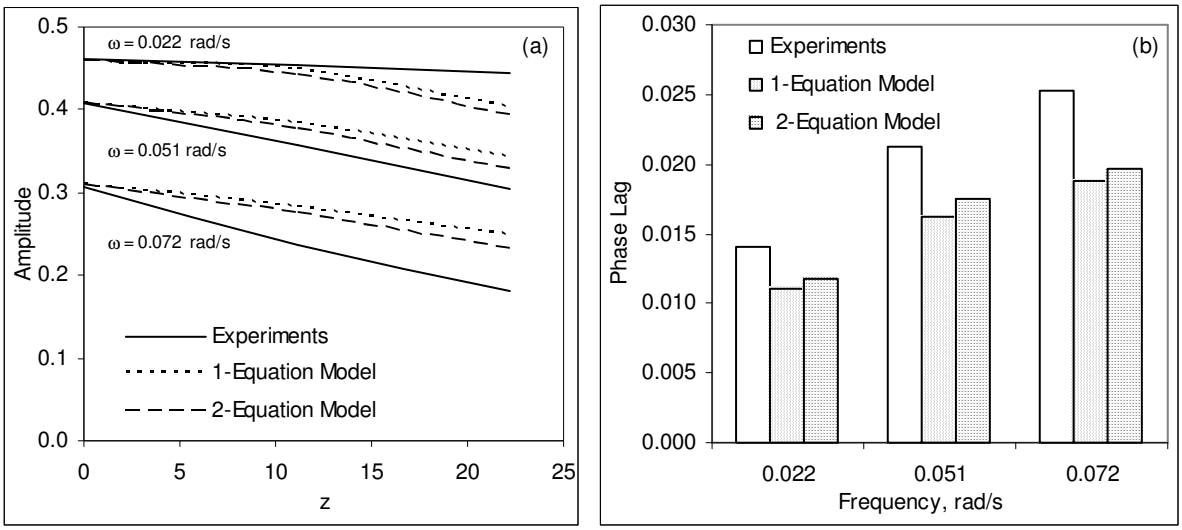

Figure 8.20: **A**ttenuation of temperature and phase lag in experiments, 1 and 2-equation models for frequency response of glass-water bed. Pe = 950, ω_{ref} = 0.021 rad/s.

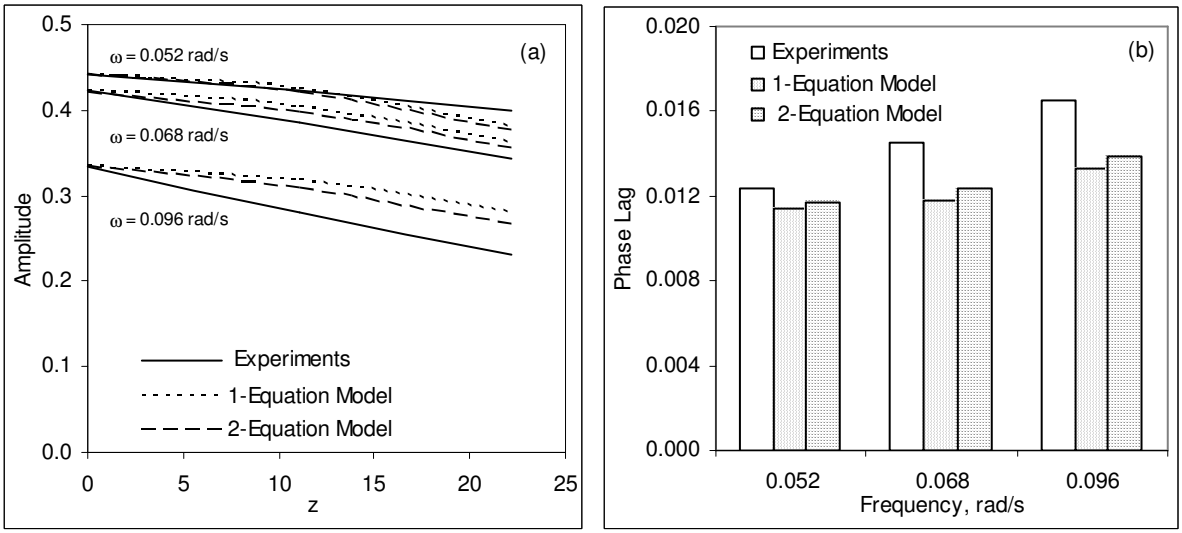

Figure 8.21: Attenuation of temperature and phase lag in experiments, 1 and 2-equation models for frequency response of glass-water bed. Pe = 1550, ω_{ref} = 0.038 rad/s.

A comparison of amplitude and phase lag between the experiments and the numerical simulation is performed to provide a qualitative validation. Figures 8.20 and 8.21 show the attenuation of temperature and corresponding phase lag for Peclet numbers of 950 and 1550 respectively. Figure 8.20(a) shows the attenuation of temperature for various frequencies. For a frequency of 0.022 rad/s, the attenuation as predicted by the experimental results is lower

as compared to that of numerical simulation. Further the attenuation as predicted by 1-equation model is lower than that of 2-equation model. At higher Peclet number of 1550, similar trends are observed but the corresponding difference between the experiments and numerical simulation is smaller.

Since the non-dimensional phase lag remains constant with distance, it is shown in the form of bar chart in Figures 8.20(b) and 8.21(b). The phase lag in experiments is higher as compared to that in numerical simulation. It varies as a function of frequency of pulsations. In all cases, the phase lag prediction of 2-equation model is higher as compared to those of 1-equation model and hence closer to the experimental results. The difference between the three results falls with an increase in frequency.

8.3.3 Pulse Speed and Spread

A comparison of pulse speed and spread is shown in Figures from 8.22 to 8.25. Figures 8.22 and 8.23 show the pulse speed for Peclet numbers of 950 and 1550 respectively The corresponding values for the hot and the cold phases are shown in these figures. The pulse speed in experiments is marginally lower than that in the numerical simulation. As expected, the 1-equation model predicts higher speed than that of 2-equation model. Further, the cold and the hot phases of the pulse move at unequal speeds; the cold phase having higher value. The experiments and numerical simulation behave in a similar manner as far as hot and cold pulse speed is concerned. In all cases, the front speed of the cold fluid is faster. The similar trends are observed at a higher Peclet number of 1550 as shown in Figure 8.23, though the individual values are marginally faster.

Pulse spread is shown in Figures 8.24 and 8.25 for the above-mentioned Peclet numbers. The pulse spread in experiments is close to that in numerical simulation. In each Figure, the variation of the hot and cold pulses with distance in experiments and numerical simulation are shown. Here the hot phase predicts higher spread than that in the cold phase. Figure 8.24 shows the pulse spread for the lower Peclet number of 950. In Figure 8.24(a), the spread at a frequency of 0.021 rad/s is shown. As discussed earlier, in experiment the spread for hot phase is higher as compared to that for the cold phase. The similar trends are also observed for simulation.

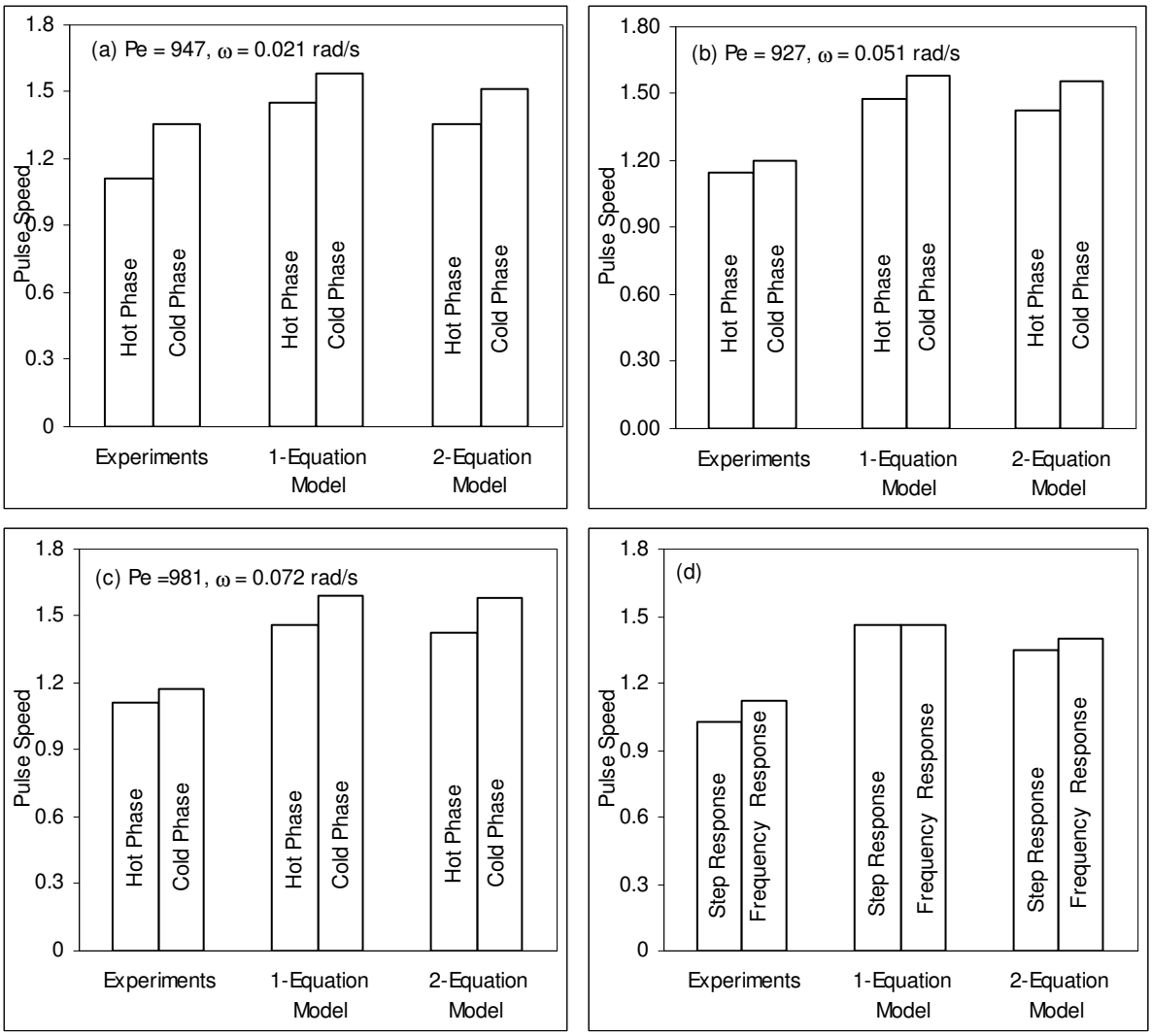

Figure 8.22: Pulse speed in experiments, 1 and 2-equation models for frequency response of glass-water bed. Pe = 950, ω_{ref} = 0.021 rad/s.

As expected, the 1-equation model predicts a lower spread than that of the 2-equation model. This is further lower than the experiments. The spread increases with distance from the inflow plane. At a higher frequency of 0.051 rad/s as shown in Figure 8.24(b), the spread falls but the overall trends are same. At a frequency of 0.072 rad/s, as shown in Figure 8.24(c), the time period is very small such that the reasonably high temperatures are not obtained at all locations; see Figure 8.4 for details. Consequently the temperatures are lower than 0.75 at locations z =11 & 22. The spread in this figure is based on maximum temperatures attained at these locations rather than the standard value of 0.75 and shown over

a length of 11 only; a similar case is shown in Figure 8.25(c). Overall, the trends do not change at higher Peclet number of 1550 as shown in Figure 8.25.

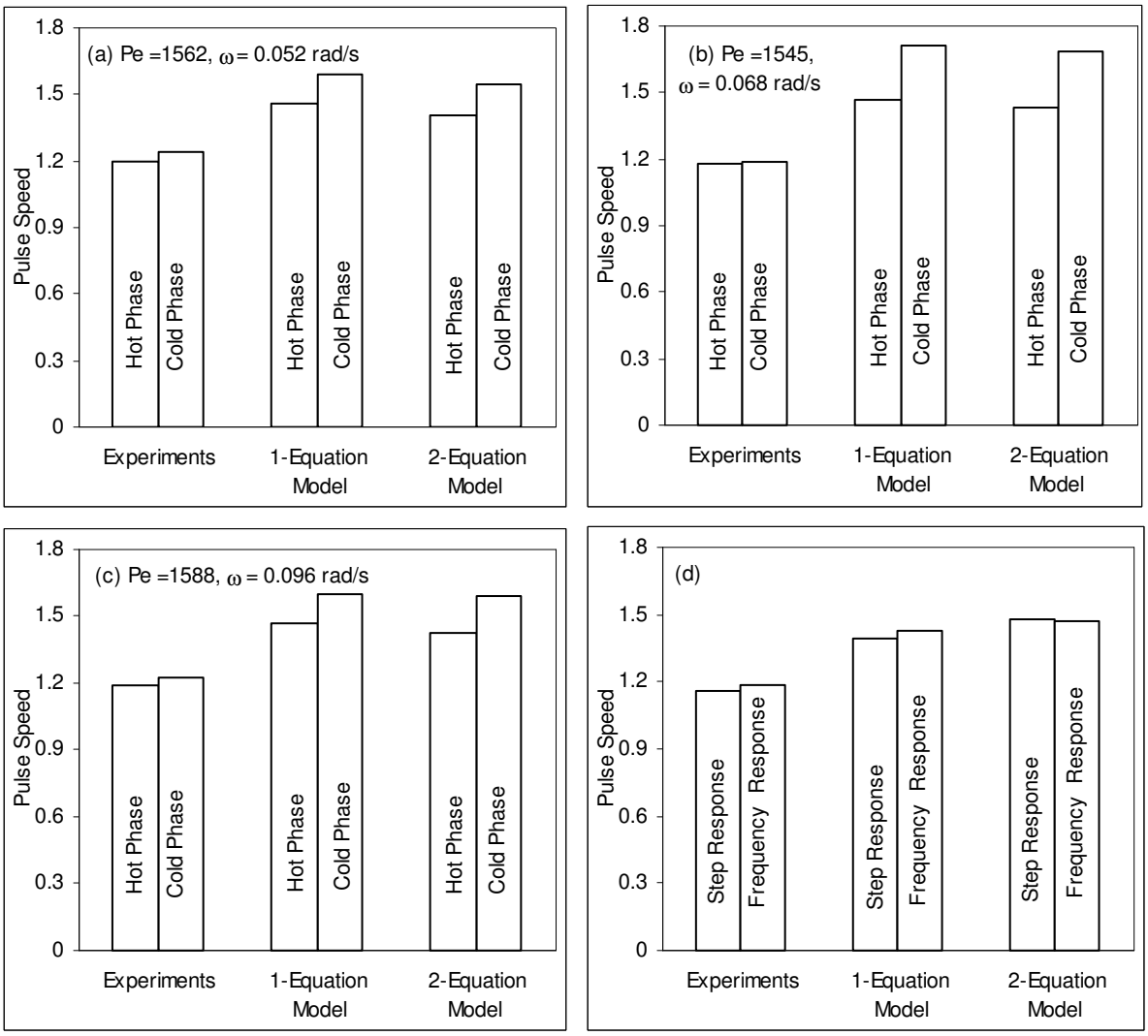

Figure 8.23: Pulse speed in experiments, 1 and 2-equation models for frequency response of glass-water bed. Pe = 1550, ω_{ref} = 0.038 rad/s.

Figures 8.22(d) and 8.23(d) compares the pulse speed as observed for a step and a frequency response. The pulse speed in experiments is marginally higher for frequency response. Overall, there is hardly any difference in two speeds. It is interesting to compare the pulse spread in the two responses. The comparison, as shown in Figure 8.26, is carried out from the experimental results as obtained from nominally similar Peclet numbers. In each figure, spread as obtained from a step response experiment along with those of frequency response at distinct frequencies of pulsations is shown. The step response has higher spread when

compared with frequency responses obtained at lower frequencies. As the frequency increases, the spread rises sharply. There seems to be only a small difference in the two figures as far as the trends are concerned. Hence, for lower frequencies the spread in a frequency response is lower than that for a step response.

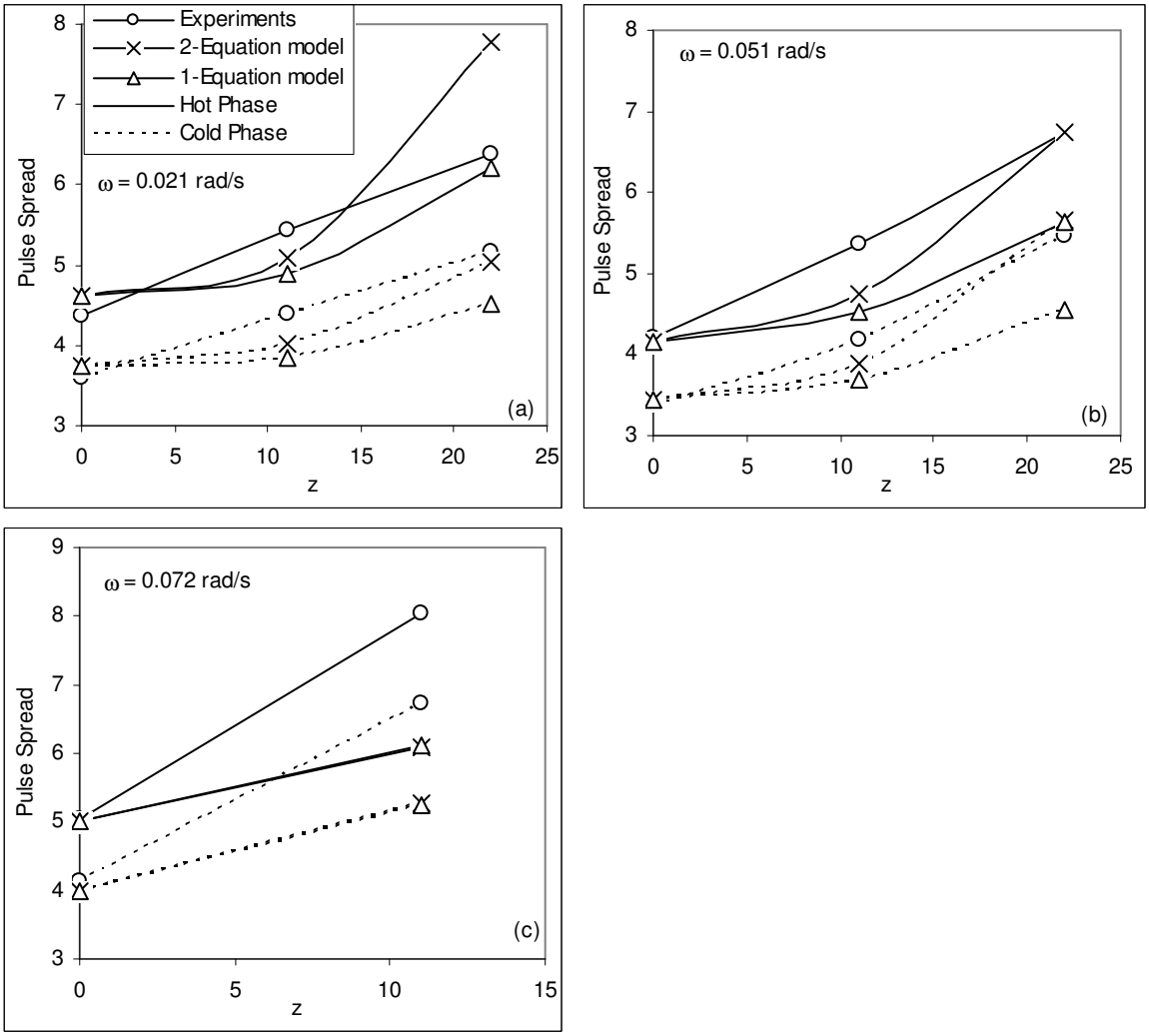

Figure 8.24: Pulse spread in experiments, 1 and 2-equation models for frequency response of glass-water bed. Pe = 950, ω_{ref} = 0.021 rad/s.

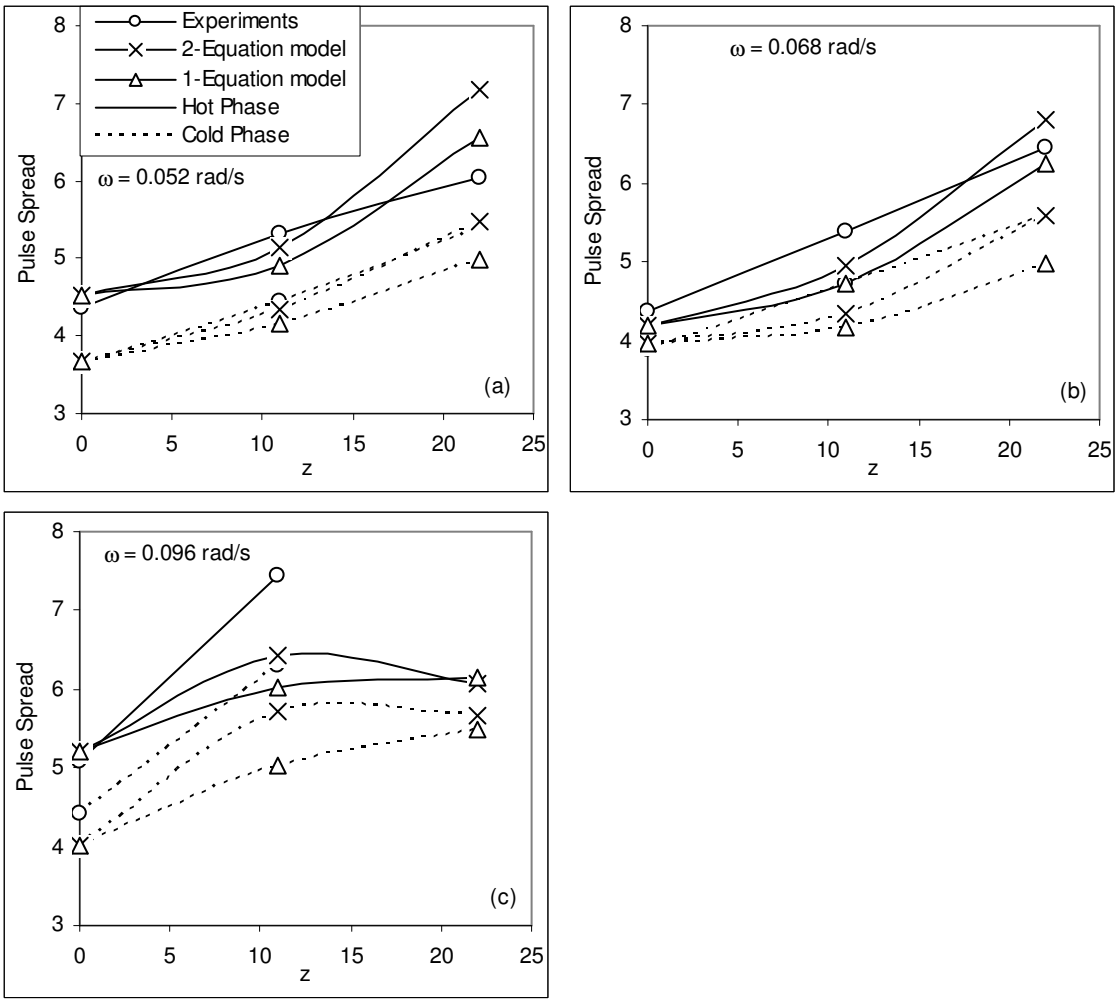

Figure 8.25: Pulse spread in experiments, 1 and 2-equation models for frequency response of glass-water bed. Pe = 1550, ω_{ref} = 0.038 rad/s.

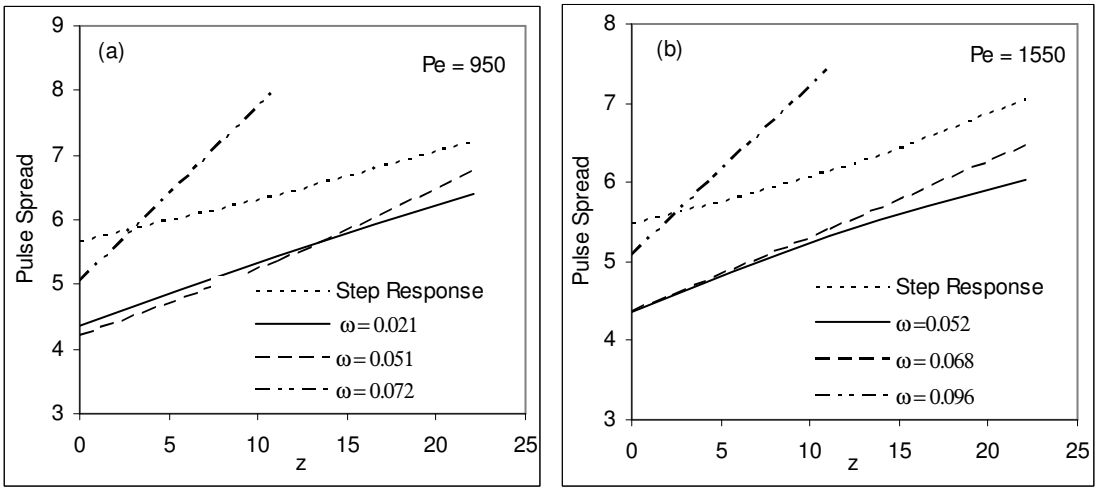

Figure 8.26: Comparison of experimental spread in step and frequency responses in glass-water bed.

8.4 THERMAL NON-EQUILIBRIUM

The thermal non-equilibrium between the fluid and the solid phases as predicted by the 2-equation model is discussed in this section. At cyclic steady state, the temperature of the two phases keeps changing periodically between the maximum and the minimum values. During the hot phase, the fluid phase has higher temperature as compared to that of the solid phase and during the cold phase, fluid temperature is lower. Hence, the thermal non-equilibrium fluctuates periodically on either side of zero.

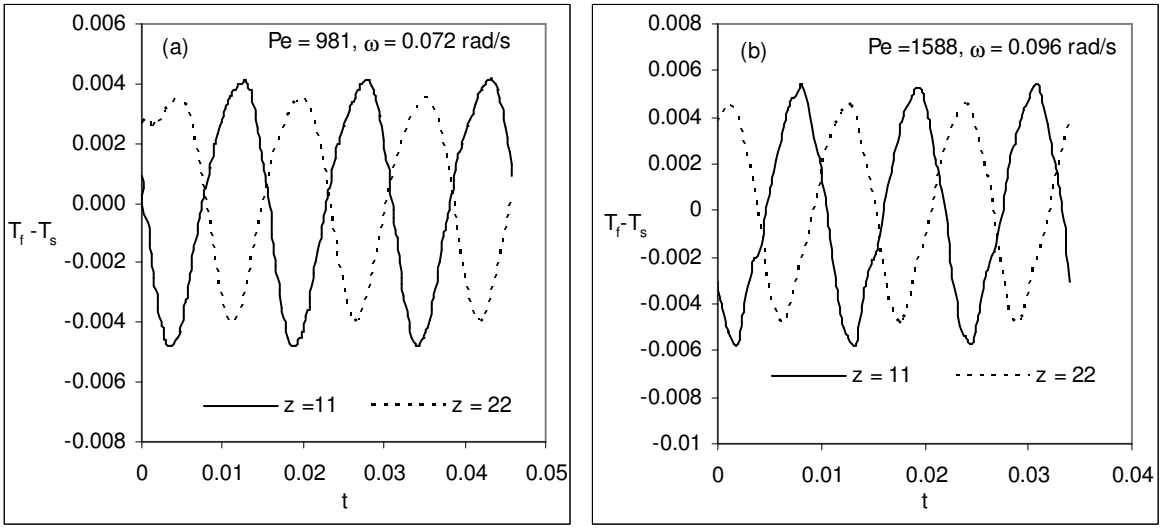

Figure 8.27: The pulse of temperature difference during frequency response in glass-water bed.

Figure 8.27 shows the thermal non-equilibrium in the glass-water bed as a function of time. The results are obtained from 2-equation model after cyclic steady state is reached. Figure 8.27(a) shows the pulse of thermal non-equilibrium for a Peclet number of 981 and Figure 8.27(b) for 1588 at two locations in the bed. The corresponding frequencies are 0.072 and 0.096 rad/s. The amplitude of pulse decreases with distance from the inflow plane but increases with Peclet number. It is interesting to see the time of occurrence of the peaks and the valleys of the pulse with respect to the fluid phase temperature. As expected, the peak occurs during the hot phase and valley during the cold phase but they occur earlier than respective peaks and valleys of the fluid phase temperature. Table 8.1 and 8.2 show the degree of thermal non-equilibrium for flow rates of 950 and 1550 respectively.

The maximum of value thermal non-equilibrium is obtained during the hot phase and the minimum value during the cold phase. The resulting amplitude is obtained by difference of the two values. All the three values fall with distance from the inflow plane. The numerical values of the minimum thermal non-equilibrium are more than that of the maximum.

Table 8.1: Degree of thermal non-equilibrium between the fluid and the solid phases at various locations. Pe = 950.

Frequency, rad/s	z = 11			z = 22		
	Maximum	Minimum	Amplitude	Maximum	Minimum	Amplitude
0.021	0.0045	-0.0056	0.0101	0.0038	-0.0046	0.0084
0.051	0.0046	-0.0056	0.0102	0.0039	-0.0046	0.0085
0.072	0.0042	-0.0048	0.009	0.0035	-0.004	0.0075

Table 8.2: Degree of thermal non-equilibrium between the fluid and the solid phases at various locations. Pe = 1550.

Frequency, rad/s	z = 11			z = 22		
	Maximum	Minimum	Amplitude	Maximum	Minimum	Amplitude
0.052	0.0056	-0.0061	0.0117	0.0048	-0.0052	0.01
0.068	0.006	-0.0063	0.0123	0.0051	-0.0053	0.0104
0.096	0.0054	-0.0058	0.0112	0.0046	-0.0049	0.0095

With an increase in Peclet number, the degree of thermal non-equilibrium increases. The amplitudes increase with frequency but its value at higher frequencies of 0.072 and 0.096 rad/s is lower.

It is interesting to consider the differences between the 1 and 2-equation models. Since the 1-equation model is faster as compared to the 2-equation model, the difference between the two is positive during the hot phase but negative during the cold phase. Its trends are similar to those of the thermal non-equilibrium. It increases during the hot phase and reaches a maximum value but falls during the cold phase. However, it changes sign before the occurrence of the maximum and the minimum temperatures. Figure 8.28 shows the pulse of temperature difference between the 1 and 2-equation models during the frequency response in glass-water bed. The difference increases with distance from the inflow plane. However, the numerical values of the peaks are higher as compared to those of the valleys in

each case. In Figure 8.28(a), the difference for a Peclet number of 981 is shown. At location z = 11, the difference between the two models fluctuates between 0.026 to 0.012; an amplitude of 0.038. It increases at location z =22. The corresponding values drop at higher Peclet number as shown in Figure 8.28(b). Tables 8.3 and 8.4 show the difference between the 1 and 2-equation models for the two Peclet numbers. For a fixed Peclet number, the difference decreases with frequency of pulsations, but increases with distance from the inflow plane, which is because of cumulative effect of heat transfer between the two phases. It is interesting to point out, that all the trends are opposite to that of degree of thermal non-equilibrium between the two phases. The difference between the two models is lower than typical values during a step response, see Table 6.6 for details.

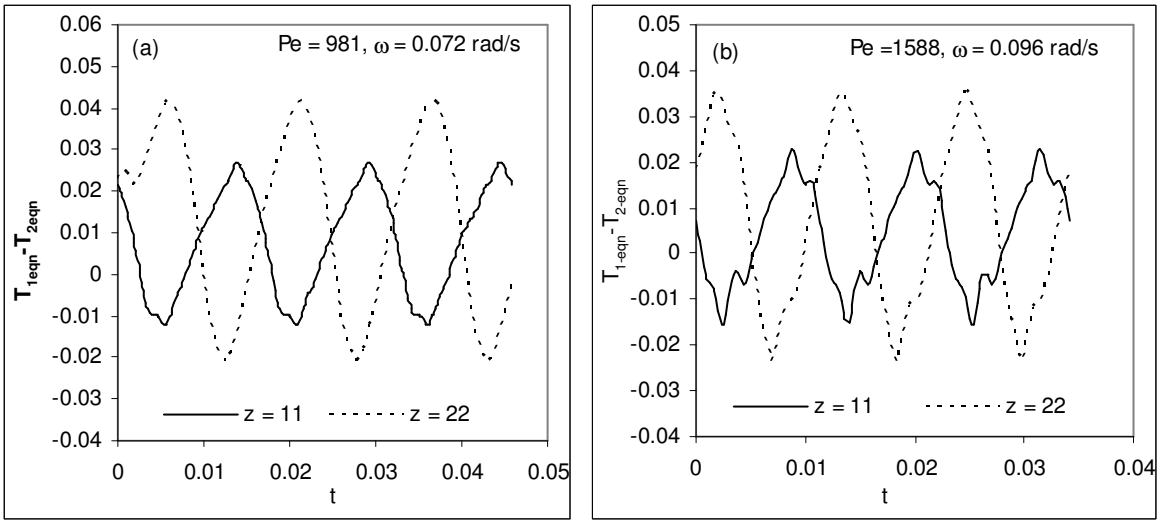

Figure 8.28: The pulse of temperature difference between 1 and 2-equation models for frequency response in glass-water bed.

Table 8.3: Difference between the 1 and 2-equations models at various locations. Pe = 950.

Frequency, rad/s	z = 11			z = 22		
	Maximum	Minimum	Amplitude	Maximum	Minimum	Amplitude
0.021	0.051	-0.055	0.106	0.085	-0.091	0.176
0.051	0.032	-0.020	0.052	0.053	-0.033	0.087
0.072	0.026	-0.012	0.038	0.041	-0.020	0.061

The values of interphase heat transfer are shown in Table 8.5. The convective resistance falls with Peclet number but the corresponding heat transfer increases. For a particular Peclet number, the heat transfer falls with distance.

Table 8.4: Difference between the 1 and 2-equations models at various locations. Pe = 1550

Frequency, rad/s	z = 11			z = 22		
	Maximum	Minimum	Amplitude	Maximum	Minimum	Amplitude
0.052	0.030	-0.022	0.052	0.051	-0.039	0.091
0.068	0.029	-0.020	0.050	0.047	-0.033	0.080
0.096	0.022	-0.015	0.037	0.035	-0.023	0.058

Table 8.5: Convective resistance and corresponding maximum interphase heat transfer at various locations in glass-water bed.

Peclet Number Pe	Dimensionless Convective Resistance (Pe / Nu A_f)	Dimensionless Interphase Heat Transfer (Nu A_f/Pe*(T_f-T_s))	
		z = 11	z = 22
981	0.135	0.031	0.026
1588	0.107	0.050	0.043

8.7 CLOSURE

A detailed analysis of frequency response of glass-water bed is performed in this chapter. The experimentally generated results are compared with those of numerical simulation using 1 and 2-equation models. The comparison is obtained using cyclic steady state temperature profiles, which are obtained after 4-5 cycles from the start of an experiment. To account for heat loss on validation, a Biot number of unity is considered in numerical simulation. A detailed analysis of attenuation of temperature, phase lag, pulse speed and spread, as obtained in during the two phases, is performed. The cold and the hot phases of the pulse have distinct speed and spread. The 1-equation model is qualitatively similar to 2-equation model though less accurate. In general, the experimental results are slower than simulation over a large distance of 11 and 22 as considered in the analysis. A comparison over a smaller distance would look better in quality. The thermal non-equilibrium between the fluid and solid phases

is also assessed. A concept of reference frequency is used such that the fluid reaches the end of the bed during the respective phases while traveling at an average velocity.

Overall, the numerical simulation provides good comparison with experiments for time varying boundary conditions. This comparison is obtained when the two phases have similar thermal properties in the next chapter a comparison but for relatively distinct properties of the two phases as in a steel-water bed is presented.

CHAPTER 9

FREQUENCY RESPONSE OF STEEL-WATER BED

9.1 INTRODUCTION

As the thermal properties of steel are quite different to those of water, the frequency response in a steel-water bed is expected to be distinct from that in a glass-water bed. The highly conductive solid particles interact with temperature pulse and distort it. These studies help to understand transport in a fluid saturated porous medium system subjected to periodic boundary conditions in a better way. The time-averaged heat transfer increase by intermittent thermal boundary conditions as compared to that for steady state can provide interesting results. In this chapter, the frequency response of the steel-water bed is discussed. The aim is to validate the numerical simulation for time periodic boundary conditions. The comparison is performed using temperature profiles obtained after cyclic steady state is reached. The properties like attenuation of temperature, phase lag, pulse speed and spread are discussed. The thermal non-equilibrium existing between the two phases during the frequency response is studied. A comparison of frequency response in glass-water bed is also carried out.

The results of frequency response as obtained from bed-2 are used for analysis. These results are compared with numerical simulation using the results of 1 and 2-equation models. As seen for a step response in steel-water bed, the 1-equation model does not predict the results accurately when minor heat losses are taking place in the bed. The 2-equation model on the other hand is very accurate under all conditions. It interesting to see the corresponding results for pulsating boundary conditions. We now discuss the experimental frequency response in steel-water bed.

9.2 EXPERIMENTAL FREQUENCY RESPONSE

The experimental frequency response in steel-water bed is discussed in this section. A frequency response has both the unsteady and the cyclic steady states as discussed in the last chapter. The unsteady state is for a brief period and afterwards the temperature fluctuates cyclically between the maximum and the minimum values. The cyclic temperature profiles

along with amplitude, phase lag, pulse speed and spread from the experiments are discussed. Both these states in a steel-water bed are demonstrated in Figure 9.1

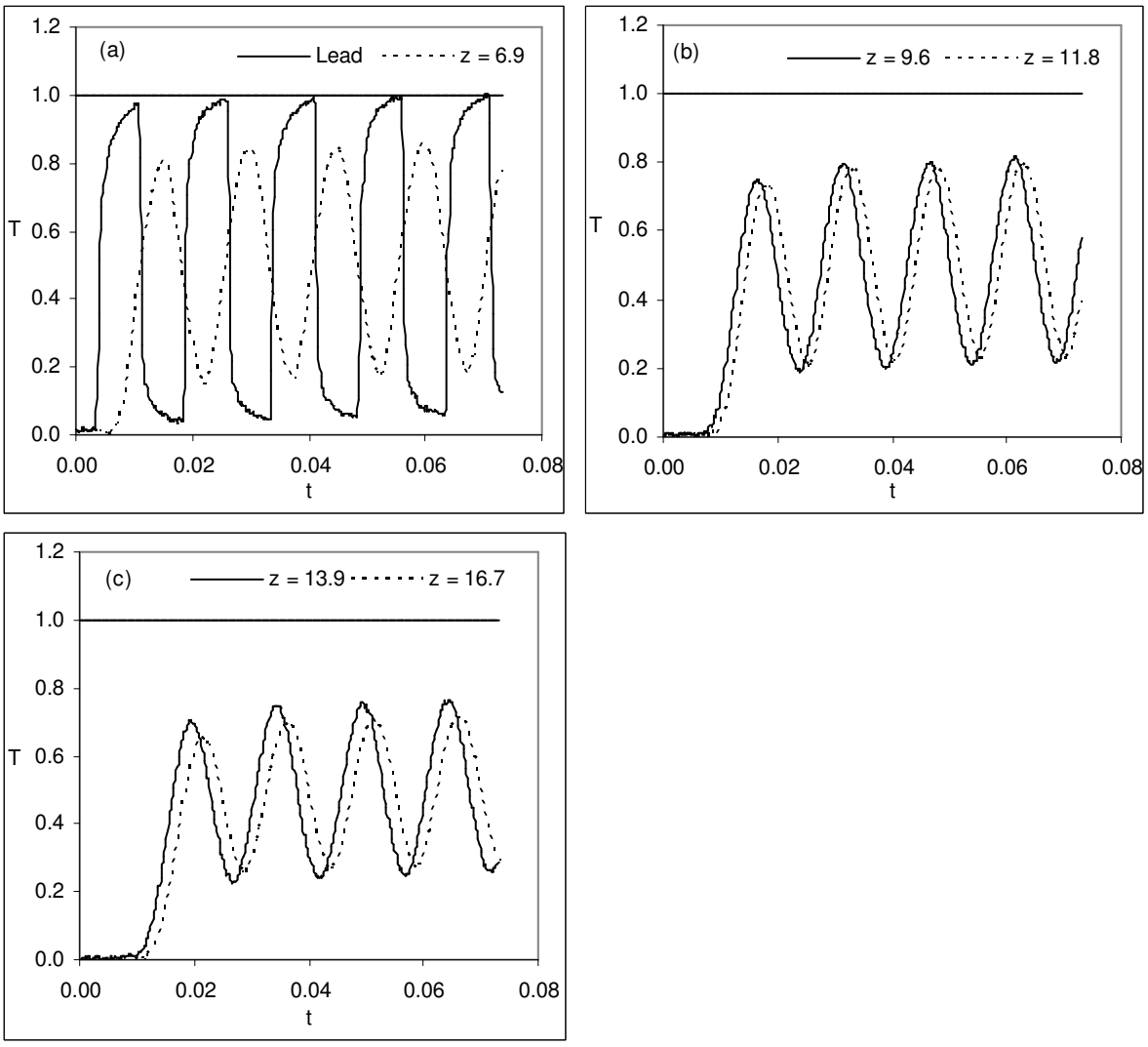

Figure 9.1: The unsteady and cyclic steady phases of the frequency response in steel-water bed. Pe = 1608, $\omega = 0.071$ rad/s.

Figure 9.1 shows the frequency response of steel-water bed at Peclet number of 1608 and the frequency of pulsation is 0.071 rad/s. Figure shows the thermal response of the bed at various locations starting from a lead location. The response has both the unsteady and cyclic steady states. The hot phase temperature of unity is also shown in each figure. Temperature at each location rises from zero, reaches a maximum temperature and subsequently falls due to cold water. Figure 9.1(a) shows the response at lead location and at $z = 6.9$ from the start of the bed. At lead location, temperature rises sharply to maximum temperature of unity and

subsequently falls to temperature marginally higher than that of the cold water of zero value. At location z = 6.9, the temperature fluctuations are smaller. Similarly Figure 9.2(b) shows the response at locations z = 9.6 and 11.8. The amplitude of temperature fluctuations fall and the response becomes slower. The amplitudes fall further at locations z = 13.9 & 16.7 as shown in Figure 9.1(c). At each location, the cyclic steady state is reached after 4-5 cycles.

9.2.1 Cyclic Temperature Profiles

The profiles obtained after cyclic steady state are plotted in this section. The profiles are shown for two Peclet numbers, which are nominally equal to 1000 and 1950. For each Peclet number, the response is discussed for three distinct frequencies of pulsations relative to the reference value. In these profiles the location of first thermocouple in bed-2 is set as z = 0 as shown in Table 7.3. The responses at various locations are shown in figures from 9.2 to 9.7.

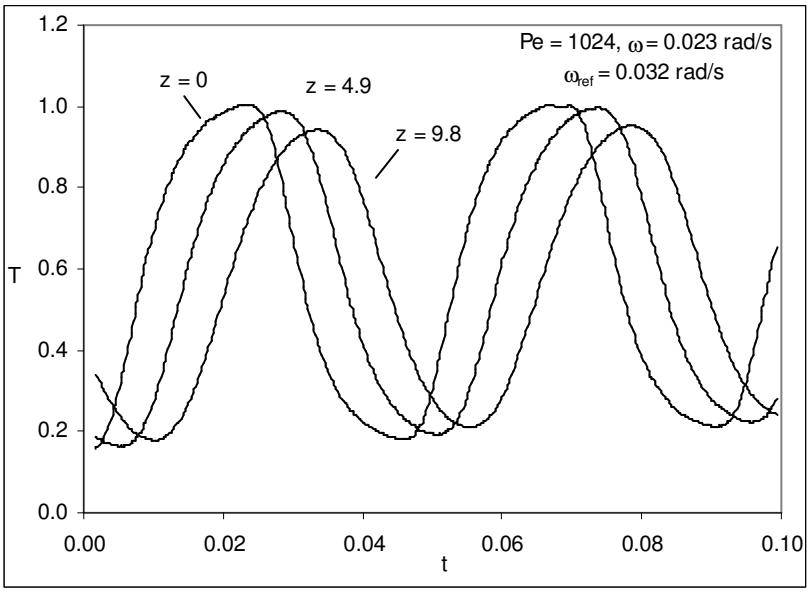

Figure 9.2: The frequency response of steel-water bed. Pe = 1024, ω/ω_{ref} = 0.718.

Figure 9.2 shows the frequency response for the bed at a Peclet number of 1048 and the frequency of pulsations is 0.023 rad/s. The corresponding reference frequency is 0.032 rad/s. Since the frequency is lower than reference, ample time is available for hot and cold fluids to reach the end of the bed. The maximum temperature at location z = 0 is unity but the minimum temperature is more than zero and hence the amplitude is less than 0.5. The

maximum temperature at each location falls with distance but the minimum temperature rises. The phase lag of location $z = 4.9$ with respect to $z = 0$ is 38°.

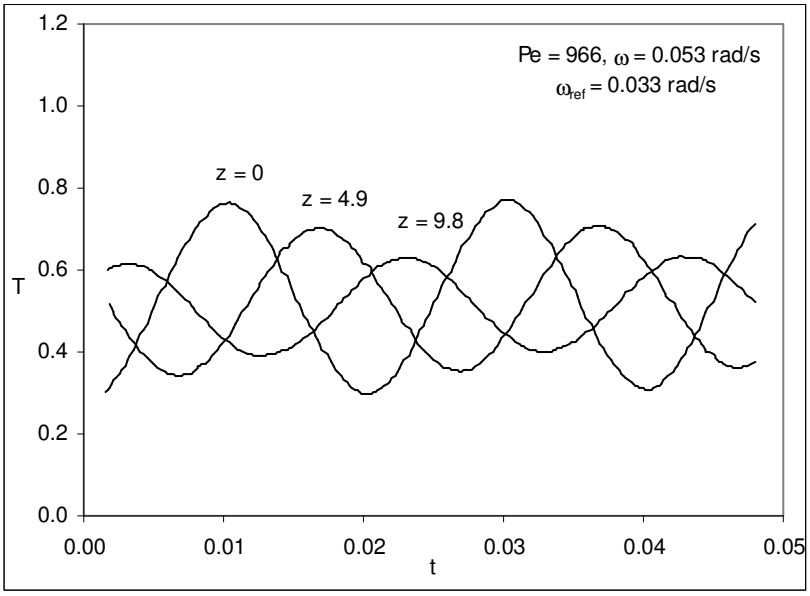

Figure 9.3: The frequency response of steel-water bed. Pe= 966, $\omega/\omega_{ref} = 1.6$.

Figure 9.3 shows the frequency response when the frequency of pulsation is increased to 0.053 rad/s, the Peclet number being 966. Since the frequency is 1.66 times the reference value, the time-period is smaller and it results into a fall in the respective amplitudes. Here the amplitudes at z =0 is less than unity and but falls with distance at a greater rate as compared to that for the previous case. The phase lag at location $z = 4.9$ with respect to $z = 0$ increases to 111°.

In Figure 9.4, the frequency increases further to 0.091 rad/s and the resulting amplitudes are extremely small and the attenuation with distance is more. The phase lag between the locations $z = 4.9$ & 0 rises to 182°.

Figures 9.5 to 9.7 show the cyclic steady states when the Peclet number is nominally equal to 1950 and the corresponding reference frequency is close to 0.065 rad/s. In Figure 9.5, the response for a frequency of 0.053 rad/s is shown, the Peclet number being 2019. The maximum temperature at each location falls but the minimum temperature increases with distance. The amplitude at $z = 0$ is marginally lower than 0.5 and falls with distance. The phase lag for location $z = 4.9$ is 52°.

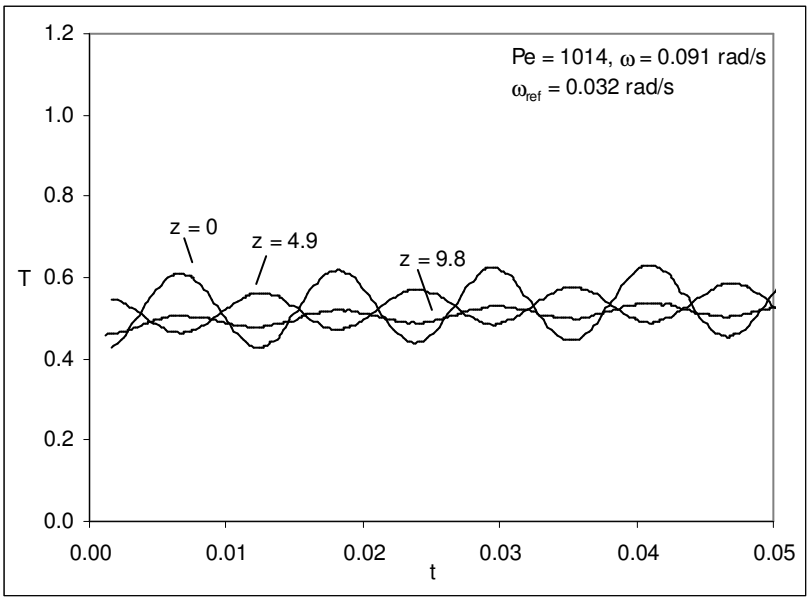

Figure 9.4: The frequency response of steel-water bed. Pe= 1014, ω/ω_{ref} =2.84.

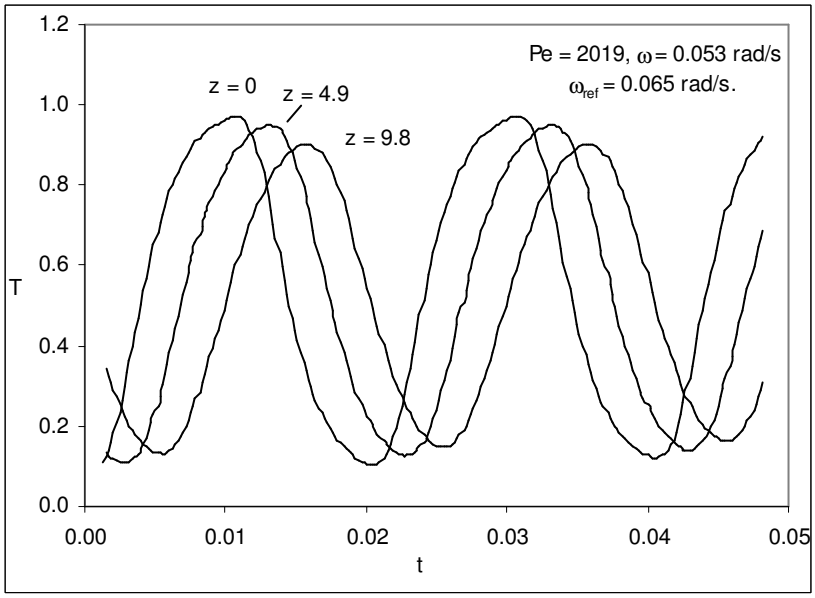

Figure 9.5: The frequency response of steel-water bed. Pe = 2019, ω/ω_{ref} = 0.815.

Figure 9.6 shows the frequency response for a higher frequency of 0.087 rad/s. It results into lower amplitudes at each location and the corresponding phase lag is more. These affects are further magnified at a higher frequency of 0.149 rad/s as shown in Figure 9.7, such that the resulting amplitudes are small and the phase lags are high.

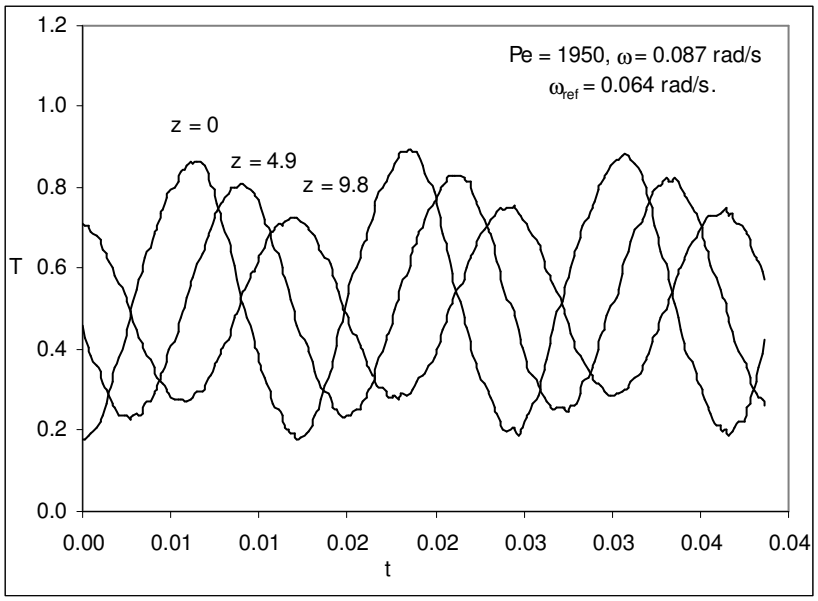

Figure 9.6: The frequency response of steel-water bed. Pe= 1950, ω/ω_{ref} =1.35.

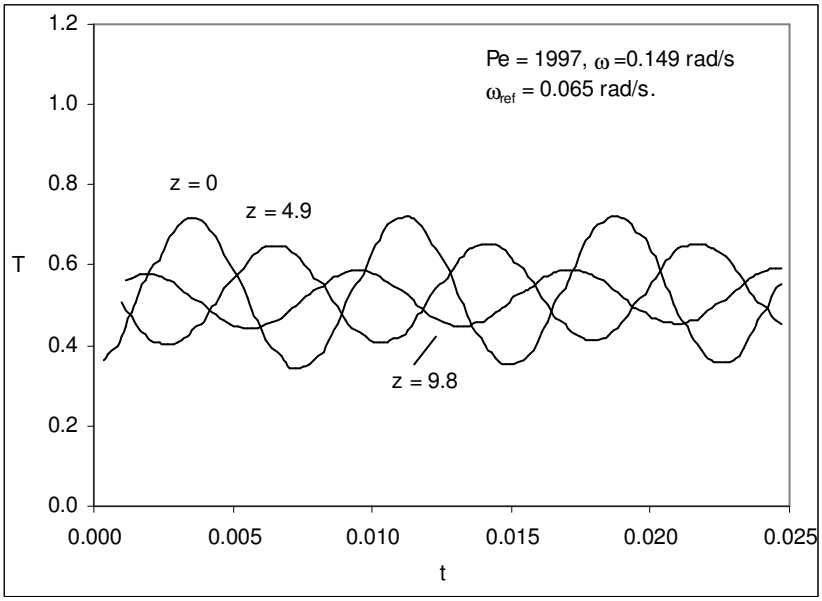

Figure 9.7: The frequency response of steel-water bed. Pe = 1997, ω/ω_{ref} = 2.3.

The amplitudes, phase lag and pulse speed and spread as observed in these experiments are presented in the subsequent sections.

9.2.2 Amplitude and Phase Lag

The amplitude and phase lag are presented as a function of distance for various frequencies.

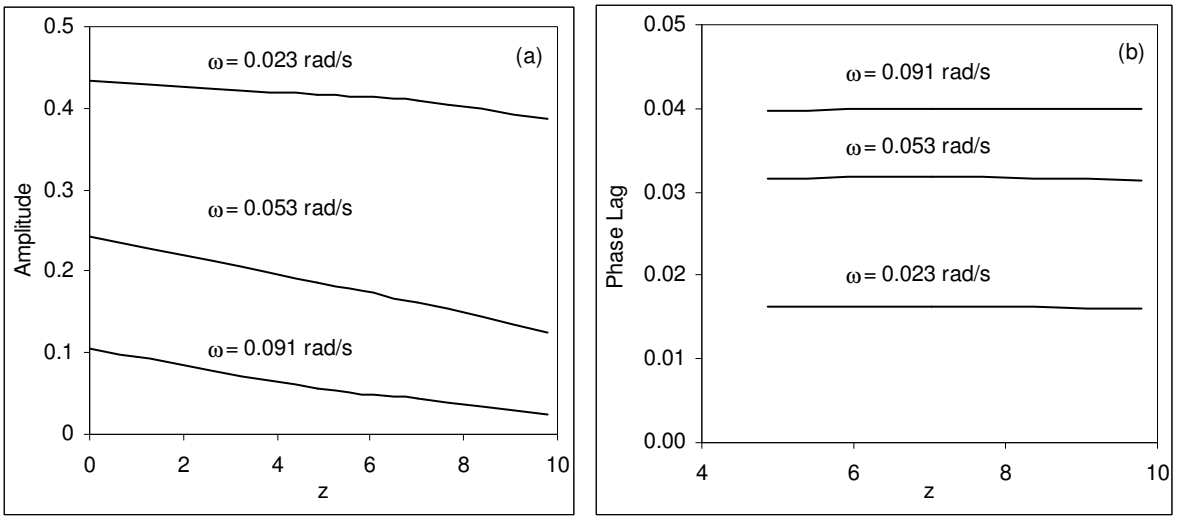

Figure 9.8: Attenuation of temperature and phase lag as a function of distance for steel-water bed . Pe = 1000; ω_{ref} = 0.032 rad/s.

Figure 9.8 shows the amplitude and corresponding phase lag when the nominal flow rate is 1000. Figure 9.8(a) shows the attenuation of temperature with distance and Figure 9.8(b) shows the phase lag at the given location with respect to that at $z = 0$. The amplitude varies inversely with frequency of pulsations such that for a frequency of 0.091 rad/s, its maximum value is 0.1. For each frequency, the amplitude falls with distance. The phase lag, on the other hand, increases directly with frequency but remains constant with distance.

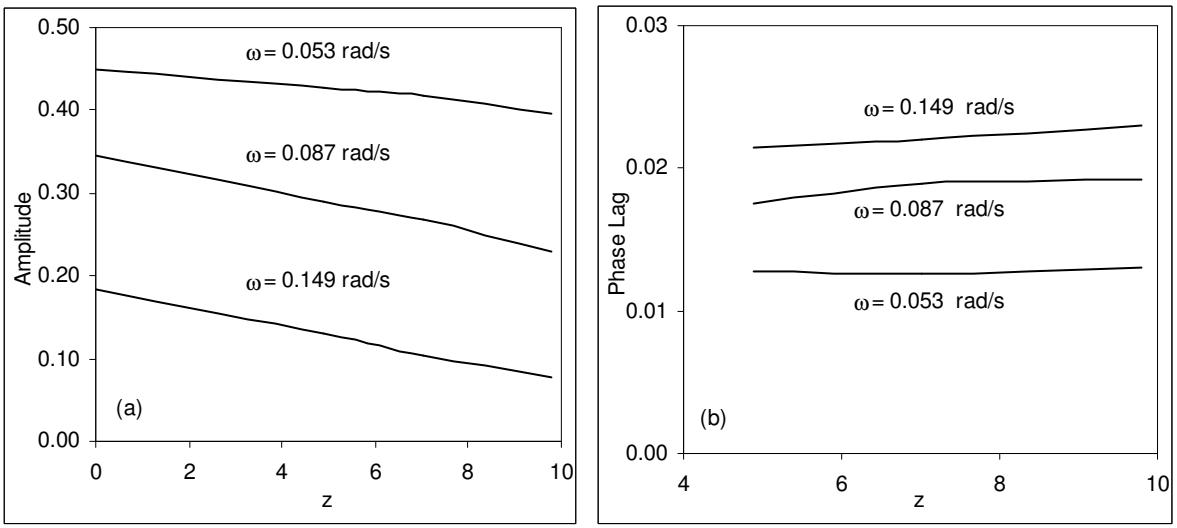

Figure 9.9: Attenuation of temperature and phase lag as a function of distance for steel-water bed. Pe = 1950; ω_{ref} =0.064 rad/s.

Figure 9.9 shows the corresponding results for a higher Peclet number of nominal value of 1950. The trends of amplitude and phase lag are almost similar to that of the previous case, but the corresponding phase lag is lower.

9.2.3 Pulse Speed and Spread

The speed of the pulse traveling through the steel-water bed and the corresponding spread is presented in this section. The speed of the pulse is calculated corresponding to a temperature of 0.5 at various locations and the spread for the corresponding temperature range of 0.25 to 0.75. These are calculated separately for both the hot and the cold phases. Figure 9.10 shows the pulse speed for various frequencies and the Figure 9.11 the corresponding pulse spread in the bed. The spread is shown for fewer cases as for the remaining cases the temperatures of 0.25 and 0.75 are not attained; see Figures 9.4 and 9.7 for details. For some cases, the spread is calculated over a temperature range of 0.35 and 0.65.

The pulse speed as shown in Figure 9.10 does not show any particular trend as in glass-water bed. The hot and the cold phases have independent values. At a higher Peclet number of 2000 as shown in Figure 9.10(b), is marginally higher than that at lower Peclet in Figure 9.10(a). The front spread as shown in Figure 9.11 increases with distance and decreases with frequency of pulsations. For a frequency of 0.087 rad/s, it is based on temperatures of 0.65 and 0.35. In most cases, the cold phase spread is higher than the hot phase.

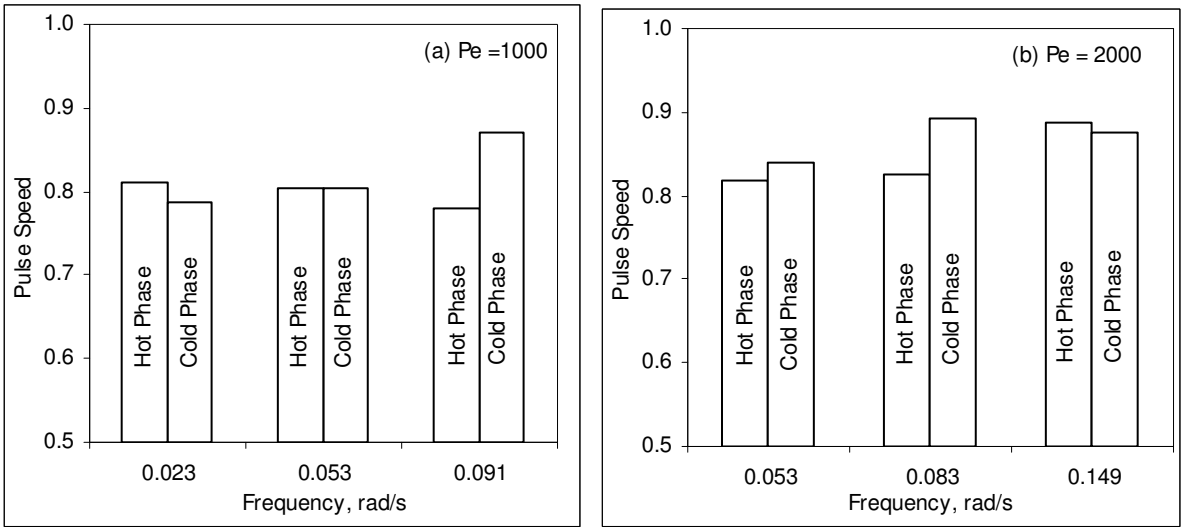

Figure 9.10: Pulse speed as a function of frequency of pulsation in steel-water bed.

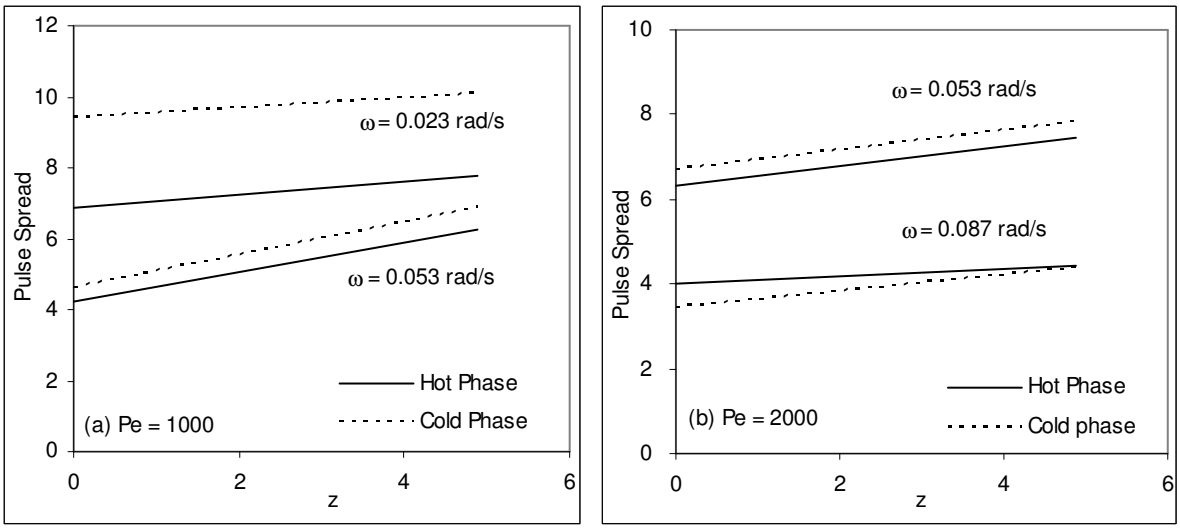

Figure 9.11: The pulse spread as a function of distance in steel-water bed.

9.3 VALIDATION OF NUMERICAL MODELS

The validation of numerical simulation is performed by using the results of the experiments. The response at first thermocouple in bed-2 is set as boundary condition for subsequent locations in simulation and the results are compared with those of the experiments. The cyclic temperature profiles are drawn and resulting amplitude and phase lag is calculated at each location. A comparison of pulse speed and spread is also performed.

9.3.1 Cyclic Temperature Profiles

Figure 9.12 shows the results of 1 and 2-equation models at a Peclet number of 1024 and frequency is 0.023 rad/s. The plots for various locations of z =0, 4.9 & 9.8 are shown in the figure. At location z = 0 the two models are set identical. The profile related to 1-equation models are shown for two Biot numbers of 0 and 0.05 whereas those of 2-equation model for a value of 0.05 only. The profiles of 1-equation model for a Biot number of 0.05 as shown in the lower portion of the figure are not compatible but predict lower values of peaks and valleys. Those for zero Biot number are similar to the experimental profiles and predict higher values of peaks and valleys than those of 2-equation model. This figure shows typical results of two models and their sensitivity to heat loss. 1-equation model is very sensitive to heat loss and shows large damping. Hence, both the models predict profiles, which are similar to the experimental profiles. The results of the experiments are subsequently

compared with numerical simulation over one time-period to show an enhanced view. Figures 9.13 to 9.15 show the comparison for a lower Peclet number of 1000. Here the 1-equation model results are shown for zero Biot number and those of the 2-equation model for 0.05.

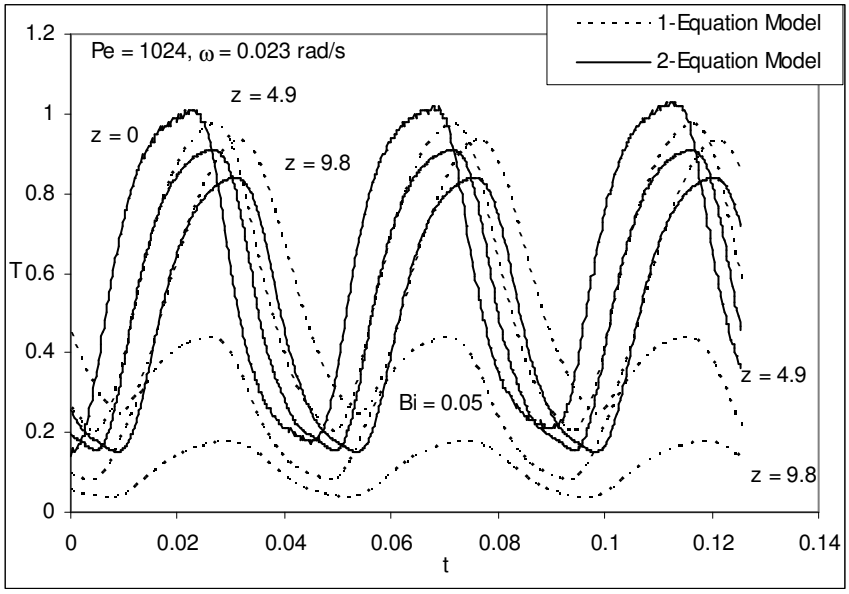

Figure 9.12: Variation of temperature with time as predicted by numerical simulation for frequency response of steel-water bed. Pe = 1024, ω = 0.023 rad/s.

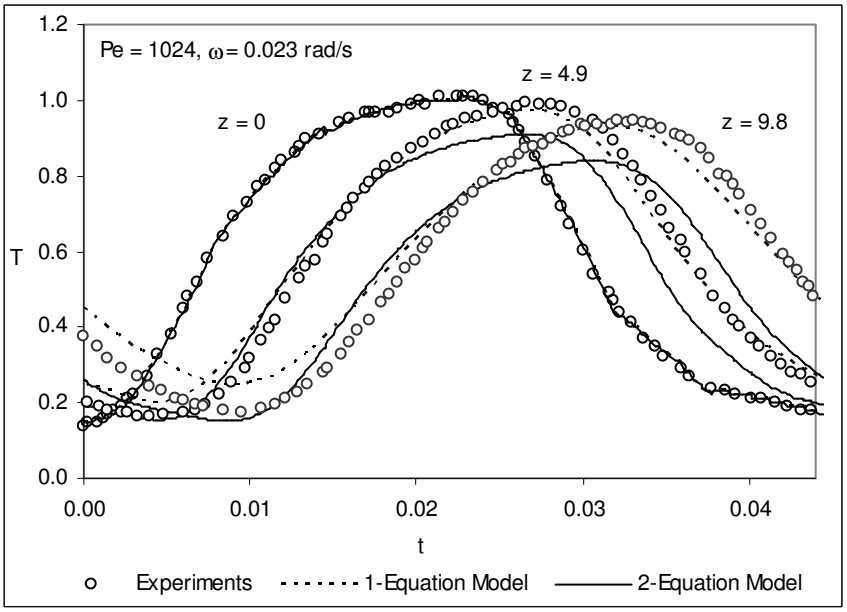

Figure 9.13: Variation of temperature with time in experiments, 1 and 2-equation models for frequency response of steel-water bed. Pe = 1024, ω = 0.023 rad/s.

Figure 9.13 shows the above comparison but over one time-period. The results of 1-equation model are shown for a Biot number of zero and those of 2-equation model for 0.05. The profiles of 1-equation model look closer to the experiments than those of the 2-equation model. The results of 2-equation model are close to the experiments during the hot phase only. In Figure 9.14, the comparison at a higher frequency of 0.023 rad/s is shown. The individual differences between the profiles of experiments and numerical simulation have increased. In Figure 9.15, the frequency being high and attenuation is large and hence the profiles are confusing.

In Figures 9.16 to 9.18, show the comparison for higher Peclet number having nominal value of 1950. In Figure 9.16, the comparison for a frequency of 0.053 rad/s is shown. At location $z = 4.9$, both the numerical simulations are quite close to the experiments. Of the numerical simulation, the 1-equation model is closer to experiments during the cold phase, and the 2-equation model on the other hand is closer to experiments during hot phase.

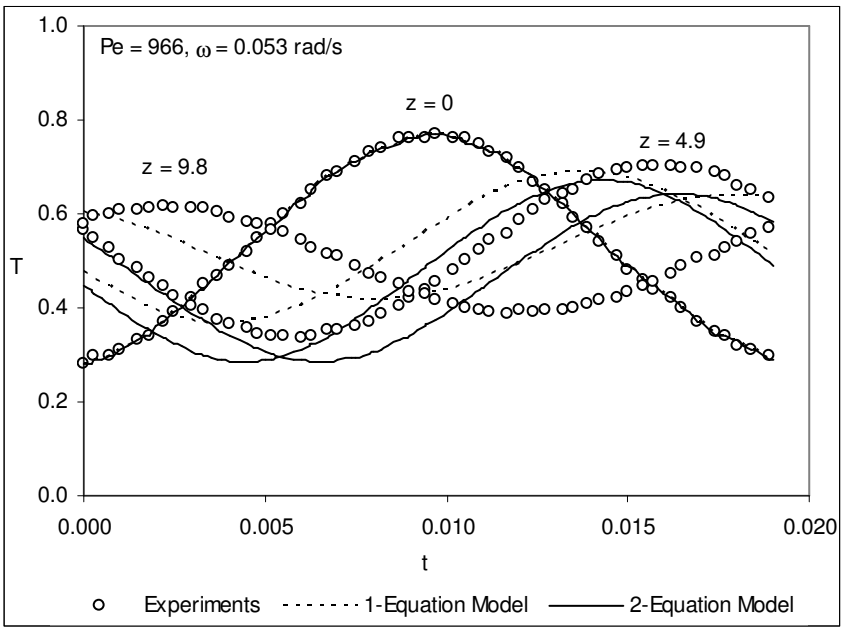

Figure 9.14: Variation of temperature with time in experiments, 1 and 2-equation models for frequency response of steel-water bed. Pe = 966, ω = 0.053 rad/s.

Figure 9.17, compares the experimental results at $z = 9.8$ with those of the numerical simulation. The profiles of 1-equation model are shown for zero Biot number but those of the 2-equation models for both the values of 0 and 0.05. At zero Biot number, the 2-equation

model predicts higher value of the maximum temperature as compared to that in the experiments. The minimum temperature for both the Biot numbers is close to that in the experiments.

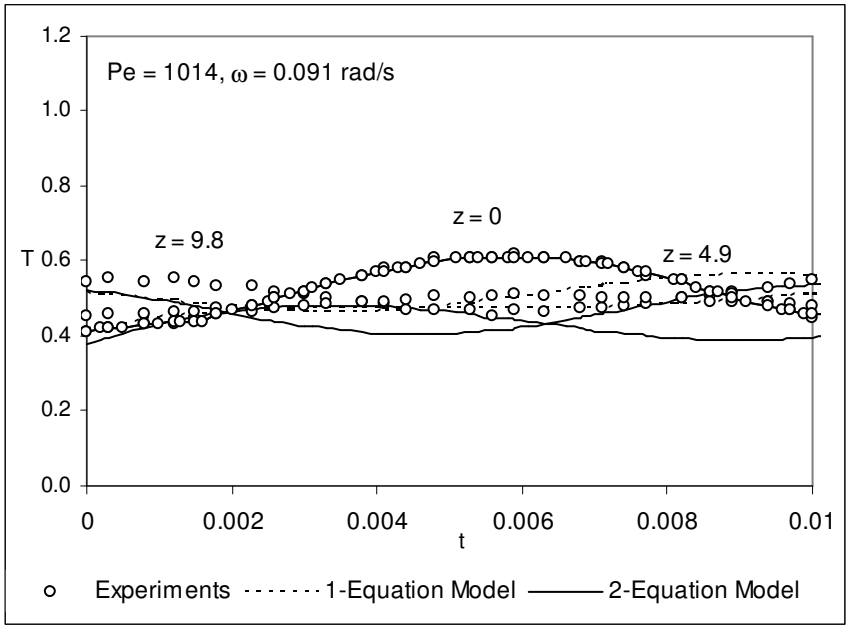

Figure 9.15: Variation of temperature with time in experiments, 1 and 2-equation models for frequency response of steel-water bed. Pe =1014, ω = 0.091 rad/s.

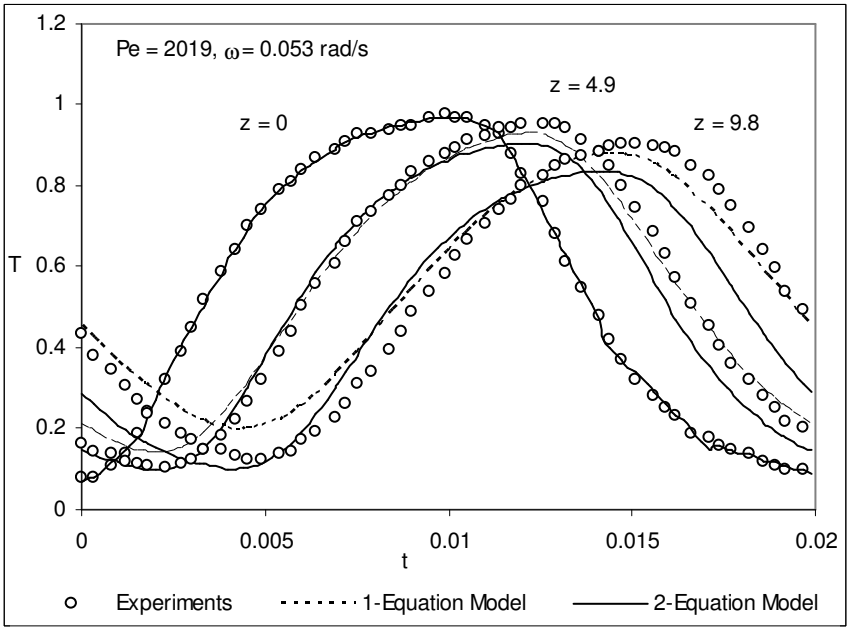

Figure 9.16: Variation of temperature with time in experiments, 1 and 2-equation models for frequency response of steel -water bed. Pe =2019, ω = 0.053 rad/s.

It is clear that the match between the 2-equation model and the experiments is sensitive to the individual phase and Biot number. For the hot phase, it improves with an increase in the Biot number but in the cold phase, it deteriorates with Biot number. During the cold phase, there is hardly any possibility of heat loss as the temperatures are falling. A variable Biot number; positive during the hot phase but zero/negative during the cold phase would improve the match. The 1-equation model, on the other hand at Bi =0, is a better match as far as the cold phase is concerned but its prediction of the minimum temperature is poor. Figures 9.18 and 9.19 show the comparison for frequencies of 0.087and 0.149 rad/s. The similar trends are seen but the individual differences are magnified.

These comparison show that 2-equation model predicts the temperature profiles well though it has higher amplitude and lower phase lag as compared to the those of the experiments. The profiles of 1-equation model at zero Biot number are reasonably close to those of the experiments but have poor sensitivity to heat loss. The abstract of the above comparison is shown in Figure 9.20 over 2-3 time-periods. The comparison for all the frequencies and both the Peclet numbers is shown for a location of z = 4.9. In Figure 9.20(a & b), the results of 1-equation model at Biot number of 0.05 are also shown in addition to those at zero. At lower frequencies, the comparison is better and still permissible at higher frequencies. Over 2-3 time periods the comparison looks good and meaningful.

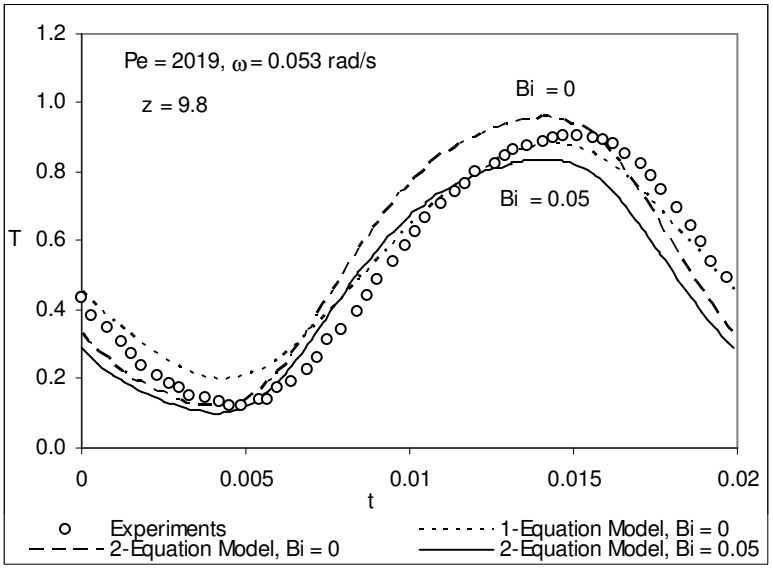

Figure 9.17: A comparison of the experimental profile with those of 1-equation model at *Bi* = 0 and 2-equation model for *Bi* = 0 & 0.05 for frequency response of steel -water bed. Pe =2019, ω = 0.053 rad/s.

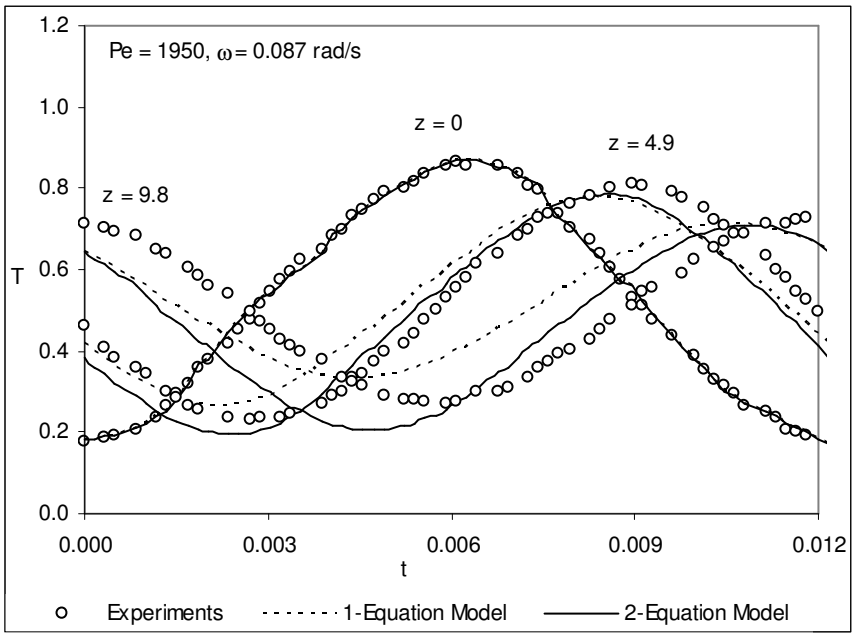

Figure 9.18: Variation of temperature with time in experiments, 1 and 2-equation models for frequency response of steel-water bed. Pe =1950, ω = 0.087 rad/s.

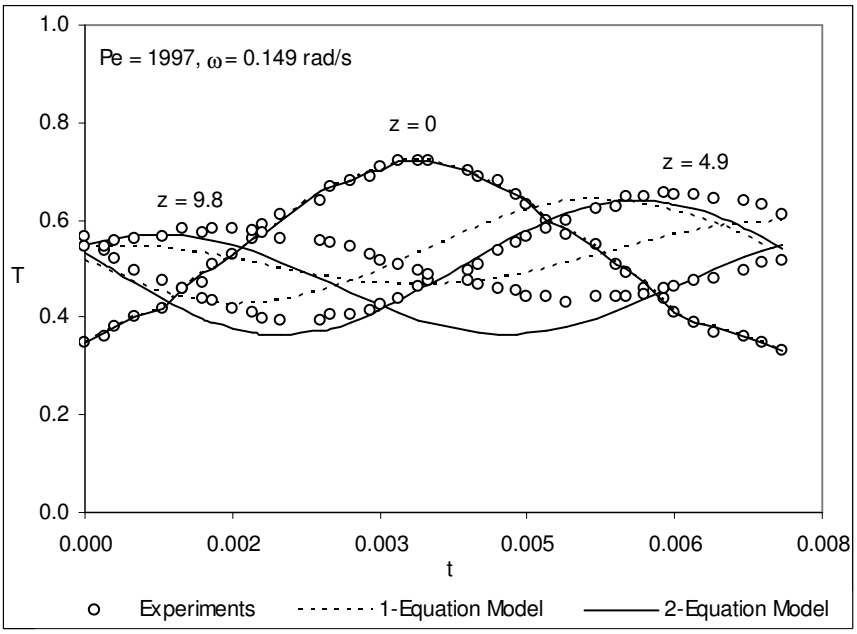

Figure 9.19: Variation of temperature with time in experiments, 1 and 2-equation models for frequency response of steel -water bed. Pe =1997, ω = 0.149 rad/s.

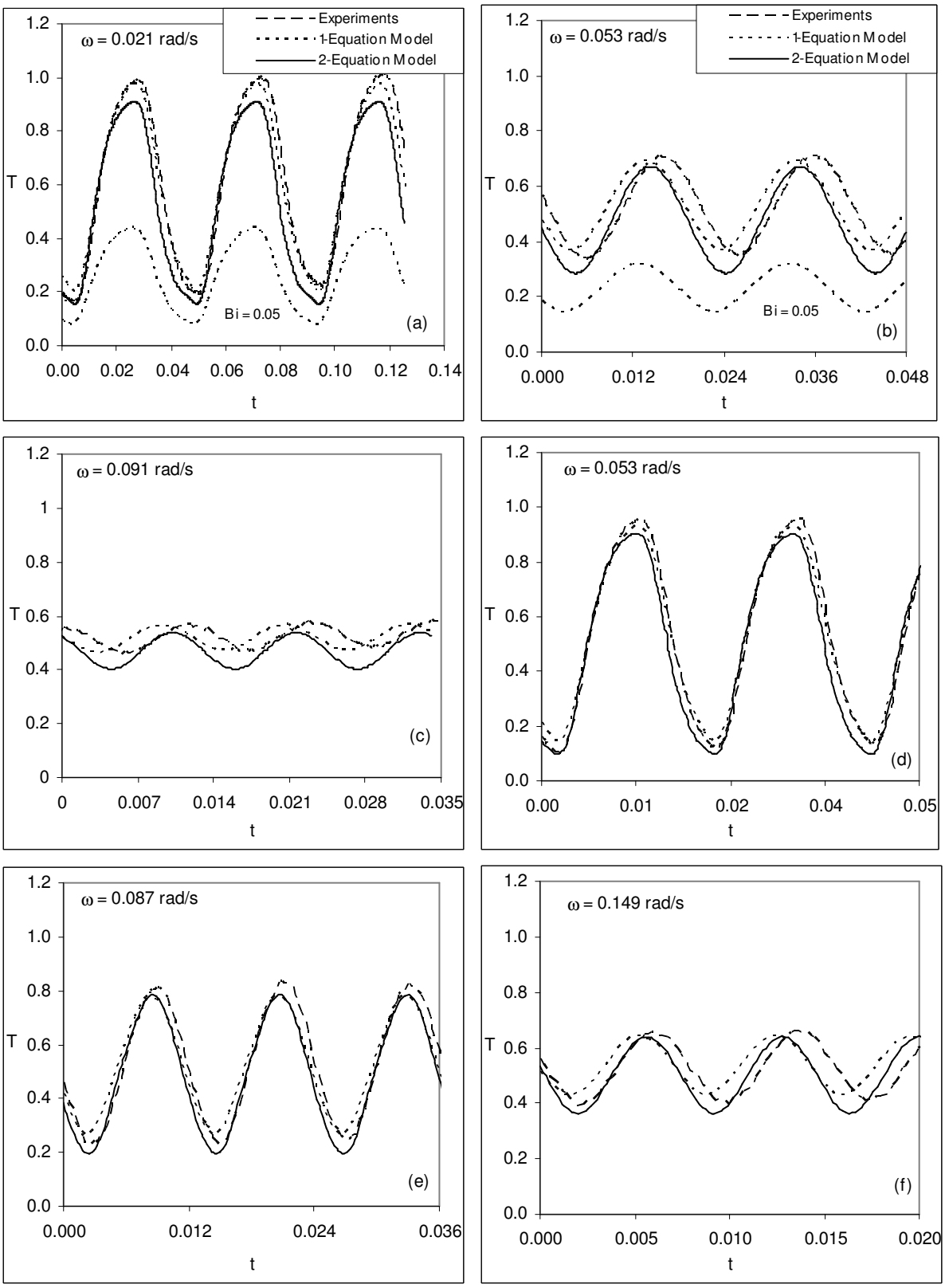

Figure 9.20: Comparison of temperature profiles in experiments, 1 and 2-equation models for frequency response of steel-water bed at z =4.9. (a-c) Pe = 1000; (d-f) Pe = 1950.

9.3.2 Amplitude and Phase Lag

The comparison of amplitude and phase lag is presented in the Figures 9.21 and 9.22 for Peclet number of 1000 and 1950 respectively. For a Peclet number of 1000, Figure 9.21(a) shows the attenuation of temperature and 9.21(b) the corresponding phase lag. For a frequency of 0.023 rad/s, the amplitudes as predicted by the experimental results are more as compared to that of numerical simulation.

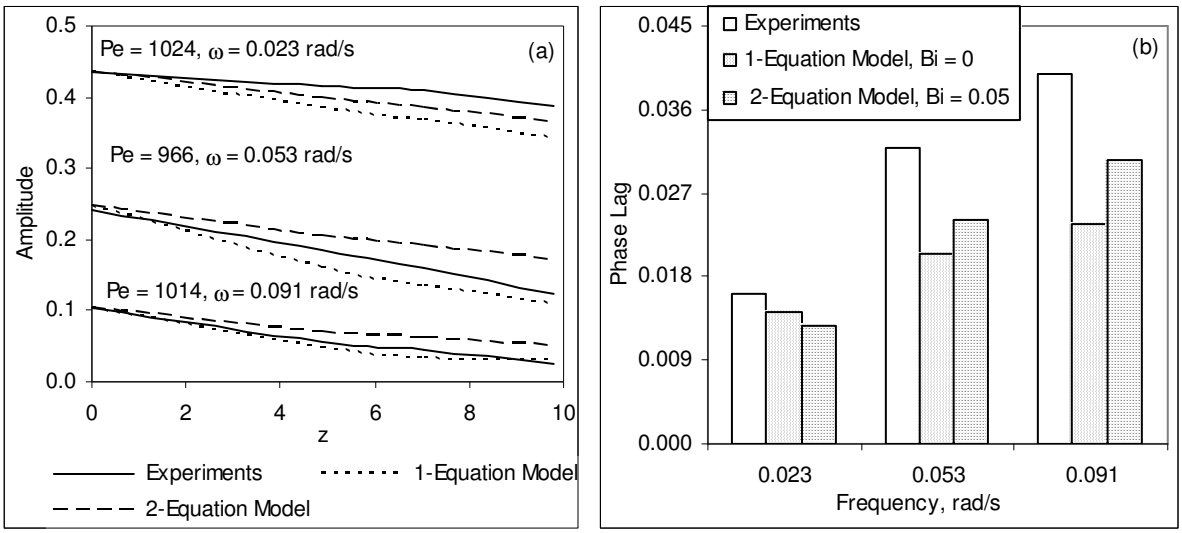

Figure 9.21: **A**ttenuation of temperature and phase lag in experiments, 1 and 2-equation models for frequency response of steel-water bed. Pe = 1000, ω_{ref} = 0.032 rad/s.

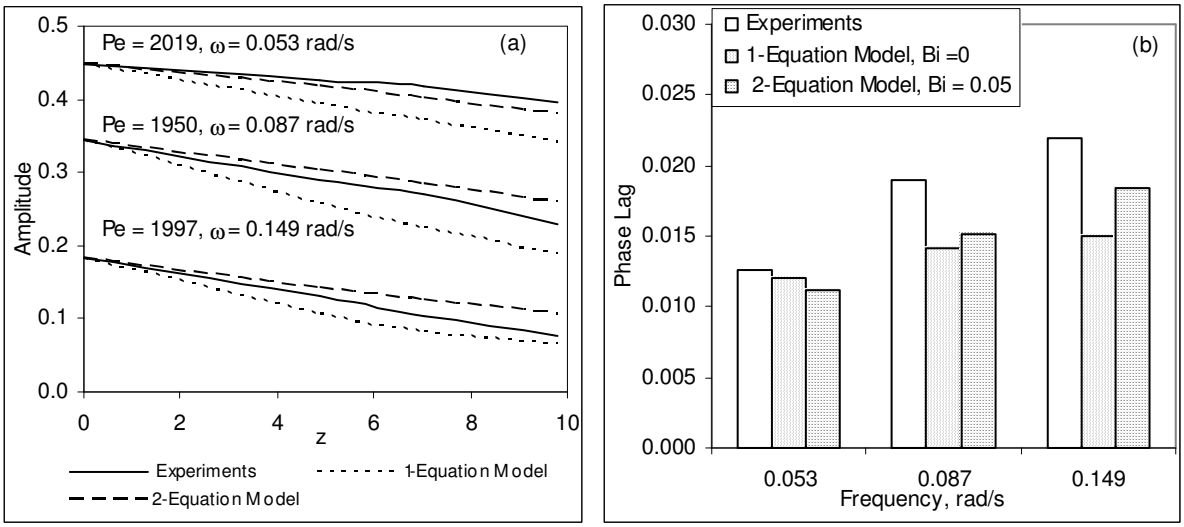

Figure 9.22: **A**ttenuation of temperature and phase lag in experiments, 1 and 2-equation models for frequency response of steel-water bed. Pe = 2000, ω_{ref} = 0.064 rad/s.

It is lower for 1-equation model than that for 2-equation model. However, for higher frequencies, the amplitude of 2-equation model becomes higher as compared to experiments and 1-equation model. The phase lag is higher in the experiments than that of the numerical simulation. In general, the results of 2-equation model are close to those of the experiments.

Almost similar trends are seen at higher Peclet number in Figure 9.22 except that the phase lag as predicted by simulation is now closer to that of the experiments.

9.3.3 Pulse Speed and Spread

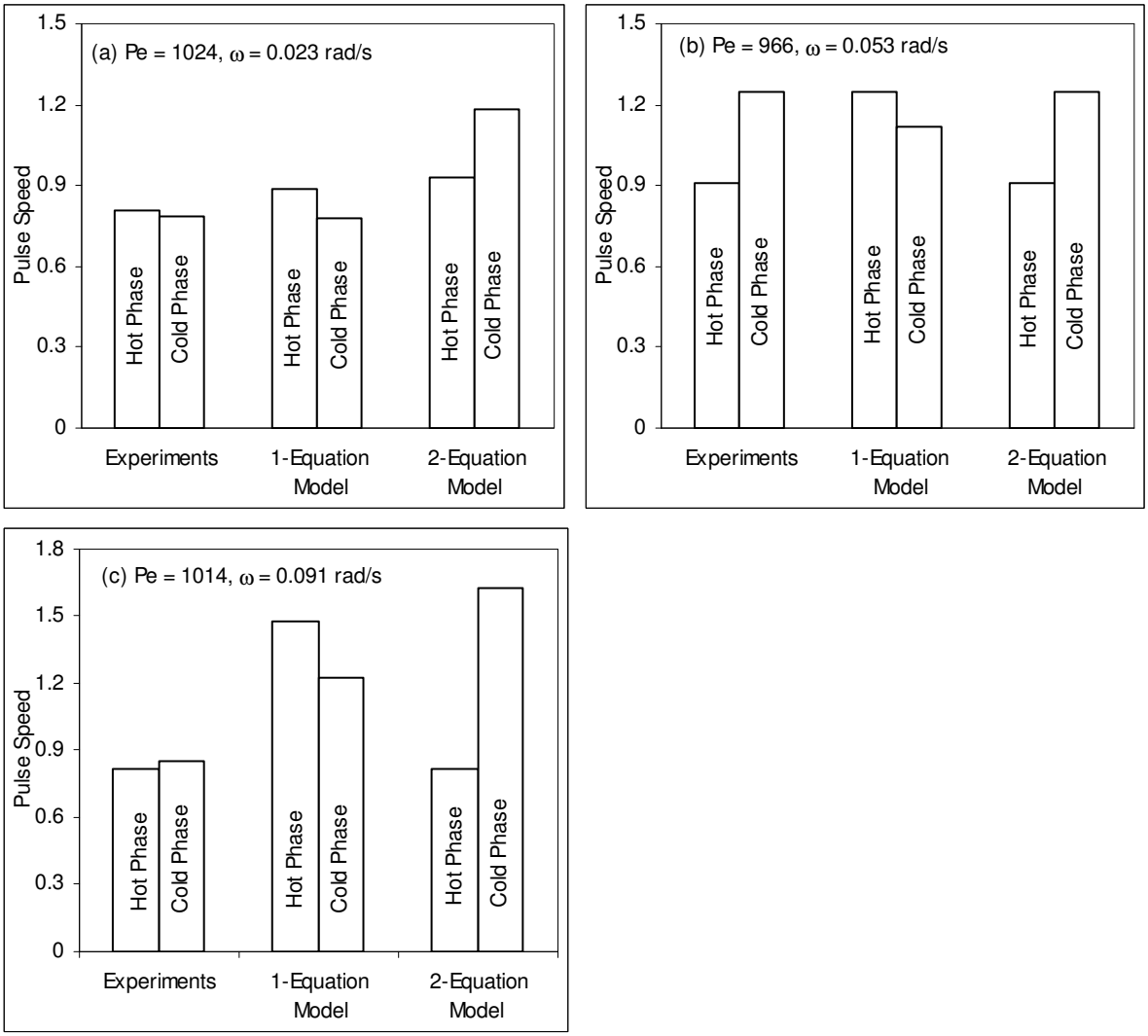

Figure 9.23: Pulse speed in experiments, 1 and 2-equation models for frequency response of steel-water bed. Pe = 1000, ω_{ref} = 0.032 rad/s.

As shown in Figures 9.16 and 9.17, there is difference in the profiles of 1 and 2-equation models during the hot and the cold phase. These are reflected in the pulse speed in Figures 9.23 & 9.24 and the corresponding spread as shown in Figure 9.25. The experiments have lower speed as compared to that of simulation. For majority of the cases, the speed of cold phase of the experiments is marginally higher as compared to that of the hot phase. The 2-equation model also follows this trend but that of the 1-equation model is opposite. Hence, the results of 2-equation model are closer to those of the experimental.

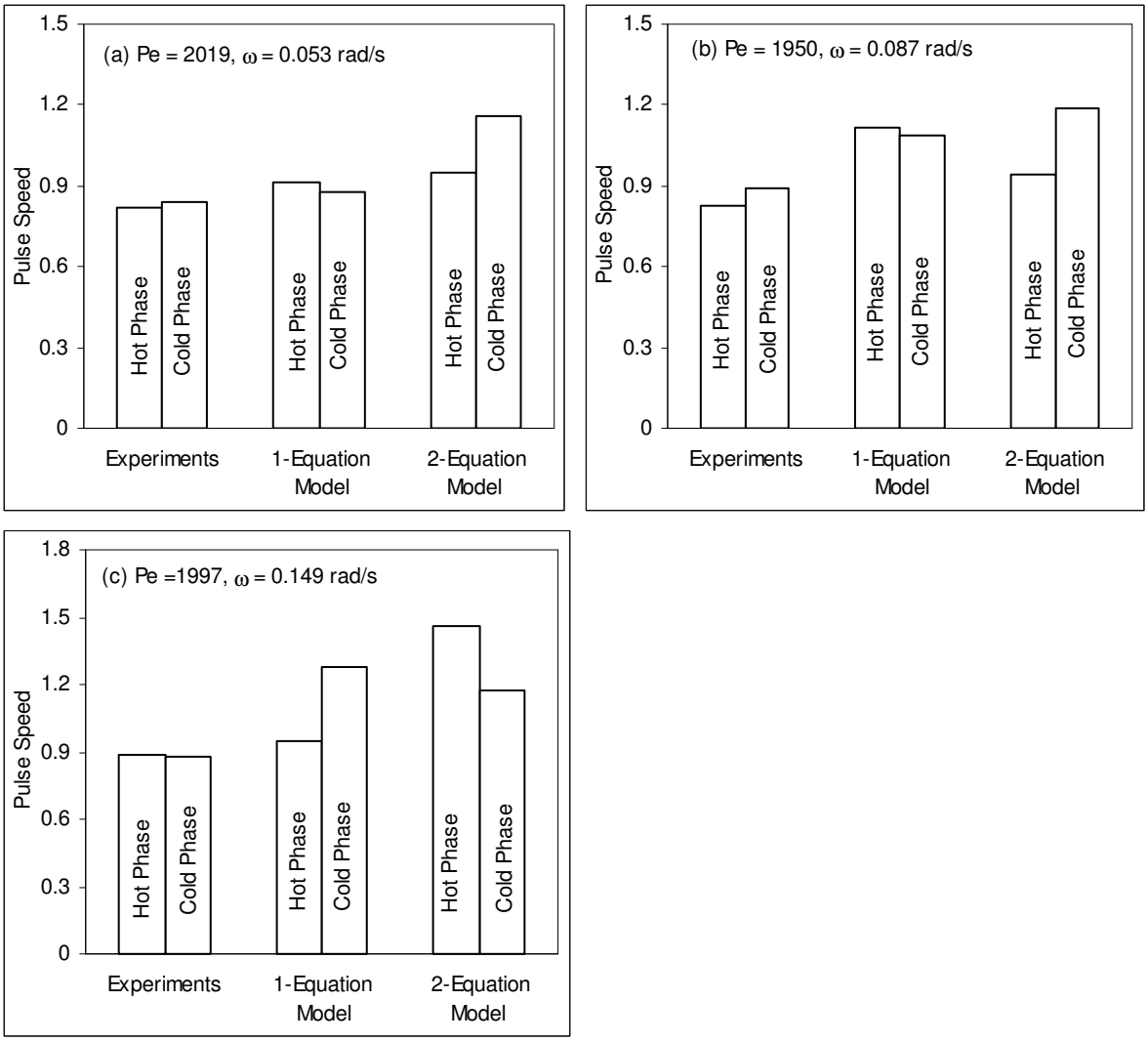

Figure 9.24: Pulse speed in experiments, 1 and 2-equation models for frequency response of steel-water bed. Pe = 1950, ω_{ref} = 0.064 rad/s.

Consider now the spread in the hot and the cold phases as shown in Figure 9.25 In each figure the results during the two phases are shown in the figure. The pulse spread is shown

for selected cases as explained earlier. The spread at a frequency of 0.023 rad/s in Figure 9.25(a) is more during the cold phase than that in the hot phase. The spread as predicted by 1-equation model is the highest and that of the 2-equation model is close to experimental results. The same trends are followed for a frequency of 0.053 rad/s as shown in Figure 9.26(b). In Figure 9.25(c), the spread is calculated over a temperature range of 0.35 to 0.65 and presented over a length of $z = 7$ only. Here the hot phase spread is more.

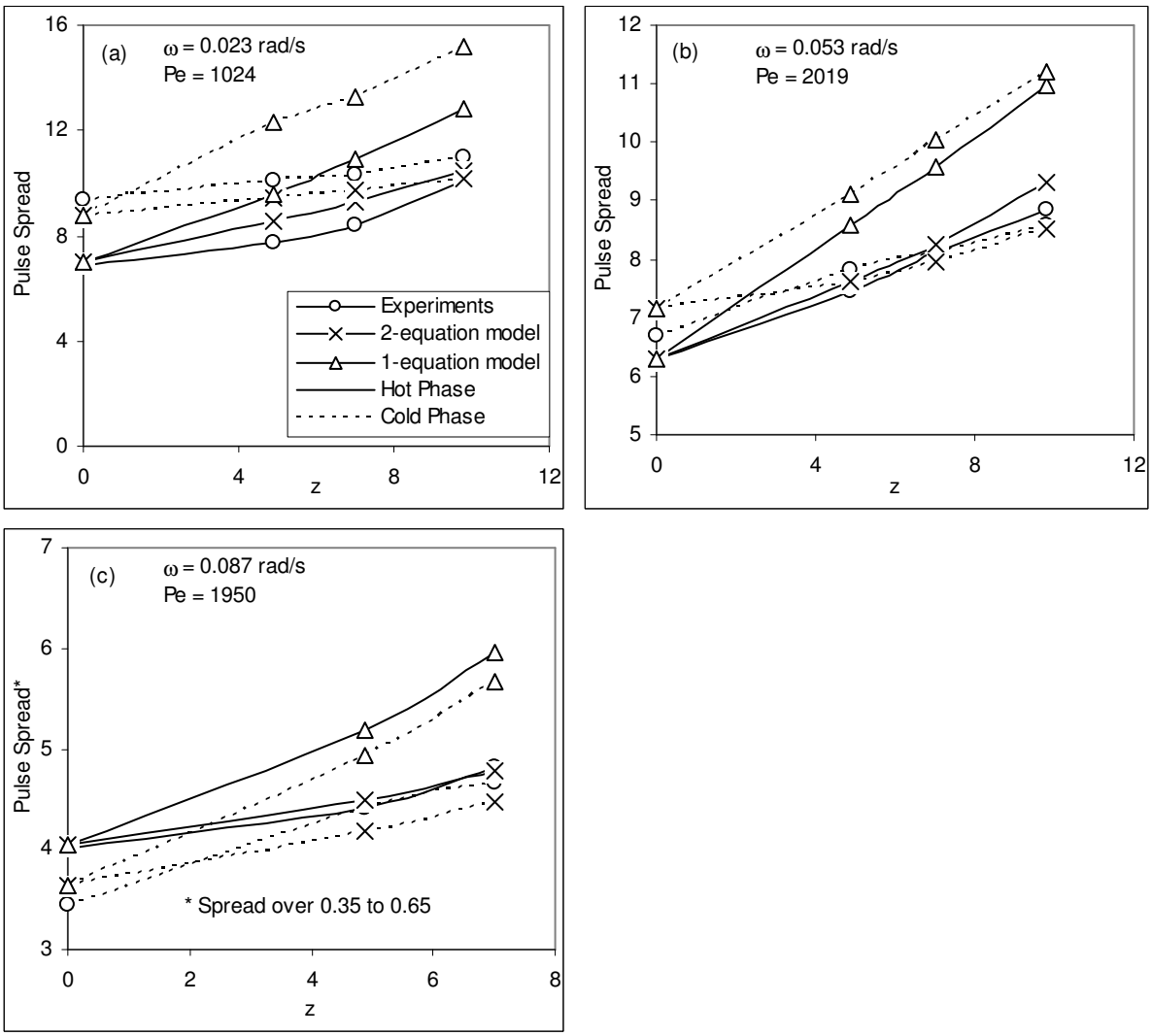

Figure 9.25: Pulse spread in experiments, 1 and 2-equation models for frequency response of steel-water bed.

Figures 9.26 and 9.27 compare the pulse speed and spread in a step response with that of the frequency response. The comparison is performed with the results of hot phase of the frequency response. The speed is almost similar for the two cases but the spread is

distinct. The spread for a step and a frequency response are shown in Figure 9.27. For a lower frequencies of 0.023 and 0.053 rad/s as shown in Figures 9.27(a & b), the results are identical to those of the step response but for a frequencies the spread is lower.

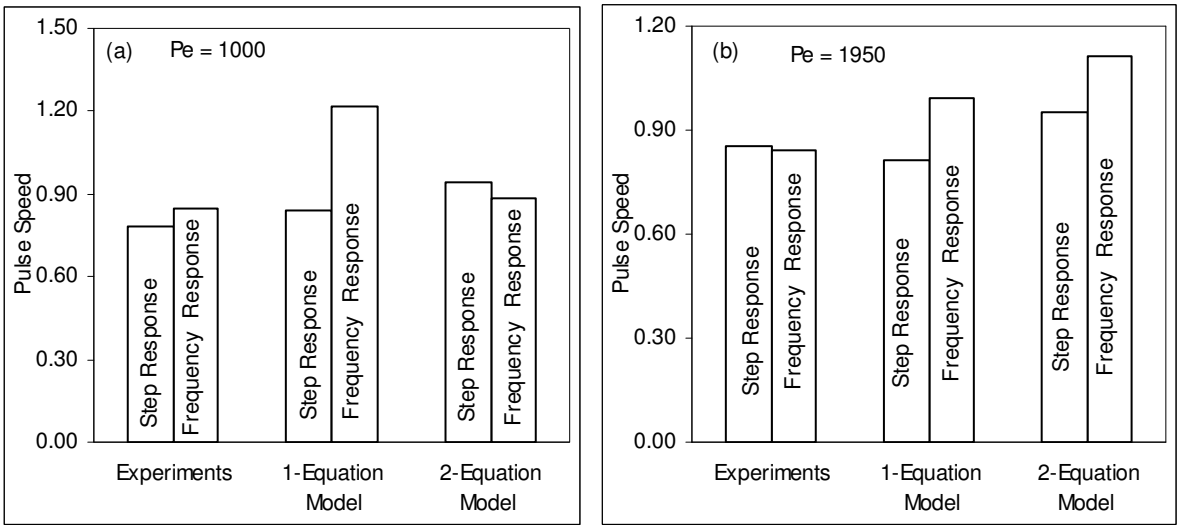

Figure 9.26: Comparison of pulse speed for step and frequency response in steel-water bed.

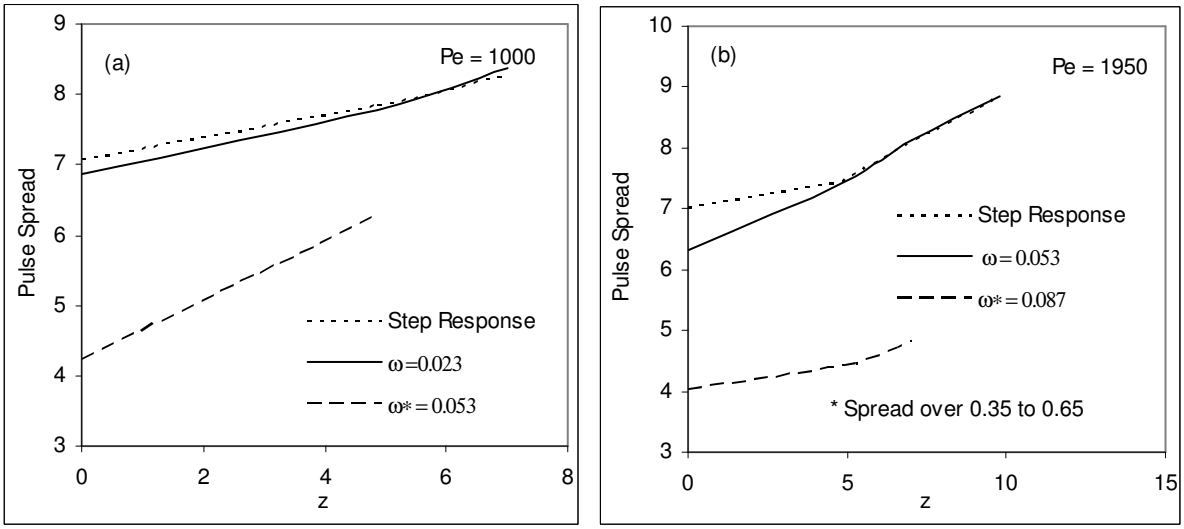

Figure 9.27: Comparison of experimental pulse spread for step and frequency response in steel-water bed.

9.4 THERMAL NON-EQUILIBRIUM

The thermal non-equilibrium between the fluid and the solid phases is discussed in this section. In cyclic steady state, the temperature of the two phases keeps changing. The thermal non-equilibrium between the two phases keeps changing periodically between the maximum and the minimum values. It varies with frequency and Peclet number.

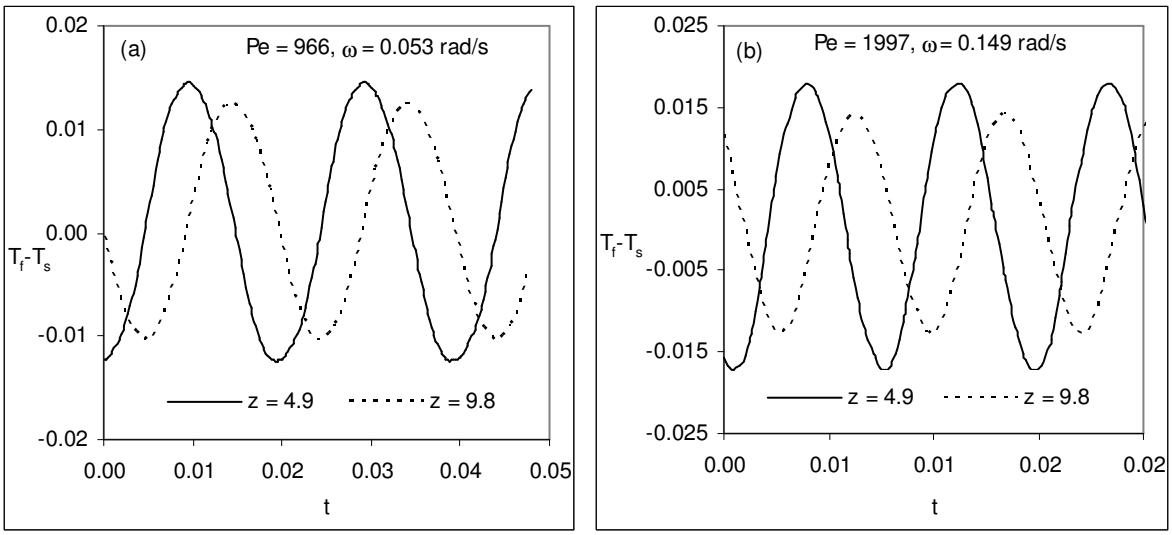

Figure 9.28: The pulse of temperature difference during frequency response in steel-water bed.

Figure 9.28 shows the thermal non-equilibrium in steel-water bed as a function of time at two locations in the bed. As the temperature fluctuates between the maximum and the minimum values, so is the thermal non-equilibrium. The amplitudes vary with distance form the inflow plane. It increases with Peclet number. The corresponding amplitudes for various frequencies are shown in Tables 9.1 and 9.2. Table 9.1 shows the thermal non-equilibrium for a Peclet number of 1000 for various frequencies. The corresponding maximum and minimum values are shown. The amplitudes fall with an increase in frequency. The maximum values are numerically higher that the minimum values for all the cases.

Table 9.1: Degree of thermal non-equilibrium between the fluid and the solid phases at various locations. Pe = 1000.

Frequency, rad/s	z = 4.9			z = 9.8		
	Maximum	Minimum	Amplitude	Maximum	Minimum	Amplitude
0.023	0.01720	-0.01580	0.03300	0.01480	-0.01310	0.02790
0.053	0.01450	-0.01240	0.02690	0.01240	-0.01030	0.02270
0.091	0.00890	-0.00690	0.01580	0.01440	-0.00460	0.01900

Table 9.2: Degree of thermal non-equilibrium between the fluid and the solid phases at various locations. Pe = 1950.

Frequency, rad/s	z = 4.9			z = 9.8		
	Maximum	Minimum	Amplitude	Maximum	Minimum	Amplitude
0.053	0.0244	-0.024	0.04840	0.0215	-0.0202	0.04170
0.087	0.0219	-0.0219	0.04380	0.0192	-0.0187	0.03790
0.149	0.018	-0.0172	0.03520	0.0141	-0.0127	0.02680

The difference between the 1 and 2-equation models is shown in the Figure 9.29. It also varies with temperature and fluctuates between the maximums and minimum values. Though the figure pattern is similar but the trends are opposite to that of thermal non-equilibrium such that it increases with distance and falls with Peclet number. Tables 9.3 and 9.4 show the amplitudes of the difference between the models for various frequencies. Numerically, the maximum values are again higher than the minimum values. The corresponding interphase convective resistance and heat transfer is shown in Table 9.5. The convective resistance increases with Peclet number and the corresponding heat transfers are also higher. It is because of higher temperature difference between the two phases. The degree of thermal non-equilibrium is higher as compared to the glass-water bed although the particle size is distinct in the two cases.

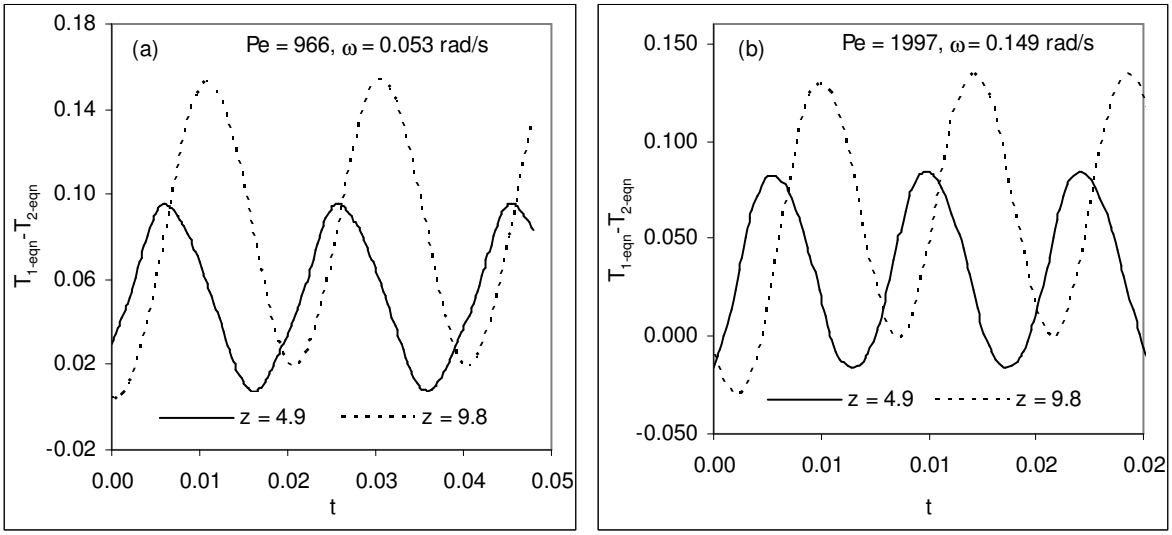

Figure 9.29: The pulse of temperature difference between 1 and 2-equation models during frequency response in steel-water bed.

Table 9.3: Difference between the 1 and 2-equations models at various locations. Pe = 1000

Frequency, rad/s	z = 4.9			z = 9.8		
	Maximum	Minimum	Amplitude	Maximum	Minimum	Amplitude
0.023	0.10440	-0.65030	0.75470	0.10800	-0.58020	0.68820
0.053	0.09570	0.00740	0.08830	0.15370	0.00390	0.14980
0.091	0.08440	-0.00500	0.08940	0.12400	-0.00380	0.12780

Table 9.4: Difference between the 1 and 2-equations models at various locations. Pe = 1950

Frequency, rad/s	z = 4.9			z = 9.8		
	Maximum	Minimum	Amplitude	Maximum	Minimum	Amplitude
0.053	0.0962	-0.0283	0.12450	0.1664	-0.0323	0.19870
0.087	0.0835	-0.0145	0.09800	0.1372	-0.0033	0.14050
0.149	0.0841	-0.0164	0.10050	0.134	-0.0298	0.16380

Table 9.5: Convective resistance and corresponding maximum interphase heat transfer at various locations in steel-water bed.

Peclet Number Pe	Dimensionless Convective Resistance (Pe / Nu A_f)	Dimensionless Interphase Heat Transfer (Nu A_f/Pe*(T_f-T_s))	
		z = 4.9	z = 9.8
966	0.408	0.036	0.030
1950	0.555	0.039	0.035

9.5 SENSITIVITY ANALYSIS

A brief sensitivity analysis of the frequency response in porous bed is presented. Byun *et al.* [2006] studied analytically the thermal behavior of porous medium under oscillating flow conditions where the hot and the cold fluids enters through the opposite ends of the porous bed. The oscillations in solid and fluid phase vary with thermal properties, interphase heat transfer of the porous medium. It varies with weighted ratio of thermal storage capacities of solid and fluid phases (K) and that of interphase heat transfer and energy convected downstream $\left(hA_{IF} / \varepsilon(\rho c_P)_f \omega\right)$ which is called as equivalent Stanton number.

In order to check the similar results for pulsating flow, a sensitivity analysis with respect to the parameter K is considered. Its value is varied from 0.1 to 10, keeping the value of the other constants as fixed. Figure 9.30 shows the effect of change in the value of K upon the thermal response in a porous bed. The other properties are kept fixed as in glass-water bed in the last chapter. As the value of K increases, the storage capacity of the solid phase

increases relative to that of the fluid phase, and the response becomes slower. The maximum temperature obtained at a location also falls. The time to reach a particular temperature; charging time is higher. Figure 9.31 shows the effect of change in thermal storage capacity ratio on the thermal non-equilibrium between the two phases. It increases directly with an increase in thermal storage capacity ratio.

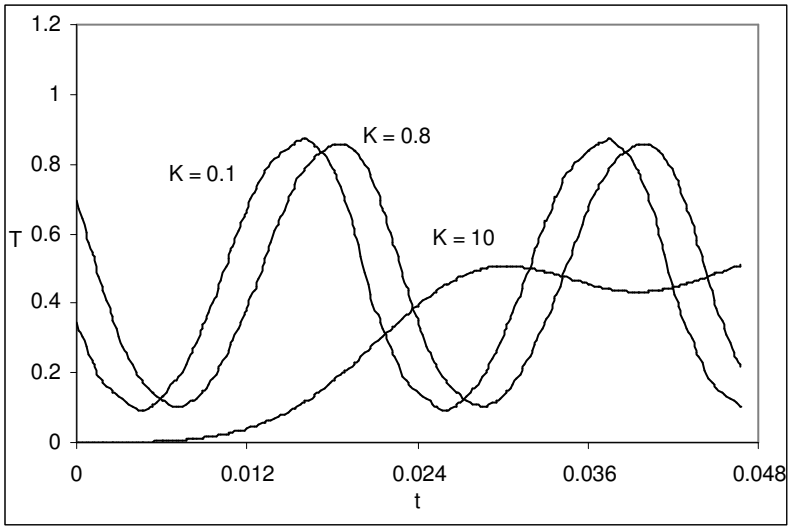

Figure 9.30: The effect of change in thermal storage capacity ratio on temperature profiles for frequency response in a porous bed. Pe = 950, $\omega = 0.052$ rad/s, $z = 9.6$.

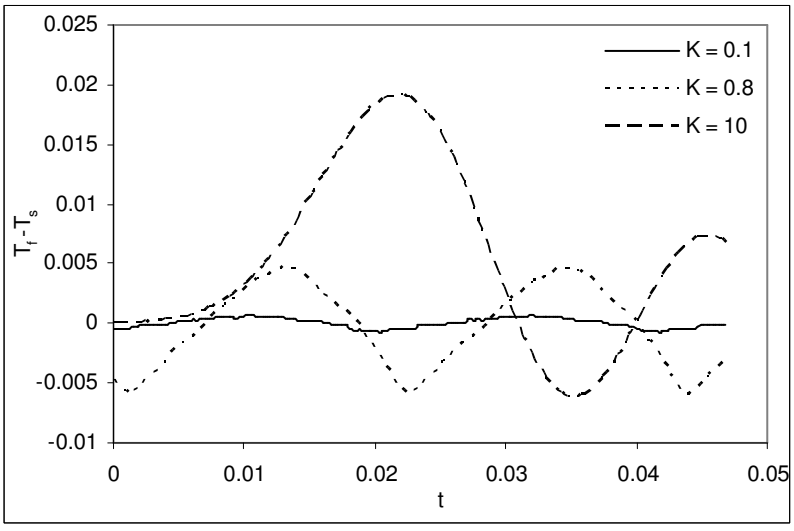

Figure 9.31: The effect of change in thermal storage capacity ratio on thermal non-equilibrium for frequency response in a porous bed. Pe = 950, $\omega = 0.052$ rad/s, $z = 9.6$.

9.6 COMPARISON OF FREQUENCY RESPONSE IN GLASS AND STEEL-WATER BEDS

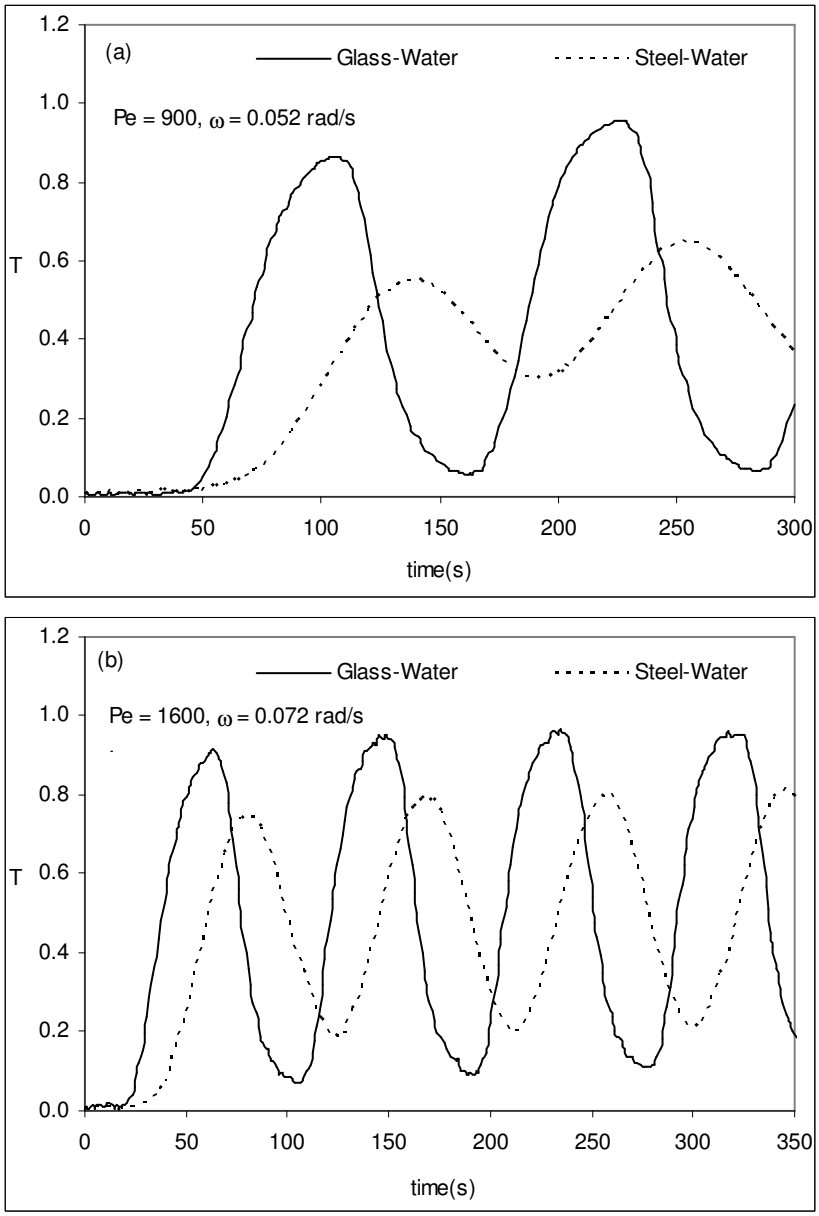

Figure 9.32: The comparison of experimental temperature profiles for frequency response in glass and steel-water beds. $z = 9.6$ from the inflow plane.

Since the nature of temperature response in a porous bed changes with the thermal properties of the solid phase, it is interesting to compare the frequency response in glass and steel-water beds. It is performed by using temperature-time profiles in experiments and numerical simulation. The parameters such as amplitude, phase lag, pulse speed and spread in the two

beds are compared. A comparison of thermal non-equilibrium in the two beds is also performed. The comparison for temperature time profiles is performed separately in experiments and simulation under similar conditions. For experiments, these profiles are plotted using nominally similar flow rates, frequency and distance from the inflow plane.

9.6.1 Time-Temperature Profiles

The time –temperature profiles as obtained from the experiments and simulation in the two beds is performed. The Peclet number is nominally equal to 900 and 1600. This comparison is obtained at location z = 9.6 in glass and steel-water beds. The comparison as obtained in the experiments is discussed first. The time of start of response is set same in the two beds. The temperature in lead pipes in the two beds is identical.

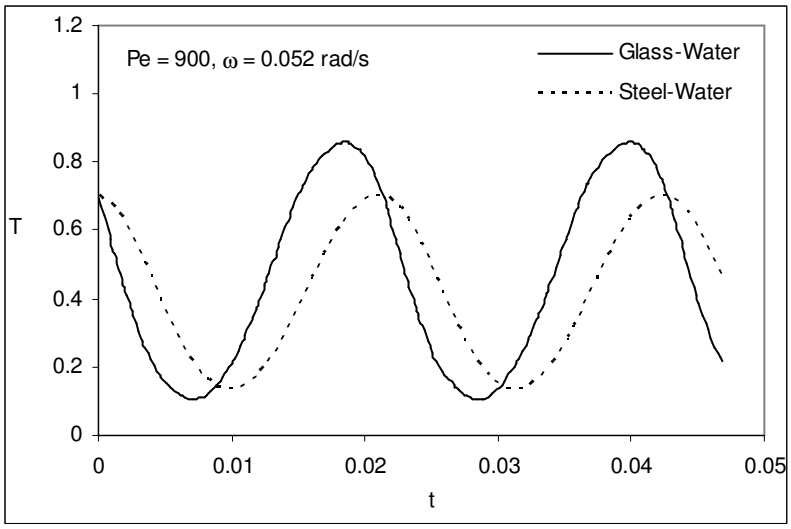

Figure 9.33: The comparison of temperature profiles as obtained from the 2-equation model for frequency response in glass and steel-water beds. z = 9.6 from the inflow plane.

Figure 9.32 shows the comparison for two Peclet numbers of 900 and 1600. In Figure 9.32(a), a comparison for a Peclet number of 900, the frequency of pulsations is 0.052 rad/s. The temperature profiles related to steel-water bed are slower as compared to those of the glass-water bed and the maximum temperature is lower & the minimum temperature is higher. The similar trends are shown at higher Peclet number of 1600 as shown in Figure 9.32(b). Hence, the response of glass-water bed is faster as compared to that of steel-water bed. The steel-water requires more time for charging to a fixed temperature.

Figure 9.33 compares the temperature profiles as obtained from 2-equarion model for glass and steel-water beds for a Peclet number of 900. The profiles are qualitatively similar to those obtained from the experiments.

9.6.2 Amplitude and Phase Lag

A comparison of amplitudes and phase lag in the two beds is shown in Figure 9.34. It is clear that under similar conditions the amplitudes is higher in a glass-water bed than that in a steel-water bed and the corresponding phase lag is lower. It is also confirmed in numerical simulation as shown.

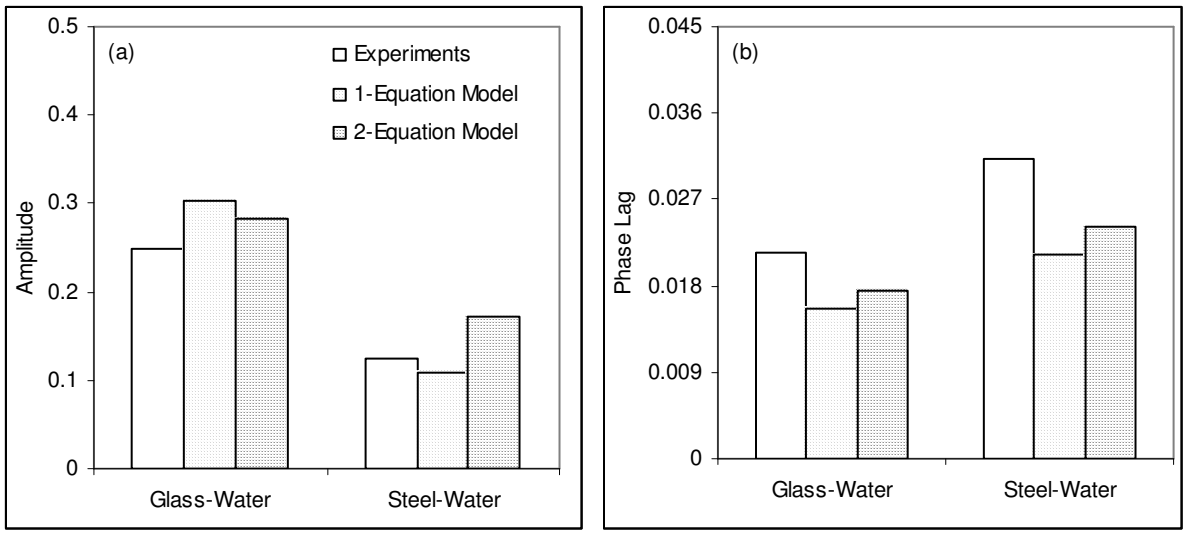

Figure 9.34: Comparison of amplitude and phase lag for frequency response in glass and steel-water beds. Pe = 950, $\omega = 0.052$ rad/s, $z = 10$.

9.6.3 Pulse Speed and Spread

Figure 9.35 compares the pulse speed and spread in the two beds. Figure 9.35(a) compares the front speed in the two beds during the hot phase. Front speed in glass water bed is more as compared to that in steel-water bed. The results of 2-equation model are closer to experimental results than 1-equation model. The comparison of spread, as obtained from the experiments, is shown in Figure 9.35(b). The spread is calculated by time rate of change of temperature from 0.35 to 0.65 under similar conditions. Hence, the heating time required for a steel-water bed is more as compared to a glass water bed.

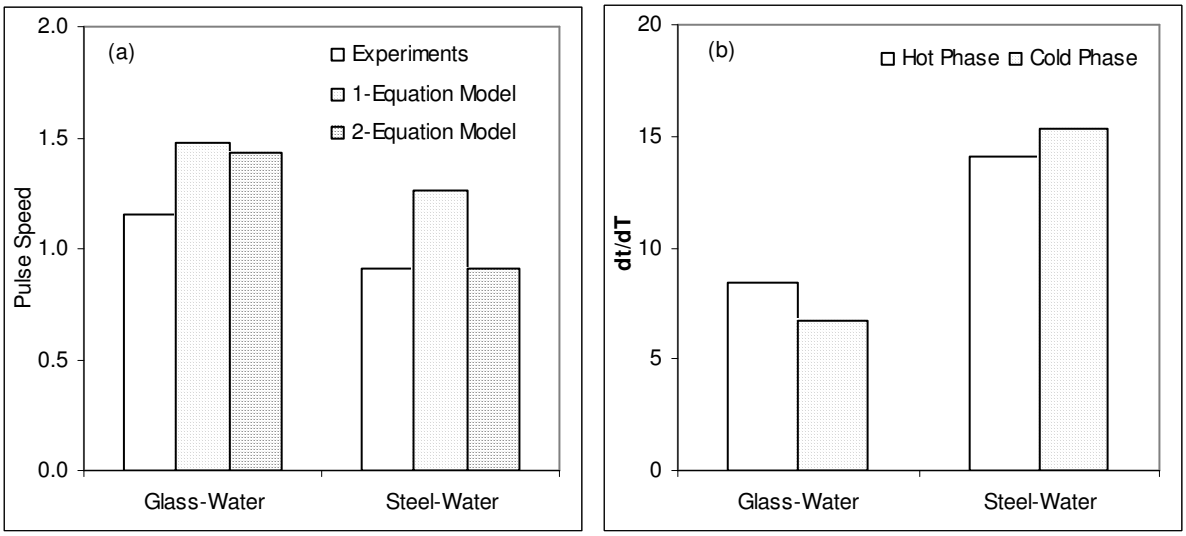

Figure 9.35: Comparison of pulse speed and spread for frequency response in glass and steel-water beds. Pe = 950, $\omega = 0.052$ rad/s.

9.6.4 Thermal Non-Equilibrium

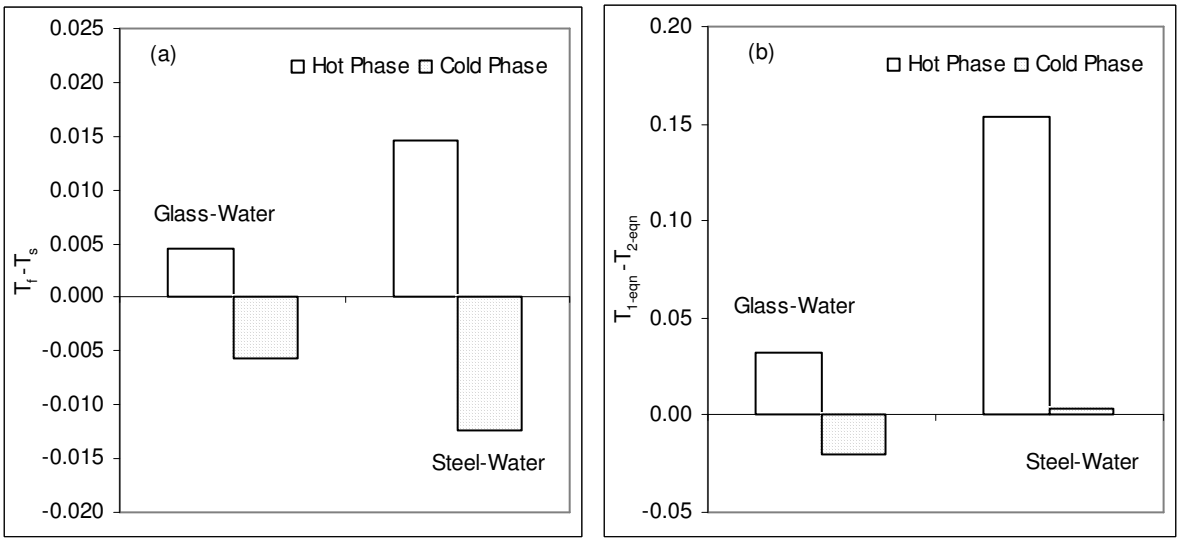

Figure 9.36: Comparison of thermal non-equilibrium for frequency response in glass and steel-water beds. Pe = 950, $\omega = 0.052$ rad/s.

The maximum degree of thermal non-equilibrium, as obtained from 2-equation models, in the two beds is shown in Figure 9.36(a). The results during the hot and the cold phases are shown in the figure. In glass-water bed, it is less as compared to that in steel-water bed during the frequency response. The maximum degree of difference between the 1-equation and 2-equation models is shown in Figure 9.36(b). In glass-water bed it is smaller as compared to that in steel–water bed. Hence, the frequency response in steel-water bed is

distinct to that in a glass-water bed. The numerical simulation predicts well, the differences between the responses in the two beds.

9.7 CLOSURE

In this chapter, the numerical simulation of frequency response in a steel-water bed is presented. The idea is to use the simulation when the thermal properties of the fluid and the solid phases are distinct. The results of the numerical simulation are compared with those of lab scale experiments using the results of 1and 2-equation models under similar conditions. The comparison is performed by using cyclic steady state temperature profiles for a qualitative validation. The corresponding amplitude, phase lag, pulse speed and spread of the thermal pulse traveling through the bed are also compared. In addition, the thermal non-equilibrium between the fluid and the solid phases is assessed. A comparison of the frequency response in glass-water and steel-water bed is also performed. The amplitude of the pulse in steel-water bed is lower and the corresponding phase lag is more. The pulse speed in this bed is also slower. The degree of thermal non-equilibrium is more in this bed. The results of 2-equation model are uniformly superior to those of 1-equation model. For a positive Biot number, the results of 1-equation model are poor.

In Chapters 8 and 9, the thermal response of distinct porous beds to time periodic boundary conditions is discussed. The results are useful in context of the energy storage in a porous bed. In Chapter 6 and 7, the validation for a single flow of hot water is performed. The analysis of energy storage in porous medium is discussed in next chapter.

CHAPTER 10

ENERGY STORAGE IN POROUS MEDIUM

10.1 INTRODUCTION

Energy storage using a porous medium is an attractive method of storing available excess energy and reusing it at a later point of time when its availability is either less than the required amount or is not available at all. The energy storage effect is obtained by using fixed porous solid mass such as closely packed mesh screens or spherical beads through which hot/cold fluid flows. Its working is similar to that of a regenerator as used in a Stirling cycle. Regenerators are also used in gas turbine cycles but they are used only to extract waste heat from the exhaust gases in order to improve the cycle efficiency. In contrast, the regenerator enables the Stirling cycle to be completed and forms a primary part of the system. The regenerator is mounted by two heat exchangers on either side. In a Stirling refrigerator, one of the heat exchangers pumps up heat into the working fluid from a low temperature heat sink and another rejects heat from the fluid to a high temperature heat source, which refers to the ambient conditions. After rejecting heat, the temperature is still hotter and hence transfers remaining energy to the regenerator. Later when the working fluid temperature is lower than that of the regenerator, same heat is transferred to the fluid from the regenerator. Hence, the regenerator first receives the energy from the working fluid, stores it in the solid phase and later releases it to the working fluid.

An energy storage system also works in a similar manner. It stores the excess available energy in its solid phase and releases when the supply of energy is less than the demand; thereby the average consumption of energy is efficiently met. It acts as a thermal sponge, absorbing energy into its solid phase when exposed to the hot medium and releasing it to the cold medium at a later stage in the same cycle. The energy may be stored in the form of either sensible or latent heat. An ideal storage system must have a high heat capacity and so must be large in mass. It should offer negligible resistance to flow and its porosity must be large in this sense. The heat transfer rate between the fluid and the solid phases must be large so that the transfer of energy takes place efficiently. However, the space occupied by the

stagnant fluid must be small; hence, the porosity should be small in this respect. It should be well insulated such that there is no heat loss to the surroundings.

The storage and the retrieval of energy from the fixed porous solid mass are obtained by back and forth flow of hot and cold fluids through the mass. This type of flow is referred to as oscillatory flow. It has two phases: hot and cold. In the hot phase, hot fluid enters the mass through one of its ends called the hot end and the transfers energy to the solid mass and in the cold phase, the cold fluid flows through the opposite cold end and retrieves the stored energy. The velocity of fluid thus follows a sine type curve, the positive half symbolizes the charging of energy into the mass through one of its ends and the negative half the discharge of energy through the opposite end, see Figure 10.1. Other than energy storage, the oscillatory flow has wide applications in waste heat recovery units of gas turbines and enhancement of cooling of electrical and electronic equipments. The porous media in presence of oscillatory flow is also considered as an effective method of rapid heat dissipation**,** Leong and Jin [2005].

As heat flows to and from the solid phase, temperature differentials are set up within the representative elementary volume. During the hot phase, heat flows from the fluid to the solid phase and temperature of the fluid phase is higher as compared to that of the solid phase and during the cold phase, the solid phase temperature is higher. Hence, the estimation of temperature differential between the two phases is important in the working of the storage system. The resulting heat transfer between the two phases is a key phenomenon in an energy storage system. This is called thermal non-equilibrium, Amiri and Vafai [1994]. Therefore, the modeling should consider separate temperatures for the two phases. It requires that individual temperatures be assigned to the two phases within the representative elementary volume along with a relationship for interphase heat transfer connecting them. Hence, the corresponding models of heat transfer will necessarily be of 2-equation type, one equation each for the fluid and the solid phase temperatures.

The use of porous medium for energy storage lies in the fact that it has a large effective surface area that can quickly store and retrieve energy during the oscillatory flow. Considering a bed of porosity, ε = 0.4 and the particle diameter, d_P as 1 mm, the effective surface area of the porous insert is given as $A_{If} = \frac{6(1-\varepsilon)}{d_p}$. Its value is 3600 m^2/m^3 of the

volume of the bed, which is very large and the resulting heat transfer from the fluid to the solid phase is thus enhanced. The other factor that is of great advantage is the flow of fluid through torturous paths through the solid phase providing intense mixing of the two phases. Once the energy enters the solid phase the corresponding rise in temperature, can be calculated from solid phase energy equation. Neglecting the heat loss to the ambient, the stored energy is retrieved during the cold phase and the temperature of the cold fluid increases, which is governed by the fluid phase energy equation. Hence, the 2-equation model predicts accurately the resulting temperatures.

The energy storage system can be used for storing both the hot and the cold mediums for human comfort. In winter months, it can store cold fluid, which can be reused effectively when the atmosphere becomes hot. Similarly, in summer months, it can store hot fluid for its reuse in the cold atmosphere. Therefore, it does not consume power for space heating and cooling but only reuses the stored energy effectively. It is a field scale problem involving huge space for storing energy such as underground storage inside natural rocks in earth. The role of mathematical model for field simulation is of great importance. The model is initially developed on a small scale and compared against lab experiments. Once validated, we can simply use larger length and time scales to simulate the practical storage system. The model will be valid equally for both the cases. One can use a length of 100 m instead of 1m and a time scale of 3 months instead of 1 hour. For a lab scale problem through a pipe containing saturated porous medium, velocity profile is practically constant. So it has been used for analysis in this chapter.

The validation of such a model has been considered in the Chapters 6 to 9. The boundary conditions of step response in Chapters 6 & 7 and frequency response in Chapters 8 & 9 are close to those for a practical storage system. The storage system considers alternate flow of hot and cold fluids through the porous bed, which has been considered in these chapters. Chapters 6 & 7 consider single flow of hot fluid through a cold domain whose effect is similar to that of hot phase of the oscillatory flow. Similarly, Chapters 8 & 9 considers the effect of time variable but periodic boundary conditions similar to the combined effect of the hot and the cold phases on the porous domain. Hence, the mathematical model is well tested against lab scale experiments. One can increase the length and time scale in numerical simulation and the results are equally valid but on a larger scale.

The thermal performance of porous medium for energy storage is discussed in this chapter. It depends on the thermal properties of the solid and the fluid phases. The other properties of interest are the frequency of oscillations, storage space, Reynolds numbers, particle size, porosity, number of cycles, thermal non-equilibrium and the effect of heat loss from the bed. Various thermal properties of the solid phase are considered. Glass and plastics have properties close to water but the steel properties are considerably different. The axial conduction in steel may distort the thermal front as seen in the previous chapters. A detailed analysis of energy storage in the porous medium is carried out using 1 and 2-equation models of heat transfer. Both the unsteady and the steady states of the storage system are discussed. The effectiveness of the porous bed for energy storage is defined and calculated for each case. The temperature profiles, governing the performance of the storage system are plotted at various instants of time in a cycle and for number of cycles elapsed. The mathematical expressions are developed for energy storage in the fluid and the solid phases, energy entering and leaving the porous bed. Further, an energy balance is carried out for the bed, which helps in choosing a reasonably fine space grid and the number of time steps.

10.2 ENERGY STORAGE IN POROUS MEDIUM

10.2.1 Physical Model

Figure 10.1 shows the systematic representation of an energy storage system. Figure 10.1(a) shows the physical model; the beads are closely packed inside a tube of radius R. The length of the tube is L in non-dimensional form. The porous bed is assumed fully water-saturated and maintained initially at zero temperature everywhere i.e. the cold-water temperature. The velocity of fluid through the bed is sinusoidal changing its direction after each phase. The temperature profiles are shown in Figure 10.1(b). The x-axis shows the distance from the respective ends, i.e. the distance from the hot end during the hot phase and the cold end during the cold phase, and the y-axis shows the temperature.

During the positive half, hot fluid enters the bed through one of the ends and the temperature of the bed rises. The rise is greater near the hot end and temperature profile with respect to distance resembles the line sloping down as shown in Figure 10.1(b). The temperature is unity, the maximum value, at $z = 0$ but its value at $z = L$ should be close to zero. It ensures that energy leaving the bed through the cold end is zero. In the negative half,

the cold water enters the domain through the opposite end and the temperature of the bed falls. The temperature profile in the cold phase follows the profile as shown by line sloping up in Figure 10.1(b). The temperature is zero at the cold end but it should be close to unity at the hot end for maximum effectiveness.

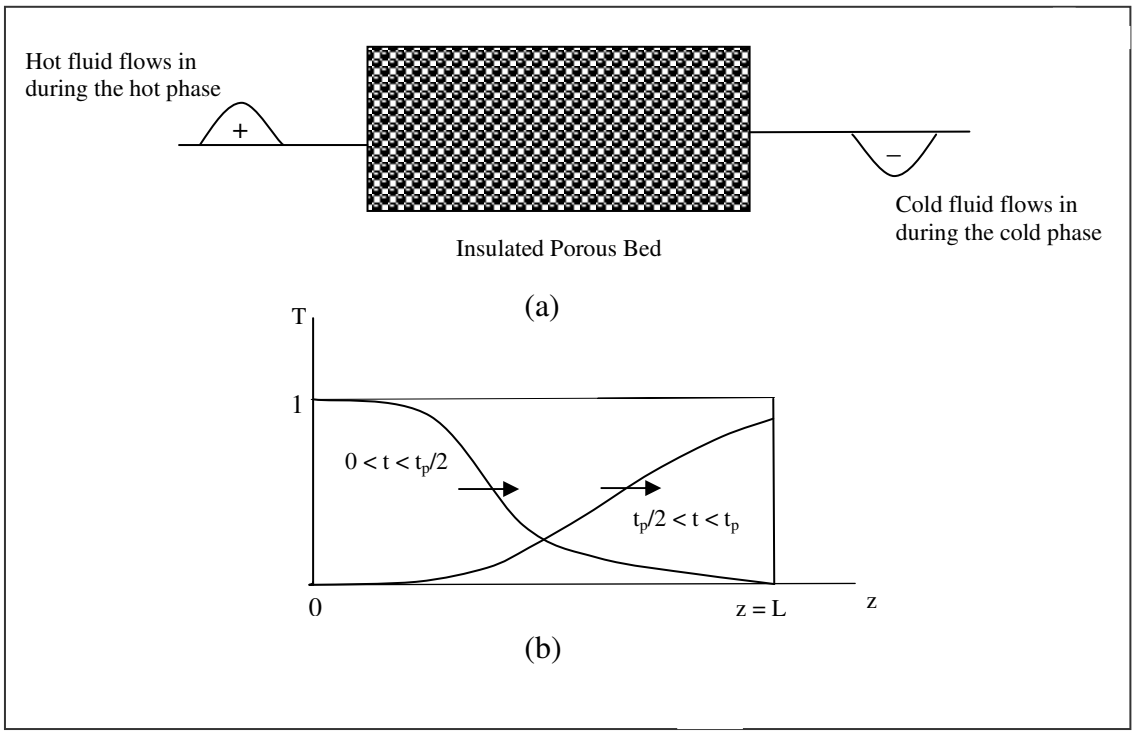

Figure 10.1: The systematic representation of an energy storage system. (a) Physical model (b) Temperature profiles.

During the hot phase the temperature at a location, say at midpoint, rises due to storage of energy but falls during the cold phase due the retrieval and hence resembles a cyclic change in temperature. The solid and the fluid phase temperatures are distinct in the bed though vary in the similar fashion. During the unsteady period, these profiles change from one cycle to another. When the cyclic steady state is reached, no change occurs at corresponding instants of two successive cycles and the performance reaches an optimum level. The idea is to use these profiles to find the parameters favorable for storage and retrieval of energy.

10.2.2 Boundary Conditions

The above-mentioned conditions of flow and temperature are incorporated in the numerical simulation through appropriate boundary conditions. The velocity is sine type and is positive during the hot phase but negative during the cold phases i.e.

$$u = u\,\sin(\omega t) \text{ and } \quad \text{Hot phase}: 0 < \omega t < 180^{\circ}; \text{Cold phase}: 180^{\circ} < \omega t < 360^{\circ} \qquad (10.1)$$

In the hot phase, the hot fluid flows in through the hot end and the fluid non-dimensional temperature is assigned unity value. The outflow boundary condition of zero temperature derivative in axial direction for both the phases at $z = L$. Hence

$$T_{z=0} = 1 \text{ and } \left(\frac{\partial T}{\partial z}\right)_{z=L} = 0 \qquad (10.2)$$

In the cold phase, the flow direction is reversed and the cold fluid enters through the opposite cold end. Here the temperature is assigned zero value. The fluid and the solid phases temperatures are assigned zero gradients in axial direction at $z = 0$. Hence

$$T_{z=L} = 0 \text{ and } \left(\frac{\partial T}{\partial z}\right)_{z=0} = 0 \qquad (10.3)$$

Along the tube axis, axi-symmetry of the temperature field is assumed for both the fluid and the solid phases:

$$\left(\frac{\partial T}{\partial r}\right)_{r=0} = 0 \qquad (10.4)$$

The heat flux is prescribed for heat loss through the tube wall for the fluid and the solid phase as follows

$$-\left(\frac{\partial T_f}{\partial r}\right)_{r=1} = \frac{\mathrm{Bi}}{\lambda}\left((T_f)_{r=1} - T_\alpha\right) \qquad \text{and} \qquad -\left(\frac{\partial T_s}{\partial r}\right)_{r=1} = \mathrm{Bi}\left((T_s)_{r=1} - T_\alpha\right) \qquad (10.5)$$

The numerical computation is carried out for temperature fields inside the porous bed. The grid size of 1% of the total length and time steps of 0.1 % of the total time are used to provide reasonable accuracy. The number of cycles is chosen such that cyclic steady state is reached.

10.2.3 Effectiveness of Energy Storage

As the hot fluid enters the bed, its energy is stored in the solid as well as the fluid phases contained in the bed. As a result, the fluid leaves the bed with negligible energy. Consequently, the temperature of the bed rises. For a perfectly insulated bed, the stored

energy is calculated by the difference of incoming and outgoing fluid energies. This difference integrated over the hot phase gives the total stored energy. Similarly, in the cold phase, the stored energy is retrieved by the flow of cold fluid from the opposite end. It can be calculated by the difference of outgoing and incoming fluid energies. During the initial unsteady period, the stored and the retrieved energies are unequal. Once the cyclic steady state is reached, these two energies become equal.

The stored energy can also be calculated by the rise in temperature of the solid and the fluid phases contained in the bed. An integration of the solid and fluid phase temperature over the length of the bed for a particular point of time gives the energy level. The stored energy over a time period can then be calculated by the difference of energy levels between the two time limits, say the start and the end of the hot phase. An energy balance based on the equality of the stored energy with the incoming and outgoing energies helps to ensure that the time and grid space is reasonably fine.

Consider the flow of hot fluid, the stored energy in this phase is obtained by integrating the energy difference of incoming and outgoing energies as

$$E_{stored} = \int_0^{t_P/2} \left(E_{In} - E_{out}\right) dt \tag{10.6}$$

The hot fluid leaves the bed at a temperature of T. Substituting for the respective energy terms we get

$$\begin{aligned} E_{stored} = & \int_0^{t_p/2} \left(\rho c_P\right)_f u \sin(\omega t) \pi R^2 \left(T_{hot} - T_{cold}\right)_{z=0} dt \\ & - \int_0^{t_p/2} \left(\rho c_P\right)_f u \sin(\omega t) \pi R^2 \left(T - T_{cold}\right)_{z=L} dt \end{aligned} \tag{10.7}$$

Since $\int_0^{t_P/2} \sin(\omega t)\, dt = \frac{2}{\omega}$ we get

$$\begin{aligned} E_{stored} = & \left(\rho c_P\right)_f u \frac{2}{\omega} \pi R^2 \left(T_{hot} - T_{cold}\right)_{z=0} \\ & - \left(\rho c_P\right)_f \pi R^2 \int_0^{t_P/2} u \sin(\omega t) \left(T - T_{cold}\right)_{z=L} dt \end{aligned} \tag{10.8}$$

Similarly, the energy retrieved during the cold phase is given as

$$E_{retrieved} = \int_{t_P/2}^{t_P} (E_{out} - E_{in}) \, dt \tag{10.9}$$

The cold fluid leaves the hot end with a temperature of *T*, substituting for the respective energy terms, we get

$$\begin{aligned} E_{retrieved} = & \int_{t_P/2}^{t_p} (\rho c_P)_f \, u \sin(\omega t) \pi R^2 \left(T - T_{cold}\right)_{z=0} dt \\ & - \int_{t_P/2}^{t_p} (\rho c_P)_f \, u \sin(\omega t) \pi R^2 \left(T_{cold} - T_{cold}\right)_{z=L} dt \end{aligned} \tag{10.10}$$

Since during the cold phase, the cold water enters through cold end, its energy is zero. We get

$$E_{retrieved} = \int_{t_P/2}^{t_p} (\rho c_P)_f \, u \sin(\omega t) \pi R^2 \left(T - T_{cold}\right)_{z=0} dt \tag{10.11}$$

The difference of stored and retrieved energies are obtained from Equations 10.8 and 10.11 as

$$\begin{aligned} E_{stored} - E_{retrieved} = & (\rho c_P)_f \, u \frac{2}{\omega} \pi R^2 \left(T_{hot} - T_{cold}\right)_{z=0} \\ & - (\rho c_P)_f \pi R^2 \int_0^{t_p/2} u \sin(\omega t) \left(T - T_{cold}\right)_{z=L} dt \\ & - (\rho c_P)_f \int_{t_P/2}^{t_p} \pi R^2 u \sin(\omega t) \left(T - T_{cold}\right)_{z=0} dt \end{aligned} \tag{10.12}$$

Dividing the above equation by the stored energy, a factor ψ can be obtained as

$$\psi = \frac{E_{stored} - E_{retrieved}}{E_{stored}} = \frac{\frac{2}{\omega} - \int_0^{t_P/2} T_{z=L} \sin(\omega t) \, dt - \int_{t_P/2}^{t_P} T_{z=0} \sin(\omega t) \, dt}{\frac{2}{\omega} - \int_0^{t_P/2} T_{z=L} \sin(\omega t) \, dt} \tag{10.13}$$

or

$$\psi = 1 - \frac{\int_{t_p/2}^{t_P} T_{z=0} \sin(\omega t) dt}{\frac{2}{\omega} - \int_0^{t_P/2} T_{z=L} \sin(\omega t) \, dt} \tag{10.14}$$

At the steady state, the value of the ψ approaches zero. The grid size and the time steps in the numerical simulation are chosen such that the factor ψ is less than 0.01.

Effectiveness

The effectiveness of porous medium for energy storage indicates the amount of energy retrieved in the cold phase to the amount of energy supplied in the hot phase. Both these energy effects occur at the hot end. The effectiveness of the porous bed for energy storage is

$$Effectiveness = \frac{Energy\ outflow\ during\ the\ cold\ \ phase}{Energy\ inf\ low\ during\ the\ hot\ \ phase} \tag{10.15}$$

Since the temperature of in coming water is unity, the effectiveness during the hot phase can be written as

$$Effectiveness = \frac{\int_{t_P/2}^{t_P} \left(\rho c_p\right)_f \ \pi R^2 u\ sin(\omega t)(T - T_{cold})_{z=0}\, dt}{\int_{0}^{t_P/2} \left(\rho c_p\right)_f \ \pi R^2 u\ sin(\omega t)(T_{hot} - T_{cold})_{z=0}\, dt} \tag{10.16}$$

Canceling common terms and writing $\frac{(T - T_{cold})}{(T_{hot} - T_{cold})}$ as the non-dimensional temperature *T*, we get

$$Effectiveness = \frac{\int_{t_P/2}^{t_P} T_{z=0}\ sin(\omega t) dt}{\int_{0}^{t_P/2} sin(\omega t)\quad dt} \tag{10.17}$$

The denominator term of $\int_{0}^{t_P/2} sin(\omega t) dt$ is equal to $\frac{2}{\omega}$. Hence

$$Effectiveness = \frac{\omega}{2} \int_{t_P/2}^{t_P} T_{z=0}\ sin(\omega t) dt \tag{10.18}$$

The effectiveness depends upon the temperature variation at the hot end during the cold phase. If it becomes unity, the effectiveness becomes 100 %. In the above equation, the parameters such as frequency and time are in dimensional form. By changing time *t* to non-

dimensional form as $\frac{\alpha t\, Pe}{R^2}$ and substituting, the corresponding non-dimensional values in the above equation remains unchanged.

In the above analysis, the energy balance is based on the fluid inlet and exit energies during the two phases. In the second approach, the fluid and solid phase energies are calculated during the hot phase and an energy balance is again established.

Approach 2

In this approach, the analysis is performed for the stored energy during the hot phase. It is given by the difference of incoming and outgoing fluid energy, is equated to that of the fluid and solid phases contained in the porous medium.

$$E_{stored} = E_{in} - E_{out} = E_{stored\ in\ fluid} + E_{stored\ in\ solid} \tag{10.19}$$

A parameter ϕ can be defined as

$$\phi = \frac{E_{in} - E_{out} - E_{stored}}{E_{in}} \tag{10.20}$$

$$= 1 - \frac{E_{out}}{E_{in}} - \frac{E_{stored}}{E_{in}} \tag{10.21}$$

The factor ϕ should approach zero for reasonably fine time and space grids.

Consider the first term in right hand side of the above equation.

$$\frac{E_{out}}{E_{in}} = \frac{\int_0^{t_P/2} (\rho c_p)_f \pi R^2 u \sin(\omega t)(T - T_{cold})_{z=L}\, dt}{\int_0^{t_P/2} (\rho c_p)_f \pi R^2 u \sin(\omega t)(T_{hot} - T_{cold})_{z=0}\, dt} \tag{10.22}$$

Rearranging the above term and writing in the non-dimensional form, we get

$$\frac{E_{out}}{E_{in}} = \frac{\omega}{2} \int_0^{t_P/2} T_{z=L} \sin(\omega t) dt \tag{10.23}$$

The second term comprises two terms belonging to the solid and the fluid phases as

$$\frac{E_{stored}}{E_{in}} = \frac{E_{solid} + E_{fluid}}{E_{in}} \tag{10.24}$$

Consider the stored energy in the solid phase. The volume occupied by the solid phase is $(1-\varepsilon)$ of the total volume. In the absence of heat loss to ambient, the energy stored in the

solid phase over the hot phase is obtained by integrating the stored energy over the length of the bed. The factor $\frac{E_{solid}}{E_{in}}$ is thus given as

$$\frac{E_{solid}}{E_{in}} = \frac{(1-\varepsilon)(\rho c_p)_s \int_0^L \pi R^2 \{T_s(z,t_{P/2}) - T_s(z,0)\} dz}{\int_0^{t_P/2} (\rho c_p)_f \pi R^2 u \sin(\omega t)(T_{max} - T_{min})_{z=0} dt} \tag{10.25}$$

Solving the above equation and writing temperature in non-dimensional form we get,

$$\frac{E_{solid}}{E_{in}} = \frac{(1-\varepsilon)}{2\beta} \frac{\omega R}{U} \int_0^{L/R} \{T_s(z,t_{P/2}) - T_s(z,0)\} dz = f_1(\text{ say }) \tag{10.26}$$

Similarly, for the fluid phase, the stored energy parameter is given as

$$\frac{E_{fluid}}{E_{in}} = \frac{(\varepsilon)}{2} \frac{\omega R}{u} \int_0^{L/R} \{T_f(z,t_{P/2}) - T_f(z,0)\} dz = f_2 \tag{10.27}$$

In the above two equations, the parameter $\frac{\omega R}{U}$ is in non-dimensional form. Substituting $t^* = \alpha \frac{t}{R^2}$, so that frequency is also non-dimensional, we get,

$$f_1 = \frac{E_{solid}}{E_1} = \frac{(1-\varepsilon)}{2\beta} \frac{\omega^*}{\text{Pe}} \int_0^{L/R} \{T(z,t_{P/2}) - T_s(z,0)\} dz \tag{10.28}$$

$$f_2 = \frac{E_{fluid}}{E_1} = \frac{(\varepsilon)}{2} \frac{\omega^*}{\text{Pe}} \int_0^{L/R} \{T_f(z,t_{P/2}) - T_f(z,0)\} dz \tag{10.29}$$

where ω^* is non-dimensional frequency.

The energy balance becomes

$$\phi = 1 - \frac{E_{out}}{E_{in}} - f_1 - f_2 \tag{10.30}$$

The value of the factor ϕ should be close to zero for energy balance in the bed over the hot phase. The factor $\int_0^{L/R} \{T(z,t_{P/2}) - T(z,0)\} dz$ gives the measure of stored energy in the solid and

the fluid phases of the bed during the hot phase. It can be calculated for various configurations of the bed and the performance can be quantitatively compared.

10.3 THERMAL PERFORMANCE

A detailed thermal analysis of the porous bed for energy storage is carried out. Various configurations of the porous bed are considered by varying the physical dimensions of the bed, thermo-physical properties of the solid particles, fluid velocity and oscillating frequency. The thermal equilibrium and non-equilibrium models of heat transfer are used for numerically solving the governing equations. Instantaneous temperature distributions inside the porous bed are plotted for judging the thermal performance of the bed. Amplitude of temperature fluctuations in the bed is considered. The extent of thermal non-equilibrium in between the two phases is discussed and the resulting difference between 1 and 2-equation models is also considered. The optimum parameters giving the maximum effectiveness are obtained. Various energy terms and energy balances, are obtained from the temperature profiles. A reference configuration, based on previous studies, is first presented and the temperature profiles are plotted to understand the working of the bed. The parameters are changed with respect to this configuration and the corresponding thermal performance is compared. Since the numerical simulation is carried out in the non-dimensional form, the results can be used for field-scale cases by scaling up the governing variables suitably, such as by increasing the tube radius, the corresponding length and time-period are also scaled up. Similarly, by knowing the hot and the cold-water temperatures, the non-dimensional temperature profile at a location can be converted into corresponding dimensional profiles.

We now discuss instantaneous temperature distributions in the porous bed for the reference geometry.

10.3.1 Temperature Profiles

Consider a porous bed of L =10 having glass beads of diameter d_P contained in an insulated tube of radius R for which R/d_P is 12. Since the velocity follows a sine curve the corresponding Reynolds number based on the tube radius, also varies in the similar fashion. Its peak value is set to 100, which occurs at the middle of the hot and the cold phases, though in opposite directions. The frequency of oscillations, ω is set to unity in the non-dimensional

form; hence, the time t in a cycle varies from zero to 2π. The non-dimensional time is obtained by multiplying the time in seconds by a factor of $\frac{\alpha Pe}{R^2}$. For a tube radius of 30mm and normal ambient temperature of 25°C, the corresponding dimensional frequency is 0.095 rad/s. The fluid phase thermal diffusivity is 0.0144 cm^2s^{-1} and the Peclet number is 621. It corresponds to a time-period of 66 sec. The particle size is 2.5mm and the length of the bed is 300 mm. The simulation is performed over a number of cycles such that the cyclic steady state is reached.

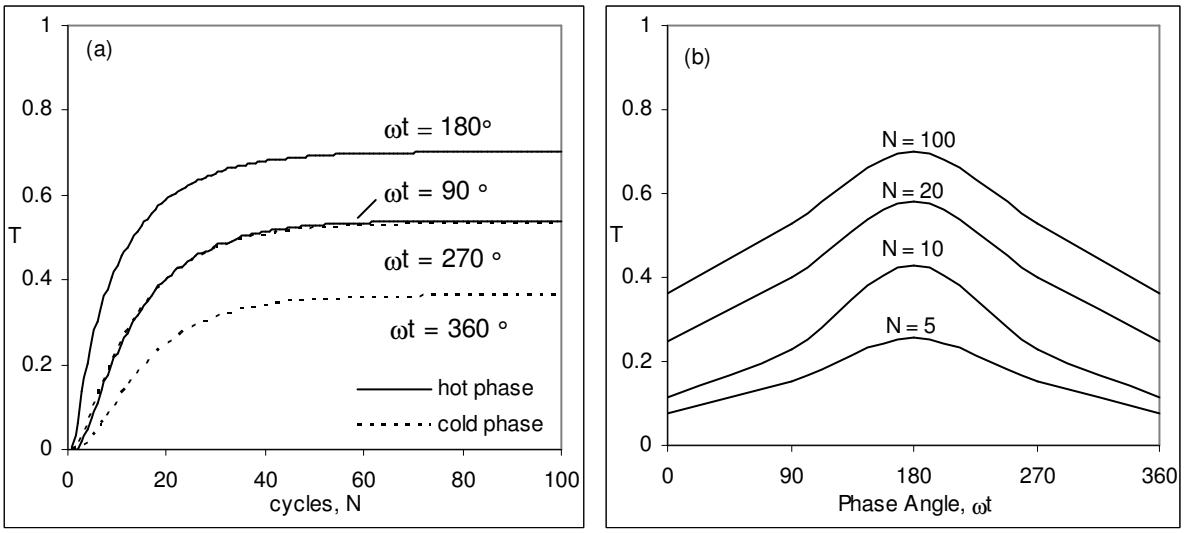

Figure 10.2: Variation of midpoint fluid temperature with time in glass-water bed: (a) Various points in a cycle; (b) Cyclic variations. Re =100, L= 10, ω =1.

Figure 10.2 shows the thermal performance of the bed over a period of 100 cycles using the 2-equation model. Figure 10.2(a) shows the temperature build up at the midpoint of the bed as a function of the number of cycles elapsed. The temperature profiles at the middle and the end of the hot and the cold phases are shown. It keeps fluctuating between these values rising during the hot phase and falling during the cold phase. These are represented by the corresponding phase angles. Phase angles ωt = 90° and 270° represent the middle of the hot and the cold phases while ωt = 180° and 360° represent the end of the two phases. At the start of simulation, the temperature is zero everywhere and but rises as a function of number of cycles elapsed. It reaches a cyclic steady state after around 60 cycles. The lowest temperature in the cycle occurs at the end of the cold phase i.e. ωt = 360° and the highest

temperature at the end of the hot phase i.e. $\omega t = 180°$. The corresponding values at steady state are 0.36 and 0.70 respectively. Hence, the temperature at midpoint fluctuates between these values cyclically and results into an amplitude of 0.34. At the middle of the hot and the cold phases, the respective temperatures are quite close at 0.53 and 0.54. Figure 10.2(b) shows the variation of temperature within a cycle from unsteady to the steady state of the bed at its midpoint. The phase angle is shown along the *x*-axis and the current cycle number is indicated. During the 5^{th} cycle, the minimum and the maximum temperatures are 0.07 to 0.25 and the amplitude of temperature fluctuation is 0.18. By 10^{th} cycle, the temperatures fluctuate between 0.11 to 0.43, and the amplitude rises to 0.32. In the 20^{th} cycle, the temperatures fluctuate between 0.24 and 0.58 and the amplitude rises to 0.34. By the steady state, the amplitude rises to 0.34 and the corresponding values of temperature are 0.36 and 0.70. The temperatures increase during the unsteady period but when the cyclic steady state is reached, theses values become constant from one cycle to another. This fluctuation is at midpoint; its value at other locations in the bed is obtained by plotting the temperatures profiles with respect to distance.

Figure 10.3 shows the temperature profiles with respect to distance as obtained at various instants of time in a cycle for the unsteady and the steady states. The sloping lines show the temperature profiles during the hot and the cold phases while the *x*-axis shows the corresponding distances from the respective ends i.e. from the hot end during the hot phase and from the cold end during the cold phase. The profiles are shown at the middle and the end of two phases. During the hot phase, the temperature at the hot end is unity but its value at the cold end should be close to zero in order to minimize the energy leaving the bed. Similarly, during the cold phase, the temperature at the cold end is zero but its value at the hot end should be close to unity in order to maximize the effectiveness, see Equation 10.18. At the start of the hot phase of any cycle *N*, the temperatures are at a minimum level but higher than zero. It rises during this phase but falls during the cold phase. The level of temperature at any instant in the bed can be judged by the length-averaged temperature.

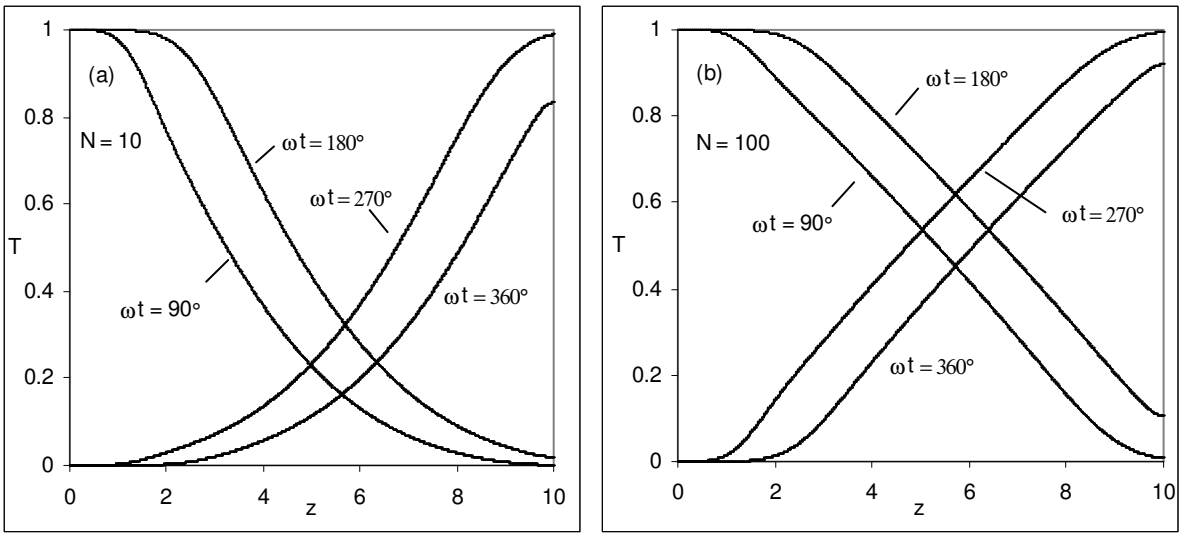

Figure 10.3: The variation of fluid temperature with distance in the glass-water bed. (a) Unsteady state, $N = 10$; (b) Steady state N= 100. Re =100, $L = 10$, $\omega = 1$.

Figure 10.3(a) shows the profiles during the unsteady period of 10^{th} cycle and Figure 10.3(b) for the steady state. The steady state profiles are much fuller and higher as compared to those at the unsteady state. In the unsteady period, the temperatures are rising in the bed and hence lower than the optimum values. The average fluid temperatures in the bed at the middle and end of the hot phase of 10^{th} cycle are 0.36 and 0.49 respectively. During the cold phase, it falls to 0.36 at the middle and to 0.23 at the end of the phase. At steady state, the average temperatures at the middle of hot phase rises to 0.52 and further rises to 0.65 by the end of the phase. During the cold phase, the values at the middle and the end of the phase fall to 0.51 and 0.38 respectively. As seen from Figure 10.3(b), the temperature at the cold end at the middle of the hot phase is nearly zero at 0.007, but it rises to 0.1 by the end of this phase. It results into loss of energy through the cold end. During the cold phase, it keeps fluctuating between 0 and 0.1. Similarly, the temperature at the hot end during the middle of cold phase is 0.99 but falls to 0.92 by the end of this phase. During the hot phase, the temperature here is unity and it fluctuates between 0.92 and 1.0. It lowers the effectiveness from the ideal value of unity. Hence, the fluctuations at the two ends should be within limits. It should fluctuate at the hot end to a value as close as possible to unity and that at the cold end to a value as close as possible to zero. The lower the fluctuations the more is the effectiveness.

10.3.2 Amplitude of Temperature Fluctuations

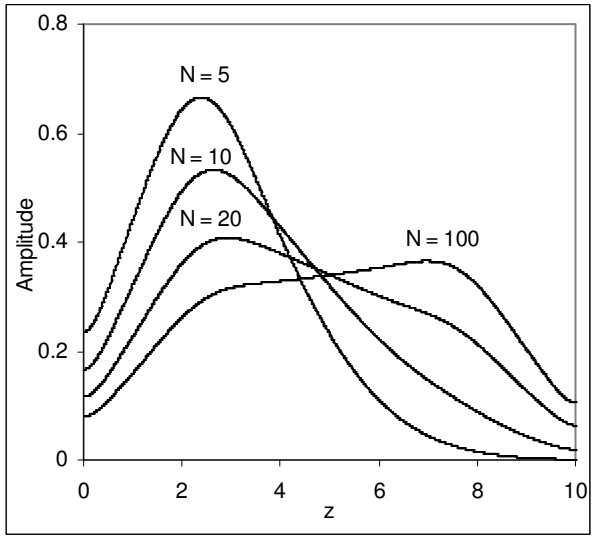

Figure 10.4: The amplitude of temperature fluctuations during the unsteady and steady period in glass-water bed. Re =100, $L = 10$, $\omega = 1$.

Figure 10.4 shows the amplitude of temperature fluctuations as a function of distance from the hot end for the unsteady and the steady states. It is calculated as the difference between the temperature profiles at the end of the hot and the cold phases in various cycles. The amplitude for the unsteady state is different from that for the steady state. The figure can be divided into two regions about its midpoint, first in which the amplitude falls with the number of cycles and the second in which it increases. Region 1 is the portion of the bed between the hot end and the midpoint whereas the midpoint and the cold end forms region 2. The trends of amplitude are distinct for the two regions. For region 1, the amplitude falls with the number of cycles but for region 2, it increases. The two regions converge at the midpoint of the bed where the amplitude is 0.33. Hence, the amplitude for the two regions approaches each other such that at steady state and becomes almost constant in most parts of the bed except near the ends where it falls. The amplitudes at the hot and the cold ends approach zero though the corresponding values in the unsteady states are different. At the hot end, it falls during the unsteady periods but at steady state remains greater than zero at 0.08. At the cold end, it increases from zero for unsteady state and reaches 0.105 at steady state.

The region 1 has a peak at its centre but falls in either direction. During the fifth cycle, the peak value is 0.66 that occurs at z =2.5 falling to 0.23 and 0.33 at the hot end and near the midpoint respectively. In region 2, the amplitude falls to zero at the cold end from its value of 0.33 near the midpoint. As the number of cycles increase, the peak in region 1 falls and region 2 becomes fuller. By 10^{th} cycle, the peak falls to 0.53 at z = 2.65 falling to a lower value of 0.16 at the hot end and to a value of 0.33 at the midpoint. In region 2, it falls from 0.33 at midpoint to a value of 0.01 at the cold end. By 20^{th} cycle the peak falls to 0.40 at z = 2.9 in region 1 thereby shifting marginally towards the midpoint. It falls to 0.11 at the hot end. In region 2, it falls from 0.33 to 0.06 at the cold end. Hence, the amplitude at the hot end falls with number of cycles elapsed but increases at the cold end. At steady state, the curve is quite flat and has a peak of 0.36 at z = 6.9. It falls to 0.08 at the hot end and to 0.105 at the cold end. The positive value at the hot end indicates that the temperature at the end of the cold phase is less than the ideal value of unity. The positive value at the cold end indicates that by the end of the hot phase, the temperature is more than zero. Ideally, these values should be zero in both the cases and the value of the constant amplitude in the bed should be large. Hence, the trends of the amplitude of temperature fluctuations in the bed are quite interesting. It provides useful information about energy storage for various beds. An ideal bed is one, which has constant amplitude falling to zero on either side.

10.3.3 Thermal Non-Equilibrium

The thermal non-equilibrium between the two phases, T_f - T_s is presented for the bed. It is obtained at various instants of time in a cycle from unsteady to steady state as shown in Figure 10.5 at the midpoint of the bed. During the hot phase, $0° < \omega t < 180°$, the fluid has higher temperature as compared to that of the solid, so the thermal non-equilibrium is positive. It becomes negative during the cold phase, $180° < \omega t < 360°$. Hence, it fluctuates periodically between the maximum and the minimum values in a cycle. These values of thermal non-equilibrium are almost equal and occur respectively at the middle of the hot phase, $\omega t = 90°$ and the cold phase, $\omega t = 270°$. At these instants, the rate of temperature change is the maximum and is approaching the corresponding optimum values. The thermal non-equilibrium is low during the unsteady states and increases as the steady state is approached. In the 5^{th} cycle, the maximum value of thermal non-equilibrium is 0.0034 but

increases to 0.0053 in the 10th cycle. By 20th cycle, there is hardly any further change in its value and hence attains a steady state. It is interesting to see that its value at the unsteady states is lower as compared to that for the steady state. The variation of thermal non-equilibrium at other locations needs to be discussed.

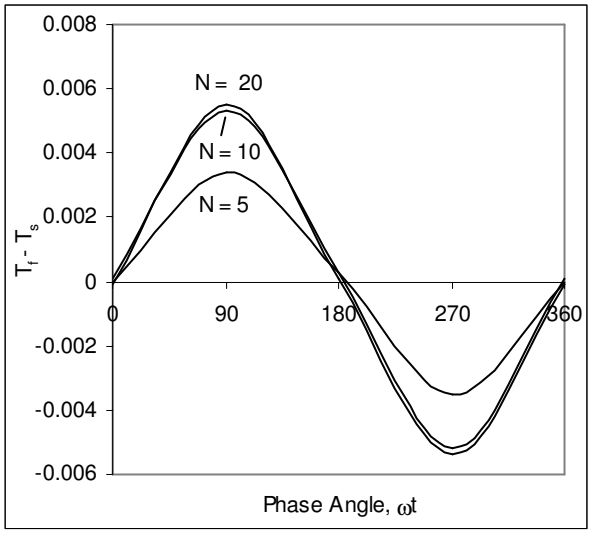

Figure 10.5: The pulse of thermal non-equilibrium for the glass-water bed at the midpoint. Re =100, L = 10, ω = 1.

Figure 10.6 shows the variation of thermal non-equilibrium with respect to distance from the hot end. Since the thermal non-equilibrium is high at the middle of the two phases, it is plotted for the hot and the cold phases in Figures 10.6 (a & b) respectively. The figure looks similar to that of the variation of amplitude of temperature fluctuations in the bed in the two regions as discussed earlier. The bed is divided into two regions, about its midpoint, and the trends of the thermal non-equilibrium are opposite in these regions. In region 1, it is initially high but falls with number of cycles elapsed and reaches a minimum at steady state. In region 2, its value is low during unsteady states, but increases with the number of cycles elapsed and becomes constant after steady state is reached. At the midpoint, the corresponding changes are very small. Here the thermal non-equilibrium is low in the 5th cycle but increases marginally and reaches a steady state by 20th cycle.

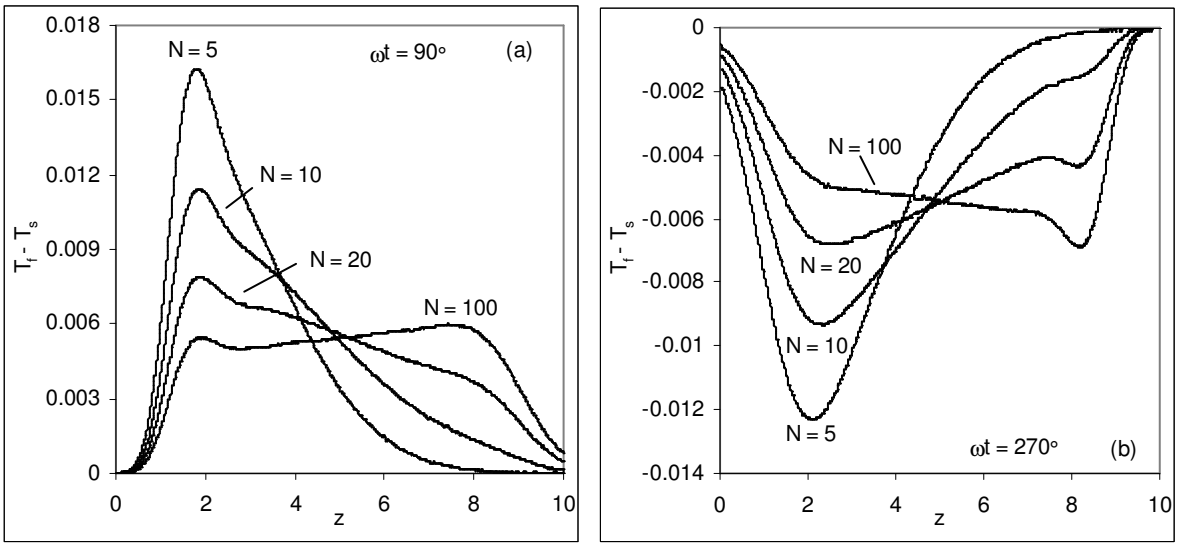

Figure 10.6: The variation of thermal non-equilibrium with distance for glass-water bed. (a) Middle of hot phase, ωt = 90°; (b) Middle of cold phase, ωt = 270°. Re =100, L = 10, ω = 1.

For a location in region 1, say z = 2.5, the thermal non-equilibrium decreases from unsteady to steady state. For a location in region 2, say z = 7.5, it increases from its value in unsteady state and reaches a maximum at steady state. At the two ends of the bed, the fluctuations are unequal for the two phases. At the hot end, z = 0, it fluctuates between zero to a negative value and at the cold end, z = 10, between a positive value and zero at the steady state. The thermal non-equilibrium is nearly constant in the bed at steady state, though marginally higher towards the cold end for both the phases.

The thermal non-equilibrium at the end of the two phases, ωt = 180° and 360°, is now discussed. Figure 10.7 shows the variation of thermal non-equilibrium at the end of the two phases. Its fluctuation at these instants is very small except for a marginal value at the two ends of the bed. While for midpoint of the two phases thermal non-equilibrium is positive for the hot phase and negative for the cold phase, at the end of the phases, it is both positive and negative in the bed. The fluctuations are again higher when heat transfer is unsteady for the hot phase but are lower for the cold phase as compared to the steady state.

The variation at the end of the hot phase, ωt = 180°, is shown in Figure 10.7(a). It is negative near the hot end but becomes positive for the remaining portion of the bed. It is zero at the hot end and becomes negative up to a location of z = 3.2 with a peak occurring at z = 2.4. It increases afterwards and reaches a peak at a location of z = 4.2 and approaches zero

at the cold end. As steady state is approached, the corresponding fluctuations become small and turn positive at the cold end.

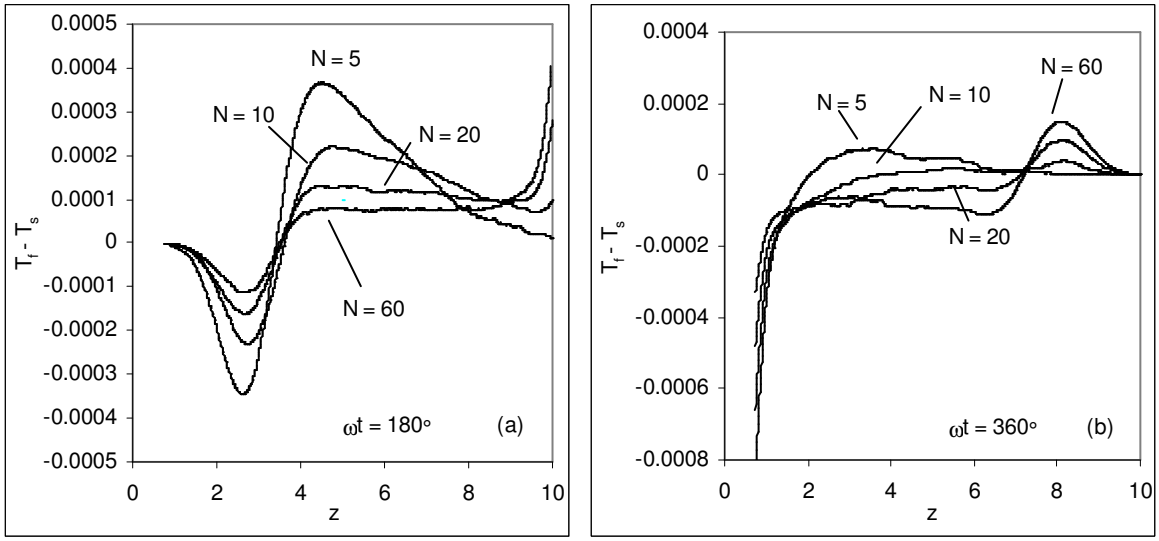

Figure 10.7: The variation of thermal non-equilibrium with distance for glass-water bed. (a) End of the hot phase, $\omega t = 180°$; (b) End of the cold phase, $\omega t = 360°$. Re =100, $L = 10$, $\omega = 1$.

A similar variation of thermal non-equilibrium, but in the opposite sense, is observed at the end of the cold phase, $\omega t = 360°$, Figure 10.7(b). It is positive near the cold end but becomes negative for the remaining portion of the bed. Its value at the cold end is zero. It increases with distance from the cold end and reaches a peak at $z = 8$ and becomes zero at $z = 7$. For the remaining portion of the bed, it is negative. The fluctuations are low for the unsteady states but increases with the number of cycles. At steady state, it has a large value at the hot end. Hence, the pattern of fluctuation is opposite to that of the hot phase though the corresponding values are smaller. The profiles shown are plotted using averaging over a large number of points and in general, the values are negligibly small as compared to that of the middle of the two phases.

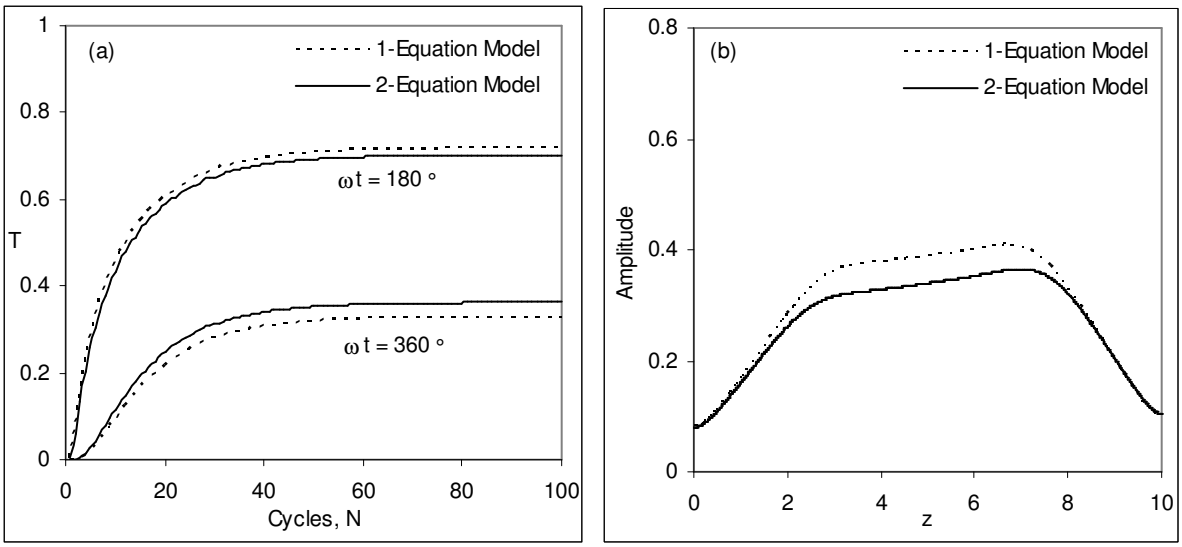

Figure 10.8: Difference between 1 and 2-equation models at the end of two phase in glass water bed. (a) Various points in a cycle at the midpoint; (b) Amplitude of temperature fluctuations. Re =100, L= 10, ω =1.

The difference between the 1 and 2-equation models is now discussed. Figure 10.8(a) shows the temperature build up at the midpoint of the bed as a function of number of cycles elapsed using 1 and 2-equation models. At the end of the hot phase, ωt = 180°, temperature as predicted by the 1-equation model is higher as compared to that of the 2-equation model and at the end of the cold phase, ωt = 360°, it is lower. The resulting amplitude of temperature fluctuations in the cycle is shown in Figure 10.8(b). Its value as predicted by 1-equation model is higher than that of the 2-equation model in most part of the bed, though at the ends they are equal for the two models. Figure 10.9 shows the difference between the two models as a function of phase angle at the steady state. The temperatures are shown along the y-axis and the secondary y-axis shows the difference between the two models. The 1-equation model predicts a faster moving temperature profile as compared to that of the 2-equation model. By the end of the cold phase, ωt = 360°, the 1-equation model predicts a lower temperature as compared to that of the 2-equation model. By the end of the hot phase, ωt = 180° the response of 1-equation model becomes faster than that of the 2-equation model. At the middle of the two hot phases, ωt = 90° and 270°, the difference between the two models is negative but unequal.

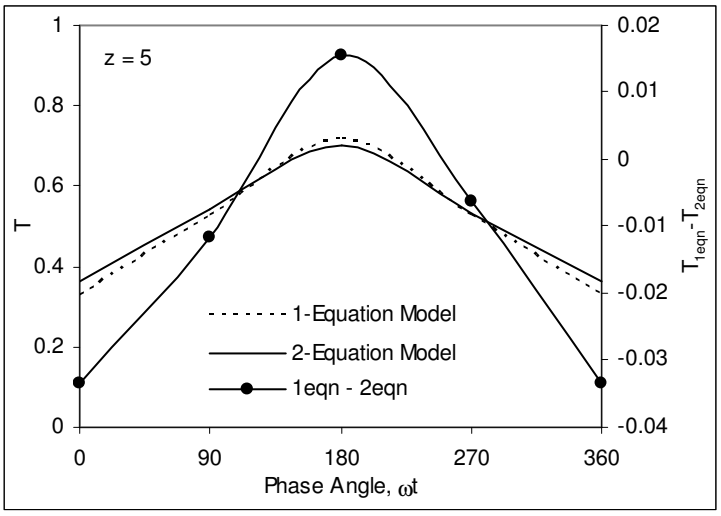

Figure 10.9: The temperature profiles of 1 and 2-equation models as a function of phase angle and the pulse of temperature difference between the 1 and 2-equation models for glass-water bed at steady state. Re =100, L= 10, ω =1.

The temperature difference between the two models, at steady state, is plotted as a function of distance from the hot end in Figure 10.10. The profiles at the middle and the end of the two phases are shown. The profiles of the hot phase, ωt = 90° and 180°, follow a particular trend such that both increase with distance from the hot end and the peak value of the profile at ωt = 180°, is higher. The profile at ωt = 90° has a peak of 0.0124 at z = 1.75, drops and becomes negative with a minimum value of -0.02 at z = 8.4 and again rises and attains a negative value at the cold end. The profile of ωt = 180° rises from the hot end to a maximum value of 0.025 at z = 3.5 and then drops to marginally negative value of 0.0048 at the cold end. The profiles of the cold phase, ωt = 270° and 360°, also follow these trends but in an opposite sense to that of the hot phase. Hence, the differences are less at the two ends of the bed. For a location close to hot end, say z =2, the difference for ωt = 180° is smaller than that for middle of the two phases, ωt = 90° and 270°. In addition, for a location near the cold end, say z =8, the difference for ωt = 360° becomes lower than that at the middle of the two phases. Hence, the normal trend of high difference at the end of the two phases is only followed in the central region of the bed. The difference between the two models chnages along the length of the bed.

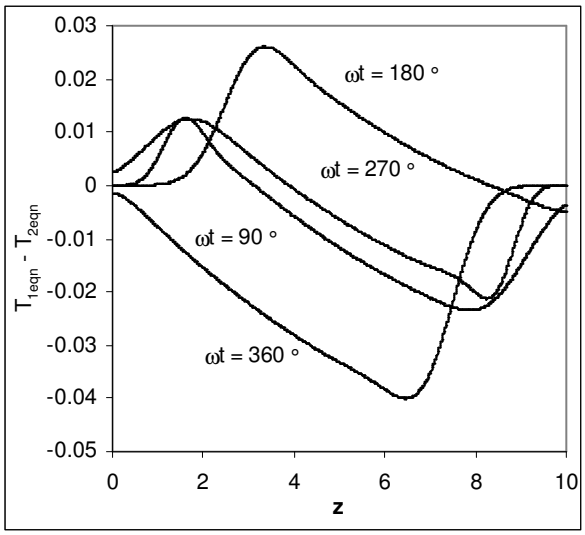

Figure 10.10: The variation of temperature difference between the 1 and 2 equation models for glass-water bed. Re =100, L= 10, ω = 1.

10.3.4 Energy Storage

The energy is stored in the bed during the hot phase, and retrieved during the cold phase by the flow of cold water. It is stored in the solid as well as the fluid phases contained in the bed, reaching an optimum level by the steady state. Apart from the energy stored, some energy is lost through the cold end during the hot phase, as given by the factor E_{out}/E_{in} in Equation 10.23. The value of this factor is 2.1 % of the incoming energy. The energy balance for the incoming and outgoing fluid energies as given by the factor ψ, Equation 10.14, has a value of 0.5 %. The effectiveness of the bed relates to temperature level of cold water attained while its flow through the hot bed in the cold phase. Since this temperature is less than the ideal value of unity, the effectiveness of the bed is 98.3 %. At steady state, the stored energy in the solid and fluid phase is 40.5 % and 52.2 % of the total supplied energy. For the stored energy, the balance is given by the factor of ϕ in Equation 10.30. The value of this factor is 5 %. The higher value of this factor is due to integration carried over the length of the bed instead of the cold ends. Hence, both the excess energy balances are quite small. The temperature fluctuations are higher in 1-equation model as compared to that of the 2-equation model and the effectiveness is marginally higher at 98.6% and energy lost, E_{out}/E_{in} is only 1.7 %.

We now consider the effect of changes of various bed parameters on temperature profiles and the energy storage.

10.4 PARAMETRIC STUDY

In this section, the effect of physical parameters such as length, frequency and the particle size of the porous bed on the thermal performance of the bed are considered.

10.4.1 Effect of Bed Length

The effect of change in bed length on the thermal performance is discussed. It is changed from its reference value of 10 to 5 and 15, keeping other conditions unchanged. It results in a change in the average temperature of the bed during the two phases. A decrease in length means that during the hot phase, the energy has to be stored in a smaller volume with respect to the reference and results in a higher value of the average temperature in the bed. During the cold phase, the stored energy has to be retrieved through a smaller volume and the average temperature becomes lower. Similarly, as the length of the bed is increased it results to a lower temperature during the hot phase but a higher temperature during the cold phase. The other effect of the change in length is the amount of energy leaving the bed via the cold end during the hot phase, E_{out}/E_{in} . It increases with a decrease in the length of the bed and lowers the effectiveness. On the other hand, an increase in length of the bed results to under-utilization of the available storage volume.

Figure 10.11 shows the temperature profiles with respect to distance at the middle and the end of the two phases for the lengths of L = 5 and 15. The temperature profiles of L = 5 as shown in Figure 10.11(a) are fuller and the corresponding deviation between the two lines is larger when compared to that for L= 15, Figure 10.11(b). The exit energy loss is higher for L= 5 as indicated by the hot phase profile at ωt = 180°, being around 4 % of the total energy supplied. The profiles shown in Figure 10.11(a) do indicate a better utilization of the bed space for energy storage as compared to that in Figure 10.11(b).

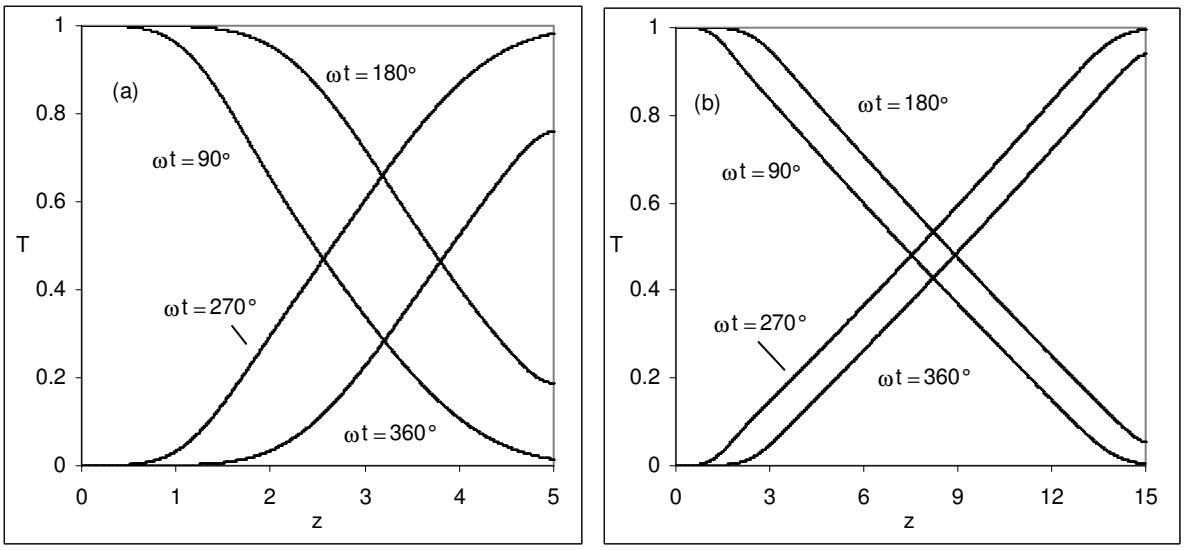

Figure 10.11: The variation of fluid temperature with distance in the glass-water bed. (a) L = 5; (b) L = 15. Re =100, ω = 1.

Figure 10.12 shows the variation of average temperature in the above-mentioned beds as a function of the number of cycles elapsed. For the ease of comparison, the reference profiles for the bed of L = 10, are also shown in the figure. At the end of the hot phase, the temperature profile corresponding to L = 5 is the highest and that for L = 15 the lowest. At the end of the cold phase, the profile for L =5 has the lowest value and that for L= 15 the highest value. The number of cycles required to reach steady state is different in each case. The bed of L = 5 reaches steady state quite early as compared to that for the other beds and the corresponding temperatures fluctuations are also higher.

Table 10.1 presents average temperatures in the bed at the middle and the end of the two phases for bed lengths of L = 5, 10 and 15. The average temperature in the bed at the end of the hot phase is the highest for L =5 and the smallest for L =15. However, at the end of the cold phase, this trend is reversed. The other observation from this table is that, for shorter bed lengths, the rise during the first half of hot phase, $0° < \omega t < 90°$, and the fall during the first half of cold phase, $180° < \omega t < 270°$ are higher as compared to that for the corresponding values in the second half. For higher lengths, the two values approach each other. Table 10.2 gives the temperatures at the cold and the hot ends corresponding to ωt = 180° and 360° respectively. At the cold end for ωt = 180°, the bed of L= 5 has the highest value at 0.1874 and this value is the lowest for L= 15 at 0.054. A higher value results into

larger exit losses through the bed. On the other hand, high temperature at the hot end for ωt = 360° ensures high effectiveness. Its value is the highest for the bed of L= 15 at 0.93.

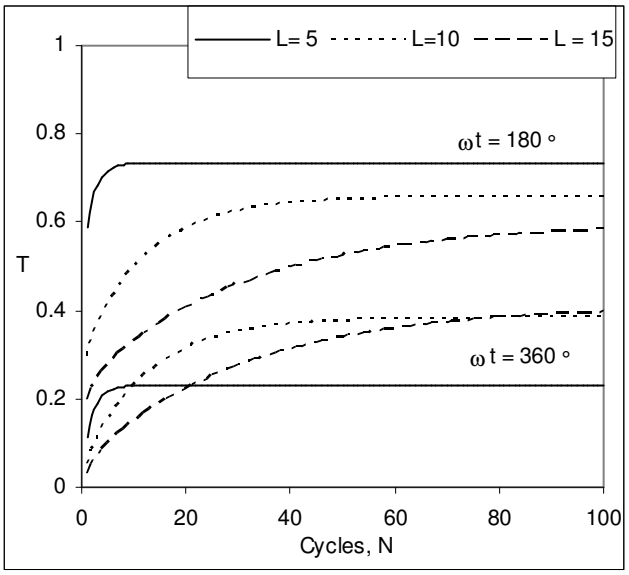

Figure 10.12: Effect of change in bed length: The variation of average temperature with time in the glass-water bed. Re =100, ω = 1.

Table 10.1: Average temperature in glass-water bed for various bed lengths. Re =100, ω = 1.

Length of the bed, L	ωt = 90°	ωt = 180°	ωt = 270°	ωt = 360°
5	0.514	0.7344	0.458	0.2319
10	0.5263	0.6571	0.5141	0.38
15	0.4923	0.5826	0.4862	0.3963

Table 10.2: Fluid temperatures at the hot and cold ends in glass-water bed. Re =100, ω = 1.

Length of the bed, L	z =L, ωt = 180°	z =0, ωt = 360°
5	0.1874	0.7589
10	0.1051	0.92
15	0.0548	0.9388

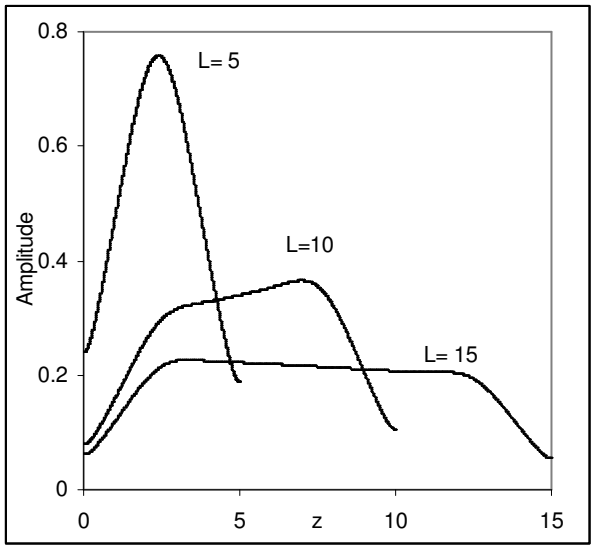

Figure 10.13: Effect of change in bed length: Variation of amplitude of temperature fluctuations in the glass-water bed. Re =100, ω = 1.

Figure 10.13 shows the amplitude of temperature fluctuations for the bed lengths of L = 5, 10 and 15. Its value is the highest for a bed of L = 5 having a peak value of 0.75 at the midpoint but falls sharply towards the ends. The bed of higher length has a moderate value of the fluctuations but is uniform throughout the bed. High temperature fluctuation indicates high energy storage in the bed. The effectiveness of energy storage for L= 5 is marginally lower at 94 % as against 98.6 % for the reference case. Hence reducing the length by 5 does not affect much as far as energy storage is concerned. For L = 15, its value is close to that of the reference at 98.7 %. However, the capacity of storage is not fully utilized in this bed.

A decrease in bed length has the same effect as that of an increase in the flow rate. The effect of change in flow rate can thus be considered qualitatively as similar to that of the change in bed length.

10.4.2 Effect of Frequency

In this section, the effect of frequency different from the reference value of unity is discussed. The change in frequency affects the time period such that as the frequency is increased, the time period falls, less time is available for the storage and retrieval of energy. If the time period increases, the supply of energy is higher. The frequency is changed from the reference value of unity to ω = 0.5 and 2. Figure 10.14 shows the effect of change in frequency of oscillations on the average temperature of the bed for various instants of time.

At a frequency of ω = 0.5, the storage of energy is higher and the resulting average temperature is higher. It is lower during the cold phase and retrieves a larger amount of energy. On the other hand, for ω = 2, the time period is smaller and the temperature build up is slower during the hot phase, and the steady state temperature is also lower. During the cold phase, the corresponding temperature drop is lower. It results in a higher steady state temperature and the temperature fluctuations are smaller. The number of cycles required for the steady state is also higher as compared to that for the lower frequencies of ω = 0.5 and 1.

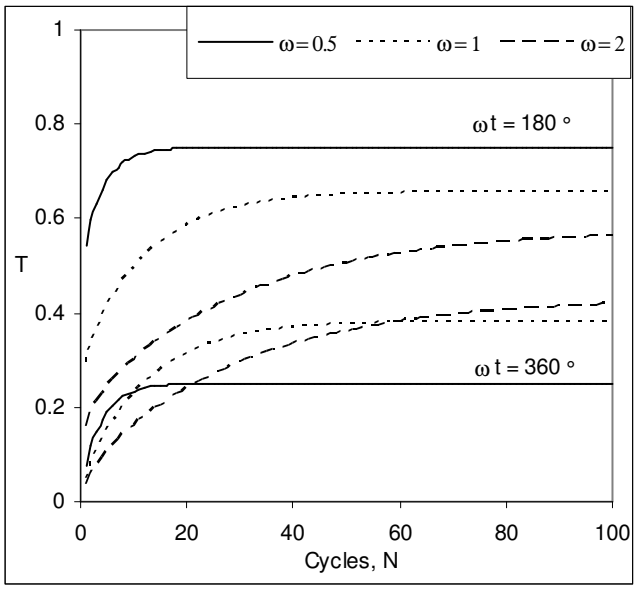

Figure 10.14: Effect of change in frequency: Variation of average temperature with time in the glass-water bed. Re =100, *L*=10.

Figure 10.15 shows the temperature profiles with respect to distance from the respective ends at steady state. It is shown at the end of the two phases for the above-mentioned frequencies. At the end of the hot phase, the profile corresponding to ω = 0.5 has the highest value of temperature and the corresponding exit losses are the highest. Higher time period results into more supply of energy and hence higher temperatures. The profile of ω =2 is of the lowest value but the exit losses are also minimum. The reference temperature profiles are in between these two profiles. The profiles at the end of the cold phase are also shown in the figure. Here the trends are reversed. The frequency of ω = 2 has the highest temperature in the bed but lower fluctuation at the hot end. The profile of ω = 0.5 has the lowest temperature and the corresponding fluctuation at the hot end is a maximum.

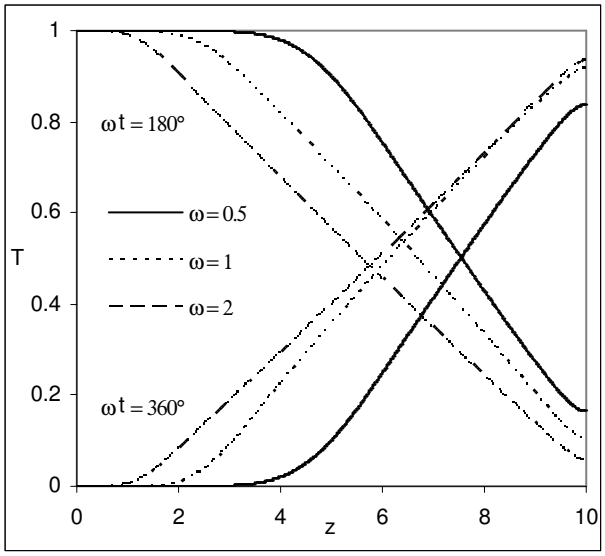

Figure 10.15: The effect of change in frequency: The variation of fluid temperature with distance in the glass-water bed. Re =100, L = 10.

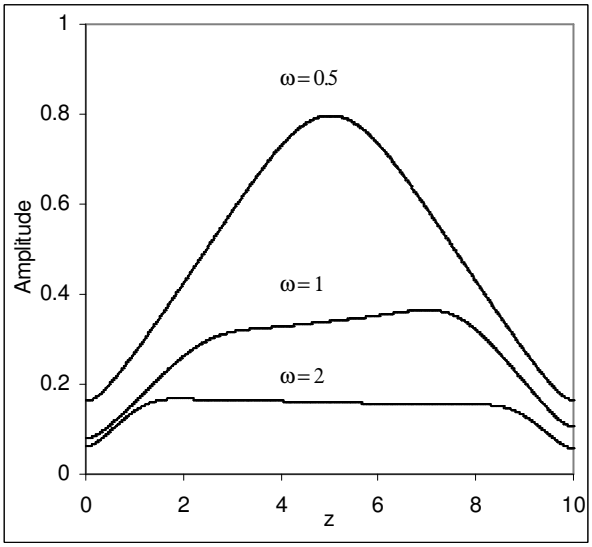

Figure 10.16: The effect of change in frequency: The variation of amplitude of temperature fluctuations with distance in the glass-water bed. Re =100, L = 10.

Figure 10.16 shows the amplitude of temperature fluctuations in the bed as a function of distance from the hot end. The fluctuations for ω =2 are the lowest but quite uniform throughout the bed. Its average value is 0.145, which is less than that of the reference whose average value is 0.36. For ω = 0.5, the peak value is very high at 0.80 but falls rapidly with distance from the midpoint on either side. Its average value is larger as

compared to that for other frequencies at 0.49. Hence, the energy stored and retrieved is large for this frequency. It increases with the temperature fluctuations and but should be uniform in the bed for maximum space utilization.

The effectiveness of energy storage is obtained in each case. For $\omega = 0.5$, its value is 97.4 % and the stored energy is large as compared to the other cases. For $\omega = 2$ its value is 98.3 % but here the stored energy is quite small. The effect of change in frequency is similar qualitatively to that of the length of the bed. An increase in both the values results in similar results. The effectiveness does not indicate the true amount of energy stored as the energy input varies with frequency. However, the fraction of energy stored in the solid phase of the incoming energy is equal for the three cases though the energy supplied is different. For $\omega = 0.5$, the energy stored is 1.82 times that of the reference case but for $\omega = 2$, it is only 0.53 times. Hence decreasing the frequency results into an increase in stored energy levels though exit losses are marginally higher. It is greater by a factor of 2.25 with respect to the reference for $\omega = 0.5$; for $\omega = 2$, this factor is only 0.37.

10.4.3 Effect of Particle Size

The effect of change of particle size d_p is discussed in this section. A change in particle size affects the porosity of the bed. The particle size is changed from 2.5 mm in the reference bed in either direction 1.3 mm and 4.76 mm. It affects the porosity, which changes to 0.3 and 0.40 respectively. Therefore, the interphase heat transfer area of the bed, as given by Equation 3.76, changes. It increases with a reduction in d_p. The other effect is on the rate of mixing of the fluids due to the presence of the porous medium; it increases with a reduction in d_p. Figure 10.17 shows the variation in particle size on average temperature in the glass-water bed as a function of number of cycles elapsed. The effect of increase in particle size results in lower average temperatures at the end of the two phases, as compared to that for d_p= 2.5 mm. The difference between the two curves however, remains unchanged. During the unsteady state, the temperature corresponding to d_p= 2.5 mm is lower in the hot phase. As the particle size decreases to 1.3 mm, the temperature changes become slow during both phases but there is no effect on steady state temperatures.

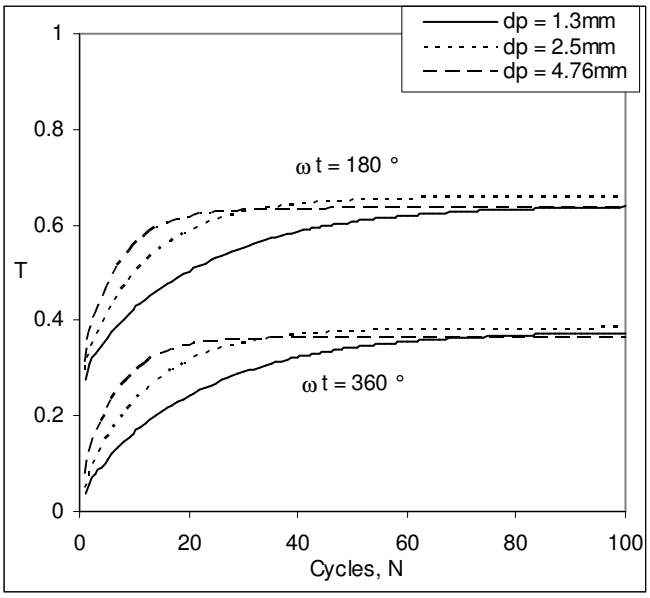

Figure 10.17: The effect of change in particle size: Variation of average temperature in the glass-water bed with time. Re =100, L=10, ω = 1.

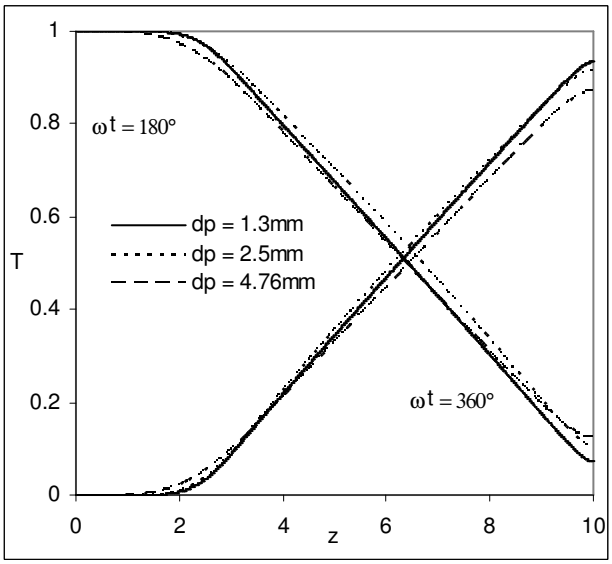

Figure 10.18: The effect of change in particle size: Variation of fluid temperature with distance in the glass-water bed. Re =100, L = 10, ω = 1.

Figure 10.18 shows the temperature profile with respect to distance in the bed. During the cold phase, the effect of an increase in particle diameter results into a marginally lower temperature. During the hot phase, the three curves look identical. Hence, most of the difference is observed only during the unsteady period.

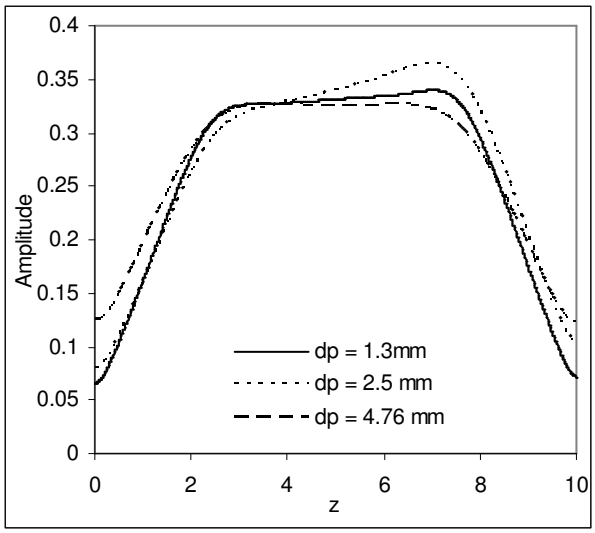

Figure 10.19: The effect of change in particle size: The variation of amplitude of temperature fluctuation with distance in the glass-water bed. Re =100, L = 10, ω = 1.

The amplitude of temperature fluctuations is shown in Figure 10.19 for various particle diameters. The fluctuation for d_p= 4.76mm is uniform throughout the bed but higher near the cold end. Those for d_p= 1.3 and 2.5 mm look unexpected. There is hardly any change in the average values for the three cases. The fluctuations near the ends are the highest for d_p= 4.76mm. Higher particle size has a lower storage space in the form of solid particles but more space for the stagnant fluid. For d_p= 1.3 mm, the energy in the solid phase is the highest but that in the fluid phase the lowest. The reverse happens for d_p= 4.76 mm. The energy stored in the solid phase is 107 and 93 % respectively of the reference case but that in the fluid phase is 78 and 106 %. The corresponding values for exit losses are 1.1 and 3.4 % respectively. The overall energy levels are the lowest for d_p= 1.3 mm but highest for d_p= 4.76 mm. The value of the factor ψ for d_p= 1.3 and 4.76 mm are respectively 0.1 and 0.05 % but that of factor ϕ are 9 and 6.6 %. Hence, the change in particle size affects the energy storage in the solid phase.

10.5 EFFECT OF SOLID PHASE PROPERTIES

In this section, the effect of change in thermal properties of the solid phase on the performance of the bed is discussed. The values of thermal storage capacity ratio β and thermal conductivity ratio λ are changed from 2.2 and 0.55 for the reference bed of glass-water keeping the other parameters of the bed unchanged. The temperature profiles are

plotted with the changed parameters and the compared with those of the reference. In addition, the comparison of the performance of the reference bed to that of steel-water is discussed in this section. A comparison of thermal performance of steel water bed with that of the reference bed is first considered.

10.5.1 Steel-Water Bed

A comparison of the performance using a steel-water bed of the configuration discussed above is considered. The thermal properties of the bed are changed to steel water configuration such that thermal capacity ratio β is now 1.1 instead of 2.2 and the thermal conductivity ratio λ is 0.04 instead of 0.55. As discussed in Section 9.6, related to comparison of the frequency response of glass and steel water beds, the maximum temperature during heating is higher in the glass-water bed as compared to that in steel-water bed and during cooling the minimum temperature are lower. Hence, the amplitude of temperature fluctuations is higher in glass-water bed. The pulse speed is also higher in the glass-water bed but the spread and thermal non-equilibrium is lower. It is interesting to see the effect of these changes on the thermal storage.

Figure 10.20 compares the temperature profiles as obtained in the two beds. Figure 10.20 (a) shows the comparison of midpoint temperature with respect to number of cycles elapsed. The temperature at the end of the hot phase is higher in glass-water bed as compared to that of the steel-water bed. A higher axial conduction in the steel-water bed lowers the temperature. At the end of the cold phase, glass-water bed has a lower temperature. However, the time to reach steady state are almost equal for the both the beds.

There are lower temperature fluctuations in a steel-water bed as compared to that in the glass-water bed. Figure 10.20(b) shows the comparison of temperature-distance profiles at the end of the two phases. By the end of the hot phase, it is higher for glass-water water as compared to that for the steel-water bed. At the end of the cold phase, glass-water bed has a lower temperature. The difference between the two profiles is lower towards the opposite ends; at the cold end during the hot phase and at the hot end during the cold phase.

At the middle of the hot phase, the average temperatures are almost same at a value of 0.52 but by the end of the phase, the respective values are 0.61 and 0.65 for steel

and glass-water beds. At the middle of the cold phase, the average temperatures are again equal at 0.511, but by the end of the phase, the respective values are 0.42 and 0.38. Hence, a lower fluctuation for steel water bed is obtained as compared to that for the glass-water. The temperature at the hot and cold ends is now discussed. During the hot phase, the maximum temperature at the cold end is 0.094 in a steel-water bed but its value is higher at 0.105 in glass-water bed. During the cold phase, the minimum temperatures at the hot end are equal for the two beds at 0.92.

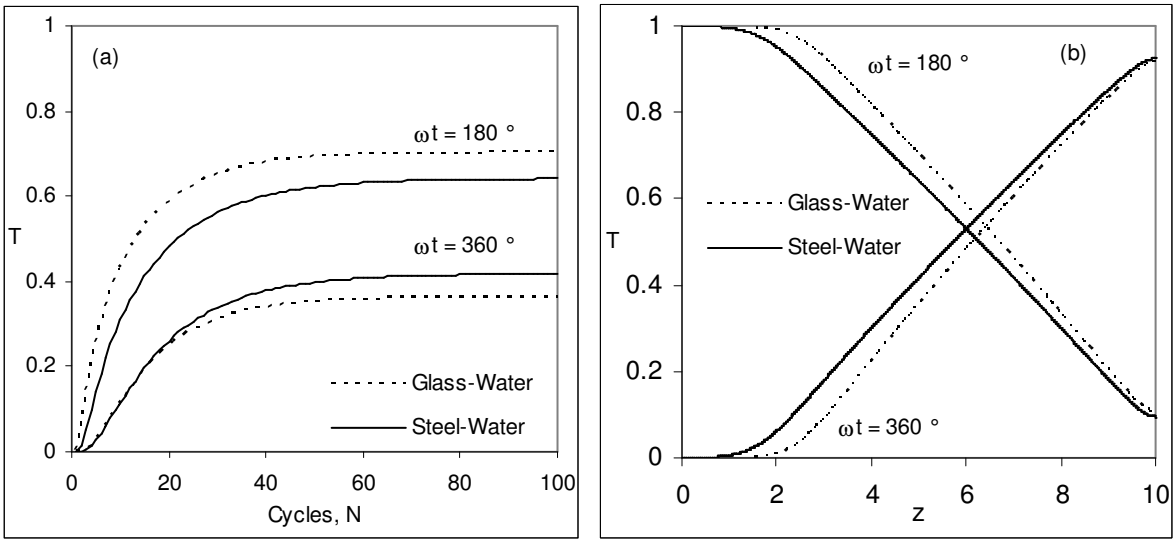

Figure 10.20: Comparison of thermal performance of glass and steel-water beds. (a) Variation of midpoint fluid temperature with time; (b) Variation of fluid temperature with distance. Re =100, L = 10, ω = 1

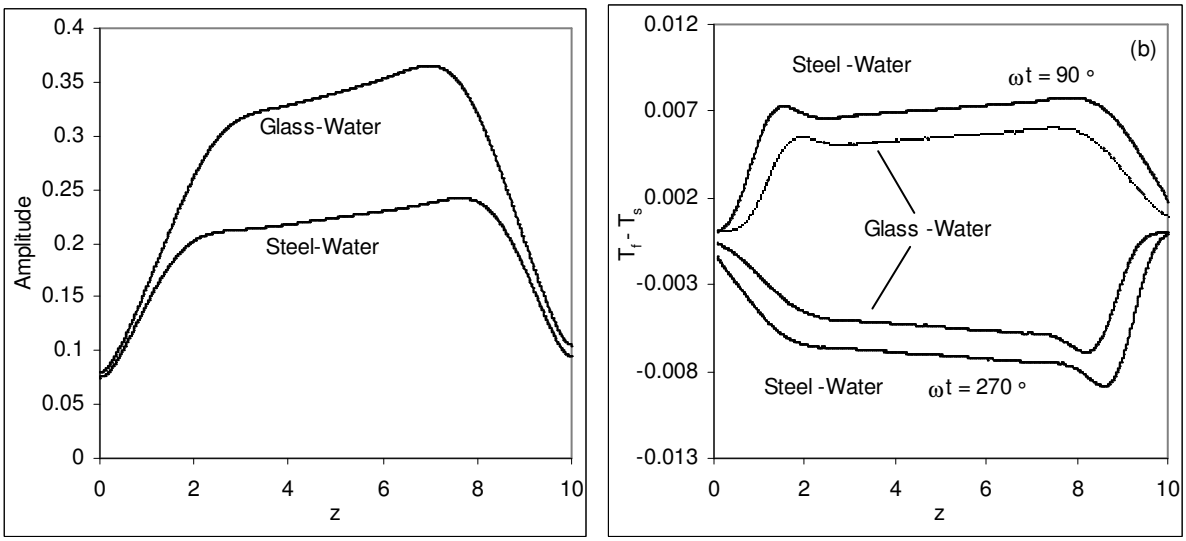

Figure 10.21: Comparison of thermal performance of glass and steel-water beds. (a) Amplitude of temperature fluctuations (b) Thermal non-equilibrium. Re =100, L = 10, ω = 1.

The amplitude of temperature fluctuation, is shown in Figure 10.21(a). It is higher in the glass-water bed as compared to that of the steel-water bed. At the respective ends, the values are almost equal. The peak of amplitude is almost at the same location in the two beds, towards the cold end, z = 8. This comparison is for insulated beds. A minor heat loss in steel-water has more severe effect as compared to that in the glass-water bed, as seen in the previous chapters. Figure 10.21(b) compares thermal non-equilibrium in the two beds at the steady state as a function of distance from the hot end. It is plotted for the middle of the hot and the cold phases. The trends are almost identical in the two beds with a peak value higher for the steel-water bed. At the middle of the hot phase, the peaks occur in both beds near z =2 and at the middle of the cold phase, near z =8. Hence, thermal non-equilibrium in steel water bed is higher as compared to that in a glass-water bed but the overall trends are similar.

In glass-water bed, the amount of energy leaving the bed during the hot phase is 2.1 % whereas it is 2.6 % in steel-water bed. The effectiveness of steel water bed is 97.9 whereas it was 98.3 % for glass-water. The fact that steel has higher storage capacity as compared to that of glass results into lower temperature fluctuations in the steel-water bed. The value of the factor ψ is 0.56 % and that of factor ϕ is 5%.

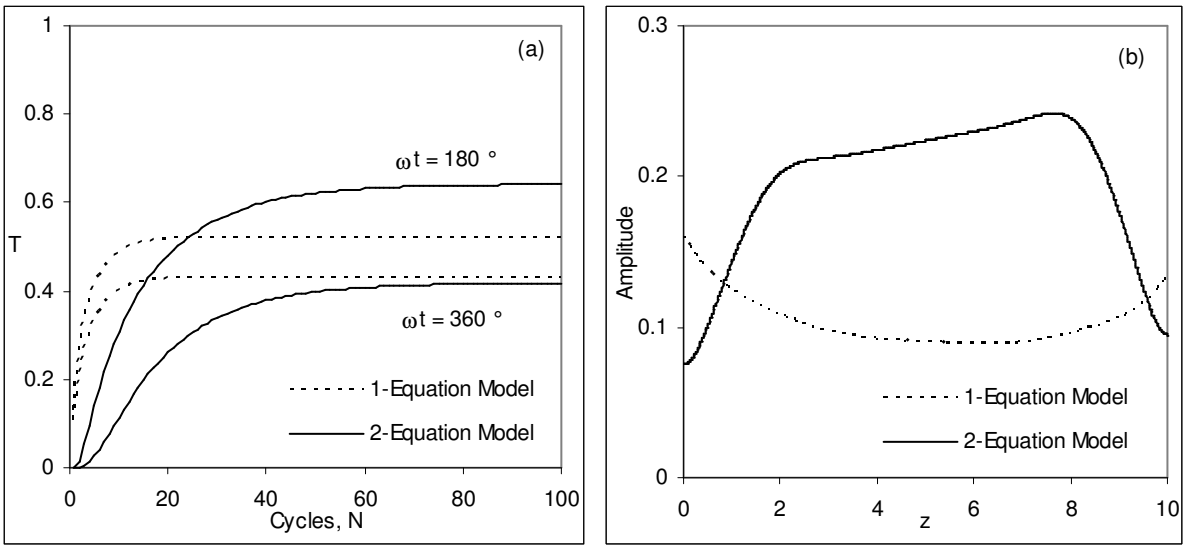

Figure 10.22: Difference between 1 and 2-equation models in steel-water bed. (a) Variation of midpoint fluid temperature with time (b) Amplitude of temperature fluctuations. Re =100, L= 10, ω =1.

The difference between the 1 and 2-equation models for steel-water bed is now discussed. Figure 10.22 (a) shows the temperature profiles at the midpoint of the bed as a function of the number of cycles elapsed. The profiles of 1-equation model are different from that of 2-equation model for this bed. During the hot phase, the 1-equation model profile changes rapidly in the unsteady period. For the cold phase, the build up is faster and the steady state temperature is marginally higher. The resulting amplitude of temperature fluctuations is shown in Figure 10.22(b), which is different for 1-equation model as compared to the 2-equation model. It has a higher value at the ends than that at the middle portion of the bed. Overall, the amplitude is lower as compared to the 2-equation model.

Figure 10.23 shows the difference between the temperature profiles of these models at steady state. At the end of the hot phase, it is negative in most parts of the bed and at the middle of the hot phase; it is again negative but by a lesser amount. During the cold phase, these become mirror images of that of hot phase. The profiles are just opposite to that of glass-water bed as shown in Figure 10.10.

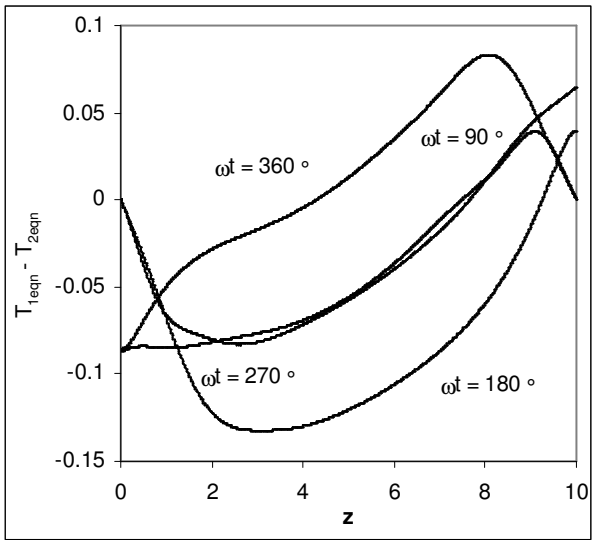

Figure 10.23: The profiles of temperature difference between the 1 and 2 equation models for steel-water bed. Re =100, L= 10, ω = 1.

Hence, for a steel-water bed the profiles are distinct from that for the glass-water bed. The temperature fluctuations are lower for the steel-water bed. The 1-equation model for this bed shows major differences over the 2-equation model. The steel-water bed stores more energy in its solid phase than that in the glass-water bed but it has higher heat losses due to a higher thermal conductivity.

A comparison of the performance of the bed is performed by changing thermal properties of the solid phase. Both the properties of thermal capacity ratio β and the thermal conductivity ratio λ are considered. The results are obtained by changing the properties significantly in either side of the reference value and subsequently compared with each other.

10.5.2 Change in Thermal Storage Capacity Ratio

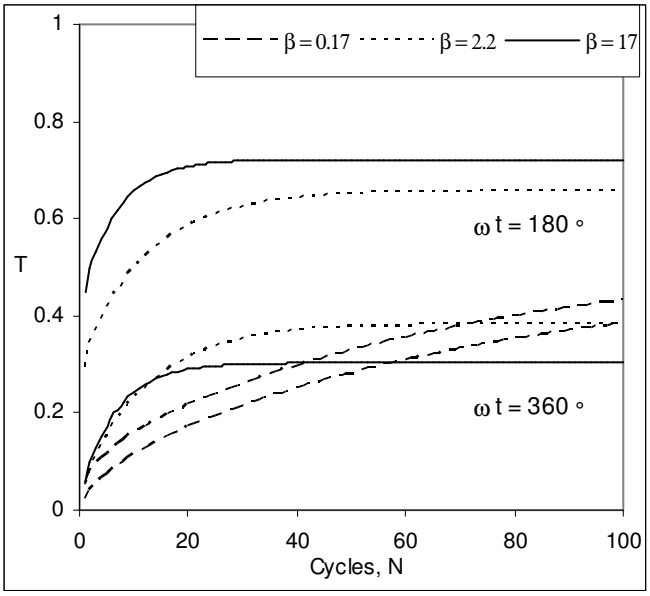

Figure 10.24: The effect of thermal storage capacity ratio: The variation of average fluid temperature with time in the bed. Re =100, L=10, ω = 1.

As discussed in Section 9.6 the major property governing energy storage is the weighted ratio of solid and fluid phase thermal storage capacities given as K. But in the present analysis, the equivalent property considered is β, the two are related to each other by $K = \frac{1-\varepsilon}{\varepsilon\beta}$. Hence the value of β is varied by keeping the porosity ε constant at 0.36 and its effect on thermal performance is considered. The value of β is changed from its normal value of 2.2 in either directions, keeping λ constant at 0.55 such that the profiles are affected considerably. Figure 10.24 shows the effect of change of properties on the average temperature in the bed. It is plotted as a function of number of cycles elapsed at the end of the two phases. Here $\beta = 2.2$

corresponds to the reference temperature profiles. A decrease in the value of β to 0.17 (K = 10), results to an increase in the storage capacity of the solid phase relative to that of the fluid phase, and the response becomes slower. The temperature at the end of the hot phase is very low as compared to that of the reference and the rate of temperature build up is very small. Its value at the end of the cold phase is marginally lower than that at the end of the hot phase. Overall, the temperature fluctuation is very small. On the other hand an increase in β to 17 (K = 0.1) results into an increase in storage capacity of the fluid phase, the resulting temperature changes are large. At the end of the hot phase, the average temperature is higher and that at the end of the cold phase is very low with respect to the reference case. Hence, the temperature fluctuations increase with an increase in the value of β.

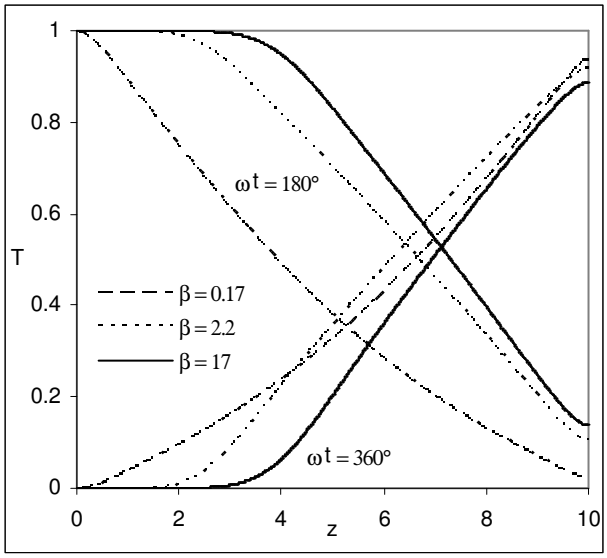

Figure 10.25: The effect of change in thermal storage capacity ratio: The variation of fluid temperature with distance in the bed. Re =100, L = 10, ω = 1.

Figure 10.25 shows temperature profiles as a function of distance from the respective ends at the steady state. The profiles corresponding to β = 0.17 have a lower value as compared to that for β = 17 during the hot phase. However, during the cold phase, the trend is reversed. The resulting amplitude of temperature fluctuations is shown in Figure 10.26. Its value for β = 0.17 is low but uniform throughout the bed and that for β = 17 is high and non-uniform. Figure 10.27 shows the corresponding thermal non-equilibrium data for these properties of the solid phase as a function of distance form the hot end. Figure 10.27(a) shows the thermal non-equilibrium at the middle of the hot phase and Figure 10.27(b) at the

middle of the cold phase. Its value, for β = 0.17, is numerically higher in both cases as compared to the higher values of β. However, its value for β = 17 is much smaller. Hence, the thermal non-equilibrium is higher when the solid phase has a larger storage capacity of the two phases. The change in thermal properties affects the relative storage capacities of the fluid and solid phases only. For a glass-water bed, the solid phase stores around 43 % of the total energy and the rest in the fluid phase. For β = 0.17, the share of the solid phase rises to 91 % but for β = 17, it is only 9 %. Hence, it is the question of storing the energy in a particular form. It is more viable to store energy in the solid phase rather than the fluid phase because it is stagnant. Storage in the fluid phase means no porous media at all, which is not advisable. The temperature fluctuations being higher for β = 17 results into higher hot phase temperatures. It result into more severe heat loss to ambient conditions as compared to the lower values of β. The exit losses are also marginally higher for β = 17 as the temperature levels are higher. Hence, the energy storage in porous beds with a high value of β is a better alternative.

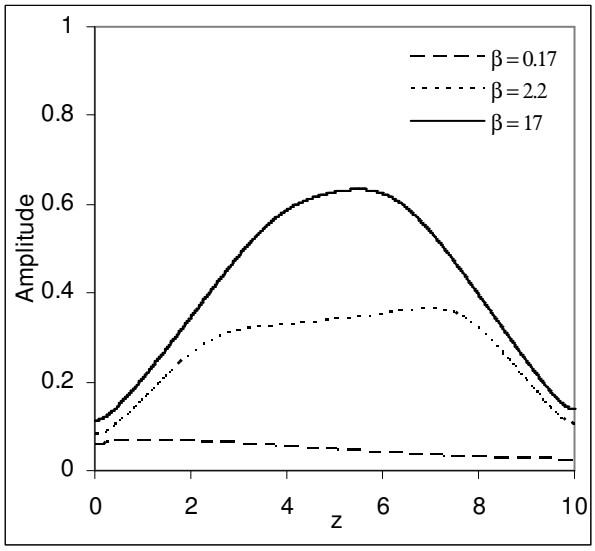

Figure 10.26: The effect of change in thermal storage capacity ratio: The variation of amplitude of temperature fluctuations with distance. Re =100, L = 10, ω = 1.

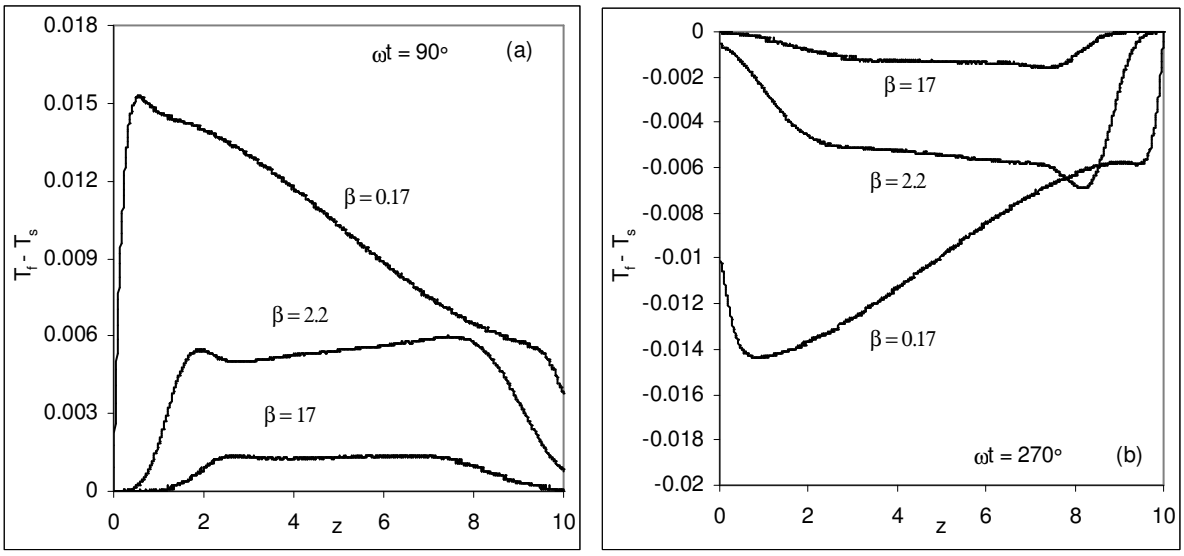

Figure 10.27: The effect of change in thermal storage capacity ratio: The variation of thermal non-equilibrium with distance in the bed. Re =100, L = 10, ω = 1.

The other property of interest is the thermal conductivity ratio λ. A higher value of thermal conductivity of the solid phase results into higher spread of the thermal front and a higher phase lag as observed in the last chapters. Its effect on the thermal storage is now discussed.

10.5.3 Change in Thermal Conductivity Ratio

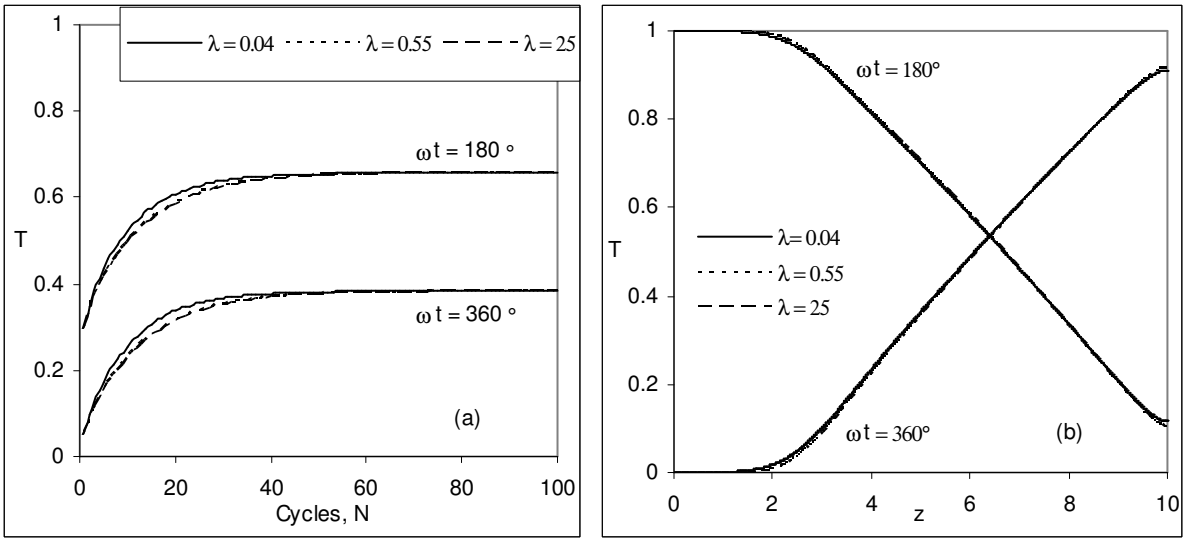

Figure 10.28: The effect of change in thermal conductivity ratio: (a) The variation of average temperature with time in the bed; (b) the variation of fluid temperature with distance. Re =100, L=10, ω = 1.

The effect of change in thermal conductivity ratio λ on the thermal performance is discussed in this section. It is changed from its normal value of 0.55, in both the directions, to 0.04 and 25. The effect of change of λ is discussed for step response in the porous bed in Section 6.7. A change in its value affects the front speed and the spread. A decrease in its value results to an increase in spread but corresponding decrease in front speed. Both the changes seem to increase with distance and hence are cumulative in nature. This aspect is negated for an oscillatory flow as indicated by the profiles in Figure 10.28. Figure 10.28(a) shows the temperature-time profiles in the bed. There is hardly any difference for these profiles over the reference profiles. In the unsteady period, there is a minor difference in these profiles; though in the same direction, but at the steady state, these profiles are similar. Similarly, there is no change in the temperature-distance profiles with a change in the value of λ as observed in the Figure 10.28 (b). Hence, the energy levels and effectiveness is unchanged from that of the reference value.

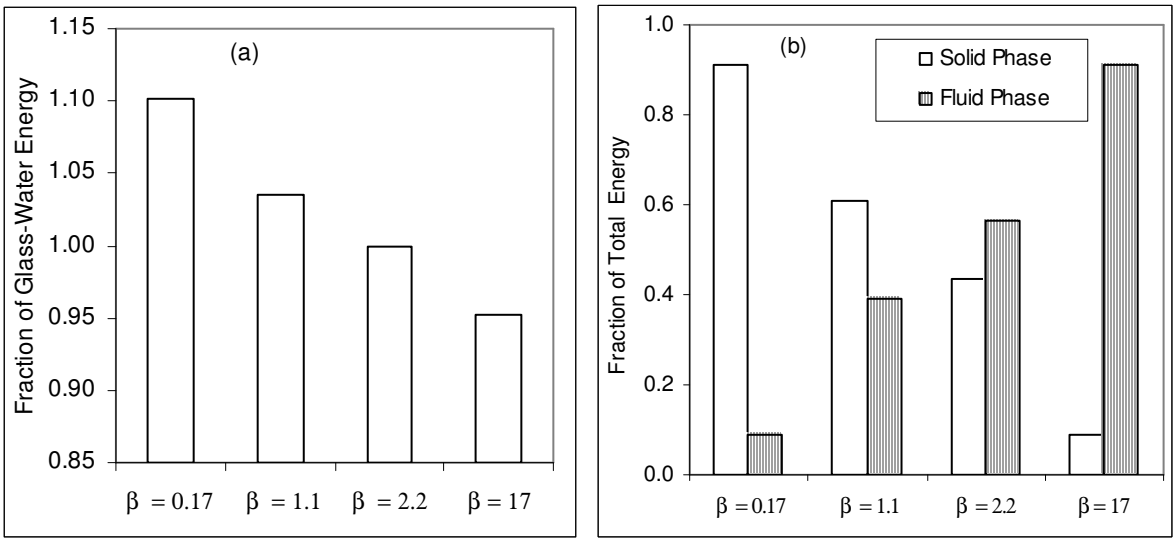

Figure 10.29: Energy Storage in porous medium: (a) Fraction of glass-water bed energy (b) Storage in the solid and the fluid phases. Re =100, L=10, ω = 1.

Figure 10.29 summaries the above discussion with respect to the energy stored as a function of solid phase property of β. Figure 10.29 (a) shows the total energy stored in various porous beds as fraction of that stored in the glass-water bed as indicated by β = 2.2 in the figure, which is considered as unity. A steel-water bed, β = 1.1 stores 4 % more energy though the

temperature levels are less. A bed having $\beta = 0.17$ stores 10 % more energy as compared to that of the glass-water bed but a bed having $\beta = 17$ stores only 95 % of the glass-water bed energy. A higher storage than glass-water bed means that the exit losses are correspondingly lower. Hence, a marginal change in the total stored energy occurs with a change in the value of β. Figure 10.29 (b) shows the fraction of energy stored in the solid and the fluid phases. A glass-water bed stores 43 % of the total energy in the solid phase whereas the corresponding value for steel-water is 61%. The storage in the solid phase for a porous bed with $\beta = 0.17$ is as high as 91% but for $\beta = 17$, it is only 9%.

It is thus concluded that the role of thermal storage is important for an energy storage system and the thermal conductivity is of less importance. These results are at zero heat loss but for the cases where heat losses occur, as in a practical storage system, it would significantly affect the performance. In that respect, the thermal conductivity of the solid phase should be low such that the value of λ is around 0.5 as for glass-water system. It has been observed in Chapter 6, that minor heat loss has practically no effect on the temperature profiles in this bed. It would ensure that minor heat losses do not affect significantly the thermal storage in this bed. On the other hand, the value of β should be low, such that more energy is stored in the solid phase of the bed.

10.6 CLOSURE

A detailed analysis of energy storage in a porous bed is presented in this chapter. The concept of energy storage originates from the regenerator as used in a Stirling cycle. Its applications can be extended on a higher scale to underground storage systems storing huge amount of energy over a longer time periods. To understand its working, a physical model is generated and the related parameters such as energy storage in the fluid and the solid phases, effectiveness, energy balances, and exit losses are discussed in this chapter.

A reference bed is first chosen and the energy storage aspects are discussed by plotting temperature profiles, thermal non-equilibrium, and amplitude of temperature fluctuations. The parameters are changed with respect to the reference case and the thermal performance compared. The analysis is performed for each case such that cyclic steady state is reached. In a practical storage system, the steady state is important but it

should occur early. It can be obtained by decreasing either the bed length or the frequency. In both the cases, a higher utilization of the porous bed for energy storage is obtained.

The average temperature variation with time in the bed relates to storage of energy. The temperature-distance profiles show the utilization of the bed for energy storage and exit losses. These profiles are plotted by changing the bed length, frequency, particle size and the solid phase properties. The temperature profiles at the opposite ends of the bed are important for energy storage.

The amplitude of temperature fluctuations in the bed is an important aspect of the energy storage. Its variation in the unsteady and the steady periods is distinct. It divides the bed in two regions such that the trends are opposite in the two regions. The extent of thermal non-equilibrium is very important for an energy storage system. Its value is high at the middle of the two phases and during unsteady period of the bed. The difference between the 1and 2-equation models is a maximum value at the end of the two phases. These values vary significantly in the bed, the variation near the hot end being opposite to the cold end.

The energy storage components in the fluid and the solid phases are important aspect of a storage system. A higher value of thermal storage capacity ratio β results into higher temperature fluctuations and hence higher temperatures are obtained during the hot phase. Its value determines the fraction of energy stored in the solid phase. It becomes very high when energy storage is large in the solid phase. The thermal conductivity ratio λ hardly plays a role in the energy storage but affects other related parameters such as pulse speed, spread and the heat loss to the ambient. However, its change does not affect significantly the temperature profiles during the oscillatory flow.

The fraction of energy storage in the fluid and the solid phases is a more important aspect as compared to the effectiveness of the energy storage. Properly chosen physical dimensions such as bed length and frequency ensure that it is close to the ideal value of unity. However, the fraction of energy stored in the solid phase of the bed indicates better utilization over a longer time periods. A comparison of glass-water and steel-water beds is also considered. The steel-water bed shows lower temperature fluctuations and more storage in the solid phase but susceptible to ambient heat losses. The 1-equation model is qualitatively similar to 2-equation model for glass-water bed, but for steel-water bed, the

trends are different. It shows the importance of thermal non-equilibrium modeling for a practical storage system.

Overall, the results show that the idea of storage can be used for energy storage in a porous bed on a larger scale. The storage in the underground reservoirs is a challenging application. The solid phase in that case would be sand and the flow is largely unsaturated. The cost for pumping hot and cold water would be an additional parameter.

A numerical analysis of flow and heat transfer in an unsaturated porous medium is considered in the next chapter.

CHAPTER 11

FLOW AND HEAT TRANSFER IN AN UNSATURATED POROUS MEDIUM

11.1 INTRODUCTION

When the pore space is fully filled with water, the medium is water saturated. As no air is present in the medium, no interface is formed with water and the pressure in the medium is the local static pressure in the fluid phase. There is no change in the volumetric water content with time and the resistance to flow is largely viscous and hence small. The flow is governed by Darcy law, a linear relationship between the flow rate and the pressure gradient. Flow in such a medium takes place under a positive pressure head. However, the pore water does not flow in a straight line; instead travels around individual particles and through varying pore sizes within the medium. It results into a much larger path between the two points than a straight line, a factor called tortuosity. The term hydraulic conductivity (K) is a proportionality constant and is a measure of how easily can water flow through the medium. It is obtained by dividing flow rate with the gradient of the pressure head. It depends on properties of both the fluid and the medium. A higher value of K means that a lower pressure gradient is required for a given flow rate. Flow in a saturated porous medium is largely time independent.

In an unsaturated medium, the pore space is not completely filled with water and air is present in the pores. An interface is formed between water and air and pressure of water falls below atmosphere. This is similar to a rise of water through connected pore spaces, which behave as capillary tubes. The presence of air lowers the effective conducting pore volume as compared to that in the saturated medium. The flow channels in the unsaturated medium thus become narrower and the flow path becomes more tortuous as compared to the saturated medium, and the flow rate reduces.

As the water in the pores is less than the maximum possible amount, the water content c of unsaturated medium is an important parameter. It is the portion of REV occupied by water in the medium. The interface between air and water is formed and by capillary action, a pressure difference across the interface is introduced. The pressure difference, called the capillary pressure is given as a function of soil water content in

literature. It is expressed as absolute value of the negative gage pressure existing at the interface. Hence, in formulations it is a positive quantity. This pressure is also called the matric potential. The air present in the medium is considered as stagnant. With the movement of water through the interface, the surface tension creates additional resistance to flow apart from the viscous resistance. The pressure being small, the negative gage pressure governs the flow through the unsaturated porous medium as against a positive pressure in the saturated medium. As the water content decreases, the matric potential also decreases, but the variation is non-linear. Hence the transport in medium is influenced substantially. When the water content in the voids is maximum, the pressure approaches the atmospheric. The hydraulic conductivity of the medium falls as compared to the saturated value and a linear relationship between flux and hydraulic gradient no longer exists. A parameter of relative hydraulic conductivity (K_r) measures how easily water can flow through this medium as compared to that of the saturated medium. Its value depends on the water content present in the pores and hence the matric potential. The relative hydraulic conductivity increases with water content and approaches unity for saturated water content. The water content varies at each point of time and for each location in the bed. Consequently, the flow in unsaturated porous media is a time dependent phenomenon. The mass flux is distinct at each location in the bed and varies with time.

Unsaturated flow is generally studied in the context of flow in soils of various types. Flow takes place from higher to lower water content through the interconnected pores. In the soil capillaries, the interface between the air and water is formed and pressure head of water falls. The relation between the matric potential and water content is called the *retention curve*. It is a characteristic of a porous medium that depends on the geometry of the pores. This relation strongly influences the movement of water in unsaturated media. As water flows in, it increases the pressure in the soils. However, the gradient is not constant along the column length, mainly due to non-uniform wetness. This gradient is constant in a saturated medium. Hence, the hydraulic conductivity cannot be obtained by dividing flow rate by hydraulic gradient.

The mathematical formulation for flow through an unsaturated medium is considerably involved. The additional factor is the surface tension between the air and water interface. The magnitude of the surface tension may be several orders of magnitude larger

than viscous forces. In a saturated medium, the flow rate of water is equal to the hydraulic conductivity times the driving force. For unsaturated media, the relative hydraulic conductivity is sensitive to and has a nonlinear dependence on the water content. Hence, the flow is combination of Darcy's law and mass conservation of water. This formulation requires knowledge of the unsaturated hydraulic conductivity, water content and matric potential, Mualem [1976]. It can quantify the movement of water in the unsaturated zone. It is also useful in the transport of contaminants. In this context, aquifer recharge rate, the flow rate of water down to the water table, is very important. It is also important in waste disposal of nuclear materials, which are buried in dry unsaturated regions of earth. The natural water movement can transfer these materials in case of leak, Muralidhar [1988].

The velocity and temperature profiles are obtained for the unsaturated porous medium and the analysis of flow and heat transfer is carried out in this chapter. The porous bed is initially considered to be at a constant matric potential and a temperature close to the ambient. The medium is exposed to atmospheric pressure and hot water flow enters the medium at the inflow plane. The velocity profiles are obtained in the unsaturated porous medium using modified Darcy law and mass conservation while the temperature profiles are derived using the 2-equation model. The velocity profiles in unsaturated medium are highly unsteady as against time independent in a saturated medium. The resulting pressure profiles, relative hydraulic conductivity and water content are also obtained. In the present problem, the diffusion into a porous medium is taken as horizontal and hence free from the gravity effects. Interphase heat transfer area and dispersion need to be repeatedly calculated as the water content varies in the REV.

11.2 TRANSPORT IN AN UNSATURATED POROUS MEDIUM

11.2.1 Properties of an Unsaturated Medium

Figure 11.1 shows the schematic representation of saturated and unsaturated porous media. The saturated porous medium has no air present and water fills the pore space completely, Figure 11.1(a). Air is present in the unsaturated porous medium, the amount of water thus becomes less than the saturated amount, see Figure 11.1(b) and the interface between the hot and cold fluids is shown in Figure 11.1(c). In the unsaturated medium, the water content, c is the portion of REV occupied by water. The degree of saturation, s on the other hand is the

portion of pore volume filled with water. The degree of saturation s relates to portion of pore volume filled with water as:

$$s = \frac{\text{Volume of liquid in the pores}}{\text{Pore - volume}} \tag{11.1}$$

It varies between zero and unity. In addition, the relation between saturation and water contents is

$$c = \frac{\text{Volume of liquid in the pores}}{\text{Volume of REV}} = s\varepsilon \tag{11.2}$$

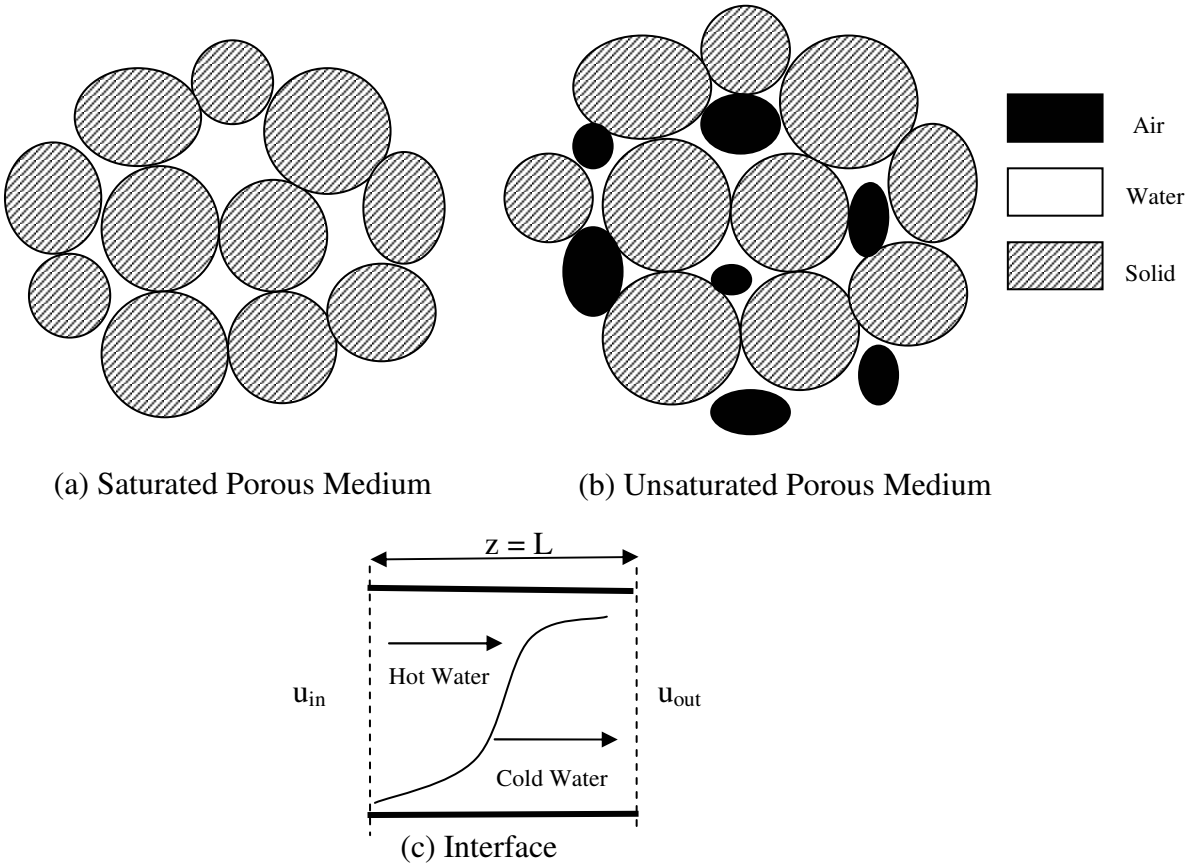

Figure 11.1: Schematic representation of porous medium. (a) Saturated; (b) Unsaturated; (c) Interface.

The relationship for pressure head and water content is available in literature, Van Genuchten [1980]. The commonly used relationship for water content and pressure head is

$$\text{Effective Saturation } \Theta = \frac{c - c_r}{c_{sat} - c_{res}} \quad = \left[\frac{1}{1+(ah)^n}\right]^m \tag{11.3}$$

here a, n and m are constants. The typical values of these constants are a = 0.005 1/cm, n= 2.0 and m=*0.5*. Putting Θ = 0.875, gives h = 110 cm. However, it is a negative value i.e. pressure head is below atmosphere. Figure 11.2 shows the plot between water content, c and pressure head on logarithmic scale. The change of pressure near the saturated c_s and residual water c_r contents is very large.

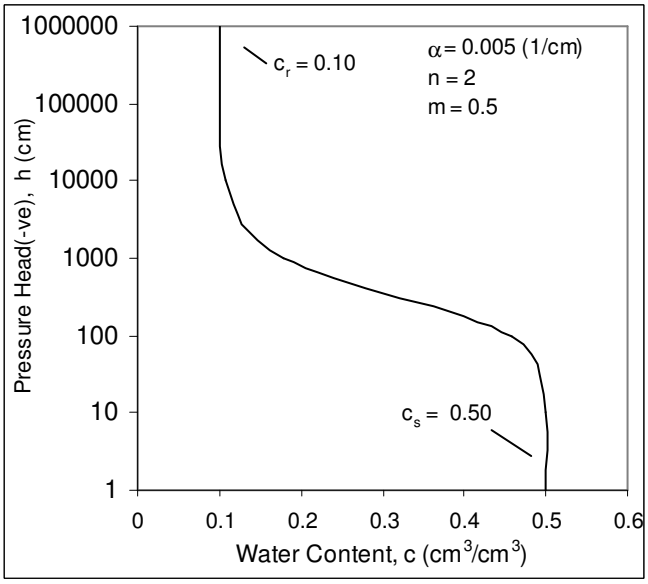

Figure 11.2: The typical variation of matric potential with water content in a clay-type soil.

The relationship between the relative hydraulic conductivity (K_r) and pressure head (h) as a function of the dimensionless water content (Θ) as derived by Mualem [1976] is given as

$$K_r = \Theta^{1/2}\left[\int_0^{\Theta} \frac{1}{h(x)}dx \Big/ \int_0^{1} \frac{1}{h(x)}dx\right]^2 \tag{11.4}$$

Solving for water content, using the Equation 11.3 for dimensionless water content, we get.

$$K_r(h) = \frac{\left\{\left[1-(\alpha h)^{n-1}\left[1+(\alpha h)^n\right]^{-m}\right\}^2\right.}{\left[1+(\alpha h)^n\right]^{m/2}} \tag{11.5}$$

Figure 11.3 shows the variation of K_r with pressure. The pressure head is indicated using logarithmic scale. Clearly as h approaches zero, the relative hydraulic conductivity approaches unity and pressure becomes atmospheric. The value of relative hydraulic conductivity is nearly zero for h = 1000 cm.

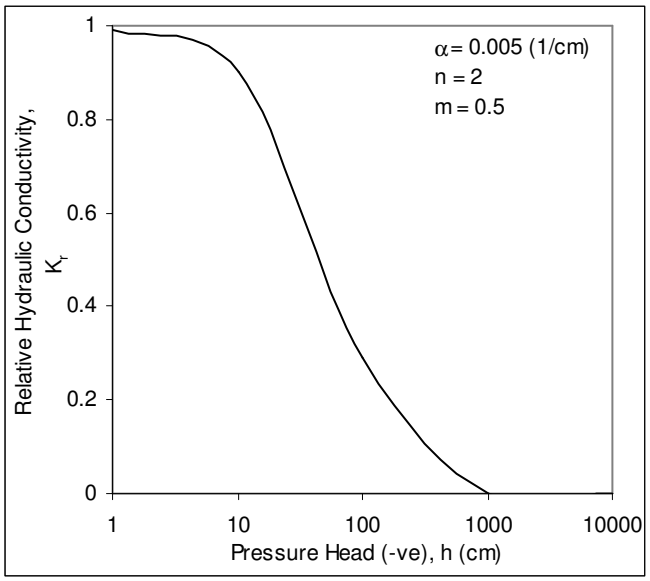

Figure 11.3: The variation of K_r with matrix potential of the unsaturated soil.

Table 11.1: Thermo-physical properties of sand-water porous bed.

Particle diameter, d_P [cm]	Porosity, ε	hydraulic conductivity, K [cm/hr]	Thermal Diffusivity α [cm^2/hr]		Thermal conductivity ratio, λ	Thermal capacity ratio, β
			α_f	α_s		
0.1	0.5	3.6	5.36	7.9	3.42	2.29

In addition, the properties of the sand-water porous bed need to be specified. The properties of the bed are given in Table 11.1. A particle size d_P of 1mm is chosen and the porosity ε of the medium corresponds to the saturated water content c_{sat}. The thermal properties of λ and β corresponds to that of fine sand.

11.2.2 Flow in an Unsaturated Medium

Darcy law governs the flow through a saturated porous medium. It states that the volume of water that passes through a bed per unit time is dependent on cross-sectional area of the medium, head difference between inlet and outlet and K, the hydraulic conductivity. Mathematically it can be written as:

$$Q = -KA\frac{\Delta h}{L} \tag{11.6}$$

The volumetric flux q can be written as

$$q = -K\frac{\Delta h}{L} \tag{11.7}$$

For steady flow, there is no change in water content of the porous medium and it is equal to porosity of the medium. Hence, the flux is proportional to the hydraulic gradient and K is merely proportionality constant the hydraulic conductivity (cm s^{-1}). The second way of writing the above equation is in the terms of permeability k and viscosity μ as

$$q = -\frac{k}{\mu}\frac{\Delta p}{L} \tag{11.8}$$

Here p is the pressure potential and k is a function of pore structure and geometry and μ is a fluid property. The conductivity of soils has a wide range of values. It is 10^{-9} cm/s for clay to 1 cm/s for clean sand. Lower values of K for clay medium arise due to smaller pore size and larger drag force by the walls of the pores.

For an unsaturated medium, the equation modifies to

$$q = -K(c)\frac{\partial h}{\partial z} \tag{11.9}$$

Here $\frac{\partial h}{\partial z}$ is the local hydraulic gradient and K(c) is the hydraulic conductivity of the unsaturated medium. The value of $\frac{\partial h}{\partial z}$ is not constant across the bed but varies with water content. Hence, the hydraulic conductivity also varies with position. We can write Equation 11.9 as:

$$q = -K_r K\frac{\partial h}{\partial z} \tag{11.10}$$

The mass balance equation in an unsaturated porous medium, Bear [1988] is written as:

$$\frac{\partial(\varepsilon \rho s)}{\partial t} + \nabla.u\rho = 0 \tag{11.11}$$

The relative hydraulic conductivity of the unsaturated medium varies between zero and unity. Substituting the product of εs as c and velocity as volumetric flux in mass balance equation, we get

$$\frac{\partial c}{\partial t} + \nabla.q = 0 \tag{11.12}$$

By combining Equations 11.10 and 11.11, we can write

$$\frac{\partial c}{\partial t} == -\nabla.\left(-K_r K \frac{\partial h}{\partial z}\right) \tag{11.13}$$

$$\frac{\partial c}{\partial h}\frac{\partial h}{\partial t} = \frac{\partial}{\partial z}\left(K_r K \frac{\partial h}{\partial z}\right) \tag{11.14}$$

The above equation is similar to the unsteady heat conduction equation

$$\frac{\partial T}{\partial t} = \frac{\partial}{\partial x}\left(\alpha(T)\frac{\partial T}{\partial x}\right) \tag{11.15}$$

An additional term of $\frac{\partial c}{\partial h}$ is present in the above equation. Hence, the matric potential varies along the bed length as a function of water content c. The relative hydraulic conductivity K_r also varies with water content. Once the values of h and K_r are calculated, the flux q can be known from Equation 11.10.

11.2.3 Heat Transfer in Unsaturated Medium

Heat transfer in unsaturated soils in the presence of air is slow. A mathematical model as used for saturated porous medium has been modified for unsaturated medium. The water content, matric potential and velocity profiles obtained from the unsaturated flow equation are substituted in the 2-equation model. It affects the Reynolds number and the interphase heat transfer namely Nusselt number and dispersion are also affected. The water content in the REV keeps varying with time. Hence the volume of liquid in REV is not a constant but that of solid phase remains unchanged. The interphase area between the fluid and solid phases keeps varying as the fluid volume in REV changes. All these changes are incorporated in the energy equations. Air present in the REV is considered as stationary. The analysis is performed in the dimensional form. As the fluid velocity is small, the resulting heat transfer rate is also small and resembles the fluid and solid phase energy equations behave effectively as diffusion equations. The fluid phase energy equation is written as:

$$Fluid: \quad c\left(\rho c_p\right)_f\left[\frac{\partial T}{\partial t} + u.\nabla T\right] = \nabla\left[k_{eff,f}.\nabla T\right] - a_{sf}h_{sf}\left(T - T^s\right) \tag{11.16}$$

Since the flow rate in the unsaturated medium is very slow, the hydrodynamic dispersion is neglected. Hence

$$k_{eff,f_Z} \quad \Leftarrow k_f \tag{11.17}$$

The fluid phase energy equation thus becomes

$$\left[\frac{\partial T}{\partial t}+u.\nabla T\right]=\frac{\alpha_f}{c}\nabla[c.\nabla T]-\frac{a_{sf}\ \alpha_f Nu_p}{c\ d_p}\left(T-T^s\right) \tag{11.18}$$

The volume of the solid phase energy is unchanged to $(1-\varepsilon)$; hence, the equation is given as

$$Solid: \quad (1-\varepsilon)(\rho c_p)_s\left[\frac{\partial T}{\partial t}\right]=\nabla\left[k_{eff,s}.\nabla T\right]-a_{sf}h_{sf}\left(T-T^f\right) \tag{11.19}$$

The solid phase dispersion is unchanged as in a saturated medium.

$$k_{eff,s_Z} = (1-\varepsilon)_S \tag{11.20}$$

The solid phase energy equation is modified to

$$\left[\frac{\partial T}{\partial t}\right]=\frac{k_s}{(\rho c_p)_s}\frac{\partial^2 T}{\partial x^2}-\frac{a_{sf}h_{sf}}{(1-\varepsilon)(\rho c_p)_s}\left(T-T^f\right) \tag{11.21}$$

$$\left[\frac{\partial T}{\partial t}\right]=\alpha_s\frac{\partial^2 T}{\partial x^2}-\frac{a_{sf}Nu_p\alpha_s\lambda}{(1-\varepsilon)d_p}\left(T-T^f\right) \tag{11.22}$$

Interphase area between the fluid and the solid phase is dependent on the soil water content and given as

$$A_{If} = \frac{6(1-c)}{d_p} \tag{11.23}$$

In addition, Nusselt number is given as

$$\mathrm{Nu}_p = 2+1.1\mathrm{Pr}^{0.33}\mathrm{Re}_P(i)^{0.6} \tag{11.24}$$

This relationship has been adapted from the heat transfer correlation for a saturated porous medium.

11.3 NUMERICAL SOLUTION

The numerical solution of the governing equations is obtained by finite difference discretization. The fluid velocity in the medium in not constant but varies with space and time and consequently the temperature profile is affected. The flow and heat transfer equations are coupled and are to be simultaneously solved.

11.3.1 Flow Equation

The numerical solution of pressure in the unsaturated bed is obtained from the finite difference discretization of Equation 11.14. The equation is solved using implicit differencing for time derivative and backward differencing for spatial derivatives as

$$\frac{h_i^{n+1} - h_i^n}{\Delta t} = \frac{K_s}{\Delta z^2}\left[K_r^{east}(h_{i+1} - h_i) - K_r^{west}(h_i - h_{i-1})\right]^{n+1} X\left(\frac{\partial h}{\partial c}\right)^{n+1} \tag{11.25}$$

Here K_r^{east} and K_r^{west} are obtained by harmonic mean of values at downstream and upstream grid points of point *i***.** These are respectively called as east and west values. In other words

$$\frac{1}{K_r^{east}} = \frac{1}{K_{r(i+1)}} + \frac{1}{K_{r(i)}} \qquad \text{and} \qquad \frac{1}{K_r^{west}} = \frac{1}{K_{r(i)}} + \frac{1}{K_{r(i-1)}} \tag{11.26}$$

11.3.2 Heat Transfer Equation

The solution of the 2-equation model is obtained by finite difference discretization of Equations 11.18 and 11.22 for the fluid and the solid phases of the medium. Using the implicit differencing for time derivative, QUICK formulation for convection terms, as discussed in Section 4.2.3, and backward differencing for diffusion terms, hence the fluid and the solid phase equations become:

Fluid Phase

$$\frac{T_i^{n+1} - T_i^n}{\Delta t} + \frac{\frac{u_r}{c(i)}T_r - \frac{u_l}{c(i)}T_l}{\Delta z} = \frac{\alpha_f}{c_i \Delta z^2}\left[c^{east}(T_{i+1} - T_i) - c^{west}(T_i - T_{i-1})\right]^{n+1} - \frac{a_{sf}(i)\alpha_f Nu_{p(i)}}{c_i d_p}\left(T_i - T_i^s\right)^{n+1} \tag{11.27}$$

Using QUICK formulation for discretization of convection term, we get

$$\frac{T_i^{n+1} - T_i^n}{\Delta t} + \left(\frac{u_r\left[\left(\frac{3}{4}\right)T_i + \left(\frac{3}{8}\right)T_{i+1} - \left(\frac{1}{8}\right)T_{i-1}\right]_r - u_l\left[\left(\frac{3}{8}\right)T_i + \left(\frac{3}{4}\right)T_{i-1} - \left(\frac{1}{8}\right)T_{i-2}\right]}{\Delta z}\right)^{n+1}$$
$$= \frac{\alpha_f}{c_i \Delta z^2}\left[c^{east}(T_{i+1} - T_i) - c^{west}(T_i - T_{i-1})\right]^{n+1} - \frac{a_{sf}(i)\alpha_f Nu_{p(i)}}{c_i d_p}\left(T_i - T_i^s\right)^{n+1} \tag{11.28}$$

The solid phase equation is similar to that for the saturated medium.

Solid Phase

$$\left(\frac{T_i^{n+1} - T_i^n}{\Delta t}\right) = \frac{\alpha_s}{\Delta z^2}(T_{i+1} + T_{i-1} - 2T_i)^{n+1} - \frac{a_{sf}(i)Nu_{p(i)}\alpha_s \lambda}{(1-\varepsilon)d_p}\left(T_i - T_i^f\right)^{n+1} \tag{11.29}$$

11.3.3 Initial and Boundary Conditions

The solution of governing equations is subjected to suitable initial and boundary conditions such that pressure and temperature profiles are obtained. The initial conditions prevailing in the bed for $0 \le z \le L$ at $t = 0$.

$$h = 100\,\text{cm}\,,\; K_r = 0.288 \;\text{ and }\; \frac{\partial c}{\partial h} = -0.071\left(\text{cm}^3/\text{cm}^3\right)/\,\text{cm} \tag{11.30}$$

and fluid contained in the medium has zero temperature and velocity. Hence

$$T = 0 \;\text{ and }\; u = 0 \tag{11.31}$$

The fluid enters the unsaturated bed at $t > 0$, its pressure is set to zero at the inflow plane and the outflow boundary condition of zero derivative in axial direction at $z = L$ is set as

$$h_{z=0} = 0 \;\text{ and }\; \left(\frac{\partial h}{\partial z}\right)_{z=L} = 0 \tag{11.32}$$

The boundary condition at outlet is referred as closed outflow boundary condition as the outflow is blocked. The length L is chosen significantly larger as compared to distance covered by fluid in the domain for the specified period of time. The inflow temperature is unity and the outflow boundary condition of zero derivatives in axial direction at $z = L$ is set, hence

$$T_{z=0} = 1 \;\text{ and }\; \left(\frac{\partial T}{\partial z}\right)_{z=L} = 0 \tag{11.33}$$

The algebraic equations resulting from Equations 11.25, 11.28 and 11.29 are solved by Gauss-Seidel iterations. The solution obtained is checked for time step independence such that the results are free from the time-steps chosen. The time steps are varied from 5000 to 20000, percentage change in each time step varying from 0.02 to 0.005 % of the total time. The simulation is carried out for L = 100 cm and a grid of 500 is chosen.

Since the analysis is carried out in the dimensional form, the choice of units is important to obtain convergence of the results. Length and velocity are chosen in meters and meters per hour, while temperature in non-dimensional form.

11.3.4 Grid Independence

Figure 11.4 shows the effect of varying the number of time-steps for a step increase in pressure and temperature at the inflow plane. Figure 11.4(a) shows the effect on the pressure profile in the medium and Figure 11.4(b) on the temperature profile. The pressure head rises, from its initial value of 100 cm, in the bed. It varies as a function of distance from the inflow plane and the time elapsed. Ultimately, it approaches the incoming pressure of zero value. The dependence on the number of time-steps used in the simulation, at location z = 20 cm, is shown in figure. The time steps for simulation are varied from 5000 to 20,000 thereby varies from 0.02 to 0.005% of the total time; see Figure 11.4(a). During unsteady state, the profile is independent of the time steps used but the steady state values are marginally different. As the time-steps are increased, the steady state value becomes higher. Overall, there is hardly any difference between the individual curves and time-steps independence is achieved at this stage.

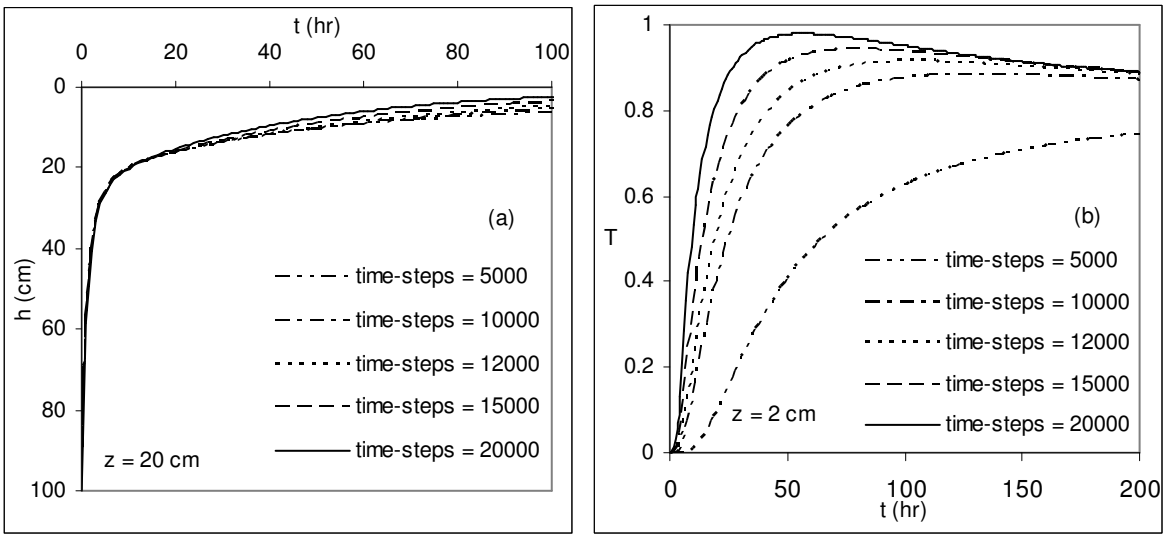

Figure 11.4: The effect of time-steps variation on the results of step change in temperature and pressure at the inflow plane of the unsaturated medium.

The corresponding temperature profiles are shown in Figure 11.4(b). The temperature profiles being very slow, are shown at an upstream location of z = 2 cm. The temperature profiles during unsteady states are distinct but as the steady state is reached, the individual temperatures approach each other. The steady state at this location is les than unity at 0.89. Increasing the time-steps further, temperatures may cross a unity value. The profiles using time-steps of 10,000 and 12,000 look reasonably accurate. The time steps of 5000 gives a

lower value of temperature at various locations in the bed. A time-steps of 12000 are used in the simulation.

11.4 FRONT PROPAGATION

The propagation of the fluid front and the thermal front is discussed in this section. The velocity profiles and hence the temperature profiles evolve slowly in time for an unsaturated porous medium. Figure 11.5 shows the pressure variation in the bed; Figure 11.5(a) shows the variation with respect to time and Figure 11.5(b) with respect to distance. In Figure 11.5(a), the pressure rises from the initial value and approaches the incoming pressure as a function of time and distance from the inflow plane. At z = 2 cm, the pressure rises rapidly from the initial value of 100 cm and settles to a value close to zero at 0.02 cm. At z = 20 cm, the rise of pressure is marginally slower and the steady state value is also lower. Similarly at z = 40 cm, the rise is further slower, and the steady state value is lower at 0.42 cm. The pressure rise is fast nearer to inflow plane as compared to those away from it. Up to 100 hrs, the pressure builds up in the bed is from initial value to one shown in Figure 11.5(b). It falls to 16 cm at the outflow plane from a zero value at the inflow plane. As the time increases, it rises further and becomes almost equal to the incoming pressure after 400 hrs, see Figure 11.5(b).

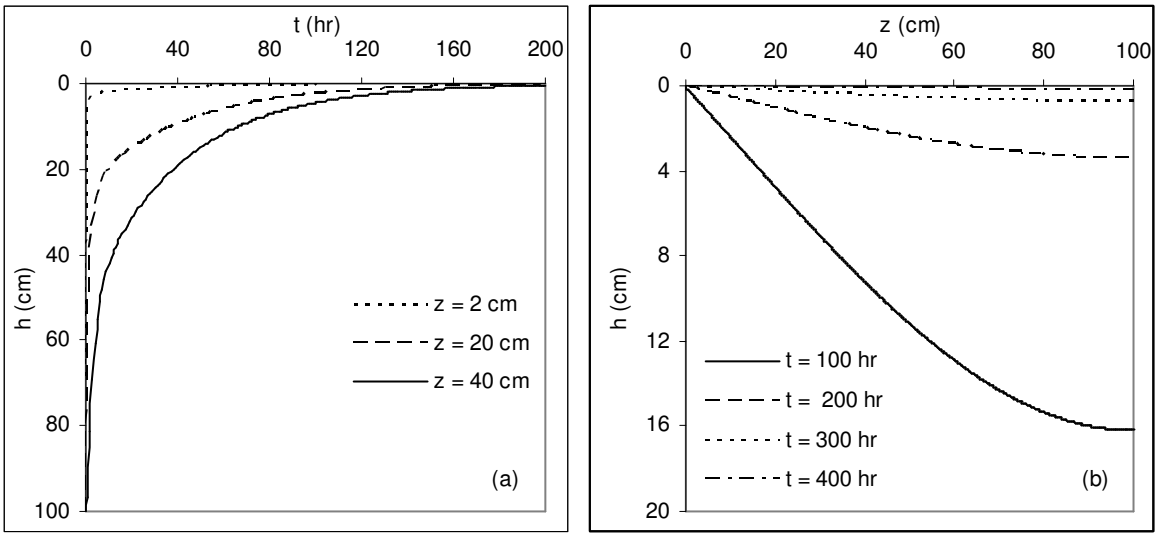

Figure 11.5: The unsteady variation of pressure head in the unsaturated porous medium.

Figure 11.6 shows the variation of velocity in the bed as a function of time and distance in the bed. Velocity at a location is initially zero but increases with the arrival of hot fluid. It increases with time to a large value and afterwards falls. At z = 2 cm, it rises sharply to 80 cm/hr at the start and falls in the bed for various points of time to a value of 0.21 cm/hr. At z =20 cm, it rises to 11 cm/hr at start but falls rapidly. At downstream points, the initial rise is small but the steady state is close to 0.2 cm/hr. In the initial 100 hrs, the pressure gradient is large in the bed but as the time increases, the pressure increases and approaches the incoming fluid pressure and the velocity falls in the bed. It becomes almost zero as the pressure rises to atmospheric value. After 200 hrs, the pressure increases, but the gradient becomes small in the bed. With further increase in time, the pressure almost becomes equal to the incoming pressure. After 400 hrs, the pressure in the bed is close to zero everywhere and hence velocity is small. The velocity profiles at various points of time as a function of distance form the inflow plane are shown in Figure 11.6(b); the fluid velocity at locations closer to the inflow plane is higher as compared to that near the end. Further, it is always higher for shorter times. After 100 hr, the velocity is quite large at z = 3 cm at the inflow plane but falls rapidly with distance. With increase in time, the value of velocity close to inflow plane becomes lower and the average value falls in the bed. It becomes nearly constant with distance. After 300 hrs, the velocity in the bed is close to low value of 0.08 cm/hr. At 400 hrs, it is almost zero in the bed.

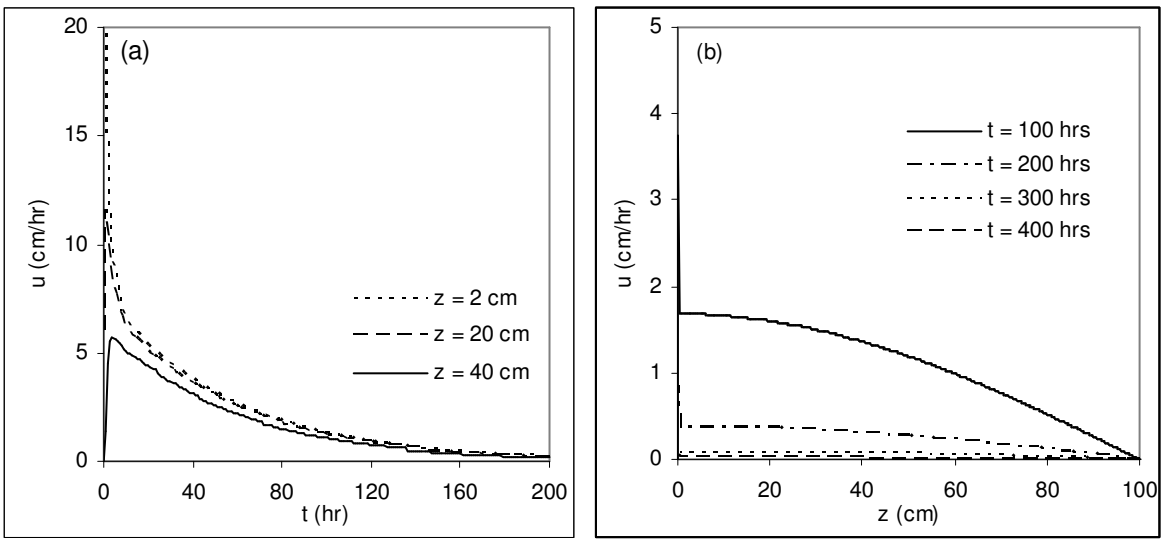

Figure 11.6: The unsteady variation of velocity in the unsaturated porous medium.

Figure 11.7 shows the variation of temperature in the unsaturated porous bed. Figure 11.7(a) shows the unsteady variation of temperature at various locations in the bed as a function of time elapsed. At locations close to inflow plane, z = 2 cm, the build up is quite fast. But the build up at downstream locations is slower. The maximum temperature attained at a location is less than unity and falls with distance from the inflow plane. As the velocity is small at locations away from the inflow plane, the build up of temperature is very slow. At z =2 cm, the maximum temperature of 0.9 is attained but falls with time. The maximum temperature at z = 4 cm is 0.65. The temperature build up at further downstream locations is very slow owing to low velocity. This is further cleared in Figure 11.7(b); the temperature profile with respect to distance. From 100 to 400 hrs, there is hardly any rise in temperature in the bed. Hence the temperature build up in unsaturated porous medium is very slow and velocity dependent. A higher pumping pressure at the inflow plane is required to further store the energy in the bed.

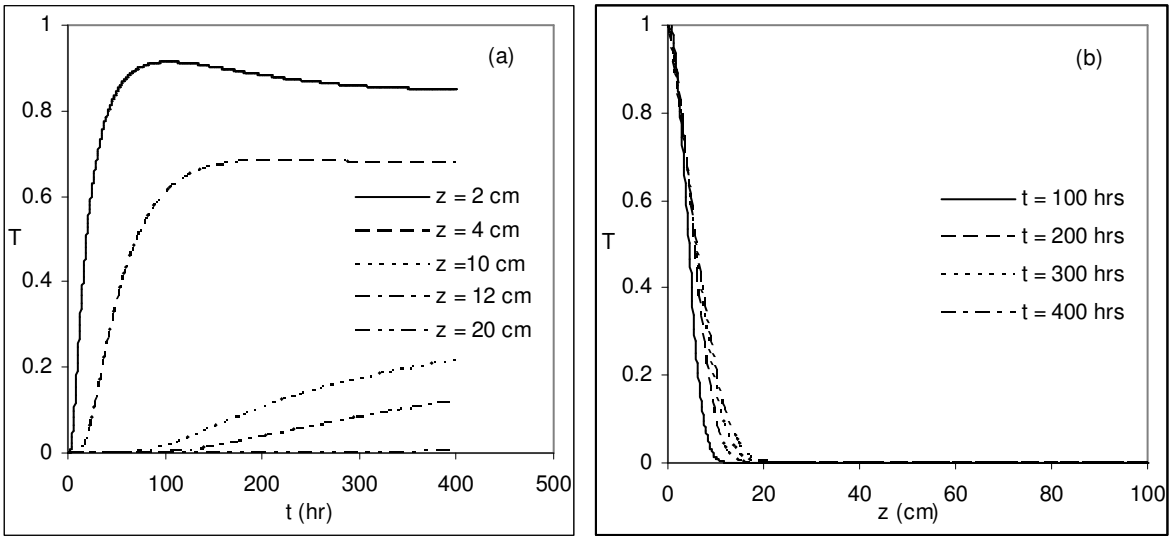

Figure 11.7: The unsteady variation of temperature in the unsaturated porous medium.

It is interesting to see the variation of relative hydraulic conductivity and water content in the bed. It is shown in Figure 11.8. Figure 11.8(a) shows the variation of water-content c in the bed as a function of distance. Initially c has a value of 0.46 corresponding to a pressure of 100 cm in the bed. It increases as the fluid enters through the inflow plane. It approaches the saturated amount c_s. After 100 hrs, the profile of h is shown in Figure 11.5(b), where its value is between zero and 16 cm, hence the water content varies

between 0.50 and 0.49 only. In other words, the bed is almost saturated after 100 hrs. Figure 11.8(c) shows the profile for relative hydraulic conductivity, K_r. At the start, it corresponds to 0.288 in the bed for a pressure of 100 cm. The K_r rises and approaches a unity value as h increases to zero. It increase to 0.96 at z = 20 cm and to 0.93 at z = 40 cm. After 100 hrs, its value at $z = L$ is 0.84, hence less than unit value. Hence, the pressure head in the bed varies and it results to a change in the value of velocity, water content, relative hydraulic conductivity and temperature.

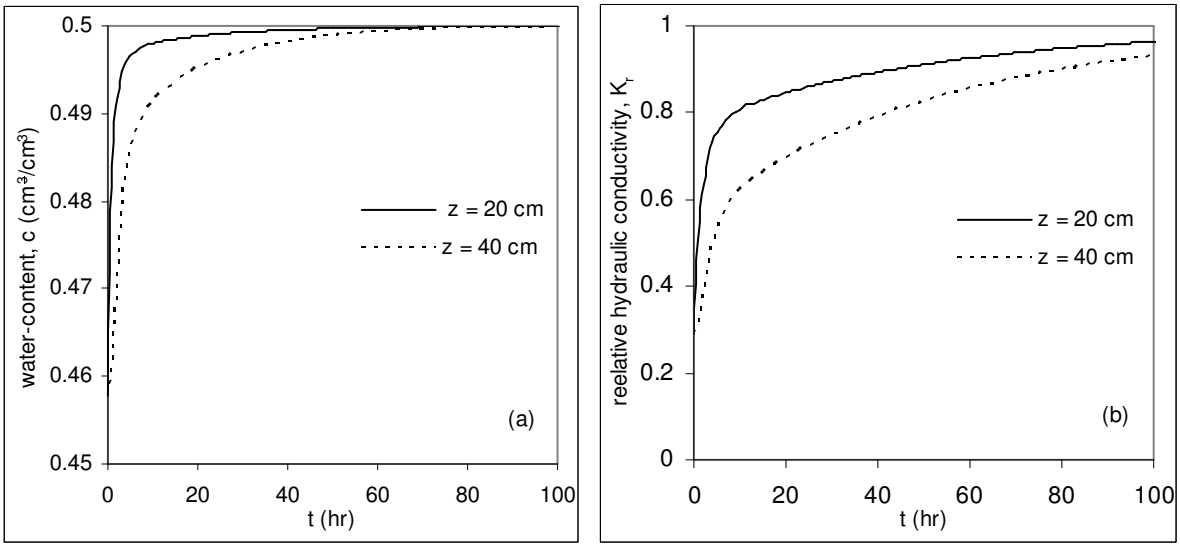

Figure 11.8: Variation of water content and hydraulic conductivity in the bed with respect to time in the unsaturated porous medium.

11.4.1 Inter Phase Heat Transfer

The interphase heat transfer plays a major role in the thermal transport through the medium. The correlation by Wakao and Kaguei [1982] is used in the present study. Since the velocity in this medium is very small, an effect of change in its value, on the temperature profiles is observed. Its value is changed from its normal value to either side. A Significant effect on the thermal front is seen with this change. Figure 11.9 shows the effect of change in its value on the temperature profiles. When its value is doubled from the normal value, the temperature profiles evolve slowly. On the other hand when it is reduced to half of its normal value, the thermal propagation becomes faster. Hence, the interphase heat transfer significantly effects the thermal propagation.

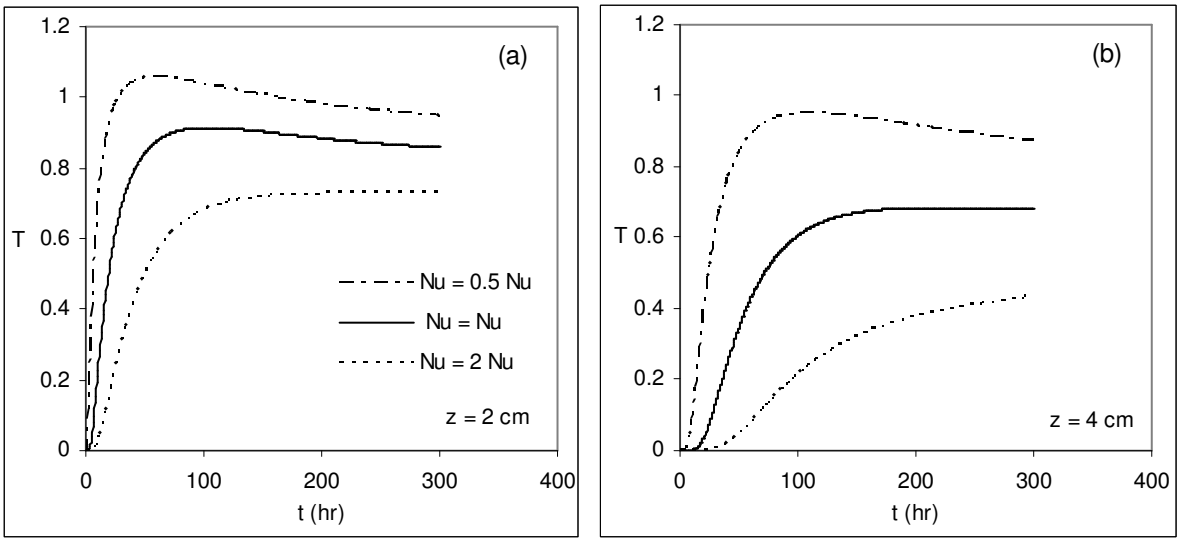

Figure 11.9: The effect of Nusselt number change on the temperature profiles in the unsaturated porous medium.

11.5 CLOSURE

An analysis of transport in unsaturated porous medium is carried out in this chapter. The pressure profiles are obtained using modified Darcy' law and mass balance. The velocity in the medium time dependent and low. The 2-equation model is modified to find the heat transfer in the medium. Since the velocity is low in the medium, the thermal front travels at a very slow speed and has large spread. The convection in the medium is small and transport is governed largely by diffusion. The chapter gives basic and vital information about energy storage in unsaturated porous medium. The maximum temperatures at any location in less than unity. Steady state is not achieved even over long periods of time.

CHAPTER 12

CONCLUSIONS AND SCOPE OF FUTURE WORK

12.1 INTRODUCTION

The present work addresses the unsteady energy transport in saturated and unsaturated porous medium with a focus on energy storage aspects. An experimental and numerical study of transport in porous media with reference to energy storage system is carried out. A mathematical model based on local volume averaging is developed to simulate the effects related to energy storage in the porous medium. The equations are solved by finite differences discretization. A laboratory scale experimental set up is developed for validating the results obtained from numerical simulation. Experiments are performed for step and frequency response of the bed. The two distinct beds comprising solid phases of glass and steel are used for validation. The energy storage in porous medium takes place in its solid phase and energy exchange processes are similar to step and frequency responses of the bed. The numerical simulation for flow and heat transfer in unsaturated porous medium is also performed.

12.2 SUMMARY

The main features of the present work are as following

- The mathematical modeling of convective heat transfer in a porous medium is performed by volume averaging of governing equations for the fluid and the solid phases. These equations are based on either thermal equilibrium or thermal non-equilibrium between the two phases.
- The finite difference discretization of these models is carried out by using an implicit approach for the time derivatives and central difference scheme for second order partial-spatial derivatives. The first order upwind method and QUICK scheme have been used for the modeling of convective terms. The resulting algebraic equations are solved by Gauss-Seidel iterations using sufficiently fine grid in space and a large number of time-steps. The numerical simulation is first compared with analytical results obtained by

neglecting various terms of the mathematical model. The numerical simulation is consequently converted to non-dimensional form for wider applications.

- A laboratory scale experimental set up is fabricated to validate the results of numerical simulation and provide vital information about the transport phenomenon in porous medium. The validation is performed for two distinct boundary conditions related to step and frequency response of the porous bed.
- The step response refers to the thermal response of an initially cold domain to hot fluid, which flows through one of its ends. For an energy storage system, it relates to charging of the bed. The results of experiments are compared with numerical simulation using the 1 and 2-equation models of heat transfer. The comparison is obtained qualitatively by examining the unsteady temperature profiles at various locations and quantitatively by comparing the front speed and the spread of the thermal front traveling through the bed.
- The response of the bed subjected to a time varying inlet temperature is one of waveforms that have peaks and valleys. During the hot phase, the temperature level of porous medium rises and reaches a maximum value at the end of the phase. During the cold phase; the level falls and reaches a minimum value at the end of the phase. Hence, the frequency response signifies the unsteady behavior of the porous medium subjected to pulsating boundary conditions. The experimental results of frequency response are compared with numerical simulation using the 1 and 2-equation models of heat transfer. In addition, the global properties such as attenuation of temperature, phase lag, pulse speed and spread are discussed.
- Energy storage using a porous medium is an attractive method of storing momentarily available excess energy and reusing it at a later point of time. It is obtained by using fixed porous solid mass such as closely packed mesh screens or spherical beads through which hot and cold fluid alternately flow. The thermal performance of a porous medium for energy storage is discussed. It depends on the thermal properties of the solid and the fluid phases. The other parameters of interest are the frequency of oscillation, storage space, Reynolds number, particle size, porosity, number of cycles elapsed, thermal non-equilibrium and the effect of heat loss from the bed.
- When the pore space is not fully filled with water and air is present in the pores, the medium is called unsaturated. The flow channels in the unsaturated medium become

narrower, the flow path becomes more tortuous as compared to that in the saturated medium, surface tension adds resistance to flow, and the overall flow rate reduces. The main property of the unsaturated medium is the water content present in the pores. The velocity profiles in the medium are obtained using the continuity equation and modified Darcy's law. The temperature profiles are subsequently obtained using the 2-equation model.

12.3 CONCLUSIONS

Following conclusions are drawn from the study.

1. The 2-equation model is an accurate method of simulating heat transfer in porous medium. The 1-equation model is qualitatively similar to 2-equation model for beds having a fluid-to-solid thermal conductivity ratio λ closer to unity such as glass-water bed. For values of λ different from unity, the thermal equilibrium model fails to simulate the convective heat transfer. It also fails when sudden temperature changes are taking place in the bed.
2. The step response in glass-water bed is faster than that in a steel-water bed. The speed of the front is higher and the corresponding spread is small.
3. A wave of temperature difference travels through the bed whose amplitude falls as it propagates downstream. Its amplitude increases with an increase in Peclet number. The amplitude in steel-water bed is higher than that in glass-water bed.
4. The front speed and spread of the thermal front traveling through a porous medium are dependent on the thermal properties of the medium. The front speed depends on factors β (the fluid-to-solid heat capacity ratio) and λ. It falls with a reduction in theses values but the front spread increases. As the thermal dispersion in transverse direction increases, the front speed falls and the spread increases. The dispersion in longitudinal direction affects only spread but the speed remains unaffected.
5. In frequency response, the amplitude as obtained from the experiments is higher than that from the simulation, when frequency is close to the reference value. It becomes lower as the frequency increases. The phase lag is higher in experiments than that in simulation and increases with an increase in frequency. The temperature amplitude in glass-water bed is higher than that in steel-water bed. However, the corresponding phase lag is lower.

6. During frequency response, cold pulse in a glass-water bed travels faster than the hot pulse but has a lower spread. Hence, the glass responds to the hot and cold pulses in a distinct manner. The steel-water bed, on the other hand, no significant difference is observed between the hot and the cold pulse speeds.
7. The degree of thermal non-equilibrium fluctuates between positive and negative values during the frequency response. Its amplitude falls with distance but the phase lag increases with distance. It is higher in steel-water bed as compared to that in glass-water bed.
8. The amplitude of temperature fluctuations and thermal non-equilibrium in the bed is important for energy storage. During oscillatory flow, it varies significantly with distance from the hot end. Its variation from transient to steady state is also quite large.
9. The energy storage in the solid phase becomes high as factor β decreases but the amplitude of temperature fluctuations is lower. The property λ is less important in thermal storage and only accounts for heat loss through the bed walls.
10. Energy transport in the unsaturated porous medium is slow and pressure dependent. As the medium becomes saturated, the peak fluid speed and hence the transport becomes slow. Overall, the 2-equation model continues to predict the storage properties of the porous bed under unsaturated flow conditions.

12.4 SCOPE OF FUTURE WORK

The present work addressed some of the unresolved issues for convective heat transfer in a porous medium. However, many issues are still left out while newer questions have arisen. The following questions will be important and have to be considered in the future.

1. Since the temperatures recorded with a thermocouple or a data acquisition system may be noisy and scattered, a validation based on sensitivity coefficient approach can be conducted which will be free from noise and disturbances in the measurement of temperature. The sensitivity coefficient does not rely on individual temperature values. It depends upon the overall trends, such as the front movement and the spread of the recorded data.
2. The experimental program based on oscillatory flow where the hot and the cold fluids enters through the opposite ends need to be performed.

3. The experimental set up developed can be used to undertake inverse calculations such as the coefficients of longitudinal and transverse dispersion, channeling, presence of wall, flow development and entrance effects on energy storage in porous medium.
4. The analysis for unsaturated flow and heat transfer can be extended in 2-D form for wider applications. The field scale test for energy storage in underground reservoirs needs to be conducted.
5. The study for saturate and unsaturated porous medium can be extended to a bed of vertical extent.

REFERENCES

1. **Alazmi B. and Vafai K.** [2000], "Analysis of variants within the porous media transport models." *ASME J. Heat Transfer*, vol. **122**, pp. 303-326.
2. **Alazmi B. and Vafai K.** [2004], "Analysis of variable porosity, thermal dispersion, and local thermal non equilibrium on free surface flows through porous media." *ASME J. Heat Transfer*, vol. **126**, pp. 389-399.
3. **Al-Juwayhel F. and El-Refaee M.M. [**1998], "Thermal performance of a combined packed bed-solar pond system- a numerical study." *App. Thermal Engg.*, vol. **18,** pp.1207-1223.
4. **Amiri A. and Vafai K.** [1994], "Analysis of dispersion effects and non-thermal equilibrium, non-Darcian, variable porosity, incompressible flow through porous media", *Int. J. Heat Mass Transfer*, vol. **37**, pp. 939-954.
5. **Amiri A. and Vafai K.** [1998], "Transient analysis of incompressible flow through a packed bed." *Int. J. Heat Mass Transfer*, vol. **41,** pp. 4259-4279.
6. **Bradean R.**, **Ingham D.B., Heggs P.J., and Pop I.** [1996], "Free convection fluid flow due to a periodically heated and cooled vertical flat plate embedded in a porous media." *Int. J. Heat Mass Transfer*, vol. **39**, pp. 2545-2557.
7. **Bear J.** [1988], Dynamics of Fluids in Porous Media, Dover.
8. **Bear J. and Bachmat Y.** [1990], Introduction to Modeling of Transport Phenomena in Porous Media, Kluwer Academic Publishers, London.
9. **Beasley D. E. and Clark J. A**. [1984]. "Transient response of a packed bed for thermal energy storage." *Int. J. Heat Mass Transfer*, vol. **27,** pp. 1659-1669**.**
10. **Bejan A.** [1978], "Two thermodynamic optima in the design of sensible heat units for energy storage." *ASME J. Heat Transfer*, vol. **100**, pp. 708-712.
11. **Bouvier P., Stouffs P. and Bardon J-P** [2005], "Experimental study of heat transfer in oscillating flow." *Int. J. Heat Mass Transfer*, vol. ***48***, pp. 2473-2482.
12. **Brisson J.G. and Swift G.W.** [1994], "Measurements and modeling of recuperator for superfluid Stirling refrigerator", *Cryogenics* vol. **34**, pp. 971-982.
13. **Byun S.Y, Ro T. S., Shin J. Y., Son Y. S. and Lee D. Y.** [2006], "Transient thermal behavior of porous media under oscillating flow condition." *Int. J. Heat Mass Transfer*, vol. **27,** pp. 1659-1669**.**

14. **Carbonell R.G. and Whitaker S.** [1984], "Heat and mass transfer in porous media." *Fundamentals of Transport Phenomena in Porous Media*, Bear and Corapcioglu, Martinus Nijhoff, eds., pp. 121-198.
15. **Cheng P. and Zhu H**. [1987], "Effects of radial thermal dispersion on fully-developed forced convection in cylindrical packed beds." *Int. J. Heat Mass Transfer*, vol. **30,** pp. 2373-2323.
16. **Dincer and Rosen M.A**. [2001], "Energetic, environmental and economic aspects of thermal energy storage systems for cooling capacity." *App. Thermal Engg*, vol. **21**, pp. 1105-1117.
17. **Dullien F. A. L.** [1979], Porous media fluid transport and pore structure, Academic Press, New York.
18. **Duval F., Fichot F. and Quintard M.** [2004], "A local thermal non-equilibrium model for two-phase flows with phase-change in porous media." *Int. J. Heat Mass Transfer*, vol. **47**, pp. 613-639.
19. **Fu W.-S., Huang H.-C. and Liou W.-Y.** [1996], "Thermal enhancement in laminar channel flow with a porous block." *Int. J. Heat Mass Transfer*, vol. **39**, pp. 2165-2175.
20. **Fu H.L., Leong K.C., Huang X.Y. and Liu C.Y.** [2001], "An experimental study of heat transfer of a porous channel subjected to oscillating flow." *ASME J. Heat Transfer,* vol. **123**, pp.162-170.
21. **Genuchten M Th.Van.** [1980] "A closed form equation for predicting the hydraulic conductivity of unsaturated soils." *Soil Sci. AM .J*, vol. **44,** pp. 892-898.
22. **Gong Z. X. and Mujumdar A. S.** [1997], "Finite element analysis of cyclic heat transfer in a shell-and–tube latent heat energy storage exchanger." *Applied Thermal Engineering* vol. **17,** pp.583-591.
23. **Hsu C.T. and Cheng P.** [1990], "Thermal dispersion in a porous medium." *Int. J. of Heat and Mass Transfer*, vol. **33**, pp. 1587-1597.
24. **Hsu C.T.** [1999], "A closure model for transient heat conduction in porous media." *ASME J. Heat Transfer*, vol. **121**, pp. 733-739.

25. **Huang P. C. and Vafai K.** [1993], "Flow and heat transfer control over an external surface using a porous block array arrangement." *Int. J. Heat Mass Transfer*, vol. **36**, pp. 4019-4032. .
26. **Hunt M. L. and Tien C.L**. [1988], "Effects of thermal dispersion on forced convection in fibrous media." *Int. J. Heat Mass Transfer*, vol. **31**, pp. 301-309.
27. **Hus C.T. and Cheng P.** [1990], "Thermal dispersion in porous medium." *Int. J. Heat Mass Transfer*, vol. **33**, pp. 1587-1597.
28. **Ismail K.A.R. and. Stuginsky Jr R.** [1999], "A parametric study on possible fixed bed models for pcm and sensible heat storage." *App. Thermal Engg*, vol. **19**, pp. 757-788.
29. **Kaviany M.** [1995], Principles of Heat Transfer in Porous Media, Springer-Verlag.
30. **Kim S. Y., Kang B. H. and Hyun J.M.** [1994], "Heat transfer from pulsating flow in a channel filled with porous media." *Int. J. Heat Mass Transfer*, vol. **37**, pp. 2025-2033.
31. **Kim S. Y., Kang B. H. and Hyun J.M.** [1993], "Heat transfer in the thermally developing region of a pulsating channel flow." *Int. J. Heat Mass Transfer*, vol. **36**, pp. 4257-4266.
32. **Kim S. J. and Kim D.** [1999], "Forced convection in microstructures for electronic equipment cooling." *ASME J. Heat Transfer*, vol. **121**, pp. 639-645.
33. **Kim S. J., Kim D. and Lee D.Y.** [2000], "On the local thermal equilibrium in microchannel heat sinks." *Int. J. Heat Mass Transfer*, vol. **43**, pp. 1735-1748.
34. **Koh J. C. Y. and Colony R**. [1974], "Analysis of cooling effectiveness for porous material in a coolant passage." *ASME J. Heat Transfer*, vol. **96**, pp. 324-330.
35. **Koh J. C. Y. and Stevens R. L**. [1975], "Enhancement of cooling effectiveness by porous materials in coolant passage." *ASME J. Heat Transfer*, vol. **97**, pp. 309-311.
36. **Krishnan S., Murthy J. Y. and Garimella S. V.** [2004], "A two temperature model for control of passive thermal control systems." *ASME J. Heat Transfer*, vol. **126**, pp. 628-637.

37. **Kuwahara F., Nakayama A. and Koyama H.** [1996], "A numerical study of thermal dispersion in porous media." *ASME J. Heat Transfer*, vol. **118**, pp. 756-761.
38. **Kuwahara F. and Nakayama A.** [1999], "Numerical determination of thermal dispersion coefficient using a periodic porous structure." *ASME J. Heat Transfer*, vol. **121,** pp. 160-163.
39. **Kuwahara F. and Nakayama A.** [1999], "Numerical determination of thermal dispersion coefficient using a periodic porous structure." *ASME J. Heat Transfer*, vol. **121**, pp. 160-163.
40. **Kuwahara F., Shirota M. and Nakayama A.** [2001], "A numerical study of interfacial convective heat transfer coefficient in two-energy equation model for convection in porous media." *Int. J. of Heat and Mass Transfer*, vol. **44**, pp. 1153-1159.
41. **Kuwahara F., Shirota M. and Nakayama A.** [2001], "A numerical study of interfacial convective heat transfer coefficient in two-energy equation model for convection in porous media." *Int. J. Heat Mass Transfer*, vol. **44**, pp. 1153-1159.
42. **Kuzay T.M., Collins J.T., Khounsary A.M. and G. Morales** [1991], "Enchanced heat transfer with metal wool filled tubes." *Proceedings of the ASME/JSME Thermal Engineering Conference*, pp. 145-151
43. **Kuznetsov A.V.** [1994], "An investigation of a wave of temperature difference between solid and fluid phases in a porous packed bed." *Int. J. Heat Mass Transfer*, vol. **37**, pp. 3030-3033.
44. **Kuznetsov A.V.** [1996], "A perturbation solution for a nonthermal equilibrium fluid flow through three-dimensional heat storage packed bed." *ASME J. Heat Transfer*, vol. **118**, pp. 508-510.
45. **Kuznetsov A.V. and Vafai K.** [1995], "Analytical comparison and criteria for heat and mass transfer models in metal hydride packed beds." *Int. J. Heat Mass Transfer*, vol. **38,** pp. 2873-2884.
46. **Lage J.L**. [1993], "On the theoretical prediction of transient heat transfer within a rectangular fluid-saturated porous medium enclosure." *ASME J. Heat Transfer*, vol. **115,** pp. 1069-1071.

47. **Lake L.W.** [1989], Enhanced Oil Recovery, Prentice Hall.
48. **Lee D.-Y. and Vafai K.** [1999], "Analytical characterization and conceptual assessment of solid and fluid temperature differentials in porous media." *Int. J. Heat Mass Transfer*, vol. **42**, pp. 423-435.
49. **Leonard B.P**. [1979], "A stable and accurate convective modeling procedure based on quadratic upstream interpolation." *Computer Methods in Applied Mechanics and Engineering*, vol. **19,** pp**.** 59-98.
50. **Leong K.C. and Jin L.W.** [2005], "An experimental study of heat transfer in oscillating flow through a channel filled with an aluminum foam." *Int. J. Heat and Mass Transfer*, Vol. **48**, pp. 243-253.
51. **Levec J. and Carbonell R.G.** [1985], "Longitudinal and lateral dispersion in packed beds." *AIChE*, vol. 31, pp. 581-602.
52. **Metzger T., Didierjean S. and Maillet D.** [2004], "Optimal experimental estimation of thermal dispersion coefficients in porous media." *Int. J. Heat Mass Transfer*, vol. **47**, pp. 3341-3353.
53. **Mualem Y**. [1976], "A new model for predicting the hydraulic conductivity of unsaturated porous media." *Water Resour. Res.*, vol.**12**, pp. 513-522.
54. **Muralidhar K. [1988], "**Flow into a fault bounded by an unsaturated porous medium**."** *Proc. 16th Nat. Conf. Fluid Mechanics and Fluid Power*, pp**.** 533-538.
55. **Muralidhar K., Verghese M. and Pillai K.M.** [1993], "Application of an operator-splitting algorithm for advection-diffusion problems." *Numerical Heat Transfer*, Part A, vol **23**, pp. 99-113.
56. **Muralidhar K. and Suzuki K.** [1997], "Regenerator models for Stirling cycles." *Thermal Science & Engg.* , vol **5**, pp. 31-40.
57. **Muralidhar K. and Suzuki K.** [2001], "Analysis of flow and heat transfer in a regenerator mesh using a non-Darcy thermally non-equilibrium model" *Int. J. Heat Mass Transfer*, vol. **44**, pp. 2493-2504.
58. **Muralidhar K. and Sundararajan T. [1995],** Computational fluid flow and heat transfer, Narosa Publisher.

59. **Nakayama A., Kuwahara F. and Sugiyama M.** [2001], "A two energy equation model for conduction and convection in porous media." *Int. J. Heat Mass Transfer*, vol. **44,** pp. 4375-4379.
60. **Nield D. A., Kuznetsov A.V. and Xiong M.** [2002], "Effect of local thermal non-equilibrium on thermally developing forced convection in a porous medium." *Int. J. Heat Mass Transfer*, vol. **45**, pp. 4949-4955.
61. **Ozisik M**. N. [1980], Heat Conduction, Wiley- Interscience.
62. **Peak J. W., Kang B.H. and Hyun J.M**. [1999], "Transient cool-down of a porous medium in pulsating flow." *Int. J. Heat Mass Transfer*, vol. *42*, pp. 3523-3527.
63. **Poulikakos D. and Renken K**. **J.** [1987], "Forced convection in a channel filled with porous medium, including the effects of flow inertia, variable porosity, and brinkman friction." *ASME J. Heat Transfer*, vol. **109**, pp. 880-888.
64. **Quintard M. and Whitaker S.** [1993], "One- and two-equation models for transient diffusion processes in two-phase systems." *Advances in Heat Transfer*, vol. **23,** pp. 369-464.
65. **Renken K. J. and Poulikakos D.** [1988], "Experiment and analysis of forced convective heat transport in a packed bed of spheres. *Int. J. Heat Mass Transfer*, vol. **31,** pp. 1399-1408.
66. **Riaz M.** [1977], "Analytical solutions for single- and two-phase models of packed-bed thermal storage systems." *ASME J. Heat Transfer*, vol. **99,** pp**.** 489-492.
67. **Schumann T.E.W**. [1929], "Heat transfer: a liquid flowing through a porous prism, *J. Franklin Inst*. Vol. **208**, pp. 405-416.
68. **Slattery, J.C.** [1981], Momentum, energy and mass transfer in continua, second edition, R.F. Krieger.
69. **Sozen M. and Vafai K.** [1990], "Analysis of the non-thermal equilibrium condensing flow of a gas through a packed bed." *Int. J. Heat Mass Transfer*, vol. **33**, pp. 1247-1261.
70. **M. Sozen M. and Vafai K.** [1991], "Analysis of oscillating compressible flow through a packed bed." *Int. J. Heat and Fluid Flow* vol. **12,** pp. 130-136.

71. **Spiga G. and Spiga M.** [1981], "A rigorous solution to a heat transfer two phase model in porous media and packed beds." *Int. J. Heat Mass Transfer*, vol. **24**, pp. 355-364.
72. **Tannehill J.C., Anderson D.A. and Pletcher R.H.** [1997], Computational Fluid Mechanics and Heat Transfer, Taylor and Francis.
73. **Tindall J.A., Kunkel J.R.** [1999], Unsaturated Zone Hydrology, Prentice Hall.
74. **Vafai K., Alkire R.L. and Tien C.L**. [1985], "An experimental investigation of heat transfer in variable porosity media." *ASME J. Heat Transfer*, vol. **107,** pp**.** 642-647.
75. **Vafai K. and Sozen M.** [1990], "An investigation of a latent heat storage porous bed and condensing flow through it," *ASME J. of Heat Transfer*, vol. **112,** pp. 1014-1022.
76. **Vafai K. and Sozen M.** [1990], "Analysis of energy and momentum transport for fluid flow through porous media." *ASME J. of Heat Transfer*, vol. **112**, pp. 690-699.
77. **Vafai K. and Kim Sung-J.** [1990], "Analysis of surface enhancement by a porous substrate." *ASME J. Heat Transfer*, vol. **112,** pp**.** 700-706**.**
78. **Wakao N., Kaguei S. and Funazkri T.** [1979], "Effect of fluid dispersion coefficient on particle-to-fluid heat transfer coefficients in packed beds." *Chem.Engng. Sci*. vol. **34**, pp. 325-336.
79. **Wakao N. and Kaguei S.** [1982], Heat and Mass Transfer in Packed Beds, Gorden and Breach, New York, pp. 243-295.
80. **Walker G**. [1983], Cryocoolers, Part 1 and 2, International Cryogenics Monographs Series, Plenum Press, New York.
81. **Welty J. R., Wicks C. E. and Wilson R.E.** [1976], Fundamentals of Momentum, Heat and Mass Transfer, John Wiley & sons.
82. **Yano Y., Ochi M. and Enya S.** {1991], "Protection against fire and high temperature by using porous media and water." *Pro. ASME/JSME Th. Engng.*, pp. 213-218.
83. **Yumrutas R. and Unsal M**. [2005], "Modeling of a space cooling system with underground storage." *App. Thermal Engg.*, vol. **25**, pp. 227-239.

84. **Young D.-L. and Vafai K.** [1999], "Analytical characterization and conceptual assessment of solid and fluid temperature differentials in porous media." *Int. J. Heat Mass Transfer* vol. **42**, pp. 423-435.

85. **Zhao T. S. and Cheng P.** [1996], "Oscillatory heat transfer in a pipe subjected to a laminar reciprocating flow." *ASME J. Heat Transfer*, vol.**118**, pp. 592-597.

LIST OF PUBLICATION FROM THE PRESENT WORK

JOURNALS

1. **Chanpreet Singh, R. G. Tathgir, K. Muralidhar**, "Experimental Validation of Heat Transfer Models for Flow through a Porous Medium." Journal of Heat and Mass Transfer, Springer Berlin / Heidelberg. Volume 43, 2006, pp 55-72.

2. **Chanpreet Singh, R. G. Tathgir, K. Muralidhar**, "Energy Storage in Fluid Saturated Porous Media Subjected to Oscillatory Flow." Communicated to Journal of Heat and Mass Transfer, Springer Berlin / Heidelberg.

3. **Chanpreet Singh, R. G. Tathgir, K. Muralidhar**, "Assessing Experimental and Numerical Data using Sensitivity Functions." Journal of the Institution of Engineers India, Mechanical Engineering Division. Volume 87, July 2006, pp 54-62.

4. **Chanpreet Singh, R. G. Tathgir, K. Muralidhar**, "Comparison of 1-equation & 2-equation Models for Convective Heat Transfer in Saturated Porous Media." Journal of the Institution of Engineers (India), Mechanical Engineering Division. Volume 84, October 2003, pp 104-113.

NATIONAL CONFERENCE

1. **Chanpreet Singh, R.G. Tathgir, K. Muralidhar**, "Heat Transfer Analysis of Oscillatory Flow In Saturated Porous Media." Proceedings of National Conference on the Recent Developments in Mechanical Engineering. TU, Pataila. October 31 and November 1, 2003.

2. **Chanpreet Singh, T. K. Jindal, R.G. Tathgir**, "Thermal analysis of Regenerator Mesh using Thermally Non-Equilibrium Model" Proceedings of 28th National Conference on Fluid Mechanics and Fluid Power. PEC Chandigarh. December 13-December 15, 2001

3. **Chanpreet Singh, R. G. Tathgir, K. Muralidhar**, "An Accurate Discretization of the Convective Diffusion Equation and its Application to Transport in Porous media" Abstract Proceedings of National Conference on Mathematical and Statistical Techniques, TU, Patiala. December 6- December 8, 2001

4. **Chanpreet Singh, R.G. Tathgir, K. Muralidhar**, "Energy Storage in Natural Reservoirs: A Porous Medium Model." 5th Punjab Science Congress.TU, Patiala Feb 7-9 2002